Investigation and Validation of a Cubic Turbulence Model in Isothermal and Combusting Flows

by

Richard Carroni

A Doctoral Thesis

Submitted in partial fulfillment of the requirements for the award of
Doctor of Philosophy at Loughborough Univeristy

October 1999

ABSTRACT

Computational Fluid Dynamics relies upon turbulence models for predicting most engineering flows. Relatively accurate models exist but are computationally intensive; simpler, more practical models, however, often return poor predictions. The new cubic, eddy-viscosity turbulence model is a compromise of these extremes, employing a nonlinear (cubic) stress-strain relationship. The primary objective of the current research is to compare the cubic model against a range of other two-equation turbulence models, for a variety of isothermal and combusting flows.

The TEACH research code is the main platform for the investigations of the new turbulence model. Other, industry-standard models (standard k-ε, ReNormalisation Group k-ε and Launder & Sharma low Reynolds-number models) are also implemented for comparative purposes. The nonlinear model is found to be numerically unstable and several remedies are required before any converged solutions can be obtained for the complex flows investigated. The turbulent, isothermal test cases are: fully-developed pipe flow, axisymmetric pipe expansion (three different flows) and strongly-swirling pipe flow (for which a Reynolds Stress Model, available in a commercial CFD code, is also utilised). In most cases, the nonlinear model provides the best results relative to the other two-equation models. A detailed analysis is carried out to account for the different ways in which the physics of the flows are represented by the various turbulence models.

A challenging, reacting flow is the bluff-body stabilised, nonpremixed flame. Initial simulations, utilising the flame sheet combustion model, reveal that the accuracy of

the computed temperature and mixture fraction distributions depends largely upon the predictions of the flow field. The nonlinear turbulence model gives slightly improved results relative to the other, standard models. However, detailed velocity distributions are required for further analysis of the cubic model. Since no flow-field data for confined, bluff-body burners exists in the public domain, an experimental combustor is designed and built on-site. An optical technique, Particle Image Velocimetry (PIV), is utilised to obtain detailed profiles of the flow; temperatures are measured using a standard thermcouple probe. After extensive processing, the experimental results are compared with the simulation predictions. The nonlinear turbulence model captures all the flow features and is seen to significantly improve results compared to the other models. Reasons for its relative success are presented.

ACKNOWLEDGEMENTS

I wish to express my gratitude and indebtedness to my supervisor Mr. Henk Versteeg for the guidance, support and constructive criticism he has provided throughout the investigation. I would like to acknowledge the invaluable assistance that Dr. G. Hargrave provided with the experimental work, and Dr. W. Malalasekera for his interest in and support of the project as director of research.

I would also like to thank all my colleagues within the Thermofluids Research Group who have been very supportive and helpful, and with whom I had many useful discussions.

Finally, I wish to thank my family for all the encouragement and support they have provided.

NOMENCLATURE

Roman Letters

A_2, A_3	Anisotropic stress invariants.
c_1 to c_7	Constants in the nonlinear stress/strain relationship.
$C_{\varepsilon 1}, C_{\varepsilon 2}$	Constants in dissipation rate transport equation.
C_f	Skin friction factor.
C_{g1}, C_{g2}	Constants in the transport equation for mixture fraction variance.
C_p	Specific heat capacity.
C_μ	Constant in the eddy-viscosity formula.
$d, d_1, d_2, d_3,$ d_4, D, D_1, D_2	Diameters in the various test cases.
E	Gradient production.
E_r	Roughness constant.
$e_\phi(X)$	Radially-averaged relative error for ϕ at location X
f_μ, f_1, f_2	Damping functions.
f	Mean mixture fraction.
H	Step height (in pipe expansions).
k	Turbulence energy.
l	Turbulence length scale.
l_{bl}	Length scale in the inertial boundary layer, defined by Equation 2.44.
m	Mass fraction.
m, n	Exponents in definition of β-pdf.
P, p	Pressure.
P_k	Turbulence energy production.
Pe	Peclet number.
r	Radial coordinate.
R, r	Radius.
R	Parameter defined in Equation 2.18.
R_t	Turbulent Reynolds number.
Re	Reynolds number
S_{ij}	Mean strain-rate tensor.
T	Temperature.
u', v', w'	Fluctuating components of instantaneous velocities.
u_τ	Wall friction velocity
$\overline{u_i' u_j'}$	Reynolds stress tensor.
U, V, W	Mean velocities.
X	Axial coordinate.
X_r	Reattachment length.
y	Perpendicular wall distance.
y^+	Dimensionless perpendicular wall distance, defined in section 2.1.3.1.
Y_c	Yap correction factor.

Greek Symbols:

δ_{ij}	Kronecker delta.
ε	Dissipation rate of k.
$\tilde{\varepsilon}$	Isotropic dissipation rate.
η	Strain-rate dependent parameter defined in Equation 2.19.
Γ	Diffusive transport coefficient.
Γ_f	False diffusion coefficient.
κ	Von-Karman constant.
μ_t	Turbulent dynamic viscosity.
ν	Kinematic viscosity.
ν_t	Turbulent kinematic viscosity.
ρ	Density.
σ_k	Turbulent Prandtl number in the k equation.
σ_ε	Turbulent Prandtl number in the ε equation.
σ_t	Turbulent Prandtl number.
τ_{ij}	Reynolds stress tensor.
τ_w	Wall shear stress.
$\overline{\omega}$	Net rate of species formation.
Ω_{ij}	Mean vorticity tensor.

Abbreviations

ASM	Algebraic Stress Model
BR	Blockage Ratio.
CARS -	Coherent Anti-Raman Spectroscopy.
CDR	Confinement Diameter Ratio (defined in Chapter 6).
CDS	Central Differencing Scheme.
CFD	Computational Fluid Dynamics.
CR	CRY turbulence model without the Yap correction term (defined by Equation 2.42).
CRY	Cubic, nonlinear turbulence model proposed by Craft et al (1996). Also referred to as the cubic NLEVM or nonlinear LRN.
CR93	Precursor to the CRY model, developed by Craft et al (1993).
CR97	Subsequent development of the CRY model.
DNS	Direct Numerical Simulation.
EBU	Eddy Break-Up.
EDC	Eddy Dissipation Concept.
EVM	Eddy-Viscosity Model.
LDV	Laser Doppler Velocimetry.
LES	Large Eddy Simulation.
LIF	Laser Induced Fluorescence.

LRN	Low Reynolds Number.
LS	Turbulence model proposed by Launder & Sharma (1974).
LSY	LS model with the addition of the Yap term (defined in Equation 2.42).
NLEVM	NonLinear Eddy-Viscosity Model.
PDF	Probability Density Function.
PIV	Particle Image Velocimetry.
RANS	Reynolds Averaged Navier Stokes.
RNG	ReNormalisation Group.
RSM	Reynolds Stress Model.
SIMPLE	Semi Implicit Method for Pressure Linked Equations.
SMC	Second-Moment Closure.
TEACH	Teaching Elliptic Axisymmetric Characteristics Heuristically.
TSL	Thin Shear Layer.
UPS	Upwind Scheme.

TABLE OF CONTENTS

CHAPTER 1: INTRODUCTION

1.1 BACKGROUND

Complex fluid motion within combustors and furnaces is known to profoundly affect the burner performance and emissions levels. Modern burners seek to enhance the combustion process by introducing swirl or by promoting highly turbulent recirculation regions in bluff-body type geometries. Accurate predictive tools for turbulent, non-premixed flames are essential from the design point of view. Computational Fluid Dynamics (CFD) is acquiring a leading role in the design of burners; it is used to gain a better understanding of the fundamental interactions between turbulent flow fields and chemical reactions, and to quantify the effects and influences of various parameters. The main limitation of CFD is turbulence closure, an issue which is of vital importance.

There are currently four main methods of treating turbulence for incorporation in CFD: eddy-viscosity models (EVM), second-moment closures (SMC), large eddy simulations (LES) and direct numerical simulation (DNS). Although the last two approaches are the most accurate, they are extremely resource-intensive and thus have no immediate prospects in practical engineering environments. Both EVM's and SMC's, on the other hand, are more viable avenues as far as industry is concerned. These approaches embody a degree of commonality in that they are both treatments for the Reynolds stresses encountered in the Reynolds-averaged Navier-Stokes (RANS) equations. SMC's involve the additional solution of a transport equation for each

Reynolds stress (the reader is referred to Launder, 1989, for a review of this family of models), whilst EVM's approximate the Reynolds stresses using relatively simple relationships. Despite SMC's having a greater potential to successfully predict complex flows, they too often require excessive computational and temporal resources. This leaves EVM's as the most feasible method for treating practical turbulent flows. EVM's have developed considerably since their introduction in the form of zero-equation models. However, the current family of so-called linear, two-equation models is still not capable of accurately predicting many flow phenomena such as recirculation vortices and highly swirling flows.

A new model, the cubic nonlinear EVM (denoted as cubic NLEVM) was recently developed by Craft et al (1993, 1996) in order to address the shortcomings of the linear two-equation models. The proposed function of this model is to bridge the gap between linear EVM's and SMC's without incurring the computational burden associated with the latter.

This thesis reports on the application of the cubic NLEVM in various isothermal flows in order to assess the model's capability of predicting recirculation and swirl, both of which feature strong streamline curvature. It reports on the initial simulations of a bluff-body combustor, and then describes the experimental work involved in obtaining velocity measurements for such a burner. Finally, the cubic NLEVM is used to simulate combustion within the experimental combustor. In all cases, the performance of the nonlinear model is compared with that of 'industry-standard' linear EVM's.

The following literature survey briefly introduces the concept of eddy-viscosity turbulence models and describes the general development of two-equation EVM's. The latter part of the survey describes recent exploits in this field regarding nonlinear EVM's, and introduces the cubic model. The survey reports on existing applications of the cubic NLEVM to various flows and shows that axisymmetric pipe expansions, highly-swirling and combusting flows have not yet been investigated using this model. The chapter ends with an outline of the thesis in section 1.3.

1.2 LITERATURE SURVEY

Drawing upon Newton's law of viscosity, Boussinesq (1877) put forward an analogous proposition in which the Reynolds stresses are directly linked to the mean rates of fluid deformation via a scalar called the eddy viscosity, μ_t:

$$\tau_{ij} = -\rho\overline{u_i u_j} = \mu_t\left(\frac{\partial U_i}{\partial x_j} + \frac{\partial U_j}{\partial x_i}\right) \qquad (1.1)$$

The problem of calculating Reynolds stresses was thus reduced to one of reckoning the eddy, or turbulent, viscosity, which is proportional to a length scale and a turbulent velocity scale. Based on thin shear layer (TSL) assumptions, zero-equation models simply assumed that the turbulent velocity scale was a function of the length scale which could in turn be prescribed algebraically. However, complex flows are characterised by convection and diffusion, thereby challenging the TSL assumptions. One-equation models attempted to account for this by incorporating a transport equation for turbulence energy, which was suggested as a measure of the turbulent velocity scale. Improvements over the zero-equation models, however, were not significant.

In recognition of the fact that the length scale characterising the large, energy-containing eddies is subject to the same transport processes as the turbulence energy, researchers proposed that a transport equation also be solved for the length scale or a related quantity. This approach is known as two-equation modelling. Harlow & Nakayama (1967) and Jones & Launder (1972), amongst others, advanced an equation for the turbulence dissipation rate $\varepsilon \propto k^{3/2}/l$ (k-ε model); Spalding (1971) and Saffman (1970) suggested the turbulence vorticity k/l^2 (k-ω model); Rotta (1968) recommended an equation for kl (k-kl model) and Kolmogorov (1942) put forward the frequency of turbulent motion $k^{1/2}/l$. A detailed analysis (Launder & Spalding, 1974) of the k-kl, k-ω and k-ε models concluded that whilst these three models are essentially the same (the different length scale-related expressions can all be written in terms of each other), the k-ε model is the most plausible (from a physical perspective) and also the simplest to implement numerically. Physically correct transport equations can be derived for both

turbulence energy (k) and dissipation rate (ε); however, these contain unknown correlations which require further modelling. References for details of these assumptions and simplifications can be found in Rodi (1980).

Utilising a single set of empirically evaluated constants, the k-ε model has been applied with reasonable success to a large number of test cases, including recirculating and jet flows as well as TSL flows. However, in instances where mediocre predictions are obtained, different constants can be adopted to improve results. For example, Rodi (1972) replaced the constants with simple functions such that the spreading rate of axisymmetric jets in stagnant surroundings were no longer overpredicted. This emphasises the fact that the approximated ε equation is largely responsible for the k-ε model's lack of universality. A concise assessment of the performance of this model and its numerous variants is given in the review by Nallasamy (1987).

One of the limiting factors affecting one- and two-equation models is that they are derived with the aid of assumptions which are strictly applicable to regions of flow in which the Reynolds number is high. In wall-bounded flows, the standard k-ε model may not be integrated directly to the wall because it is unable to account for the low Reynolds number interactions between the turbulent flow field and the viscous sublayer. Instead, so-called wall functions are employed; these relate the mean-velocity at a point near the wall to the wall shear stress. Several different proposals for wall functions are reviewed by Launder (1981) and Nallasamy (1987). They are based on assumptions which are only valid for near-equilibrium conditions in the inertial sublayer (fully turbulent region of boundary layer) of fully-developed flow over larger surfaces (e.g. pipes, channels, plates). Further details are given in Chapter 2.

Wall functions do not perform correctly in flows where recirculation (or some other complex phenomenon) exists in the proximity of solid boundaries. In order to overcome this obstacle, Jones & Launder (1972,1973) developed a low Reynolds number (LRN) k-ε model which requires integration to the wall and application of the no-slip boundary condition. The steep gradients and viscous effects in the inertial sublayer were resolved by employing damping functions, f_μ and f_2, for the turbulent

viscosity and the dissipation rate destruction term, respectively. Application of this model to various flows led Jones & Launder (1972, 1973) to conclude that the simulated near-wall gradients were markedly improved compared with those calculated by the standard high Reynolds number k-ε model.

A number of LRN k-ε models were subsequently proposed by various researchers. The numerical study of several TSL's by Patel et al (1985) concluded that of the many LRN k-ε models reviewed, that of Launder & Sharma (1974) returned the best performance. This model shared the basic structure of the Jones & Launder model, but employed different damping functions. Subsequent studies, including DNS, quantified the near-wall, asymptotic behaviour of the turbulence quantities, which affected the limiting behaviour of the damping functions. Numerous LRN k-ε models were proposed, amongst them those suggested by Nagano & Hishida (1987), Myong & Kasagi (1990a), Nagano & Tagawa (1990), Abe et al (1994), Cho & Goldstein (1994) and Kobayashi & Tagashi (1996). Nagano & Shimada (1995) reviewed several different forms of the dissipation rate equation in LRN k-ε models and reported that some models were indeed able to correctly predict the near-wall trends for ε. However, the damping functions in all the above models depend on either the wall distance y or the friction velocity u_τ, or both. This causes difficulties to arise when the models are applied to complex geometries or when separation/reattachment is present.

Since LRN k-ε models are only applicable to wall-bounded flows, there exists a requirement for turbulence models to cater for both wall-bounded and free-stream low Reynolds number flows without the necessity of making case by case adjustments. One approach is to use a multiple time-scale (MTS) turbulence model (e.g. Duncan et al, 1993, Nagano et al, 1994a). The MTS model was designed to explicitly represent the energy cascade, thus enabling it to calculate wall and free flows. The review by Nagano & Shimada (1995) reported that excellent results were obtained for simple free and wall-bounded flows. Nallasamy (1987) reported that the MTS model of Hanjalic et al (1979) accurately predicted the spreading rates of both plane and axisymmetric free jets, but no further computations were performed.

A further limitation of two-equation eddy-viscosity models is the fact that the constant C_μ $(=0.09)$ was derived for flows close to local equilibrium, where the production (P_k) and dissipation (ε) rates of turbulence energy are approximately equal. This condition only applies to thin shear layers, but not in weak shear flows. Launder & Spalding (1972) therefore recommended that functional forms of C_μ be investigated. Rodi (1972) created an empirical formula for C_μ based on P_k and ε; this improved weak shear flow predictions but was only a case-specific procedure. A different avenue was afforded by the DNS work of Lee et al (1990). Their study revealed that there existed a dimensionless parameter (the strain invariant $\tilde{S}$) which had an element of universality embedded in it. This was concluded from their observation that, given comparable levels of $\tilde{S}$, a homogeneous shear flow and an inhomogeneous channel flow possessed very similar turbulence structures and statistical correlations. Based on this information, Cotton et al (1993) suggested that C_μ be a function of $\tilde{S}$. The strain invariant was also implemented to good effect by Yakhot et al (1992); however, rather than altering C_μ, it was used as a modification to the ε equation of the ReNormalisation Group Theory (RNG) model of Yakhot & Orszag (1986). As pointed out by Speziale & Thangam (1992), the original RNG k-ε model was no better than the standard k-ε model, but the improved version is capable of accurately predicting the reattachment length of flow over a backward facing step (Thangam & Speziale, 1992). However, Lien & Leschziner (1994) reported that the strain invariant parameter in the RNG k-ε model is actually detrimental in other turbulent flows, e.g. plane and round jet flows and flows across a staggered tube-bank assembly.

Unlike thin shear layers, practical engineering flows often exhibit complex mean strains associated with any of the following, amongst others, phenomena: streamline curvature, separation, swirl, strong streamwise pressure gradients and impingement. These features are susceptible to the nature of the turbulence structure, in particular anisotropy. A major shortcoming of the linear eddy viscosity model is the isotropic assumption, i.e. the turbulent viscosity is identical for all the Reynolds stresses. As discussed by Speziale (1987) and Thangam & Speziale (1992), this leads to the predictions $\tau_{xx} = \tau_{yy} = \tau_{zz} = \frac{2}{3}k$ in plane channel flow and $\tau_{xx} + \tau_{yy} = 2\tau_{zz}$ in flow over

backward facing steps, which contradicts experimental results. Furthermore, Thangam & Speziale (1992) demonstrated that the normal stress difference $\tau_{yy} - \tau_{zz}$ is non-zero and contributes directly to the prediction of the mean velocity field. Speziale (1987) proved that in order to reproduce secondary flows in square ducts, the streamwise mean velocity must cause a non-zero cross-stream normal stress difference; a forecast clearly unresolvable by linear EVM's. In order to overcome these limitations, nonlinear EVM's were introduced. In these models, the Boussinesq approximation is extended such that the Reynolds stress also becomes a function of higher-order terms involving mean-velocity gradients. The function of the nonlinear terms is to mimic the response of turbulence to complex strains. These models are also referred to as being anisotropic because their effect is to promote unequal normal Reynolds stresses.

According to the review of Speziale (1991), Lumley (1970) and Saffman (1977) appeared to be amongst the first to propose such a relationship. Yoshizawa (1984) derived a quadratic stress/strain relation using a Direct Interaction Approximation (DIA) method. The values of the additional constants were derived from purely theoretical considerations; Speziale (1991) reported that unfortunately these constants required empirical adjustments when applied to channel and Couette flows. Results for this model's performance in a backward facing step configuration are discussed by Kobayashi & Togashi (1996). Speziale (1987) created a quadratic model by assuming that the effect of turbulence on mean flow could be represented by a non-Newtonian stress/strain relationship. He applied this model to channel flow, square duct flow and back-facing step flows; significant improvements were achieved in all cases. Rubinstein & Barton (1990) derived a quadratic model using RNG theory. This method was selected because the RNG theory is valid for both high and low Reynolds number flows, and the anisotropy of certain flows (e.g. in noncircular ducts) arises in the low Reynolds number regime. A mathematical comparison with previous nonlinear models is made, but no numerical calculation is performed. Several other quadratic models were suggested, including those of Myong & Kasagi (1990b) and Shih et al (1993). A review by Lien & Leschziner (1994) concluded that many quadratic NLEVM's returned poor representations of anisotropy. It should also be noted that these models, with the exception of that of Rubinstein & Barton (1990), are high Reynolds number models and thus require the application of viscous damping in wall-bounded flows. Furthermore,

unlike most linear EVM's, many anisotropic models are not intrinsically realisable (i.e. the production of turbulence energy is not unconditionally positive). An oft-quoted observation in favour of nonlinear models is the fact that all the quadratic models discussed are of similar form, regardless of the method of derivation. However, the model constants vary considerably, reflecting the fact that they were obtained empirically from a variety of flows. Craft et al (1993) and Apsley & Leschziner (1998) stated that whilst quadratic expressions allow normal-stress anisotropy to be captured, third-order terms are required so as to sensitise the Reynolds stresses to streamline curvature and swirl effects. Sharif & Wong (1995) conducted simulations of rotating pipe flows utilising the quadratic model of Speziale (1987); their report that the quadratic model was not able to overcome the defects of the standard k-ε model supports the conclusion that cubic terms are necessary.

Craft et al (1993) proposed a third order nonlinear EVM (CR93) in which the turbulence production rate was a function of dimensionless strain and vorticity parameters ($\tilde{S}$ and $\tilde{\Omega}$); the model constants were calibrated over a wider range of flows (homogeneous shear flow, fully-developed swirling pipe flow and curved channel flow) which theoretically bestowed upon the model a greater element of universality. Slightly modified versions of the damping functions of Launder & Sharma (1974) were employed. In the flows studied, the nonlinear model returned better results than the LRN eddy-viscosity model of Launder & Sharma (1974); nevertheless, further modifications were recommended. Rabbitt (1997) utilised this model, in conjunction with wall functions, to simulate flow through pipe expansions and contractions. However, the predictions barely improved upon those of the standard k-ε model and the normal Reynolds stresses were found to be inaccurate. In Rabbitt's case, the unexceptional performance of the nonlinear model is at least partly due to the fact that complex strains often arise in the vicinity of walls (i.e. $\overline{v'^2} = 0$ but $\overline{u'^2}$ and $\overline{w'^2}$ are non-zero); Apsley & Leschziner (1998) stated that in this case wall functions are simply not adequate, and integration to the viscous sublayer is necessary. Chen & Leschziner (1999a) applied the LS and CR93 models to the unsteady flow through the inlet guide vanes and one rotor-stator stage of an axial compressor. Whilst the LS model failed to capture the vortex shedding and wake unsteadiness at the trailing edge of the blade, the

nonlinear model returned a significant (although not entirely accurate) shedding frequency. Magagnato (1999) reported similar behaviour for flow past a turbine blade. Chen & Leschziner (1999b) also compared the performance of the LS and CR93 models with that of an SMC model, for flow over various blade profiles (a turbine blade and two compressor vanes). Although the nonlinear model matched the RSM results for the turbine blade computations, it was unable to predict the suction-side separation occurring along on of the compressor profiles.

In a later version of the CR93 cubic NLEVM, Craft et al (1996) retuned the model coefficients (CR96). It was pointed out that, in common with the CR93 model, a damping term f_μ was still required for near-wall flows, but that its influence was significantly diminished compared to when used in linear EVM's. This was attributed to the functional form of C_μ (which depends on $\tilde{S}$ and $\tilde{\Omega}$) contributing considerably to near-wall strain-related damping. Relatively good results, especially for weakly-swirling flows, were obtained for a number of different cases (not including recirculation), at a computational cost only marginally greater than for linear EVM's. However, in a further application of CR96 to transitional pipe and channel flows, Craft et al (1997) found that the CR96 model predicted turbulence intensities which were too similar to each other. Specifically, the Reynolds stress normal to the wall ($\overline{v^2}$) was incorrectly predicted; it is upon this component that the accurate calculation of heat fluxes rests. In an effort to enable the model to simulate flows which were far from equilibrium (including transitional flows), Craft et al (1997) drew upon the work of Suga (1995) and sensitised the normal stresses to a term known as the stress anisotropy invariant (A_2), for which a complete transport equation is additionally solved. The new model (CR97) was able to improve the resolution of near-wall normal Reynolds stresses. A further improvement was incorporated in the cubic model of Apsley & Leschziner (1998) whereby the coefficients of the various nonlinear terms are modified by different low Reynolds number damping functions. This allows the different behaviour of the individual stresses to be captured and enhanced. In simulations of flow over airfoils and through diffusers, the Apsley & Leschziner (1998) model has been shown to out-perform the quadratic model of Speziale (1987) and the cubic model of Lien et al (1996) (the latter is a LRN cubic extension of the quadratic high Reynolds

number model of Shih et al, 1993). However, less satisfactory results were obtained in the case of strongly separated flow over a backward facing step.

This section has demonstrated that within the eddy-viscosity framework of turbulence closure, the cubic, nonlinear models are the most promising. The literature survey has also summarised the latest developments in nonlinear EVM's. Of the cubic models reviewed, the CR96 model apparently offers the best compromise between accuracy and complexity; despite this, the literature review reveals that the model has not been extensively validated, particularly for recirculating and strongly-swirling flows, nor has it been utilised in combusting cases. We are thus presented with the need for a more thorough validation of this auspicious turbulence model.

1.3 THESIS OUTLINE

Chapter 2 states the aim of turbulence and combustion modelling and presents the models employed. The issue of variable-density effects is discussed and it is shown that no modifications are required for bluff-body combustor simulations.

The third chapter is devoted to describing the CFD code, listing guidelines with which to obtain meaningful, converged solutions, and prescribing the various boundary conditions. The last part of Chapter 3 reports on special numerical considerations regarding the nonlinear turbulence model.

Chapter 4 is a comprehensive description of simulations of three different geometries: fully-developed pipe flow, axisymmetric pipe expansion flow (three different cases) and highly-swirling pipe flow. The performance of the nonlinear turbulence model is compared to the standard k-ε, RNG and LS models, and reasons for the relative success or failure of the various models are discussed.

Turbulent diffusion flames are introduced in Chapter 5, and further evidence of the suitability of the flame-sheet model is presented. The flow characteristics of bluff-

body combustors are summarised and the effects of confinement on such flows are discussed. Simulations of a bluff-body combustor are then performed. Two turbulence parameters affecting combustion predictions are examined, and the performance of the nonlinear turbulence model is reported on.

Chapter 6 defines the modelling requirements for an experimental confined, bluff-body combustor. The salient design features of the experimental combustor are highlighted. Application of the optical diagnostics technique, Particle Image Velocimetry (PIV), to the experimental rig is discussed, and the general procedure, including causes of error, is described. The experimental results are then compared with the CFD predictions for this geometry, and the performance of the turbulence models, particularly the cubic EVM, is discussed.

The final chapter begins with a closing discussion which summarises the performance of the various turbulence models in the flows investigated, and notes the numerical problems and remedies involving the nonlinear model. The conclusions are presented and the contributions of the thesis are listed. Finally, recommendations for further work are made.

CHAPTER 2: TURBULENCE AND COMBUSTION MODELS

Turbulent combustion is a complex phenomenon involving the interaction between flow and thermo-chemical fields. As such, accurate mathematical descriptions are only possible when using the transport equations in their original, complete form. The solution of these equations is known as a Direct Numerical Simulation (DNS). For DNS in non-reacting, turbulent flows, one needs to resolve the computational grid down to the Kolmogorov micro-scale, and the time steps must be correspondingly small. The necessary grid density is intensified by a factor of three as the Reynolds number increases. Combustion scales in chemical reactions are even smaller than the Kolmogorov scales, which signifies that the magnitude of DNS computations is further compounded. Hence a more feasible approach is to employ turbulence and combustion models.

The present chapter describes in some detail the various turbulence (EVM) and combustion (flame sheet) models utilised during the current research. Three of the four turbulence models are commonly used in commercial CFD codes, whilst the cubic nonlinear model is a recent development and is therefore the focus of the current investigation[1]. The combustion model is relatively unsophisticated but reasonably effective; more complex combustion models were avoided because they require more

[1] The latest releases of the commercial CFD codes STAR-CD and FIDAP make use of this cubic model. Commercial issues, however, precluded the publication of the relevant validation and performance studies.

resources and the incremental improvements are overshadowed by the effects of using different turbulence models. The final section assesses the effects of variable-density flows on turbulence modelling.

2.1 TURBULENCE MODELLING

To put turbulence modelling into context, it should be noted that all flows obey the general conservation laws for mass and momentum.

Continuity: $$\frac{\partial \rho}{\partial t} + \frac{\partial (\rho u_i)}{\partial x_i} = 0 \qquad (2.1)$$

Momentum: $$\rho \frac{Du_i}{Dt} = \frac{\partial (-p + \tau_{ij})}{\partial x_j} + \rho g_i \qquad (2.2)$$

where τ_{ij} are the stresses and g_i are external (body) forces. In laminar cases, Newton's law of viscosity is invoked and simply substituted into equation (2.2), resulting in the Navier-Stokes equation. However, the RANS approach in turbulent flows decomposes the instantaneous velocity u_i into mean (U_i) and fluctuating (u_i') components. Upon substitution into equation (2.2) and time averaging the various terms (and assuming constant dynamic viscosity μ), the following equations are obtained

Continuity: $$\frac{\partial \rho}{\partial t} + \frac{\partial (\rho U_i)}{\partial x_i} = 0 \qquad (2.3)$$

Momentum: $$\rho \frac{DU_i}{Dt} = -\frac{\partial p}{\partial x_i} + \frac{\partial}{\partial x_j}\left(\mu \frac{\partial U_i}{\partial x_j}\right) + \frac{\partial}{\partial x_j}\left(-\rho \overline{u_i' u_j'}\right) + \rho g_i \qquad (2.4)$$

All terms in these equations contain only mean quantities, with the exception of the so-called Reynolds stresses $-\rho \overline{u_i' u_j'}$ in the Reynolds Averaged Navier Stokes (RANS) equation. The aim of classical turbulence modelling is to close the set of transport equations by finding expressions for these Reynolds stresses.

The standard k-ε model is probably the most widely used turbulence model in engineering applications. Although it is thoroughly reviewed in the public literature, a brief outline of its derivation will currently be given in light of the fact that the various

other turbulence models under consideration possess similar fundamental structures. The ReNormalisation Group (RNG) theory and the popular Launder & Sharma low Reynolds number models are also depicted, and finally the cubic nonlinear model of Craft et al (1996), upon which rests the bulk of the research, is presented.

2.1.1 Standard *k*-ε, RNG and Launder & Sharma Models

As with all eddy-viscosity models (EVM's), Boussinesq's (1877) representation of the Reynolds stresses is drawn upon. Its applicability is extended to normal Reynolds stresses (i.e. when $i = j$) by the addition of a term involving the Kronecker delta (δ_{ij}):

$$-\rho\overline{u_i'u_j'} = \mu_t\left(\frac{\partial U_i}{\partial x_j}+\frac{\partial U_j}{\partial x_i}\right)-\frac{2}{3}k\delta_{ij} \tag{2.5}$$

As suggested by Jones & Launder (1972), the eddy viscosity is defined by

$$\mu_t = \rho C_\mu \frac{k^2}{\varepsilon} \tag{2.6}$$

where k is the turbulence (i.e. kinetic) energy and ε is the dissipation rate. Complete transport equations for k and ε are derived from the Navier Stokes equation.

k equation:

$$\rho\frac{Dk}{Dt} = d_k \underbrace{-\rho\overline{u_i'u_j'}\frac{\partial U_i}{\partial x_j}}_{P_k} \underbrace{-\mu\overline{\frac{\partial u_j'}{\partial x_i}\frac{\partial u_j'}{\partial x_i}}}_{\rho\varepsilon} \tag{2.7}$$

$$d_k = \underbrace{\frac{\partial}{\partial x_i}\left(\mu\frac{\partial k}{\partial x_i}\right)}_{d_k^\mu} \underbrace{-\frac{\partial}{\partial x_i}\left(\rho\overline{u_i'k}\right)}_{d_k^t} \underbrace{-\frac{\partial}{\partial x_i}\left(\rho\overline{u_i'\frac{p}{\rho}}\right)}_{d_k^p} \tag{2.8}$$

ε equation:

$$\rho\frac{D\varepsilon}{Dt} = d_\varepsilon + P_\varepsilon + \Phi_\varepsilon \tag{2.9}$$

$$d_\varepsilon = \underbrace{\frac{\partial}{\partial x_k}\left(\mu\frac{\partial \varepsilon}{\partial x_k}\right)}_{d_\varepsilon^\mu} \underbrace{-\frac{\partial}{\partial x_k}\left(\mu u_k\overline{\frac{\partial u_i'}{\partial x_j}\frac{\partial u_i'}{\partial x_j}}\right)}_{d_\varepsilon^t} \underbrace{-\frac{\partial}{\partial x_k}\left(2\mu\overline{\frac{\partial p}{\partial x_i}\frac{\partial u_k'}{\partial x_i}}\right)}_{d_\varepsilon^p} \tag{2.10}$$

$$P_\varepsilon = \underbrace{-2\mu\frac{\partial U_i}{\partial x_k}\frac{\overline{\partial u_i'}}{\partial x_j}\frac{\partial u_k'}{\partial x_j}}_{P_{\varepsilon 1}} \underbrace{-2\mu\frac{\partial U_i}{\partial x_k}\frac{\overline{\partial u_j'}}{\partial x_i}\frac{\partial u_j'}{\partial x_k}}_{P_{\varepsilon 2}} \underbrace{-2\mu u_k'\frac{\overline{\partial u_i'}}{\partial x_j}\frac{\partial^2 U_i}{\partial x_j \partial x_k}}_{P_{\varepsilon 3}} \underbrace{-2\mu\frac{\overline{\partial u_i'}}{\partial x_j}\frac{\partial u_i'}{\partial x_k}\frac{\partial u_k'}{\partial x_j}}_{P_{\varepsilon 4}} \tag{2.11}$$

$$\Phi_\varepsilon = -2\overline{\left(\mu\frac{\partial^2 u_i'}{\partial x_j \partial x_k}\right)^2} \tag{2.12}$$

These exact equations contain numerous unknown terms involving higher-order correlations of fluctuating velocities. In the k equation, P_k is the production of turbulence energy. The dissipation of k is brought about by the smallest eddies working against viscous stresses. At elevated Reynolds numbers, the viscous transport (by diffusion) term d_k'' is small compared to the turbulent diffusion d_k', and is thus neglected. An analogy of the gradient diffusion concept is used to model the turbulent transport of k. The pressure diffusion (d_k'') is often deemed to be negligible, but is nevertheless assumed to be adequately accounted for in the gradient diffusion term (Tennekes & Lumley, 1972, state that the pressure-work term, as it is also known, is of the same order of magnitude as the production and dissipation rates, but cannot be properly modelled due to insufficient knowledge). Hence the diffusion term in the k equation is modelled as

$$d_k = \frac{\partial}{\partial x_j}\left(\frac{\mu_t}{\sigma_k}\frac{\partial k}{\partial x_j}\right) \tag{2.13}$$

where σ_k is an empirical constant, and the complete k equation becomes

$$\rho\frac{Dk}{Dt} = \frac{\partial}{\partial x_j}\left(\frac{\mu_t}{\sigma_k}\frac{\partial k}{\partial x_j}\right) + P_k - \rho\varepsilon \tag{2.14}$$

Similarly, the diffusive terms in the ε equation are modelled as

$$d_\varepsilon = \frac{\partial}{\partial x_j}\left(\frac{\mu_t}{\sigma_\varepsilon}\frac{\partial \varepsilon}{\partial x_j}\right) \tag{2.15}$$

Of the terms in equation (2.11), the mixed production ($P_{\varepsilon 1}$) and production by mean velocity gradients ($P_{\varepsilon 2}$) terms are supposed to be small relative to the turbulent production ($P_{\varepsilon 4}$) term. As Rodi (1980) noted, the dissipation production and destruction terms, P_ε and Φ_ε respectively, cannot be modelled individually; rather, only their difference can be approximated. Furthermore, the gradient production term $P_{\varepsilon 3}$ is only of significance in viscous layers (i.e. near a wall). Thus Hanjalic & Launder (1972) modelled equation (2.11) as

$$P_\varepsilon = C_{\varepsilon 1}\rho\frac{\varepsilon}{k}P_k - C_{\varepsilon 2}\rho\frac{\varepsilon^2}{k} \tag{2.16}$$

and the complete ε equation becomes

$$\rho\frac{D\varepsilon}{Dt} = \frac{\partial}{\partial x_j}\left(\frac{\mu_t}{\sigma_\varepsilon}\frac{\partial\varepsilon}{\partial x_j}\right) + C_{\varepsilon 1}\rho\frac{\varepsilon}{k}P_k - C_{\varepsilon 2}\rho\frac{\varepsilon^2}{k} \tag{2.17}$$

The empirical constants given in table 2.1 take on the values prescribed by Launder & Spalding (1974).

C_μ	σ_k	σ_ε	$C_{\varepsilon 1}$	$C_{\varepsilon 2}$
0.09	1.0	1.3	1.44	1.92

Table 2.1: Constants in the turbulence transport equations.

All the simplifications made whilst modelling the k and ε equations hinged upon the assumption of high Reynolds number flows. This implies that the standard k-ε model is not applicable to low Reynolds number regions. In fact, when employed in wall-bounded flows, the k-ε model cannot be integrated directly to the wall; rather, empirically-derived wall functions must be adopted in place of the no-slip boundary condition. The nature of these boundary conditions is described in section 2.1.3.

Starting from fundamental principles and using ReNormalisation Group theory, Yakhot & Orszag (1986) derived a set of equations for k and ε. In the high Reynolds number limit, these matched the corresponding equations in the standard k-ε model, but the constants (also calculated explicitly rather than empirically) were somewhat different (see table 2.2). The fact that the equations in the two models were the same, yet

yet constructed from different approaches, leant them an element of credibility with regard to physical validity. Yakhot et al (1992) subsequently implemented several corrections to the constants, made by Yakhot & Smith (1992), and further introduced a strain-dependent modification to the constant $C_{\varepsilon 1}$ which is influential in highly-strained flows.

RNG Model	C_μ	σ_k	σ_ε	$C_{\varepsilon 1}$	$C_{\varepsilon 2}$
Yakhot & Orszag (1986)	0.085	0.72	0.72	1.063	1.72
Yakhot et al (1992)	0.085	0.72	0.72	1.42-R	1.68

Table 2.2: Constants in RNG model.

where
$$R = \frac{\eta(1-\eta/4.38)}{1+0.012\eta^3} \tag{2.18}$$

$$\eta = S\frac{k}{\varepsilon} \tag{2.19}$$

$$S = \left(\tfrac{1}{2}S_{ij}S_{ij}\right)^{1/2} \tag{2.20}$$

where S_{ij} is the mean strain rate as defined in Appendix A.

An attractive feature of the RNG model, as noted by Speziale (1991), is the fact that it automatically accounts for viscous effects on buffer layer turbulence as a wall is approached, thereby eliminating the need for empirical wall functions or damping functions. However, Rubinstein & Barton (1990) explained that whilst the RNG theory is valid for both high and low Reynolds number flows, it is not applicable to viscosity dominated regions (e.g. viscous sublayers). Thus the RNG model can be applied up to the boundary between inertial and viscous sublayers, which in practice implies that wall functions are employed (as done by Speziale & Thangam (1992), Yakhot et al (1992) and Lien & Leschziner (1994)).

In an effort to remove the dependence upon empirical wall functions, Jones & Launder (1972) proposed a low Reynolds number version of the k-ε model which was designed to take into account viscous effects:

$$\rho\frac{Dk}{Dt} = \frac{\partial}{\partial x_j}\left[\left(\mu+\frac{\mu_t}{\sigma_k}\right)\frac{\partial k}{\partial x_j}\right] + P_k - \rho\varepsilon \tag{2.21}$$

$$\rho\frac{D\tilde{\varepsilon}}{Dt}=\frac{\partial}{\partial x_j}\left[\left(\mu+\frac{\mu_t}{\sigma_\varepsilon}\right)\frac{\partial\tilde{\varepsilon}}{\partial x_j}\right]+C_{\varepsilon 1}f_1\rho\frac{\tilde{\varepsilon}}{k}P_k-C_{\varepsilon 2}f_2\rho\frac{\tilde{\varepsilon}^2}{k}+\underbrace{2\mu\upsilon_t\left(\frac{\partial^2 U_i}{\partial x_j\partial x_k}\right)^2}_{\rho E} \tag{2.22}$$

where

$$\tilde{\varepsilon}=\varepsilon-\underbrace{2\upsilon\left(\frac{\partial k^{1/2}}{\partial x_j}\right)^2}_{D} \tag{2.23}$$

$$\mu_t=\rho C_\mu f_\mu\frac{k^2}{\tilde{\varepsilon}} \tag{2.24}$$

A transport equation for the isotropic dissipation rate, $\tilde{\varepsilon}$, is solved because the value of $\tilde{\varepsilon}$ at the wall is zero, thereby simplifying the implementation of boundary conditions. The gradient production term $P_{\varepsilon 3}$ in equation (2.11) is also included due to its non-zero value in viscous regions; it is denoted as E in equation (2.22) and serves to control near-wall levels of k. Damping functions are used to bridge the viscous and turbulent boundary layers. The turbulent Reynolds number (R_T) dependent functions proposed by Launder & Sharma (1974) are

$$f_\mu=\exp\left[\frac{-3.4}{\left(1+R_T/50\right)^2}\right] \tag{2.25}$$

$$f_1=1.0 \tag{2.26}$$

$$f_2=1.0-0.3\exp\left(-R_T^2\right) \tag{2.27}$$

$$R_T=\frac{k^2}{\upsilon\tilde{\varepsilon}} \tag{2.28}$$

and the constants are as given in table 2.1. Savill (1993) concluded in his review of modelling transitional phenomena, that "of all the low Reynolds number model treatments examined to date, the Launder-Sharma type damping factor is recommended for the most accurate predictions of mean-flow quantities;" this is evidenced by the relatively extensive use of the LS model and its inclusion in certain commercial codes (e.g. CFX4).

2.1.2 Cubic Nonlinear Model

Speziale (1991) summed up the major deficiencies of linear two-equation eddy-viscosity models as a) the inability to properly account for streamline curvature, rotational strains and other body-force effects, and b) the neglect of non-local and history effects on the Reynolds-stress anisotropies. These problems are potentially overcome by second-moment closures because a separate transport equation is solved for each Reynolds stress; this indicates that these models are inherently superior to their two-equation counterparts. However, Lumley (1978) stated that there exists a viable alternative to second moment modelling. He noted that the information contained in the six components of the Reynolds stresses can be reduced to three parameters: the turbulence energy, k, and two anisotropic stress invariants, A_2 and A_3, defined as

$$A_2 = a_{ij}a_{ij} \tag{2.29}$$

$$A_3 = a_{ij}a_{jk}a_{ki} \tag{2.30}$$

where the anisotropic stress is

$$a_{ij} = \frac{\overline{u_i'u_j'}}{k} - \frac{2}{3}\delta_{ij} \tag{2.31}$$

Suga (1995) therefore developed an eddy-viscosity model which tackled the above shortcomings by a) utilising a nonlinear stress-strain equation, and b) sensitising the damping functions to the anisotropic stress invariant A_2, for which an additional transport equation is solved. A cubic stress-strain relationship was adopted because quadratic formulations lack generality. For example, Suga (1995) demonstrated that a_{23} contains both linear and cubic terms which are important in swirling flows; in quadratic models, a_{23} contains only the linear term. The three-equation, non-linear model is an extension of the cubic two-equation model described by Craft (1996); Suga (1995) reported that both yielded significant improvements over the Launder & Sharma model but that the differences between the two- and three-equation versions were minor. Thus the cubic two-equation model, from now on denoted as CRY, theoretically improves upon linear EVM's without incurring large computational penalties.

The distinguishing aspect of the CRY model is the cubic stress-strain formulation (allowing for variable-density flows) employed instead of the Boussinesq relationship:

$$
\begin{aligned}
-\rho\overline{u_i'u_j'} = {} & \mu_t S_{ij} - \frac{2}{3}\rho k\delta_{ij} \\
& - c_1\mu_t\frac{k}{\tilde{\varepsilon}}\left(S_{ik}S_{jk} - 1/3\,S_{kl}S_{kl}\delta_{ij}\right) \\
& - c_2\mu_t\frac{k}{\tilde{\varepsilon}}\left(\Omega_{ik}S_{jk} + \Omega_{jk}S_{ik}\right) \\
& - c_3\mu_t\frac{k}{\tilde{\varepsilon}}\left(\Omega_{ik}\Omega_{jk} - 1/3\,\Omega_{kl}\Omega_{kl}\delta_{ij}\right) \\
& - c_4\mu_t\frac{k^2}{\tilde{\varepsilon}^2}\left(S_{kl}\Omega_{ij} + S_{kj}\Omega_{il}\right)S_{kl} \\
& - c_5\mu_t\frac{k^2}{\tilde{\varepsilon}^2}\left(\Omega_{il}\Omega_{lm}S_{mj} + S_{il}\Omega_{lm}\Omega_{mj} - 2/3\,S_{lm}\Omega_{mn}\Omega_{nl}\delta_{ij}\right) \\
& - c_6\mu_t\frac{k^2}{\tilde{\varepsilon}^2}S_{ij}S_{kl}S_{kl} - c_7\mu_t\frac{k^2}{\tilde{\varepsilon}^2}S_{ij}\Omega_{kl}\Omega_{kl}
\end{aligned}
\qquad (2.32)
$$

The individual stress-strain relations are written out in full in the thesis of Suga (1995). The constants in equation (2.32) are given in table 2.3. They were calculated by Suga (1995) and Craft et al (1996) using DNS solutions as well as the properties of homogeneous shear flows, fully-developed swirling pipe flows and curved channel flows.

C_1	C_2	C_3	C_4	C_5	C_6	C_7
-0.1	0.1	0.26	$-10C_\mu^2$	0.0	$-5C_\mu^2$	$5C_\mu^2$

Table 2.3: Constants in the cubic stress-strain relation.

The k and $\tilde{\varepsilon}$ transport equations used in the CRY model are as follows:

$$\rho\frac{Dk}{Dt} = \frac{\partial}{\partial x_j}\left[\left(\mu + \frac{\mu_t}{\sigma_k}\right)\frac{\partial k}{\partial x_j}\right] + P_k - \rho\varepsilon \qquad (2.33)$$

$$\rho\frac{D\tilde{\varepsilon}}{Dt} = \frac{\partial}{\partial x_j}\left[\left(\mu + \frac{\mu_t}{\sigma_\varepsilon}\right)\frac{\partial\tilde{\varepsilon}}{\partial x_j}\right] + C_{\varepsilon 1}f_1\rho\frac{\tilde{\varepsilon}}{k}P_k - C_{\varepsilon 2}f_2\rho\frac{\tilde{\varepsilon}^2}{k} + \rho E + \rho Y_c \qquad (2.34)$$

These are similar to the equations in the Launder & Sharma low Reynolds number model, and the eddy-viscosity is as defined in equation 2.24. The constants are given in

table 2.1. Unlike in the LS model, C_μ attains a functional form dependent upon the strain invariant:

$$C_\mu = \frac{0.3}{1+0.35M_{\tilde{S},\tilde{\Omega}}^{3/2}} \times \left[1-\exp\left[\frac{-0.36}{\exp\left(-0.75M_{\tilde{S},\tilde{\Omega}}\right)}\right]\right] \tag{2.35}$$

where $M_{\tilde{S},\tilde{\Omega}} = \max\left(\tilde{S},\tilde{\Omega}\right)$ and the dimensionless strain and vorticity invariants are

$$\tilde{S} = \frac{k}{\tilde{\varepsilon}}\sqrt{\tfrac{1}{2}S_{ij}S_{ij}} \tag{2.36}$$

$$\tilde{\Omega} = \frac{k}{\tilde{\varepsilon}}\sqrt{\tfrac{1}{2}\Omega_{ij}\Omega_{ij}} \tag{2.37}$$

The mean strain and vorticity rates, S_{ij} and Ω_{ij} respectively, are given in Appendix A. Figure 2.1 illustrates the dependence of C_μ upon $M_{\tilde{S},\tilde{\Omega}}$. The damping functions are

$$f_\mu = 1-\exp\left[-\left(\frac{R_T}{90}\right)^{1/2}-\left(\frac{R_T}{400}\right)^2\right] \tag{2.38}$$

$$f_1 = 1.0 \tag{2.39}$$

$$f_2 = 1.0-0.3\exp\left(-R_T^2\right) \tag{2.40}$$

The gradient production term in the dissipation rate equation is modelled as:

$$E = 0.0022\frac{\tilde{S}\mu_t k^2}{\tilde{\varepsilon}}\left[\left(\frac{\partial^2 U}{\partial r^2}\right)^2+\left(\frac{\partial^2 V}{\partial x^2}\right)^2\right] \quad \text{for } R_T < 250$$

$$E = 0 \quad \text{for } R_T > 250 \tag{2.41}$$

The Yap term found in the dissipation rate equation (2.34) of the nonlinear model is defined as:

$$Y_C = \max\left[0.83\frac{\tilde{\varepsilon}^2}{k}\left(\frac{k^{3/2}}{2.5\tilde{\varepsilon}y}-1\right)\left(\frac{k^{3/2}}{2.5\tilde{\varepsilon}y}\right)^2,0\right] \tag{2.42}$$

Y_C acts to augment the production term in the dissipation rate equation and was first introduced by Yap (1987) in an attempt to correct the overprediction of the turbulence length scale in separated flows. The functional form of this correction term ensures that the turbulence budgets are manipulated in regions where y is small and k is large. The term $k^{3/2}/(2.5\tilde{\varepsilon}y)$ can be explained as a ratio of turbulent and inertial length scales, respectively given as:

$$l_t = C_\mu^{3/4}\frac{k^{3/2}}{\tilde{\varepsilon}} = 0.16\frac{k^{3/2}}{\tilde{\varepsilon}} \tag{2.43}$$

$$l_{bl} = \kappa y = 0.4y \tag{2.44}$$

The latter scale is derived for that part of the inertial boundary layer which is in local equilibrium; i.e. when the assumption "production = dissipation" holds true. Thus the Yap term only contributes to the destruction of k in the event that $l_t/l_{bl} \geq 1$ in the vicinity of a rigid boundary.

In order to examine the specific role of the nonlinear terms in the cubic model independently of the Yap term, it was decided to run the nonlinear model with and without this corrective measure. To assess the effect of Y_C in a second context it was also decided to run the Launder & Sharma model *with* the Yap correction. Details of all the turbulence models described can be found in the references in table 2.4. The abbreviations used to denote these models are also tabulated.

Turbulence model	Identification	Reference
Standard $k-\varepsilon$ model	k-ε	Launder & Spalding (1974)
ReNormalisation Group model	RNG	Yakhot et al (1992)
Launder & Sharma low Re model	LS	Launder & Sharma (1974)
Launder & Sharma model with Yap term	LSY	non-standard
Craft et al cubic non-linear model	CRY	Craft et al (1996)
Craft et al model without Yap term	CR	non-standard

Table 2.4: Abbreviations used for the various turbulence models.

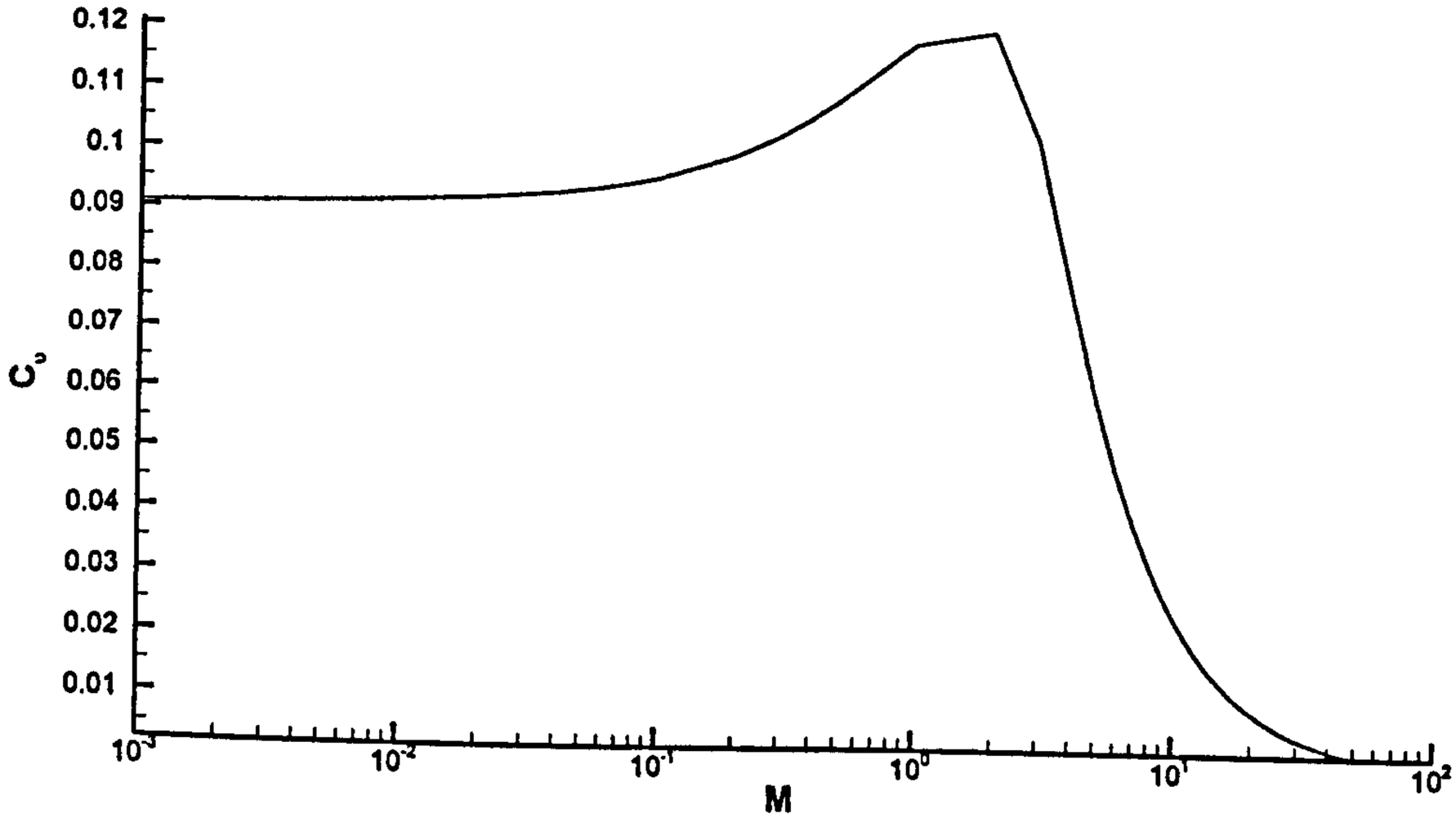

Figure 2.1: Dependence of C_μ upon $M_{\tilde{S},\tilde{\Omega}}$.

2.1.3 Near-Wall Treatment

Numerical solution of the momentum and turbulence equations requires the input of additional information in the guise of boundary conditions. Whilst the specification of boundary values is discussed in Chapter 3, the current section briefly describes two methods of near-wall treatment required for the momentum and turbulence transport equations.

2.1.3.1 Wall Functions

Since the k-ε and RNG models are not valid in regions dominated by viscosity, wall functions are utilised to bridge the gap between turbulent and laminar boundary layers. Generally, a Couette flow is assumed to occur in the vicinity of the walls and it is characterised by constant total shear stress (τ_w = constant) and negligible streamwise velocity gradients. Such a situation is described by a one-dimensional, ordinary differential equation which can be cast into dimensionless form to provide a relationship between U^+ $(=U/u_\tau)$ and y^+ $(=yu_\tau/\upsilon)$. Launder (1981) reviewed several different proposals for this relationship and found that in the case of a uniform-stress wall layer in local equilibrium, all the reviewed formulae are equivalent; significant differences, however, arise as separation is approached. A common simplification in the description of near-wall flows is to neglect the buffer layer and assume that the velocity profile undergoes an abrupt transition from the viscous sublayer to the fully-developed turbulent layer (although three-layer models also exist; see the review of Nallasamy, 1987, for details). In the TEACH code, this transition point is taken at $y^+ = 11.63$ and the near-wall velocity is given as:

$$U^+ = y^+ \qquad \text{for } y^+ < 11.63 \tag{2.45}$$

$$U^+ = \frac{1}{\kappa}\ln\left(E_r y^+\right) \qquad \text{for } y^+ \geq 11.63 \tag{2.46}$$

where the friction velocity is defined as

$$u_\tau = \sqrt{\frac{\tau_w}{\rho}} \tag{2.47}$$

The von Karman constant κ and the constant of integration E_r (also known as the roughness constant) are of an empirical nature; their values for simple flows attached to smooth walls are 0.4187 and 9.0, respectively.

Application of wall functions also supposes the shear stress in the boundary layer to be constant. Furthermore, the equation for turbulence energy can, upon assuming that local equilibrium holds true in the inertial sublayer ($30<y^+<400$), be simplified to:

$$-\overline{u'v'}\frac{\partial U}{\partial y} = \varepsilon \tag{2.48}$$

Further manipulation yields an expression for the shear stress in the inertial boundary layer (equal to the wall shear stress):

$$\tau_w = \rho C_\mu^{1/2} k \tag{2.49}$$

Recalling that the friction velocity is a function of wall shear stress, equation 2.49 can be rewritten as

$$\tau_w = \rho C_\mu^{1/4} k^{1/2} \frac{U}{U^+} \tag{2.50}$$

which is applied to the momentum equations parallel to the wall, in the boundary layer. Due to the staggered grid (see Chapter 3), no special consideration is required for the velocity normal to the wall, nor for the pressure.

Near-wall treatment of the k-equation involves recasting the source terms using the above relations. The boundary value for the dissipation rate is given as:

$$\varepsilon = \frac{C_\mu^{3/4} k^{3/2}}{\kappa y} \tag{2.51}$$

which is simply a combination of the definition of turbulent length scale with the value for said quantity in the inertial sublayer (see equations 2.43 and 2.44).

2.1.3.2 Damping Functions

The wall boundary conditions in low Reynolds number turbulence models which solve the $\tilde{\varepsilon}$-equation are $U = V = k = \tilde{\varepsilon} = 0$. Damping functions are employed in the near-wall region so as to mitigate the excessive production of turbulence energy which would otherwise be predicted by the high Reynolds number equations, given the same boundary conditions. A role of the damping functions is to ensure that the calculated variable distributions mimic the asymptotic variation of their experimental counterparts. At the wall, the limiting behaviour (as $y \rightarrow 0$) of the variables is:

$$k \propto y^2, \quad \varepsilon \propto y^0, \quad \mu_t \propto y^3, \quad -\overline{u'v'} \propto y^3, \quad \tilde{\varepsilon} \propto y^2 \qquad (2.52)$$

The damping function f_μ is of greater consequence than f_2 because it simulates the direct effect of the molecular viscosity on the turbulence energy and total shear stress. Patel et al (1985) showed that a dimensional analysis of the eddy-viscosity formula (equation 2.24) allows one to deduce that if C_μ is constant or not directly dependent on y, then f_μ should vary as y^{-1} or y^1, respectively, depending on whether the ε or $\tilde{\varepsilon}$ equation is adopted. Examination of the f_μ expressions for the LS and CRY models (equations 2.25 and 2.38) reveals that their asymptotic behaviour is $f_\mu \propto y^0$ and $f_\mu \propto y^1$, respectively (see table 2.5). Thus the formulation in the Launder & Sharma model is inconsistent with the eddy-viscosity relation, whilst that of the cubic EVM is correct. This has repercussions upon near-wall gradients; Chang et al (1995) stated that the correct prediction of the near-wall f_μ distribution is a prerequisite for the attainment of accurate heat and mass transfer rates at the boundary.

	LS	CRY
$R_T \rightarrow 0$	$f_\mu \rightarrow 0.03337$ $f_2 \rightarrow 0.70$	$f_\mu \rightarrow 0$ $f_2 \rightarrow 0.70$
$R_T \rightarrow$ large	$f_\mu \rightarrow 1.0$ $f_2 \rightarrow 1.0$	$f_\mu \rightarrow 1.0$ $f_2 \rightarrow 1.0$

Table 2.5: Asymptotic behaviour of damping functions.

2.2 COMBUSTION MODELLING

2.2.1 Background

Combustion is a process involving multiple species, each of which must be represented. The conservation of molecular species equation, as given in equation (2.53), is essentially a form of continuity for each species; upon addition of all the individiual species equations, the overall mass continuity (equation 2.1) is obtained.

$$\frac{Dm_{i'}}{Dt} + \frac{\partial}{\partial x_j}\left(m_{i'} V_{i',j}\right) = \omega_{i'} \qquad (2.53)$$

where $m_{i'}$ is the mass of species i', $V_{i',j}$ is the mass diffusion velocity of species i' in the direction j and ω_i is the net rate of mass production of species i' due to chemical reaction. The unknown quantity $V_{i',j}$ can be found by solving the physically-correct multi-component diffusion equation (Kuo, 1986), which states that the concentration gradients depend on diffusion velocities, pressure gradients, differences in the body force per unit mass on molecules of different species, and thermal-diffusion (Soret) and diffusion-thermometric (Dufour) effects. Upon making certain simplifying assumptions, this equation reduces to Fick's law (an analogy of the gradient diffusion hypothesis) for a binary system; this provides the following relationship between $V_{i',j}$ and the mass fraction ($Y_{i'}$) of each species:

$$V_{i',j} = -\frac{D_{i'}}{Y_{i'}} \frac{\partial Y_{i'}}{\partial x_j} \qquad (2.54)$$

where $D_{i'}$ is the multi-component diffusion coefficient of species i' with regard to the rest of the mixture. Hence the simplified species transport can be written as:

$$\frac{Dm_{i'}}{Dt} = \frac{\partial}{\partial x_j}\left(\Gamma_{i'} \frac{\partial m_{i'}}{\partial x_j}\right) + \omega_{i'} \qquad (2.55)$$

where Γ_i is the diffusion coefficient of species i'.

The full energy conservation equation describes the transport of the stagnation enthalpy. If it is assumed that thermal diffusion obeys Fourier's law (again an analogy of the gradient diffusion hypothesis), then the energy transport equation can be simplified to

$$\frac{Dh}{Dt} = \frac{\partial}{\partial x_j}\left(\Gamma_h \frac{\partial h}{\partial x_j}\right) + S_h \qquad (2.56)$$

where h is the static enthalpy, Γ_h is the diffusion coefficient and S_h is a source term which can include radiation heat transfer, pressure work and viscous energy dissipation. The static enthalpy of the mixture is the sum of the enthalpies of all the species:

$$h = \sum_{i'} Y_{i'}\left(h^0_{fi'} + \int_{T_0}^{T} Cp_{i'}\,dT\right) \qquad (2.57)$$

where $h^0_{fi'}$ is the enthalpy of formation of species i' and the second term on the right in the parenthesis is the sensible enthalpy of species i'.

In turbulent reacting flows where significant density variations occur, the scalars are also decomposed into mean and fluctuating components. However, the ensemble averaging approach leads to the additional terms $\overline{\rho' u_i'}$ and $\overline{\rho' \phi'}$ being present in the transport equations, for which no models are available. In order to circumvent this problem, Favre, or mass-weighted, averaging is used for the variables, where $\phi = \tilde{\phi} + \phi''$. Substituting these decomposed variables into their respective transport equations and subsequently employing time averaging techniques, results in mean transport equations which are identical in form to the original ones (i.e. 2.3, 2.4, 2.55, 2.56), except that the ensemble-averaged means are replaced by the density-weighted means. Although Favre-averaging is an artificial technique used in aiding the closure of variable-density transport equations for turbulent flows, Favre-averaged variables, whilst physically of little meaning, are accepted as being sufficiently near in value to their ensemble-averaged counterparts.

The Favre-averaged scalar transport equations are still not closed, however, because they involve the following unknown quantities:

- Turbulent diffusion fluxes, $\overline{\rho u_i'' m_{i'}''}$ and $\overline{\rho u_i'' h''}$, which are normally much larger than the corresponding laminar fluxes and
- Mean reaction rate $\overline{\omega_{i'}}$.

In the first instance, eddy-diffusivity (i.e. gradient transport) analogies of Fick's and Fourier's laws are commonly used for the turbulent species and energy equations, respectively:

$$\overline{\rho u_i'' m_{i'}''} = -\frac{\mu_t}{\mathrm{Sc}_t}\frac{\partial \tilde{m}_{i'}}{\partial x_i} \tag{2.58}$$

$$\overline{\rho u_i'' h''} = -\frac{\mu_t}{\mathrm{Pr}_t}\frac{\partial \tilde{h}}{\partial x_i} \tag{2.59}$$

where Sc_t is the turbulent Schmidt number and Pr_t is the turbulent Prandtl number. These dimensionless quantities are assumed to be constant and near unity in high Reynolds number flows. A more accurate alternative to the eddy-diffusivity concept is the General Gradient Diffusion Hypothesis (GGDH) of Daly & Harlow (1970). However, it is commonly used with second moment closures since it requires accurate knowledge of the Reynolds stresses. Craft et al (1997) used the GGDH for heat transfer in conjunction with their cubic nonlinear model, but did not report on its contribution.

The final unknown is the mean reaction rate $\overline{\omega_{i'}}$, the quantifying of which is the essence of combustion modelling. In laminar cases, reactions occur over a finite period of time and phenomenological chemical-kinetic expressions (based on the Arrhenius model and using mean quantities) are employed. The reaction rate is a highly nonlinear function of temperature and concentration (Jones & Whitelaw, 1982; Kuo, 1986; Libby & Williams, 1980; Warnatz et al, 1996). This is significant in turbulent combustion, where reactions can proceed at different rates depending on the local nature of the flow field. Areas dominated by finite-rate chemistry can still be adequately described by the Arrhenius-type models. However, in regions where combustion occurs sufficiently rapidly and the turbulent mixing rates are high, (i.e. zones of extensive

turbulence/chemistry interaction), Jones & Whitelaw (1982) reckoned the errors resulting from the application of an Arrhenius-type model to be up to three orders of magnitude. It is clear that in the context of turbulent combustion, the reaction rate $\overline{\omega_i}$ is a strong function of turbulent and chemical time scales, and that laminar tools are not suitable.

Two common modelling approaches can be taken in order to overcome this hurdle. The first is the Eddy Break-Up (EBU) model of Spalding (1976), which was improved and renamed as the Eddy Dissipation Concept (EDC) by Magnussen & Hjertager (1976). Essentially, the reaction rate $\overline{\omega_i}$ is related to the turbulent mixing time scale k/ε which controls combustion. The second approach is sometimes known as the mixed-is-burned method, which is described in the next section. Gran & Magnussen (1996) reported that in the case of fast chemistry situations, the conserved-scalar, flame-sheet model (also known as the mixed-is-burned method), in conjunction with a 'β' probability density function (described later), yields better predictions for species concentrations than the EDC. Lau (1995) also found that the EDC concentration predictions could be in error by orders of magnitude. Thus the flame-sheet approach was selected for use in the combustion simulations for two reasons:

- Fortran subroutines for this method already existed.
- The EDC approach is computationally intensive and was reported as not yielding significantly better results (Gran & Magnussen, 1996).

This decision was further justified by a comparison of the two different approaches as applied to a bluff-body combustor; the results are presented Appendix B.

2.2.2 Flame-Sheet Model

A popular modelling approach for non-premixed flames is the the flame-sheet model developed by Pun & Spalding (1967). It avoids the issue regarding the determination of the reaction rate $\overline{\omega_i}$ by considering the transport of a conserved scalar, for which there are no source terms. The mean mixture fraction $\overline{f}$ is normally selected as the conserved scalar, and the associated transport equation is:

$$\rho\frac{D\overline{f}}{Dt}=\frac{\partial}{\partial x_j}\left(\frac{\mu_t}{\sigma_t}\frac{\partial\overline{f}}{\partial x_j}\right) \tag{2.60}$$

where σ_t is the turbulent Prandtl number, normally assigned the value 0.7.

Also known as the Simple Chemical Reacting System (SCRS), the flame-sheet method treats combustion as a one-step reaction (although a different, chemical-equilibrium approach does permit intermediate reactions within the conserved scalar framework; further information is available in the Fluent 4.3 manual and in the review by Jones & Kakhi, 1996). It is assumed that fuel and oxidant cannot coexist in a given location; thus combustion occurs stoichiometrically and infinitely quickly as soon as fuel and oxidant are transported to a point. Hence the mean mixture fraction $\overline{f}$ is defined as:

$$\overline{f}=\frac{\left[sm_{fu}-m_{ox}\right]-\left[sm_{fu}-m_{ox}\right]_0}{\left[sm_{fu}-m_{ox}\right]_1-\left[sm_{fu}-m_{ox}\right]_0} \tag{2.61}$$

where the meaning of subscripts is:

s is the stoichiometric oxygen/fuel ratio,

fu refers to fuel,

ox refers to oxidiser,

1 refers to the fuel inlet and

0 refers to the oxidiser inlet.

This equation yields information regarding the mass fractions of fuel, oxidant and products at a point. Further linear relationships are used to compute the mass fractions of individual species. The limits of the mixture fraction $\overline{f}$ are 0 and 1, depending on whether the mixture at a point contains only oxidant or only fuel. Assuming that no

oxidant is present in the fuel inlet and that no fuel is present in the air inlet, the stoichiometric mixture fraction is defined as:

$$\overline{f}_{st} = \frac{m_{ox,0}}{sm_{fu,1} + m_{ox,0}} \tag{2.62}$$

By definition, fast chemistry requires that no fuel be present in the products of reaction in the case of excess oxidant. Similarly, if there is an excess of fuel, then no oxidant will be present in the products.

In an adiabatic system, the enthalpy and temperature are linear functions of the mean mixture fraction and are defined as:

$$h = h_0 + \overline{f}(h_1 - h_0) \tag{2.63}$$

$$T = \frac{h - m_f H_f}{C_{p,mix}} \tag{2.64}$$

where m_f is the local mass fraction of fuel, H_f is the calorific value of the fuel and $C_{p,mix}$ is the specific heat of the local gas mixture (this is temperature dependent and is calculated from empirical formulae). The density is calculated from the equation of state

$$\overline{\rho} = \frac{P}{RT\sum_i \frac{m_i}{W_i}} \tag{2.65}$$

where W_i is the atomic mass of species i and R is the universal gas constant.

The flame-sheet model is adequate for predicting flame lengths and yields acceptable spatial variations of major species (i.e. fuel and oxidant). However, the temperature field is a direct function of mean mixture fraction only and is not affected by the actual transport of enthalpy, which is a significant factor in turbulent flows. In other words, there is no mechanism within the model to account for the interaction between turbulence and chemistry. Jones & Whitelaw (1982) expressed this problem in a more fundamental manner by stating that the main fault of the flame-sheet model is its inability to account for the fluctuations in mixture fraction, caused by the highly non-linear

relationship between reaction rates and concentration and temperature levels. This problem can be remedied by adopting a probability density function (pdf).

The probability density function $p(f)$ describes the fraction of time that the fluctuating variable (instantaneous mixture fraction f) takes on a value between f and $f + \Delta f$. Figure 2.2 demonstrates this concept in a graphical manner.

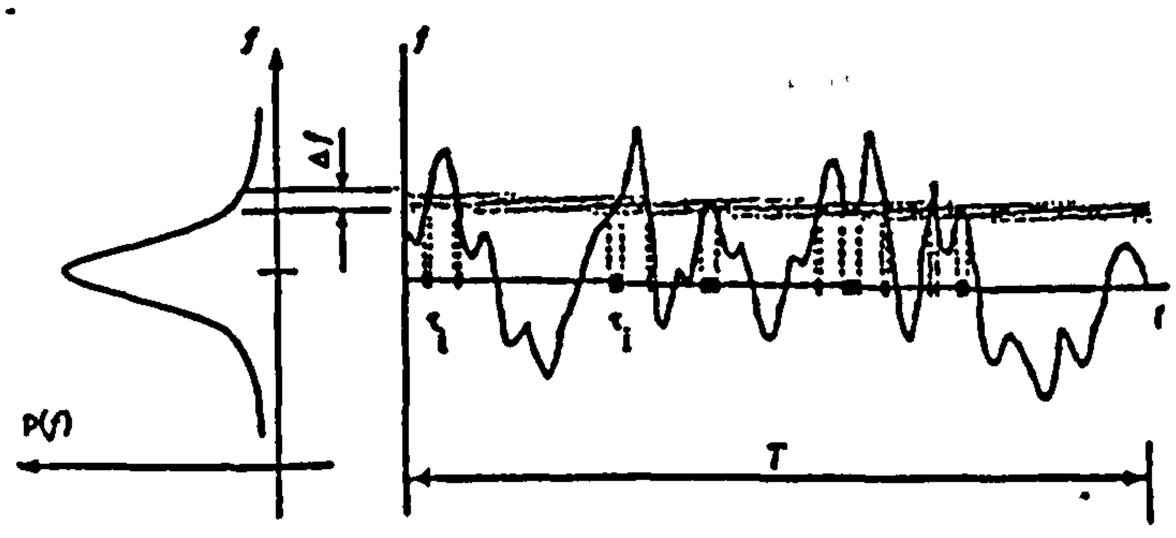

Figure 2.2: Graphical description of probability density function (Fluent 4.3 manual)

In a given period of time T (variable not to be confused with temperature), the fluctuating variable f has a value in the band Δf for a certain fraction of the period T under consideration. The pdf is a curve plotted such that the area under it in the band Δf is equal to the time fraction that f is in this range. Expressed mathematically,

$$p(f)\Delta f = \lim_{T\to\infty} \frac{1}{T} \sum_i \tau_i \qquad (2.66)$$

where τ_i is the fraction of time that f is in the $f + \Delta f$ region. The nature of the function $p(f)$ depends on the turbulent fluctuations of f. Ideally, $p(f)$ curves should exactly match experimental results.

The time averaged values of all the scalars which depend on mixture fraction f can be calculated using the probability density function. Thus, mean density, species concentration and temperature are computed from

$$\overline{\phi_i} = \int_0^1 p(f)\phi_i(f)df \tag{2.67}$$

It should be noted that during this integration, the incremental scalar $\phi_i(f)$ is found using the linear relationships involving $\bar{f}$; in the case of temperature and density, for instance, relations 2.64 and 2.65 are used.

Probability distributions tend to be functions of the mean mixture fraction $\bar{f}$ and its variance $\overline{f'^2}$, the latter being found from a transport equation:

$$\rho\frac{D\overline{f'^2}}{Dt} = \frac{\partial}{\partial x_j}\left(\frac{\mu_t}{\sigma_t}\frac{\partial\overline{f'^2}}{\partial x_j}\right) + C_{g1}\mu_t\left(\frac{\partial\bar{f}}{\partial x_j}\right)^2 - C_{g2}\rho\frac{\varepsilon}{k}\overline{f'^2} \tag{2.68}$$

where the constants take on the values $C_{g1} = 2.86$ and $C_{g2} = 2.0$. The best distributions are those which most closely resemble experimental observations of species concentrations. The clipped-Gaussian and β profiles are the most successful (Jones & Whitelaw, 1982). The β-pdf is defined as follows:

$$p(f) = \frac{f^{m-1}(1-f)^{n-1}}{\int_0^1 f^{m-1}(1-f)^{n-1}df} \tag{2.69}$$

$$m = \bar{f}\left[\frac{\bar{f}(1-\bar{f})}{\overline{f'^2}} - 1\right] \tag{2.70}$$

$$n = (1-\bar{f})\left[\frac{\bar{f}(1-\bar{f})}{\overline{f'^2}} - 1\right] \tag{2.71}$$

The variance must comply with the condition

$$0 \le \overline{f'^2} \le \bar{f}(1-\bar{f}) \tag{2.72}$$

thereby implying that $m \ge 0$ and $n \ge 0$. Furthermore, the upper limit of $\overline{f'^2}$ is 0.25. The exact shape of the β-pdf is seen to depend on the values of m and n; this is clearly demonstrated in figure 2.3.

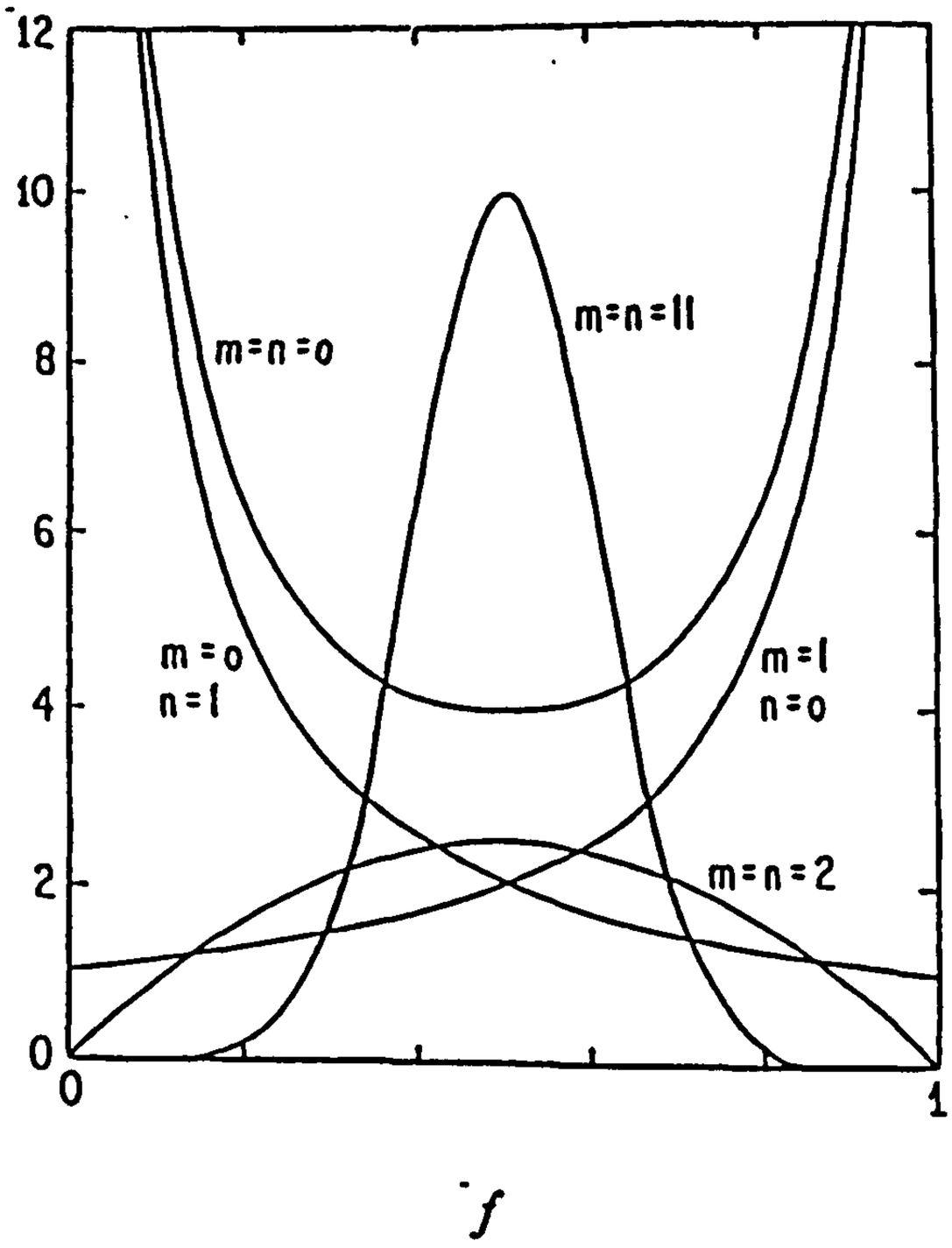

Figure 2.3: Variation of β-pdf with the parameters *m* and *n* (Libby & Williams, 1994).

Singularities occur when $\tilde{f} = 0$ or 1; these are generally avoided by simply reverting to the standard flame-sheet model for asymptotic values of mean mixture fraction.

The major assumptions pertaining to the conserved-scalar approach are listed below (Kuo, 1986).

- Infinitely fast chemistry.
- Simple, one-step, forward, irreversible reaction.
- Ideal gas law.
- Equal mass diffusivities of all species.
- Fick's law of diffusion is valid.
- Schmidt (*Sc*) and Prandtl (*Pr*) numbers are near unity.
- Lewis number ($Le = Sc/Pr$) is unity (i.e rate of energy transport equals rate of mass transport).
- Dufour and Soret effects are negligible.
- Negligible combustion-generated turbulence.

The issue of combustion-generated turbulence is also touched upon in the following section which examines variable-density effects.

2.2.3 Variable-Density Effects

Variable-density flowfields can raise issues which are not specifically addressed by the turbulence and combustion models described previously. However, it has been shown that in certain cases variable-density effects can be safely assumed to be negligible. This section outlines the key issues and explains why the turbulence and combustion models require no modification for the bluff-body combustor case.

A standard practice in turbulent combustion modelling is to simply utilise the isothermal transport equations and exchange the ensemble-mean variables with their Favre-averaged equivalents. This is confirmed in the reviews by Jones & Whitelaw (1982) and Borghi (1988), in which it is also noted that the turbulence model constants are not altered. However, it is recognised that variable-density flows do have an effect on scalar transport. This is manifested by the tendency of lower-density eddies to be more strongly accelerated when subjected to a pressure gradient, than those of higher density. This differential acceleration results in the motion of eddies relative to each other, thereby effectively enhancing turbulence generation and the non-gradient transport of scalars. Starner & Bilger (1980) were the first to experimentally investigate diffusion flames subjected to mean pressure gradients (achieved by placing the flame in a converging passage). They revealed that the pressure-density interactions strongly influence the turbulence fluctuations and that the flame is susceptible to shortening of up to 25% in moderate pressure gradients. Faced with these possible consequences, it is expedient to assess how variable-density and Favre-averaging effects bear upon the modelled scalar transport equations and the auxiliary thermodynamic relations.

Turbulent diffusion fluxes of any scalar in variable-density flows are not only due to gradients of the scalar; rather, significant contributions are made by pressure gradients between zones of variable density (known as non-gradient diffusion). In the review of Borghi (1988), it is noted that the isothermal gradient diffusion is applicable to rapid,

single-step combustion. Jones & Whitelaw (1982) make the same observation, and assume that the influence of density variations is entirely taken into account by the use of density-weighted averaging. The influence of combustion on pressure-driven scalar transport is manifested by a modification of the diffusion coefficients; Pr_t and Sc_t are assumed to be less than unity (they are also equivalent). Values of 0.7 and 0.9 are commonly used for the turbulent diffusion coefficient in, respectively, free flows and near-wall flows (Jones & Kakhi, 1996).

Variable-density effects are also apparent in the turbulence equations. If the original k and ε equations are derived whilst employing Favre-averaging techniques, then additional terms containing products of fluctuating quantities and mean gradients are obtained. In the k equation, these terms are interpreted as turbulence generation due to thermal effects, and are commonly modelled as

$$P_{k'} = P_k - \frac{\mu_t}{\overline{\rho}^2}\frac{\partial \overline{\rho}}{\partial x_i}\frac{\partial \overline{p}}{\partial x_i} \tag{2.73}$$

where P_k is the standard turbulence generation term (Jones & Whitelaw, 1982). The corresponding source term in the ε equation is also modified accordingly. Chomiak & Nesbitt (1995) reviewed various models for these pressure-related terms, and proposed several of their own. However, they noted that in the absence of significant axial gradients, the variable-density effects on turbulence generation can be ignored.

Dilatation effects on the equations were also surveyed. Velocity divergence, as it is also known, is attributable to heat release causing an expansion of the flow, and results in a decrease in turbulence energy. It is often accounted for by adding the term

$$C_{\varepsilon 3}\overline{\rho}\varepsilon\frac{\partial \tilde{U}_j}{\partial x_j} \tag{2.74}$$

in the ε equation, where the value of the constant $C_{\varepsilon 3}$ depends on the specific application. Chomiak & Nesbitt (1995) validated the variable-density and dilatation models in the k-ε framework by comparison with the standard k-ε model and also with

the experimental diffusion flame data of Starner & Bilger (1980). It was found that dilatation is negligible and hence need not be accounted for.

Once Favre-averaging has been adopted, it should be applied to all the auxiliary thermodynamic relations (e.g. sensible enthalpy equation for each species, ideal gas law) as well as to the transport equations. In practice, this introduces further complications due to the existence of correlations between mass fractions and fluctuating temperature (Chung, 1993). An error analysis by Brizuela (1995) reveals that when an assumed β-pdf profile is used, the errors associated with density and temperature at low mean mixture fractions can be significant (order of 1% and 7.5%, respectively, for a premixed methane flame). These errors become smaller, but remain significant, for the temperature as the mean mixture fraction is increased. As per common practice, though, this issue is not specifically treated.

This section has explained the subtleties of variable-density flows which generally need to be accounted for by turbulence and combustion models. Listed below is a summary of actions taken:

- $Pr_t < 1$ and $Sc_t < 1$ to account for non-gradient diffusion.
- No modifications required for the turbulence production term.
- Dilatation effects are ignored.
- Standard averaging is used for all auxiliary thermodynamic relations.

CHAPTER 3: NUMERICAL METHODOLOGY

The present chapter examines the CFD tools and methodology utilised in order to perform successful simulations. A general description of the TEACH research code is given, which is then followed by a catalogue of all the major modifications made to the code as regards implementing turbulence models and incorporating new physics. Guidelines are prescribed concerning discretisation schemes, grid quality and convergence criteria. Boundary conditions are listed and their influences are quantified. Finally, stability considerations particular to the nonlinear turbulence model are discussed, as well as the remedial measures taken.

3.1 CFD CODE

3.1.1 General Description

The TEACH (Teaching Elliptic Axisymmetric Characteristics Heuristically) code was originally written by Gosman & Pun (1974) at Imperial College for research purposes. It is based on finite volume methodology and employs a staggered, structured, orthogonal computational grid, thereby restricting the flow geometries to those with simple, smooth surfaces. A staggered grid is used so as to avoid a so-called checkerboard solution. The SIMPLE solution algorithm of Patankar & Spalding (1972) is employed. TEACH only caters for uniform radial and nonuniform axial grid generation; thus non-uniform, orthogonal meshes were generated using the pre-processing facilities of Fluent. The hybrid (first-order upwind (UPS), second-order

central differencing (CDS)) discretisation scheme of Spalding (1972) is employed so as to avoid the unphysical oscillations which can arise as a result of the convection terms being discretised with CDS.

3.1.2 Code Development

The original TEACH algorithm was designed with steady, turbulent, two-dimensional (plane and axisymmetric), incompressible flow in mind, although its architecture allowed for relatively straightforward implementation of new physics. The standard k-ε model accounted for turbulence effects; the original test case was the pipe expansion of Back & Roschke (1972). In order to achieve the research aims described in Chapter 1, the code required modification in the following areas:

- Geometry (to cater for various test cases).
- Turbulence Modelling (implementation of established and new models).
- Swirl (introduction of relevant equations so as to enable prediction of swirling flows).
- Combustion Modelling (introduction of combustion model).

The discretised partial differential equations in the TEACH code are based on Cartesian/cylindrical coordinates, thereby requiring that the flow geometries investigated consist of straight boundaries. Introducing new geometries necessitated many changes in the code; thus the only configurations examined were straight pipes, pipe expansions and coaxial combustors.

Several turbulence models were added to the TEACH code. The first, the RNG model, simply required a different value for the constant $C_{\varepsilon 2}$ and the addition of a strain related source term (via $C_{\varepsilon 1}$) to the dissipation rate equation. The Launder & Sharma (1974) low Reynolds number model was implemented for the simple reason that its basic structure is similar to that of the nonlinear model, hence allowing for facilitated, step-wise coding and testing of the cubic model. Furthermore, it is arguably the most popular low Reynolds number model in use and therefore serves as a benchmark with which to compare the nonlinear model. A new subroutine solving the isotropic

dissipation rate equation (equations 2.22 and 2.34 for the LS and CRY models, respectively) was introduced, as well as a subroutine which calculated all the strain rates, damping functions, turbulence generation and higher-order terms in the nonlinear stress-strain relations. The nonlinear elements of the Reynolds stresses were incorporated in the momentum equations by inclusion in the source terms. Direct integration to the solid boundaries was required by the low Reynolds number models; thus the wall treatment described in section 2.1.3.2 was also added to the code.

The capability for simulating swirling flows was achieved by implementing a transport equation for tangential momentum. This was somewhat simplified by the assumption of axisymmetry, but still contained convection and diffusion terms with both axial and radial gradients. Again, the equation had to be integrated directly to the wall for use with the low Reynolds number models. Many of the existing subroutines required the addition of swirl-related terms. The momentum transport equations describing swirling flows are written out in Appendix A. Confirmation that the swirl-related modifications were correctly implemented is available in Appendix C, which briefly compares the TEACH and Fluent code predictions for a swirling pipe flow.

Subroutines accounting for combustion (i.e. solution of the transport equations 2.60 and 2.68 for mixture fraction mean and variance) were obtained from a suitably modified version of the TEACH code. The only necessary changes were those concerning chemistry definition and the appropriate modifications in the common variable blocks of all the relevant subroutines. Modifications were also made to cater for fuels which contained non-combusible components. Whilst the relevant inlet conditions (discussed in section 3.3.1) still hold true in these cases, the linear relationships between mean mixture fraction, species mass fraction and enthalpy needed to be reformulated to reflect this.

3.2 SIMULATION GUIDELINES

3.2.1 Minimising and Quantifying False Diffusion

The upwind component of the hybrid discretisation scheme is only first-order accurate and thus tends to introduce numerical diffusion which can be in excess of actual turbulent diffusion. Details of the precise generation mechanism are given by Leschziner (1980). The purpose of this section is to briefly describe the situations in which this phenomenon arises and then to provide guidelines on:

- Quantifying the extent of numerical diffusion.
- Generating computational grids in which false diffusion is minimised.

Within a 2-D system, the false diffusion coefficient Γ_f for first-order upwinding can be computed from the formula derived by Vahl-Davis & Mallinson (1976):

$$\Gamma_f = \frac{\rho U_r \Delta x \Delta y \sin(2\theta)}{4\left(\Delta y \sin^3\theta + \Delta x \cos^3\theta\right)} \qquad (3.1)$$

where θ is the angle made by the resultant velocity U_r with the grid lines. The magnitude of Γ_f is seen to depend on cell size and on the skewness of the flow with respect to the computational grid. Thus false diffusion is minimised in flows which are predominantly aligned with fine grids. To give an idea of the effects of artificial diffusion, Launder (1981) showed that in the case of flow over a backward-facing step, the false diffusion due to employing only first-order upwinding could affect the computed reattachment length by 0.3 step heights (the predicted and experimental reattachment lengths were 5.5H and 7.5H, respectively).

The hybrid discretisation scheme only employs upwinding when the magnitude of the Peclet number, or cell Reynolds number ($Pe = \rho U_i \Delta x_i / \mu_t$), is greater than 2. For smaller values, central-differencing is used and no numerical diffusion arises. Thus an ideal computational grid is one in which $|Pe| < 2$ everywhere. Clearly, this is an uneconomical approach resulting in excessively large meshes.

An alternative is to concentrate the mesh in areas where diffusion is most important and where the flow is not aligned with the grid. For example, in pipe expansion flows, diffusion in the radial direction is as significant as convection within the recirculation region, and is dominant elsewhere. In light of this, the radial grid is refined such that $|Pe| < 2$ in this orientation. Convection is the dominant process in the axial direction, so the density of the longitudinal grid is not as critical, particularly since the axial flow is mostly aligned with the grid. Ramos (1993) and Jones (1994) stated that numerical diffusion caused by first-order upwinding is negligible at high cell Reynolds numbers mainly because the second derivatives, on which diffusion is based, become insignificant.

A comparison of the TEACH and Fluent codes for a pipe expansion case indicates that false diffusion effects become small when an adequate grid is utilised (see Appendix D for details).

In the present work, computational grids were created according to the two guidelines below, which permit the extent of false diffusion to be minimised and thereafter quantified:

- Grids are selectively refined so as to promote the use of central differencing where diffusion is important.
- Equation 3.1 is used to quantify false diffusion for a given grid. It should be noted that the result is a worst-case estimate because this formula was derived for upwinding only.

3.2.2 Grid Quality and Independence

The quality of a CFD solution is a strong function of the associated computational grid. In order to resolve complex flows, meshes must be refined in areas of steep gradients, thereby necessitating the use of non-uniform grids. This is particularly true near solid boundaries in wall-bounded flows, although the exact gridding employed depends on the turbulence model. This issue is resolved in section 3.3.3.

Numerical predictions are only meaningful if they can be shown to be independent of the grid. Proving a solution to be thus can be achieved by comparing skin friction factors

$$C_f = \frac{\tau_w}{\frac{1}{2}\rho U_0^2} \tag{3.2}$$

for successively larger grids (as recommended by McGuirk, 1998). In recirculating flows, the reattachment length provides a further measure. For flows in which the walls are far removed from any important flow features, profiles of U and k which bisect these features are better indicators than the skin friction factor. In the case of the low Reynolds number turbulence models, grid independence was ascertained using the nonlinear model. This is due to the fact that the cubic model tends to decrease turbulent viscosity, thereby increasing cell Peclet numbers for a given grid and potentially increasing velocities too. Since grid-independence is affected by velocity magnitudes, then if the CRY model is shown to be grid independent, the LS model certainly is so too. It was thought that the same procedure could be used for the high Reynolds number models (since the RNG model diminishes turbulence energy in recirculating flows), but it was found that in some cases a given grid was sufficiently dense for the RNG model but not so for the k-ε model. Hence grid independence for computations using high Reynolds number models was checked using both the k-ε and RNG models.

3.2.3 Convergence Criteria

During each simulation, normalised residuals were reported for the momentum and continuity equations. The documentation accompanying the TEACH code (Gosman & Pun, 1974) asserts that convergence is attained when the residuals are of the order 10^{-3} relative to the reference values (i.e. inlet mass and momentum flow rates). However, in the case of the low Reynolds number turbulence models, solutions to a turbulent pipe flow simulation which met the above criterion were found to be not entirely correct. This was deduced by taking a force balance along a fully-developed section of said pipe and applying computed pressure gradients and wall shear stresses to the following equation, where it was found that the two sides of equation 3.3 were distinctly unequal.

$$\frac{dP}{dx} = \frac{4\tau_w}{D} \tag{3.3}$$

This fundamental force balance was only satisfied once the normalised pressure residuals had dropped to $O(10^{-4})$. This, therefore, was the adopted convergence criterion. Launder (1981) also found that 10^{-3} was not always sufficient as a convergence criterion for recirculating flows, stating that the predicted reattachment lengths could vary according to the final residual level.

Residuals for the turbulence quantities k and ε were also computed, but their absolute nature meant that convergence could not be judged by them. No specific residual levels were aimed for with the turbulence quantities because the final residuals were seen to depend on grid size (denser grids resulted in higher final residuals for k and ε), but it was generally found that the final residuals were about five orders of magnitude smaller than the intial levels. The values of all the variables were monitored at a key location (e.g. near the wall or in the recirculation zone, depending on the flow); as an additional convergence test, these values were checked for invariance with iteration number. In combusting flows, the desired level for the final residuals of mean mixture fraction and variance was of the order 10^{-6} (Fluent 4.3 Manual).

3.3 BOUNDARY CONDITIONS

The purpose of this section is to present guidelines regarding the specification of inlet, exit and wall boundary conditions, particularly with reference to the turbulence models used and the various flows which were simulated.

3.3.1 Inlet Conditions

Inlet levels for velocities, turbulence energy and dissipation rate are case-dependent, whilst inlet values for the combustion quantities are always those shown in the table:

	$\tilde{f}$	$\widetilde{f''^2}$
Fuel stream	1	0
Oxidant stream	0	0

Table 4.1 : Inlet conditions for combustion quantities.

The inlet value of the velocity is normally readily available, but this is not usually the case for the turbulence quantities k and ε (or $\tilde{\varepsilon}$) which must therefore be estimated. The turbulence energy can be related to the mean velocity by means of the turbulence intensity T_i, which is typically of the order of several percent:

$$k = \frac{T_i}{100} U^2 \qquad (3.4)$$

The dissipation rate is commonly estimated from a rearrangement of the definition of turbulent length scale:

$$\varepsilon = \frac{k^{3/2}}{L} \qquad (3.5)$$

where L is a characteristic dimension of the flow geometry in question. A generally accepted formula is

$$\varepsilon = \frac{C_\mu^{3/4} k^{3/2}}{0.07L} \qquad (3.6)$$

but Nallasamy (1987) recommended that the formula

$$\varepsilon = \frac{C_\mu k^{3/2}}{0.03R_1} \qquad (3.7)$$

be used for flow in a pipe expansion (where R_i is the inlet pipe radius).

It is of course important that the nature of the numerical conditions reflect, as far as possible, those actually encountered in the flow. For example, if the actual inlet flow is fully-developed, then such a profile should also be used for the numerical inlet conditions. A numerical study for a pipe expansion (see Appendix E) demonstrates that when the actual flow is indeed fully-developed at the inlet, then the best predictions are obtained by using fully-developed profiles for U, k, and ε (or $\tilde{\varepsilon}$), rather than just for the mean velocity.

In the present work, the cases involving fully-developed inlet flows generally had experimental inlet profiles for both the mean velocity and the turbulence energy. In such instances, the experimental inlet profiles were mapped onto the inlet section of the computational grid by using interpolation functions in MATLAB. The dissipation rate was found by applying a relation of the form given by Equation 3.5 to each discrete point along the inlet profile. When the isotropic dissipation rate was required, it was generally assumed that $\tilde{\varepsilon} \approx \varepsilon$; justification for this simplification is given in the various cases in Chapter 4 where this assumption was indeed made.

Various formulae exist for specifying inlet dissipation rate, even for one type of flow. Relations 3.6 and 3.7 are just two examples of such formulae which are applied to pipe expansion flows. A numerical study for a pipe expansion (carried out in Appendix F) assesses the sensitivity of certain predicted parameters to the application of various inlet specifications for dissipation rate (equations 3.6 and 3.7). It is found that the computed reattachment was not in fact a strong function of the inlet dissipation rate. Data from the literature is also presented; it confirms this finding for a wider range of inlet specifications.

The degree of development of the inlet boundary layer can have significant effects on the flow further downstream. The frequent practice of assuming flat (plug) profiles is only valid when the inlet boundary layer is relatively thin. In the presence of a significantly-developed boundary layer, flat inlet profiles can only be assumed if certain measures are taken. For example, in the case of a pipe expansion, the flat inlet

profiles should be specified 5 step heights upstream of the expansion (Thangam & Speziale, 1992) in order to permit the development of a boundary layer.

3.3.2 Exit Conditions

Several types of exit boundary treatments exist; the method used by TEACH applies zero axial gradients at the exit (for all variables bar pressure). This assumption is valid provided that the exit is located far downstream from any major flow features.

The redevelopment length in a pipe is taken as 80d (Durst et al, 1995), so the exit condition in the fully-developed pipe flow is placed that distance downstream of the inlet. The situation regarding highly swirling flow is somewhat more complex and is thus discussed specifically in section 4.5.

Launder (1981) found that reattachment lengths in backward-facing steps are affected by the location of the outlet if the computational domain is shorter than 25 step heights (H). Similarly, Thangam & Speziale (1992) recommend $30H$ whilst Eaton & Johnston (1980) specify $50H$. These guidelines are used for the pipe expansion cases studied in the present thesis.

In the reacting cases, the issue of outlet condition placement is discussed in the relevant sections in Chapters 5 and 6.

3.3.3 Solid Boundaries

The treatment of the momentum and turbulence transport equations in the vicinity of a wall was discussed in Chapter 2. The purpose of the current section is threefold:

1. To establish the location of near-wall nodes.
2. To provide guidelines for the treatment of side walls.
3. To give the wall boundary conditions for the combustion-related variables.

When wall functions are utilised in conjunction with the k-ε and RNG models, the near-wall nodes should be placed in the inertial sublayer ($30 < y^+ < 400$). Opinions vary somewhat regarding the location of the solid-boundary nodes when utilising low Reynolds number models. McGuirk (1996) recommended utilising at least five nodes within the viscous sublayer when using the Launder & Sharma model. Craft et al (1997) placed the near-wall node at $y^+ < 0.3$ for transitional flow over a flat plate, whilst Apsley & Leschziner (1998) used $y_p^+ = 1$ for a back-step case. At the expense of erring on the side of caution, all the low Reynolds number simulations performed in the present research work employed grids such that $y_p^+ \leq 0.3$.

In geometries involving a solid boundary which is perpendicular to the main flow (i.e. in pipe expansions and bluff-body combustors), the momentum and turbulence transport equations for the low Reynolds number models (LS and CRY) should ideally be integrated directly to the side walls too. This poses the problem of having to use a separate set of damping functions for each wall. Furthermore, integration to the side walls would necessitate very dense, nonuniform axial grids, thereby causing an unacceptable increase in computing requirements. For this reason, wall functions are also applied to the side walls when low Reynolds number models are used. In the pipe expansion geometry, the main flow is a strong jet that is almost parallel to the pipe wall, and the velocities near the vertical wall are at least an order of magnitude smaller. The effects of using standard wall functions at the side wall, on flow predictions is likely to be small. Gran & Magnussen (1997) also adopted this technique during their application of the Launder & Sharma (LS) model in a bluff-body burner; they found that the results were not compromised by this practice.

In cases involving combustion, the mean mixture fraction and variance were both simply set to zero at the walls.

3.4 NUMERICAL PRACTICES REGARDING THE NONLINEAR MODEL

Obtaining a stable, converged solution with the nonlinear turbulence model proved to be an intricate proposition. The main difficulty lay in the stability of the solution; in the absence of special treatment, the simulation would diverge or crash. Three causes for this behaviour were found; the necessary remedies are described in the following sections.

3.4.1 Turbulence Generation

Introduction of third-order terms in the nonlinear model is required for resolving complex flow features, but also results in the realisability criterion not being met. Whilst the k-ε, RNG and LS models predict unconditionally positive values for turbulence generation P_k, the cubic model can yield negative normal stresses (Rabbitt, 1997, Apsley & Leschziner, 1998). This results in negative values for turbulence energy and causes the TEACH program to crash. From the point of view of stability, this problem was rectified by recalculating P_k, in the event that P_k should be negative when computed with the nonlinear contributions, using the LS methodology. The purpose of the stability measure is thus to avoid significant negative contributions from any of the Reynolds stresses in the developing stages of a simulation. In other words, negative values for P_k only arise when a simulation is first started and the initial flow field estimates yield excessive velocity gradients.

Theoretically, this stability measure should affect the final solution. In practice, however, this was not found to be the case. The Tropea et al (1989) pipe expansion flow was simulated using the nonlinear turbulence model, with the above stability measure in place. Upon convergence, this artificial device was removed and it was possible to obtain a second converged solution. Several aspects of the two predicted flow fields were compared. The reattachment lengths were virtually identical (X_r/H=1.87 and 1.89), as were the respective radial profiles of U, k and $\overline{u'v'}$ at six axial locations (graphs of these are not shown because the respective curves are almost indistinguishable from one another). Skin friction factor plots proved to be nearly the same (figure 3.1). The slight discrepancies encountered are probably related to small

variations in degrees of convergence; inspection of the residuals of the two solutions revealed differences of 6%, 5.9% and 3.3% between the axial momentum, radial momentum and mass residuals, respectively. The stability measure described does not interfere with the final solution and is therefore a valuable tool for ensuring that meaningful, converged solutions are obtained.

3.4.2 Gradient Production Term

A second area of numerical concern with the nonlinear model was the form of the gradient production term E (see equation 2.41). In complex flows such as those involving recirculation, it was found that the condition $E = 0$ for $R_T > 250$ would lead to instability. The role of this constraint was examined in the simpler turbulent pipe flow, for which stable solutions could be obtained both with and without the above constraint for E. A radial plot of E for these two solutions is shown in figure 3.2; it reveals that the condition $E = 0$ for $R_T > 250$ imposes a discontinuity in an otherwise smooth distribution of E, which appears to be the cause of numerical instability in more complex flows. The graph indicates that if the $E = 0$ constraint is removed, the value of E as the centreline is approached is small compared to the peak near the wall, where gradient production is expected to have the largest effect. Furthermore, in both cases the value of E was always at least an order of magnitude smaller than the main source terms in the $\tilde{\varepsilon}$ equation. The effect on U and k of lifting the constraint on E, is not detectable because radial profiles for these quantities were the same for the two cases.

Whilst this investigation showed that lifting the constraint on E in a fully-developed pipe flow simulation had no effect on the results, it did not yield information pertaining to this issue in complex flows. It was initially thought that the occurrence of this instability in the pipe expansion case could be due to the fact that the nonlinear model had not been calibrated for recirculating flow. To test this hypothesis, an annular mixing layer (two concentric air jets of differing velocities) was simulated, but the above problem persisted. This seemed to indicate that instabilities occurred whenever the abrupt behaviour of the E term coincided with a flow feature in which high gradients are involved. Thus it was not possible to quantify the effect of the constrained E in a complex flow. However, the above evidence (for a pipe flow) suggests that removing

the constraint should not matter. Based on this reasoning, the constraint was lifted in all the simulations of complex flows.

3.4.3 Under-Relaxation

The last numerical issue involving specifically the nonlinear model is the matter of under-relaxation; for the main variables these factors had to be smaller than those of the high Reynolds number turbulence models. Additional under-relaxation was also required for the nonlinear contributions to the Reynolds stresses; the factors had to take on values of 0.05 or smaller in order to avoid instabilities. This resulted in the computations requiring significantly more time to reach a fully-converged solution which met the criteria set out in section 3.2.2.

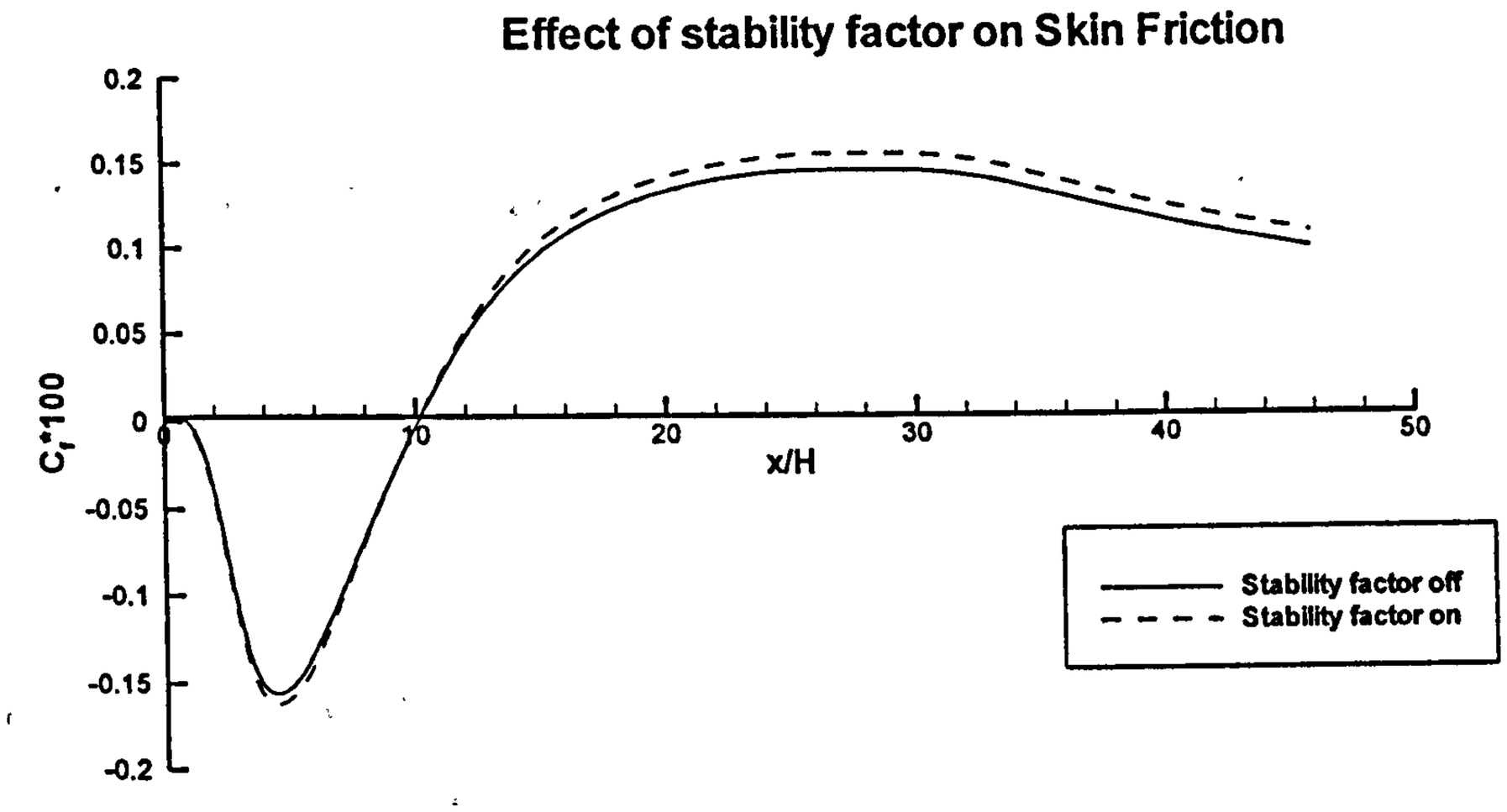

Figure 3.1: Effect of stability factor on skin friction, for the pipe expansion of Tropea et al (1989).

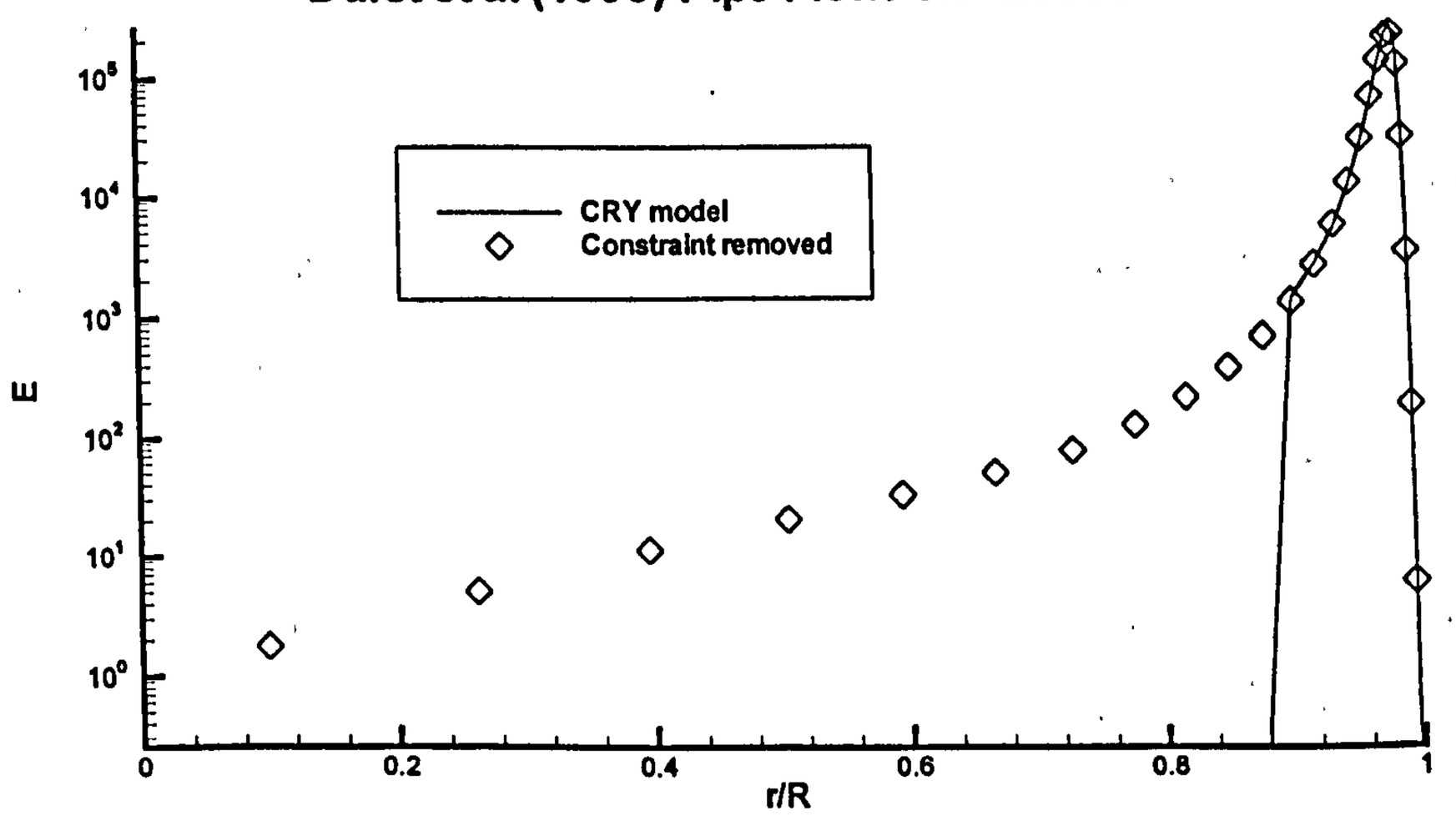

Figure 3.2: Effect of constraint on the term *E*, for the fully-developed pipe flow of Durst et al (1993).

CHAPTER 4: VALIDATION SIMULATIONS

The main flow features in the bluff-body combustor described in Chapter 6 are recirculation and swirl. Prior to the application of the cubic turbulence model to the burner, it was necessary to assess the performance of this model in several cases which isolate these individual flow phenomena. This would give an indication of the potential effectiveness of the nonlinear model in the combustor environment. Furthermore, the performance of the cubic model could be compared to three commonly used EVM's (k-ε, RNG, LS). The test cases selected for comparison and validation purposes are fully-developed, turbulent pipe flow, pipe expansion flow and finally highly-swirling pipe flow. At the time of writing, nowhere in the public domain was there any documentation concerning the application of the nonlinear model to the last two flows.

4.1 PIPE FLOW - DURST et al (1993,1995)

Although not a complex flow, the fully-developed pipe flow of Durst et al (1993, 1995) was selected to ensure that the LS and CRY models had been correctly implemented in the TEACH code. Several noteworthy conclusions were drawn despite the simplicity of this case. The working fluid is oil (kinematic viscosity 4.3×10^{-6} m^2/s, density 860 kg/m^3) which flows through a D=50mm diameter pipe of 4.0m length. Experimental profiles (obtained using laser doppler velocimetry, LDV) for mean axial velocity and normal Reynolds stresses were available for two different Reynolds numbers, Re≈20500 and Re≈7500, which correspond to mean inlet velocities of 1.85m/s and 0.64m/s, respectively (the paper reported a flow rate of 1.79m/s, but integration of the experimental profiles yielded the figure of 1.85m/s). Both cases were simulated assuming flat inlet profiles for U, k and ε, using equations 3.4 and 3.7 (where $T_i = 3\%$).

Since the inlet profile was flat, the assumption $\tilde{\varepsilon} \approx \varepsilon$ is valid. Various computational grids were utilised; grid independence was assessed by comparing the radial turbulence energy distributions (in the fully-developed area) for the different meshes. It emerged that a 500×40 mesh was sufficiently dense to support a valid solution obtained with the LS model (the coarser grid, 200×30, yielded identical results so that grid independence was also ensured for the nonlinear model). In order to reduce the computational effort, the pipe length was reduced to 60D and the grid was scaled down accordingly (375×40); the results hardly changed. The radial distribution of cells located the near wall node at $y^+ < 0.3$ for the higher flow rate. A 325×25 grid was utilised for the high Reynolds number models such that $y_p^+ > 13$ (again, based on the higher flow rate). Convergence was judged by the criteria set out in Chapter 3. No amount of numerical manipulation, though, would diminish the relative axial momentum residual below 5×10^{-3} for the Re≈7500 case (using the CRY model). However, tests showed that the force balance of equation 3.3 could still be satisfied by ensuring that the pressure residual was of the order 10^{-4}.

4.1.1 Results

Global characterizations of pipe flow are given by axial pressure gradients and friction velocities. Table 4.1 compares these experimental and computed quantities for the various turbulence models, at the two flow rates considered by Durst et al (1993, 1995). The predicted friction velocities are found from

$$u_\tau = \sqrt{\frac{\tau_w}{\rho}} \tag{4.1}$$

where the wall shear stresses for the low and high Reynolds number models are, respectively,

$$\tau_w = \mu \frac{\partial U}{\partial y} \tag{4.2}$$

$$\tau_w = \rho C_\mu^{1/2} k_w \tag{4.3}$$

Durst et al (1993, 1995) computed friction velocities based on near-wall LDA measurements; experimental pressure gradients were thus obtained from the force balance in equation 3.3. Predicted pressure gradients were computed from the simulated pressure field. Agreement between experimental and predicted values is generally good; in fact the CR model gives the best results for both flow rates. Introduction of the Yap factor in the nonlinear model, however, is seen to cause a deterioration in predicted pressure gradient and friction velocity. A third, less common parameter in pipe flows, is the dimensionless wall dissipation rate:

$$\varepsilon_w^+ = \frac{\upsilon \varepsilon_w}{u_\tau^4} \tag{4.4}$$

Patel et al (1985) suggested that this parameter could be described by $\varepsilon_w^+ = 2A^+$ where A^+ is based on pipe experiments. Myong & Kasagi (1990) report details on the variation of A^+ with Reynolds number; the values of A^+ for Re=20500 and Re=7500 are approximately 0.043 and 0.035, respectively. The CFD predictions for ε_w^+ are compared to the empirically-derived values. Table 4.1 indicates that all the low Reynolds number models significantly underpredict ε_w^+, with the nonlinear model improving somewhat over the LS model. This underprediction was also reported by Myong & Kasagi (1990) in their application of the LS model to the pipe flow of Laufer (1954). Suga (1995) obtained similar trends when applying the nonlinear model to channel flow.

	Re = 20500			*Re = 7500*		
	dP/dx (Pa/m)	U_τ (m/s)	ε_w^+	dP/dx (Pa/m)	U_τ (m/s)	ε_w^+
Experimental	-734	0.1033	0.086	-127	0.0430	0.07
k-ε	-760	0.1029	-	-123	0.0408	-
RNG	-716	0.1016	-	-118	0.0405	-
LS	-718	0.1022	0.0121	-112	0.0405	0.0092
LSY	-718	0.1024	0.0124	-113	0.0405	0.0090
CR	-736	0.1038	0.0317	-115	0.0409	0.0223
CRY	-685	0.0999	0.0209	-109	0.0399	0.0160

Table 4.1: Comparison of pressure gradients, friction velocities and asymptotic values of dissipation rate.

No values of ε_w^+ are given for the high Reynolds number models because of the relatively large distance of the near-wall node from the solid boundary.

The computed radial profiles for mean axial velocity U, U^+ ($=U/u_\tau$), turbulence energy k, normalised Reynolds shear stress $-\overline{u'v'}/u_\tau^2$ and normalised normal stresses $\overline{u'^2}/u_\tau^2$ and $\overline{v'^2}/u_\tau^2$ are plotted in figures 4.1 to 4.6 for the case Re = 20500. The respective curves for the smaller flow rate are depicted in figures 4.7 to 4.12; these match the trends of their higher Reynolds number counterparts. Figure 4.1 indicates that all the models slightly underpredict the centreline mean velocity, especially the k-ε model. The predictions for U^+ are shown by figure 4.2 to possess the same tendencies as the mean velocity.

The data for turbulence energy (obtained by combining the experimental normal stresses $k=\frac{1}{2}\overline{u_i'u_i'}$) exhibits a sharp near-wall peak in figure 4.3, which is not quite matched by the computed values. The simulations also overpredict the centreline values of k. As regards the maximum level of k, the CR model yields the highest whereas the LS, LSY, k-ε and RNG models all predict similar, lower values. Additional confirmation that the LS model was correctly implemented in the TEACH code is provided by the fact that the above profiles obtained with this model exhibit the same tendencies as those in a simulation by Myong & Kasagi (who also used the LS model), of the Laufer (1954) pipe flow (Re=50000). Furthermore, the k profiles for turbulent channel flow obtained by Craft et al (1996) with the CRY model are very similar to those calculated presently. Suga (1995) reported identical trends in his application of the CRY model to the pipe flow of Laufer (1954). As well as diminishing $\partial P/\partial x$, u_τ and ε_w^+, employment of the Yap factor by the nonlinear model also causes a reduced peak for k.

The predicted profiles of Reynolds shear stress at Re=20500 are plotted in figure 4.4. Durst et al (1993) did not provide experimental data for this parameter. The main difference between high and low Reynolds number models is the level of peak Reynolds shear stress near the wall. Only the k-ε and RNG models return a normalised value of

unity. This apparent discrepancy is even more marked in the case of the lower flow rate (Re=7500).

The cubic model distinguishes itself from the linear EVM's when a comparison is made of the normal stresses (figures 4.5, 4.6, 4.11 and 4.12). Whilst the LS, k-ε and RNG models predict values which are several orders of magnitude smaller than those of CRY, the nonlinear model is in closer agreement with the experimental profiles of $\overline{u'^2}$. Although still severely underpredicting the axial normal stresses, the nonlinear model does correctly locate the point at which the maximum value of $\overline{u'^2}$ occurs. Despite this improvement over the linear EVM's, the nonlinear model computes negative $\overline{v'^2}$ profiles, which is not physically realistic. It is alarming to note that Craft et al (1996) predicted positive profiles for *all* normal stresses in a turbulent channel flow; Suga (1995) did likewise for the Laufer (1954) Re=50000 pipe flow. The cause of this anomaly, and its potential effects in other flows, is considered in the following section.

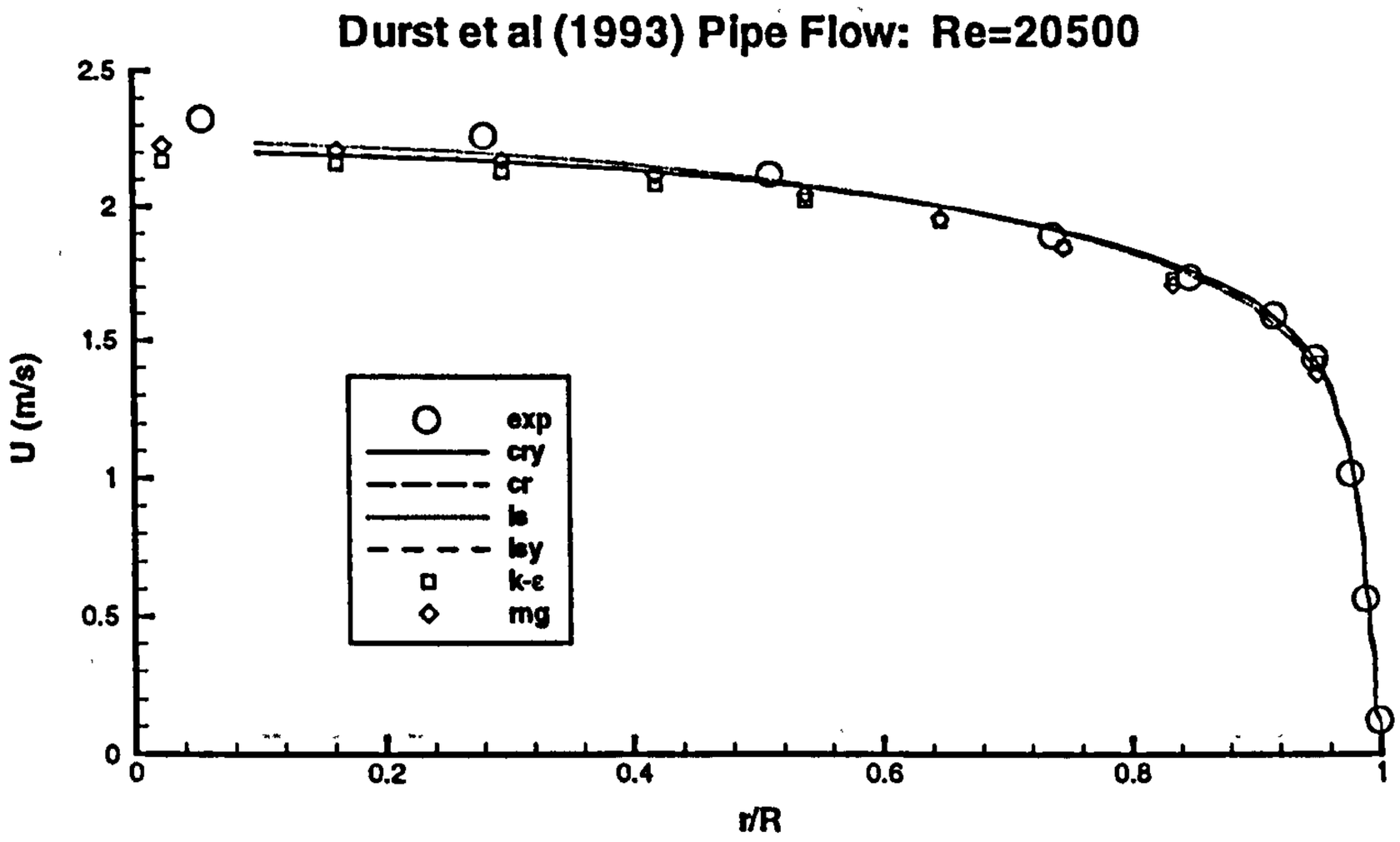

Figure 4.1: Comparison of axial velocities.

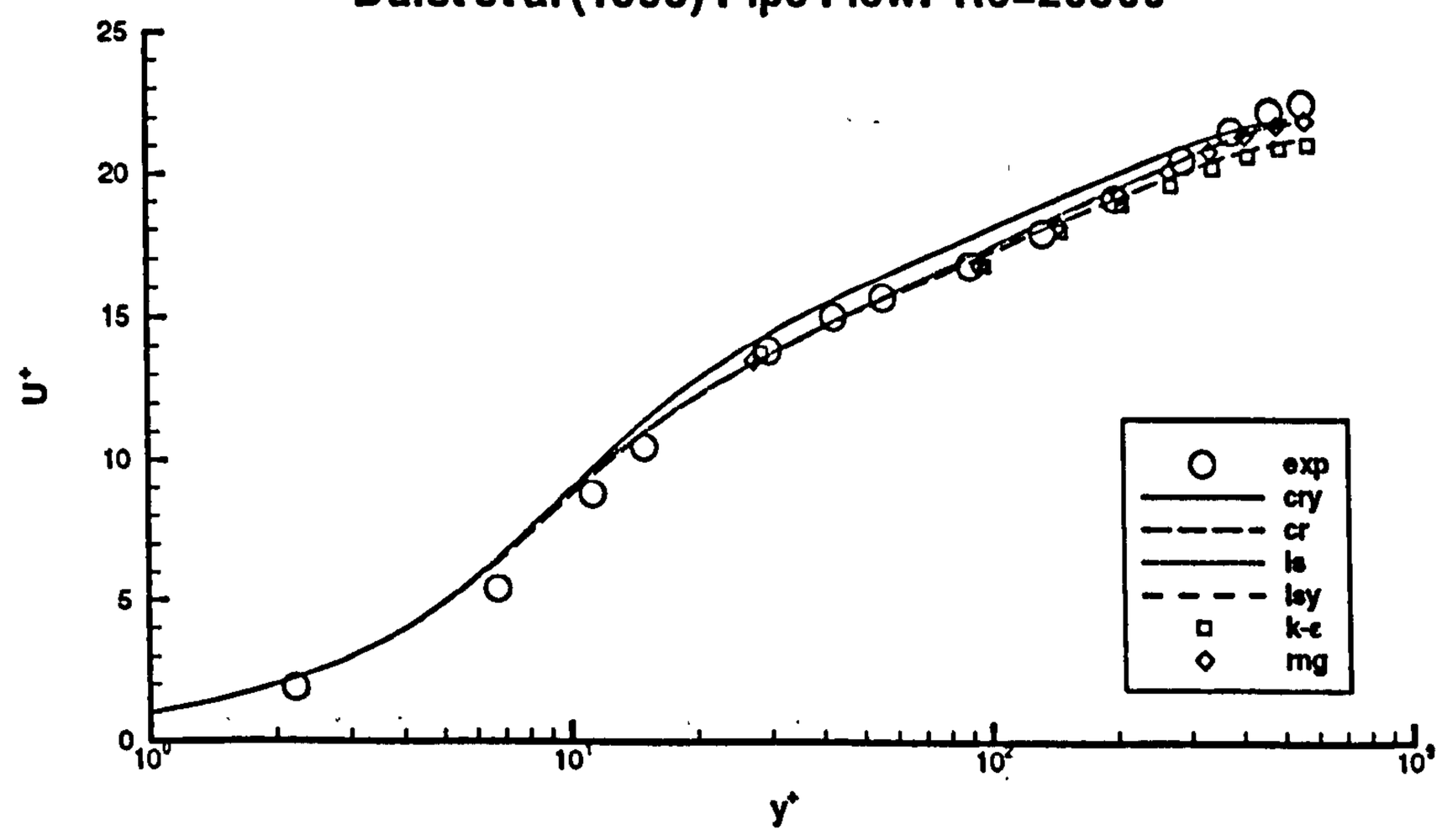

Figure 4.2: Comparison of U^+.

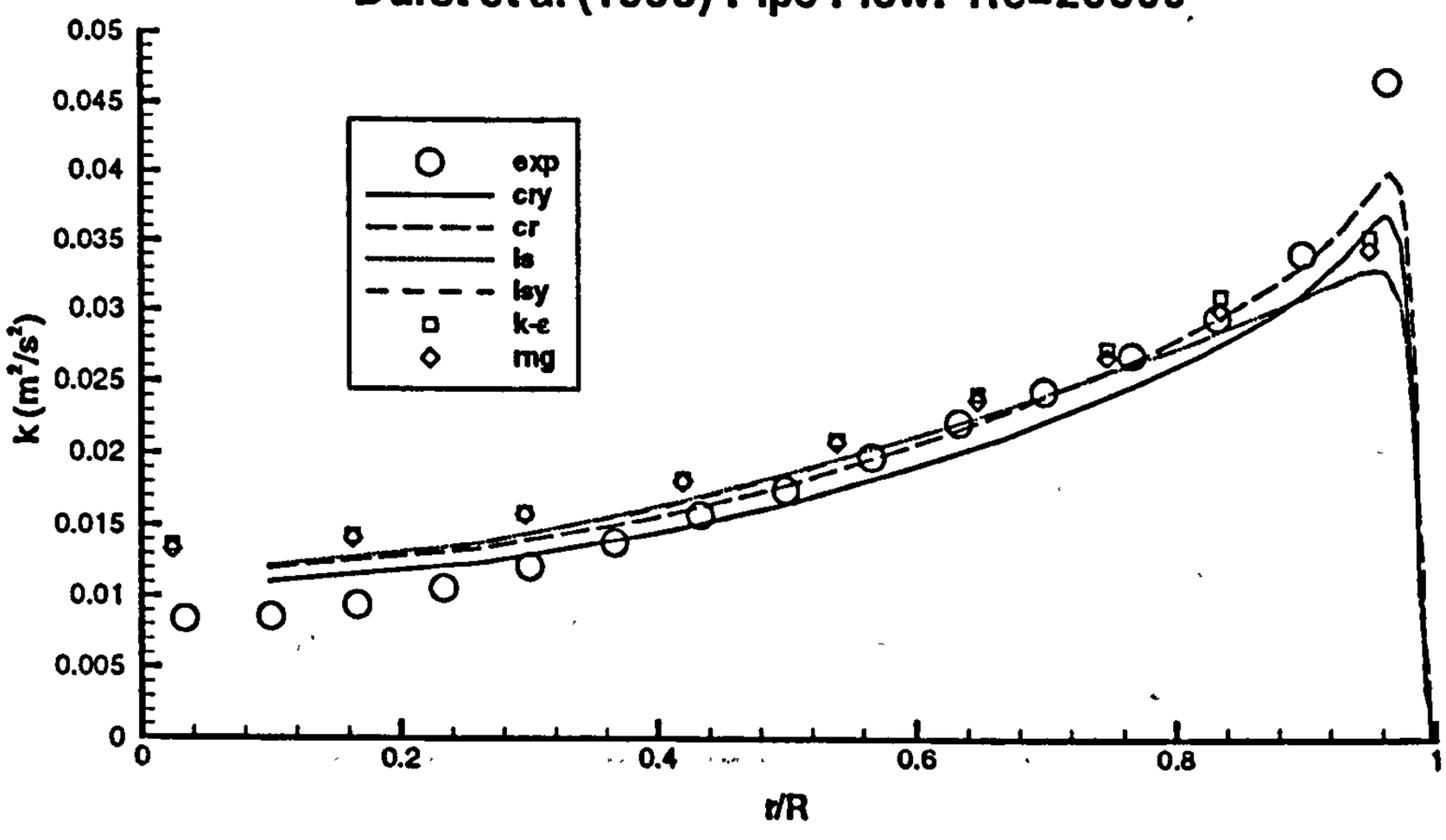

Figure 4.3: Comparison of turbulence energy.

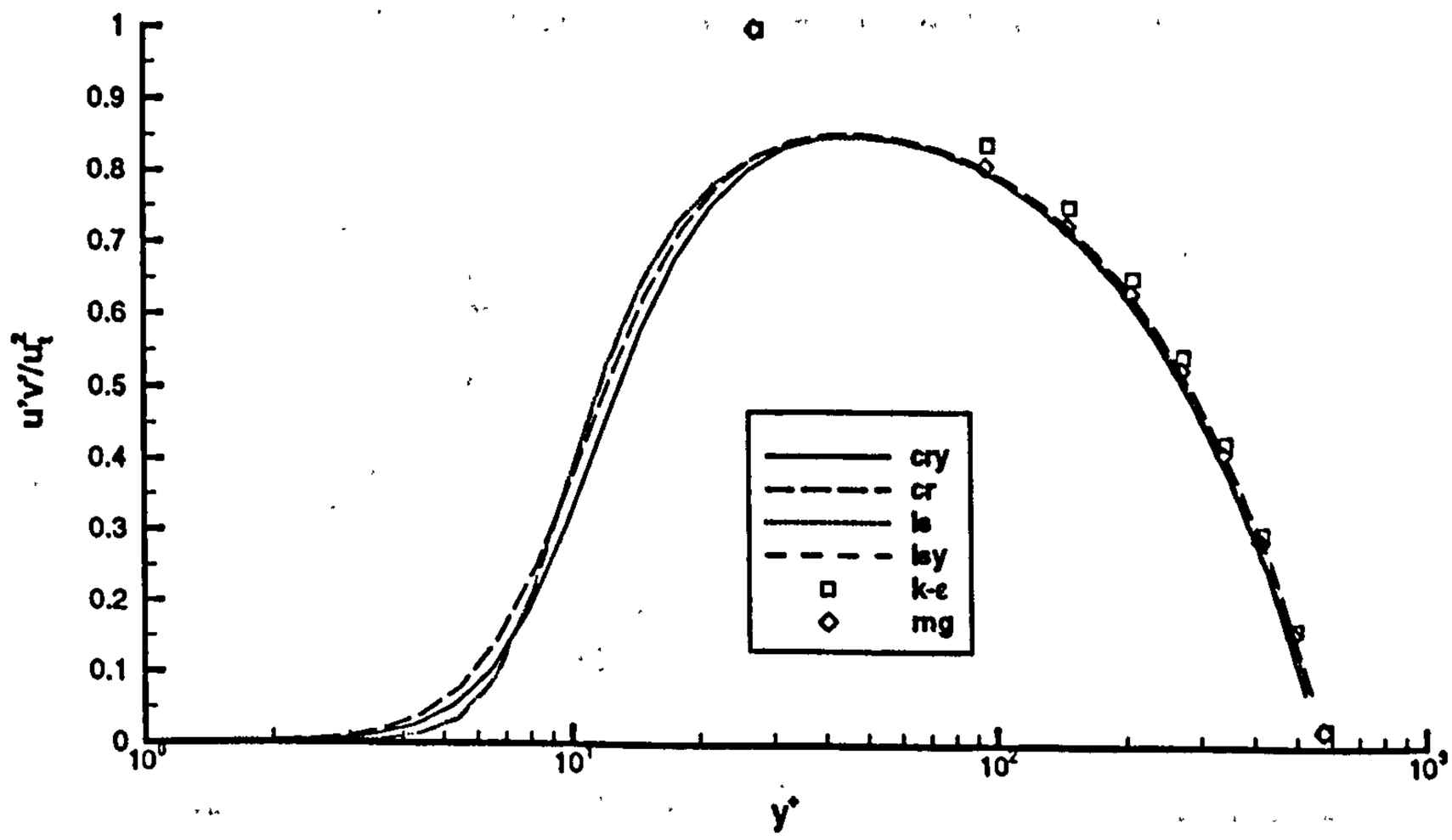

Figure 4.4: Comparison of Reynolds shear stress.

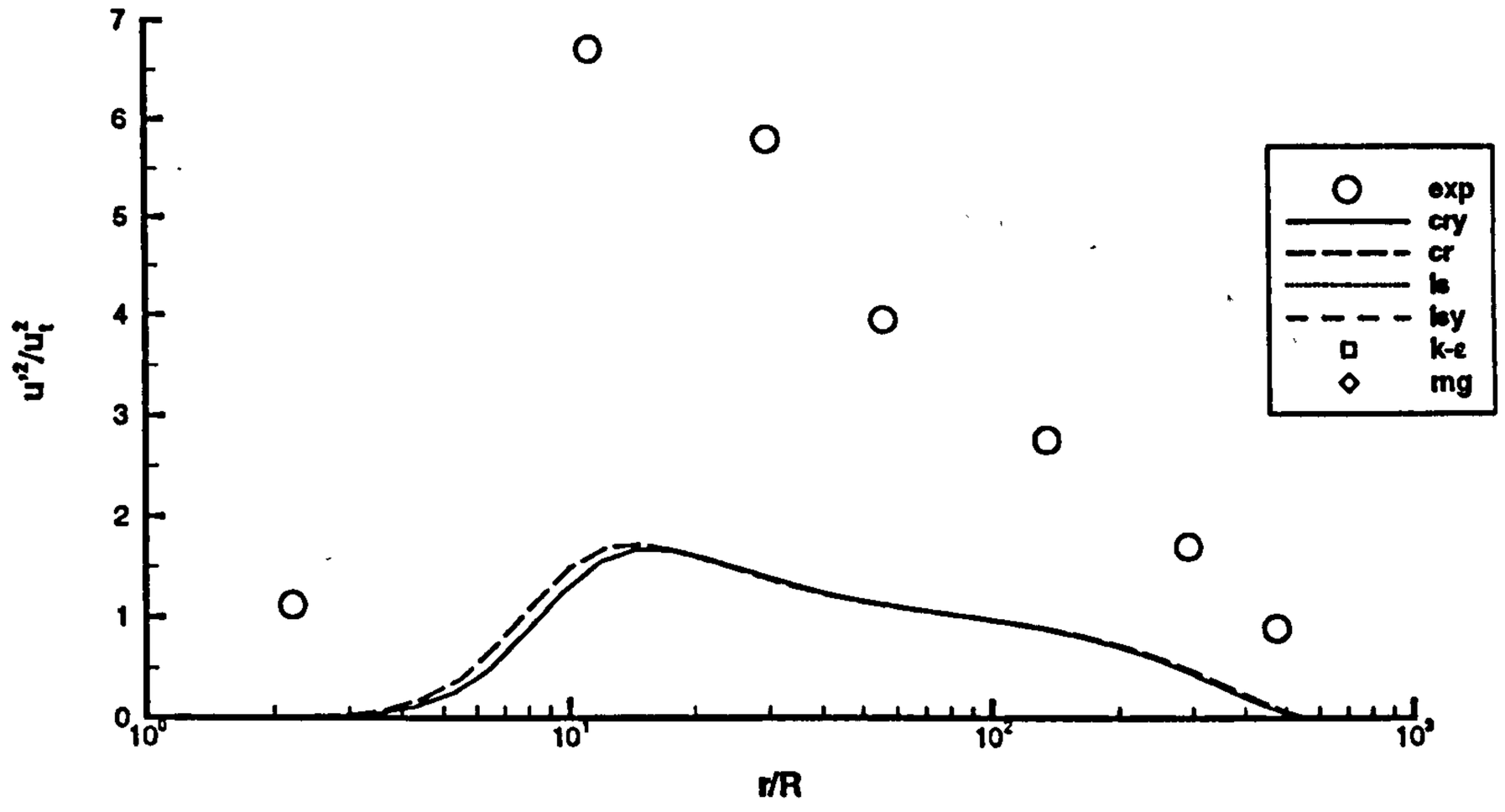

Figure 4.5: Comparison of normal Reynolds stress (axial). Note that the linear EVM predictions are at least three orders of magnitude smaller.

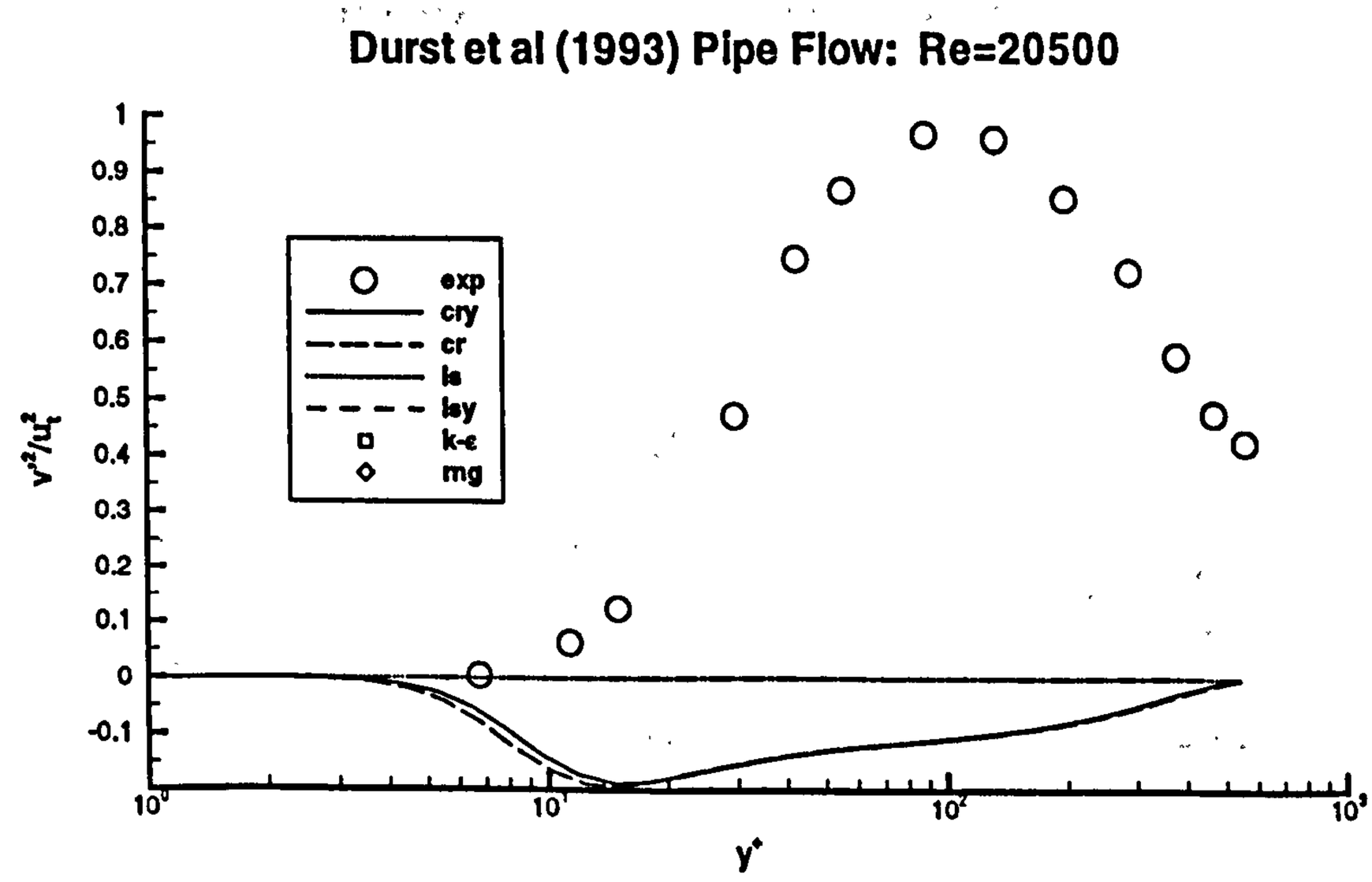

Figure 4.6: Comparison of normal Reynolds stress (radial). Note that the linear EVM predictions are at least three orders of magnitude smaller.

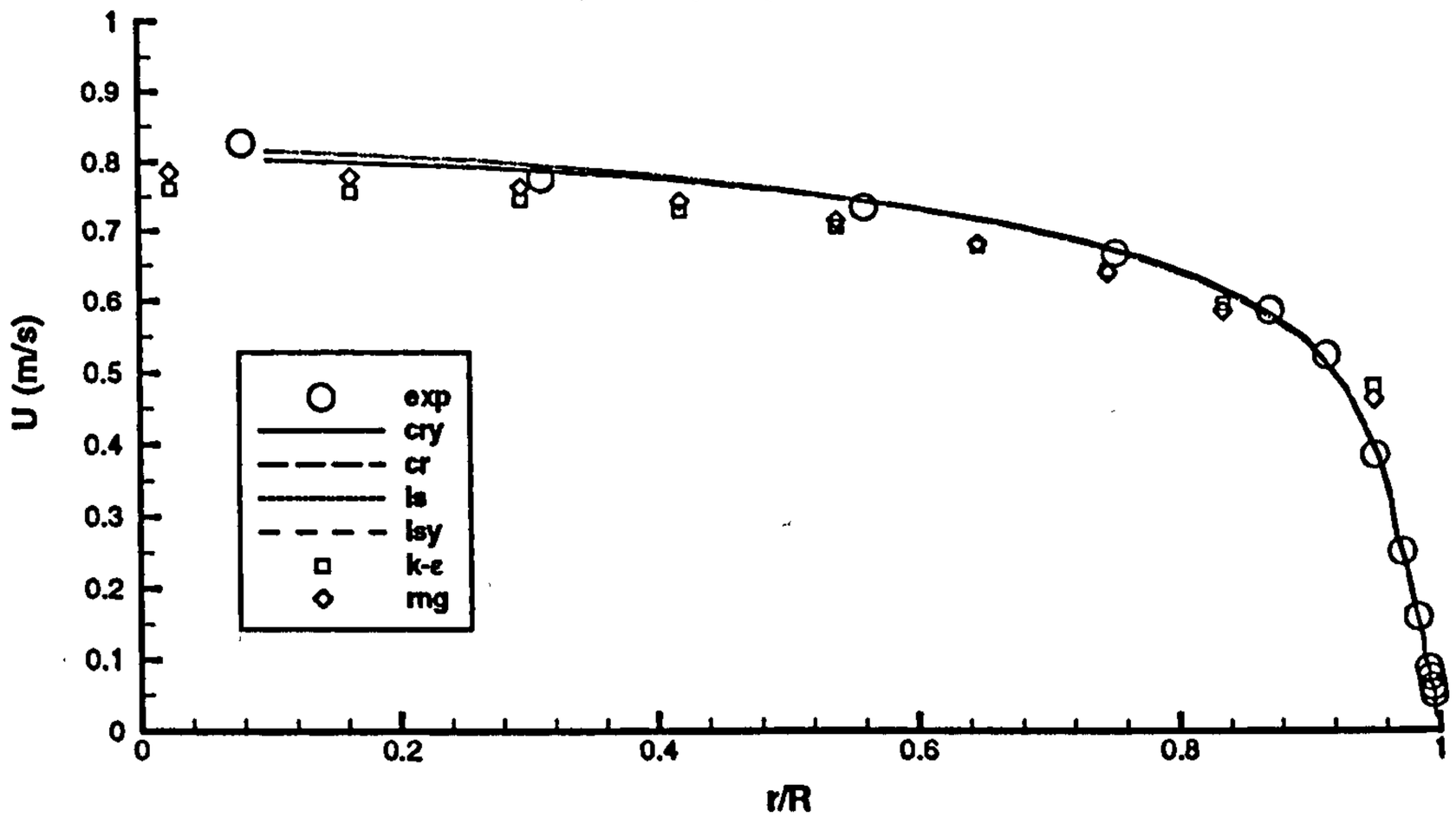

Figure 4.7: Comparison of axial velocities.

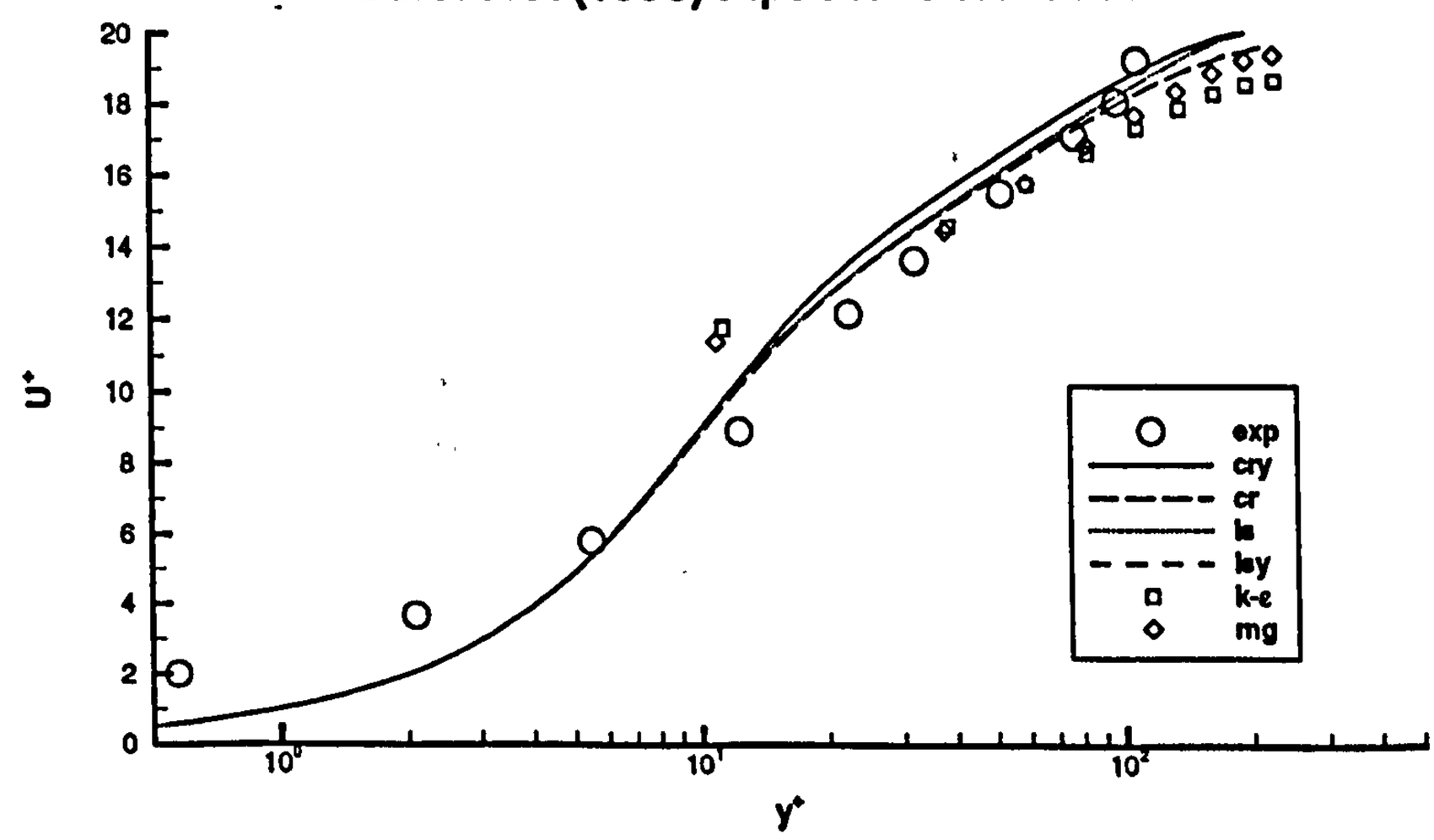

Figure 4.8: Comparison of U^+.

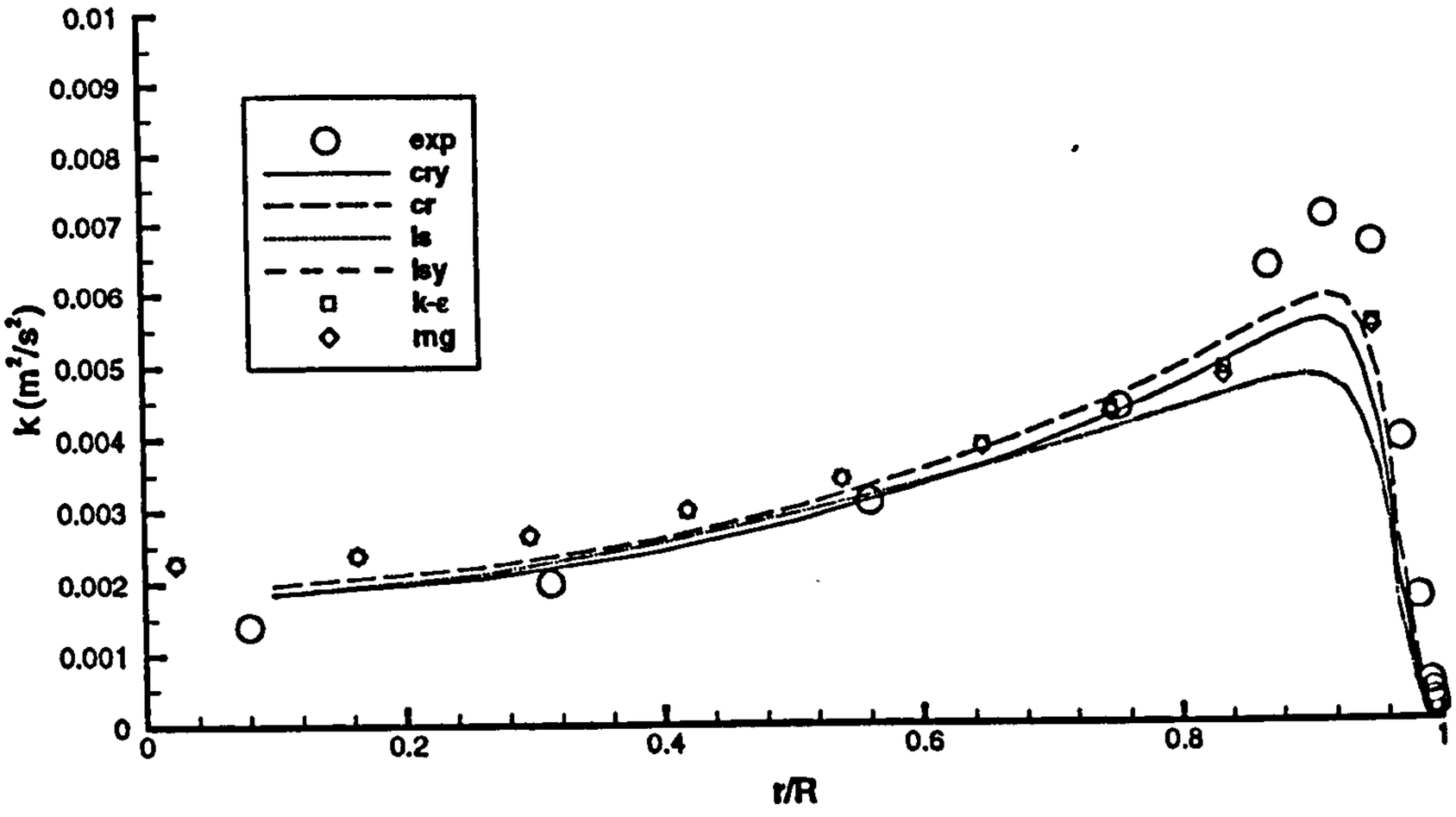

Figure 4.9: Comparison of turbulence energy.

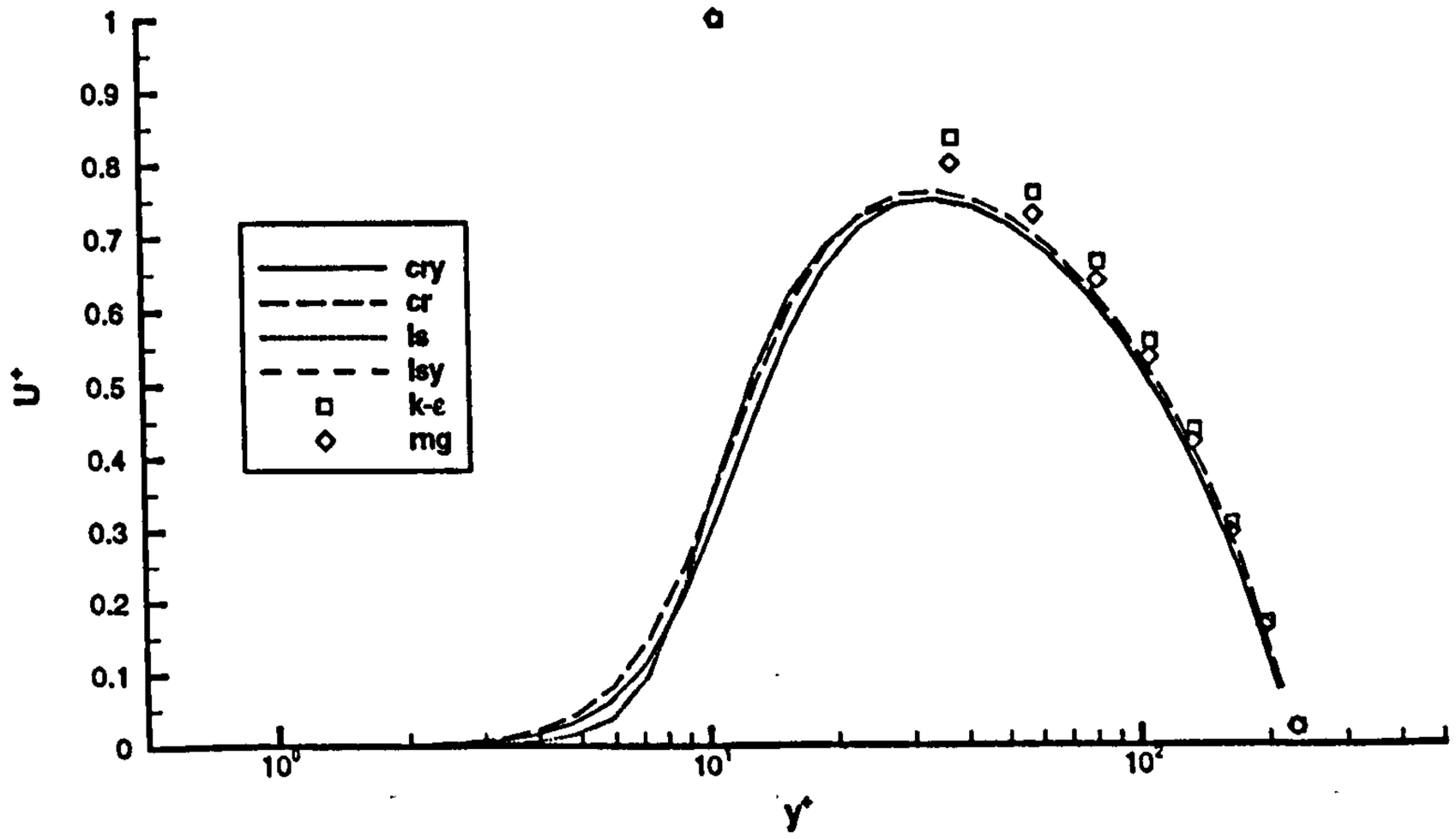

Figure 4.10: Comparison of Reynolds shear stress.

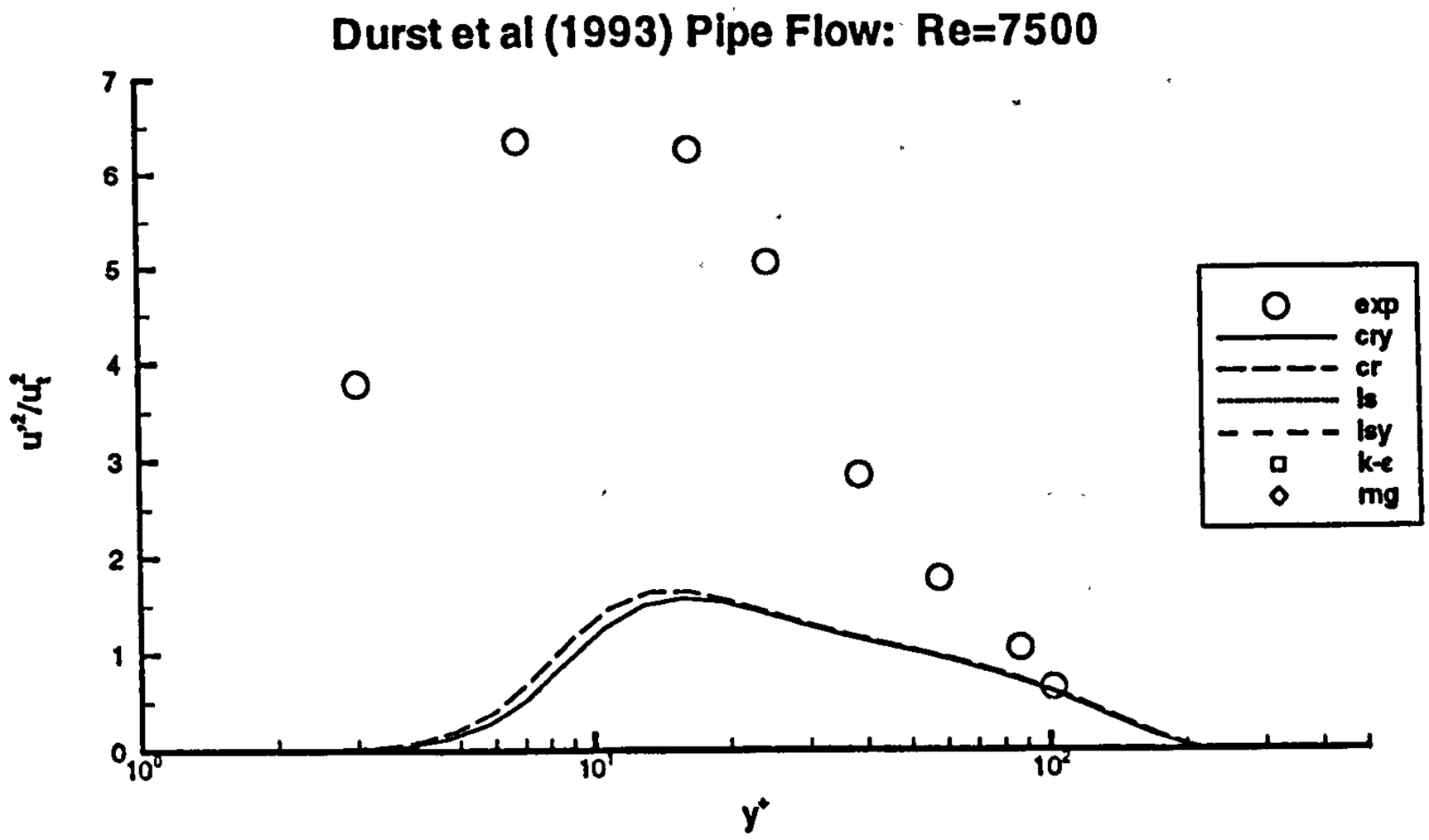

Figure 4.11: Comparison of normal Reynolds stress (axial). Note that the linear EVM predictions are at least three orders of magnitude smaller.

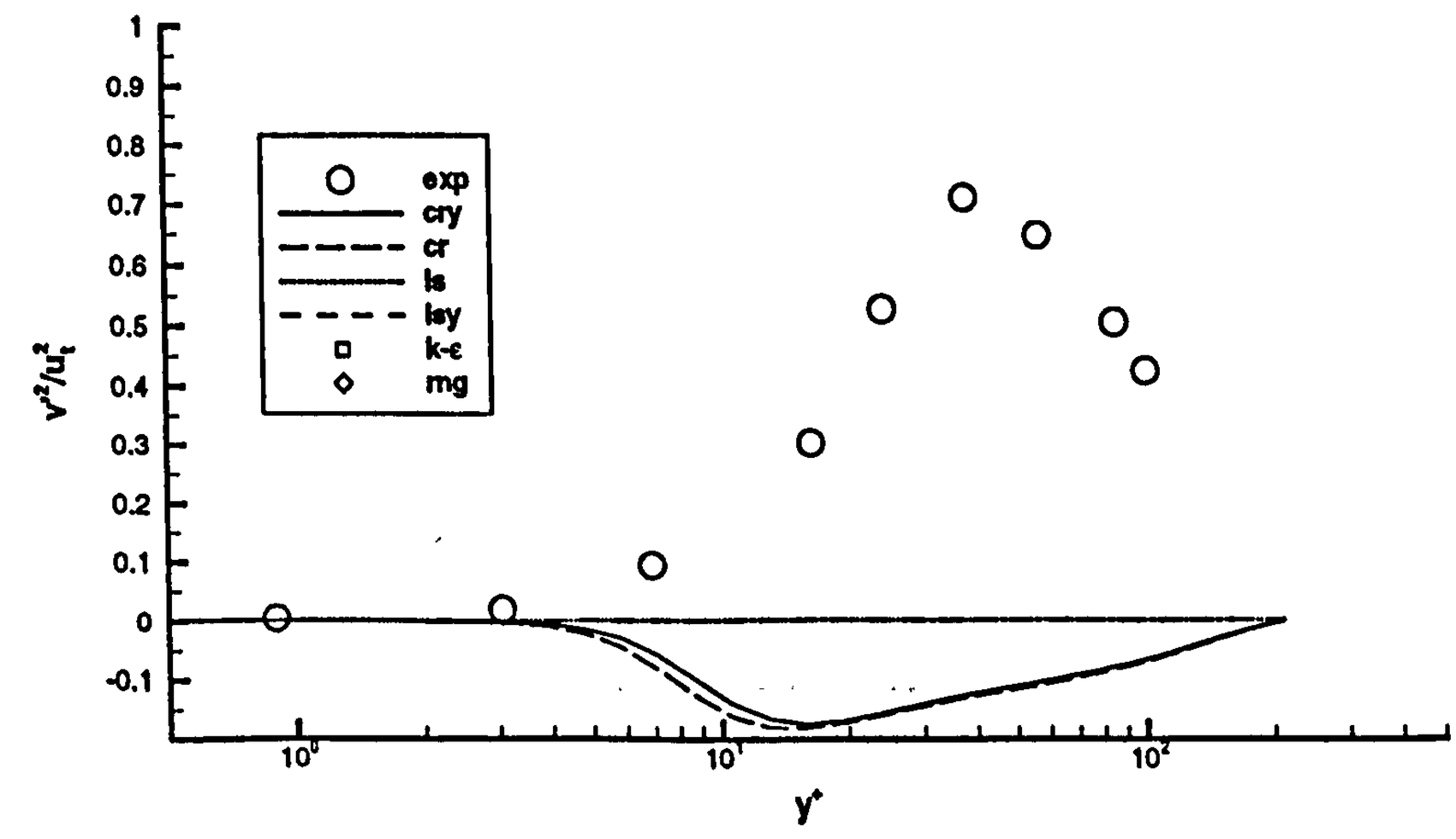

Figure 4.12: Comparison of normal Reynolds stress (radial). Note that the linear EVM predictions are at least three orders of magnitude smaller.

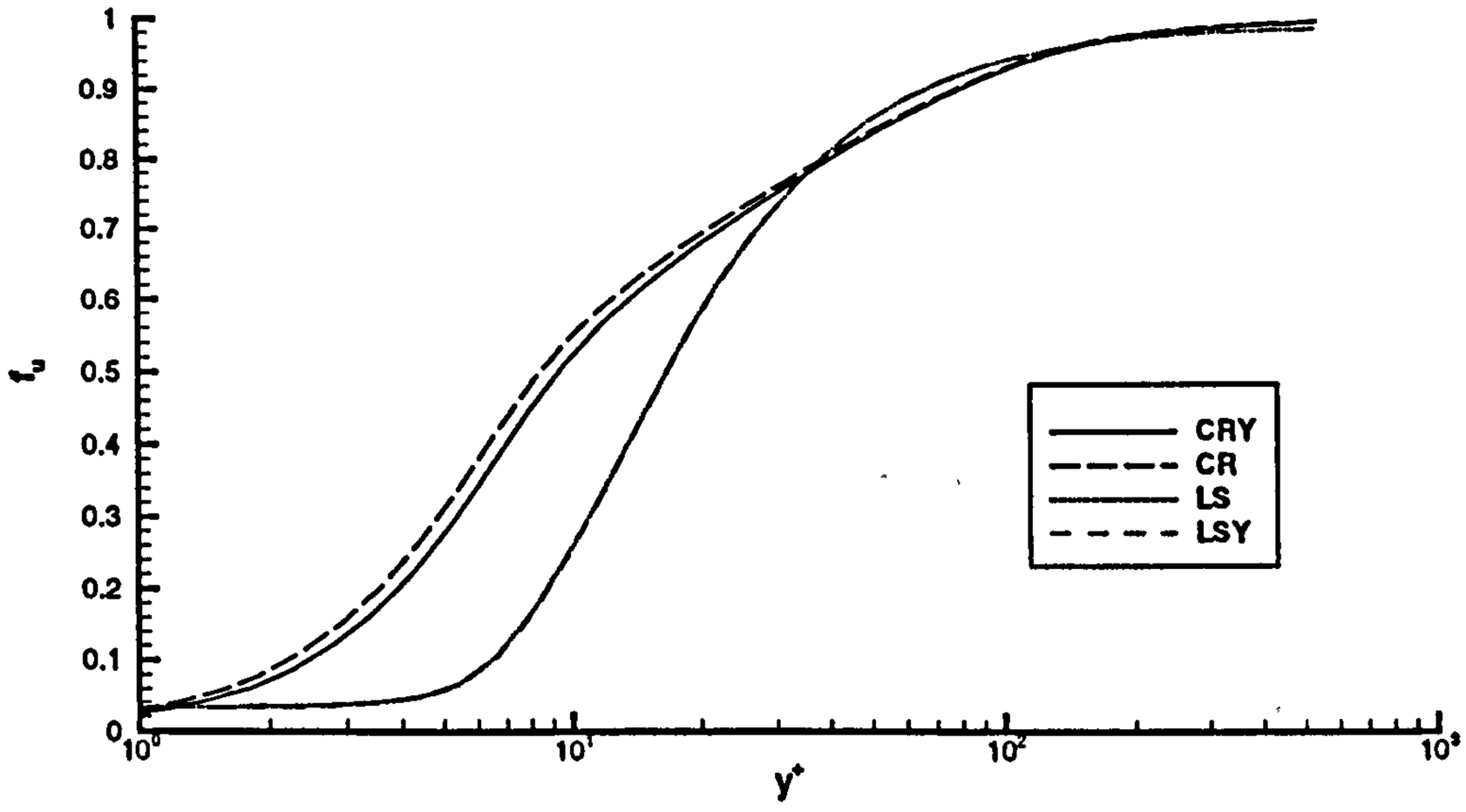

Figure 4.13: Comparison of damping function f_μ.

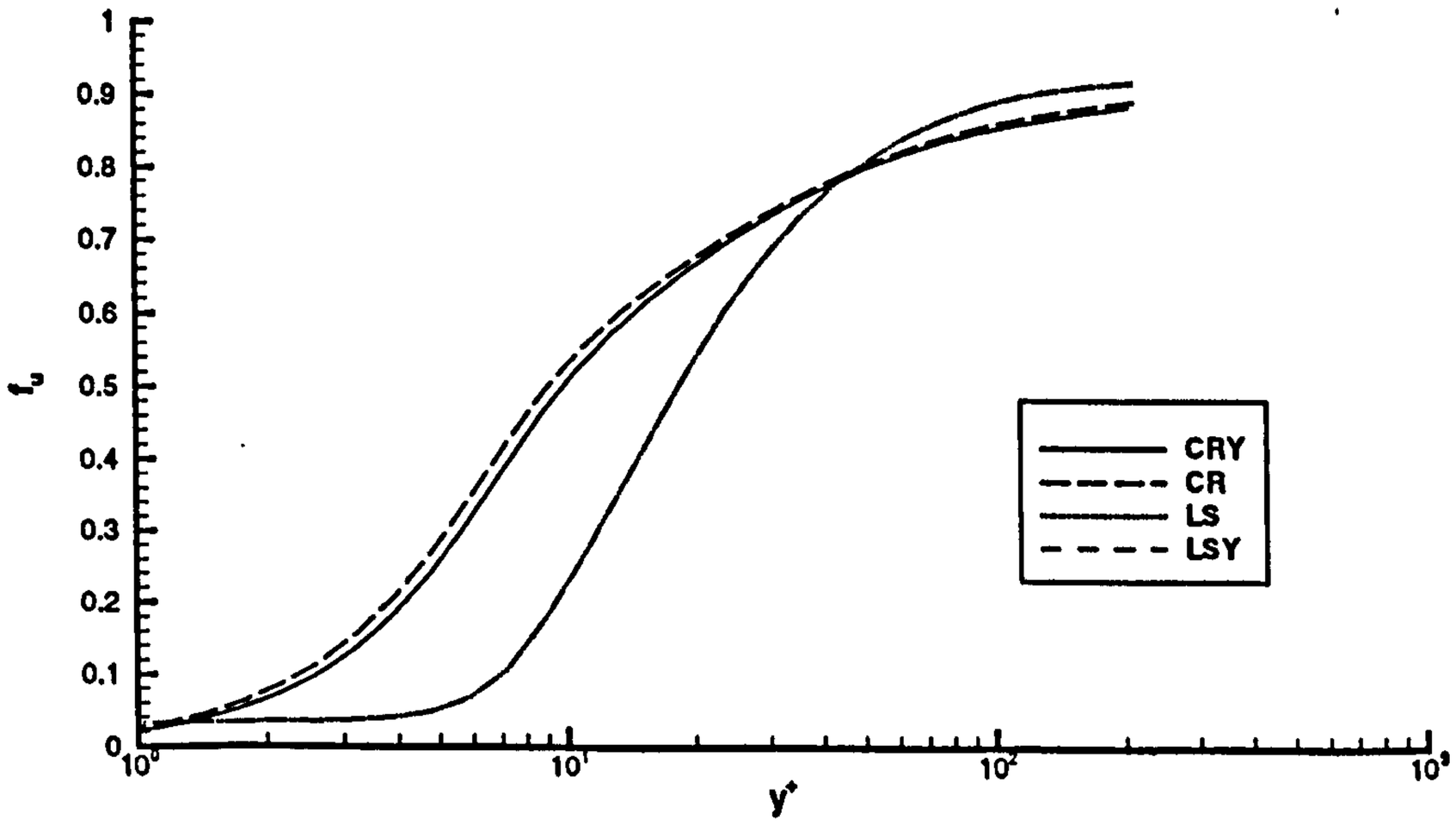

Figure 4.14: Comparison of damping function f_μ.

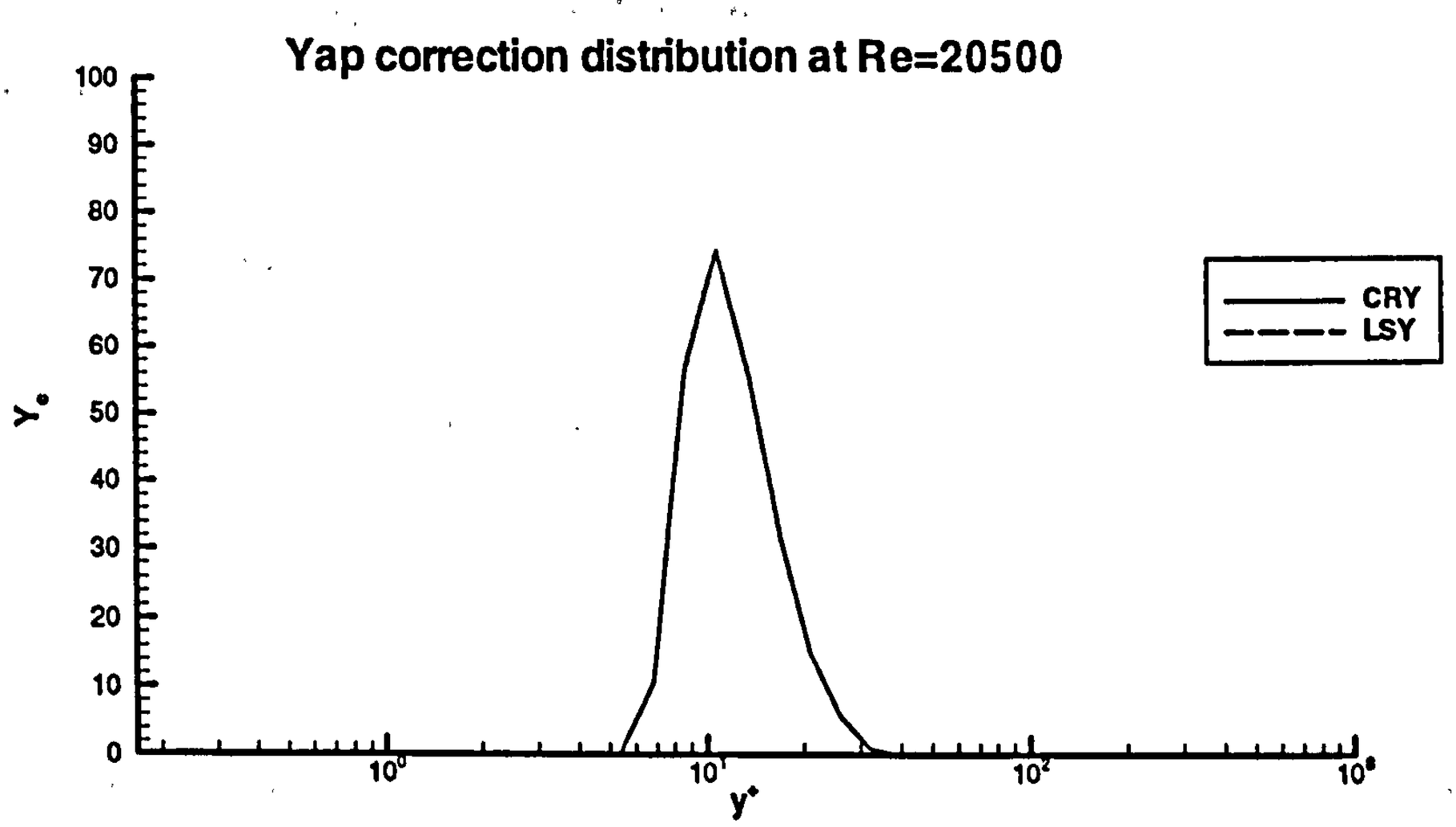

Figure 4.15: Radial distribution of the Yap correction term Y_c. Note that the LSY curve is zero for all y^+.

4.1.2 Discussion

An overview of the results reveals that the turbulence models generally yielded similar results for the pipe flow, which tended to agree with experimental trends. The sole major difference occurred in the normal stresses. Only the nonlinear model was able to predict unequal stresses, although negative normal stresses in the radial direction were calculated. One of the main concerns of the present discussion is to resolve this issue and to determine how other simulations can be affected. The remainder of the section is devoted to explaining the differences in predictions between the various turbulence models.

A thorough examination of the numerical methodology adopted by Suga (1995) revealed that the tangential normal stress was not calculated explicitly as in the TEACH code; rather, the following relationship was used:

$$\overline{w'^2} = 2k - \overline{u'^2} - \overline{v'^2} \tag{4.5}$$

This formulation provides a closer link between turbulence energy and normal stresses, and seems to prevent negative normal stresses from arising. In fully-developed pipe and channel flows, the only important Reynolds stress in momentum equations (see Appendix A) is τ_{xy} because the terms $\partial\overline{u'^2}/\partial x$ and $\partial\overline{v'^2}/\partial y$ are zero. Thus the normal stresses do not contribute to the predictions of U, k and $\overline{u'v'}$ and the negative values of $\overline{v'^2}$ are not problematic in simple flows. Similarly, in more complex flows the gradients of normal stresses are significantly smaller than the gradients of shear stresses, thereby indicating that the normal stresses themselves do not directly affect results. Supporting evidence for this is given by an order-of-magnitude analysis of the axial momentum equation in the case of swirling pipe flow (described later in this Chapter).

Results indicated that the high Reynolds number turbulence models accurately predicted the shear stress in the turbulent boundary layer whilst the low Reynolds number models returned smaller values.. The correct predictions by the k-ε and RNG models is not surprising in light of the fact that the derivation of wall functions is based on thin shear layer considerations which are valid in pipe flows. At the same radial

location ($y^+ \approx 42$) the LS and CRY models return $\overline{u'v'}/u_\tau^2 = 0.85$. Since this point is close to the wall, viscous effects can be significant. The normalised, laminar shear stress for the CRY model was computed as approximately 0.07 (at Re=20500), resulting in a total shear stress of $\left(\upsilon \partial U/\partial r + \overline{u'v'}\right)/u_\tau^2 = 0.92$. Thus consideration of viscous effects brings the low Reynolds number model predictions in line with the correct near-wall behaviour.

Comparison of the radial distributions of the damping function (figures 4.13 and 4.14) with U^+ (figures 4.2 and 4.8) reveals that the entire boundary layer is influenced by the effects of f_μ. Thus the near-wall differences (notably in k) between the LS and CRY models is mainly due to the differing damping functions (equations 2.25 and 2.38). This observation is closely linked to the detrimental influence of the Yap factor on the cubic model but not on the LS model. Inspection of the radial profile in figure 4.15 (for the Re = 20500 case) reveals that $Y_c = 0$ along the entire radius in the case of the LSY model, whereas the CRY model predicts a sharp, non-zero peak in the buffer layer at $y^+ = 10.5$. Further analysis shows that the maximum values of the quantity l/l_{bl} (see equations 2.42 to 2.44) are 0.962 and 1.121 for the LSY and CRY models, respectively. As documented in section 2.1.2, the Yap term is only included if this ratio is larger than unity. In the present case, only the CRY model 'triggers' the Yap correction, which brings about a reduction in turbulence energy. The reduced peak for k in the LS and LSY models is caused by the excessive damping of the eddy viscosity, and hence turbulence production P_k, which is brought about by the fact that the damping function f_μ remains at its near-wall asymptotic value until well into the buffer layer (see figures 4.13 and 4.14), causing l/l_{bl} to be smaller than unity. This explains why the Yap factor produces no difference between the LS and LSY results. A consequence of the non-zero Yap correction in the CRY model is the modification of near-wall gradients, resulting in the underpredicted quantities in table 4.1. This poses interesting questions as regards the suitability of the CRY model for general purpose computations. The Yap term could be adjusted for pipe flow if the coefficient 0.83 in equation 2.42 is retuned, but this could have negative repercussions when applied to other flows.

The main findings and conclusions of the fully-developed pipe flow investigation are as follows:

- The nonlinear model can predict negative values for $\overline{v'^2}$ because all three normal stresses are computed explicitly rather than using equation 4.5.
  - This has no bearing on the pipe flow predictions (and thin shear layers in general).
  - It is expected to have little effect in more complex flows. Supporting evidence is supplied in the investigation of highly-swirling pipe flow (section 4.5).
- Damping functions are influential in near-wall regions. This case did not provide much scope for testing the contributions of the nonlinear terms. The main purpose, though, was to confirm that the cubic model was correctly implemented in the TEACH code.
- The Yap correction term has a detrimental effect on the near-wall predictions of the nonlinear model in this particular flow.

4.2 PIPE EXPANSION - TROPEA et al (1989)

In order to test the performance of the turbulence models for recirculating flow, the pipe expansion studied by Tropea et al was selected. High quality LDV data was provided in the form of detailed radial distributions at various axial locations. This data was available on the well-known ERCOFTAC web site. The inlet and exit diameters are D_1=50mm and D_2=80mm, respectively, and the domain length is 0.7m. The fluid is an oil mixture of density 863.5 kg/m^3 and kinematic viscosity 6.3×10^{-6} m^2/s. The Reynolds number of 15600 is based on D_1 and the inlet centreline velocity (2.51 m/s), where the flow is fully developed. Figure 4.16 shows the geometry.

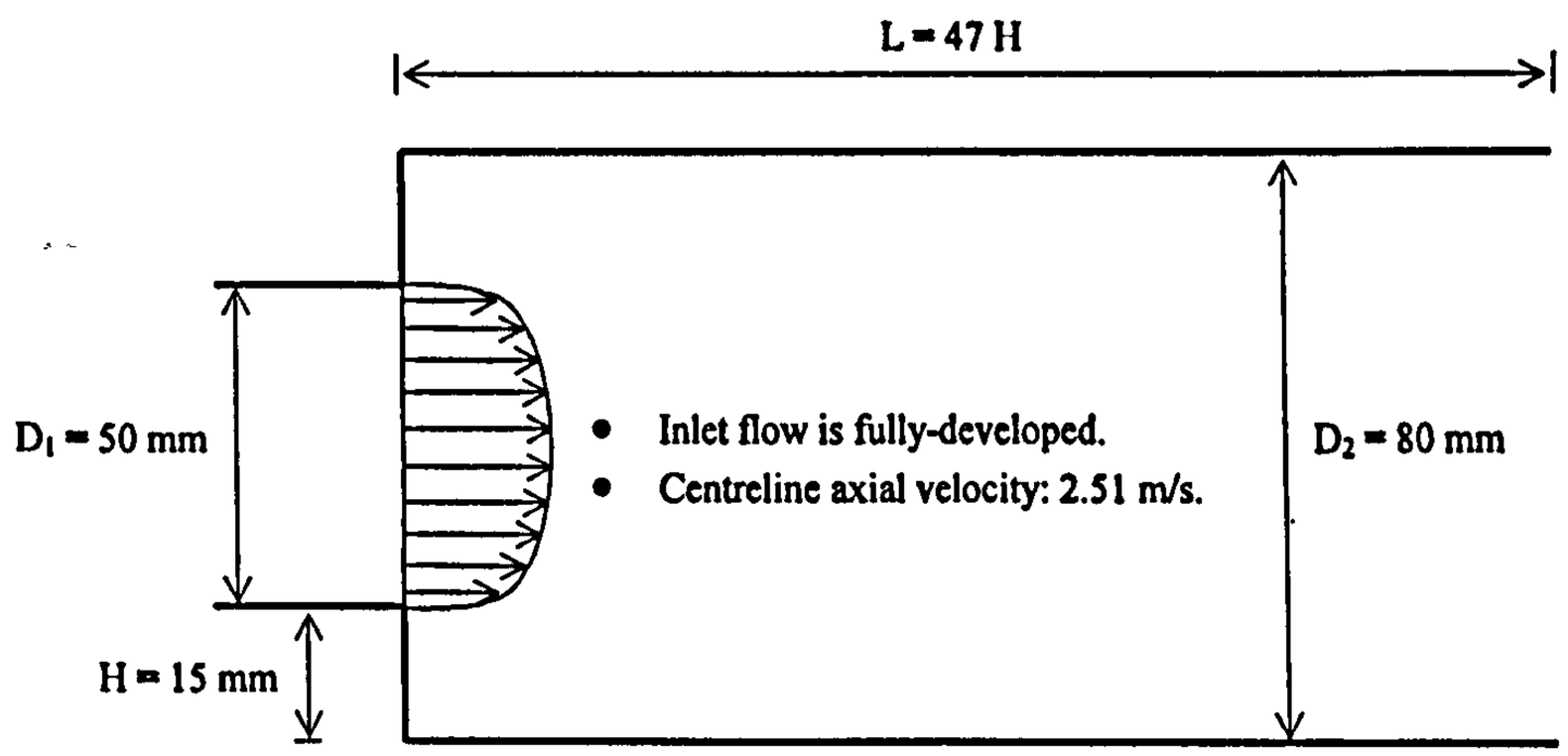

Figure 4.16: Schematic representation of the pipe expansion.

Experimental inlet profiles were available for the mean velocity U and for the normal stresses $\overline{u_i'^2}$; inlet values of k were computed with $k=\frac{1}{2}\overline{u_i'u_i'}$ and an entry profile for ε was obtained from relation 3.6 where L=D_1. It was assumed that $\tilde{\varepsilon}_{in}=\varepsilon_{in}$, despite the fully-developed nature of the inlet flow implying that $\partial\sqrt{k}/\partial r\neq 0$. In similar computations Chang et al (1995) found that the assumed profiles of k and $\tilde{\varepsilon}$ do not significantly affect the flow field calculations for pipe expansions, except in the presence of high turbulence intensity and in a very short region immediately behind the step. This is further supported by the study in Appendix F which shows that the reattachment length did not change when a different formulation was used for the inlet dissipation rate.

All the computational meshes used were sufficiently dense so as to provide a solution independent of the grid. The radial meshes were refined near the top wall and the axial grid was refined near the step. Grid independence was ascertained by comparing skin friction plots and reattachment lengths for progressively larger meshes. The simulations with the standard k-ε and RNG models utilised a 200×39 mesh to ensure that the near-wall nodes were placed in the inertial sublayer (52% of near-wall nodes were located at $y^+ > 30$ whilst 98% were located at $y^+ > 13$). The grid for the high Reynolds number models is depicted in figure 4.17.

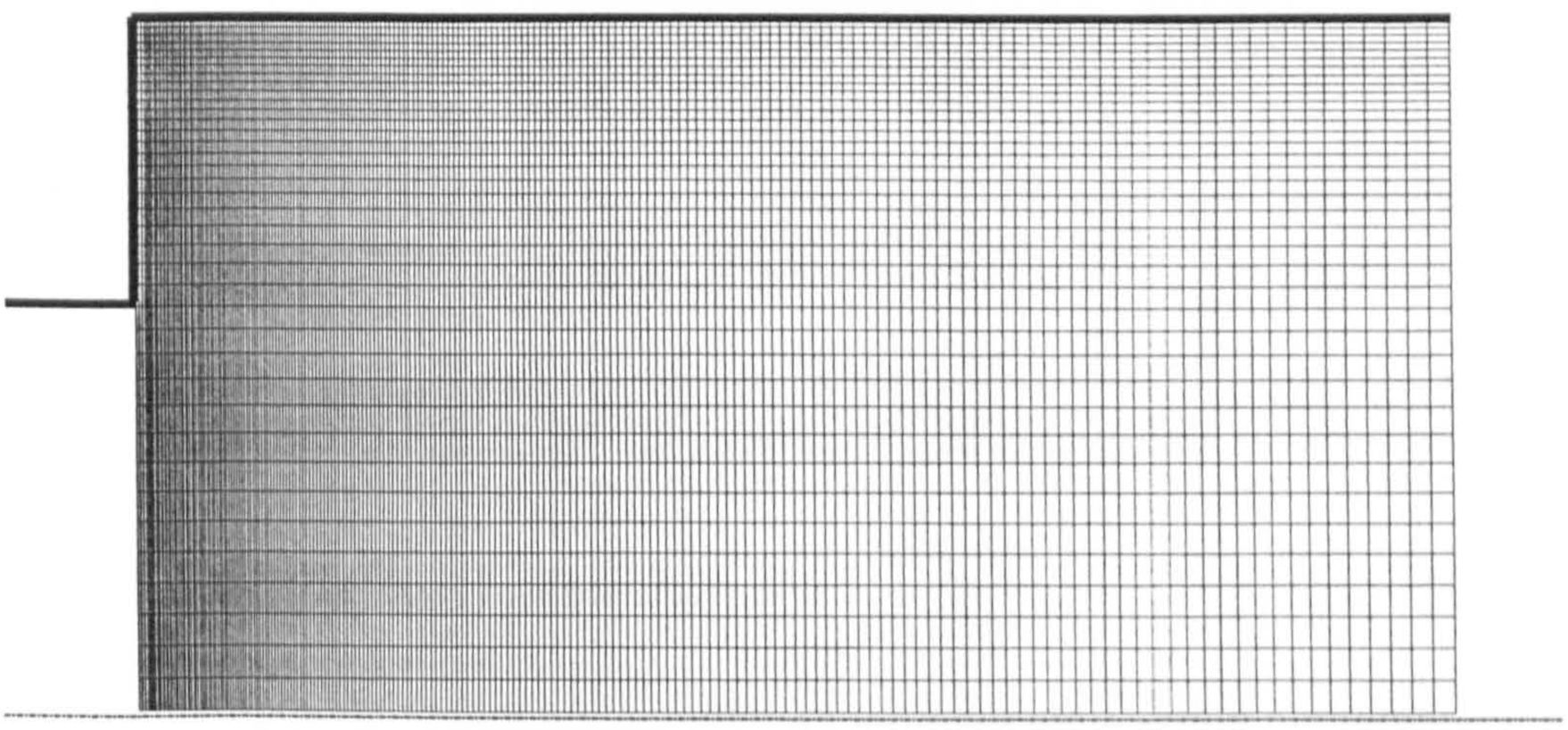

Figure 4.17: The 200×39 computational grid as used by the high Reynolds number turbulence models.

Figure 4.18 proves that 39 radial nodes are sufficient. The simulations involving low Reynolds number models were performed on a 200×70 grid. Figure 4.19 shows that the low Reynolds number model results are grid independent. The boundary layer was further resolved with many more radial nodes (100 in total, whilst maintaining the same characteristics as the smaller grid), but this made no difference. The radial distributions of nodes ensured that the maximum Peclet numbers in the radial direction were less than 2 (0.124 and 0.734 for the CRY and k-ε models, respectively). The largest axial Peclet number was approximately 10; it occurred at the centreline near the inlet. Some concern existed as to the effect of numerical diffusion in the free shear layer, where the streamlines are at an angle to the grid and the axial Peclet number is greater than 2. However, figures 4.20 and 4.21, which are contour plots of Γ_f / μ_{eff} for the k-ε and

CRY solutions (where Γ_f is the false diffusion as computed with equation 3.1), respectively, reveal that this area of the flow is virtually free from error. The high values of this ratio near the back of the step are due to very low values of effective viscosity rather than excessively large numerical errors.

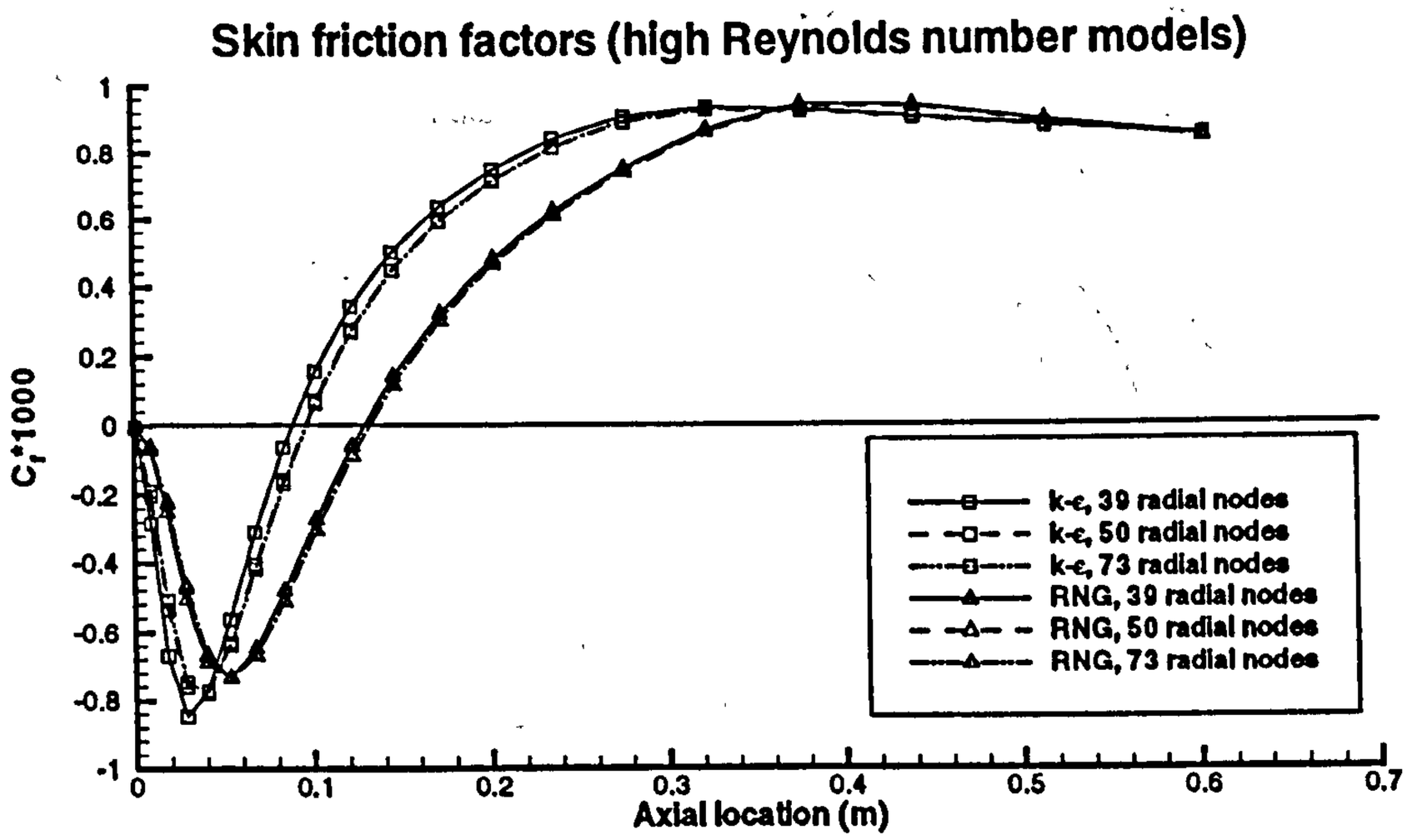

Figure 4.18: Demonstrating that the 200*39 mesh yields grid independence for the high Reynolds number models.

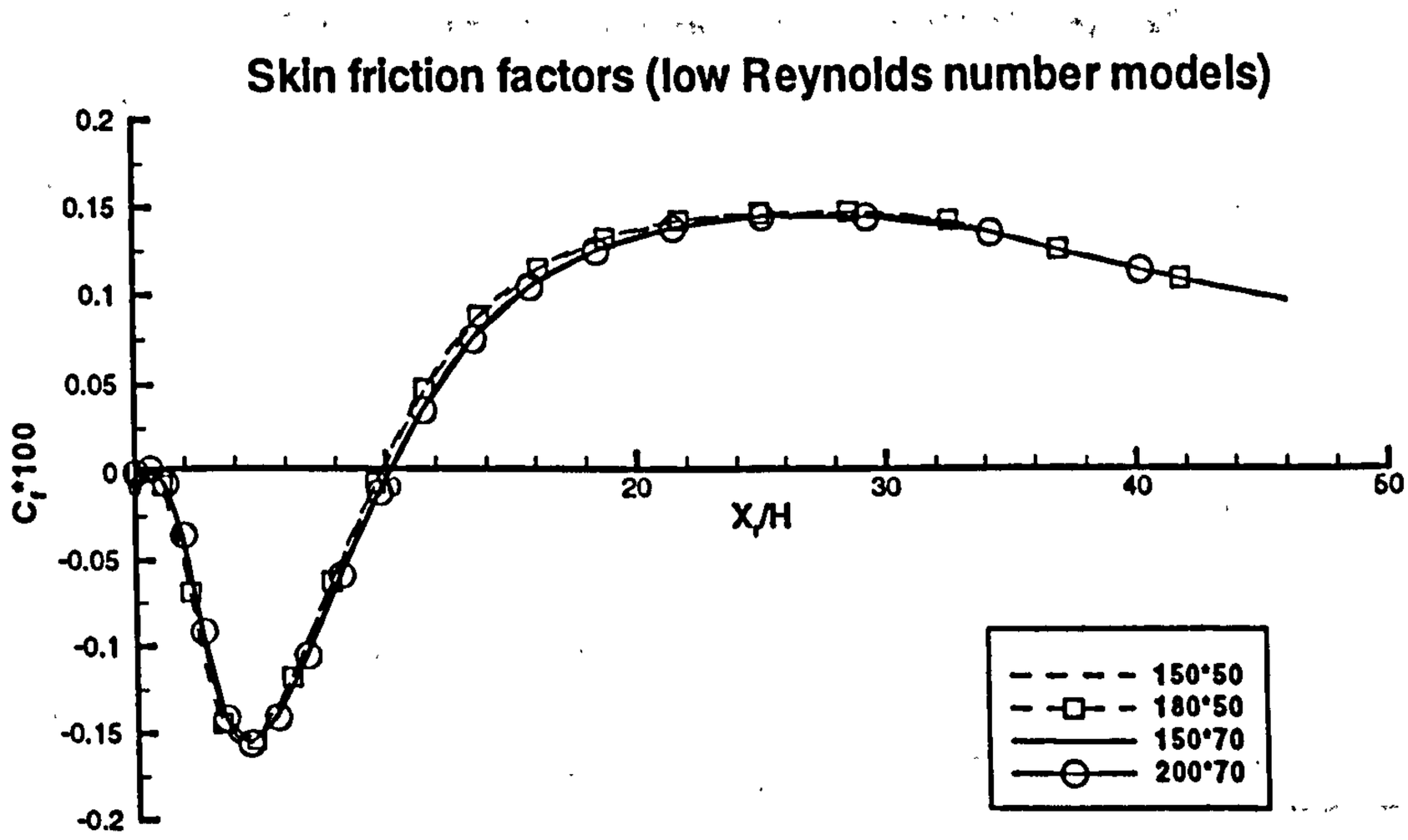

Figure 4.19: Demonstrating that the 200*70 mesh yields grid independence for the CRY model (and hence also for the LS model).

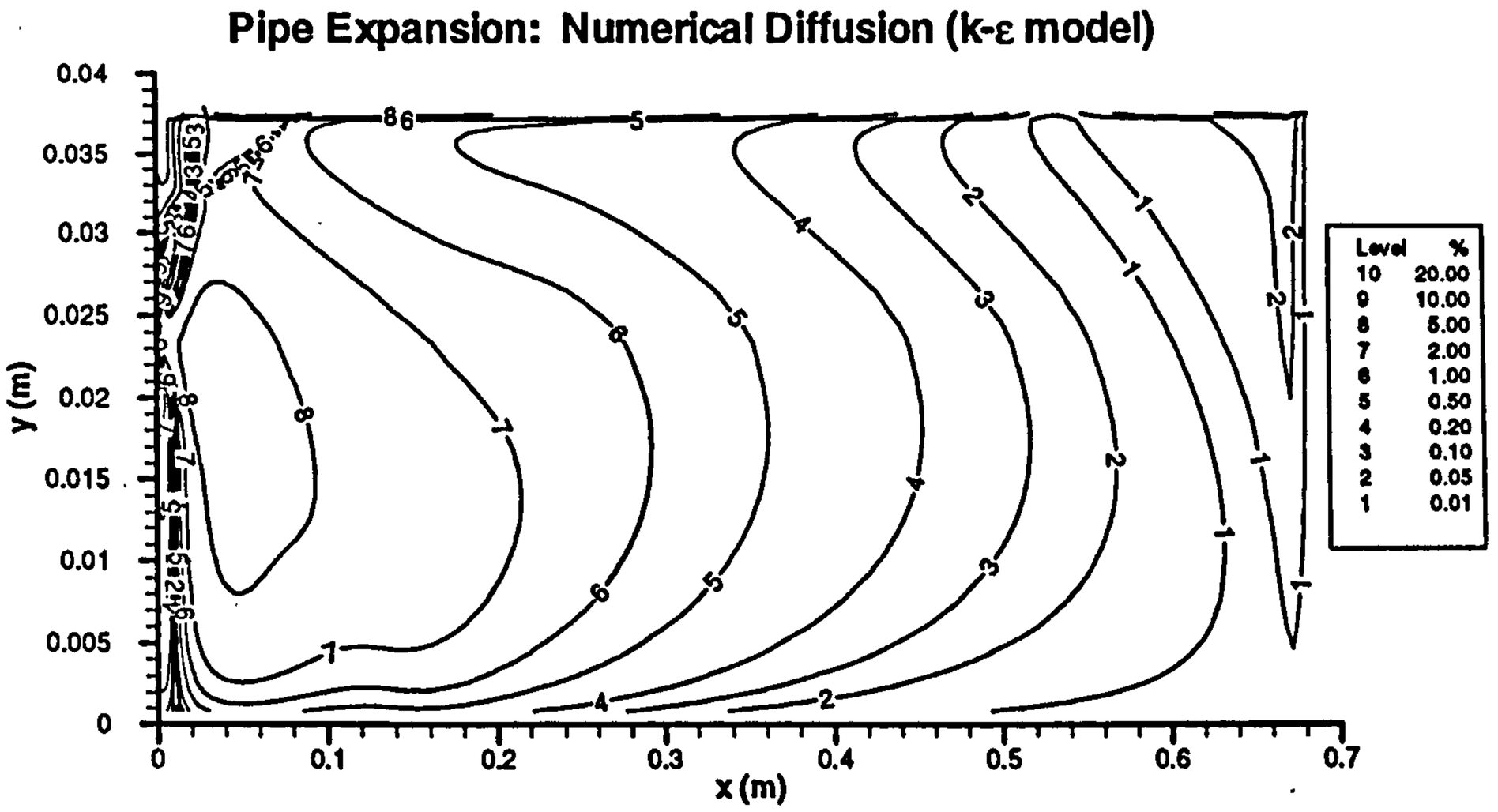

Figure 4.20: *k-ε* model: ratio of numerical diffusion and effective viscosity (Tropea et al (1989) case).

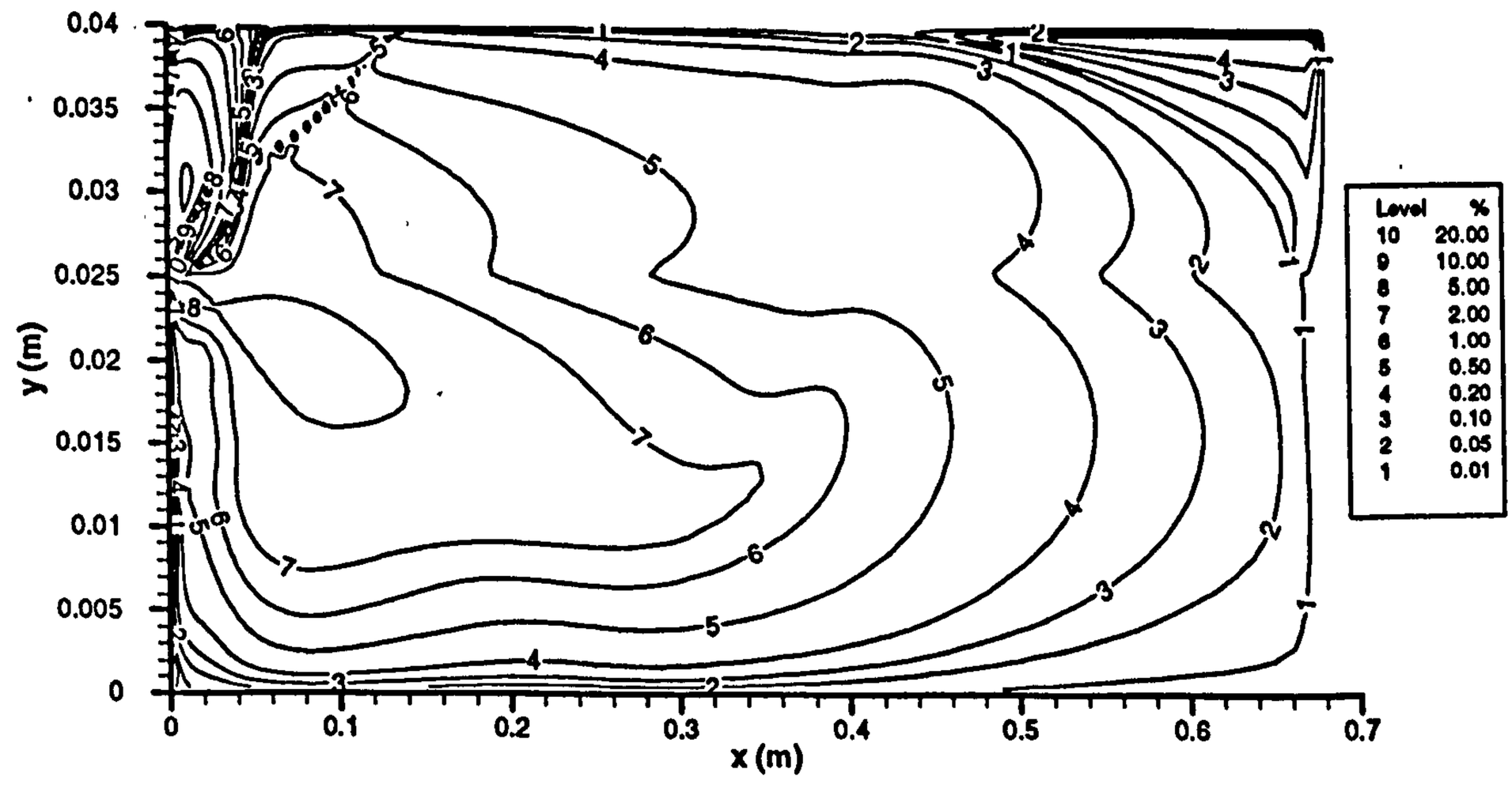

Figure 4.21: CRY model: ratio of numerical diffusion and effective viscosity (Tropea et al (1989) case).

4.2.1 Results

The most common parameter used in determining the success of CFD simulations of the backward-facing step and the pipe expansion is the reattachment length X_r. Table 4.2 compares the measured and computed values of the reattachment length non-dimensionalised with respect to the exit diameter $D2$.

	Experi-mental	*k-ε*	*RNG*	*LS*	*LSY*	*CR*	*CRY*
X_r/D_2	1.87	1.20	1.65	1.25	1.68	1.52	1.87
Error(%)	--	-36.5	-13.1	-33.2	-10.2	-18.7	-0.2

Table 4.2: Experimental and computed reattachment lengths.

The table highlights the substantial differences between the various turbulence models. The standard *k*-ε model underpredicts the reattachment length by 36.5% and the LS model underpredicts by 33%. The RNG, LSY and CR models all give reasonable agreement with the measured reattachment length. The RNG prediction is somewhat less accurate than those reported by other workers for similar flows. The Craft model with the Yap correction (CRY) gives a near-perfect match of the reattachment length, which is possibly somewhat fortuitous.

The comparison between the experimental and computed values of mean velocity U, turbulent kinetic energy k, Reynolds shear stress $\overline{u'v'}$ and normal stresses $\overline{u'^2}$ and $\overline{v'^2}$ (normalised with the maximum inlet experimental values U_0 and k_0) is presented in the form of a series of radial profiles in Figures 4.22 to 4.26. These show that the RNG and CRY models most closely match the experimental curves, and that the standard *k-ε* model is always the worst. Although the reattachment lengths are significantly different, the radial profiles are very similar when comparing the LS results with those for the LSY model and the CR results with those for the CRY model (the LSY and CR results are not plotted). Hence, the Yap correction term does not appear to have a large effect on the main flow features in this case.

The velocity profiles in Figure 4.22 show that the RNG model most closely matches the experimental curve, except right behind the step (X=5mm). Downstream of

X=80mm, CRY significantly overpredicts the mean velocity at the centreline, but underpredicts nearer the wall. The LS model, on the other hand, underpredicts the centreline velocity and overpredicts the mean velocity closer to the wall. The k-ε model substantially underpredicts the centreline velocity downstream of X=80mm.

Figure 4.23 reveals that the RNG model also provides the best match with the experimental results for turbulent kinetic energy k, except at X=5mm where none of the profiles are particularly close to Tropea's data. The CRY model yields profiles which are nearly as good as those of the RNG model, except far downstream (X=200mm) where the centreline k is underpredicted. The LS and standard k-ε models generally overpredict k with excessive peak values in the shear layer and high centreline k values in the region far downstream.

The RNG and CRY models best predict the Reynolds shear stress (see Figure 4.24). It is interesting to note that the non-linear CRY model accurately predicts the radial location of the peak value of the normalised stress, at all axial locations. The other models are not so good at predicting this location (especially at X=5mm). The standard k-ε and LS models predict a higher peak closer to the centreline, downstream of X=80mm. It is worth noting that in the recirculation zone (from step to X=120mm) the models which take streamline curvature into account (i.e. RNG and CRY) yield superior Reynolds shear stress predictions. The difference is smaller in the flow redevelopment region downstream from the reattachment point, where anisotropic effects are less important.

The normal stresses $\overline{u'^2}$ and $\overline{v'^2}$ are plotted in figures 4.25 and 4.26. Significantly, only the nonlinear model is able to predict axial fluctuations which resemble the experimental data, although the peak values are underpredicted by 40%. All models returned poor representations of $\overline{v'^2}$. In their simulation of a back-step flow using a modified cubic model, Apsley & Leschziner (1998) noted that the severely underpredicted normal stresses had no effect on the shear stress. This implies that only the latter is of consequence in the current flow.

One last result deserving attention is the ability (or otherwise) of the various turbulence models to predict corner-eddy length. Table 4.3 reveals that neither high Reynolds number model is capable of resolving the pocket of secondary recirculation which occurs just behind the step; confirmation of this is obtained from the simulations carried out in Fluent. Lien & Leschziner (1994) also note that their predictions for the Driver & Seegmiller (1985) back-step flow yielded no secondary vortex with the k-ε model and only a very small region of secondary recirculation, using the RNG model. Although Tropea et al (1989) did not take measurements in this area, Driver & Seegmiller (1985) reported that the corner eddy behind the step was roughly one step height (1H) in length. The CRY model is thus in rather good agreement, but removal of the Yap correction diminishes the secondary vortex significantly. The same trend is observed with the LS and LSY models.

	k-ε	RNG	LS	LSY	CR	CRY
TEACH	none	none	0.32	0.78	0.53	0.95
Fluent	none	none	n/a	n/a	n/a	n/a

Table 4.3: Computed corner eddy lengths X_s/H.

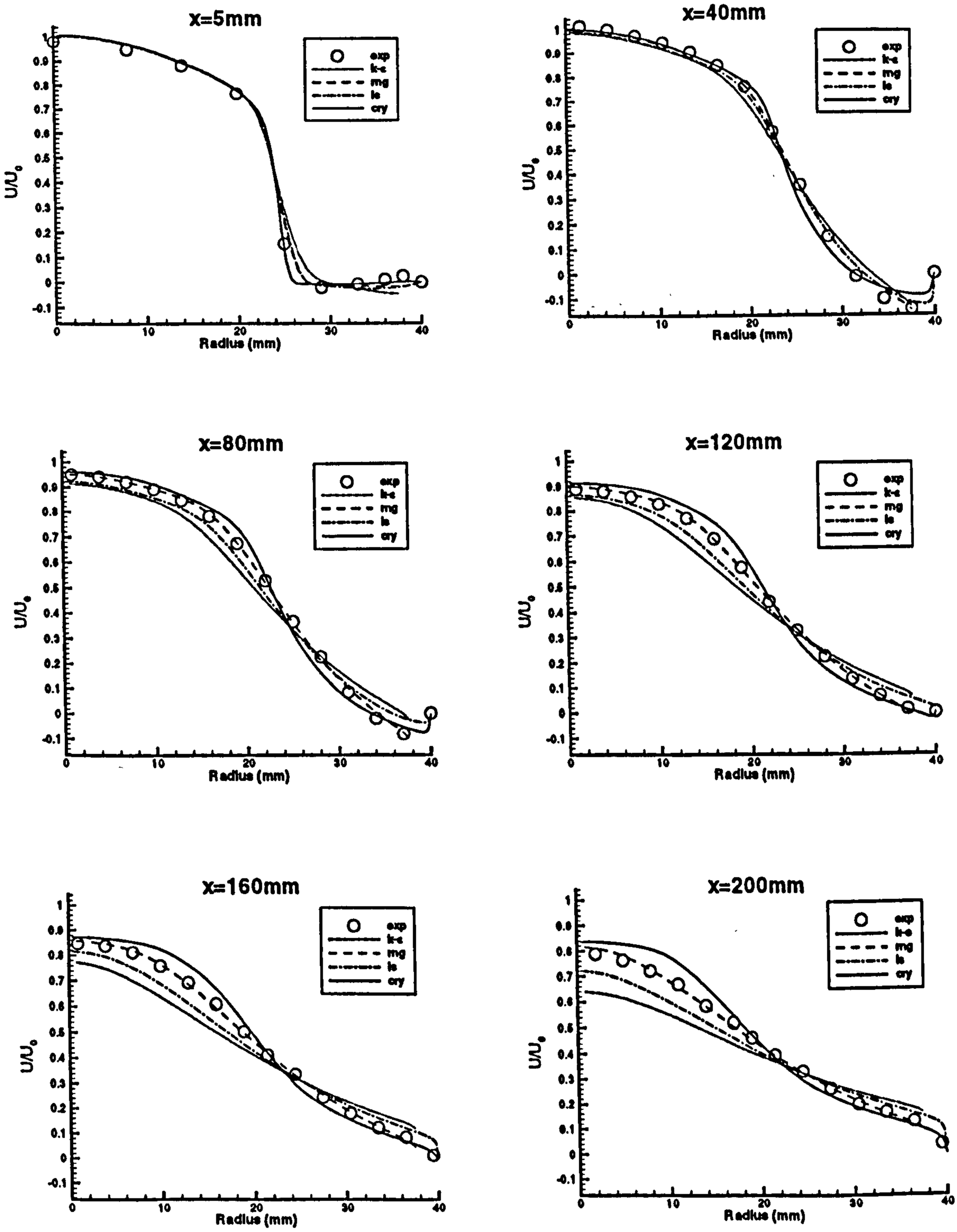

Figure 4.22: Radial distributions of axial velocity, Tropea et al (1989) pipe expansion.

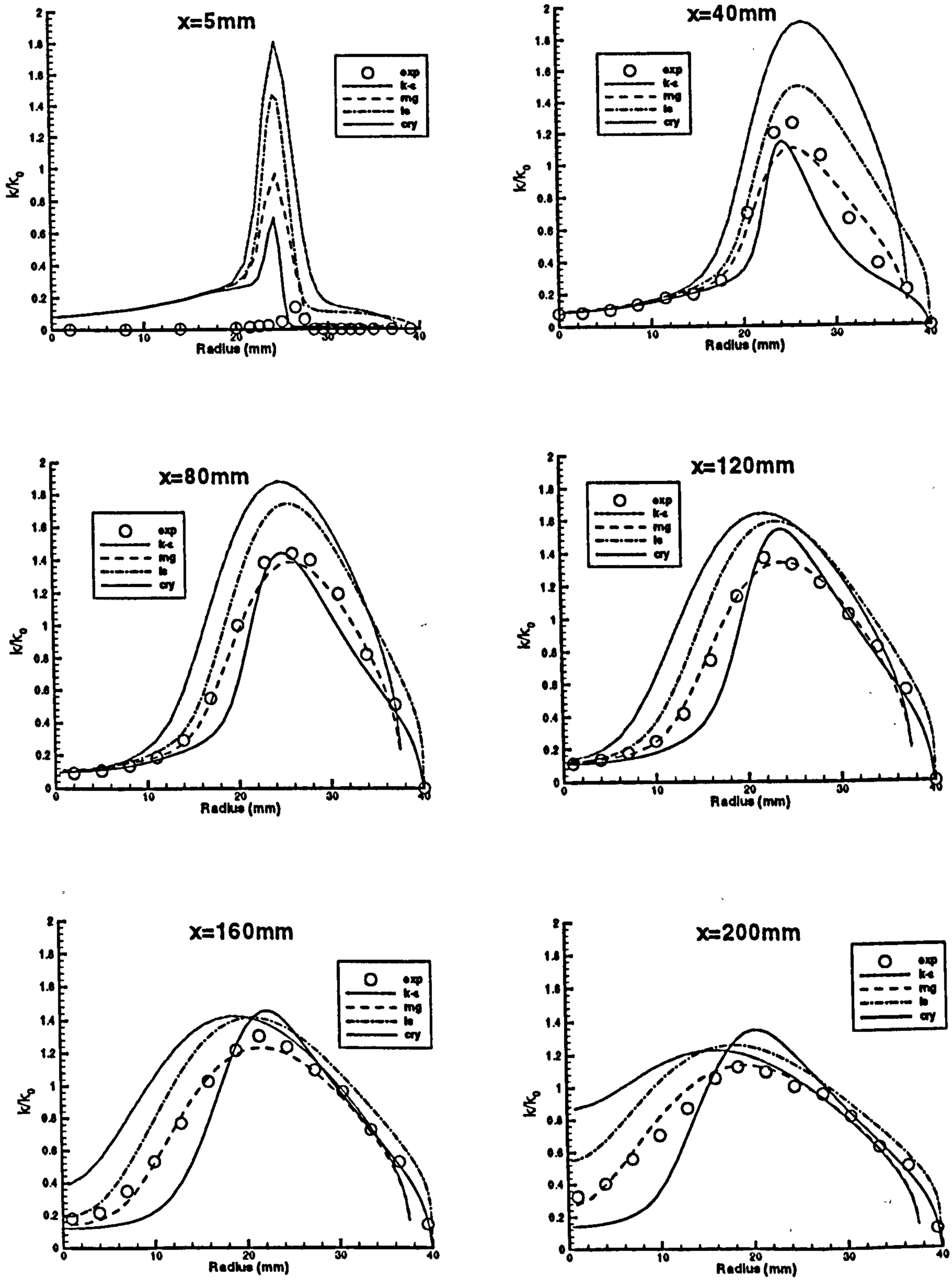

Figure 4.23: Radial distributions of turbulence energy, Tropea et al (1989) pipe expansion.

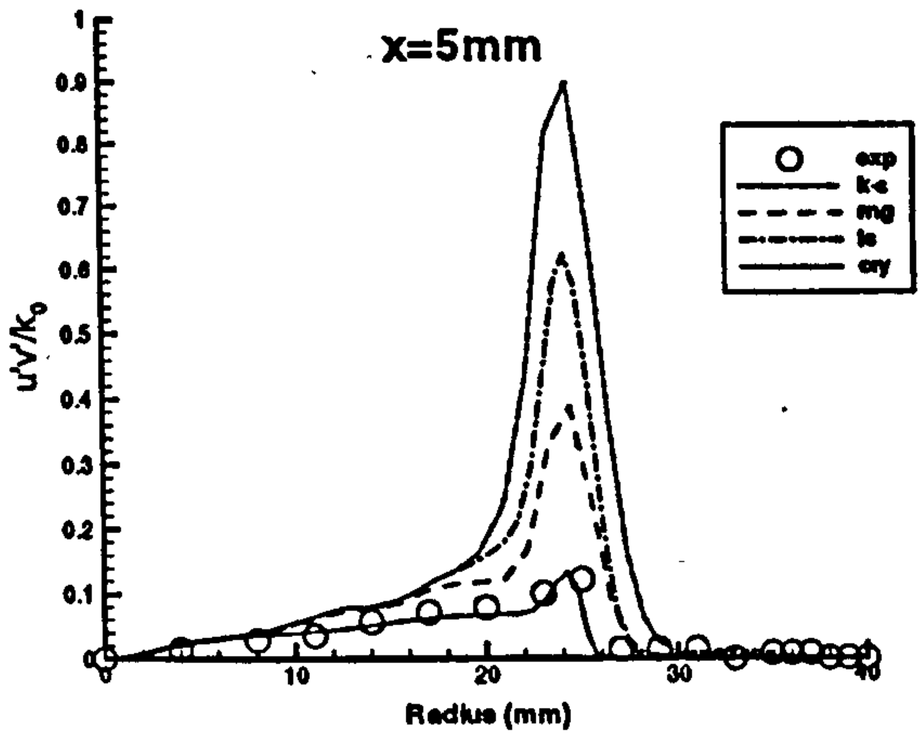

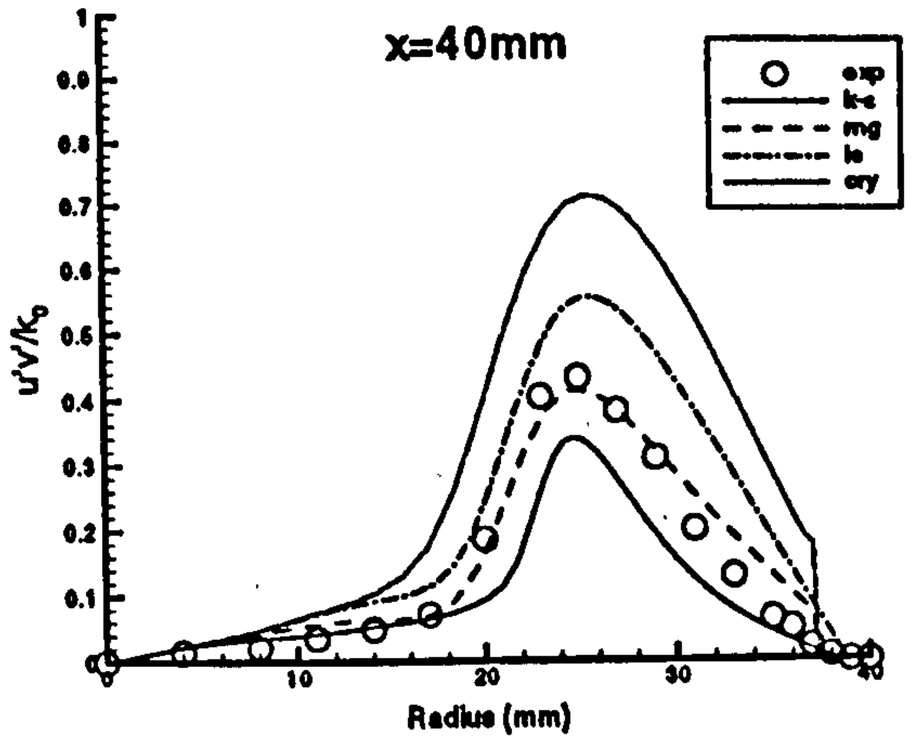

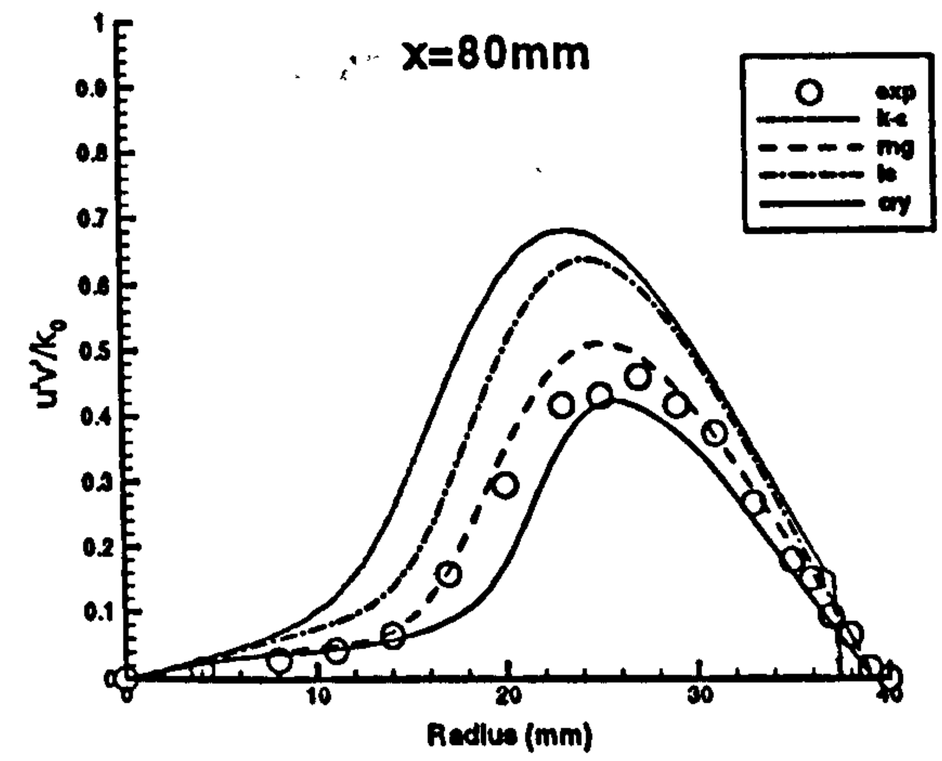

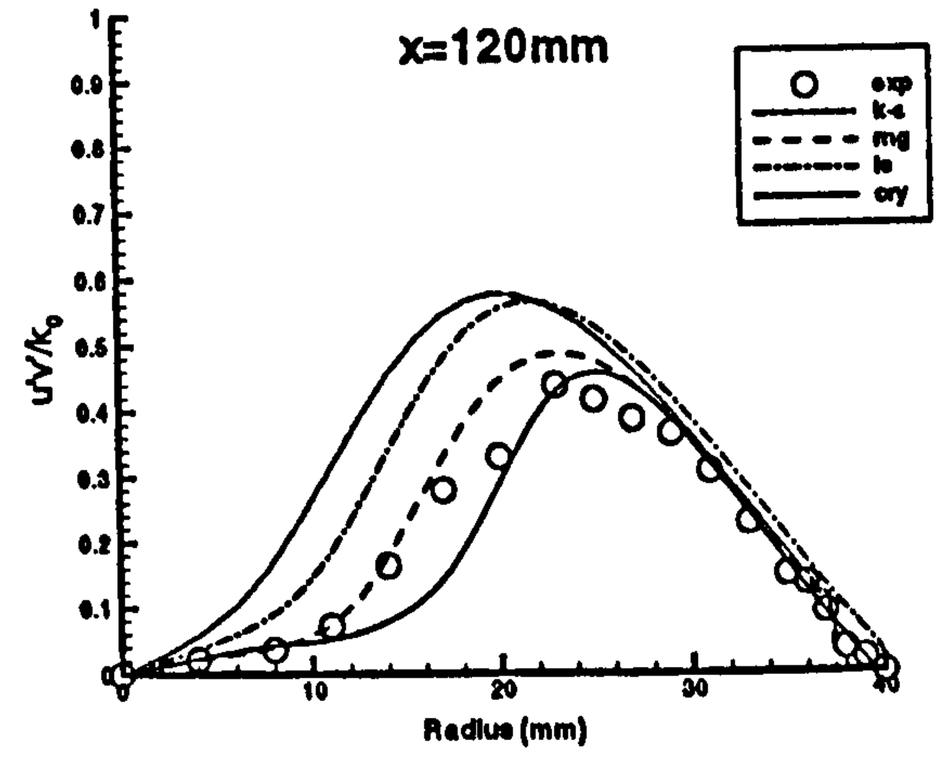

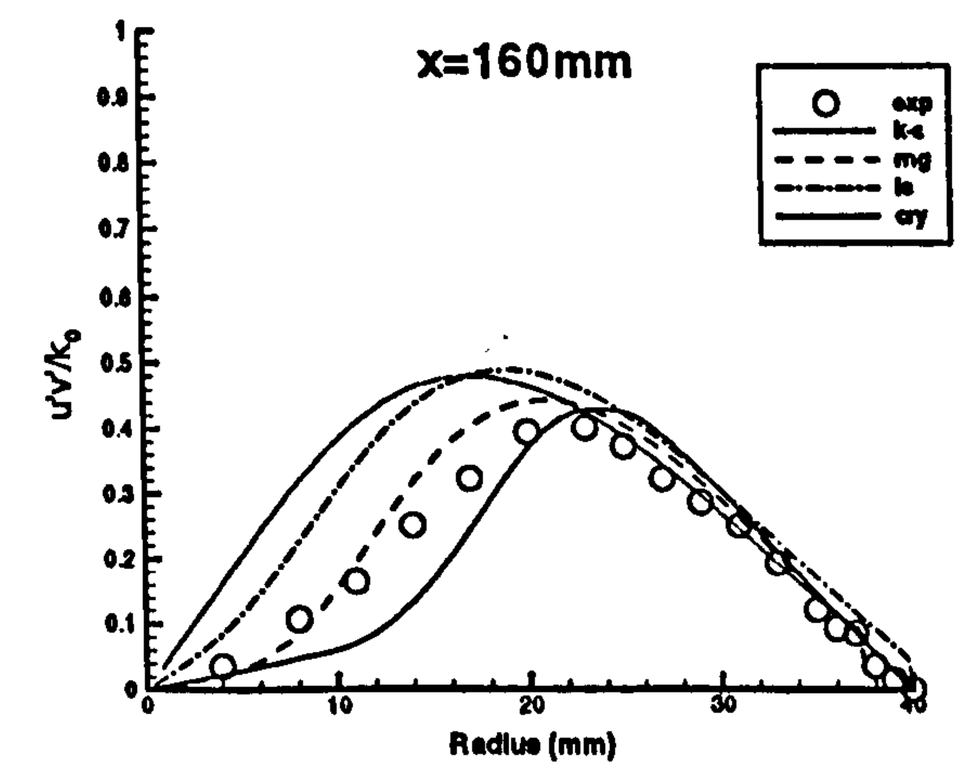

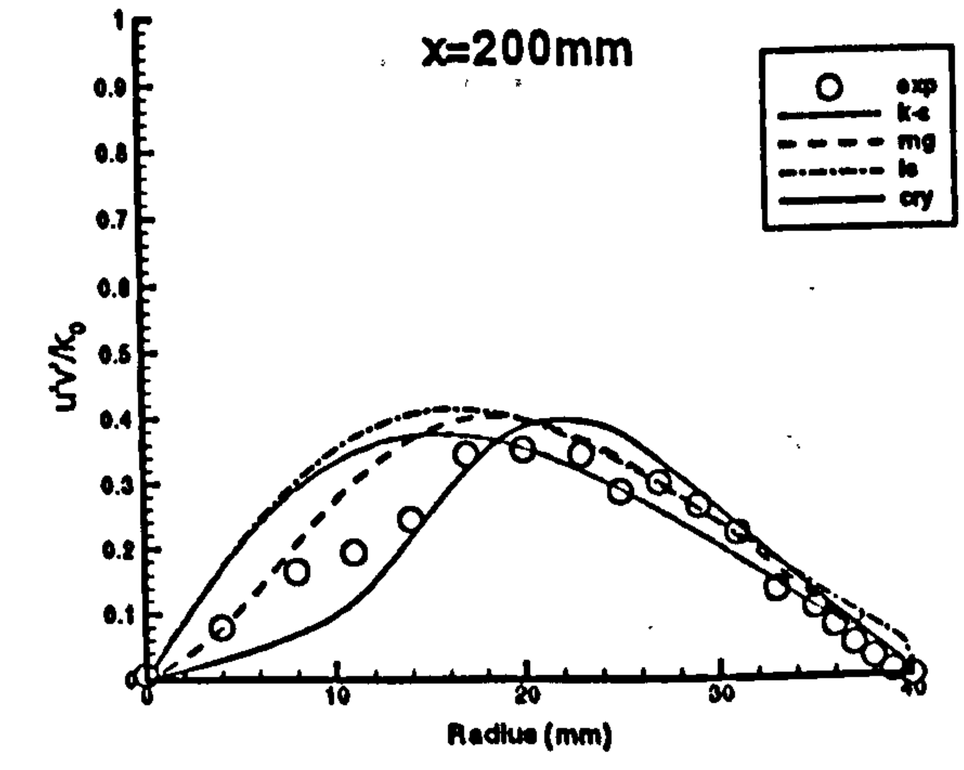

Figure 4.24: Radial distributions of Reynolds shear stress, Tropea et al (1989) pipe expansion.

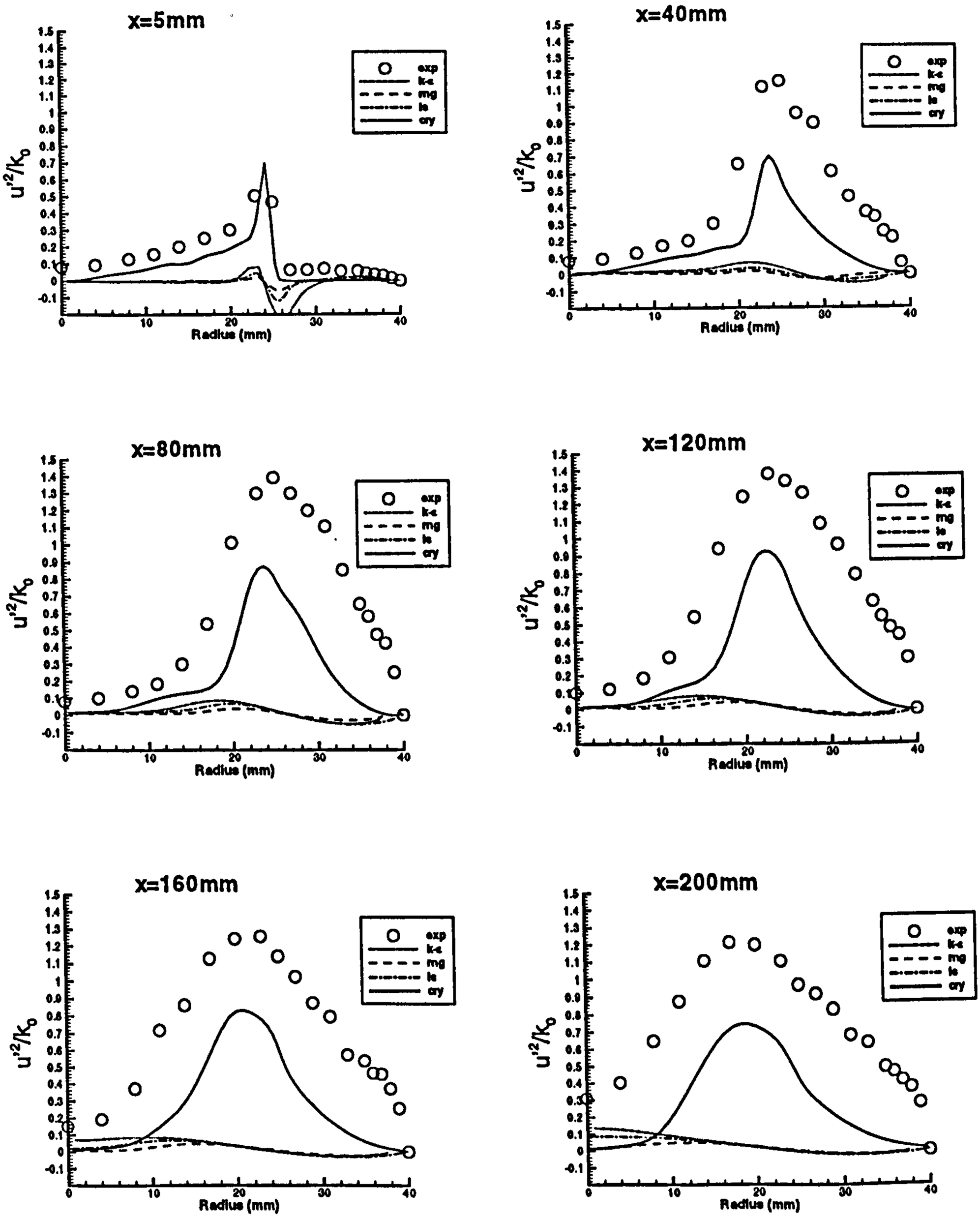

Figure 4.25: Radial distributions of normal (axial) Reynolds stress, Tropea et al (1989) pipe expansion.

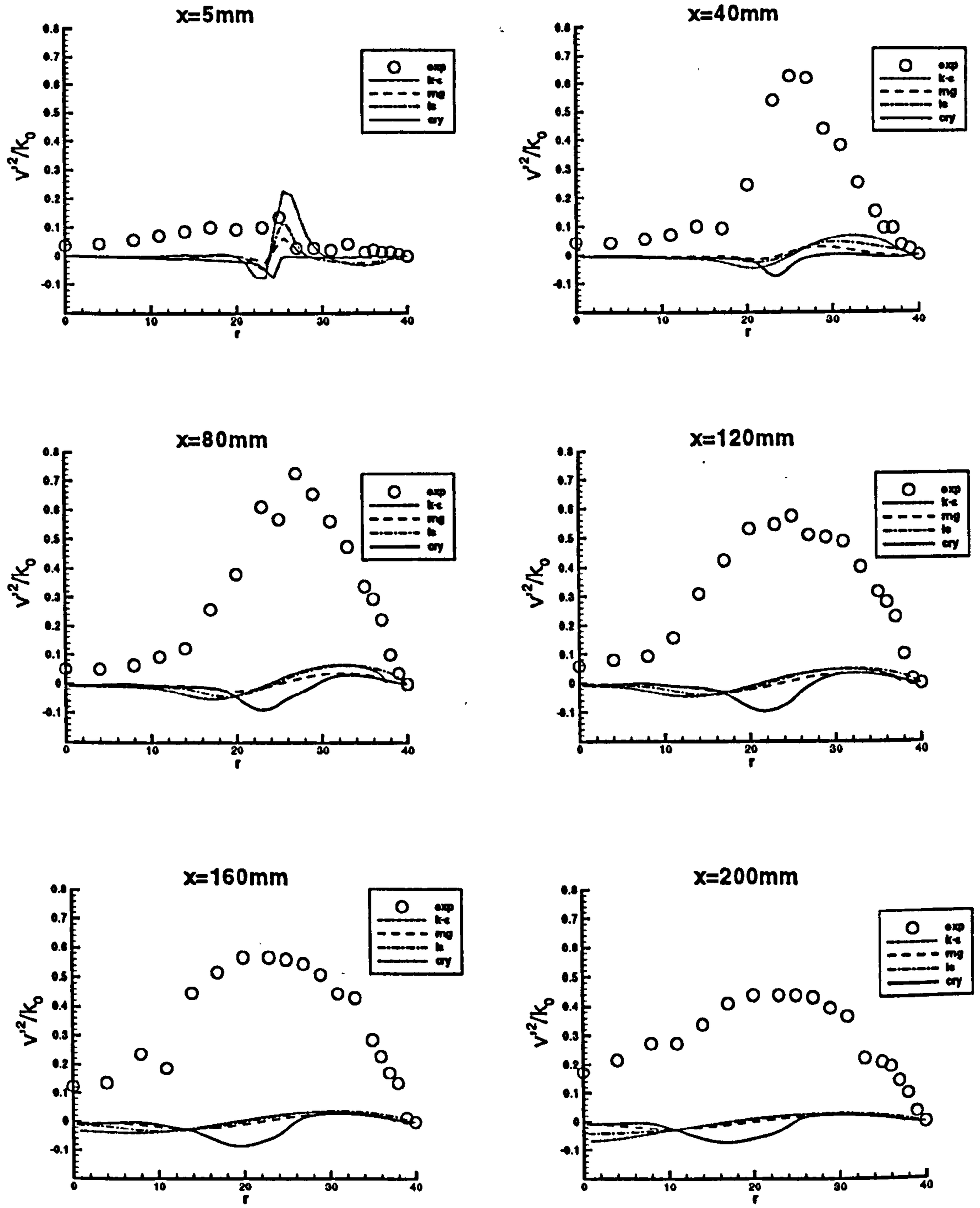

Figure 4.26: Radial distributions of normal (radial) Reynolds stress, Tropea et al (1989) pipe expansion.

4.2.2 Error Analysis

The reattachment length is a sensitive indicator of the success or failure of the simulation of a flow with recirculation and it is usually implied that a satisfactory match of the reattachment length corresponds to a successful simulation of the whole flow development in a recirculating flow. However, the possibility of a freak result must not be ruled out *a priori*. In order to quantify the deviation between experimental and computed values we tabulate, for each axial location X, the following overall relative error measure:

$$e_{\phi}(X) = \frac{\sum_{i} \left| \phi_{i,exp}(X) - \phi_{i,CFD}(X) \right| \times 2\pi r_i \Delta r_i}{\sum_{i} \phi_{i,exp}(X) \times 2\pi r_i \Delta r_i} \qquad (4.6)$$

Relative velocity error $e_U(X)$						
X (mm)	*k-ε*	*RNG*	*LS*	*CR*	*LSY*	*CRY*
5	0.121	0.063	0.081	0.057	0.078	0.055
40	0.123	0.048	0.092	0.111	0.092	0.106
80	0.184	0.027	0.127	0.108	0.106	0.100
120	0.176	0.020	0.120	0.099	0.104	0.096
160	0.175	0.024	0.128	0.098	0.115	0.093
200	0.168	0.023	0.125	0.101	0.112	0.092
Relative turbulence kinetic energy error $e_k(X)$						
5	25.32	11.94	18.68	8.254	16.43	8.372
40	0.803	0.142	0.453	0.255	0.374	0.251
80	0.370	0.063	0.265	0.142	0.223	0.134
120	0.283	0.063	0.223	0.130	0.185	0.115
160	0.177	0.067	0.180	0.122	0.109	0.111
200	0.161	0.076	0.177	0.175	0.103	0.134
Relative Reynolds shear stress error $e_{\overline{u'v'}}(X)$						
5	3.178	1.036	1.772	0.310	1.763	0.311
40	1.190	0.204	0.568	0.335	0.534	0.334
80	0.597	0.143	0.402	0.163	0.365	0.157
120	0.415	0.152	0.397	0.144	0.309	0.129
160	0.245	0.136	0.322	0.239	0.206	0.179
200	0.184	0.161	0.254	0.278	0.182	0.187

Table 4.4: Overall relative errors.

The summation is taken over all the experimental points in a radial profile so $e_{\phi}(X)$ is a radially averaged relative error for variable ϕ at axial location X. Table 4.4 gives

this measure of the relative error for the mean velocity, the turbulent kinetic energy and for the Reynolds shear stress.

The smallest overall error at each axial location is highlighted in ***bold*** typeface in each of the tables. The tabulated overall error measures confirm the impressions gained from inspection of Figures 4.22 to 4.26. The RNG model performs best in terms of the quantities for which measured data was available and the CRY model comes a close second in terms of the overall error measure.

The overall uncertainty in the comparison between experiments and CFD is, of course, influenced by the uncertainty in the experimental measurements. Tropea et al (1989) noted that an element of swirl was present in the experimental flow; this was estimated to be 6% and 1% of the inlet axial velocity at, respectively, the inlet and elsewhere. They further reported that the volumetric flow rate at each axial location varied by up to 5% relative to the inlet flow rate. Table 4.4 shows that the typical experimental uncertainty is an order of magnitude smaller than the uncertainty due to the turbulence models. Since the experimental uncertainty makes a negligible contribution, the errors reported in Tables 4.2 and 4.4 can be taken as a good indication of the overall uncertainty in the CFD work. The following discussion will look in more detail at the influence of the turbulence model.

4.2.3 Discussion

The flow through the pipe expansion is characterised by the following features: strong streamline curvature, recirculation, reattachment and flow redevelopment. Many early studies have focused on reattachment length predictions. The failure of the standard k-ε model in the case of the 2D backward-facing step is well documented in the literature. For example, Sindir and Launder - referenced in Driver and Seegmiller (1985) - used the model in the TEACH code for the Kim et al case (1980) and severely underpredicted the reattachment length. Sindir (1982) reports computations of a back-step flow and predicted a reattachment length X_r/h that was 33% below the measured value. However, in both cases the computational grid was probably too coarse. Early simulations were affected by numerical details such as the number and distribution of

the grid cells and the location of the downstream outlet boundary. The influence of these subtle effects is now better understood. Speziale and Thangam (1992) investigated the back-step configuration of Eaton and Johnston (1980) and found that the reattachment length predicted by the standard k-ε model was about 12% less than the experimental value for a grid-independent solution. Nallasamy (1987) reviewed the reattachment lengths obtained with the standard k-ε model for three different pipe expansions and found that the results were all within the margins of experimental uncertainty. Moon & Rudinger (1977) even overpredicted the reattachment length for a very high Reynolds number case; however, no numerical details were given so it was not possible to judge the accuracy of the simulation. In our calculations the performance of the standard k-ε and LS models is remarkably poor; they underestimate the reattachment length by 36% and 32%, respectively. The similarity between these two simulated results is consistent with the statement of Chieng & Launder (1980, quoted in Nallasamy, 1987) that modifying near-wall treatments does not change the reattachment region but only improves heat transfer predictions. Thangam & Speziale (1992) note that low Reynolds number models only slightly improve the reattachment length.

A likely explanation for the discrepancy between the current calculated reattachment lengths and those reported for similar separated flows, lies in the observation that the predicted results from the literature were all for much higher Reynolds number flows. For example, Qin (1984, referred to in Nallasamy, 1987) used Re = 50000 whilst Moon & Rudinger (1977) investigated a pipe expansion of Re = 2.8×10^5. The back-step flows of Eaton & Johnston (1980) and Driver & Seegmiller (1985) had Reynolds numbers of 9.5×10^4 and 3.06×10^5, respectively (all these dimensionless quantities are derived using the same parameters). On the other hand, the Tropea axisymmetric expansion has a flow corresponding to Re = 15600, which is very low compared to the above cases. It is a well known fact that the extent of the energy cascade, by which turbulence energy is passed from the largest to the smallest eddies, depends on Reynolds number. Only beyond a certain point does this range become approximately constant; it is for this regime that the k and ε equations were formulated. This would account for the excessive underprediction of the k-ε model. The LS model

suffers from the same deficiency; even though it is a low Reynolds number model, this description simply refers to the provision of viscous damping for near-wall flows. Even though the RNG and CRY models are based on the k and ε (or $\tilde{\varepsilon}$) equations, the deficiencies are moderated by the use of strain-dependent treatments.

Yakhot et al (1992) used the RNG model and found that the predicted reattachment length was only 6% below the experimental value for the back-step geometry of Eaton and Johnston. Lien and Leschziner (1994) also used the RNG model and underpredicted the experimental value by 8.5% for a stepped diffuser consisting of a backward-facing step followed by a 6 degree expansion (Driver and Seegmiller, 1985). Table 4.3 shows that the current results obtained with the RNG model are a little worse than those reported by Yakhot et al (1992) and Lien & Leschziner (1994) for similar flows. On close inspection the difference appears to be mainly due to the location of the near-wall node. In the results reported in table 4.3, care was taken to locate the near-wall nodes in the inertial sublayer. In subsequent simulations a 200×45 grid was employed, which more closely resembles the one used by Lien and Leschziner. The near-wall nodes were now placed inside the viscous sublayer without application of wall functions. Interestingly, this improved the predictions of the reattachment length to $X_r/D2 = 1.71$, only 8.6% less than the experimental value; the main flow hardly changed. It is also worth noting that this practice did not influence the results obtained with the k-ε model. The RNG model appears to be sensitive to this issue in complex flows because the modification in the dissipation rate equation is a function of strain rate, k and ε, all of which exhibit steep gradients in the buffer layer. Reasonable predictions of the reattachment length were obtained using the CR and LSY models. The Craft et al model with the Yap correction (CRY) gives a near-perfect match with experiments.

Table 4.2 shows that the Yap correction term Y_C is responsible for a major improvement in the predictions of reattachment length. The effect of this term, introduced in Chapter 2, is examined. As a function which manipulates the turbulence budgets where y is small and k is large, Y_C acts near reattachment points in the context of separated flows. The term yields improved reattachment length predictions without

influencing the solution in the bulk of the flow. Figures 4.27 and 4.28 show the effect of the Yap term on the near-wall mean velocity and turbulence kinetic energy. Y_C reduces the peak level of k at the wall by two orders of magnitude (figure 4.28), which in turn reduces shear layer spreading and shifts the reattachment point downstream (figure 4.27). Figure 4.29 gives a contour plot of the Yap correction term relative to the production and dissipation terms in the $\tilde{\varepsilon}$ equation for the CRY model calculations which confirms that the Yap term is close to zero in most of the flow field.

Correct resolution of the free shear layer in the pipe expansion is the key to successful prediction of the entire flow field. The standard k-ε model and its low Reynolds number variants (such as the LS model) perform poorly in free shear layer flows due to problems that were originally attributed to deficiencies in the ε (or $\tilde{\varepsilon}$) equation in flows with high strain rates. These can sometimes be overcome by minor adjustments to the model constants. For example, in the case of a free jet flow the constant $C_{\varepsilon 1}$ in the ε-equation (of the standard k-ε model) can be changed from 1.42 to 1.6 (Masri, 1998). This gives an improved match between experiments and computations in this particular case, but the validity of such case-by-case adjustments is restricted. Further evidence of this is supplied by Moon & Rudinger (1977) who reported that individual flow features could be correctly predicted by manipulating the constants $C_{\varepsilon 1}$ and $C_{\varepsilon 2}$; however, this had negative effects on other aspects of the flow.

Lien and Leschziner (1994) note that the turbulence anisotropy in a free shear layer has a substantial impact on the mean-flow field. This is due to (i) the strong relationship between the turbulent normal stresses and the strain rates caused by streamline curvature and (ii) the sensitivity of the turbulent shear stresses to the anisotropy of the normal stresses. In light of this, attention should be drawn to the vastly different predictions of $\overline{u'^2}$ by the CRY and RNG models (see figure 4.25).

The RNG and CRY models contain devices which are used to sensitise the k and ε (or $\tilde{\varepsilon}$) equations to strain rate dependent and anisotropy effects. Figure 4.30 illustrates the effect of these devices. The diagrams show contour plots of the Reynolds shear stress $\overline{u'v'}$, as predicted by (a) the standard k-ε model, (b) the RNG model and (c)

the CRY model. Figure 4.30(a) shows that the standard k-ε model predicts very high Reynolds shear stresses, which cause excessive spreading of the shear layer and premature reattachment. The RNG model clearly yields a major improvement in the representation of the shear layer (figure 4.30(b)). Figure 4.30(c) gives the Reynolds shear stress contours for the CRY model and reveals an even narrower shear layer and longer recirculation zone. Figures 4.30 (b) and 4.30(c) clearly show that the RNG and CRY models substantially alter the predictions of the free shear layer, which is much thinner and the recirculation zone is also larger than in the case of the standard k-ε model.

The RNG model was designed to be applicable to a wide variety of flows and uses a strain-rate dependent modification R to the constant $C_{\varepsilon 1}$ in the ε-equation, as described in Chapter 2. In the presence of high strain rates S_{ij} in the free shear layer, η becomes large, thereby causing R to attain negative values. This increases ε-production, which in turn reduces the levels of turbulence energy and the Reynolds shear stress. The effect of R is investigated in figure 4.31, which gives the ratio of R to $C_{\varepsilon 1}$. The diagram shows that R modifies the ε-production term by up to ±50%. However, along the free shear layer (which is partly outlined by contour 6 in figure 4.31) it is seen that the ratio $R/ C_{\varepsilon 1}$ small; thus the value of R in this region is nearly zero. It seems, therefore, that the reduced value of the constant $C_{\varepsilon 2}$ plays a significant role in moderating the shear stresses.

The non-linear CRY model accounts for anisotropy by means of a cubic relationship between Reynolds stresses and mean strain-rate and vorticity. In addition, the constant C_μ and source term E in the dissipation rate equation are also strain-rate dependent in the CRY model. Since the non-linear terms and the other strain-rate dependent adjustments are inextricably linked together, it is not possible to isolate the effects of each on the outcome of the simulations. Nevertheless, we can get an indication of the likely importance of the effects by comparing figures 4.30(c) and 4.30(d).

Figure 4.30(c) shows the total Reynolds shear stress for the CRY simulations and figure 4.30(d) gives the linear part – i.e. the total Reynolds shear stress minus the sum of all non-linear terms. The distribution due to the linear part of the Reynolds shear stress is not unlike that obtained in figure 4.30(b) with the RNG model. Hence the strain-rate dependent adjustments of the model constant C_μ and source term E appear to have an effect of similar magnitude to that due to the RNG parameter R. Comparison of figures 4.30(c) and 4.30(d) also shows that the effect of the non-linear terms in the CRY model is to cause a small but important further reduction of the peak levels of Reynolds shear stress in the free shear layer.

The influence of the non-linear terms is highlighted in a different way in figure 4.32, where we have plotted the ratio of non-linear terms to the linear part of the turbulent shear stress. The non-linear terms change the total turbulent shear stress by up to ±10%. It should be noted that a negative ratio causes an increase in the shear stress and vice versa. The maximum stress in the free shear layer is seen to be reduced by 10% whilst the stresses nearer both the wall and the centreline (downstream of X=60mm) are increased by 7% or so. In the first half of the recirculation zone the non-linear terms also cause substantial changes.

In summary, the study has shown that the RNG and CRY models successfully predict the flow through the Tropea et al pipe expansion. Both models reduce shear stresses in the portion of the free shear layer adjacent to the recirculation zone. The RNG model accomplishes this by manipulating the ε-production and destruction terms. There are, however, strong indications (Lien and Leschziner, 1994) that the strain-rate dependent parameter R in the RNG model is actually detrimental in other turbulent flows, e.g. plane and round jet flows and flows across a staggered tube-bank assembly. The non-linear CRY model uses a combination of devices including a cubic relationship between Reynolds stresses and mean strain-rate and vorticity and strain-rate dependent model constant C_μ and source term E in the dissipation rate equation. This improves predictions for the pipe expansion.

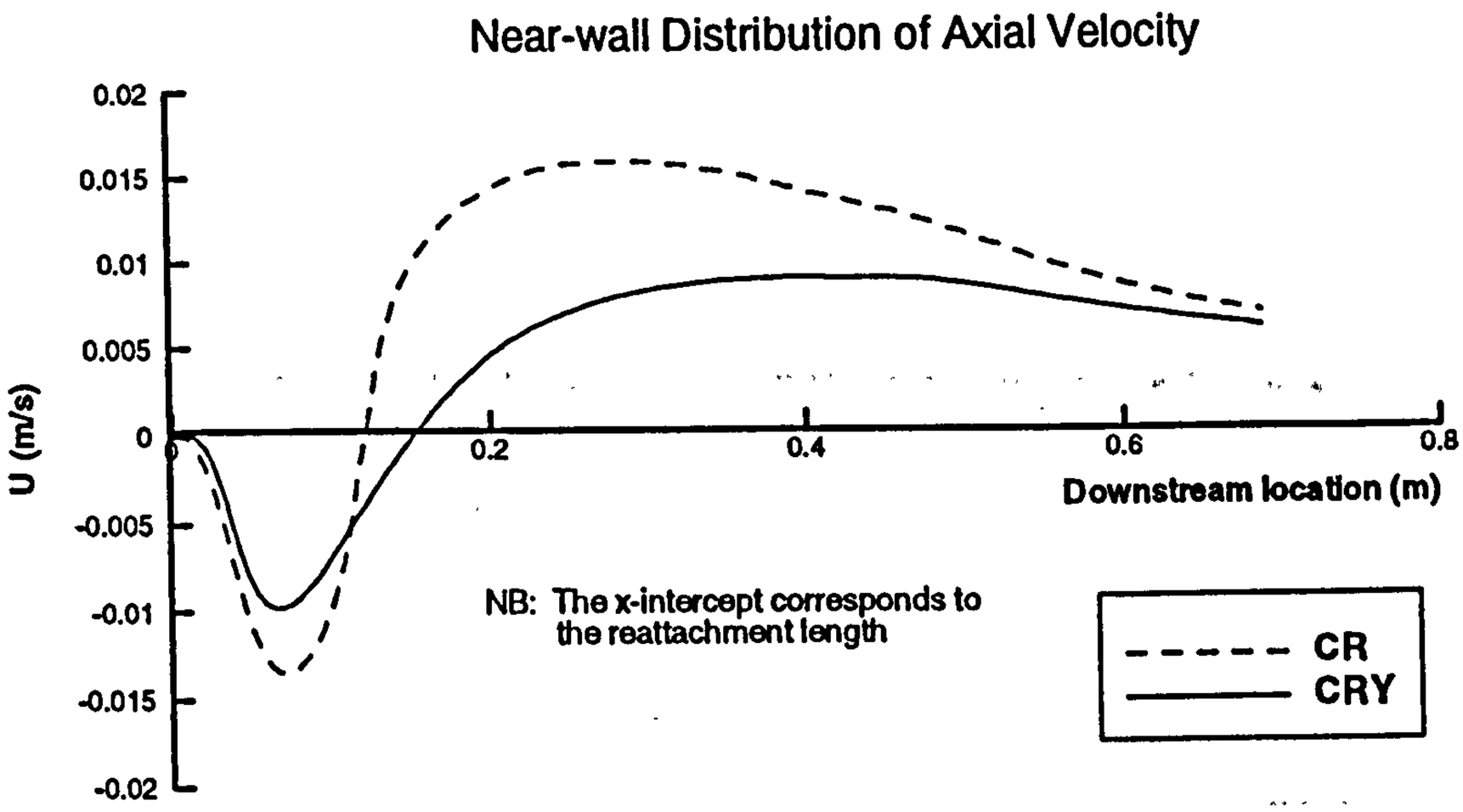

Figure 4.27: Effect of Yap correction on near-wall axial velocity distribution.

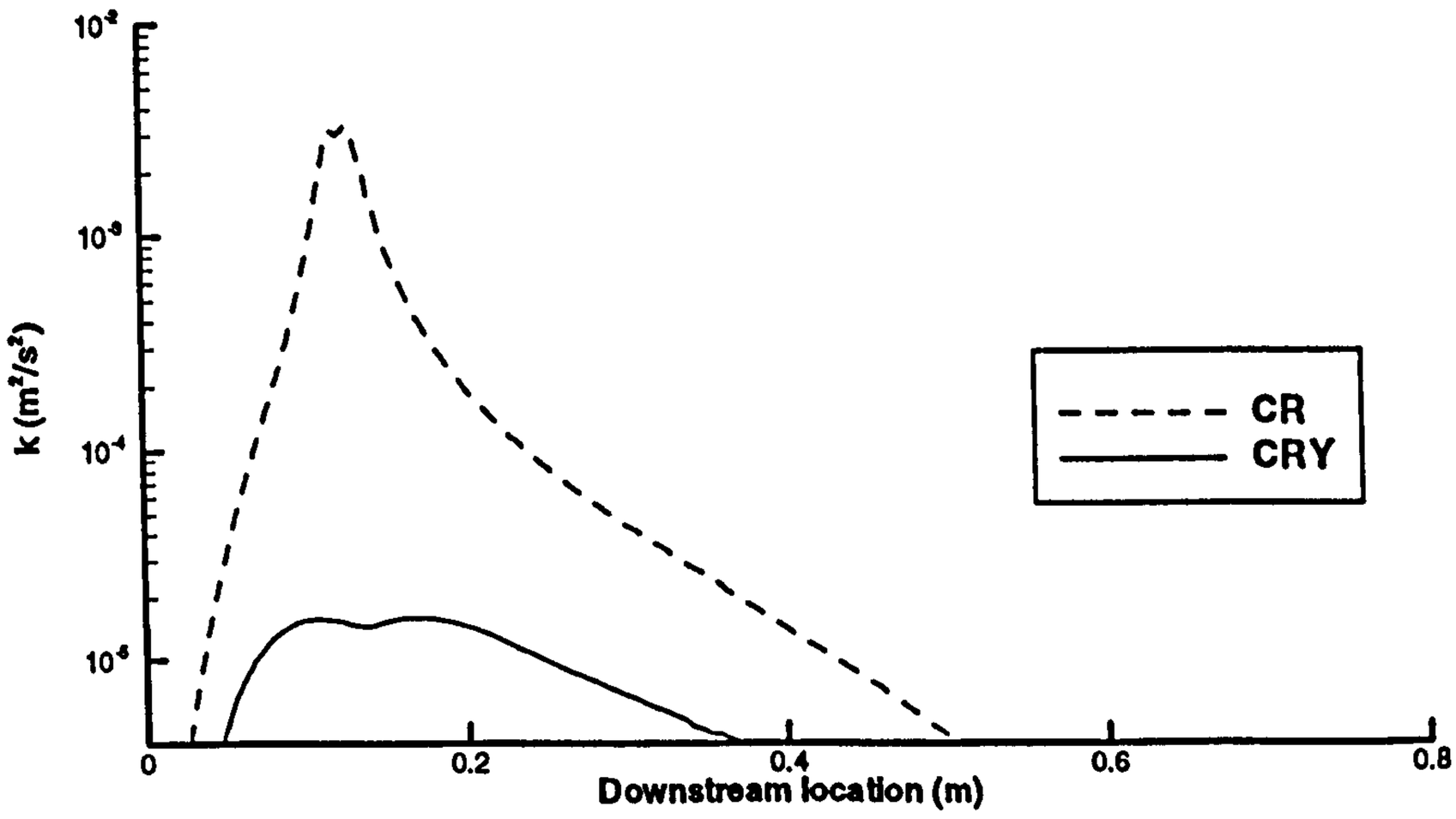

Figure 4.28: Effect of Yap correction on near-wall turbulence energy distribution.

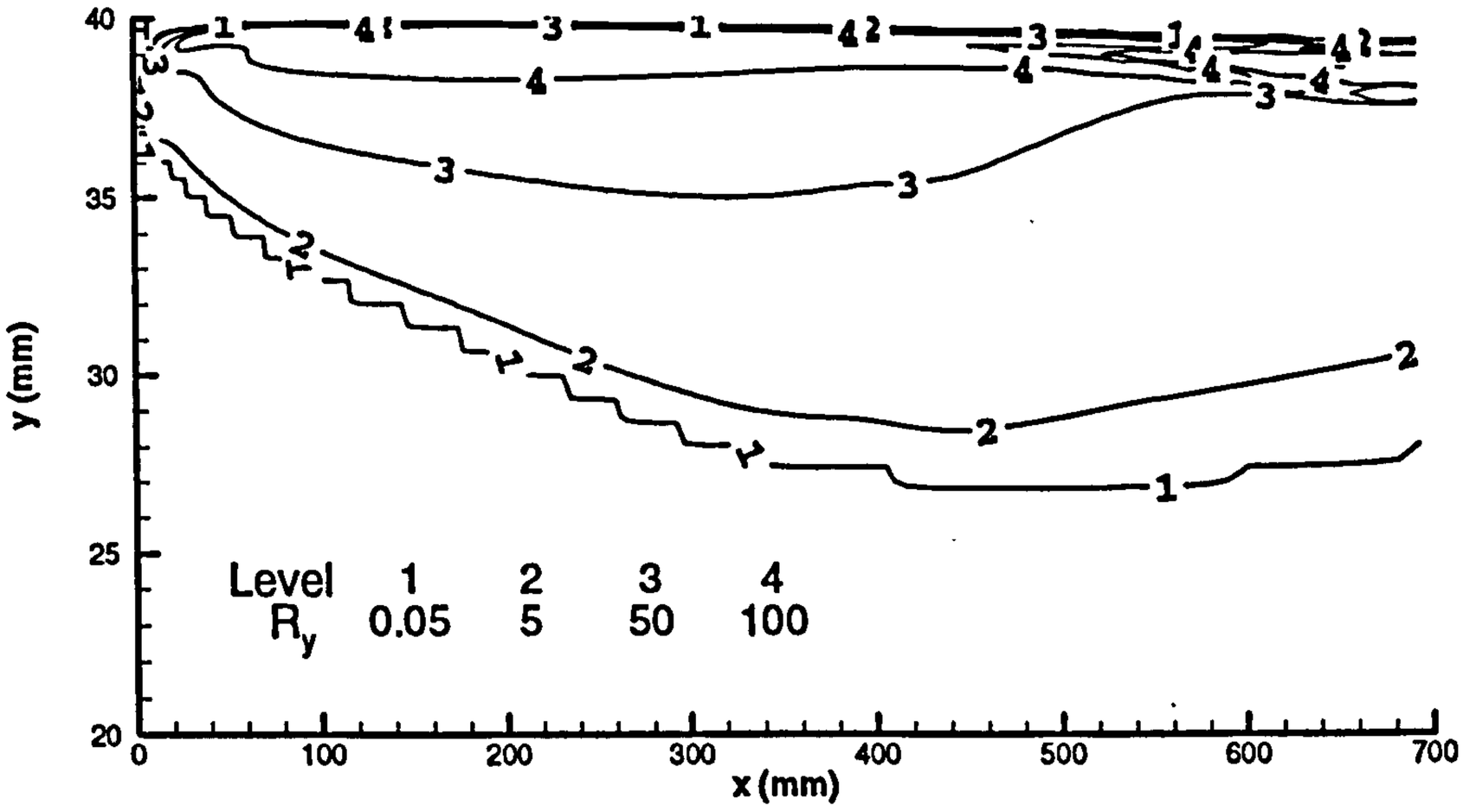

Figure 4.29: R_y: Ratio of Yap factor to the terms $f_1 C_{\varepsilon 1} \frac{\tilde{\varepsilon}}{k} P_k - f_2 C_{\varepsilon 2} \rho \frac{\tilde{\varepsilon}^2}{k} + \rho E$.

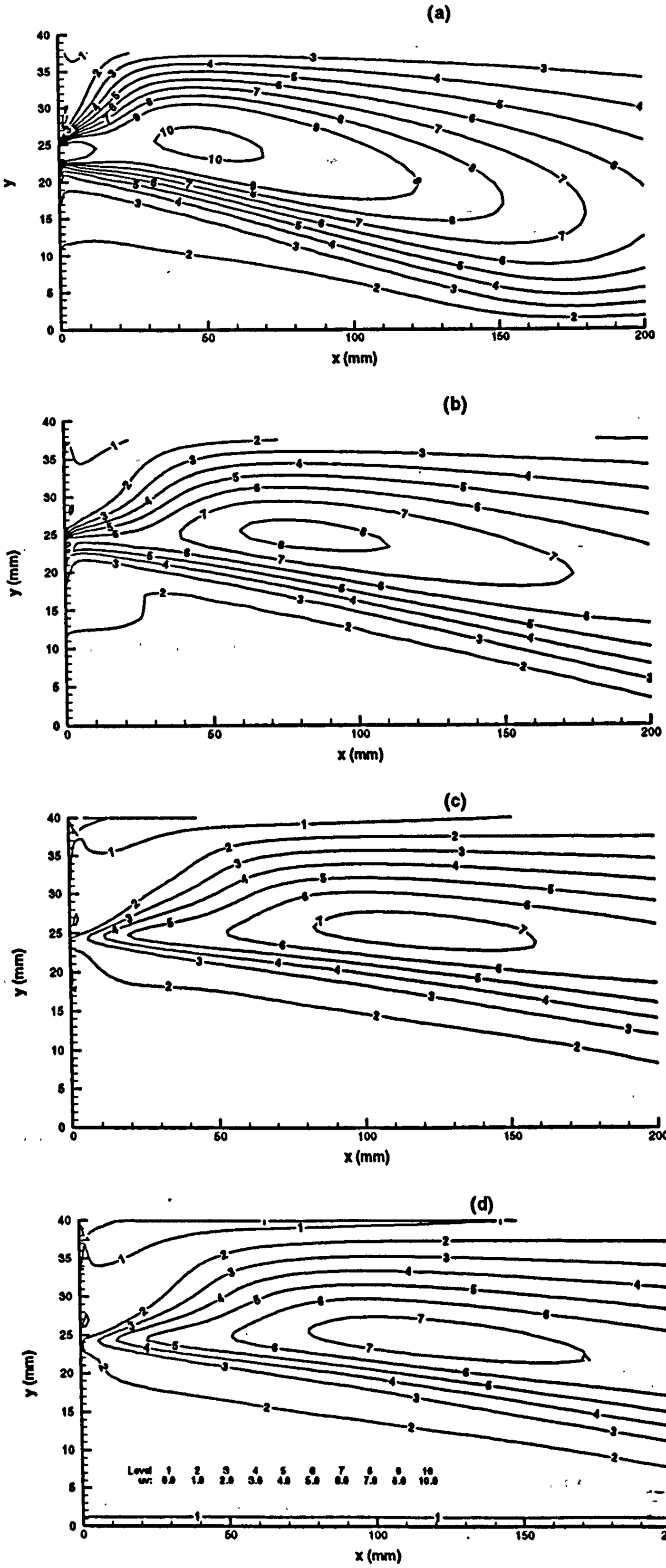

Figure 4.30: Turbulent shear stress as calculated by (a) standard *k-ε* model, (b) RNG model, (c) CRY model and (d) linear part of shear stress in CRY model. All values are multiplied by 100 (units m^2/s^2).

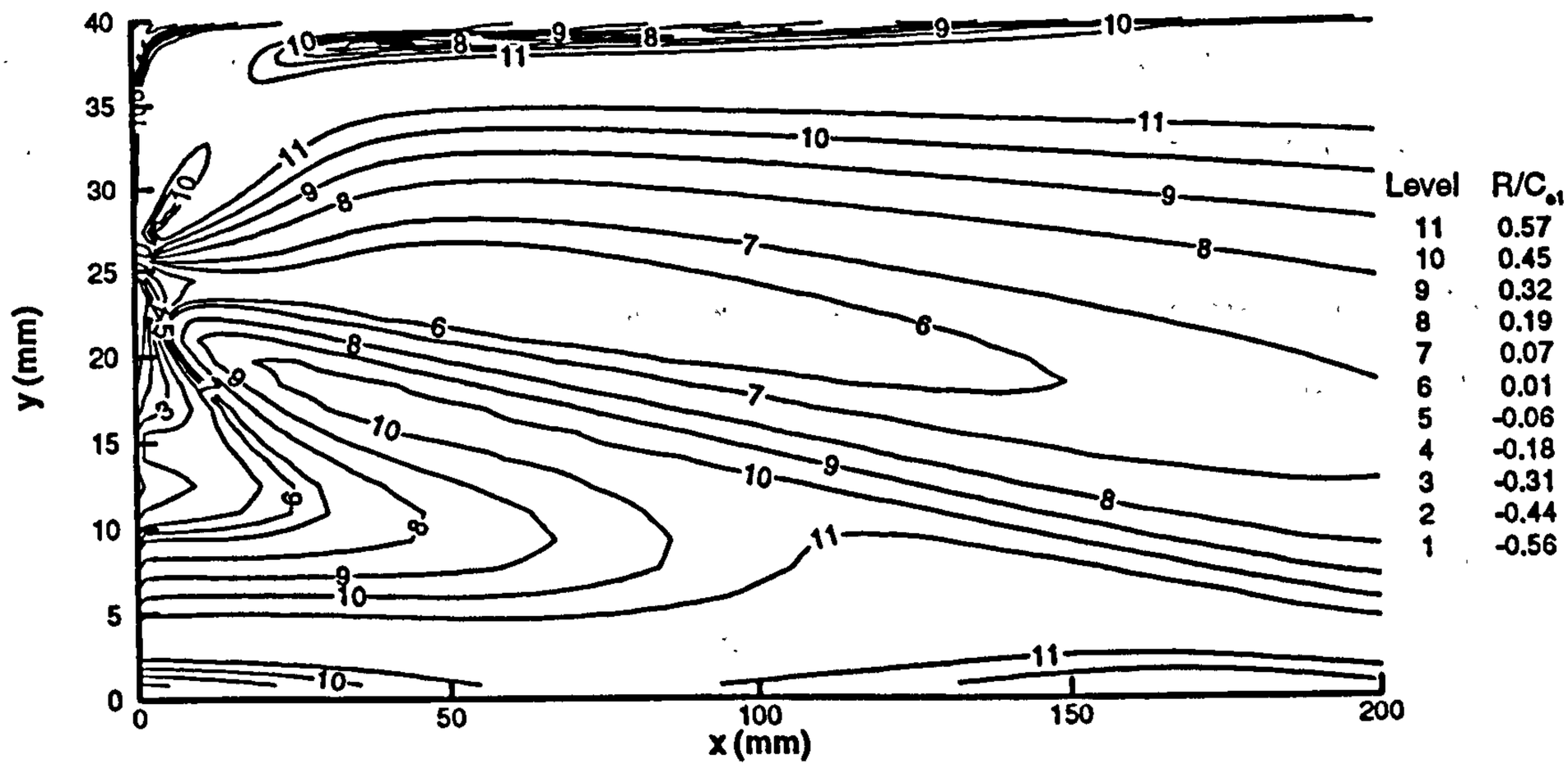

Figure 4.31: Ratio of $R/C_{\varepsilon 1}$ in the RNG model computations.

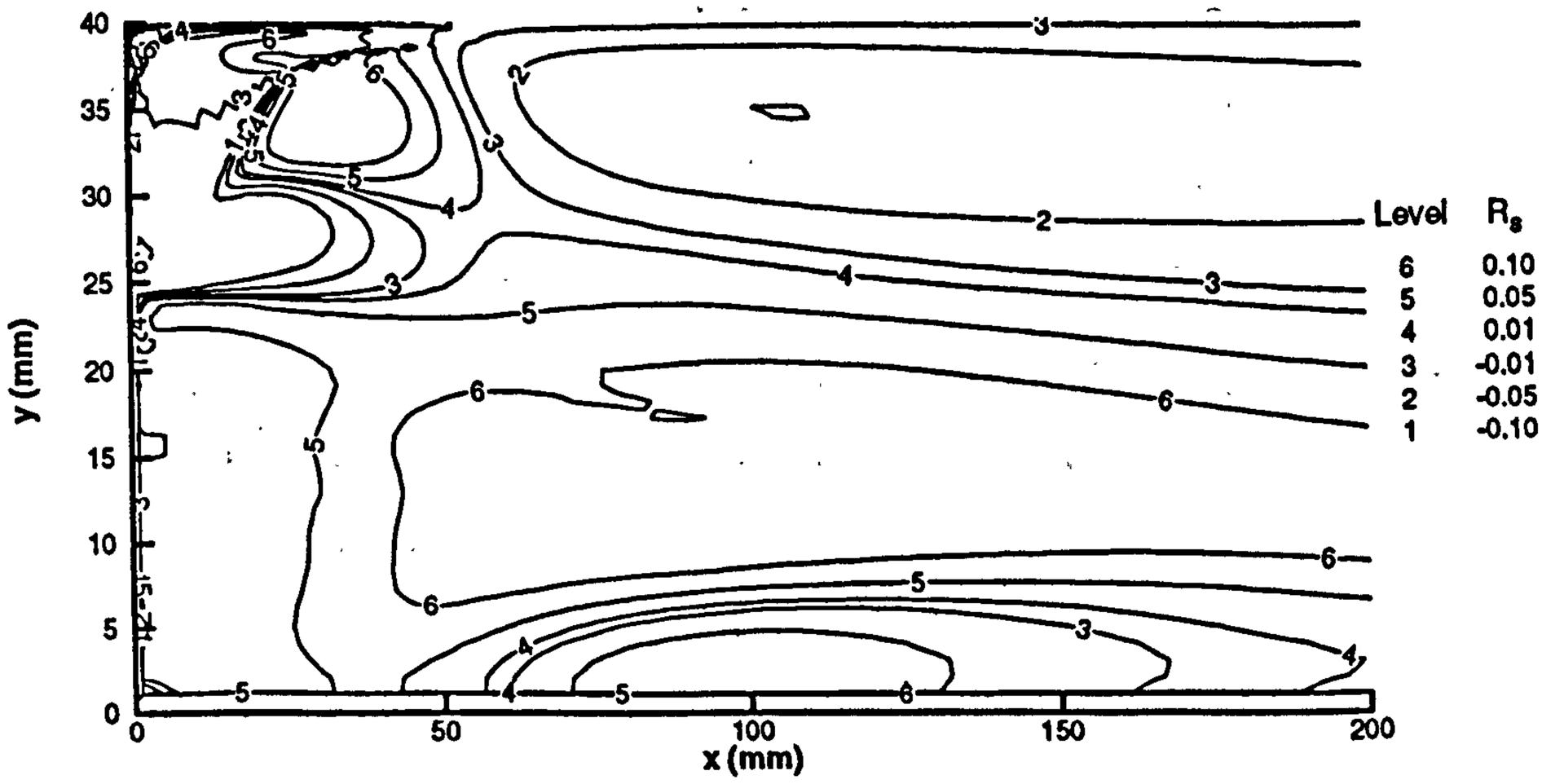

Figure 4.32: CRY model: ratio of non-linear terms (in the shear-stress equation), to the 'linear' shear stress. This ratio is denoted as R_S.

4.3 FURTHER PIPE EXPANSION SIMULATIONS

The reattachment lengths in pipe expansion flows are known to depend on Reynolds number and even geometry, particularly at lower flow rates. Thompson et al (1984) and Moon & Rudinger (1977) provide a survey of experimental cases which explore this dependence. In order to truly determine the effectiveness of turbulence models, particularly in light of the poor representation of reattachment length by linear EVM's in the study of the Tropea et al (1989) case, the higher Reynolds number pipe expansion of Durrett et al (1988) was investigated. The ensuing discussion considers this particular case, but also draws in elements from the Tropea et al (1989) simulation as well as from a third flow briefly described in Appendix G.

Detailed LDV data for the Durrett et al (1988) case was provided by Thompson et al (1984) in the form of radial distributions at various axial locations. The inlet and exit diameters are $D_1 = 50$mm and $D_2 = 95.2$mm, respectively, whilst the expanded flow was permitted to redevelop over a length of 3m (the test section was 610mm long). The fluid is air of density 1.2 kg/m^3 and dynamic viscosity 1.79×10^{-5} Pa·s, resulting in Re = 8.4×10^4 based on the inlet diameter. The inlet flow is virtually flat, with a boundary layer thickness of only 1.2mm (4.8% of the pipe radius); thus flat inlet profiles were specified in the simulation. The reported bulk velocity is 27.9 m/s[1] and turbulence intensity is approximately 2%. Inlet turbulence energy and dissipation rate were obtained using equations 3.4 and 3.7, respectively. In this instance, the assumption $\tilde{\varepsilon}_{in} = \varepsilon_{in}$ is valid. Durrett et al (1988) disclosed that the flow was nearly fully developed after 40 step heights, but that it was similar at only 20H. For this reason, a computational domain length of 27H was selected. Wall treatments for the top and side boundaries are identical to those described in section 3.3.3.

The computational grids were of a similar nature to those utilised in the previous pipe expansion case (section 4.2). Grid independence was ascertained by comparing

[1] Prior to obtaining the reports of Durret et al, the simulation was performed using the inlet velocities quoted by Chang et al (1995) in their investigation of the Durret et al case. This figure was 12% lower than that given by Durret et al (1988), and led to unrealistic reattachment lengths. The k-ε model in TEACH predicted a reattachment length which coincided with the experimental value whilst Chang et al (1995) overpredicted this point by 7%).

skin friction plots for 200×70 and 200×100 grids (see figure 4.33), using the CRY model. Both grids resulted in a reattachment length of $X_r/D_2 = 2.48$, thereby confirming that the smaller mesh is indeed sufficient. The 200×40 grid for the high Reynolds number models was created by removing radial nodes adjacent to the wall until y^+ for the near-wall nodes was mostly greater than 30 (typically in the range 50 to 90). The maximum Peclet numbers in the radial direction were 0.787 and 1.83 for the CRY and k-ε models, respectively, whilst that in the axial orientation was 4.8. Figures 4.34 and 4.35 are contour plots of the ratio Γ_f/μ_{eff} for the k-ε and CRY simulations, respectively. The errors introduced by artificial diffusion are negligible, especially in view of Γ_f being computed for first-order discretisation along *both* axes.

4.3.1 Results

Table 4.5 lists the experimental and predicted reattachment lengths. Only the k-ε model behaves as expected. The CRY and RNG models, which gave the best results in the Tropea et al (1989) case, now overpredict the reattachment length by a significant margin; the Yap correction causes the LSY model to do likewise. Interestingly, the CR model yields the most accurate reattachment length.

	Experimental	k-ε	RNG	LS	LSY	CR	CRY
X_r/D_2	1.97	1.74	2.17	1.74	2.31	2.05	2.48
Error	-	-11.7%	+10.2%	-11.7%	+17.3%	+4.1%	+25.9%

Table 4.5: Experimental and computed reattachment lengths for the pipe expansion of Durrett et al (1988).

All turbulence models predicted secondary recirculation (see table 4.6); introduction of the Yap correction term was seen to have a large effect on corner eddy size, particularly in the case of the LS model. Durrett et al (1988) only reported an experimental secondary eddy length ($X_r/H = 1.2$) for a pipe expansion involving a larger step height and smaller inlet diameter; since the bulk velocity was increased to maintain a constant Reynolds number, it is expected that the corner eddy be similar to that in the lower flow rate.

	Experimental	k-ε	RNG	LS	LSY	CR	CRY
X_r/H	≈1.2	0.13	0.20	0.15	0.59	0.27	0.53

Table 4.6: Experimental and predicted corner-eddy lengths.

Experimental and computed radial profiles (normalised with the inlet velocity) of mean velocity U, turbulence energy k and Reynolds shear stress $\overline{u'v'}$ are plotted at six axial locations (see figures 4.36 to 4.38). Durrett et al (1988) stated that the experimental errors were approximately ±3% for the mean axial velocity, and 3% and 6%, respectively, of the maximum turbulence energy and Reynolds stress. Thompson et al (1984) assumed zero swirl and only made axial and radial measurements for normal stresses. However, even in the absence of swirl the normal Reynolds stress in the tangential direction is non-zero. As noted by Hinze (1975), $\overline{v'^2} \approx \overline{w'^2}$ for a free jet. Since a major feature of pipe expansion flows is the free shear layer, the experimental turbulence energy was calculated from

$$k = \frac{1}{2}\left(\overline{u'^2} + 2\overline{v'^2}\right) \tag{4.7}$$

Figures 4.36 to 4.38 indicate the presence of trends broadly similar to those found in the Tropea et al (1989) pipe expansion. However, several differences exit. Downstream of the reattachment point (X_r/H = 8.3), the standard k-ε model most accurately resolves the axial velocity, particularly at the centreline. This is in stark contrast to this model's predictions in the previous case. The turbulence energy still remains best predicted by the RNG model, but again, the profiles predicted by the k-ε model are in much better agreement with the experimental data, than previously. The cubic model underpredicts the centreline value of k beyond the reattachment location, but very far downstream (X/H = 20) there is a substantial overprediction of k, which is linked with the excessive centreline level of U. The Reynolds shear stresses computed by the nonlinear model are in almost as much error as those of the k-ε model, whilst the RNG predictions are in excellent agreement. Once again, the Yap correction term did not influence the bulk flow; only the distributions right at the wall were altered.

4.3.2 Discussion

The most striking aspect of the comparison between Tropea et al (1989) and Durrett et al (1988) simulations is the amelioration of the k-ε model, both in terms of reattachment length (which is now in line with predictions reported in the literature) and actual flow profiles. This is largely due to the flow being of a much higher Reynolds number (Re=84000) than the previous pipe expansion (Re=15600). The RNG model returns predictions which are fairly consistent with those of the Tropea et al (1989) case, apart from the excessive reattachment length. The nonlinear model, on the other hand, does not perform so well as in the previous case, particularly far downstream of the step.

It is clear from figures 4.37 and 4.38 that the relatively poor performance of the nonlinear model is due to insufficient generation of turbulence energy within the free shear layer, consequently resulting in shear stresses which are too low. This explains the overprediction of the reattachment length; the Yap correction exacerbates the situation by further reducing the near-wall k and $\overline{u'v'}$ levels. Similar behaviour was reported by Apsley & Leschziner (1998) who applied a newer cubic turbulence model to the back-facing step flow explored by Driver & Seegmiller (1985) (Re=3×10^5); despite several theoretical improvements over the present CRY model (including a replacement for the Yap term), the reattachment point was overpredicted by 11%. Apsley & Leschziner (1998) noted that this problem can be traced to the strain-dependent expression for C_μ; in areas of high strain rates (e.g. in the separated shear layer), C_μ can be decreased by an order of magnitude compared to the standard value of 0.09 (see figure 2.1). The resulting underpredicted shear stresses cause the free shear layer computed with the CRY model to persist far downstream of the step where, according to the experimental results of Durrett et al (1988), the redevelopment process is in fact quite advanced (figure 4.38). The other parameter directly affecting the eddy viscosity is the damping function f_μ.. Examination of this variable reveals that f_μ. attains the high Reynolds number limit of unity close to the wall (at r/R=0.96), thus confirming that the above trends are in fact due to C_μ.

The deterioration in performance of the CRY model, due to low values of C_μ, seems to be directly linked to the much larger Reynolds number (Re=84000 in the

Durrett et al, 1988, flow; Re=15600 in the Tropea et al, 1989, case). Since levels of turbulence energy are proportional to the Reynolds number, it is reasonable to conclude that the strain invariant (equation 2.36), which is used to calculate C_μ (equation 2.35), is also higher in the present case, thus causing reduced values of C_μ (see figure 2.1).

A third pipe expansion flow was simulated (see Appendix G for details) just to provide an additional set of predicted reattachment lengths to compare with the computations for the Tropea et al (1989) and Durrett et al (1988) cases. The Back & Roschke (1972) flow was characterised by a Reynolds number of 20000, which is comparable to that of the Tropea et al (1989) case. A useful comparison of the relative performance of each turbulence model, for the three pipe expansions investigated, can be made by assigning cardinal positions to the various models which correspond to the predicted reattachment lengths. For example, since the CRY model predicts the longest recirculation zone for a given case, it is assigned a value of unity.

	k-ε	RNG	LS	LSY	CR	CRY
Tropea et al (1989)	6	3	5	2	4	1
Durrett et al (1988)	=5	3	=5	2	4	1
Back & Roschke (1972)	6	3	5	4	2	1

Table 4.7: Relative predictions of reattachment length for three pipe expansion cases.

Table 4.7 reveals at a glance that the turbulence models behave in a consistent manner, as far as recirculation is concerned, across the variety of pipe expansions examined. The CRY model always predicts the longest recirculation zone whilst the k-ε and LS models continuously underpredict the reattachment length by the greatest amount. Only in the Back & Roschke (1972) case do the LSY and CR models exchange relative positions.

Another noteworthy issue is the ability of the turbulence models to compute corner eddies. The low Reynolds number models always predict a secondary recirculation zone, the length of which is subject to modification by the Yap correction

term. The high Reynolds number models are less consistent. No corner eddies are predicted in the Tropea et al (1989) case, whereas secondary recirculation is forecast in the Durrett et al (1988) flow.

The main conclusions drawn from the simulations of three different pipe expansion flows are listed below:

- The CRY model always predicts the longest recirculation region whilst the k-ε model consistently underpredicts this feature.
- The Yap correction term affects the computed reattachment length in all pipe expansion flows by acting in the vicinity of the wall.
- The performance of the models is affected by Reynolds number:
    - The k-ε model is seen to improve predictions as the Reynolds number increases.
    - Increasing the Reynolds number has a detrimental effect on the CRY model.
    - The RNG model is not strongly affected by Reynolds number.
- Turbulence models which employ damping functions (i.e. LS and CRY models) always predict secondary recirculation zones.

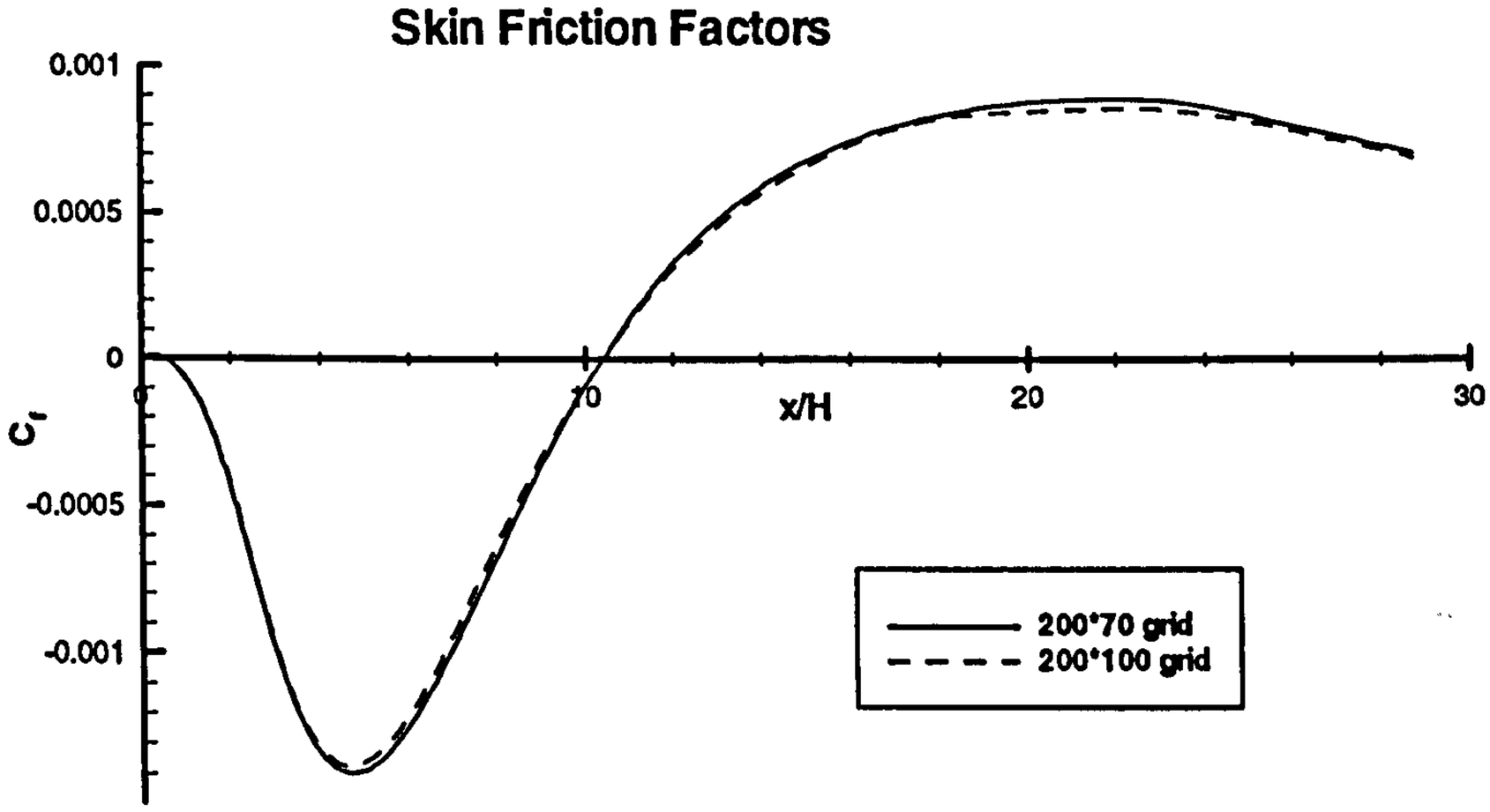

Figure 4.33: C_f plots confirming grid independence for the 200×70 mesh.

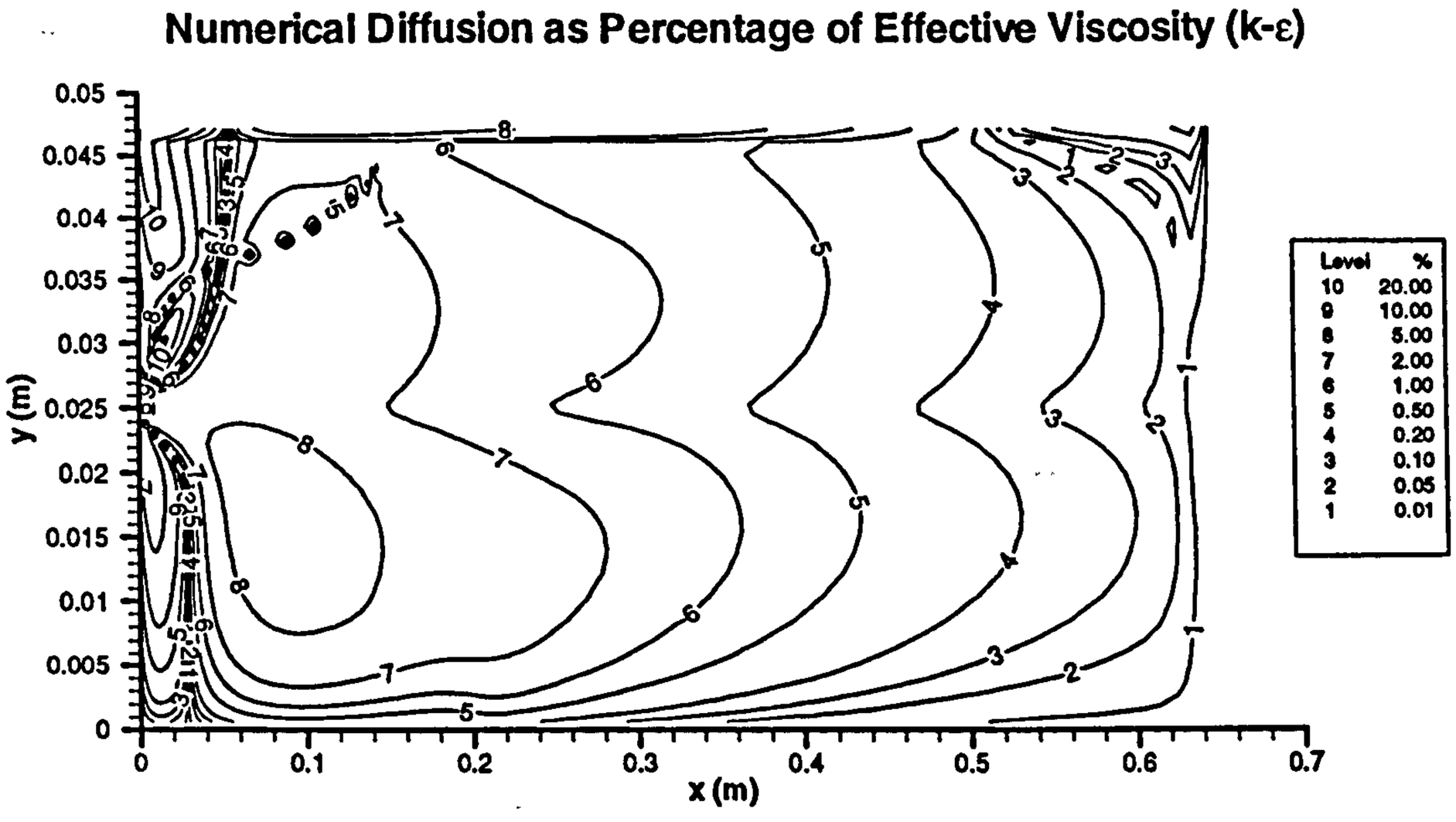

Figure 4.34: Contour plot of artifical diffusion (*k-ε* model), Durrett et al (1988) pipe expansion case.

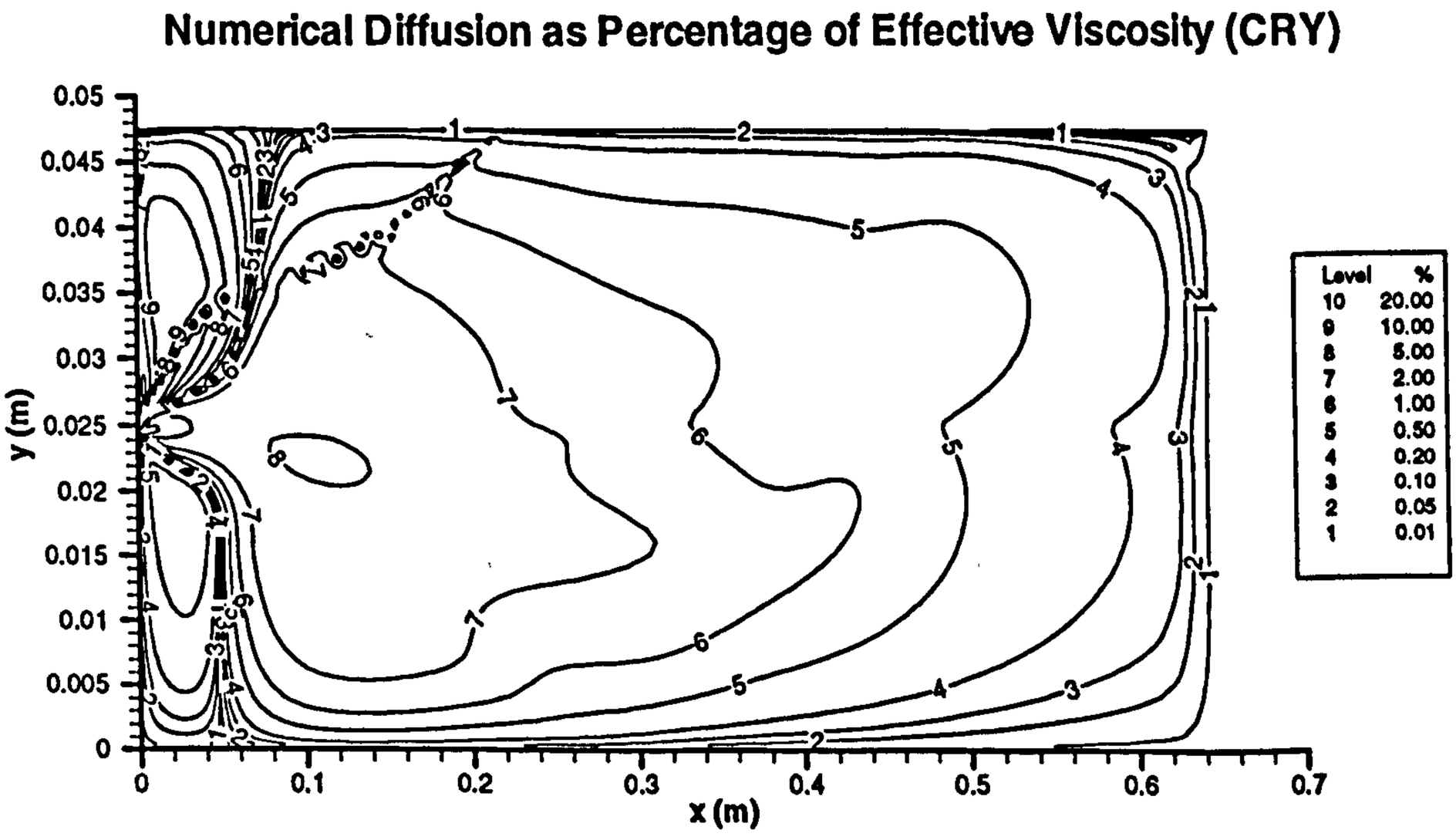

Figure 4.35: Contour plot of artifical diffusion (CRY model), Durrett et al (1988) pipe expansion case.

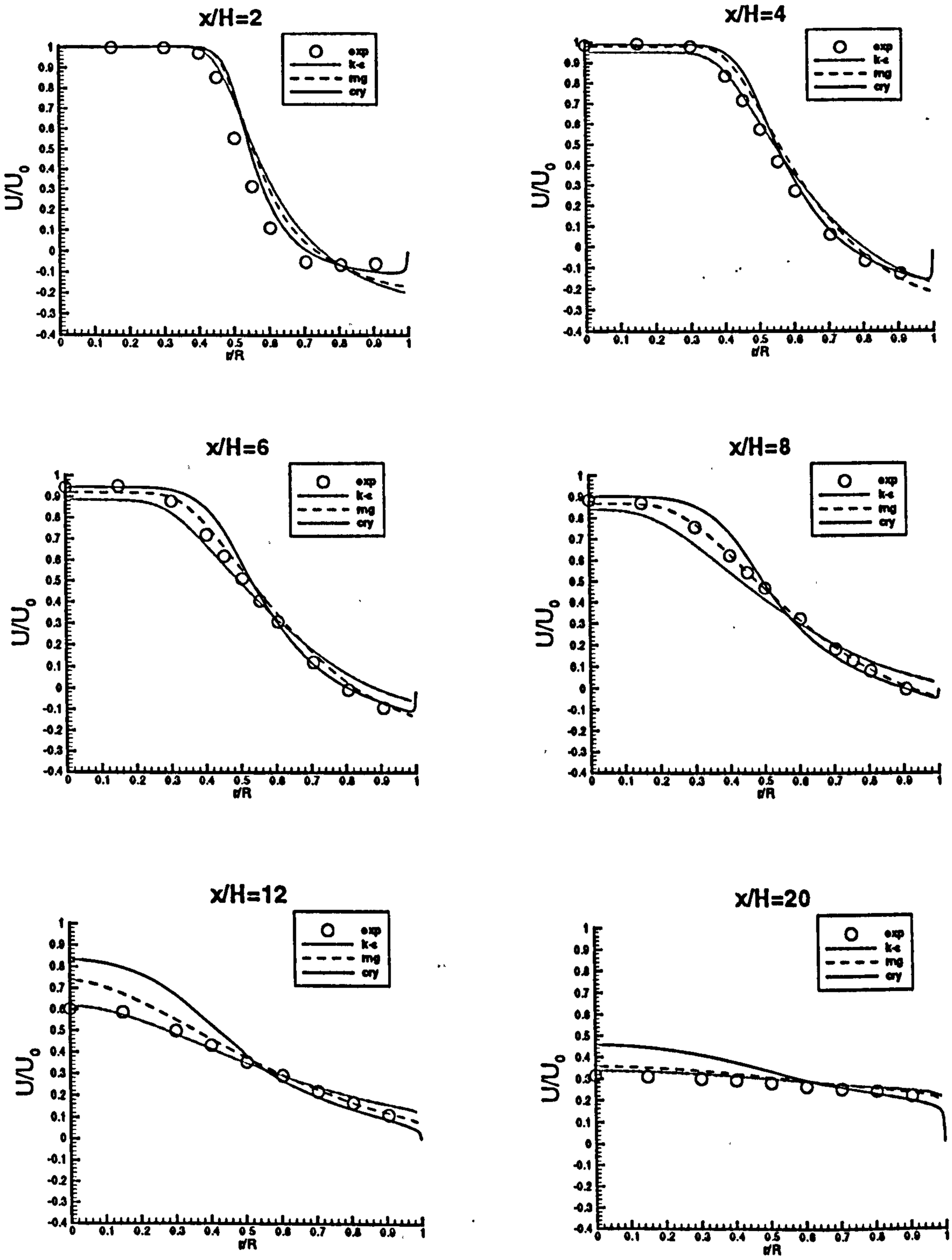

Figure 4.36: Radial distributions of axial velocity, Durrett et al (1988) pipe expansion.

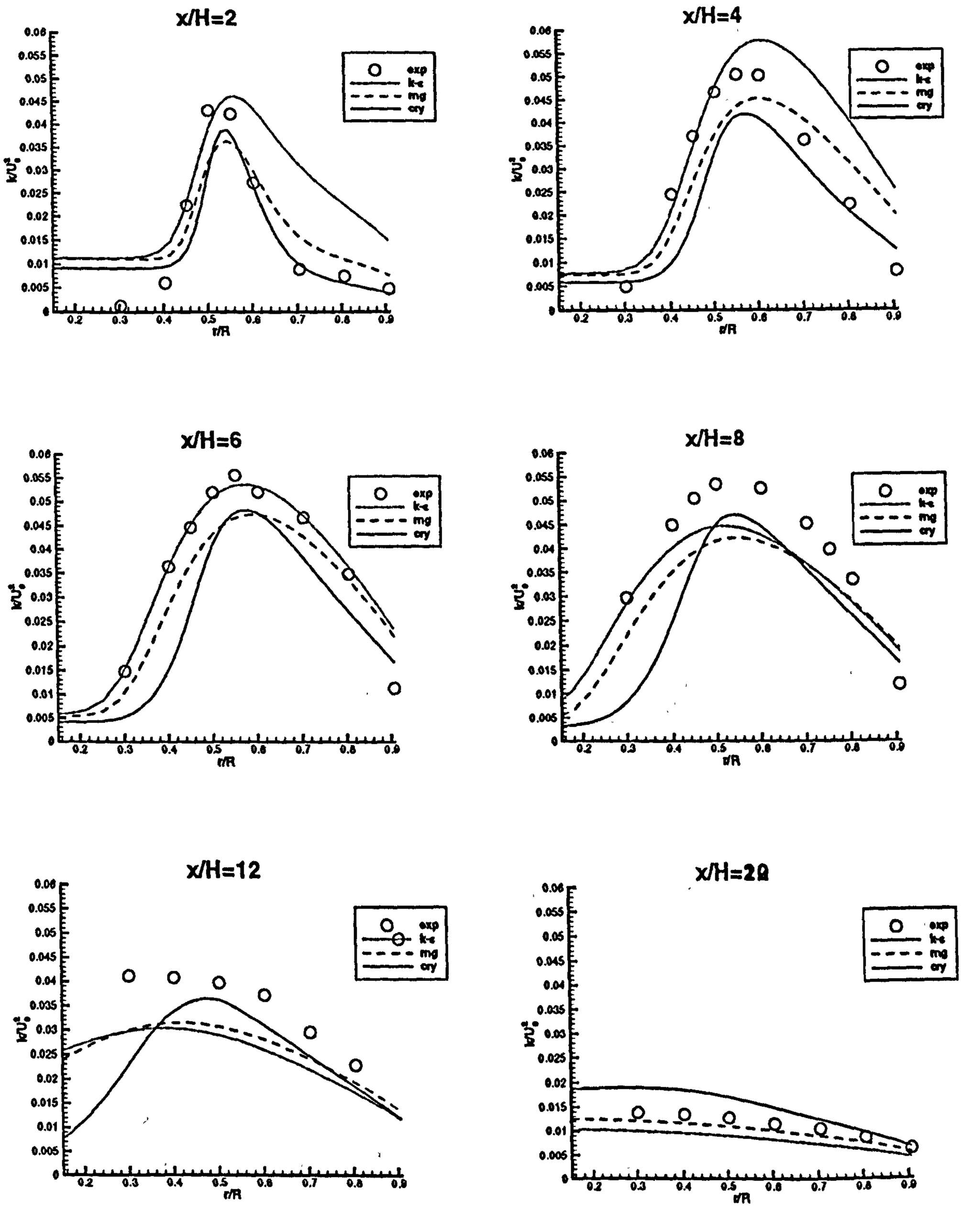

Figure 4.37: Radial distributions of turbulence energy, Durrett et al (1988) pipe expansion.

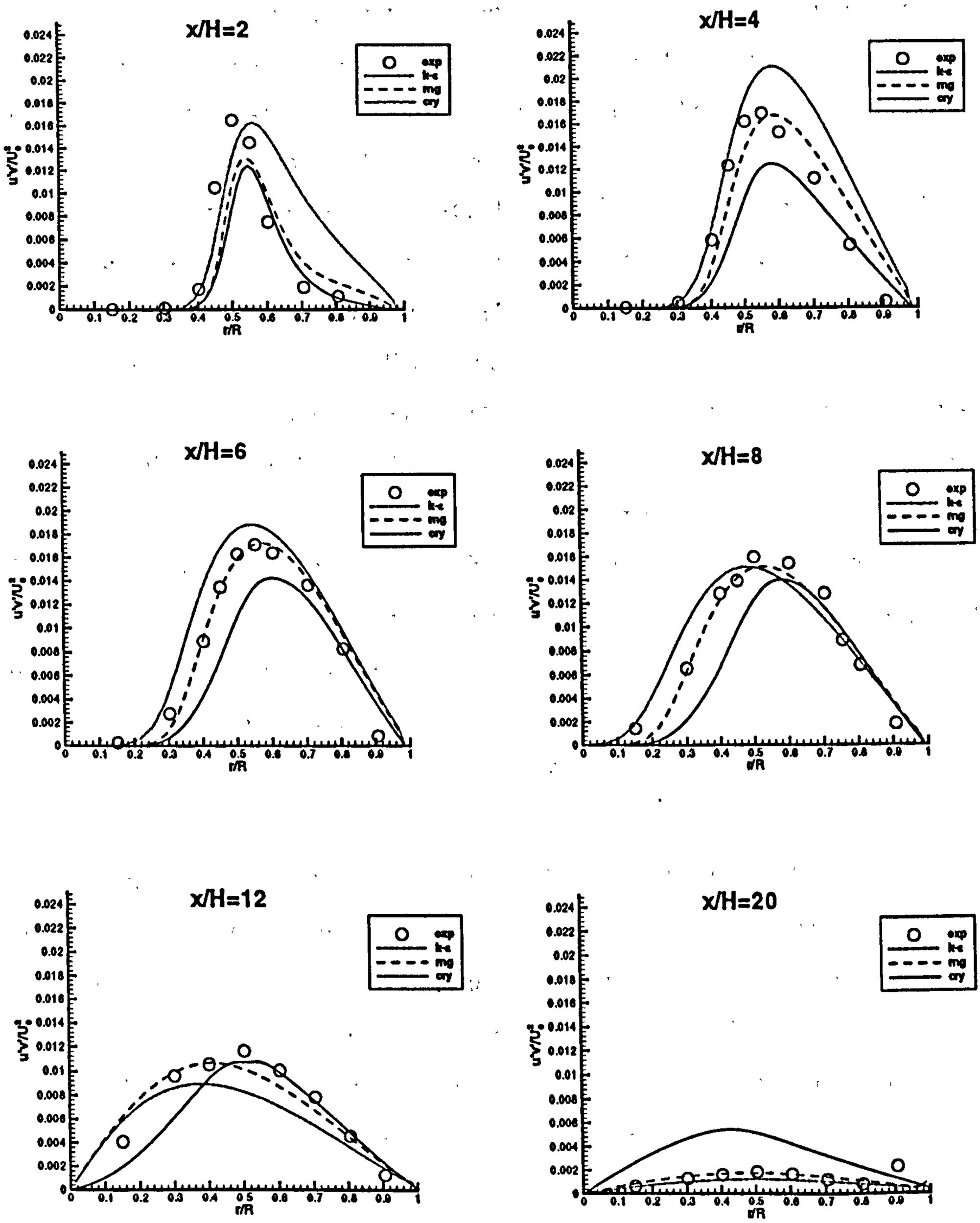

Figure 4.38: Radial distributions of Reynolds shear stress, Durrett et al (1988) pipe expansion.

4.4 SWIRLING PIPE FLOW - KITOH (1991)

Swirling flows are generally complex and of a three dimensional nature. Their properties often lend themselves to promoting flame stability and mixing in combustors. Providing the initial swirl intensities are sufficiently high, the decaying swirl results in adverse pressure gradients which are large enough to form a recirculation zone. The ensuing convection process serves to stabilise the flame. More importantly, though, mixing can be enhanced by the additional rotational shear strains which generate higher levels of turbulence. Hogg & Leschziner (1989) remark that the pressure field created by swirling motion can either amplify or attenuate turbulent mixing, depending upon the specific radial distribution of tangential velocities. The link between swirl and pressure field lies in the fact that the production of stresses, both shear and normal, contains contributions from swirl-related strains which also increase normal-stress anisotropy. Hogg & Leschziner (1989) specify that forced-vortex (i.e. solid body) rotation moderates the stresses whilst free-vortex tangential patterns magnify the stresses. In the extreme case of high levels of swirl, turbulent transport, and hence mixing, is actually dampened, thereby negating the potential advantage of introducing swirl in combustors. It is therefore vital to be able to accurately model swirling flows.

Highly-intensive, swirling pipe flow is the simplest configuration which includes the physical phenomena outlined above. The driving feature of such a flow is the centrifugal force variation in space, resulting in both adverse and favourable pressure gradients. These cause the pitch (number of twists per unit length) of the spiral-like streamlines to diminish in the axial direction, promoting a flow which is skewed relative to the orthogonal coordinate axes. Kitoh (1991) notes that the precise nature of the associated vortex-type motion depends largely on swirl intensity; at lower swirl numbers ($\Omega \leq 0.1$) the flow patterns resemble those of a forced vortex. Higher swirl numbers, however, result in a combination of forced and free vortex patterns; recirculation zones are linked with this regime.

Kitoh (1991) made available a comprehensive set of results obtained during the experimental investigation of various swirling pipe flows. Those featuring higher swirl numbers are depicted as consisting of three main regions: a near-wall boundary layer,

an annulus and a core. High swirl intensities result in a recirculation zone within the core, which is characterised by large, negative axial velocities. The tangential velocities are characteristic of a forced vortex in the core and a free vortex in the annulus. Kitoh (1991) reported that the flow in the boundary layer was free from skewing up to a certain point; furthermore, the centrifugal force (created by streamline curvature) was the dominating factor whilst anisotropy in this region was weak.

Bearing the complexity of the flow in mind, the nonlinear CRY model is expected to yield significant improvements over the standard k-ε model's predictions for swirling pipe flow. The case is also simulated with the Reynolds Stress Model (RSM) in Fluent. This type of model is acknowledged (see the review of Launder, 1989) as being the most comprehensive in terms of physical realism and hence sets a target against which the nonlinear EVM can be compared. The flow characterised by Reynolds number 50000 and swirl intensity $\Omega \approx 1$ was selected for computational study because the largest number of experimental data was available for this particular case. The high swirl number signifies that the flow is considerably more complex than the fully-developed, forced-vortex type swirling flow investigated by Craft et al (1996) and Suga (1995) with the CRY model (indeed, this is the flow with which the swirling aspects of the cubic model were calibrated), and thus provides a serious validation challenge.

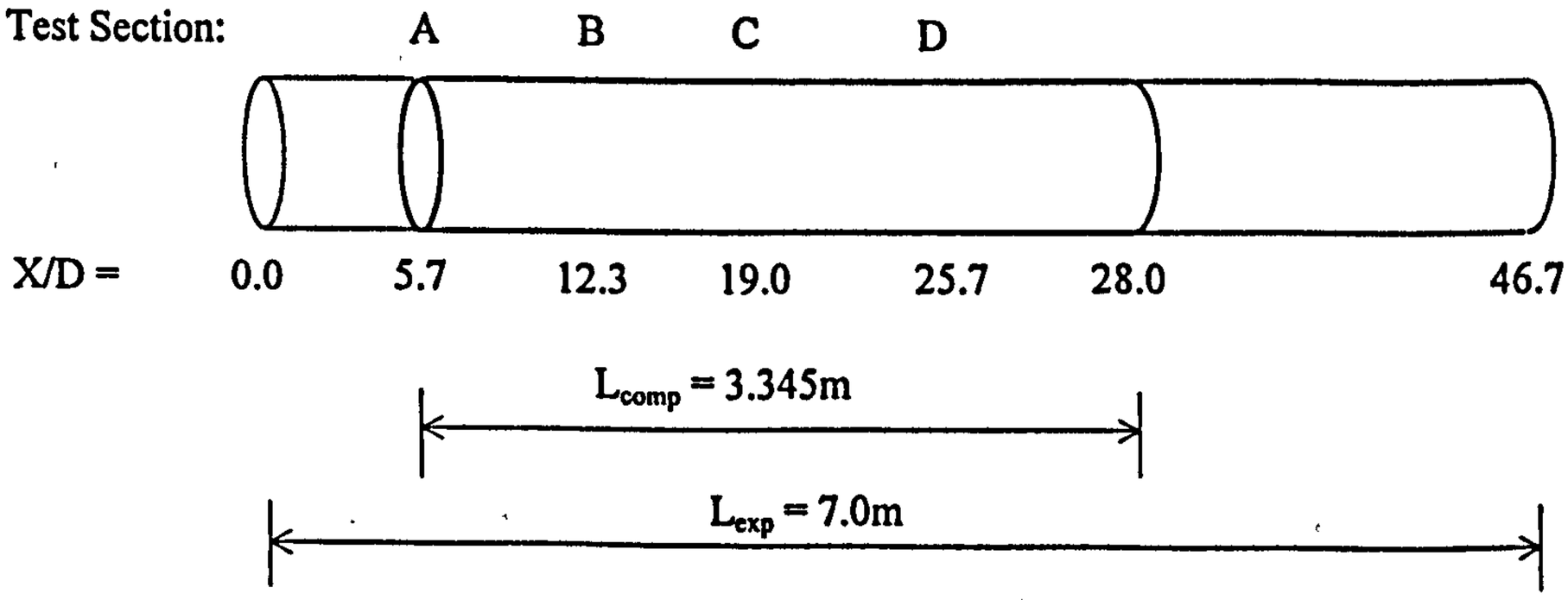

Figure 4.39: Schematic drawing of the test sections of interest.

The test pipe was 7.0m long and of diameter D=0.15m. Air (density 1.225 kg/m^3, viscosity 1.79×10^{-5} Pa·s) was used as the working fluid to measure radial profiles

of velocity and Reynolds stress (using hot-wire anemometry), at various axial locations shown in figure 4.39. The first data point (A) was utilised to set the computational inlet conditions. Thus the computational domain begins at X/D=5.7. The experimental profiles of *U*, *V*, *W*, and *k* used as inlet boundary conditions are shown in figure 4.40. In the case of the RSM, the inlet normal stresses are taken as 2/3*k* whilst the shear stresses are estimated automatically by Fluent from the inlet profiles.

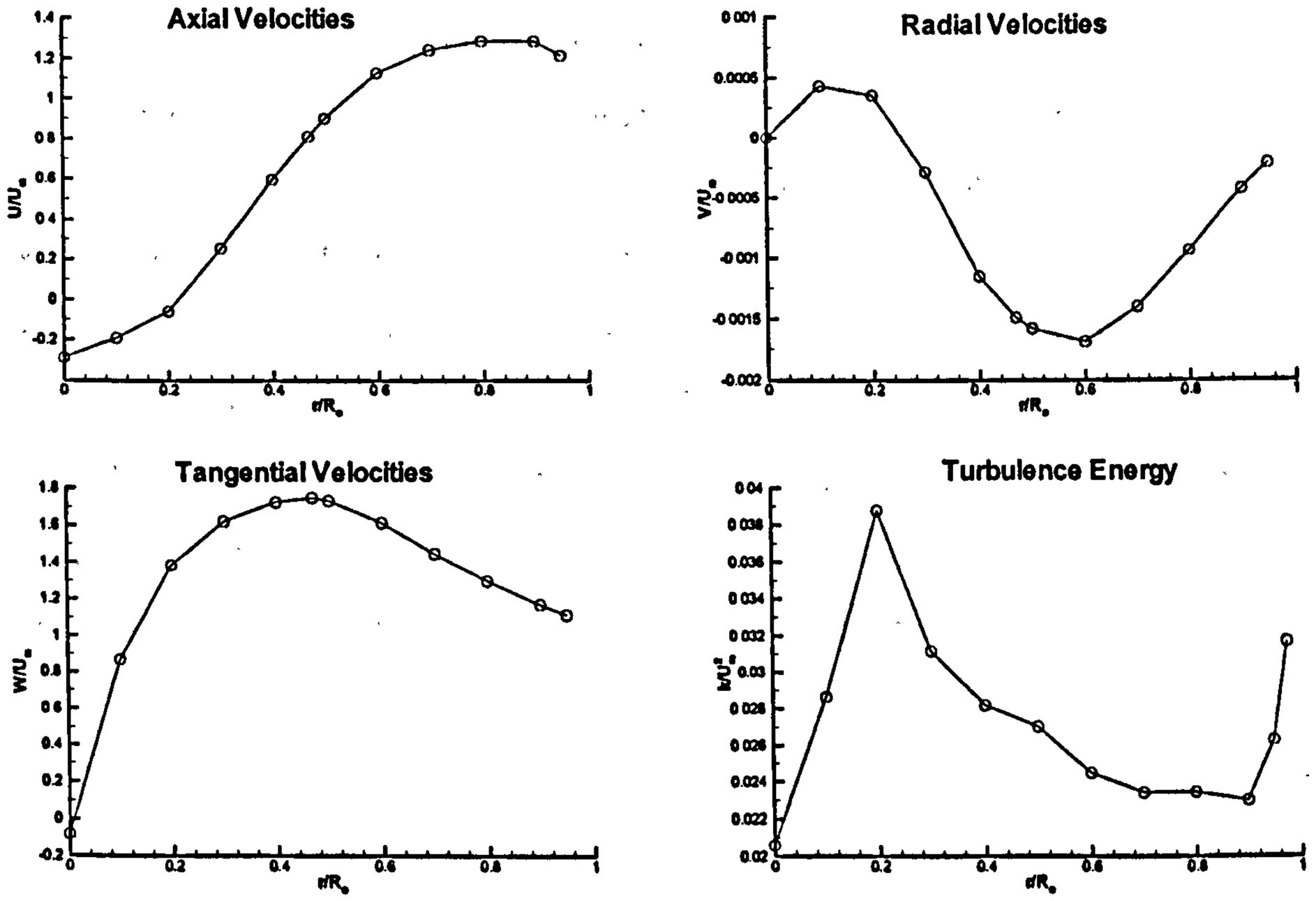

Figure 4.40: Experimental profiles used as inlet conditions.

The inlet values for dissipation rate were obtained from the formula recommended by Sampers et al (1993):

$$\varepsilon_{in} = \frac{k_{in}^{3/2}}{0.5R} \tag{4.8}$$

As in the pipe expansion flow simulations, it was assumed that $\tilde{\varepsilon}_{in} \approx \varepsilon_{in}$; figure 4.40 further indicates that the inlet radial variation of $k^{1/2}$ is not large, hence this assumption is valid. The approximation in equation 4.8 is very different from that given by equation 3.5. However, this specification is justified by comparison with the work of other researchers. Chen & Nieuwstadt (1993), who simulated the current case using

RSM and ASM (Algebraic Stress Model) models in the Fluent and Phoenics commercial CFD codes, specified $\varepsilon_{in} = k^{3/2}/0.2D$ (where D is the pipe diameter). Hogg & Leschziner (1989), computed the swirling flow in an annulus surrounding a central jet, and recommended $\varepsilon_{in} = k^{3/2}/0.36R$ (where R is the outer radius of the annulus).

The experimental test section farthest downstream occurred at X/D=39.0. However, the flow there did not at all resemble fully-developed pipe flow; instead, the axial centreline velocities were still negative at this point. Judging from the experimental trends throughout the length of the pipe, recirculation still existed at the pipe exit (L=7m). In order to lessen the numerical effort, it was decided to simulate a much shorter pipe and to study the results at the first four test sections only. For this reason, the outlet condition was applied at X/D=28.0 (2.3D downstream of the nearest test section D), resulting in a computational length of 3.345m. A simulation employing the CRY model was also carried out for a computational length of 6.0m (the number of axial cells was increased accordingly); identical centreline results were obtained for test sections B, C and D, thereby indicating that the shorter domain does not compromise the results.

Hogg & Leschziner (1989) stated that experiments of swirling flows in a combustor type geometry revealed a recirculation bubble which, no matter how long the combustor, could not be made to recover towards a fully-developed pipe flow. This is a problem because negative axial velocities persist at the pipe exit, thereby invalidating the use of the zero-gradient exit boundary condition. Hogg & Leschziner (1989) utilised an RSM for their swirling flow and noted that it fairly accurately predicted negative axial velocities at the exit. For this reason, they prescribed an axial velocity profile at the outlet rather than simply implementing a zero-gradient boundary condition; however, this had detrimental effects on the results. In the current case the zero-gradient exit condition is still applied because it is assumed that, despite not being strictly valid, it will not greatly affect results much further upstream. Chen & Nieuwstadt (1993) made a similar assumption in their simulation of this flow (using various RSM and Algebraic Stress Models) by applying this exit condition at L=7m.

A 120×28 grid (uniform in the axial direction but progressively refined in the radial orientation) was constructed for use with the high Reynolds number models, such that the near-wall node lay at $y^+ \approx 150$. Comparison of skin friction plots and axial profiles of *U*, *W* and *k* in the core region (where the flow is recirculating), obtained with denser meshes, reveals that the 120×28 grid is indeed sufficient (see figure 4.41 for the graph of skin friction variation). This mesh was also used to support the Fluent simulations conducted using the RSM model, for which standard wall functions were applied at the solid boundary. A grid for use with the low Reynolds number models was based upon the 120×28 mesh; nodes were added in the boundary layer until the near wall node lay at $y^+ < 0.3$. Comparisons (using CRY) of C_f (figure 4.42) show that the 120×55 grid is satisfactory for use with the LS and CRY models. A 300×55 mesh was also utilised for the simulation involving the extended axial domain. The radial cell Reynolds numbers were of order 10^{-3} and 10^{-2} for the *k*-ε and CRY models, respectively, whilst the axial Peclet numbers were of order 10^2. Reducing *Pe* such that central differencing is applied in the axial direction requires an extraordinary amount of additional nodes; besides, the axial *Pe* are so high that convection is clearly dominant. Application of equation 3.1, using the values of *U*, *V* and cell dimensions for which the largest axial and radial *Pe* were calculated, revealed that false diffusion is at most 1% of the eddy viscosity. Furthermore, the Fluent simulations used to verify the TEACH code (using the *k*-ε model and second order UPS/CDS scheme) yield radial profiles which agree well with those predicted by TEACH (see Appendix C), thus proving that the first-order hybrid scheme does not introduce large levels of numerical diffusion in this case.

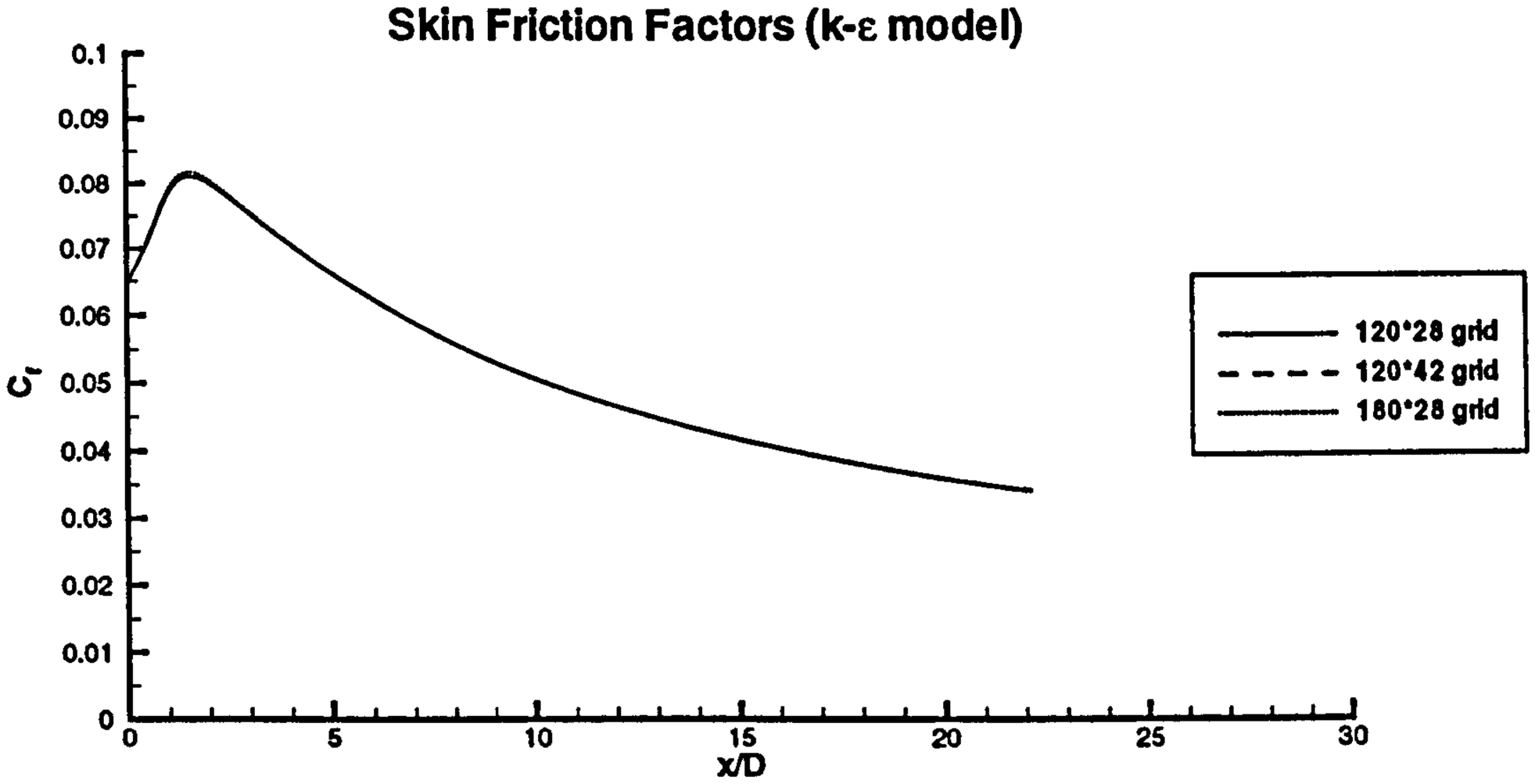

Figure 4.41: C_f plots confirming grid independence for the 120x28 mesh (note that the horizontal orgin corresponds to x/D=5.7 along the experimental axis).

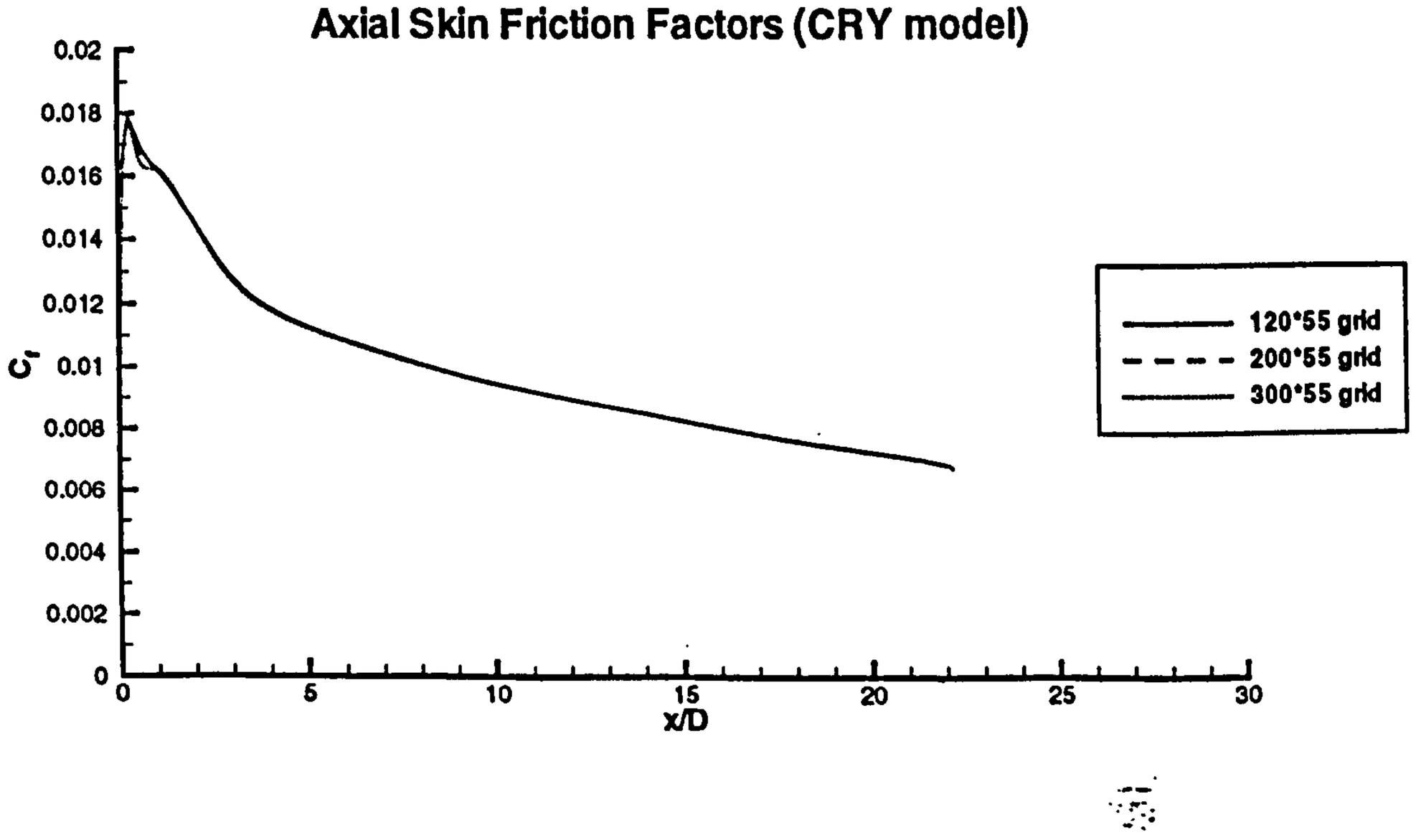

Figure 4.42: Axial C_f plots confirming grid independence for the 120x55 mesh (note that the horizontal orgin corresponds to x/D=5.7 along the experimental axis).

4.5.1 Results

The swirl number is defined by Kitoh (1991) as:

$$\Omega = 2\pi\rho \int_0^{R_0} \frac{UWr^2 dr}{\rho\pi R_0^3 U_m^2} \tag{4.9}$$

where R_0 is the pipe radius. The axial distribution of swirl number is presented in table 4.8 and plotted in figure 4.43.

Test Section	experimental	k-ε	RNG	LS	CR	CRY	RSM
B	0.83	0.76	0.76	0.56	0.61	0.69	0.79
C	0.67	0.59	0.60	0.39	0.43	0.53	0.69
D	0.60	0.47	0.48	0.29	0.31	0.42	0.60

Table 4.8: Experimental and computed swirl numbers (Ω) at the various test sections (the RSM results are obtained with the code Fluent).

It is immediately apparent that the high Reynolds number, linear EVM's compute the swirl numbers more accurately than the nonlinear model, with the k-ε and RNG values being almost identical. The second moment model closely matches the experimental curve. Of all the turbulence models, the LS model returns the lowest swirl numbers. The reason for the apparent success of the high Reynolds number models is immediately obvious when the radial profiles of the tangential velocity (see figure 4.46) are examined. The k-ε and RNG models predict significantly higher values of W than the other EVM's in the region where the product Wr^2 is greatest, and also overpredict axial velocities in the core region. Another observation drawn from the table is that the Yap factor has a significant influence on the predictions of the nonlinear model; it acts to increase the swirl number.

Radial distributions of U, V, W, k, $\overline{u'v'}$, $\overline{v'w'}$, $\overline{u'w'}$, $\overline{u'^2}$, $\overline{v'^2}$, $\overline{w'^2}$ and P are presented in figures 4.44 to 4.54, at the three axial locations depicted in figure 4.39. The data is normalised with either U_m or U_m^2, where U_m is the bulk velocity (4.87m/s). The most striking feature in figure 4.44 is the varying degree with which the different turbulence models are able to resolve the flow in the region $0 < r/R_0 < 0.5$. The linear

EVM's predict virtually flat U profiles in this area, although the RNG model does diminish the centreline velocity somewhat. The nonlinear model predicts a significantly lower centreline velocity, whilst only the RSM is able to closely match the negative experimental velocities which constitute the central recirculation zone. The Yap factor causes small changes in the computed flow near the boundary and has larger effects near the centreline. Figure 4.44 indicates that the experimental centreline velocity increases in magnitude as the flow proceeds downstream. Again, this trend is only captured by the RSM model, whilst the two-equation models predict the opposite. The nonlinear model is the only EVM to approach the experimental U curves. The RSM model is generally able to accurately duplicate the experimental results across the annulus region and to the wall.

The radial velocities are seen to be typically three orders of magnitude smaller than their axial counterparts, and hence play a small role in the swirling flow. This further implies that any small error in axial velocity has a large effect on the radial momentum equation due to the preservation of continuity.

The high inlet swirl intensity gives rise to an experimental, tangential velocity distribution which is similar to a free vortex in the annulus region and approaches a forced vortex in the core. Although the tangential velocities eventually decay completely, this does not happen within the experimental nor computational domains. In fact, the azimuthal velocities are larger than the axial velocities. In contrast to the experimental data, figure 4.46 reveals that all the two-equation turbulence models substantially underpredict the tangential velocity in the annulus and core regions. Furthermore, they are unable to resolve the free-vortex type distribution in the annulus and hence do not distinguish between the core and annulus zones. A relatively weak forced-vortex pattern is computed instead. The RSM model, on the other hand, does predict a free/forced-vortex structure (known as a Rankine combined vortex) but locates the interface between the two vortices at too great a distance from the centreline. Compared to the other two-equation models, the nonlinear model predicts a slightly steeper gradient $\partial W/\partial r$ in the core region. The k-ε and RNG models overpredict W in the region near the wall; the respective curves are very similar at all three axial locations considered. The LS model, on the other hand, underpredicts the tangential velocity

across the entire radius. The Yap factor is seen to promote *W*, particularly in the area $r/R_0 > 0.4$ at locations X/D = 19 and X/D = 25.7.

Examination of figure 4.47 reveals that no single turbulence model can be identified as most accurately predicting the turbulence energy. The linear EVM's constantly underestimate *k* everywhere; even so, significant differences between the *k*-ε, RNG and LS models exist. The RSM model, too, underpredicts *k*, sometimes by as much as the linear EVM's. The performance of the nonlinear model is observed to be somewhat inconsistent; the levels of *k* are either excessive or underpredicted, depending on axial location. Only within the region $r/R_0 > 0.7$ does the cubic model constantly return lower values than given by the experimental data.

Kitoh (1991) reported that the radial location of the peak experimental value of the axial velocity did not coincide with the point at which $\overline{u'v'}$ changes sign. This is a plausible observation since these points are only expected to be in accord in fully-developed flows where the axial gradients are zero and only the cross-stream gradients are sizeable. In the current swirling pipe flow, the axial variation of variables is relatively small. This corroborates the observation that the linear EVM's predict the peak *U* as occurring at the point where $\overline{u'v'} = 0$ (see figure 4.48), resulting from the fact that the only meaningful gradient in the axial momentum equation, as far as the linear EVM's are concerned, is $\partial U/\partial r$. This point is seen to approach the centreline as one progresses downstream (from $r/R_0 = 0.8$ at X/D = 12.3 to $r/R_0 = 0.6$ at X/D = 25.7). The $\overline{u'v'}$ profile computed by the nonlinear model displays 'wiggles' in the vicinity of the x-intercept. These oscillations can be ascribed to the higher-order terms in the nonlinear stress-strain relationship, and are also evident in the $\overline{v'w'}$ plots (see figure 4.49). In fact, they also coincide with the x-intercepts of the $\overline{u'w'}$ curves in figure 4.50. The RSM model does not provide better results than the CRY model, which in turn does improve upon linear EVM predictions of $\overline{u'v'}$. Again, the RNG model behaves as do the *k*-ε and LS models.

An immediately apparent feature of figure 4.49 is the extreme overprediction of $\overline{v'w'}$ by the *k*-ε and LS models and, to a lesser extent, by the RNG model. The

nonlinear model overpredicts $\overline{v'w'}$ by varying degrees but mimics the correct overall trend, whilst the RSM model tends to underpredict $\overline{v'w'}$. Figure 4.50 provides a stark contrast: the nonlinear model returns excessive values of $\overline{u'w'}$ (the Yap term causes a deterioration of the results) but the linear EVM's predict a flat, near-zero profile. In this case, the RSM model clearly outperforms the others.

Figures 4.51 to 4.54 are radial plots of the normal stresses and the relative static pressures. In large portions of the flow, the nonlinear model consistently returns better agreement with the experimental normal stresses than does the RSM. However, some anomalies do occur, such as the trends near the centreline ($\overline{u'^2}$) and in the boundary layer (all normal stresses). The linear EVM's underpredict the normal stresses by several orders of magnitude. No detailed experimental results for pressure are given in figure 4.54 because none were reported by Kitoh (1991). Nevertheless, it is obvious that the various turbulence models return rather diverse values. Although all models predict the smallest pressure at the centreline and the highest at the wall, the RSM seems to forecast the largest radial pressure gradient. The pressure distribution along the centreline is mapped out in figure 4.55; clearly the various models predict rather different trends. The linear EVM's predict a recovery of the pressure immediately downstream of the inlet, which is associated with the extreme overpredictions of centreline axial velocity. The nonlinear model computes a similar trend, but to a milder extent, whilst the RSM predicts a slight negative axial gradient before the pressure increases again much further downstream.

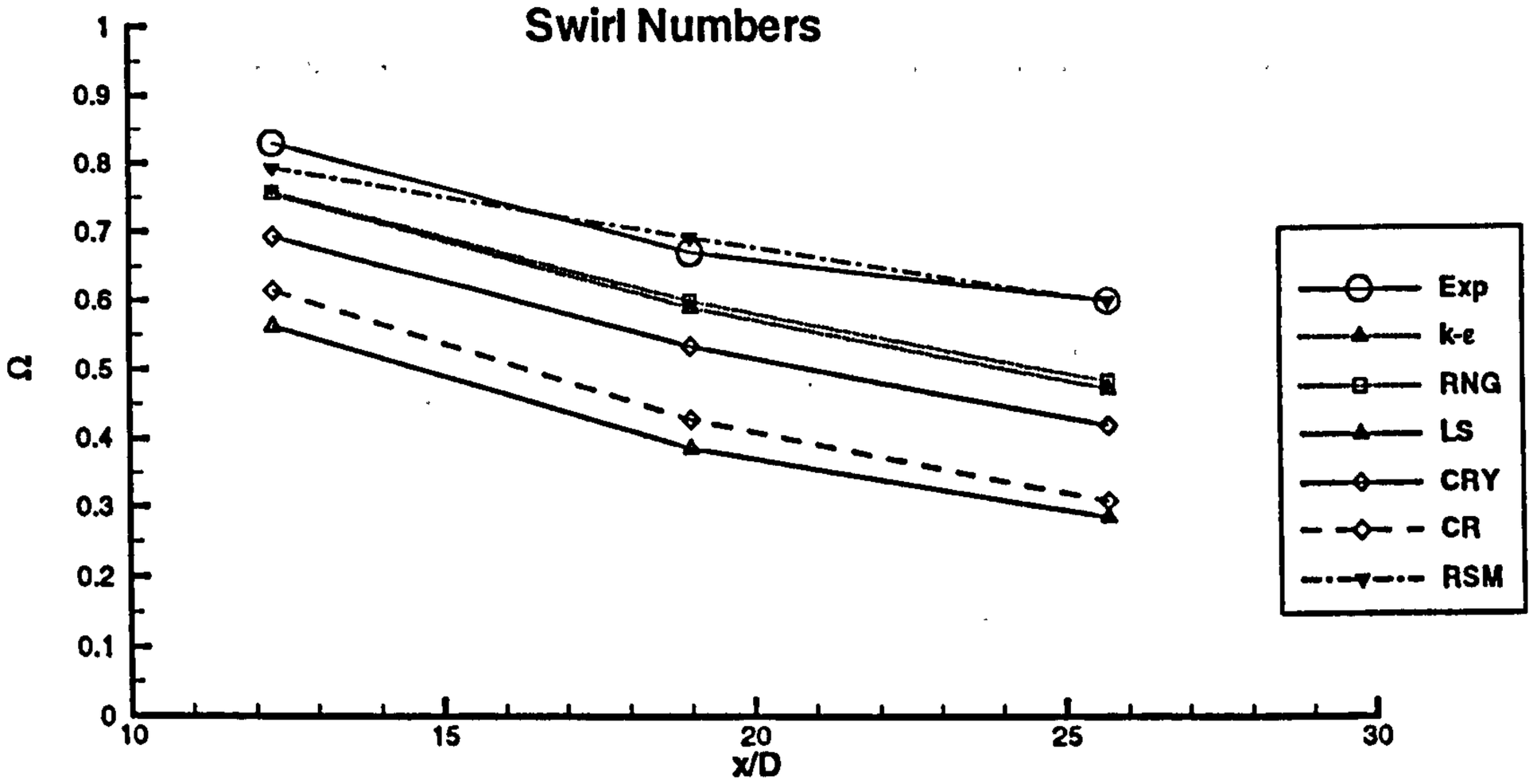

Figure 4.43: Experimental and computed axial variation of swirl number Ω (note that the 'experimental' x-axis is used).

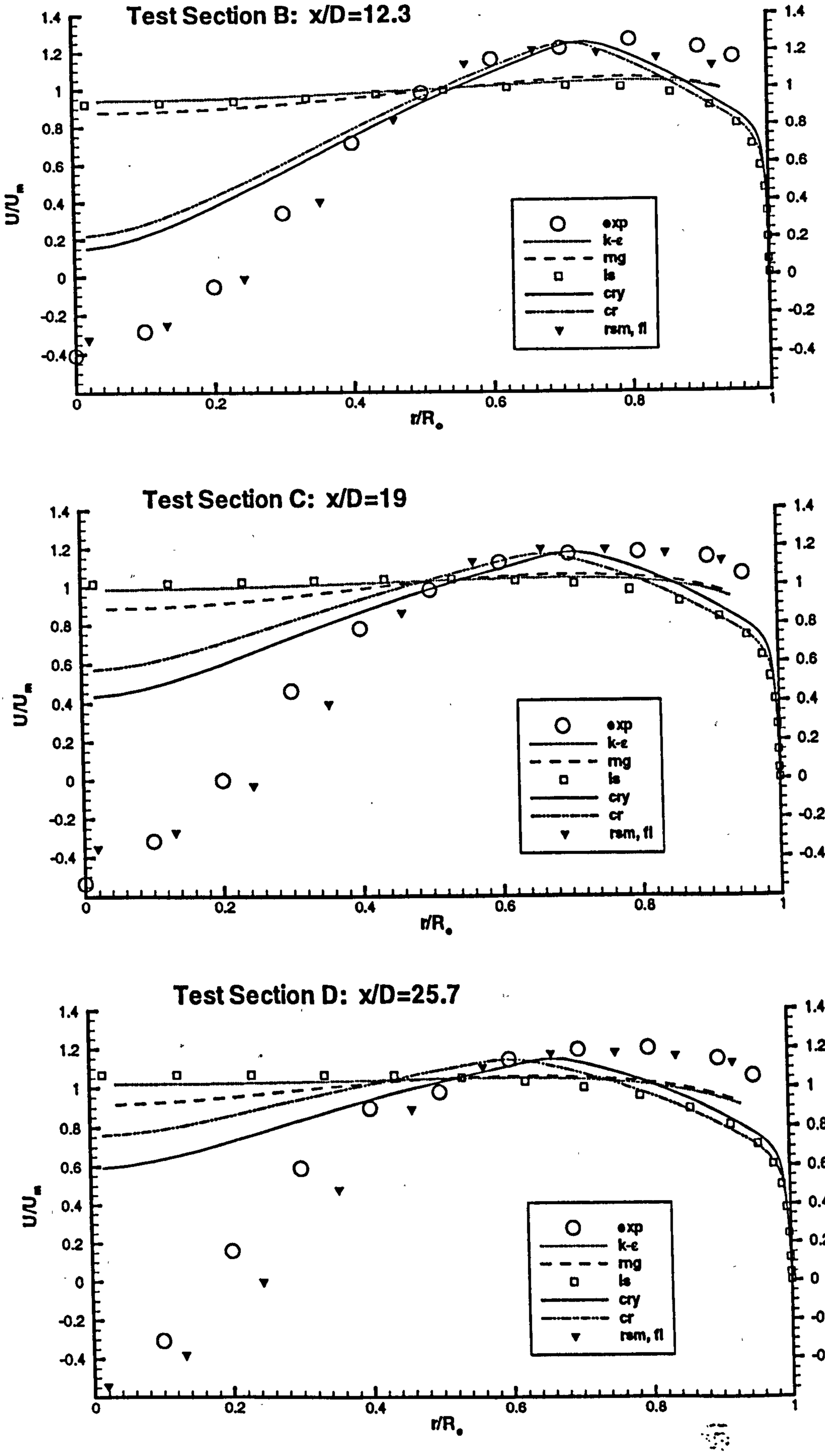

Figure 4.44: Radial distributions of axial velocity, swirling pipe flow (Kitoh, 1991).

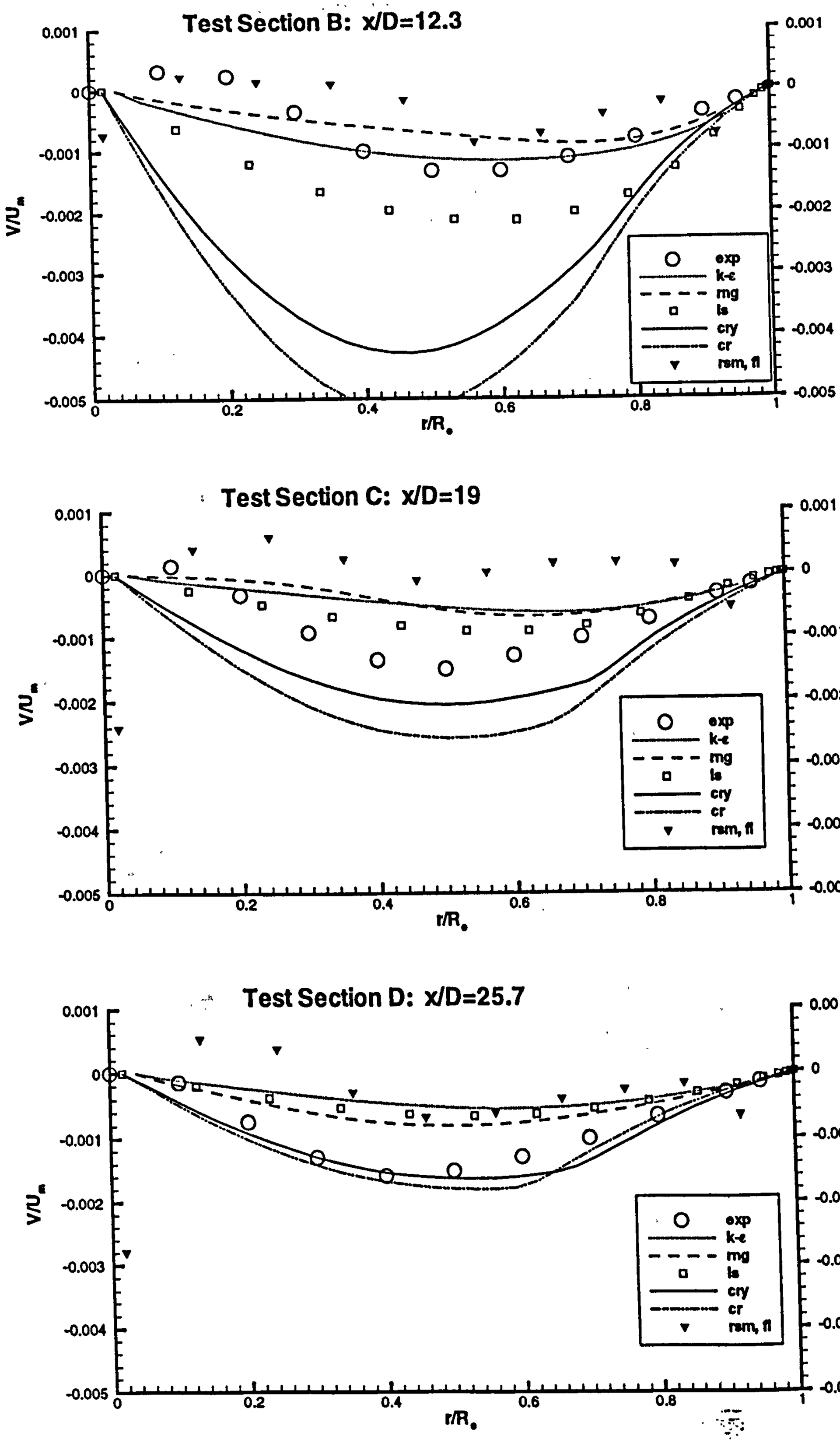

Figure 4.45: Radial distributions of radial velocity, swirling pipe flow (Kitoh, 1991).

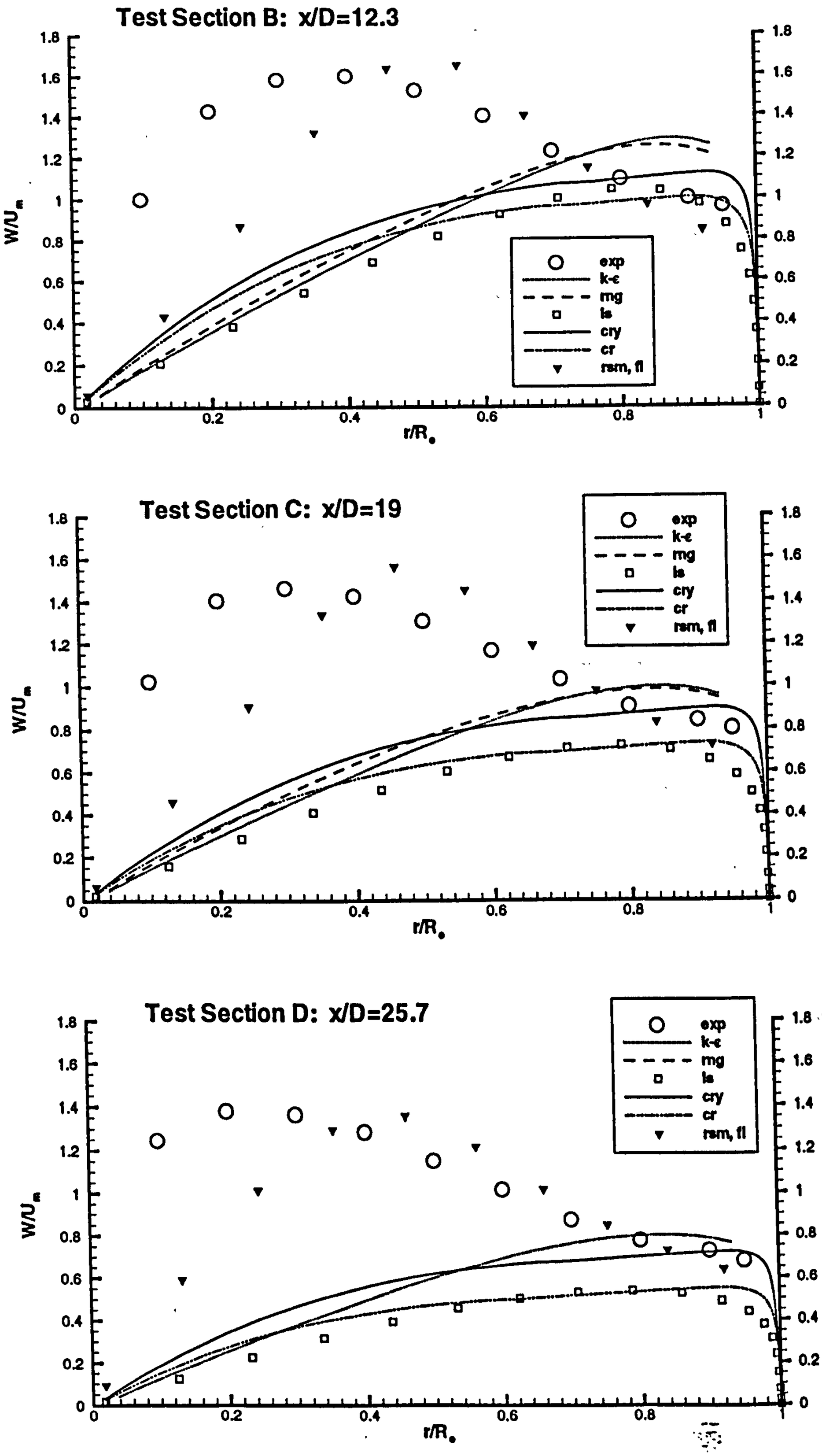

Figure 4.46: Radial distributions of tangential velocity, swirling pipe flow (Kitoh, 1991).

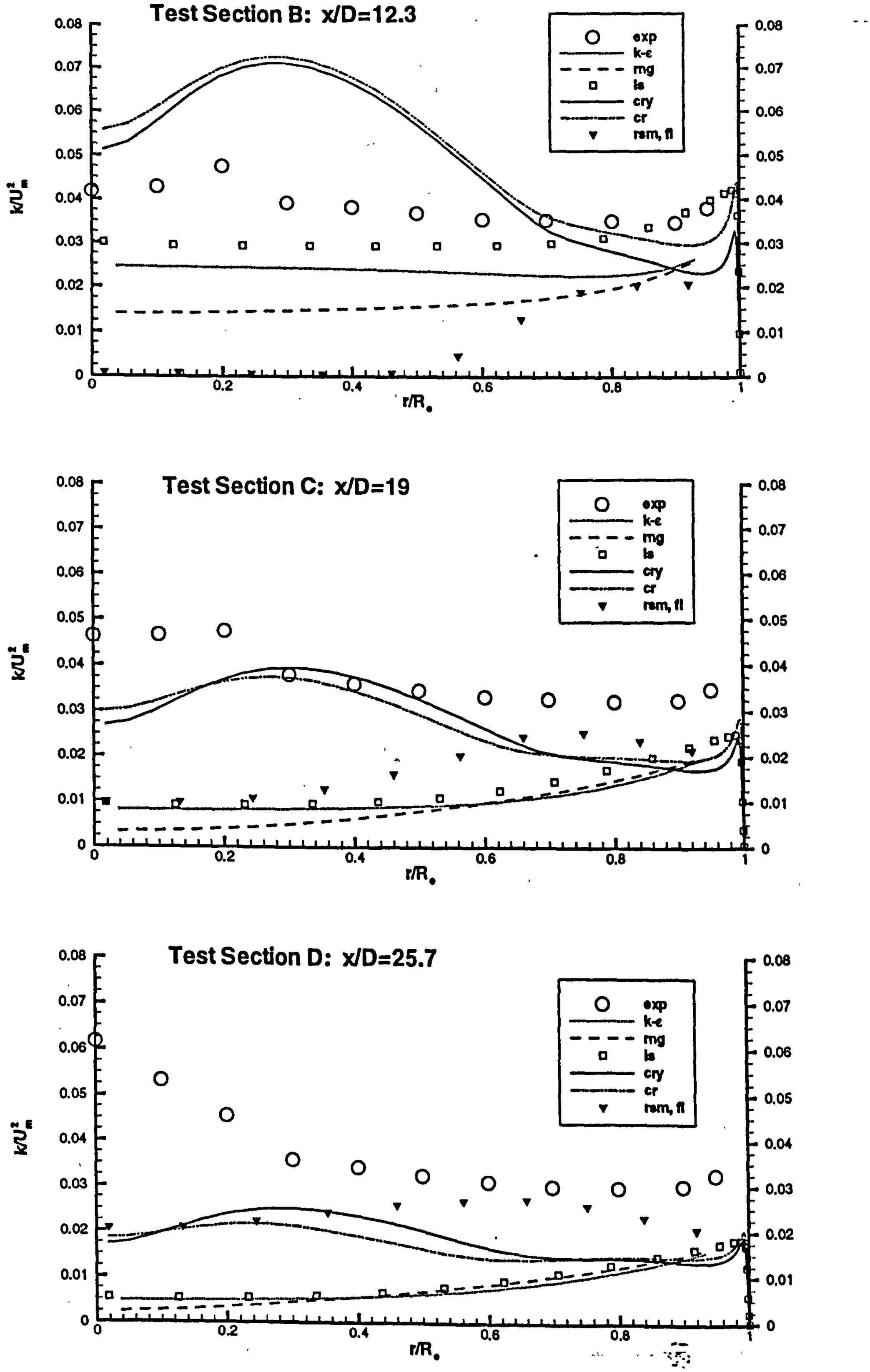

Figure 4.47: Radial distributions of turbulence energy, swirling pipe flow (Kitoh, 1991).

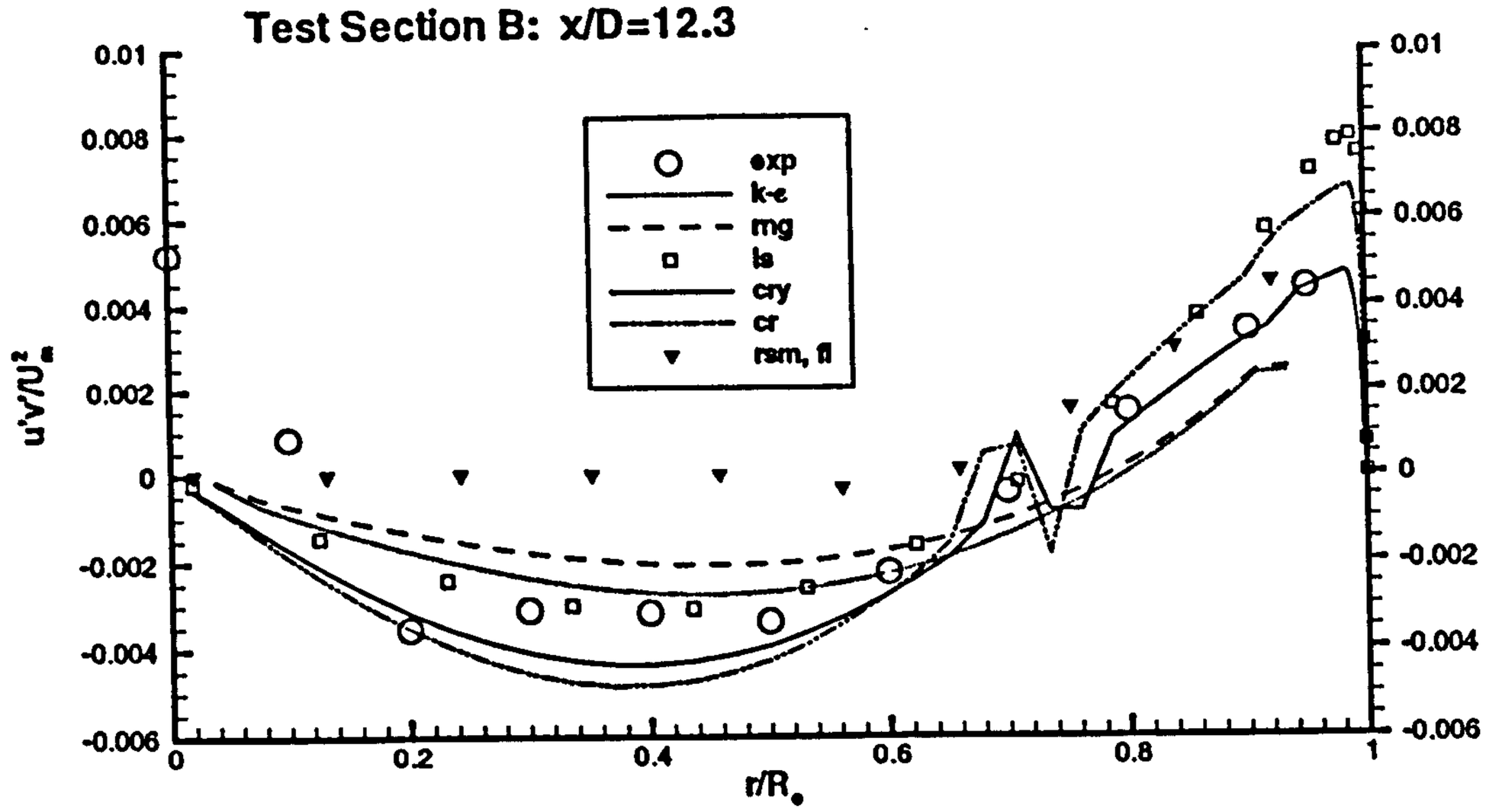

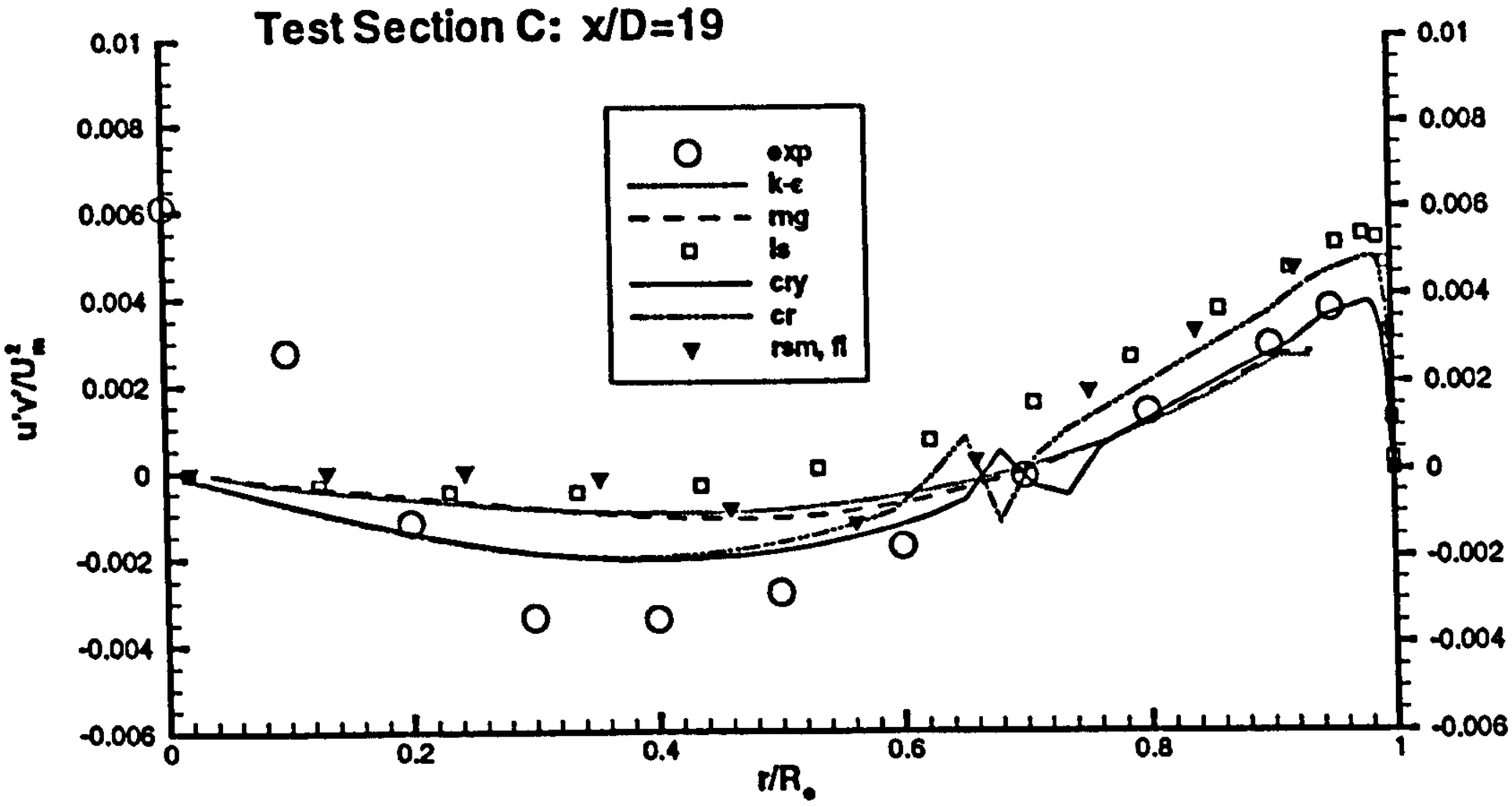

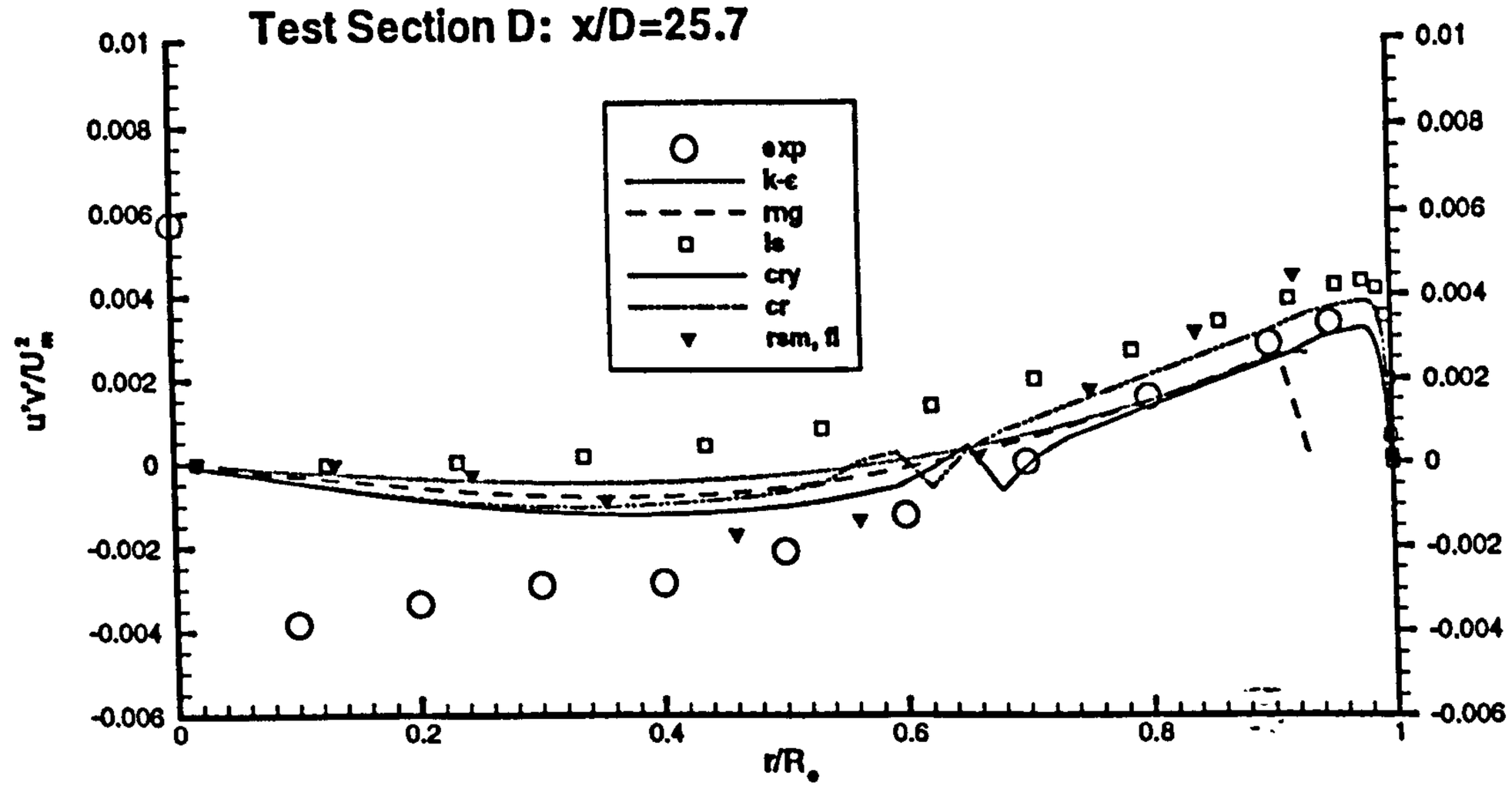

Figure 4.48: Radial distributions of Reynolds shear stress, swirling pipe flow (Kitoh, 1991).

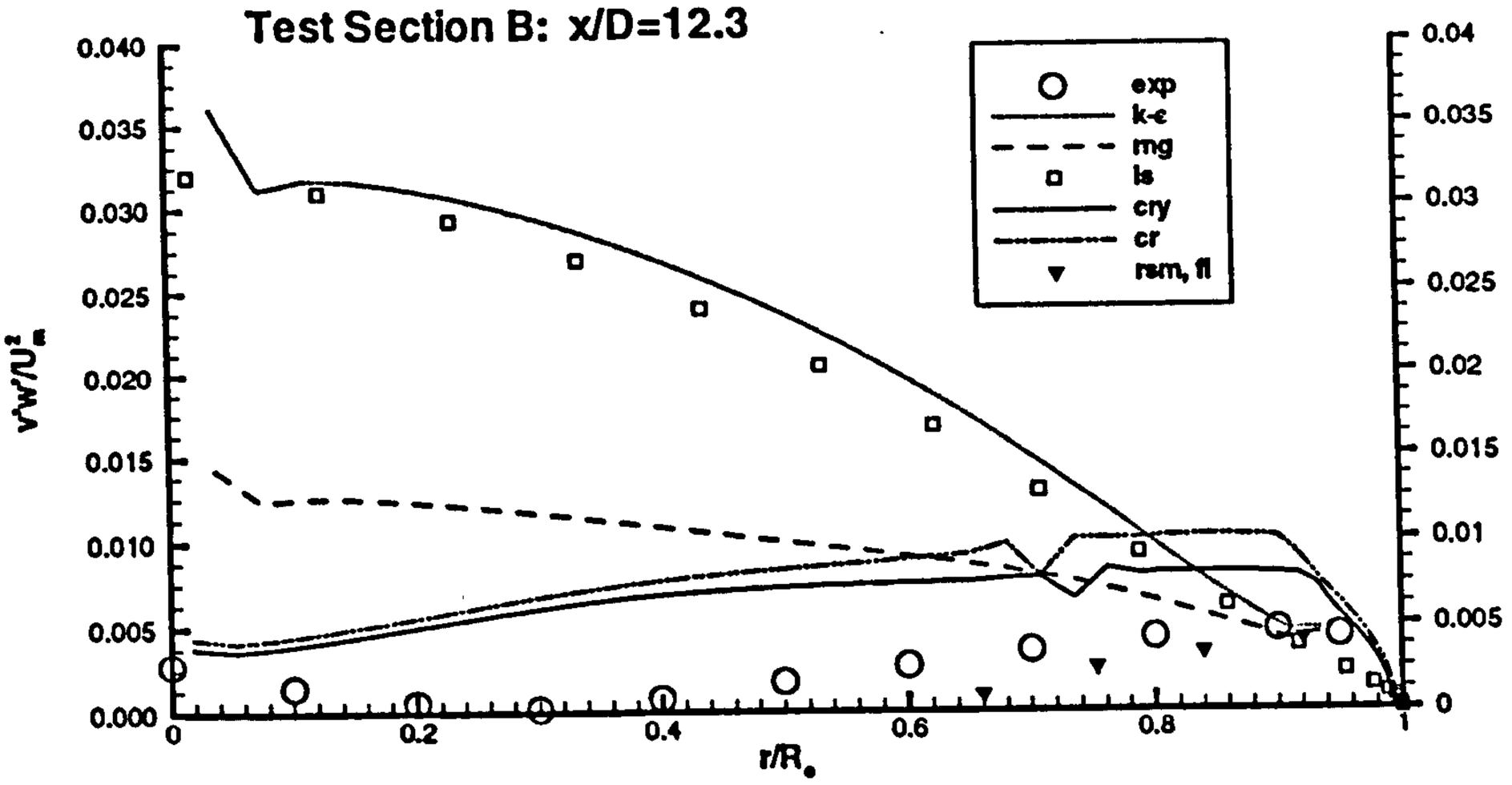

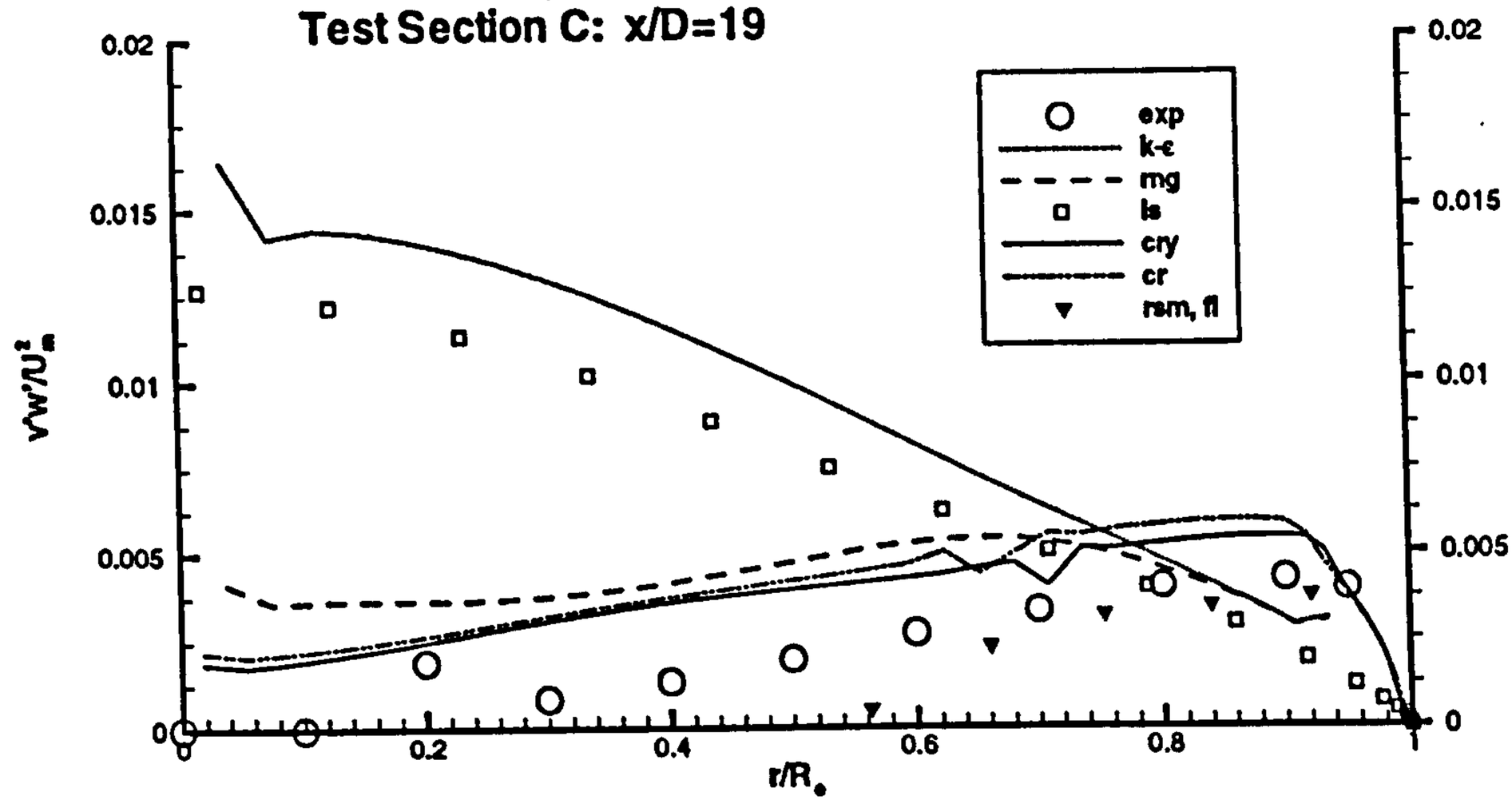

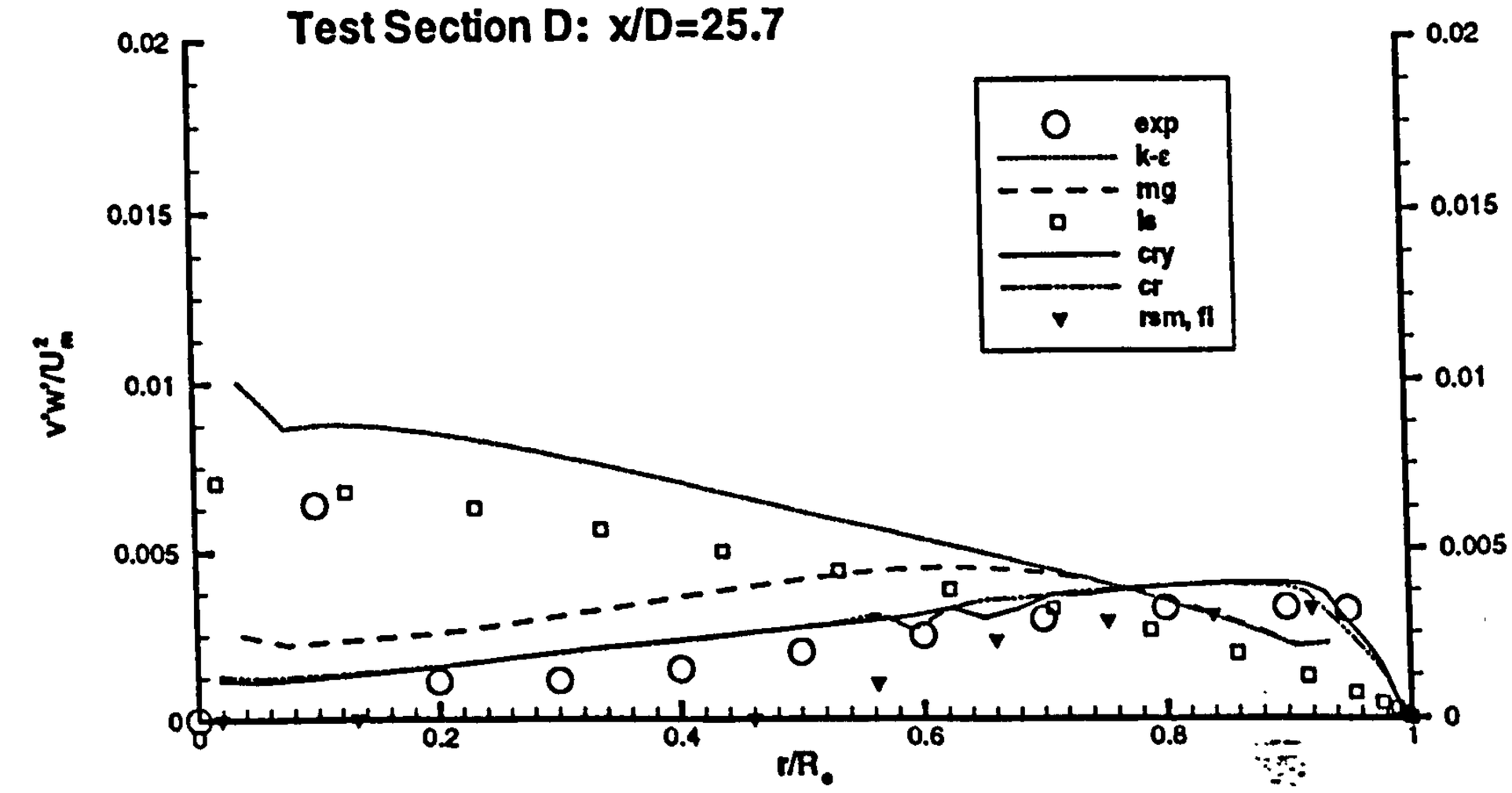

Figure 4.49: Radial distributions of Reynolds shear stress, swirling pipe flow (Kitoh, 1991).

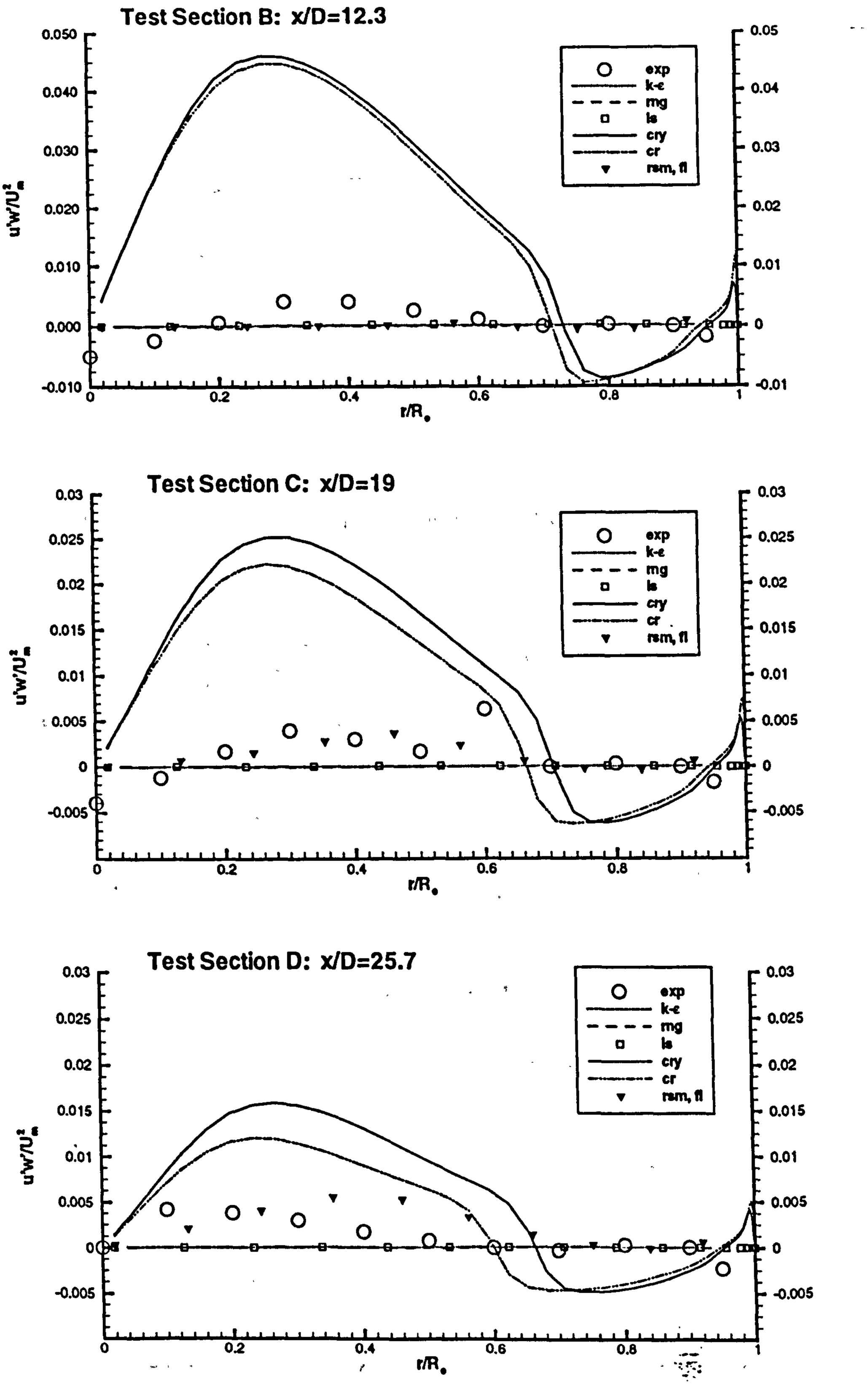

Figure 4.50: Radial distributions of Reynolds shear stress, swirling pipe flow (Kitoh, 1991).

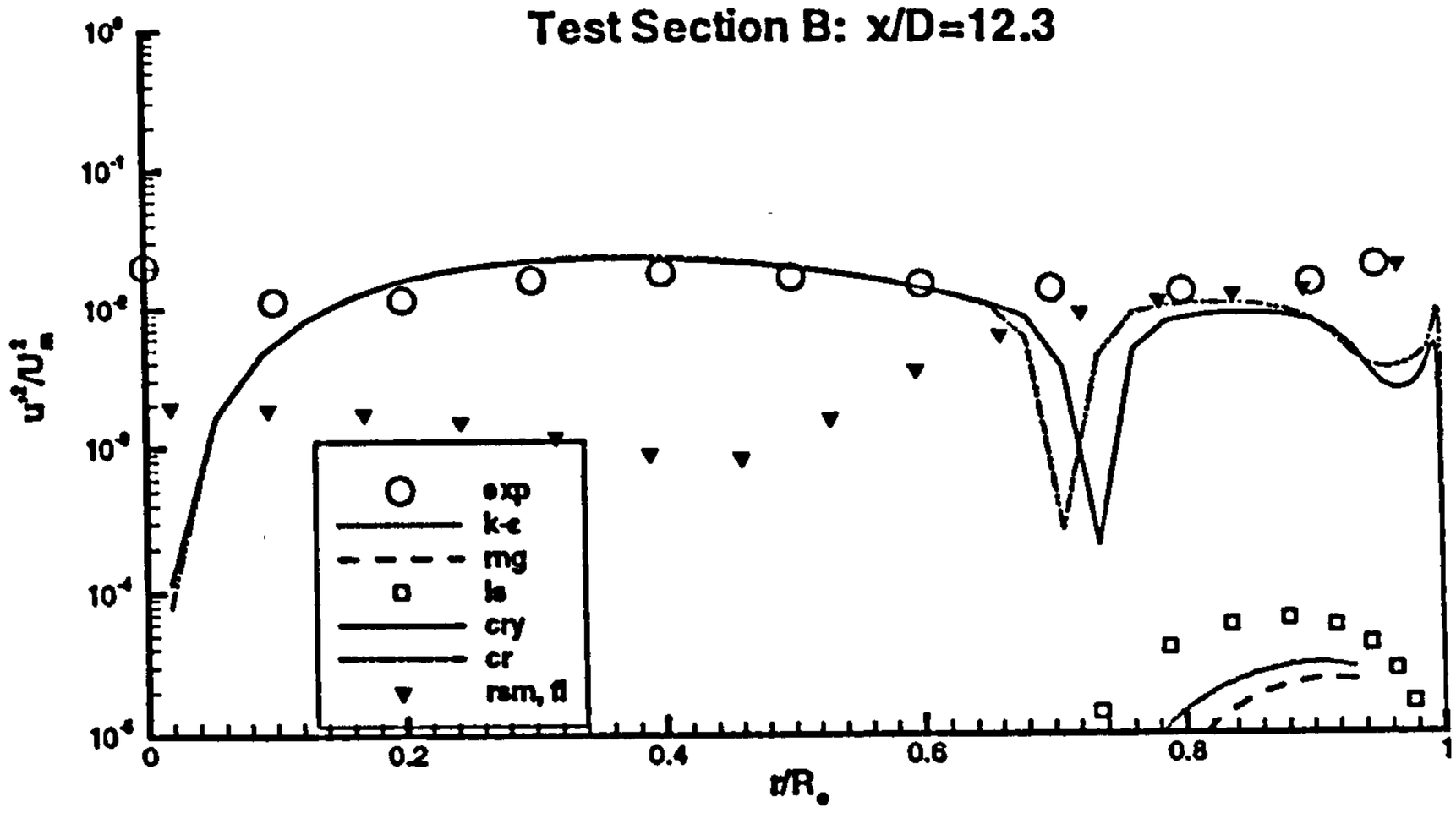

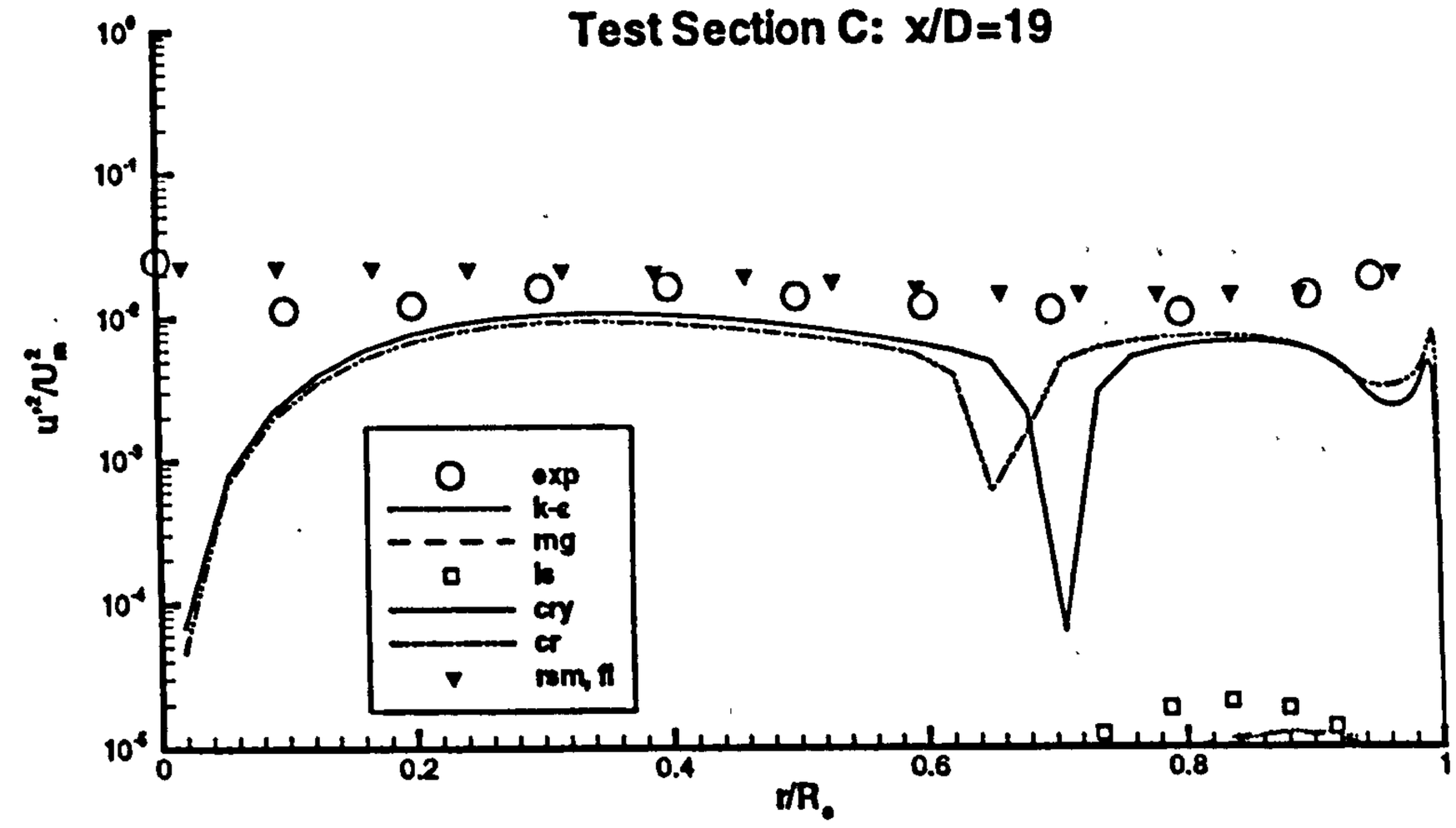

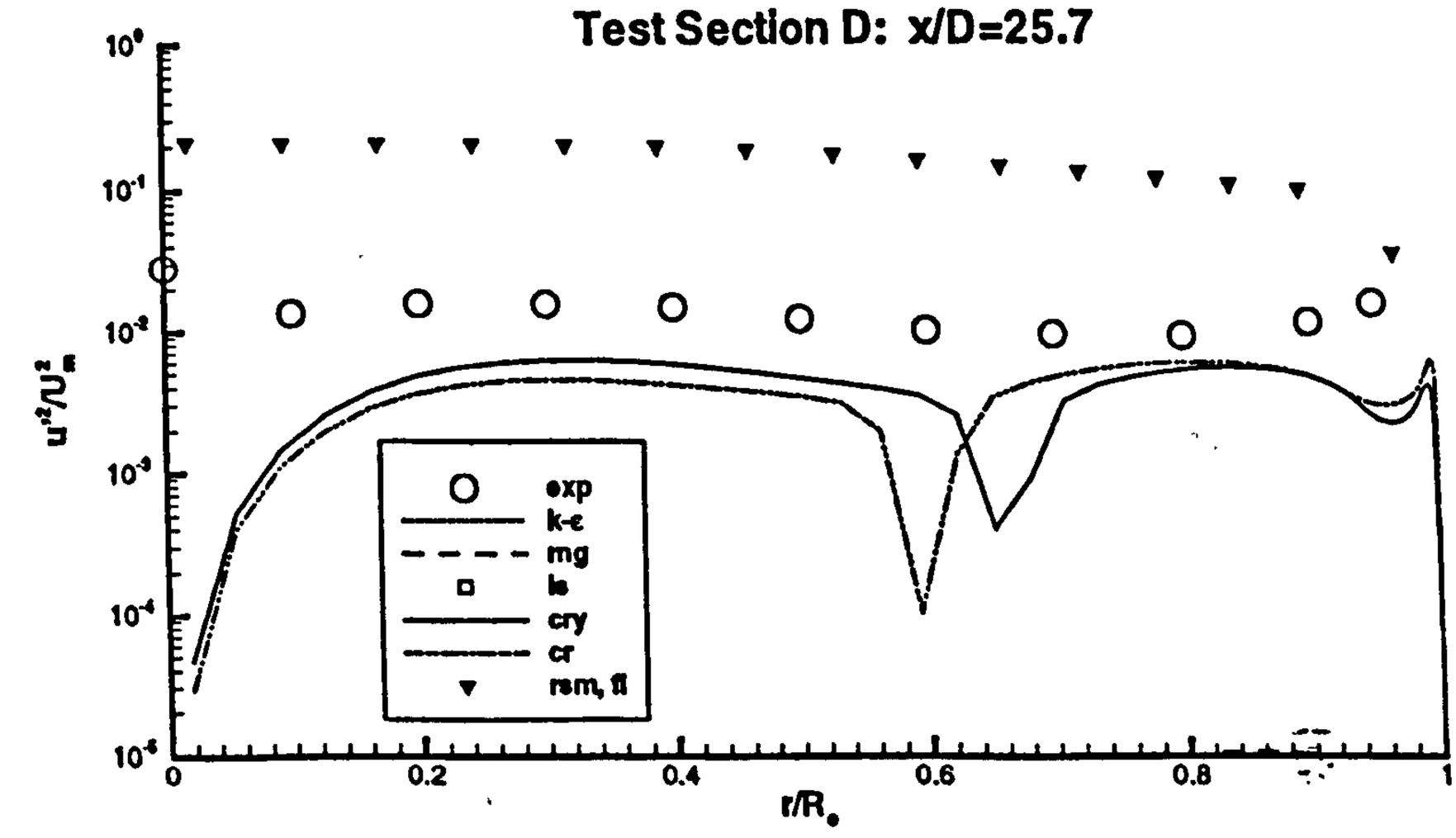

Figure 4.51: Radial distributions of normal stress, swirling pipe flow (Kitoh, 1991)

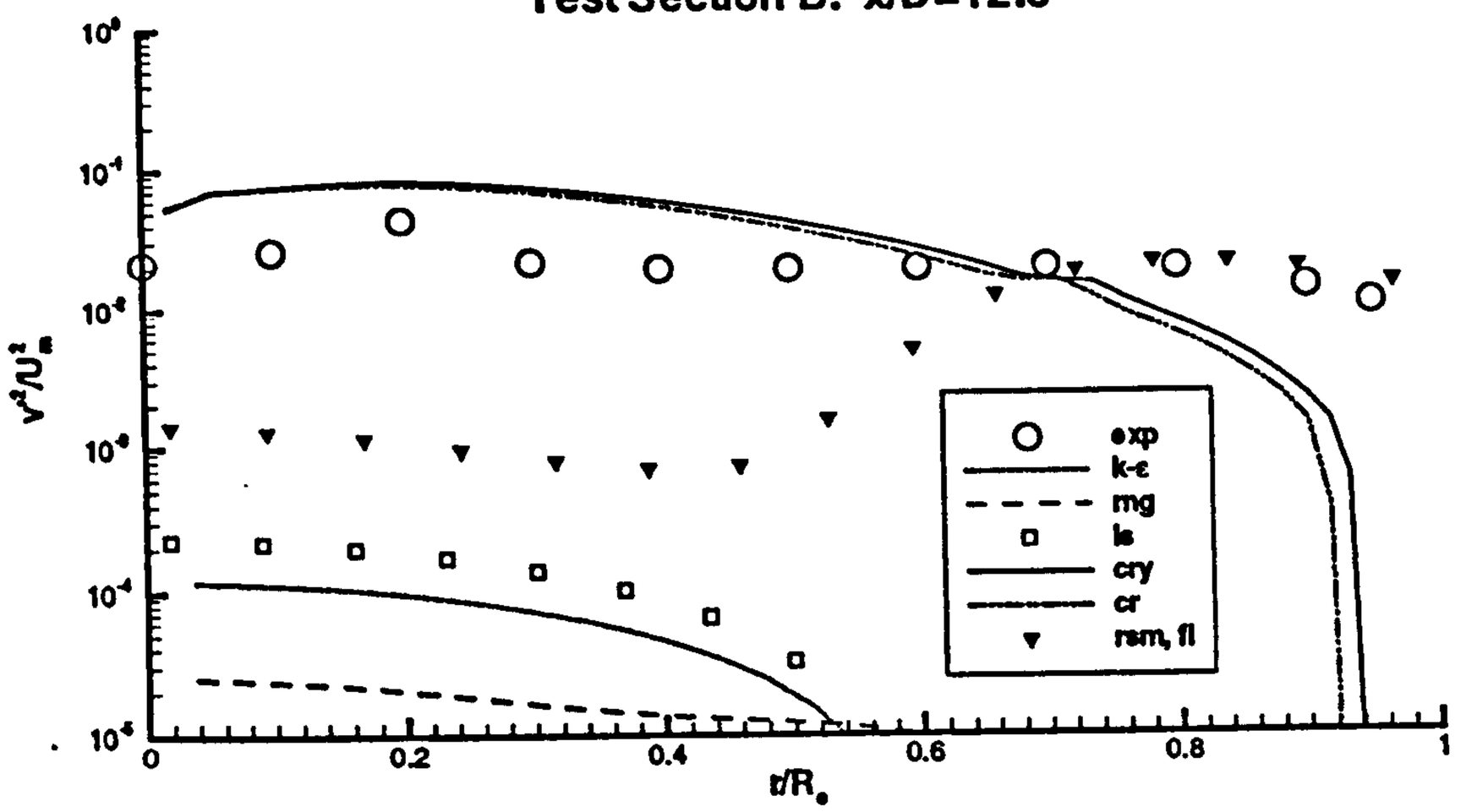

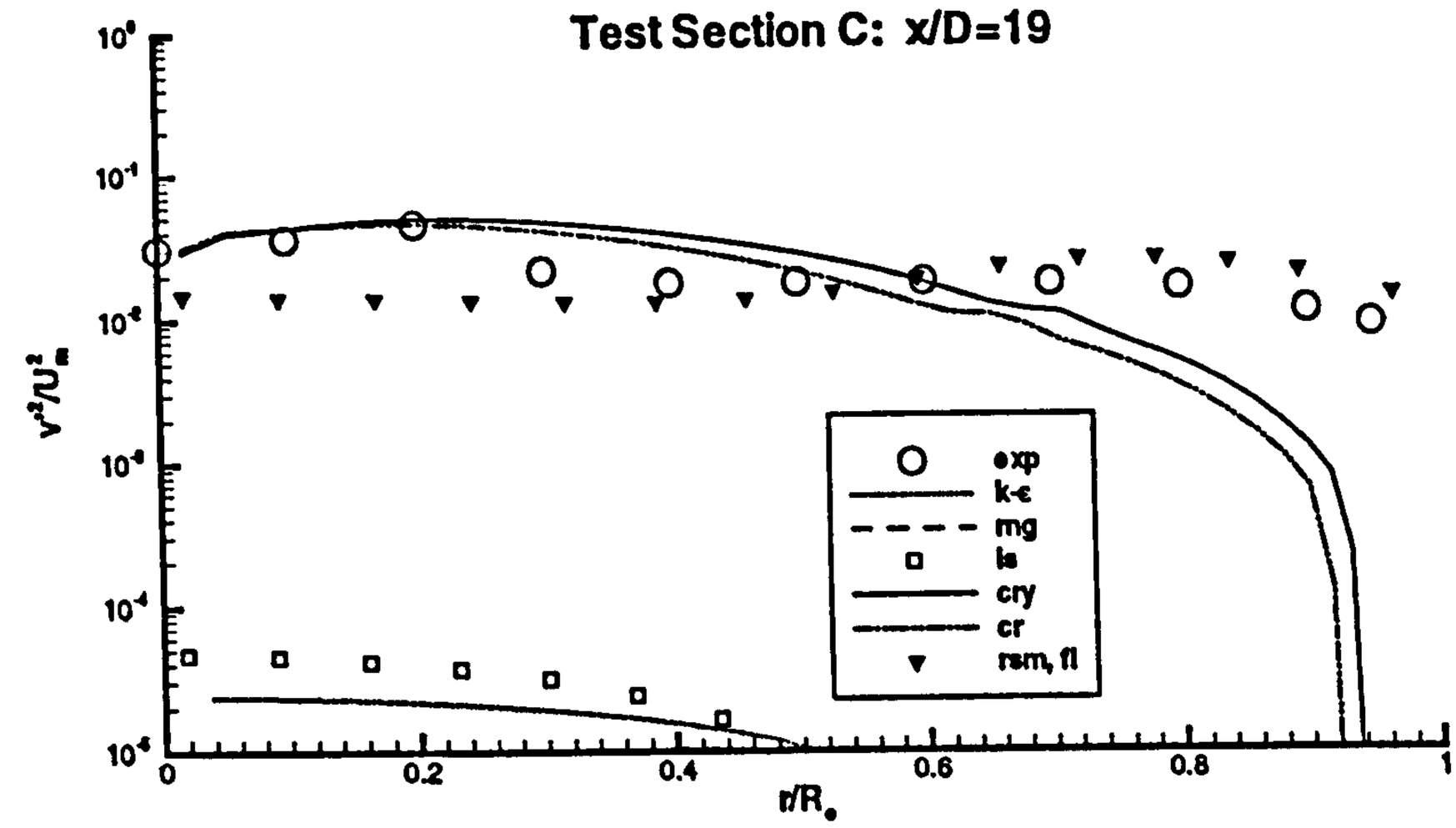

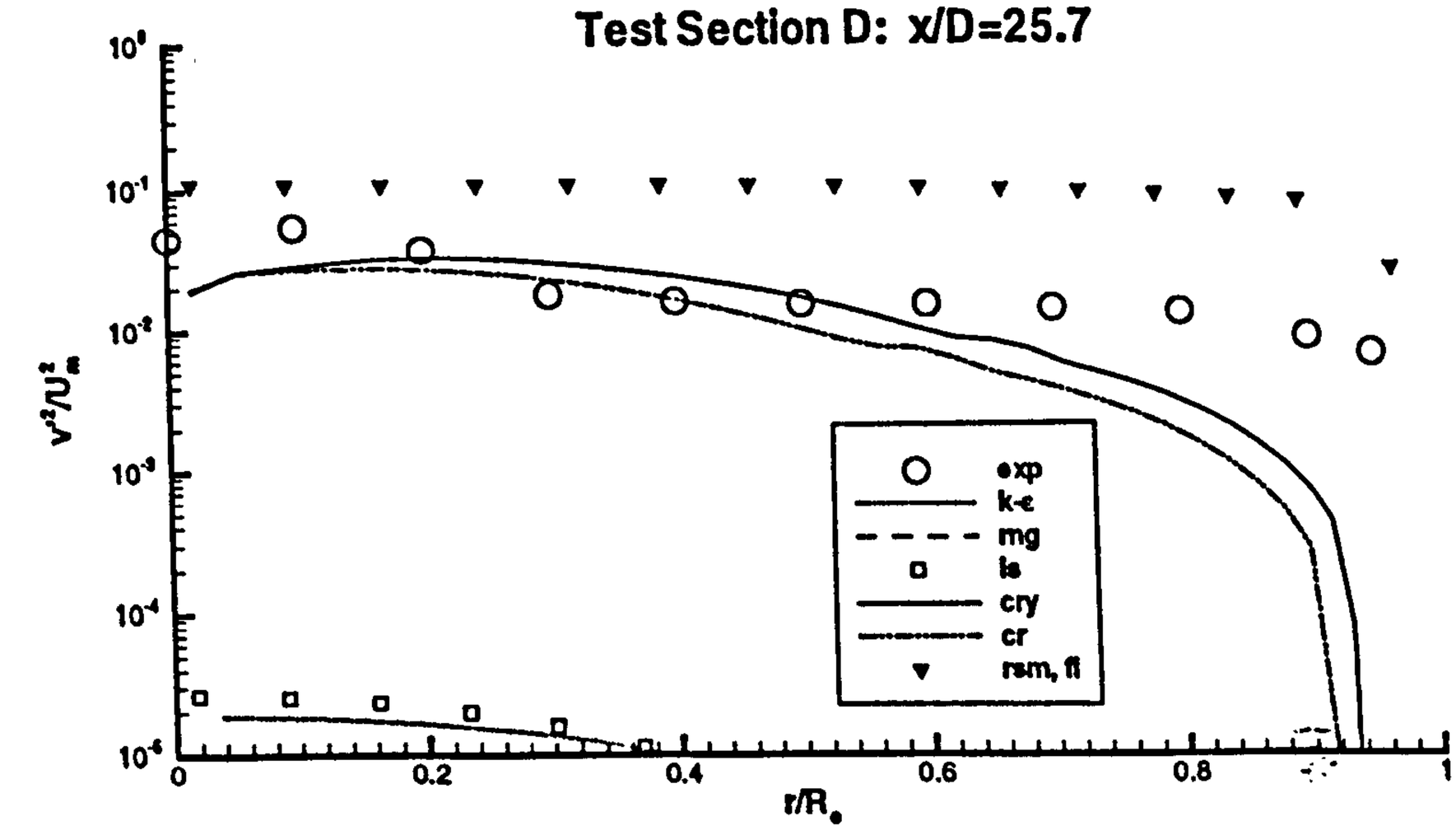

Figure 4.52: Radial distributions of normal stress, swirling pipe flow (Kitoh, 1991)

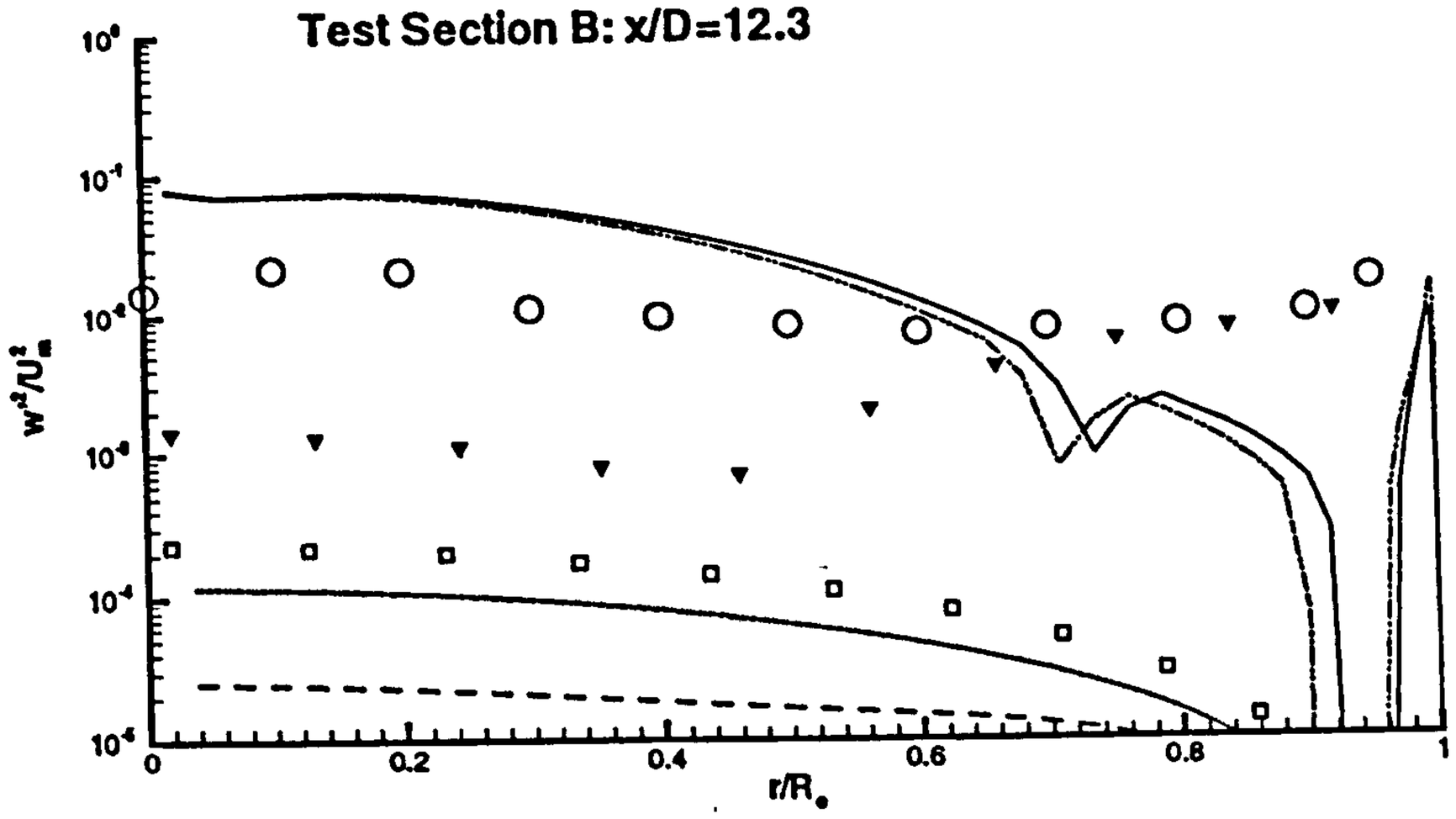

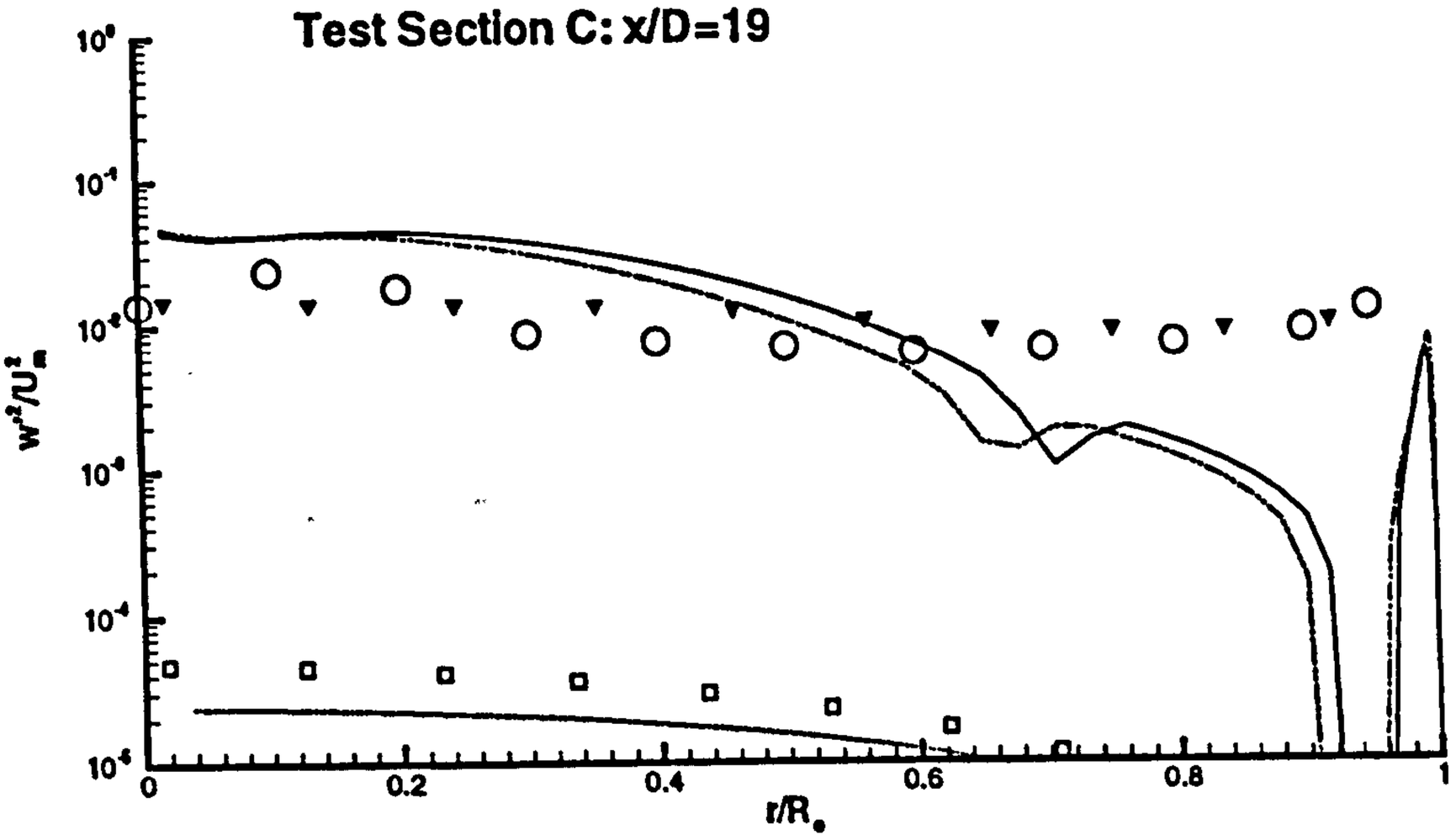

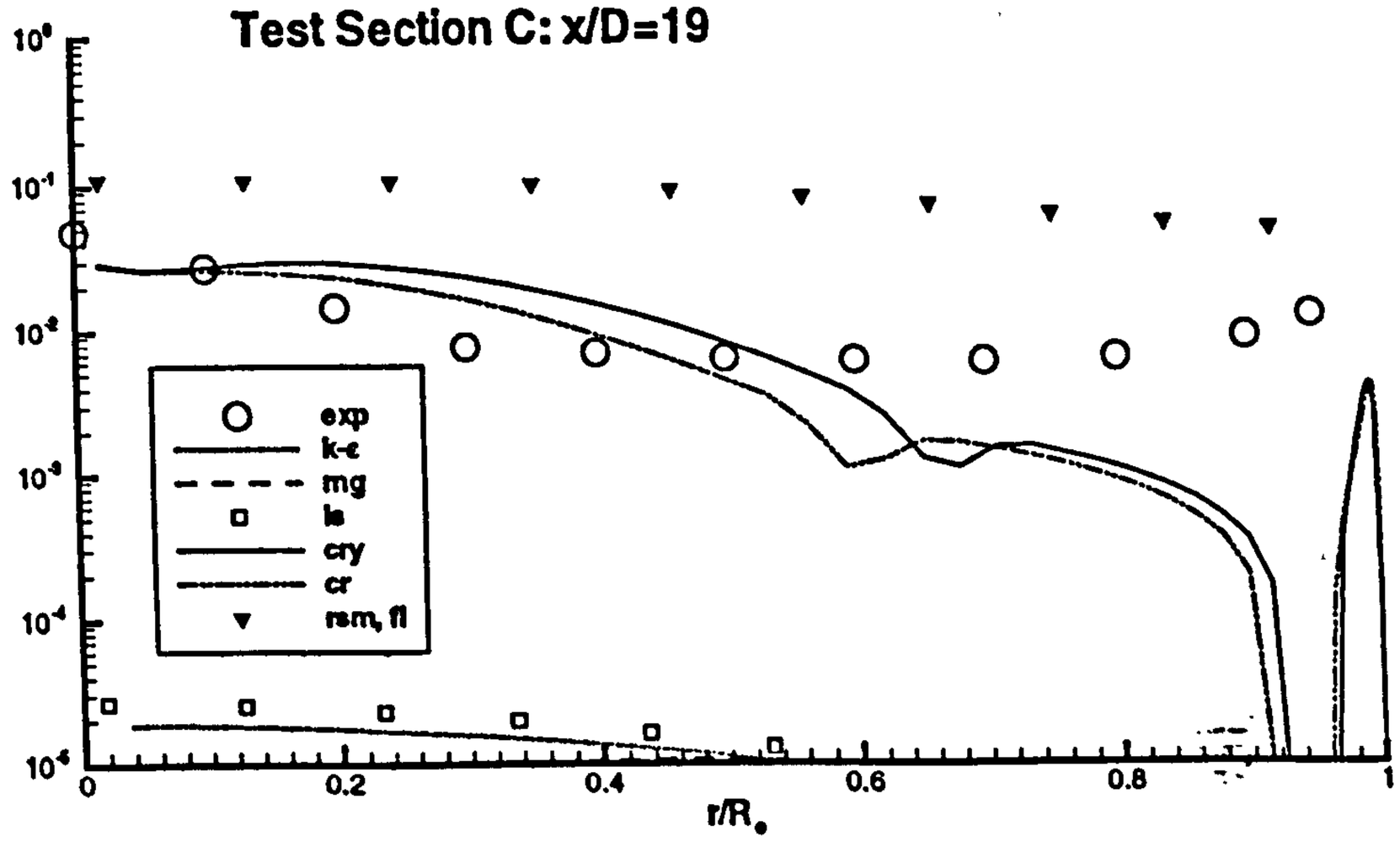

Figure 4.53: Radial distributions of normal stress, swirling pipe flow (Kitoh, 1991)

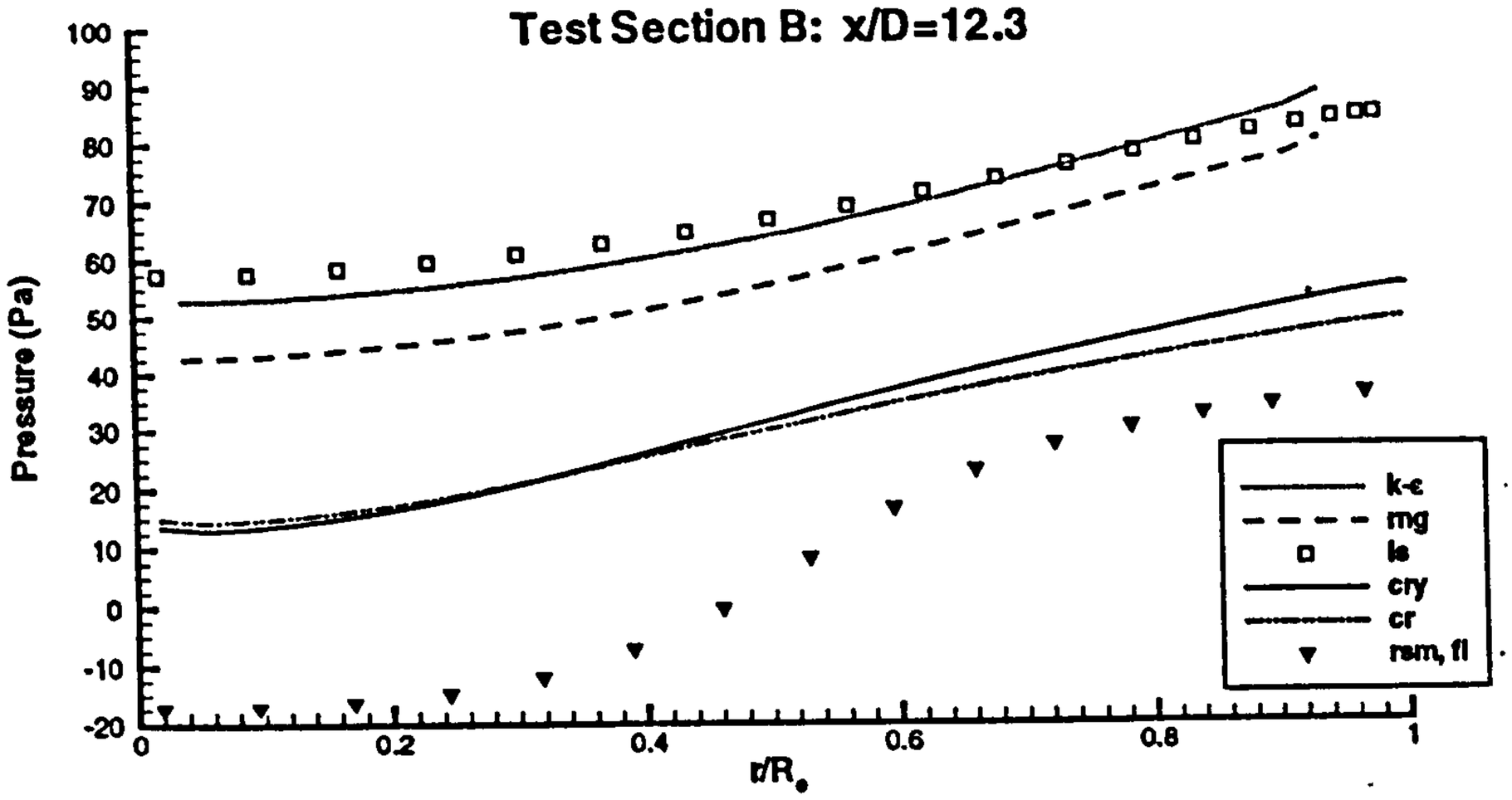

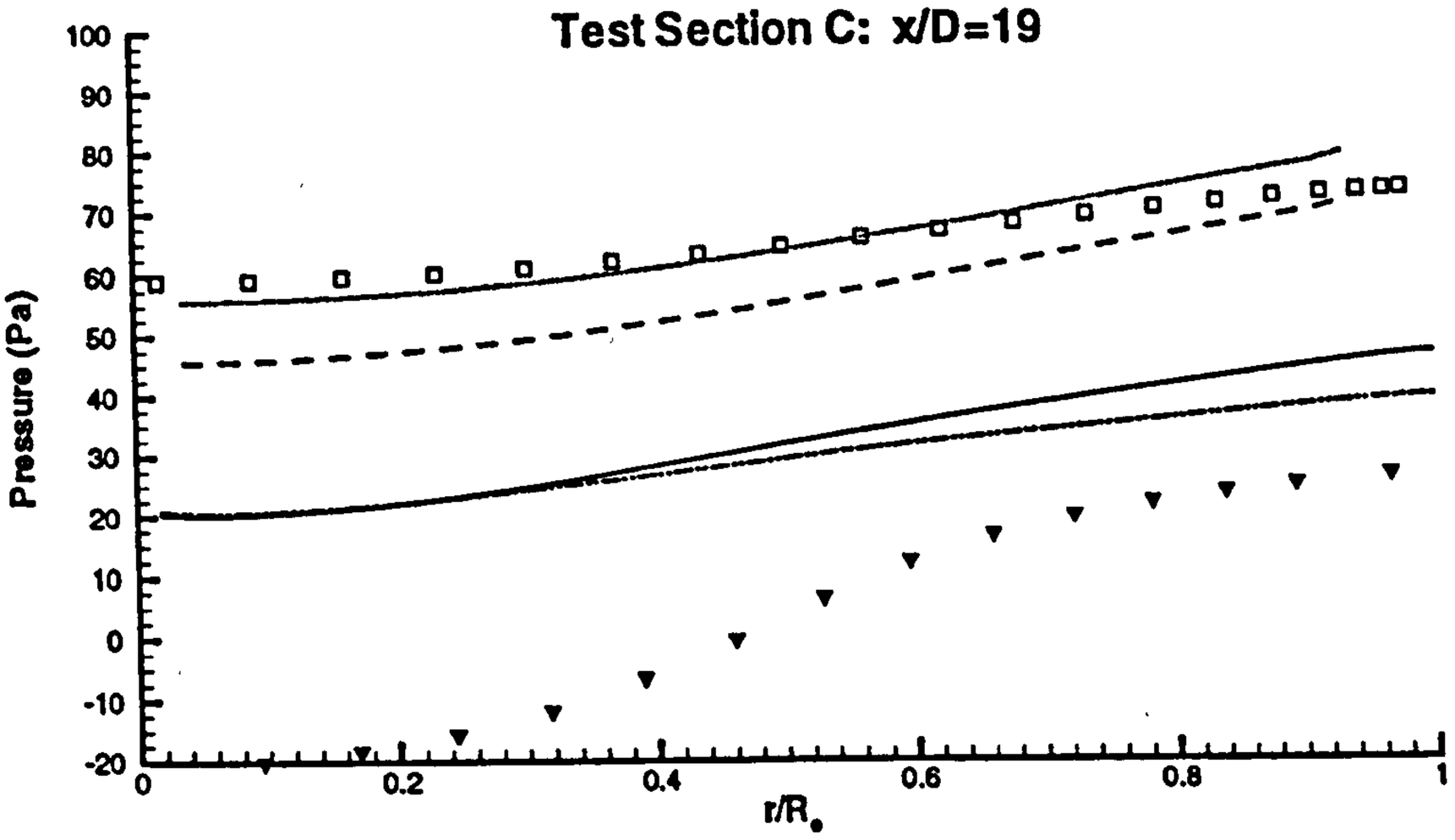

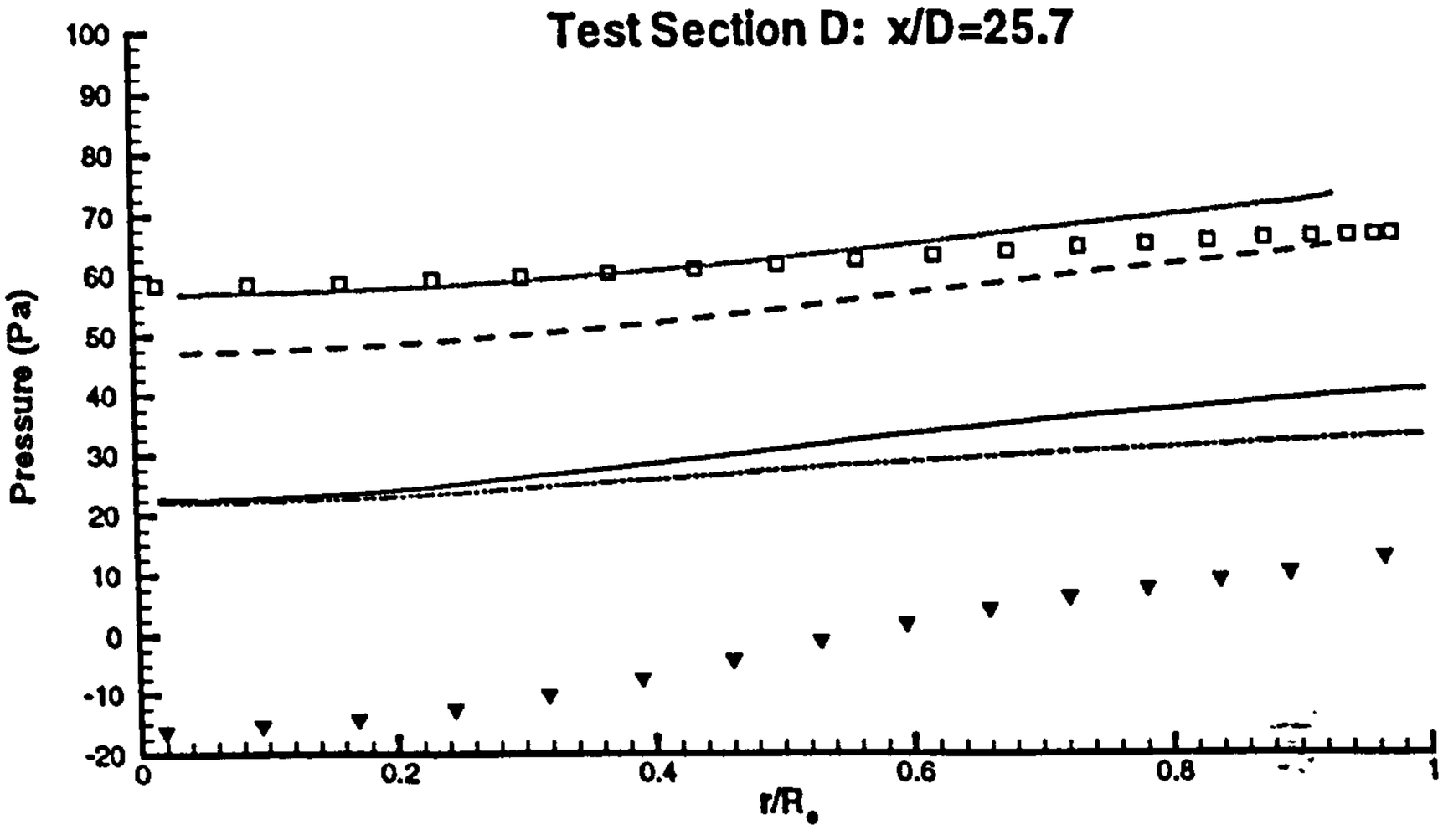

Figure 4.54: Radial distributions of relative static pressure, swirling pipe flow (Kitoh, 1991)

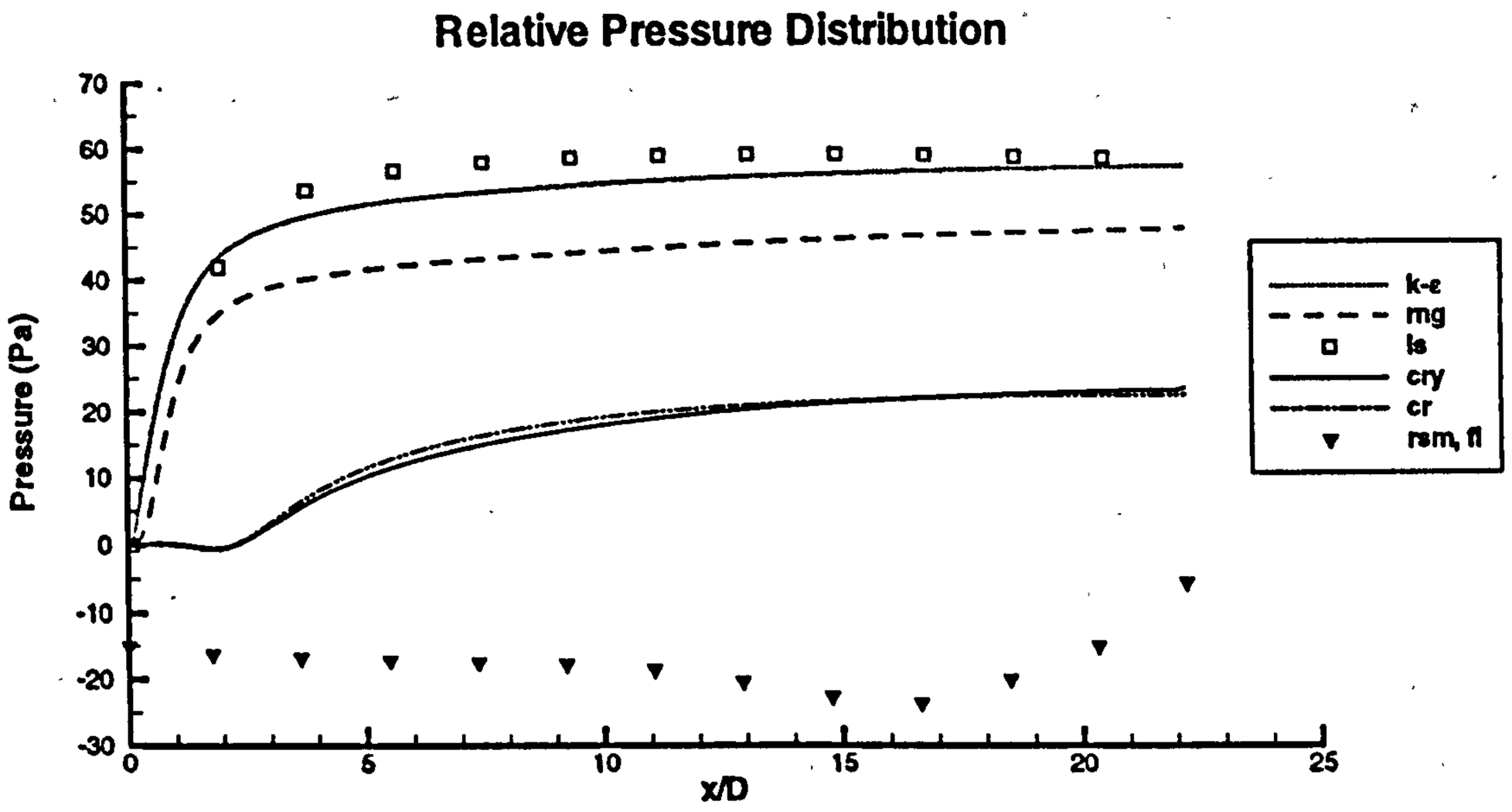

Figure 4.55: Relative static pressures along the centreline, swirling pipe flow (Kitoh, 1991). Note that the horizontal origin corresponds to x/D = 5.7 on the experimental axis.

4.5.2 Discussion

The main process occurring in the flow is the decay of swirl which results in complex pressure fields. An effect of the high swirl intensity is the reduction of turbulence transport, ultimately resulting in recirculation zones. Whilst the linear EVM's are unable to correctly predict these features, the results show that the RSM returns the most plausible profiles and captures the essence of the Rankine combined vortex in the tangential plane and the recirculation zone within the core. The nonlinear model is a compromise which departs, in the correct direction, from the linear EVM predictions. None of the models provide superior predictions for turbulence energy and shear stresses, although the cubic model does return better normal stresses than the RSM. The following discussion examines why the various turbulence models yield different predictions.

As far as the results are concerned, the main distinction between the EVM's and the RSM is the ability to predict the recirculation zone on the pipe axis. Examination of the computed flowfields near the inlet reveals that all the turbulence models predict a recirculation zone. However, the k-ε model predicts this to be only 0.5D long whilst CRY forecasts an improved length of 4.8D (relative to the computational inlet). This is due to the large redistributions of the flow field (as computed by the EVM's) soon after the inlet. Such short toroidal vortices are caused by the near-immediate pressure recovery (in the axial direction) of the EVM's (figure 4.55). Essentially, the radial pressures are redistributed and no longer support large tangential velocities; the small radial pressure gradients are evident in figure 4.54. Continuity, and the fact that the radial velocities are several orders of magnitude smaller, therefore dictates an increase in axial velocity. The sharp change in flow patterns between inlet (figure 4.40) and the test section B (in figures 4.44 to 4.46) indicates that large shear stresses are predicted by the EVM's just downstream of the inlet. By virtue of the link between turbulence energy and shear stresses in EVM's, the excessive diffusion implies that the EVM's are not able to capture the damping effect that large swirl intensities are known to have on turbulent transport. The cubic EVM is seen to suffer from this handicap, but to a lesser extent (as demonstrated by the better axial velocity profiles in figure 4.44). Figure 4.54 reveals that the RSM predicts the largest radial pressure gradients; this is reinforced by the profiles of dP/dr in figure 4.56 and accounts for the higher tangential velocities.

The improvement of the CRY model relative to the other EVM's is attributable to the nonlinear terms present in the stress-strain formulation, which effectively promotes anisotropy. Linear EVM's are known to be poorly equipped for coping with swirling flows, principally because of their inherently isotropic nature whereby the eddy viscosity is identical in all orientations. Swirling flows are marked by high levels of anisotropy; Lilley & Chigier (1971) noted that in these cases the eddy viscosity was a strong function of swirl intensity. This conclusion was arrived at by inserting experimental data into the linear stress-strain relationships to compute the effective viscosity. It was found that the isotropic assumption was acceptable for weak swirl but definitely not for strong swirl. Kitoh (1991) computed the eddy viscosities in the swirling pipe flow by working backwards from the experimental shear stresses and velocity gradients; it was found that μ_t was highly anisotropic in the bulk of the flow, but less so near the wall. In fact, $\mu_{t,\theta x}$ (i.e. the eddy-viscosity calculated from quantities in the θ,x plane) was found to be up to two orders of magnitude larger than the other two components. For comparative purposes, the range of values of $\mu_{t,xr}$, $\mu_{t,\theta r}$, and $\mu_{t,\theta x}$ obtained by Kitoh (1991) along the axis at radius r/R_o=0.2, is presented in table 4.13; the turbulent viscosities predicted by the standard k-ε and CRY models are also presented.

Units: Pa·s	μ_t (isotropic)	$\mu_{t,\theta x}$	$\mu_{t,xr}$	$\mu_{t,\theta r}$
Exp.	n/a	-0.045 to 0.224	0 to 1.12×10^{-3}	0 to 4.48×10^{-4}
k-ε	2.8×10^{-3} (at exit) to 1.9×10^{-2} (at inlet)	n/a	n/a	n/a
CRY	1×10^{-4} (at exit) to 1×10^{-3} (at inlet)	n/a	n/a	n/a

Table 4.9: Comparing axial distributions of experimental and simulated eddy-viscosities, at radius r/R_o=0.2.

The table reveals that the standard k-ε model predicts an eddy-viscosity which is typically an order of magnitude larger than that computed by the nonlinear model, thereby accounting for the excessive diffusion upstream. The CRY model is seen to predict a range of eddy-viscosities which compare very favourably with $\mu_{t,xr}$ and $\mu_{t,\theta r}$. Sharif & Wong (1995) introduced their swirling simulations by remarking that the

standard k-ε model cannot predict the size and strength of core recirculation zones and fails to anticipate the forced/free vortex; again, this was attributed to the isotropic background of the linear EVM. Kobayashi & Yoda (1987) adapted the standard k-ε model for a swirling pipe flow (Re=50000, Ω=1.176) by inserting an anisotropy coefficient in the eddy-viscosity formulation (i.e. a different coefficient for each combination of x,r,θ). It was found that the Rankine combined-vortex, tangential velocity distribution was accurately predicted, and that the axial velocity profile was correct along the entire radius bar at the centreline, where there was a relatively small overprediction. A stress-strain relation involving higher-order terms (quadratic), proposed by Pope (1975) was also tested, but this gave identical results to the standard k-ε model. Suga (1995) put forward another reason for superiority of the CRY model; he demonstrated that within the EVM structure, in a low swirl-intensity context, cubic terms were definitely required in the formulation for $\overline{v'w'}$. Suga (1995) and Craft et al (1996, 1997) cite this as the main reason for the LS model's inability to predict a curved radial distribution of tangential velocities, in a fully-developed, swirling pipe flow.

Although the cubic model improves upon the linear EVM's, it still falls short of the accuracy obtained with the RSM in swirling flows. One inhibiting factor is related to the manner in which Suga (1995) made use of a swirling flow to tune several constants in the nonlinear stress-strain relationship (equation 2.32). When applied to a fully-developed, swirling pipe flow (swirl is constantly generated by the rotation of the pipe about its longitudinal axis), the CRY model provided the correct radial distributions of tangential velocities. This was attributed to the presence of cubic terms in the stress-strain correlations, particularly in the case of $\overline{v'w'}$. In light of this benchmark case, the performance of the nonlinear model in the present swirling flow is particularly disappointing. However, the relatively tractable nature of the flow utilised for calibration of the constants, provides the explanation for this discrepancy. The flow investigated by Suga (1995) and Craft et al (1996,1997) is fully-developed and thus contains no axial gradients (thus no special consideration was made for $\overline{u'w'}$, which is of importance in the Kitoh, 1991, flow). Tangential velocity distributions are of a forced vortex pattern, which is characteristic of low swirl intensities. A consequence of low levels of swirl is the absence of swirl-induced turbulence damping and recirculation

zones. Thus the flow is less complex than that of Kitoh (1991) which is currently under investigation.

Examination of the shear stresses and turbulence energy predicted by the various models shows that not even the RSM is capable of accurately resolving these variables. Occasionally, the RSM predictions are rivalled, if not surpassed, by those of the nonlinear model. It is difficult to correlate the Reynolds stress trends with those of the mean velocities (this is true for all turbulence models). For example, the high Reynolds number models predict excessive levels of $\overline{v'w'}$, yet the core distribution of W is not steep and is very similar to that obtained with the nonlinear model (whose computations of $\overline{v'w'}$ much more closely resemble the experimental profile). This is also true of the RSM; for example, its core levels of $\overline{v'w'}$ are nearly zero but the gradient $\partial W/\partial r$ is large. Kitoh (1991) reported that the flow orientation, shear direction and velocity gradient alignment diverged considerably in the skewed flow within the annular region. This has important consequences for all eddy-viscosity type models. The eddy-diffusivity concept implies that the principal axes of the Reynolds stresses and mean strains are aligned (Sharif & Wong, 1995), which is a clear contradiction of the experimental results. Although the cubic model is anisotropic, the leading order term in equation (2.32) does assume that the stresses and strains are aligned. However, the higher order terms provide a measure of anisotropy which partially cancels this deficiency. It is interesting to note the success of the Kobayashi & Yoda (1987) model in which only the eddy-viscosity is modified for each Reynolds stress; vastly improved velocity distributions were obtained despite the fact that the linear EVM framework was used. It is therefore quite possible that the CRY model could return improved results if the constants in the nonlinear terms are recalibrated for a highly swirling flow. In contrast to EVM's, the RSM is naturally anisotropic because the Reynolds stresses are obtained from the solution of individual transport equations; furthermore, the matter of stress/strain alignment is not an issue[1].

The normal Reynolds stresses were seen to be most accurately predicted by the CRY and RSM models (figures 4.51 to 4.53). Their values are of the same order of

magnitude as the shear stresses. However, Kitoh (1991) remarked that resolution of the normal stresses in the current flow was of little import because they affected the pressure field by less than 3%. This is echoed by Tennekes & Lumley (1972) who stated that in many flows the normal stresses contribute little to the transport of mean momentum. In swirling flows, Lilley & Chigier (1971) reported that the pressure term in the axial momentum equation gains significance as the swirl intensity increases. For $\Omega > 0.6$, the pressure term is dominant. The main terms, excluding convection, in the axial momentum equation are:

$$\frac{\partial P}{\partial x}, \quad \rho\frac{\partial \overline{u'^2}}{\partial x} \quad \text{and} \quad \rho\frac{\partial}{\partial r}\left(\overline{u'v'}\right)$$

The radial variations of these terms at one axial location, are plotted in figure 4.57, whence it is immediately clear that the axial variation of normal stress is at least one order of magnitude smaller than the other two terms. In fact, these graphs confirm the important roles of the pressure and shear stress. The turbulence energy is a measure based on the normal stresses. Although the RSM grossly underpredicts the turbulence energy, it is of little consequence because k is simply derived from the normal stresses (no pde is solved for k) which were shown to be insignificant. It is worth noting, though, that the severely underpredicted turbulence energy is a reflection of mediocre predictions of normal stresses. In the EVM context, however, the turbulence energy plays a vital role; it has a direct impact on the eddy viscosity and links together stresses and strains. It also obtains feedback from the Reynolds stresses via the turbulence generation term, so the poor representations of these quantities is partly attributable to this link. The nonlinear model is no exception to this, although broadly speaking it does predict more accurate k profiles than the linear EVM's. A reason for the low levels of turbulence energy predicted by the linear EVM's is the excessive upstream diffusion causing flat U profiles, and hence low shear stresses and turbulence production.

Thus far little distinction has been made between the performances of the three linear EVM's, mainly because the differences were relatively small when compared with those regarding the CRY and RSM models. Several interesting observations can be made. Although the LS model generally mimics the k-ε model throughout the core

---

[1] This so-called flow skewness is not so important at lower swirl numbers ($\Omega \approx 0.4$) because Bish (1998) reported that the RSM and standard k-ε models yield similar results in this case.

region of the flow, it deviates significantly as the wall region is approached. This is particularly true of the axial and tangential velocities and Reynolds stress $\overline{u'v'}$, and is a manifestation of the fact that the LS model employs damping functions rather than wall functions, both of which are sensitised to simple boundary layers. In his experimental paper, Kitoh (1991) reviewed the work of other researchers, most of whom concluded that the boundary layer in swirling flows was partially free from skewing. In other words, the flow in the boundary layer was parallel to the wall and the orientation of the velocity vectors was approximately constant. Thus a portion of the boundary layer in a swirling flow is similar to that for which wall functions and damping functions were developed. Kitoh plotted near-wall data which indicated that the standard logarithmic law was still applicable up to $y^+ \approx 200$, for weakly swirling flows. However, higher swirl intensities ($\Omega > 0.3$) were shown to result in data which collapses along a single curve (for $y^+ < 1000$) whose slope is smaller than that generated by the standard logarithmic law. The current simulations involving the k-ε and RNG models were based on near-wall nodes at $y^+ \approx 180$. The f_μ damping function attains the high Reynolds number limit at $r/R_0 = 0.97$, which lies much closer to the wall and is therefore at a point which departs less from the conventional logarithmic law. The skin friction plots (figures 4.41 and 4.42) highlight the discrepancy (which cannot be explained by the fact that we are comparing total with axial friction factors) between high and low Reynolds number models in the boundary region. The overprediction by the k-ε model is likely to be due to the inapplicability of the standard logarithmic wall function to the boundary layer. Kitoh (1991) provided an experimental curve relating axial C_f to swirl number; these are compared in table 4.10 with the predictions of the low Reynolds number models. It was not possible to calculate the axial C_f with the high Reynolds number models (including RSM) because the wall function is required for finding the total skin friction (a relation incorporating k is used instead of velocity gradients). Both LS and CRY models are seen to represent the axial friction factor reasonably well.

Test Section	Exp. Ω	Axial C_f		
		Exp.	LS	CRY
B	0.83	0.0132	0.0178	0.0106
C	0.67	0.0114	0.0121	0.0088
D	0.60	0.0108	0.0097	0.0062

Table 4.10: Experimental and computed axial skin friction factors, at various test sections.

The performance of several turbulence models in a highly swirling pipe flow has been assessed. The standard k-ε, RNG and LS models were seen to be incapable of predicting the main features of the flow because of the absence of cubic terms (which are required for swirl) and the assumption of stress/strain alignment. The RNG model has not been discussed in detail in this section, mainly because it fared no better than the k-ε model. The discussion pertaining to the performance of the RNG model in the Tropea et al (1989) pipe expansion (section 4.2.3) concluded that anisotropic effects could be successfully accounted for by modifying the dissipation rate production term. Clearly, this is not satisfactory for all complex flows. The CRY model was seen to improve results relative to the linear EVM's; however it too failed to predict the extended recirculation zone. It is suspected that recalibration of the constants in the nonlinear terms related to swirl, would solve this problem (without affecting the performance in non-swirling flows). Finally, the RSM was found to yield the best results, which confirms its standing as the most general of the classic turbulence models.

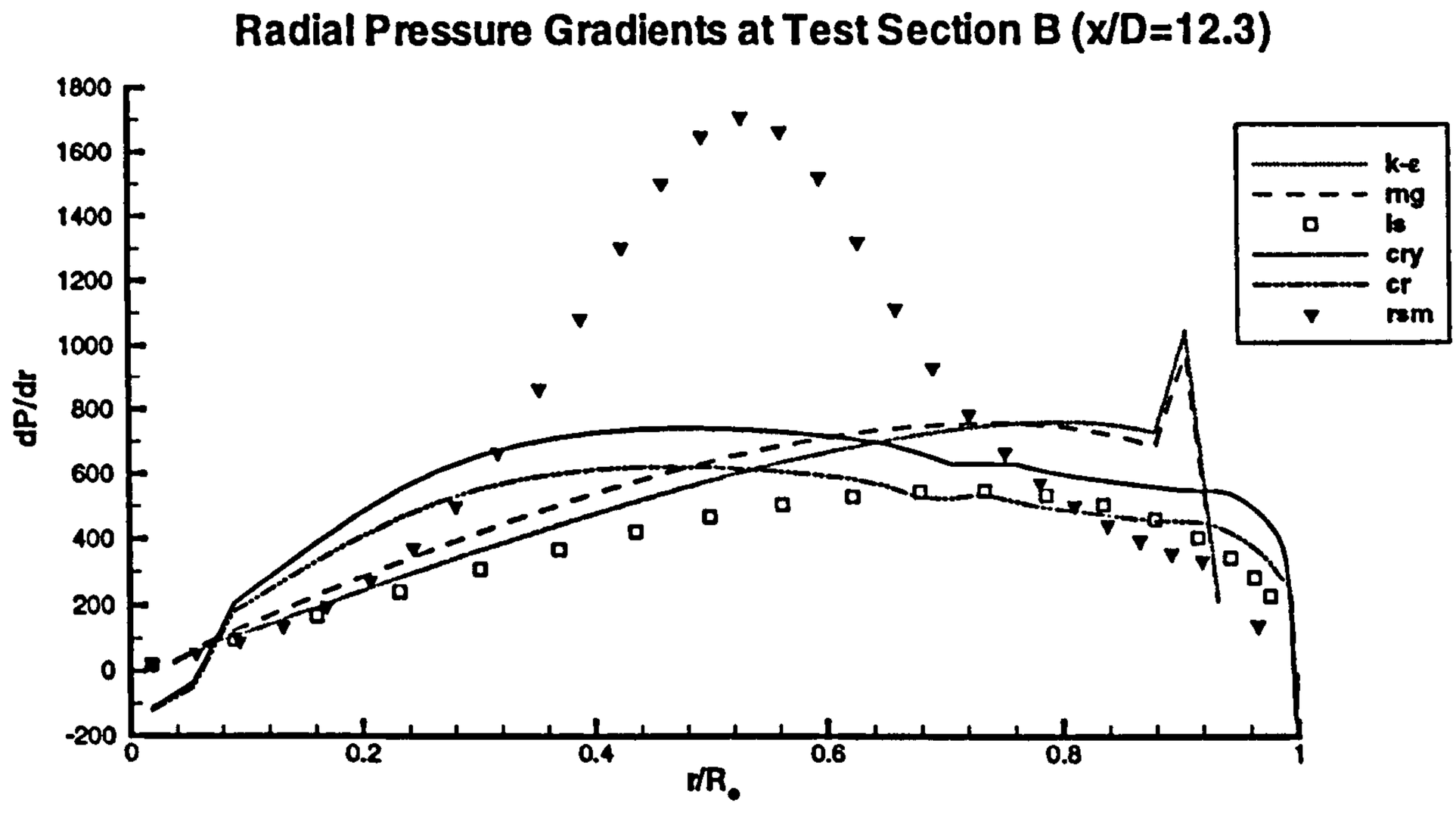

Figure 4.56: Radial profiles of radial cross-stream pressure gradients at test section B, swirling pipe flow (Kitoh, 1991)

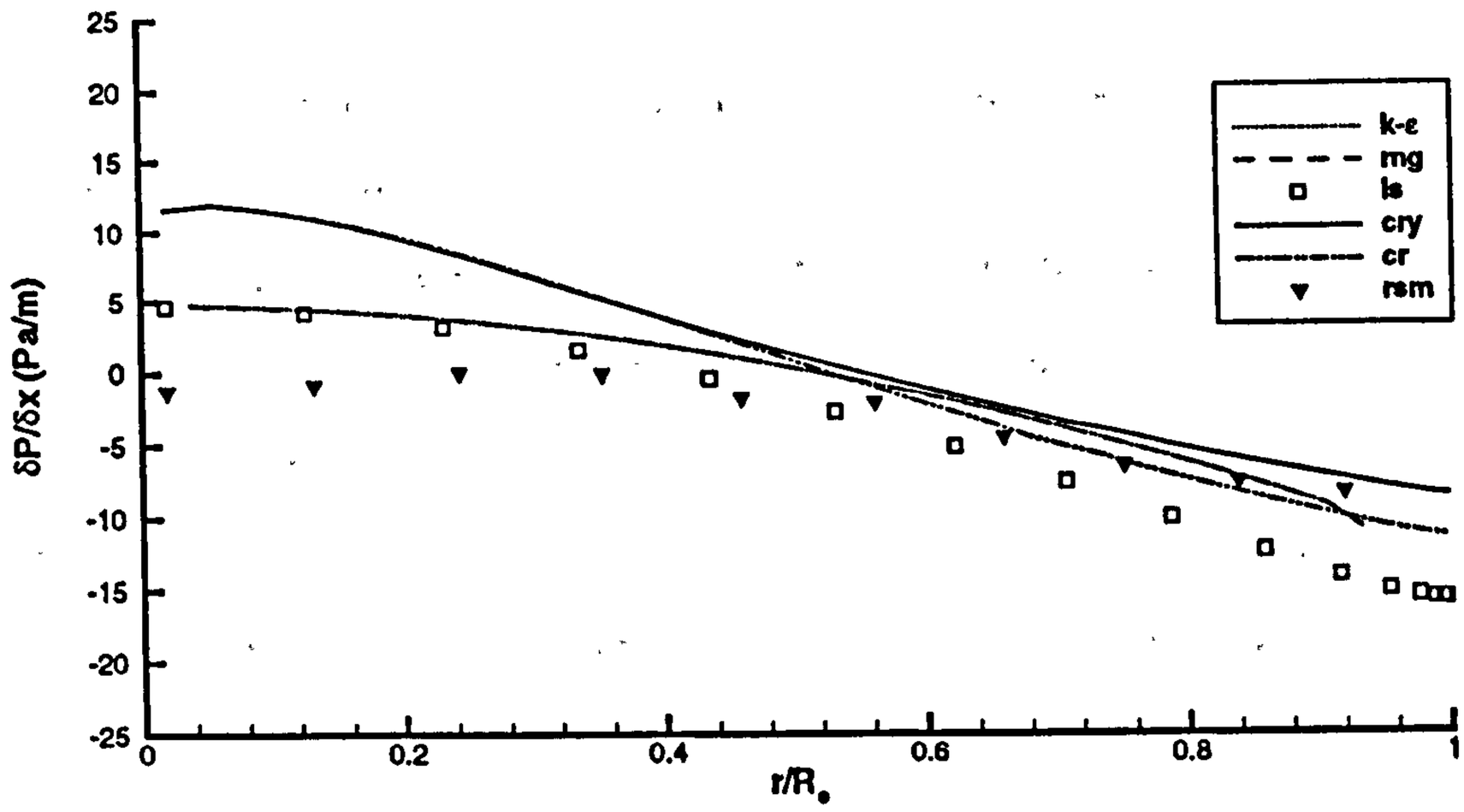

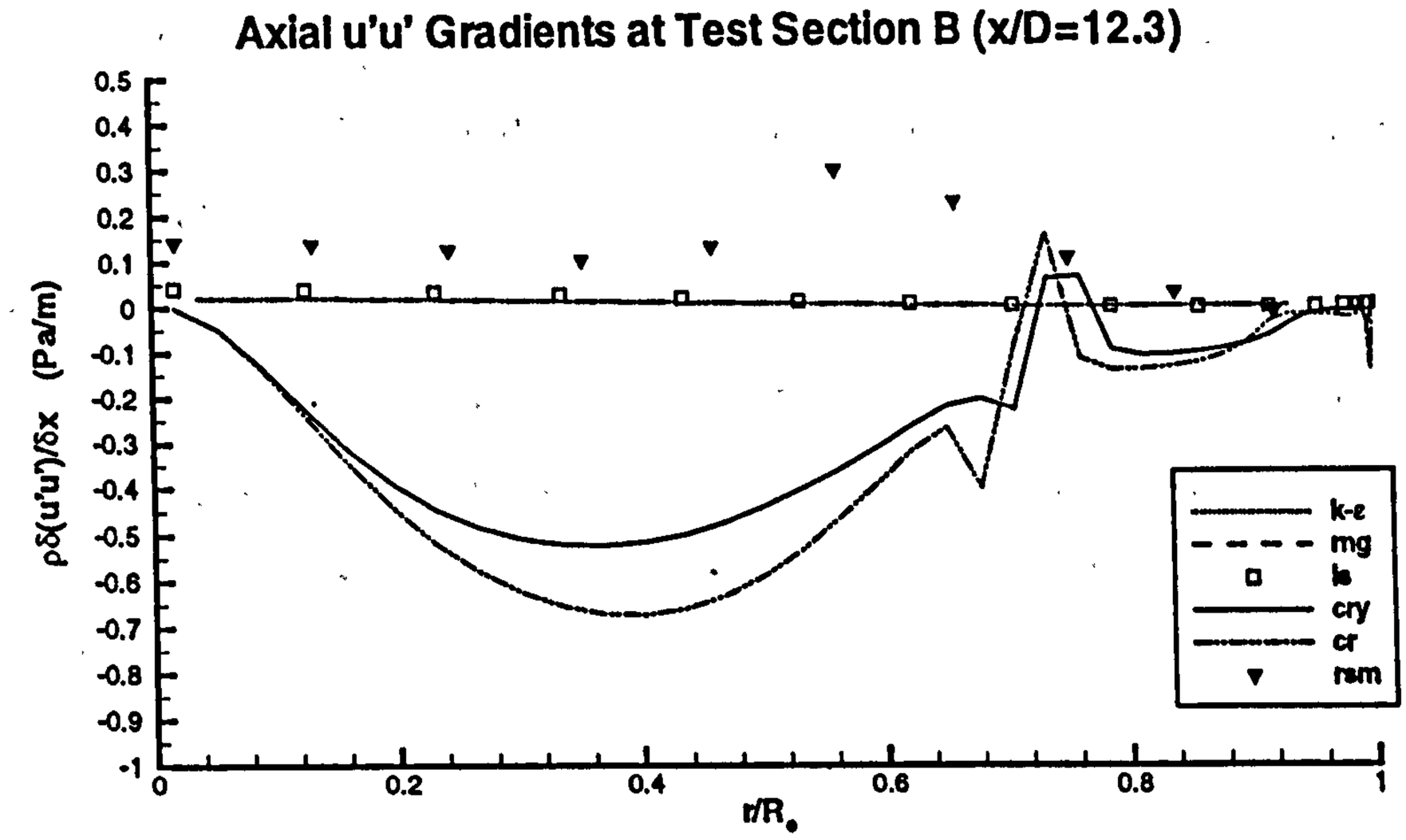

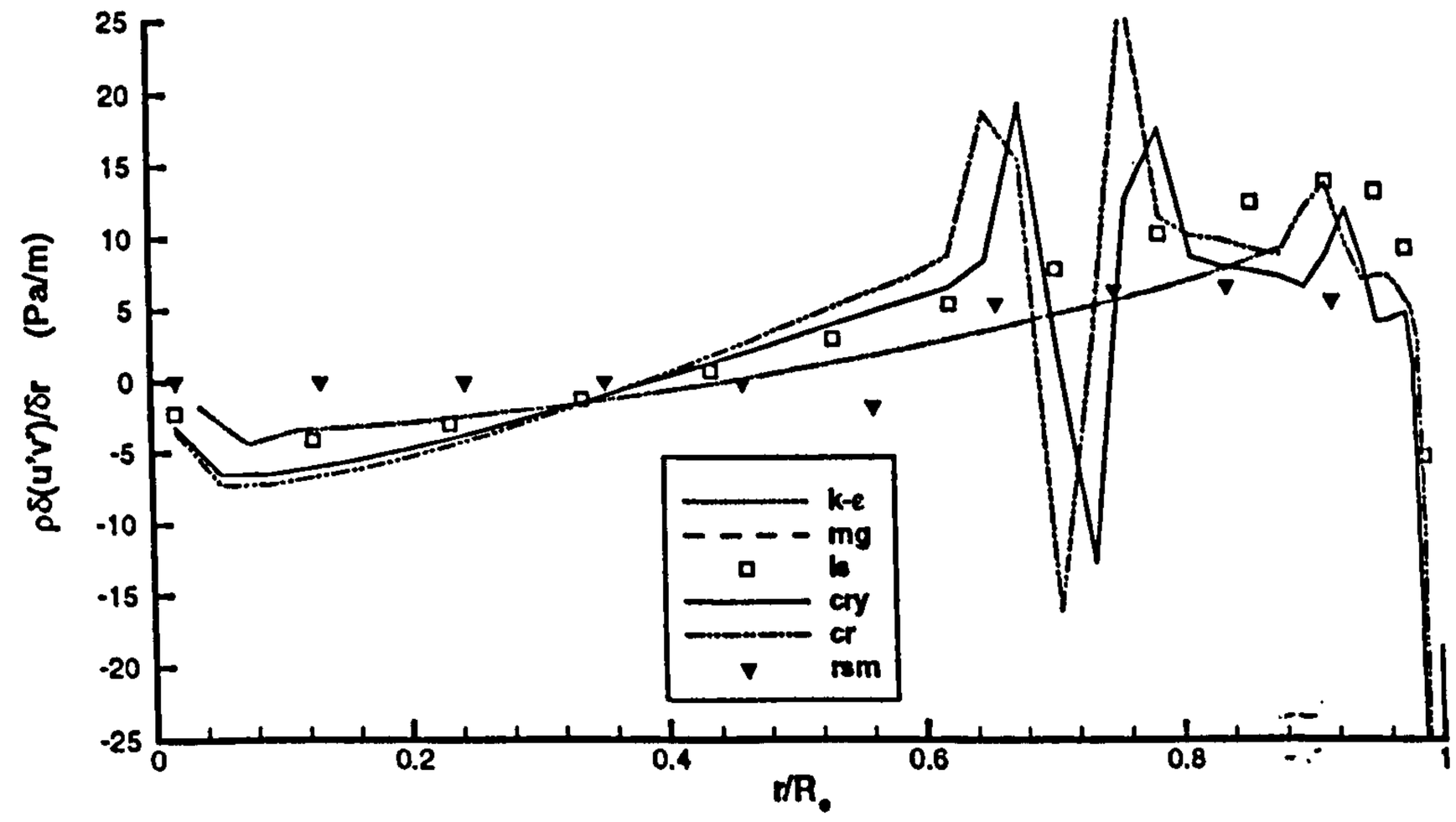

Figure 4.57: Radial profiles of the main terms in the axial momentum equation, swirling pipe flow (Kitoh, 1991)

4.6 SUMMARY

The principal conclusions drawn from the isothermal simulations carried out in this chapter are as follows:

- Over the range of flows studied (fully-developed pipe, pipe expansion and highly-swirling pipe flows), the nonlinear turbulence model generally improved upon the predictions of the other EVM's.
- The standard k-ε, RNG and LS models generally yielded similar results except for pipe expansion flows, in which case the RNG model performed similarly to the nonlinear model.
- The Yap correction term was seen to affect predictions near the wall for fully-developed pipe and pipe expansion flows. In the case of swirling pipe flow, Y_C also influenced results far from the solid boundary. The presence of this correction term was generally not beneficial.
- The nonlinear model predicts negative values for $\overline{v'^2}$ because all three normal stresses are computed explicitly in the TEACH code. This was found to have little bearing on overall computations in both simple and complex flows (as demonstrated in the discussions for the fully-developed pipe and highly-swirling pipe flow simulations).

CHAPTER 5: NON-PREMIXED COMBUSTION

Turbulent, non-premixed combustion is a complex phenomenon comprising turbulent flow, chemical kinetics, thermal transfer and pollutant formation. The fact that these events are highly interdependent emphasizes the challenge behind modelling turbulent, diffusion flames. The purpose of this chapter is to briefly describe non-premixed flames and provide supporting evidence that the flame sheet combustion model presented in Chapter 2 is suitable for the present non-premixed burner simulations. The characteristics of bluff-body combustors, including the issue of confinement, are then discussed. Finally, the effects of several parameters on the quality of bluff-body simulations are assessed, and the predictions obtained with the nonlinear turbulence model are reported.

5.1 TURBULENT DIFFUSION FLAMES

Non-premixed flames are the consequence of two consecutive events: mixing by diffusion and subsequent reaction. Diffusion is generally the slower of these processes and thus dictates the rate at which the entire sequence evolves. Although diffusion flames are relatively robust (i.e. they do not require much control and are self-sustaining) and safe, they are subject to distinct disadvantages. Weinberg (1986) noted that "diffusion flames have the interesting attribute of automatically adjusting themselves so as to maximise every kind of pollutant." The stoichiometric regions of

such flames are characterised by high temperatures and therefore large levels of NO_x, whilst incomplete combustion and pyrolysis occurs in the oxygen-starved zones. Changes in the flow velocity of either reactant only relocates the stoichiometric contour and the flame envelope. The rate-controlling mixing process leads to low combustion intensities and therefore reduced thermal efficiencies. The principal means of promoting combustion intensity is to enhance the diffusion process via turbulent mixing and to increase the contact between fuel and oxidant.

Turbulent, non-premixed flames are predominantly characterised by the extent of the interactions between turbulence and chemistry. Relative levels of turbulence and chemical activity can be quantified by a dimensionless parameter known as the Damkohler number (*Da*); it is defined as the ratio of a characteristic mixing time to a representative chemical time (Schefer et al, 1996). The Damkohler number diminishes as the turbulent mixing rate grows with respect to the reaction time scales; heat removal from the reaction zone attains an increasingly dominant role. This results in the chemical species deviating from a state of near chemical equilibrium, thereby introducing finite-rate effects. Partial or even complete flame extinction occurs once the chemical heat release rate (as a result of reaction) is significantly slower than the rate at which heat is transported due to mixing (Schefer et al, 1996). Flames typified by low *Da* are said to be approaching blowoff, and cannot be properly modelled using the fast-chemistry techniques described in Chapter 2.

Far from the blow-off limit, the turbulent mixing time is generally much greater than that required for the chemical reactions to occur. In other words, combustion occurs quickly compared to flow phenomena, and sufficient heat is maintained locally to ensure that the reaction process continues in a stable manner. The fast-chemistry equilibrium assumption is thus applicable for major species when the flame Damkohler number is high.

In the flame-sheet combustion model, the fast-chemistry assumption is complemented by the conserved scalar approach; this assumes that temperature, enthalpy and the mass fractions of the major species are linearly related to the mixture fraction. This methodology is based on the fact that combustion is believed to be a local

phenomenon depending on the local, stable composition of the gas mixture, regardless of the fluid's history. Again, this avenue is strictly valid for flames that are far from blowoff. This was proven by Masri et al (1992) when measurements of major species at various locations in turbulent flames were found to be invariant when plotted against the mixture fraction, thereby lending credence to the conserved-scalar combustion models.

5.2 THE BLUFF-BODY COMBUSTOR

The predominant feature of a bluff-body combustor is clearly seen in figure 5.1; the diameter of the fuel jet d is small compared to that of the bluff body D. Intense toroidal vortices are formed behind the bluff body (usually a cylinder pierced by a central tube), which promotes mixing and prolongs the contact between cold reactants and hot products; heat transported within this recirculation zone serves to stabilise the flame by preheating the cold reactants and also by compensating for the heat of reaction which is convected away.

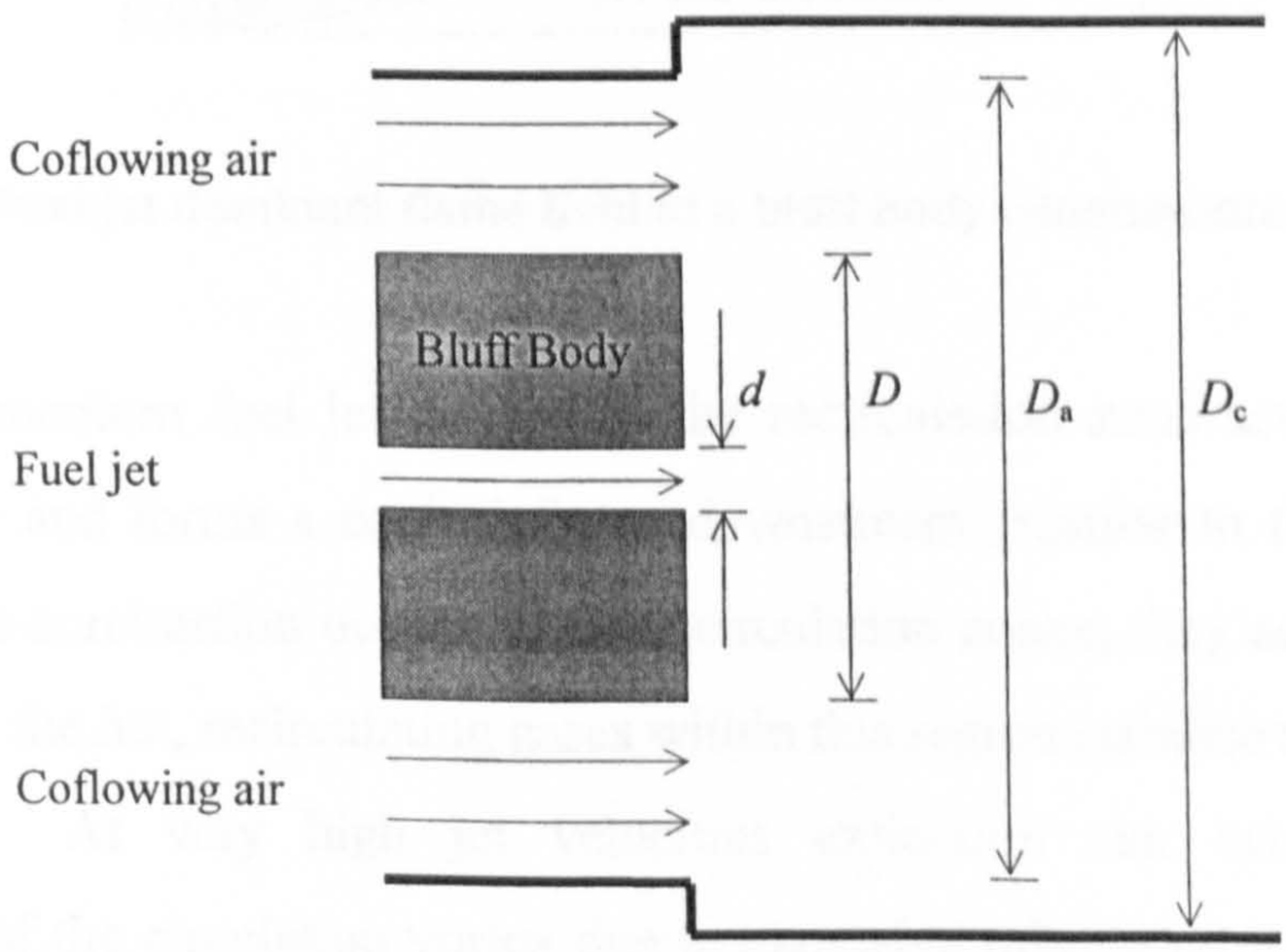

Figure 5.1: Schematic of a bluff-body burner.

The flow patterns downstream of the bluff body are rather complex; one, sometimes two, recirculation zones are formed by the coflow air and the fuel jet. There are three main controlling parameters:

1. Circulation vortex strength, which is dictated by the coflowing air velocity.
2. Fuel-jet momentum (function of fuel velocity).
3. Ratio of diameter of bluff body to that of the fuel jet (D/d).

The nature of the flow-field depends on the above parameters; the resulting bluff-body flames can be broadly classified as one of the two categories depicted below.

- Fuel-jet dominant flames are those in which the initial velocity of the fuel is much larger than that of the coflowing air. Experiments by Roquemore et al (1983) have shown that the recirculation structures produced by the two jets can be of comparable size, as seen in figure 5.2.

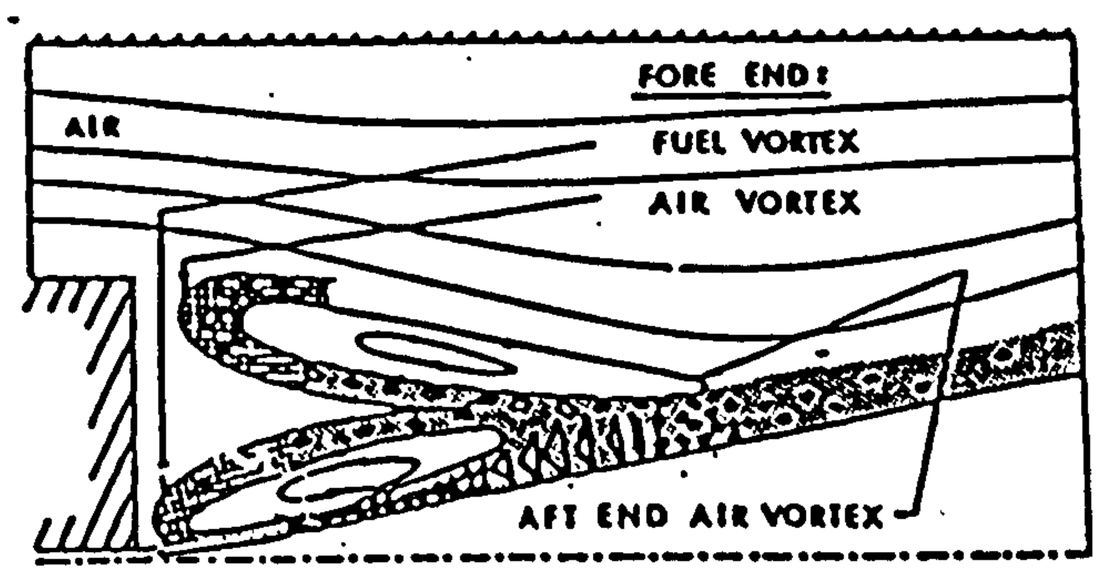

Figure 5-2: Fuel-jet dominant flame behind a bluff body (Roquemore et al, 1983).

The high-momentum fuel jet penetrates the recirculation zone established by the coflowing air and forms a conical flame downstream (similar to that of a free-jet flame). Little combustion occurs in the recirculation zones; they act as the base of the flame and the hot, recirculating gases within this region stabilise the flame further downstream. At very high jet velocities extinction can occur immediately downstream of the circulation vortex due to excessive mixing rates. Reignition can occur yet further downstream where mixing rates have reverted to lower values.

- Coflow-air dominant flames are characterised by an air recirculation zone which prevails over the circulation vortex established by the fuel jet. Fuel is entrained into the larger circulation vortex (as in figure 5.3), resulting in a luminous recirculating

flame behind the bluff-body face. The majority of the reactions occur within or near the recirculating region.

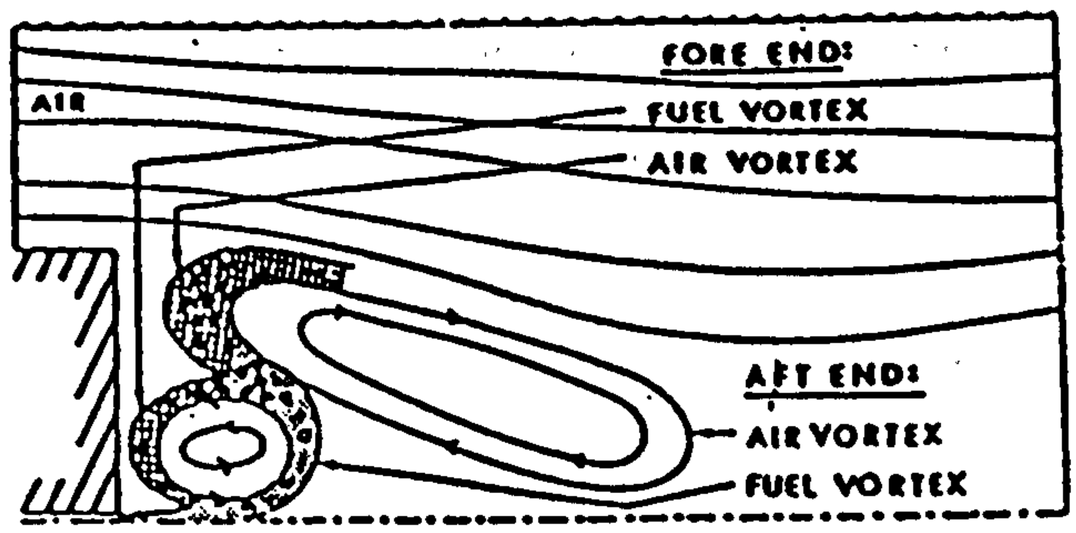

Figure 5.3: Air-jet dominant flame behind a bluff body (Roquemore et al, 1983).

When the air flow rate is high, the flow field is never dominated by the fuel jet. However, at a high enough fuel flow rate, both types of flames co-exist.

5.3 EFFECTS OF CONFINEMENT

A brief excursion into the effects of confinement on bluff-body flames is undertaken principally because most industrial burners are confined and the side-walls enable the relatively straightforward, stable, near-wall boundary conditions to be applied in CFD. Schefer et al (1996) noted that many industrial burners utilise bluff-bodies to enhance flame stability as well as mixing. Enhancement of stability is of paramount significance in the case of low-emission combustors where NO_x production is inhibited by the containment of temperatures (which has an adverse effect on stability). Confinement can affect flow patterns and thus influences the nature of the flame.

The addition of confinement generally forces the fuel jet to penetrate further downstream (due to the introduction of axial pressure gradients); hence the fuel distributions are also affected. In fact, the fuel concentrations in the recirculating region are of great importance in terms of flame regimes; the fuel distributions define whether the flame is attached to the burner, detached (lifted) from it or completely blown off. As the fuel concentration deviates from the range of values bounded by the flammability

limits, the chemical reaction times become significantly larger. This, in conjunction with turbulent mixing rates, has an enormous impact on the overall flame structure.

A parameter often used in classifying bluff-body burners is the blockage ratio, BR, defined as the ratio of the cross-sectional area of the bluff body (blockage) to that of the coflowing air duct; i.e. BR = $(D/D_a)^2$. In the case of confined burners, an additional dimensionless quotient, the confinement diameter ratio (CDR), is utilised. This is the ratio of bluff-body and confinement diameters; CDR = D/D_c. The two parameters are directly related only when the confinement diameter is the same as the outer diameter of the air-annulus (i.e. no step exists between the air jet and the confining wall).

In both unconfined and confined flows the recirculation zone length and stagnation point locations (i.e. centre of the recirculation vortex) are functions of radial and axial pressure gradients. In high blockage-ratio configurations (i.e. relatively narrow air jets) streamline curvature away from the centre is significant, whereas low BR's result in less pronounced streamline curvature. The addition of confinement to a burner with a low BR (for a given annulus air velocity) does not cause a large change in flow patterns because the confining walls are at a relatively large distance from the centreline and thus have little effect on the radial pressure distribution. Confining the flames of higher BR burners, though, generally causes the recirculation zone to increase in length (Schefer et al, 1996, found the length could increase by a factor of up to 2.7) and to relocate the stagnation point(s) further downstream. This occurrence is explained by the fact that confinement causes a pressure decrease in the axial direction (as in pipe flow); there is also a reduced radial pressure gradient which causes streamline curvature to be diminished.

Given certain fuel and air velocities, confinement and various BR's can act in opposite directions. Confinement can increase the recirculation length (for a given BR), but the recirculating vortex length is also dependent on the blockage-ratio (increasing the BR causes the vortex to be curtailed). The effects of confinement on bluff-body burners can be summarised as follows:

- Given certain fuel and air velocities, the addition of confinement to a burner with a low blockage ratio, does not cause any significant change in flow patterns.
- For geometries involving larger blockage ratios, confinement tends to lengthen the recirculation bubble.

5.4 BLUFF-BODY COMBUSTOR: EXPLORATORY SIMULATIONS

Correa & Gulati (1992) and Correa & Pope (1992) reported limited experimental results (temperatures and mean mixture fractions only, at two different locations) for an axisymmetric bluff-body combustor. Although this case had already been thoroughly explored, from a turbulence and combustion modelling perspective, by Gran et al (1996, 1997), it was investigated again for the following reasons:

- To prove that the flame sheet combustion model had been properly implemented in the TEACH code[1].
- To assess the effects of changing various parameters on simulation results.
- To obtain an initial idea of the nonlinear turbulence model's performance in combusting cases.

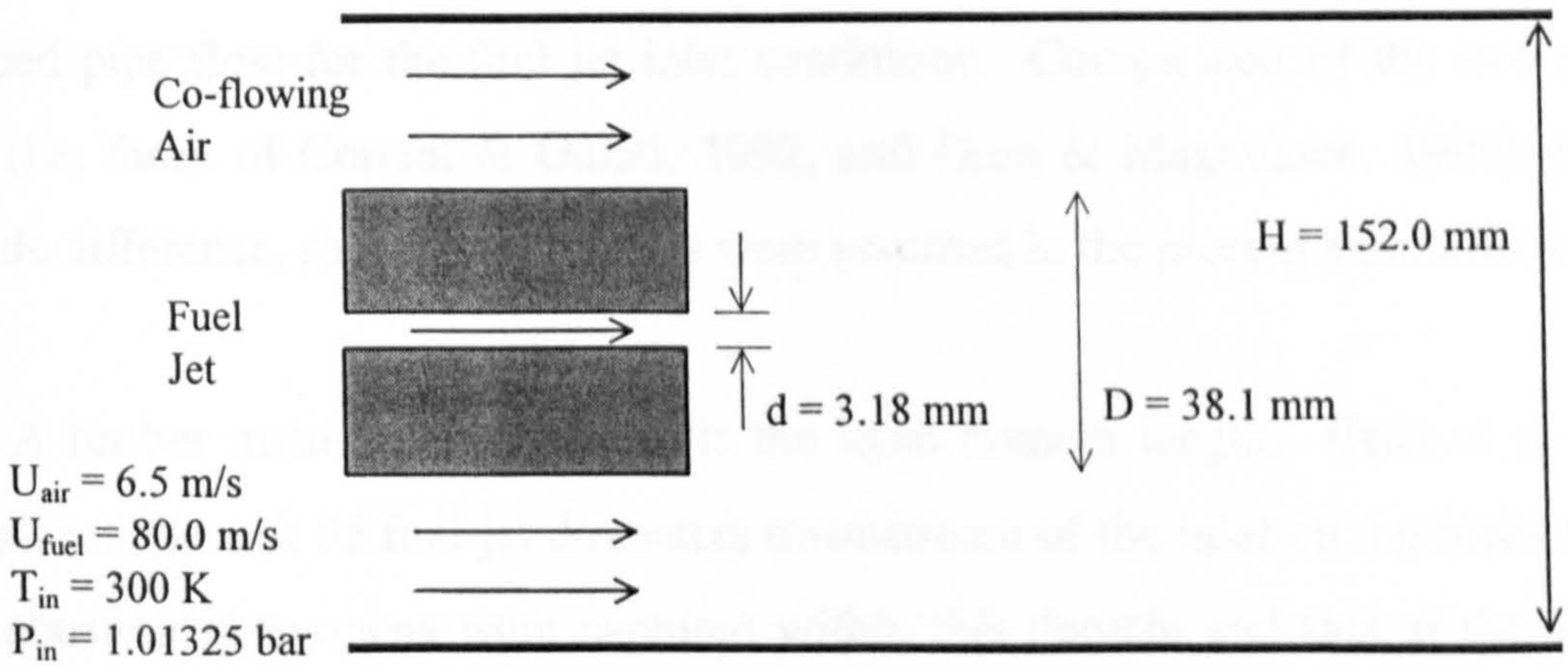

Figure 5.4: The Correa & Gulati (1992) bluff-body combustor.

The precise geometry of the burner is depicted in the above figure. The confining effect of the walls is minimal due to their location far from the bluff body. Wall insulation was adopted by the experimentors so as to promote adiabatic conditions, thereby allowing the enthalpy to become a linear function of the mean mixture fraction. The volumetric composition of the fuel, syngas, is listed in table 5.1; Gran &

---

[1] Actually, I had attempted this exercise for the furnace investigated experimentally and numerically by Elghobashi & Pun (1974) and Lockwood et al (1974), as well as being simulated by Kim & Chung (1989). However, significant variations in predictions were evident, as a result of differing numerical practices (e.g. very coarse grids, choice of numerical scheme (FV vs FE)) and the adoption of different calorific values for the fuel components. The discrepancies were sufficiently large such that it was not possible to confidently state that the TEACH predictions for this case were consistent with others' results.

Magnussen (1996) reported the stoichiometric mixture fraction to be 0.323, resulting in an adiabatic equilibrium temperature of 2181K.

Component	Volume fraction
CO	27.5 %
H_2	32.3 %
N_2	40.2 %

Table 5.1: Composition of Syngas.

Correa & Gulati (1992) assumed flat inlet profiles for both the fuel jet and air coflow flow, with a turbulence intensity of 0.5% and characteristic length of 3% of *d* and *H-D*, respectively. It was stated that the flow was relatively insensitive to the inlet profiles, although Gran & Magnussen (1996) reckoned otherwise and utilised a fully-developed pipe flow for the fuel jet inlet conditions. Comparison of the two sets of results (i.e. those of Correat & Gulati, 1992, and Gran & Magnussen, 1996) showed very little difference, so flat inlet profiles were assumed in the present simulations.

A further matter of importance is the axial domain length. Gran et al (1996, 1997) placed the exit 55 fuel-jet diameters downstream of the inlet on the basis that all the combustion phenomena were captured within this domain and that at the exit the mixture fraction is zero less than half-way from the centreline to the wind-tunnel wall. This approach was also adopted in the TEACH simulations. Although inspection of the simulated results showed that the flow had not fully redeveloped at the exit, the axial variations were small and thus the zero-gradient outlet condition described in Chapter 3 was valid.

All the simulation results presented in the following sections can safely be considered as grid-independent. Gridding studies were carried out and eventually 100×110 and 100×100 meshes were used for the cubic and k-ε turbulence models, respectively. The k-ε results were very similar to those obtained by Gran et al (1996, 1997), who stated that a 75×75 grid was fine enough. The grids utilised by the CRY and LS models were identical to those employed by the k-ε and RNG models, with

additional cells being located in the boundary layer. The majority of cells were located between the centreline and the bluff-body radius ($0.5\times D$ in figure 5.4).

5.4.1 Parameters Affecting Combustion Predictions

There exist two parameters in the current modelling framework which affect predictions for combusting flows. The first is the turbulent Prandtl number σ_t the value of which is commonly taken as 0.7 in free flows and 0.9 for wall-bounded flows (Jones & Kakhi, 1996). Secondly, Dally et al (1995) and Masri (1998) reported that the constant $C_{\varepsilon 1}$ in the dissipation rate transport equation of the standard k-ε model improves predictions for free-jet flows when the value is changed from 1.42 to 1.60. It is instructive to assess the effects of such adjustments on the standard k-ε model in order to gauge which parameters most influence the results in combusting flow simulations. Therefore, these parameters are investigated by comparing predictions obtained with the various k-ε model configurations outlined in table 5.2.

Configuration	σ_t	$C_{\varepsilon 1}$
PDF1	0.7	1.42
PDF2	0.9	1.42
PDF3	0.7	1.60

Table 5.2: Various model configurations.

Although no experimental velocity data is given, it is nevertheless helpful to briefly remark on the flow field. Figure 5.9 reveals the shape of the computed flow; there is no indication of the presence of a recirculating structure brought about by the central fuel jet (Roquemore et al, 1983, generally found such a recirculation zone in fuel-jet dominant flames, as shown in figure 5.2). The computed streamlines in figure 5.9 clearly show a large recirculation region caused by the coflowing air.

Axial and radial distributions of mean mixture fraction and temperature are plotted in figures 5.5 and 5.6. It is immediately obvious that PDF3 predicts the correct axial decay rate of f and is significantly more accurate than PDF1 and PDF2 as far as

radial profiles are concerned. If the flame length is taken as the axial centreline point at which the mixture fraction attains the stoichiometric value (0.323), then PDF3 also predicts the correct flame length; PDF1 and PDF2 significantly underpredict this feature. The PDF3 temperature trends reflect the improved mixture fraction predictions. Contour plots of f and T are provided in figures 5.7 and 5.8. The respective plots are very similar in that the PDF3 contours appear to be axially stretched versions of the PDF1 outlines. This is also true of the streamlines (see figure 5.9); PDF3 predicts a longer recirculation zone than does PDF1.

The success of PDF3 is seen to rest upon its ability to forecast the correct axial decay rate of the mixture fraction. This in turn is due to the constant $C_{\varepsilon 1}$ affecting the spreading rate of the jet. The standard k-ε model is known to overpredict the spreading rate of axisymmetric jets (Masri, 1998). Modifying the turbulent Prandtl number, on the other hand, results in only minor changes. It is clear, then, that altering the turbulence transport equations has a larger effect on results than the adjustment of the turbulent Prandtl number.

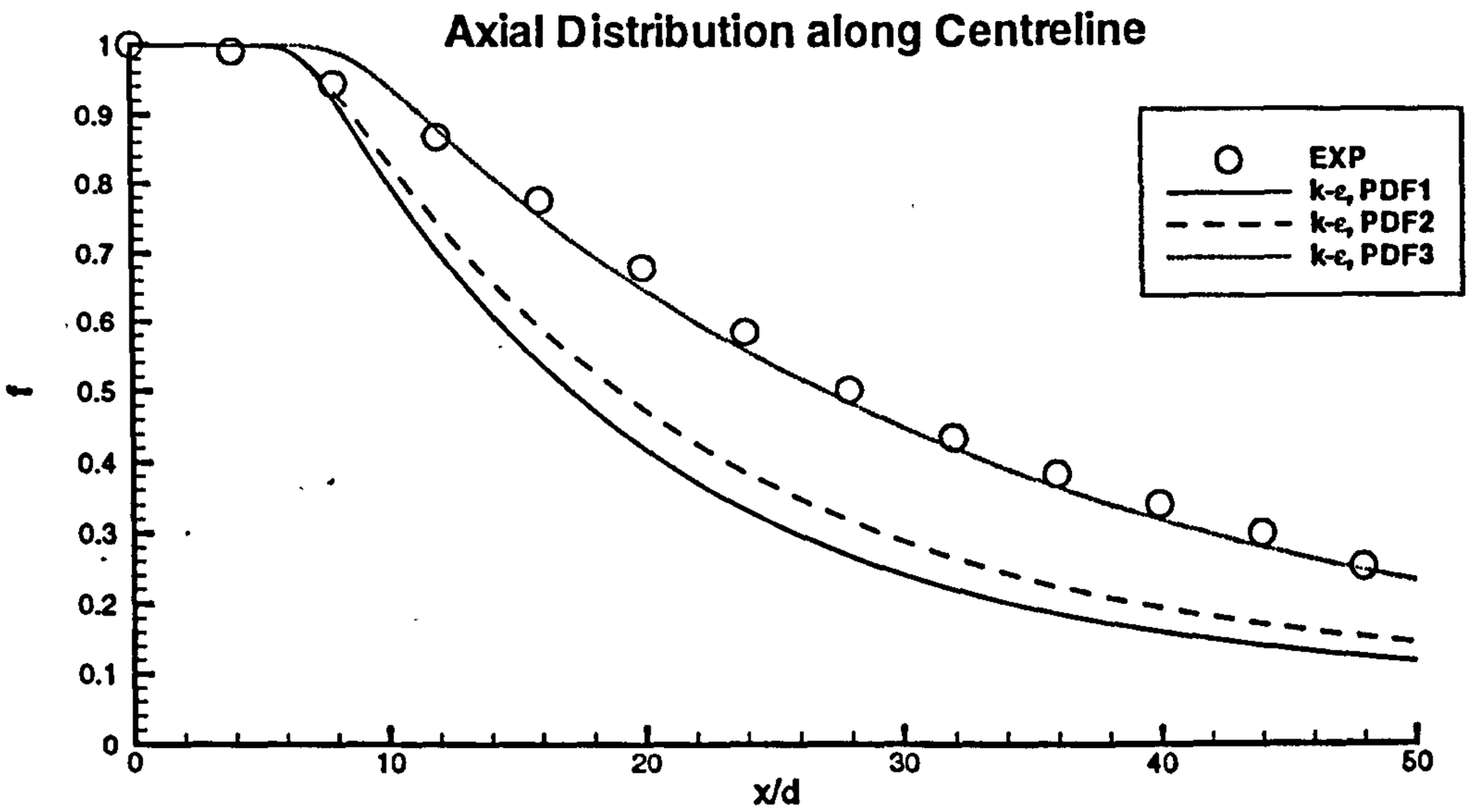

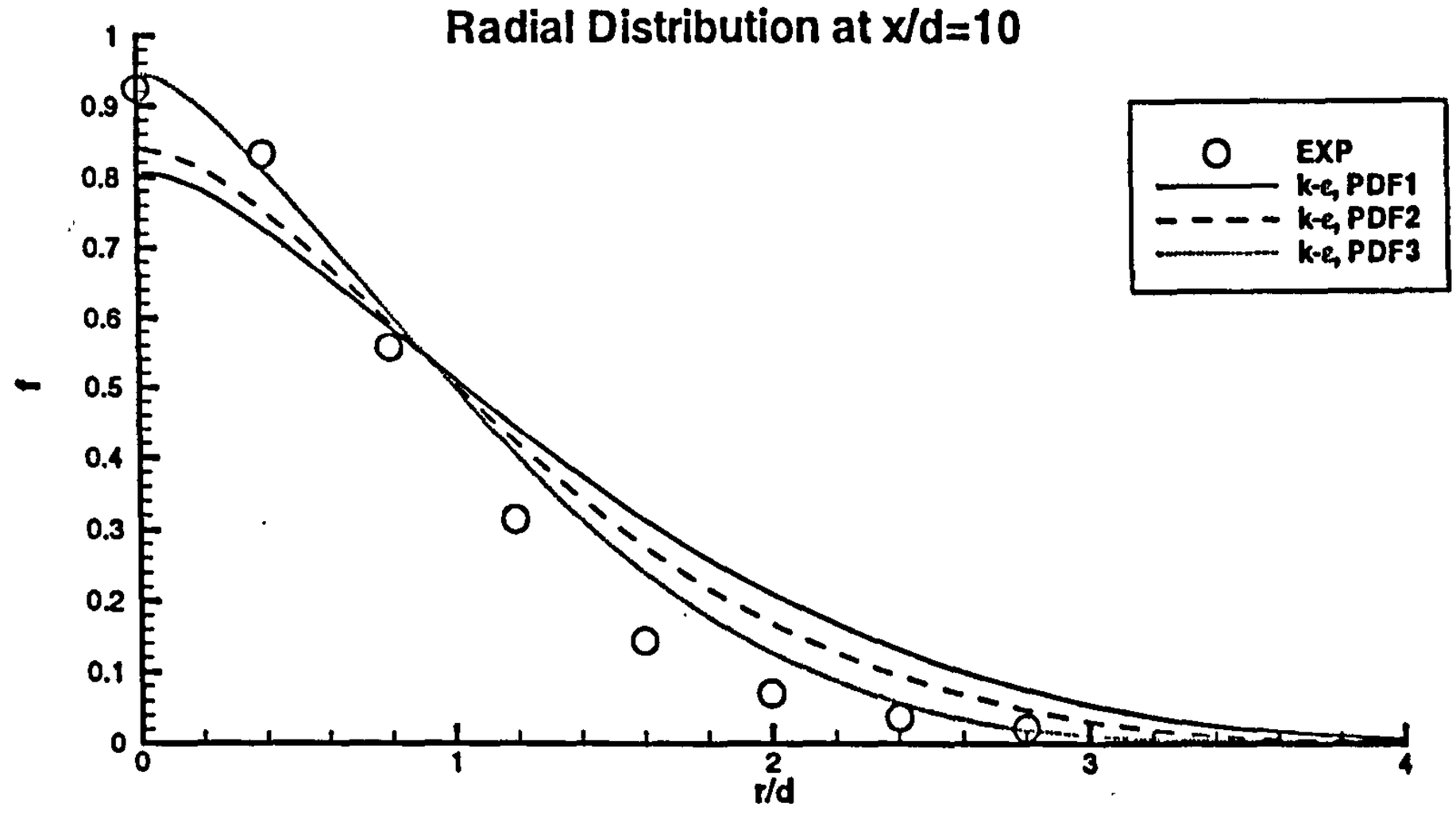

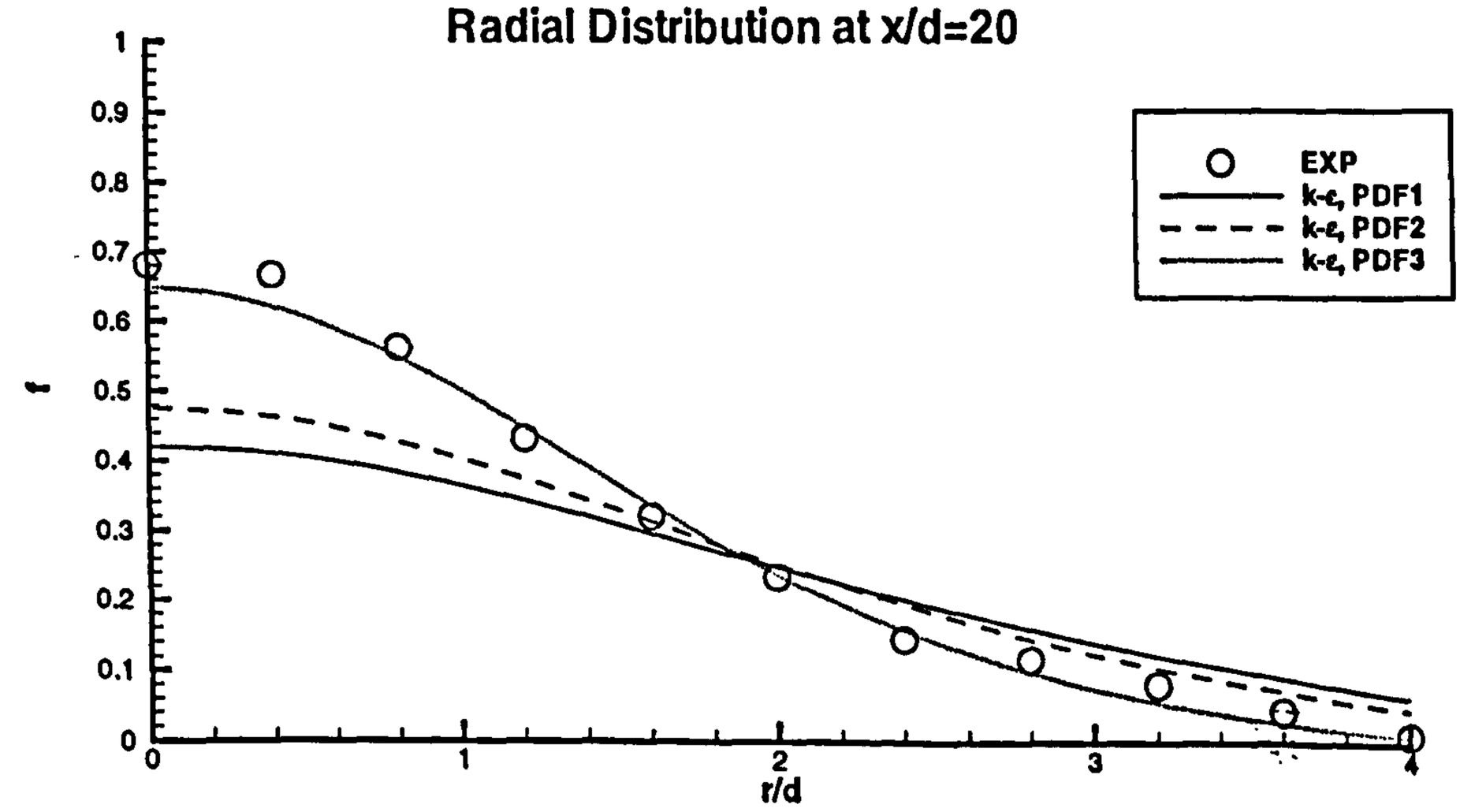

Figure 5.5: Mixture fraction distributions.

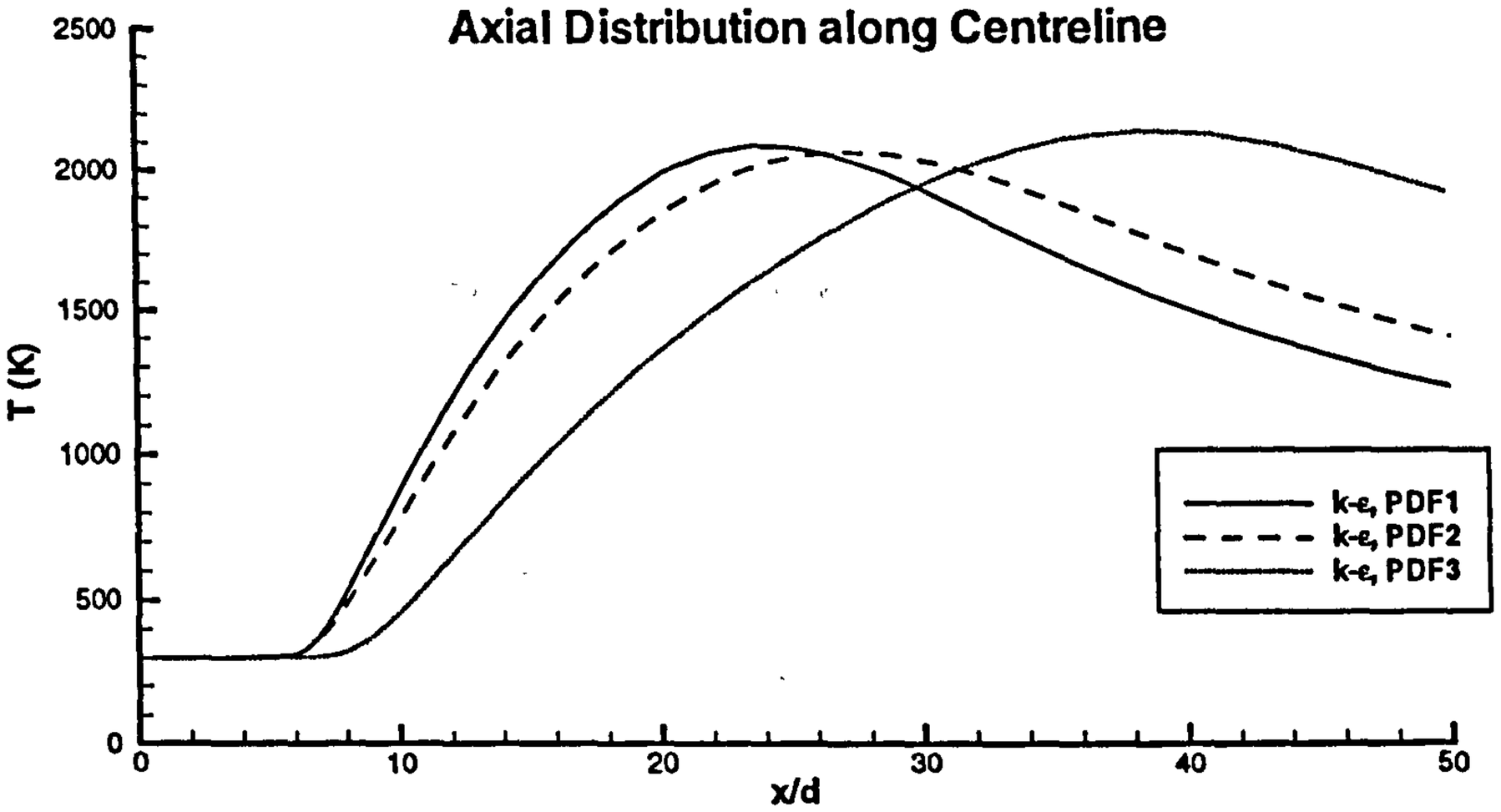

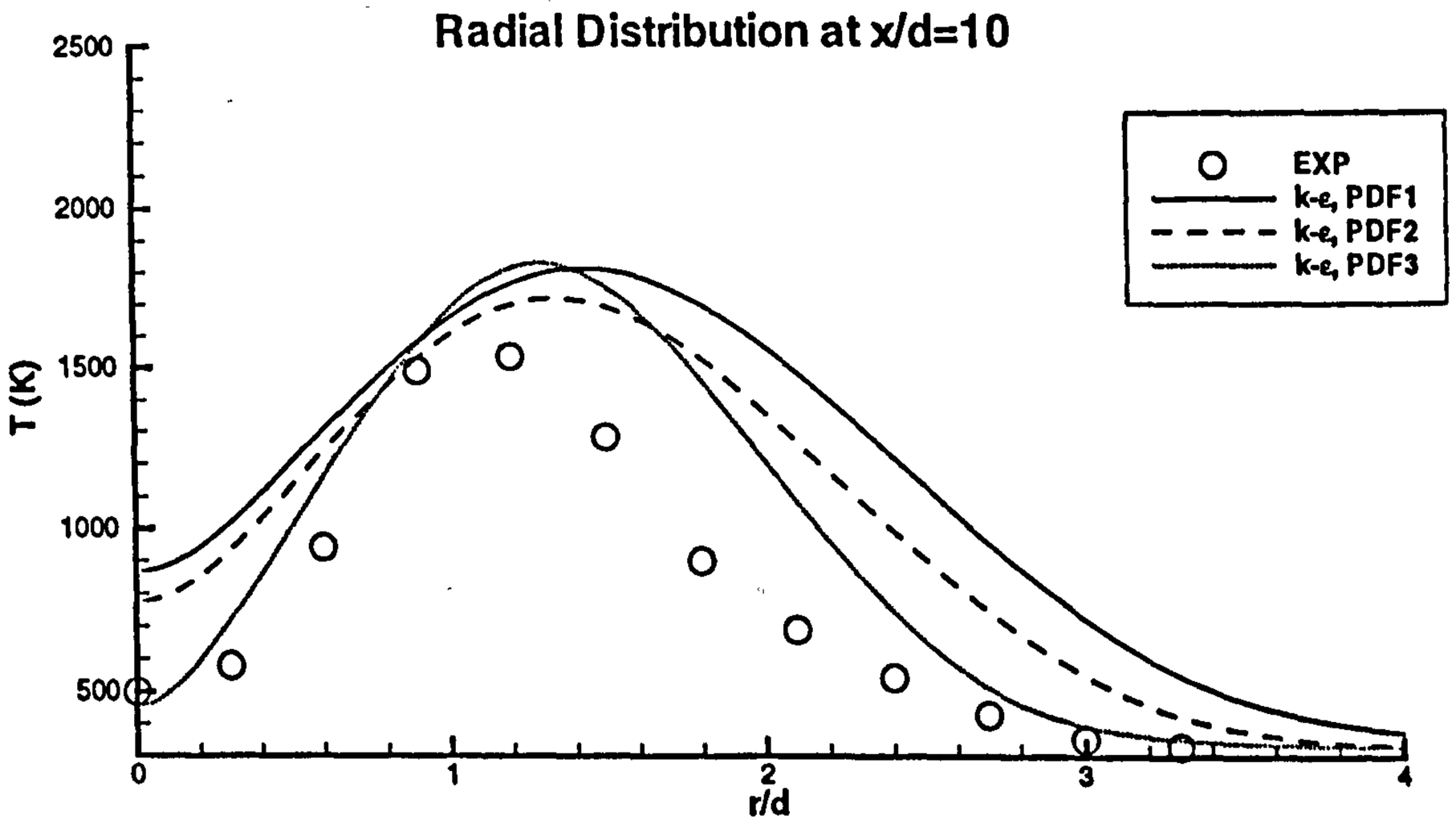

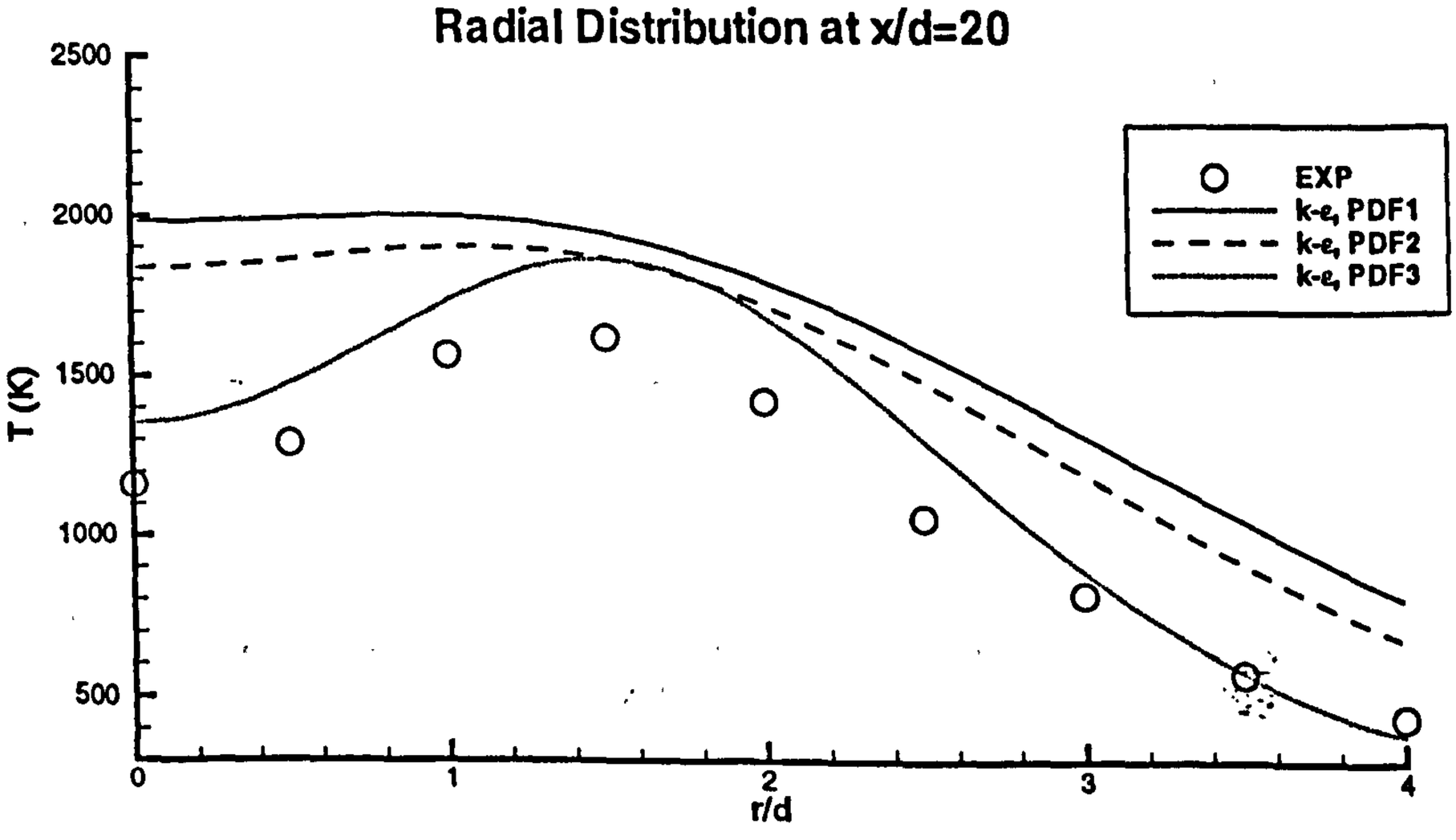

Figure 5.6: Temperature distributions. No experimental data was available for the axial distribution of temperature along the centreline.

(a)

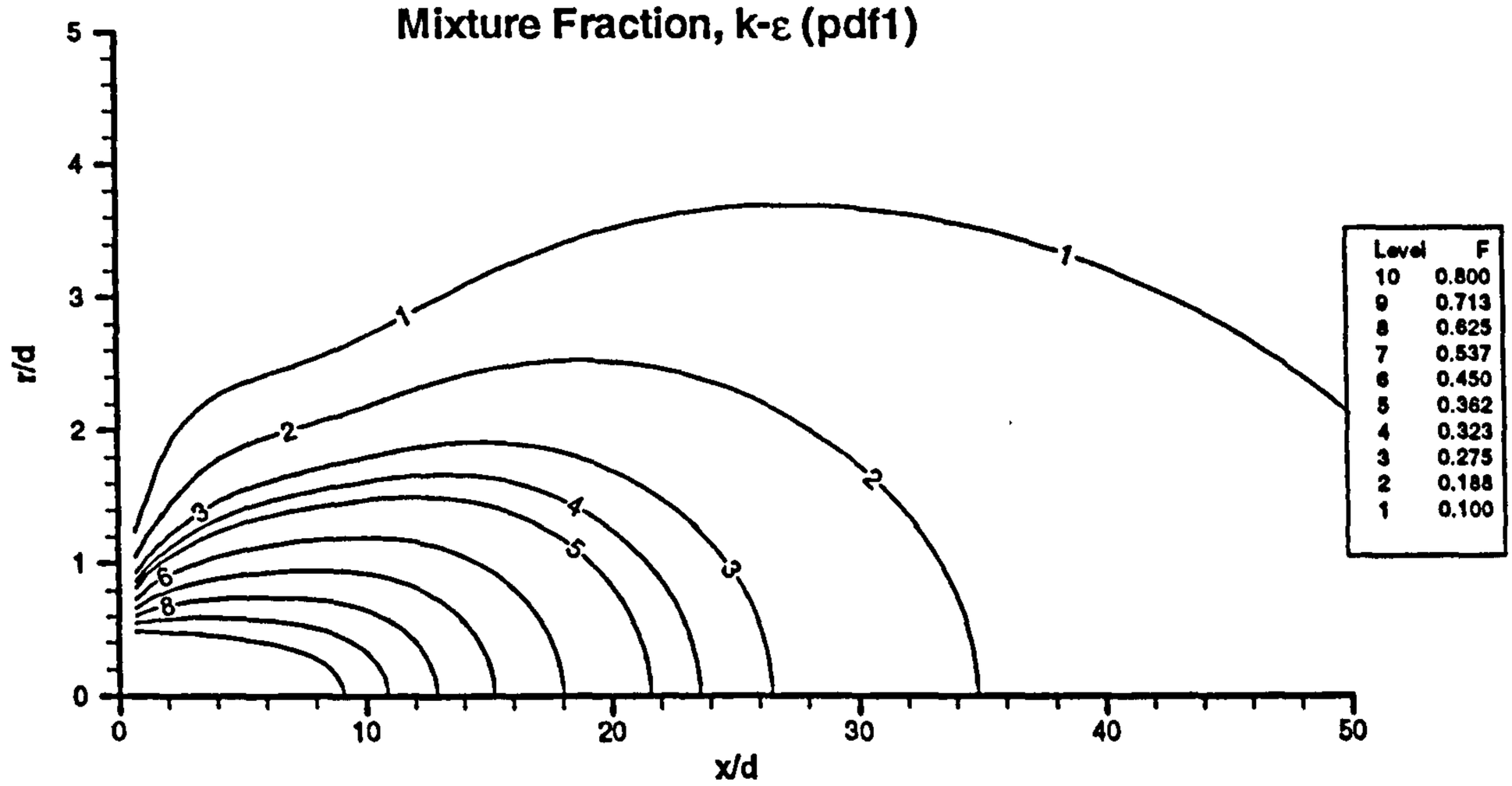

(b)

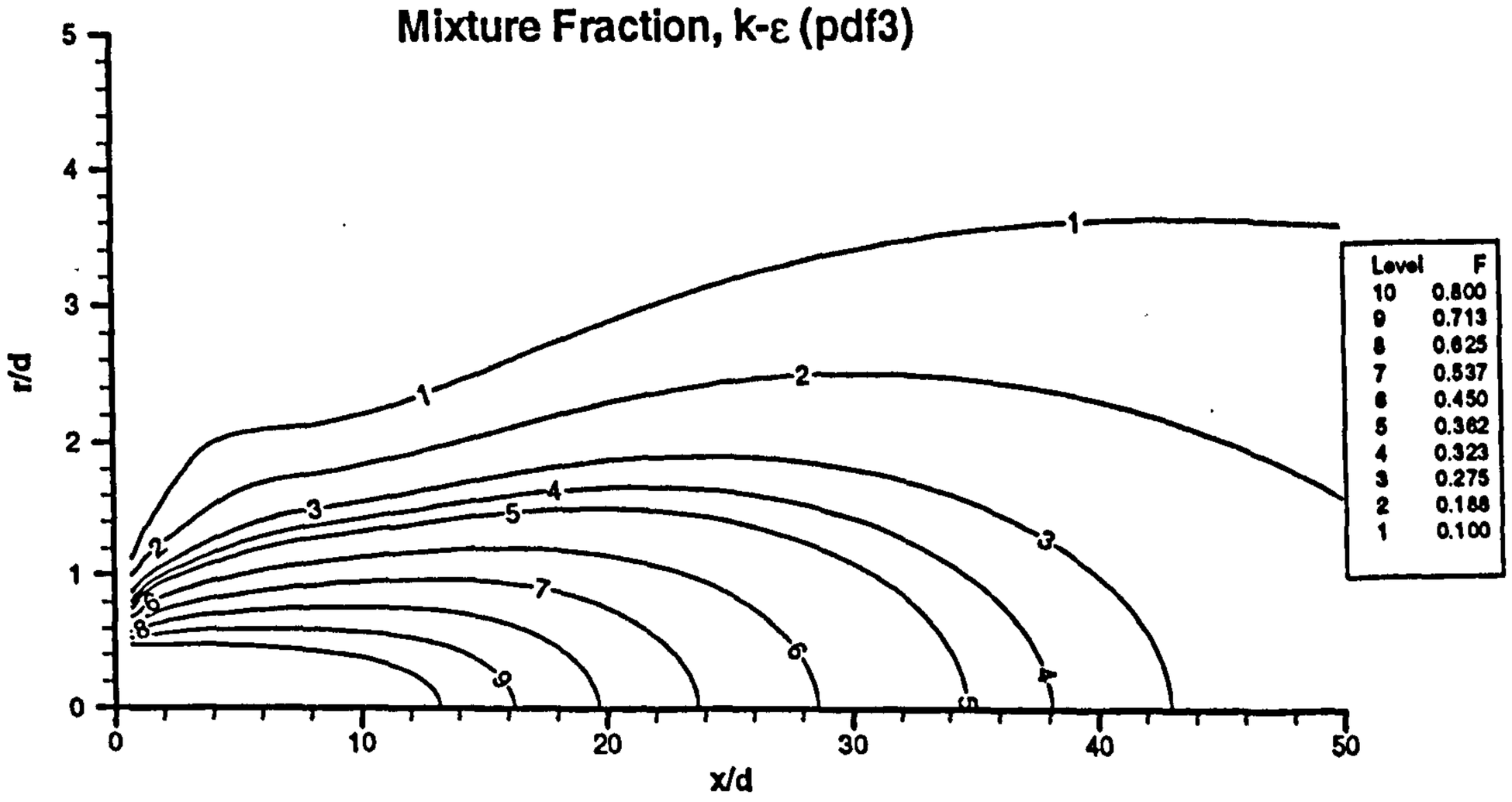

Figure 5.7: Mixture fraction contour plots, for (a) PDF1 and (b) PDF3 configurations.

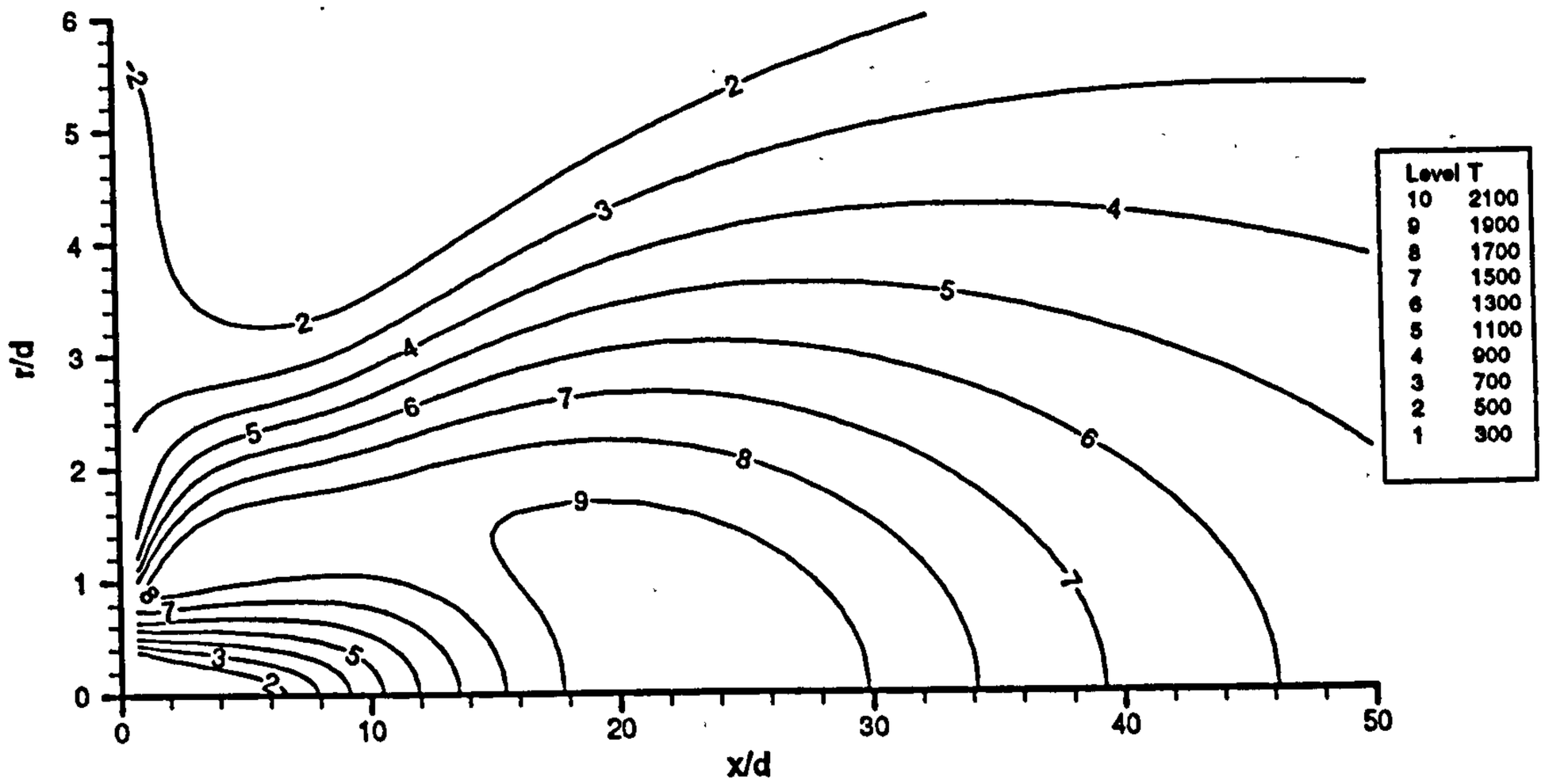

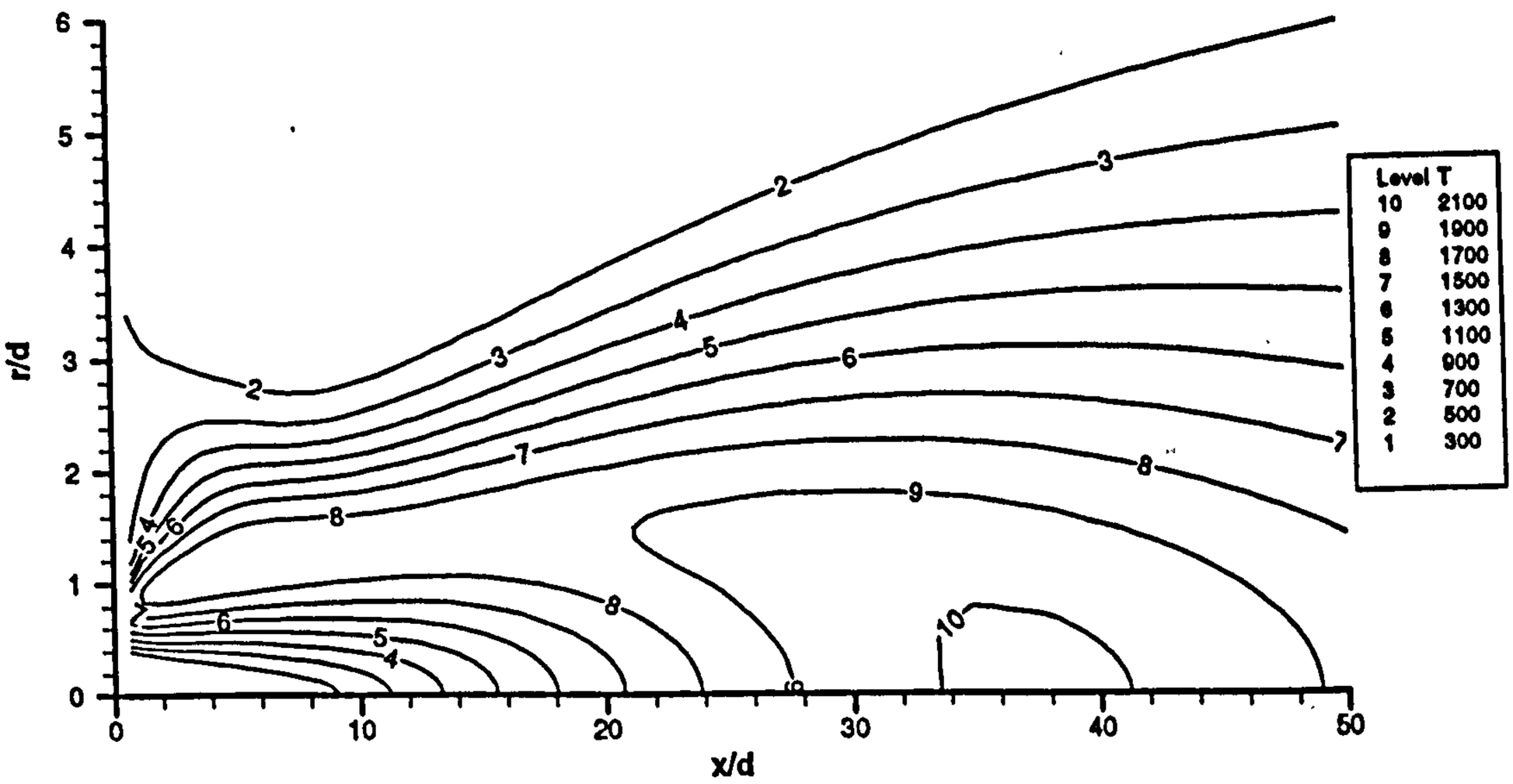

Figure 5.8: Temperature contour plots, for (a) PDF1 and (b) PDF3 configurations.

(a)

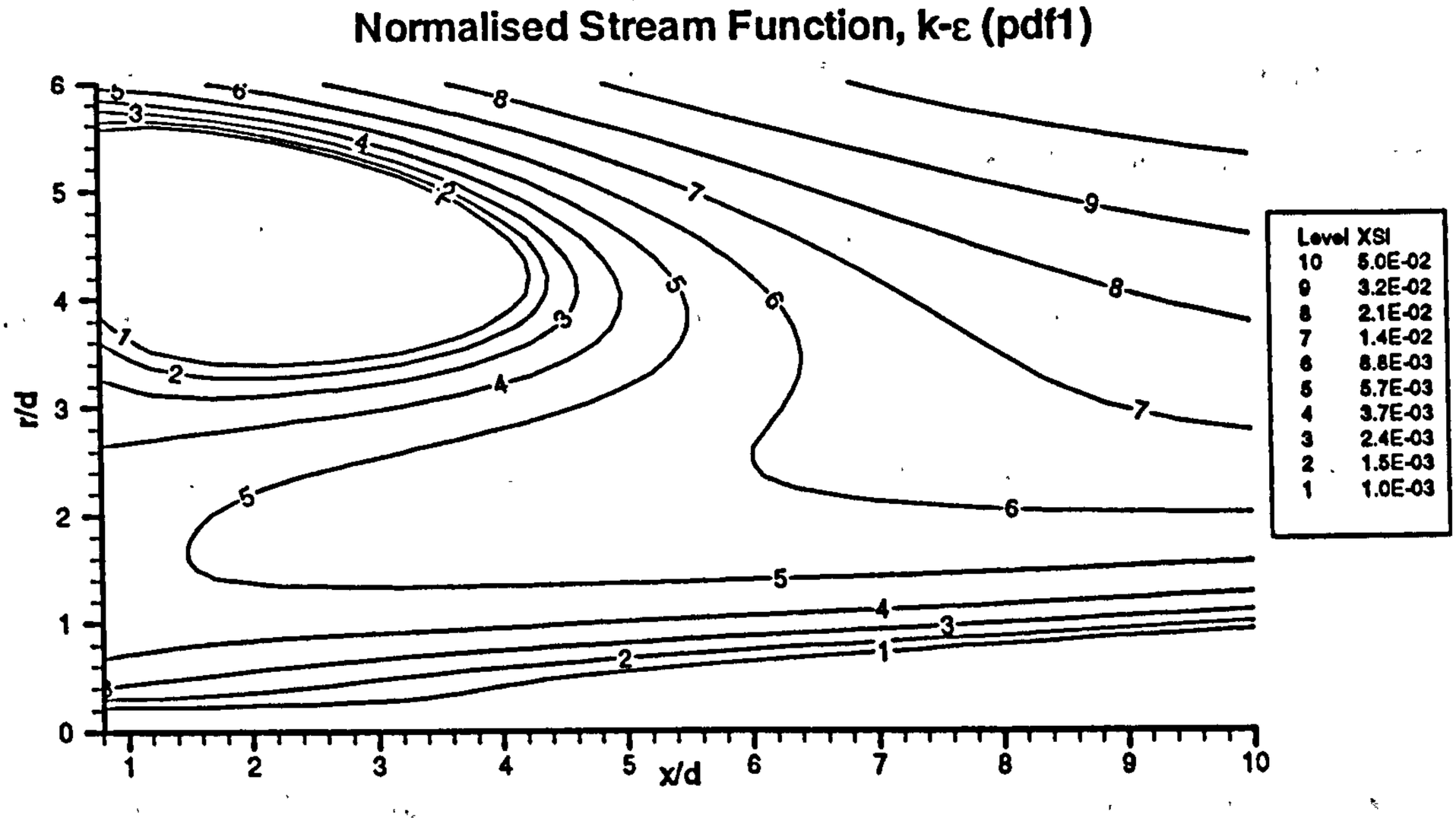

(b)

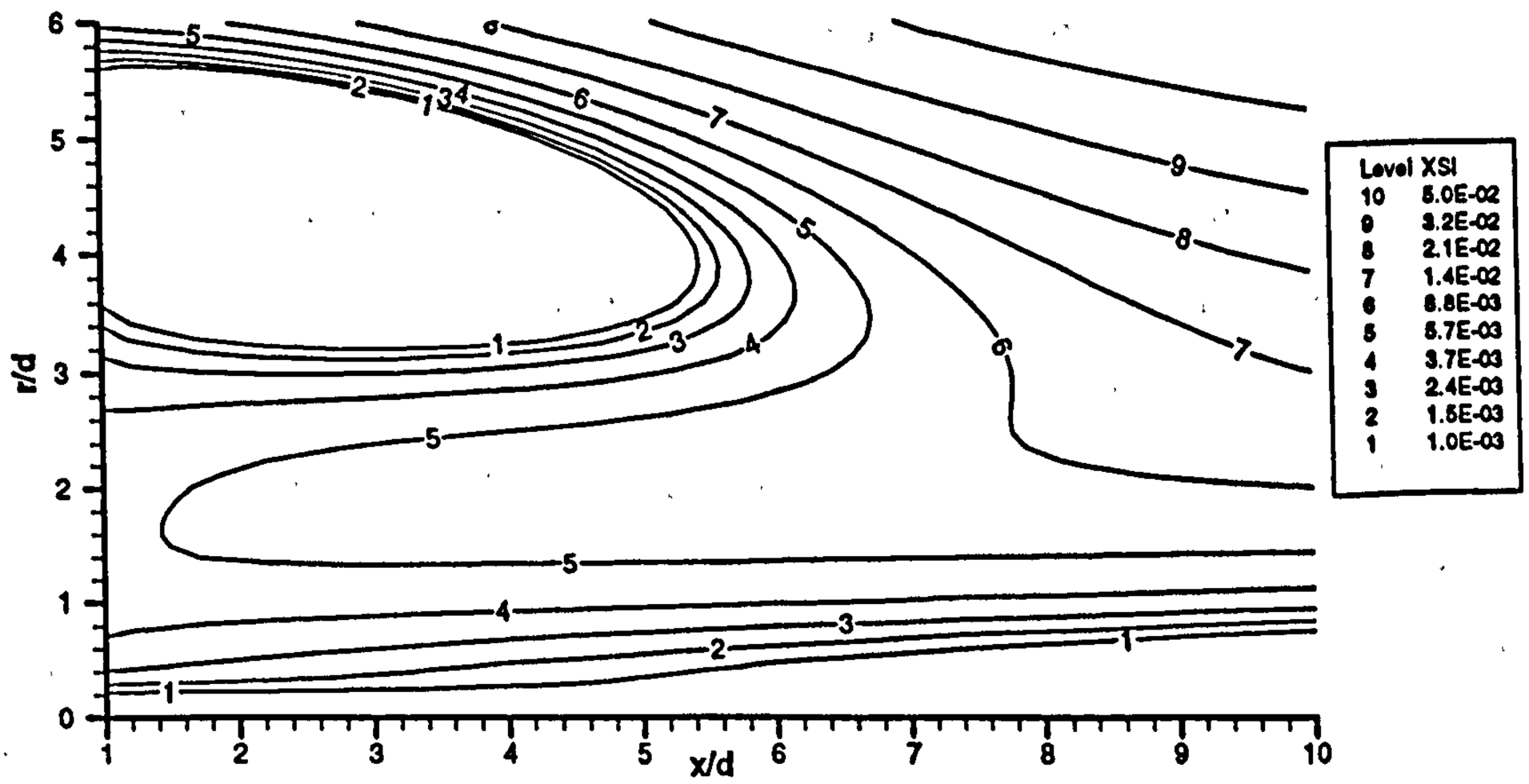

Figure 5.9: Normalised stream function contour plots, for (a) PDF1 and (b) PDF3 configurations.

5.4.2 Performance of the Nonlinear Turbulence Model

This section reports on the performance of the nonlinear turbulence model when applied to the Correa & Gulati (1992) bluff-body combustor, and the results are compared with the predictions of the standard k-ε, RNG and LS models. A turbulent Prandtl number of 0.7 was used, and the standard value of 1.42 was adopted for the constant $C_{\varepsilon 1}$. Although the PDF3 configuration was shown to significantly improve results in section 5.4.1, it was only used to demonstrate the effects of altering parameters on an ad-hoc basis. Thus it is not investigated any further.

The main feature of the mixture fraction profiles in figure 5.10 is the cubic model's prediction of a jet core which extends much further downstream than experiments indicate. The same is true, to a reduced extent, of the LS model. This is seen to modify the radial profiles of mixture fraction and has large repercussions upon the temperature distributions (figure 5.11). The radial profiles in both figures, however, do indicate that the nonlinear model returns better agreement with the experimental results (relative to the other models), away from the centreline.

The persistent jet cores indicate that the diffusion process in the centreline region is overwhelmed by convection. An examination of the effective viscosities reveals that the levels of μ_t are significantly lower for CRY and LS than for the two high Reynolds number models. Perusal of the distributions of the damping function f_μ discloses that the centreline values are much smaller than the high Reynolds number asymptotic value of unity, which should be attained at the centreline of a turbulent jet. Similarly, the function C_μ (in the case of the CRY model only) returns values much smaller than the customary 0.09. The fact that the effective viscosity depends on f_μ and C_μ explains the penetration of the fuel jet to locations much further downstream than otherwise encountered with the high Reynolds number models.

The cause of this anomaly can be traced to the dependence of f_μ on the turbulent Reynolds number, R_T, which is itself reliant on turbulence energy (equation 2.28). The function C_μ (in the case of the CRY model) is also directly related to k. It seems that the prescribed inlet levels of k are so low that the high Reynolds number asymptotic

behaviour $f_\mu \rightarrow 1$ is not satisfied. A partial remedy is to utilise fully-developed profiles for turbulence energy at the inlet. This practice enabled Gran et al (1997) to obtain a somewhat higher fuel jet spreading rate during their assessment of the LS model. The high Reynolds number models (k-ε and RNG) are excessively diffusive, and are thus less influenced by the nature of the inlet conditions. This was shown to be the case in Appendix B when the Fluent and TEACH results for the k-ε model were very similar, despite the former using a fully-developed inlet profile whilst the latter prescribed a flat inlet distribution. The results of this comparison prompted the use of flat inlet profiles in the TEACH code simulations. Consequently, the CRY and LS models predict significantly longer flame lengths (figure 5.13).

Inspection of the stream functions (figure 5.12) reveals that the CRY and LS models predict somewhat longer recirculating regions which are formed by annulus air flow past the bluff body. Bearing in mind the effects of the damping function on eddy-viscosity, f_μ was examined in the annulus inlet region and was found to generally take on values between 0.5 and 0.7. Correa & Gulati (1992) reported that the coflowing air turbulence level was very low and the velocity profile was virtually flat, so it seems that the damping function (and C_μ in the case of the CRY model) is simply responding to the fact that the turbulence levels are low. Thus the CRY and LS models compute longer recirculating zones because of the reduced shear stresses resulting from the damping mechanism provided by f_μ (and also C_μ in the case of the cubic model).

Figure 5.14 shows that the CRY and RNG, and LS and k-ε models, respectively, predict similar temperatures within the recirculation area, although the former are generally lower than the latter. At the bluff-body face (from r/d = 1 to r/d = 3), furthermore, the nonlinear model predicts a lower temperature than do all the other models. This is indicative of the CRY model predicting a stronger recirculation zone (i.e. greater velocities) in which combustion products are more quickly convected away. Examination of the temperatures reveals that the gases in the recirculation bubble are not particularly hot (less than 500K); the slightly lower densities probably only account for a small decrease in f_μ (since R_t is a function of density) relative to the effects of low turbulence energy.

5.5 SUMMARY

The main conclusion to be drawn from the discussions in the two previous sections is that the predicted flow field strongly affects the temperature and mixture fraction distributions. This is to be expected in light of the fact that in actual combustors, the purpose of the bluff body geometry is to enhance the combustion process. Given this strong link between vector and scalar quantities, it follows that the correct velocity distributions are required in order for accurate temperature and species patterns to be obtained. Complete investigation of any turbulence model necessitates high quality, experimental flow fields. Chapter 6 reports on a study whose principal aim is to measure the flow field by PIV and to validate the CFD results obtained with the cubic turbulence model.

The exploratory simulations of the Correa & Gulati (1992) bluff-body combustor yielded the following principal conclusions:

- Combustion simulations are highly sensitive to the turbulence model.
- Improved predictions using the standard k-ε model can be obtained with the use of ad-hoc adjustments, such as modifying the constant $C_{\varepsilon 1}$ in the dissipation rate equation.
- The nonlinear turbulence model computes improved temperature profiles relative to the standard k-ε, RNG and LS models. The mixture fraction predictions are markedly different too, but not necessarily more accurate.
- Further validation of the cubic turbulence model is only possible if experimental flowfield data is available for a bluff-body combustor.

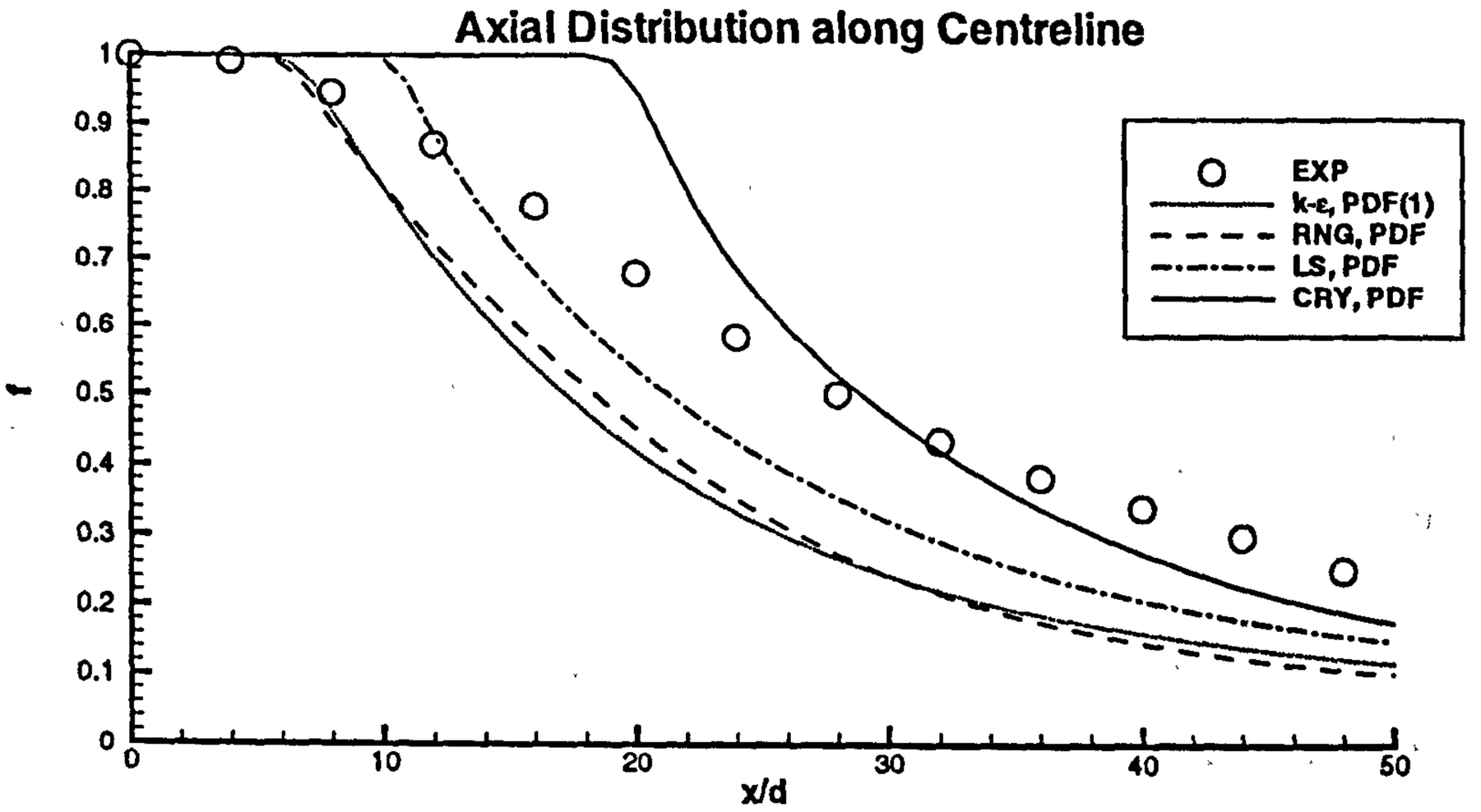

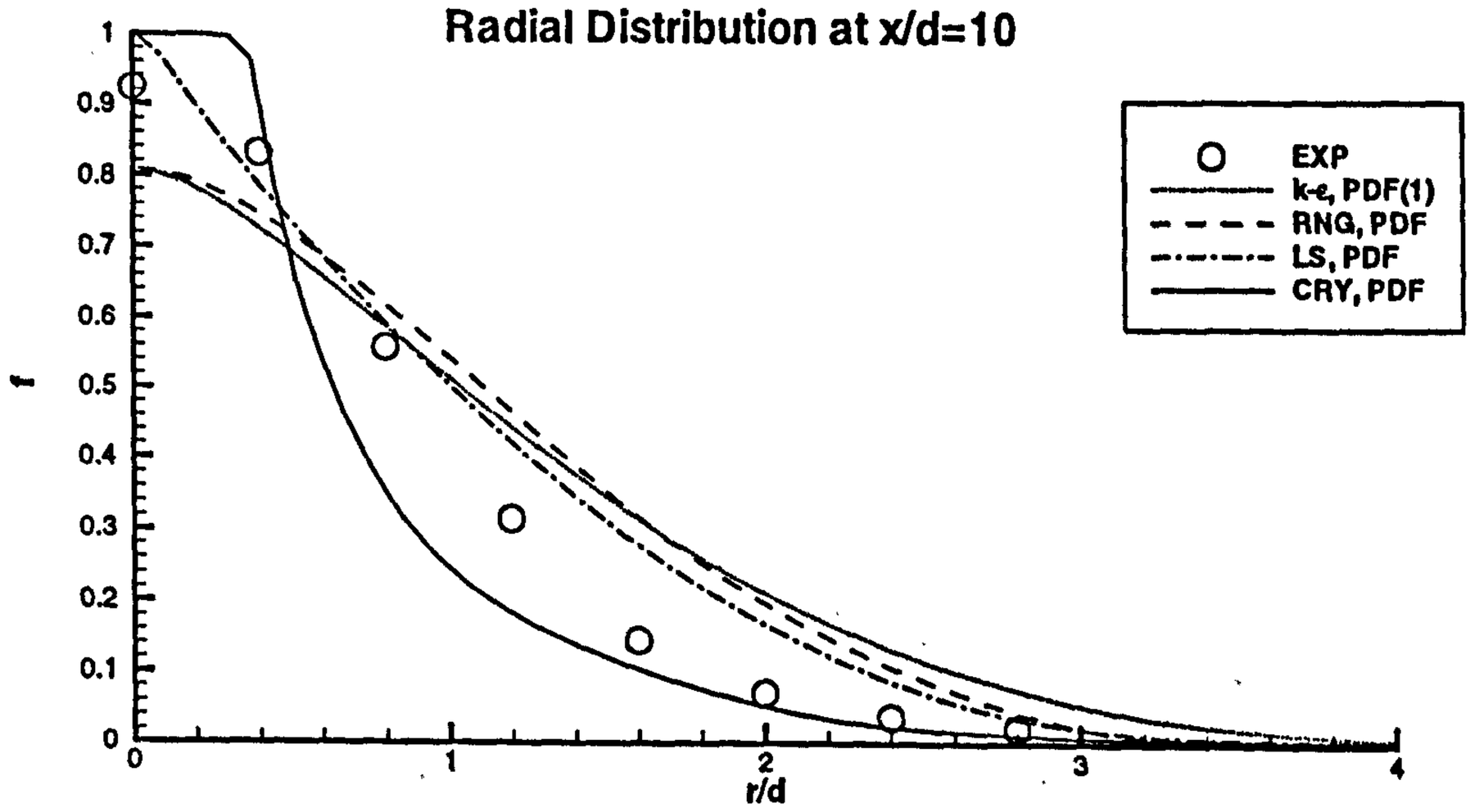

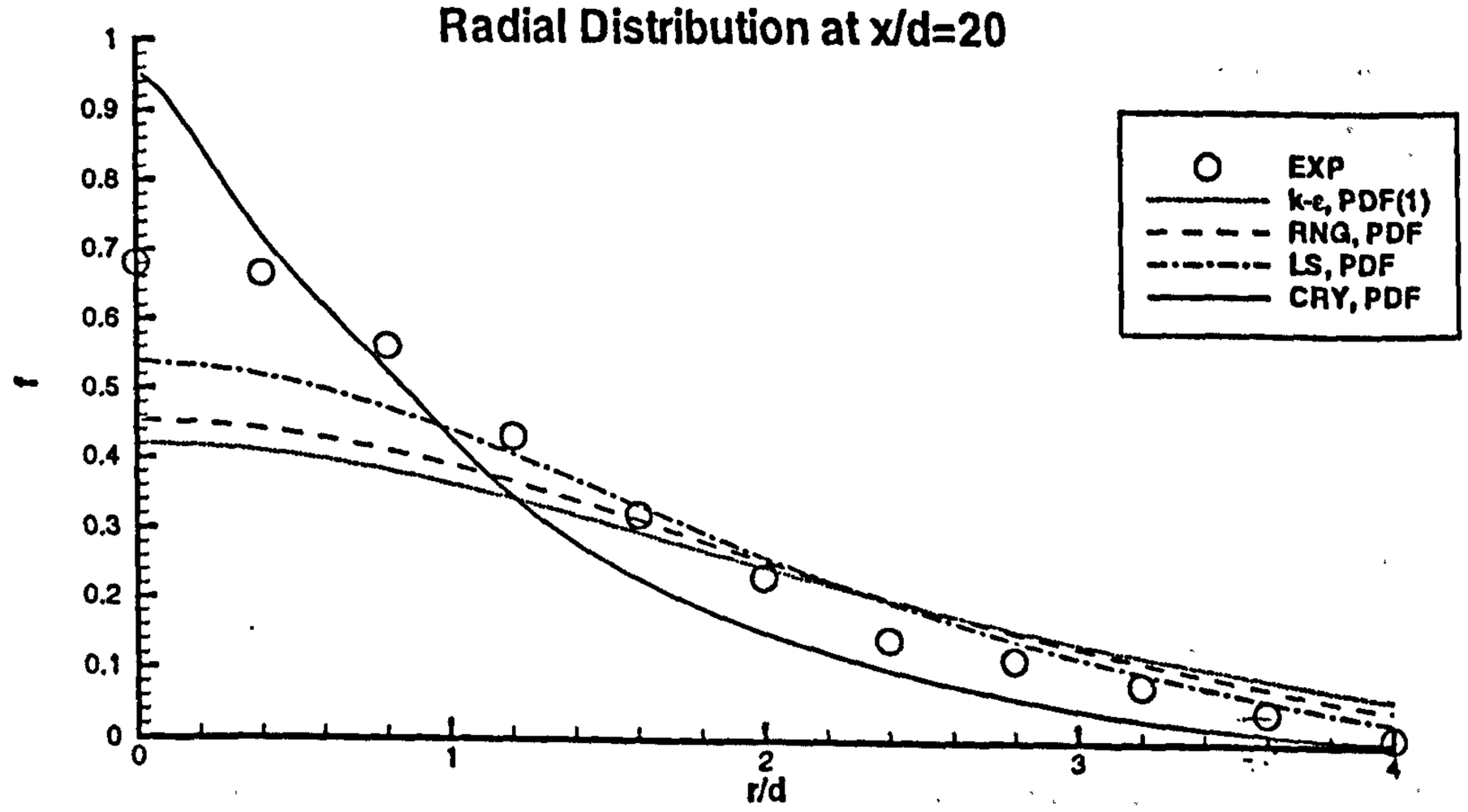

Figure 5.10: Mixture fraction distributions.

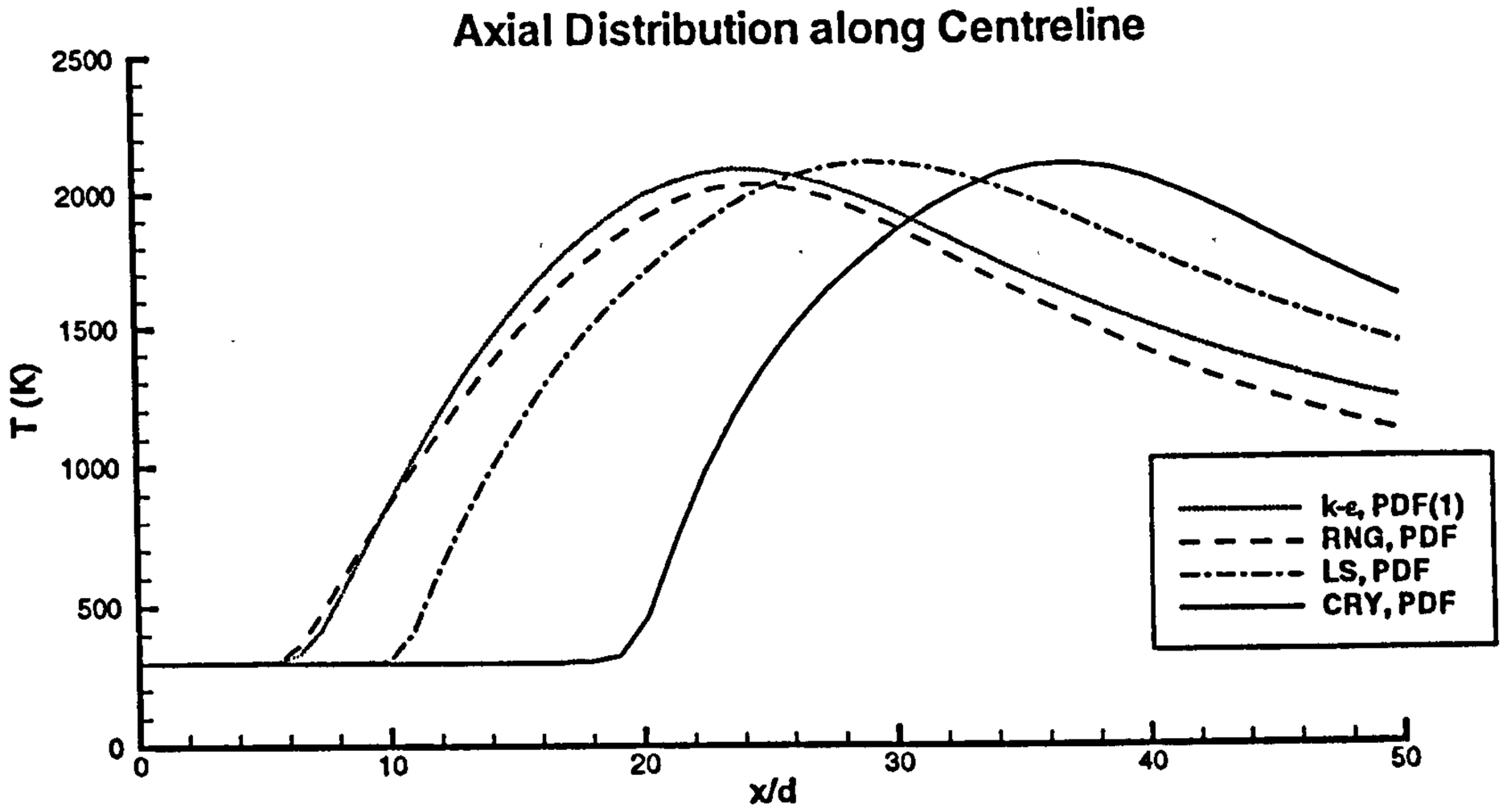

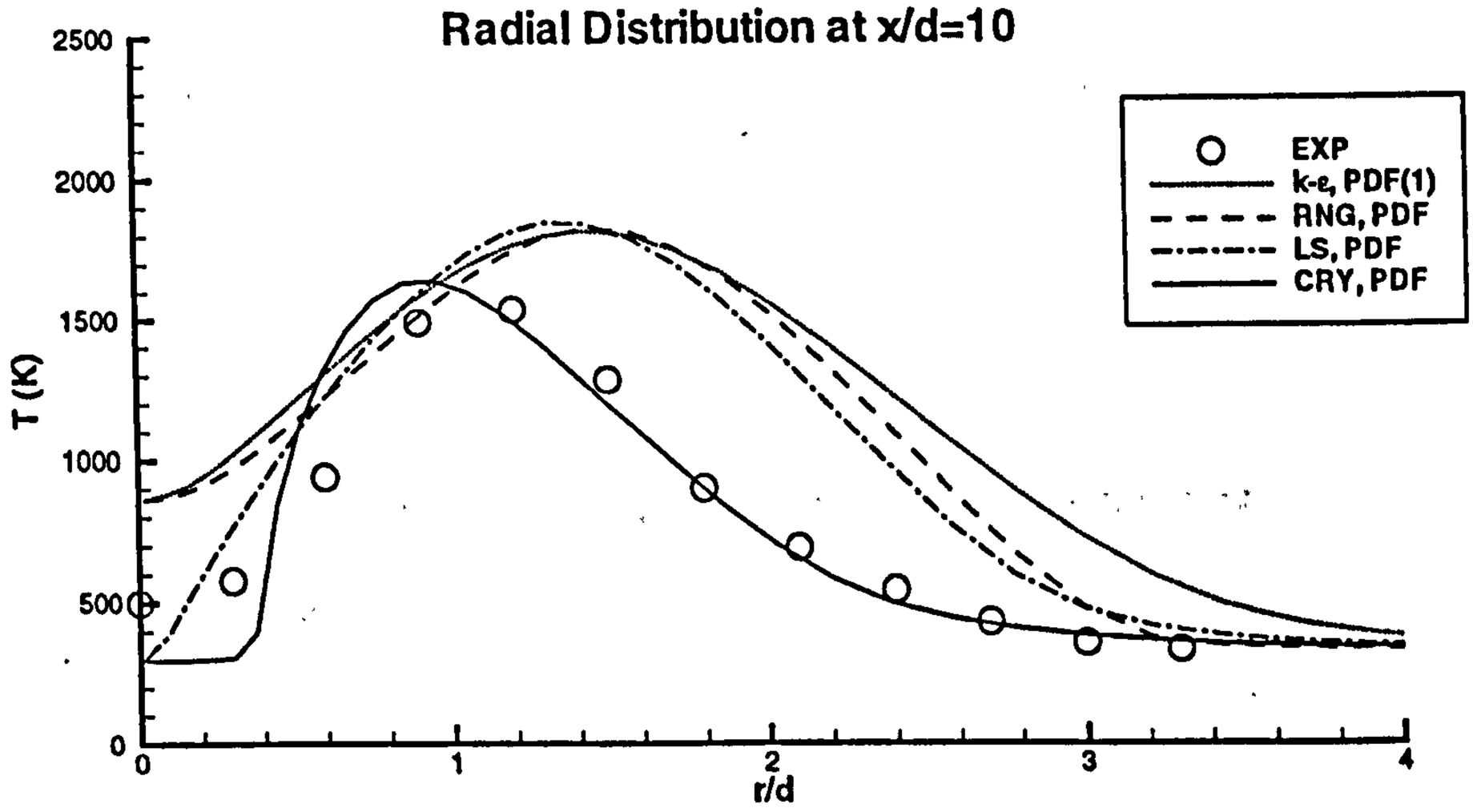

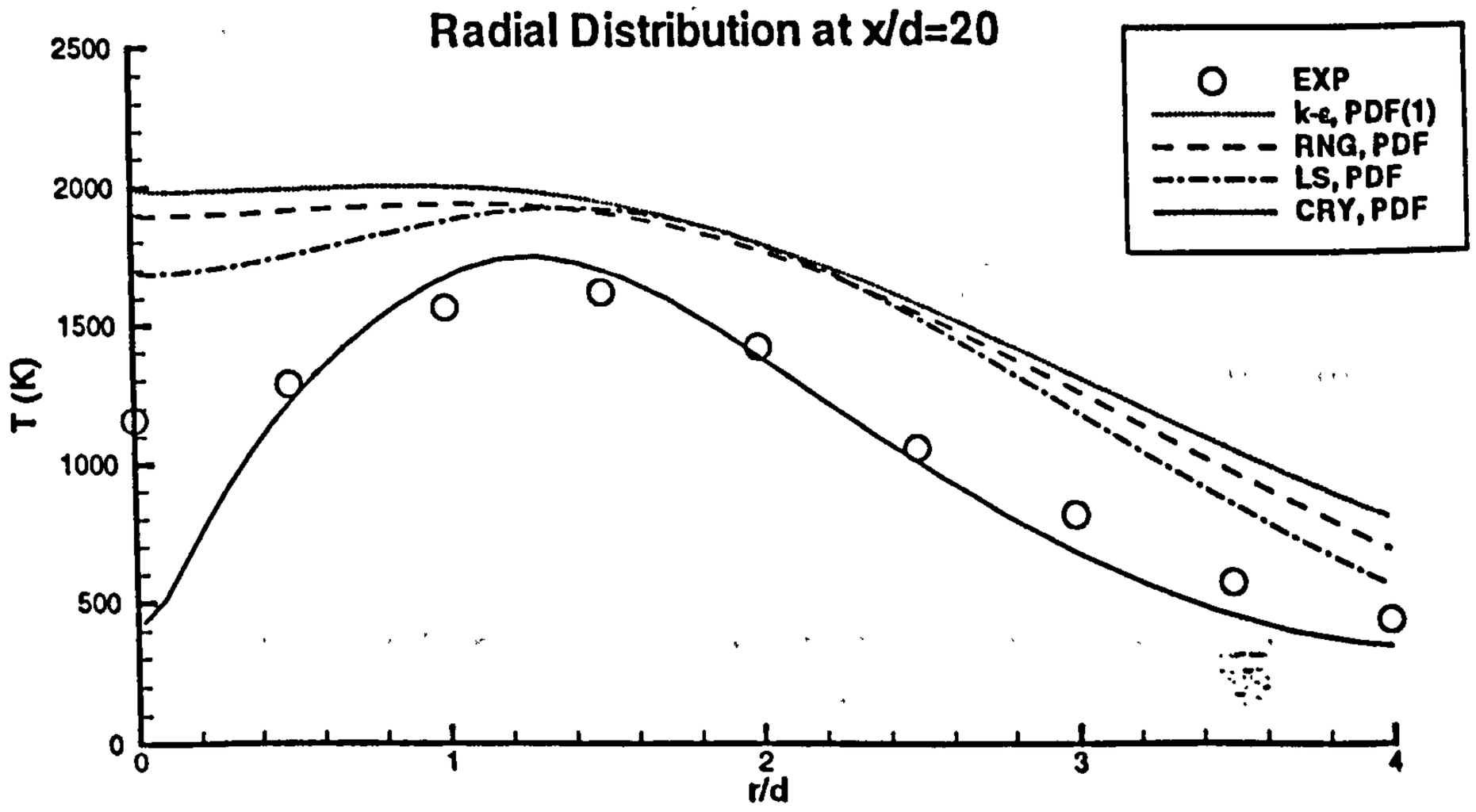

Figure 5.11: Temperature distributions. No experimental data was available for the axial distribution of temperature along the centreline.

(a)

Normalised Stream Function, k-ε model (PDF1)

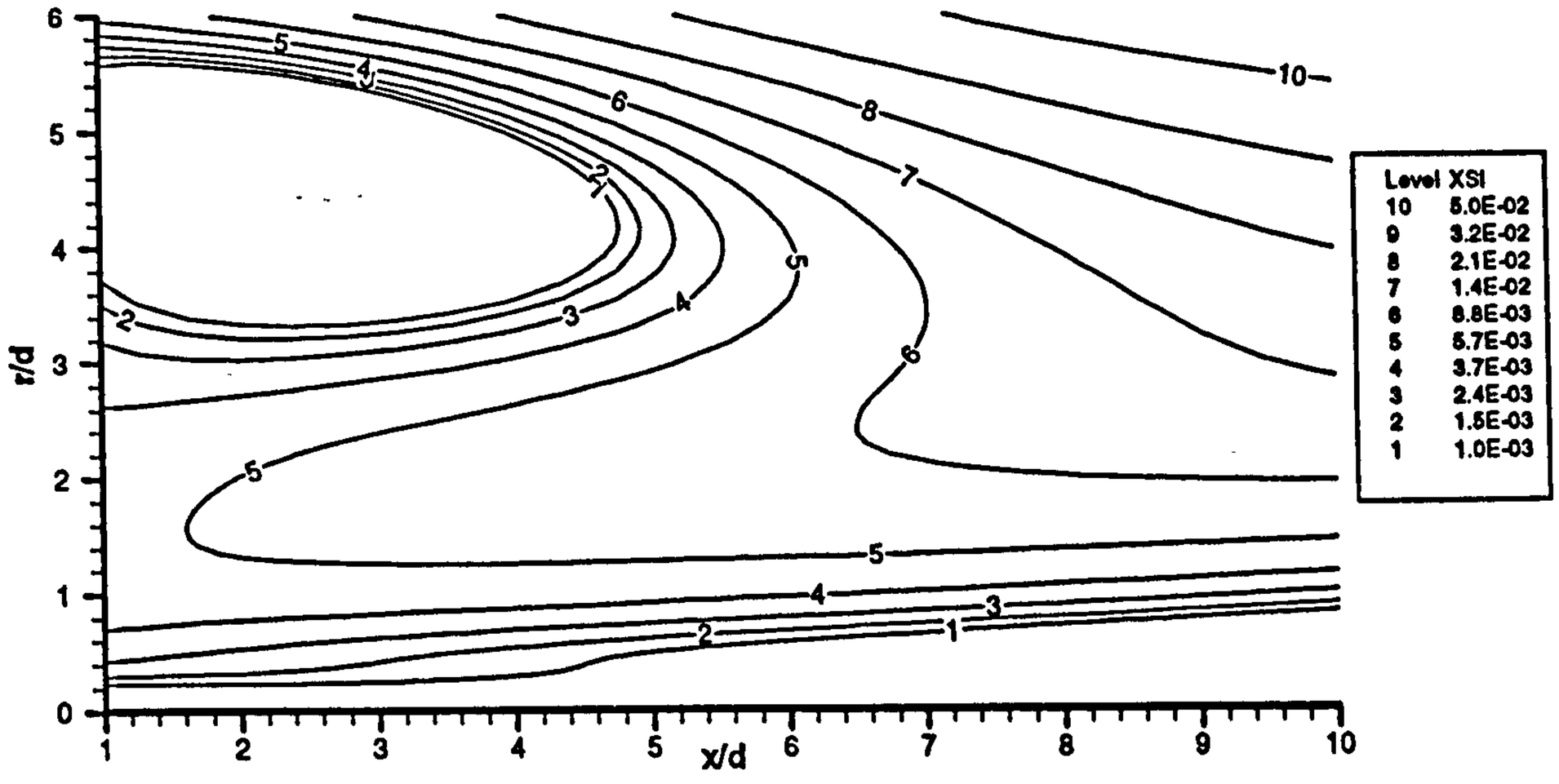

(b)

Normalised Stream Function, RNG model (PDF)

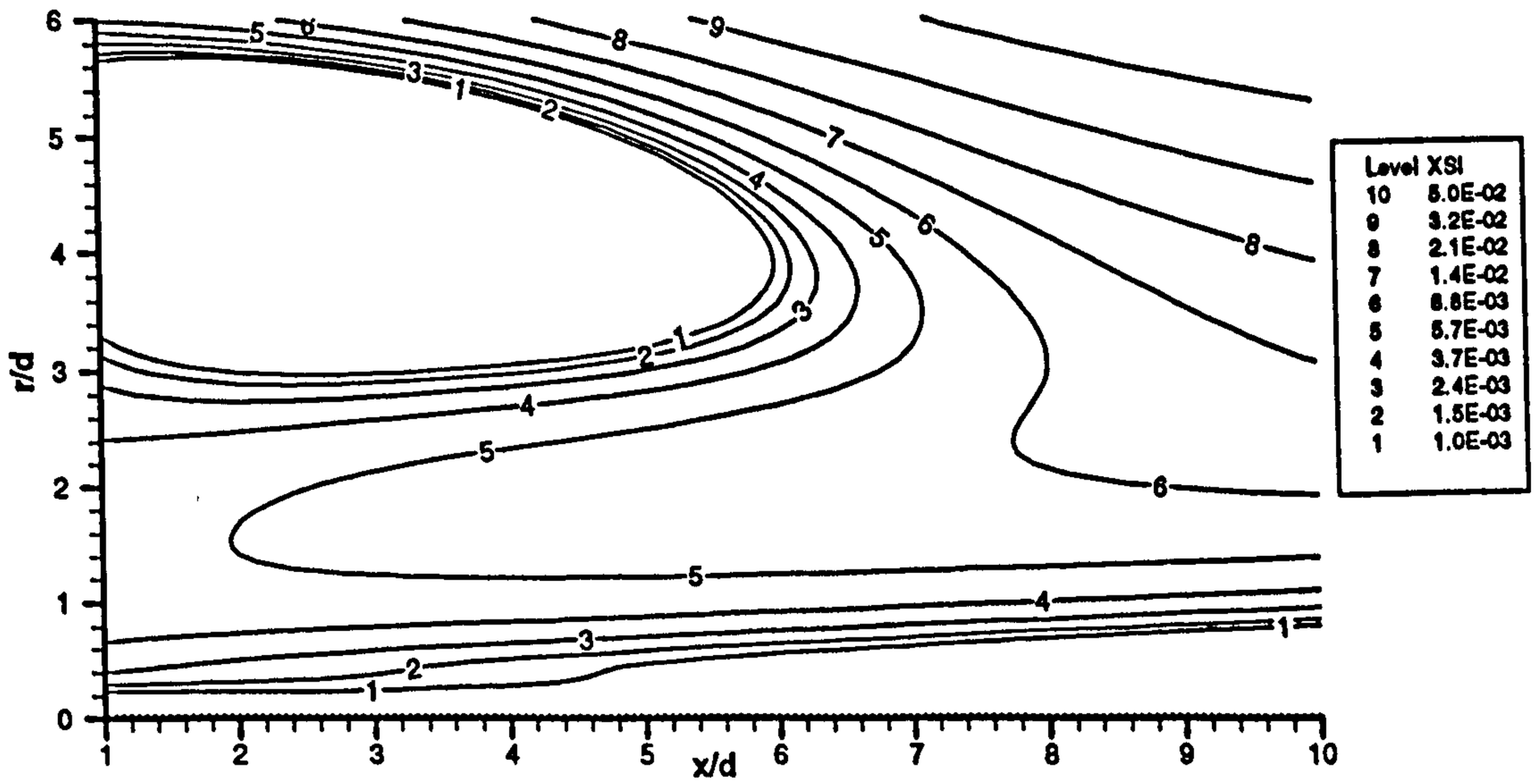

Figure 5.12: Normalised stream function contour plots for the various turbulence models.

(c)

Normalised Stream Function, LS model (PDF)

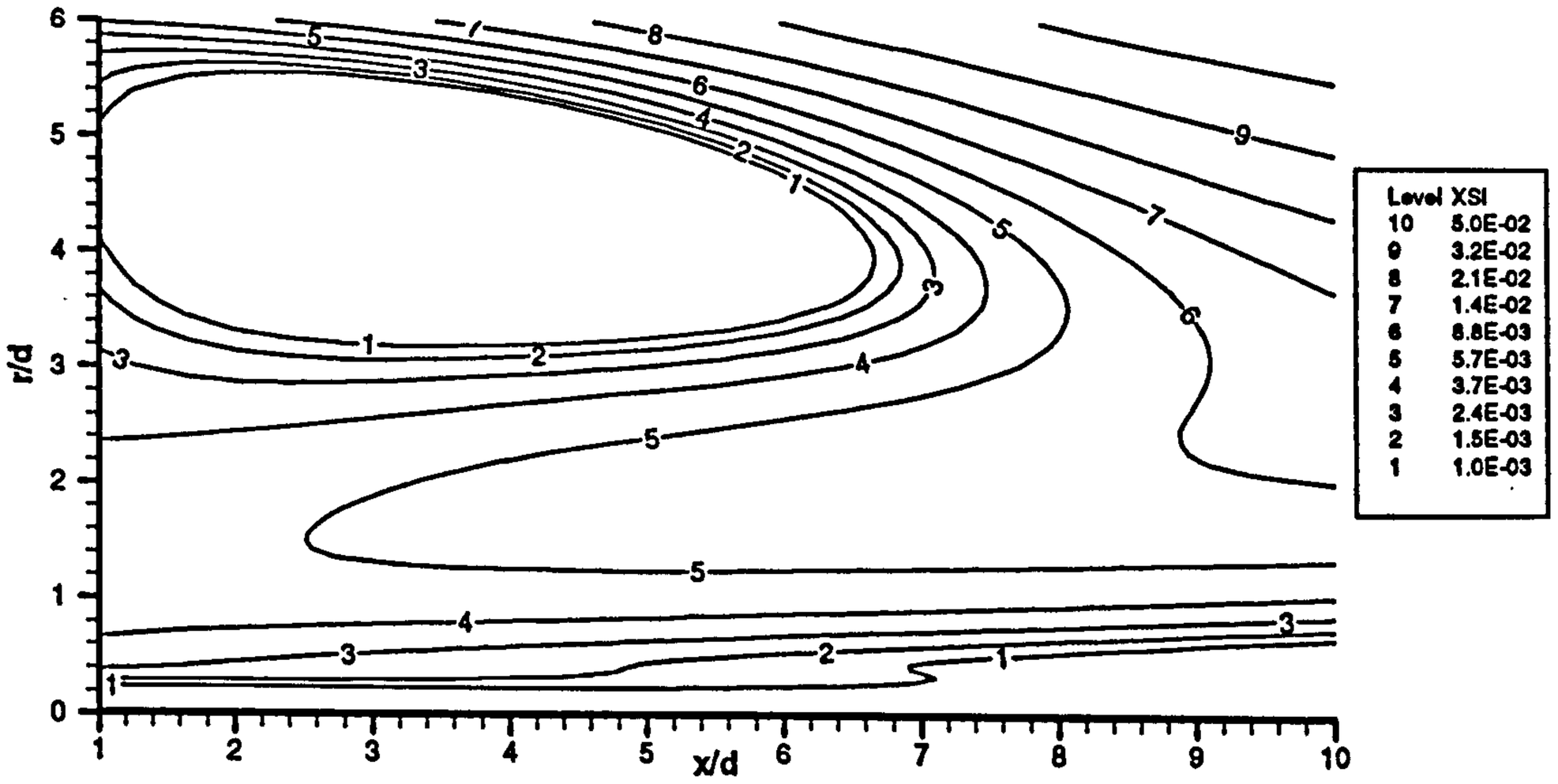

(d)

Normalised Stream Function, CRY model (PDF)

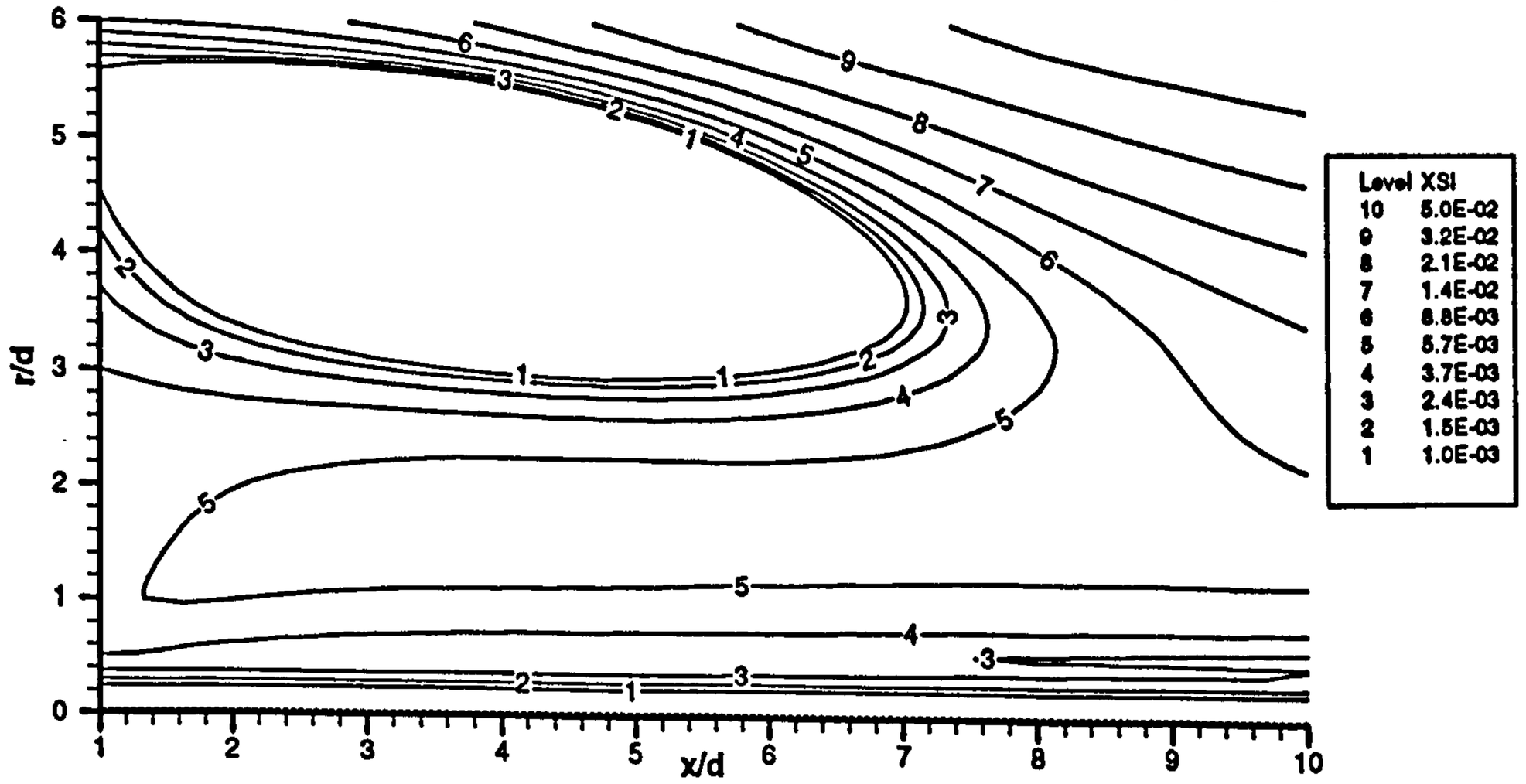

Figure 5.12 - continued.

(a)

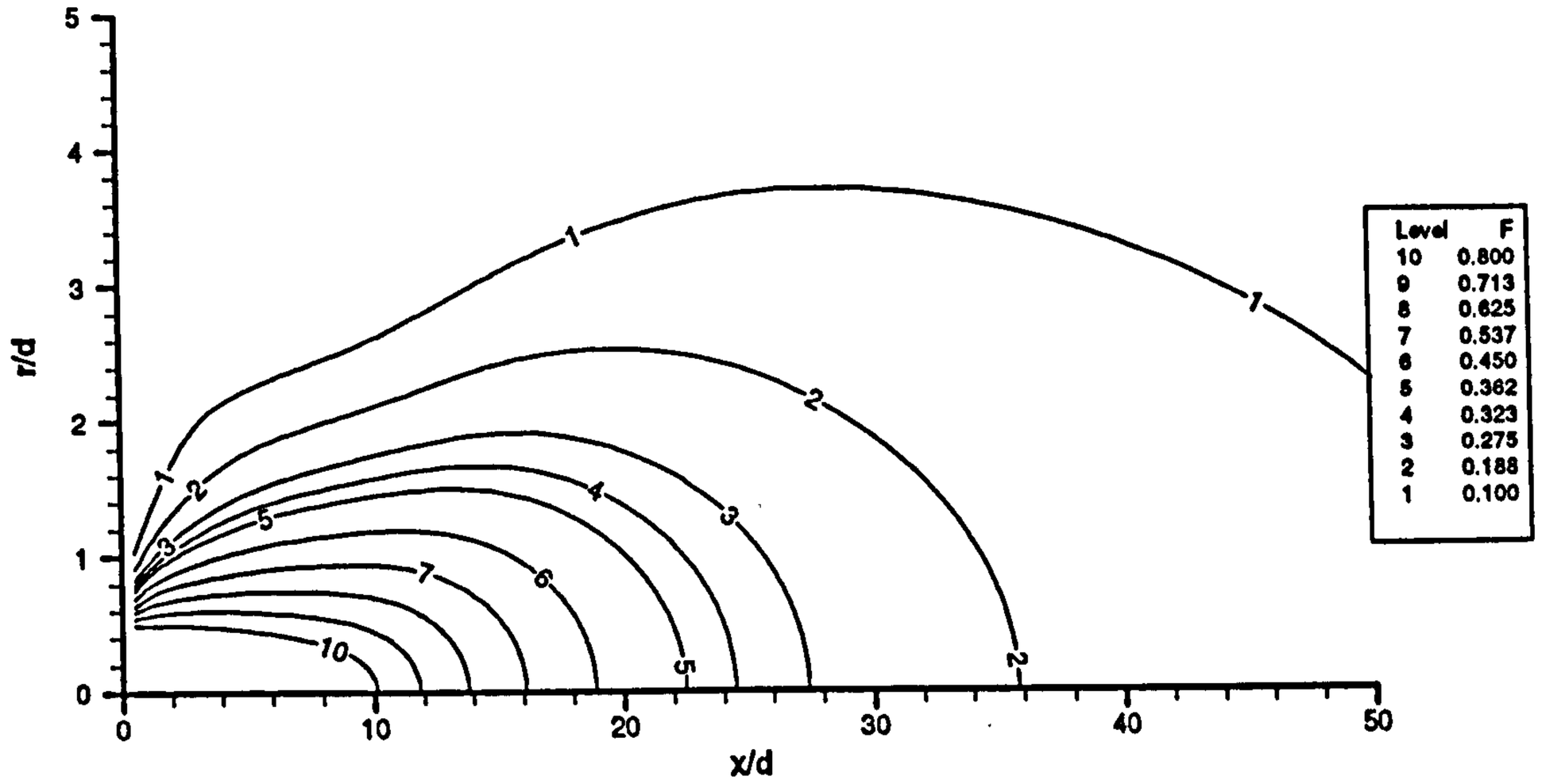

(b)

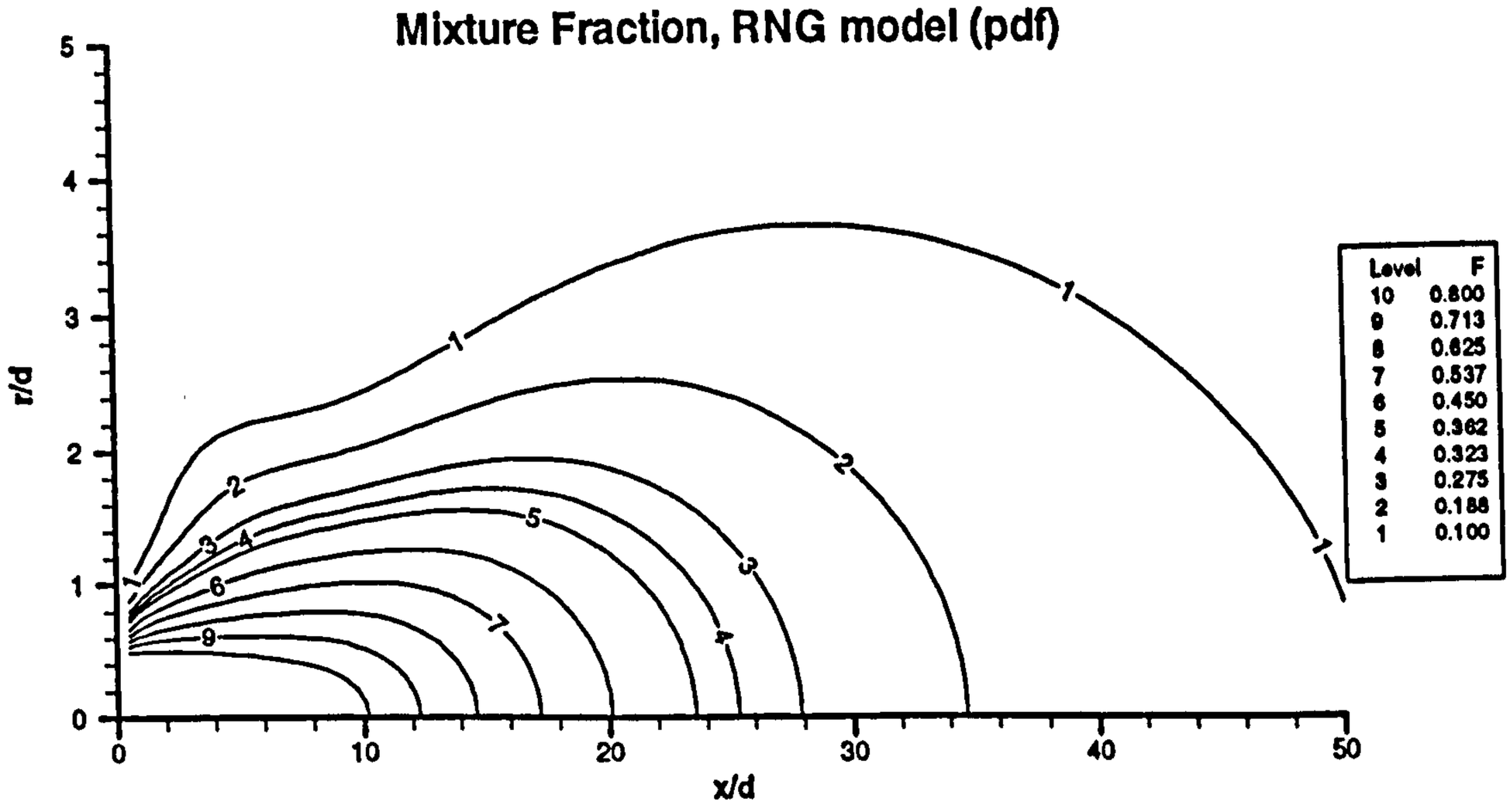

Figure 5.13: Mixture fraction contour plots for the various turbulence models.

(c)

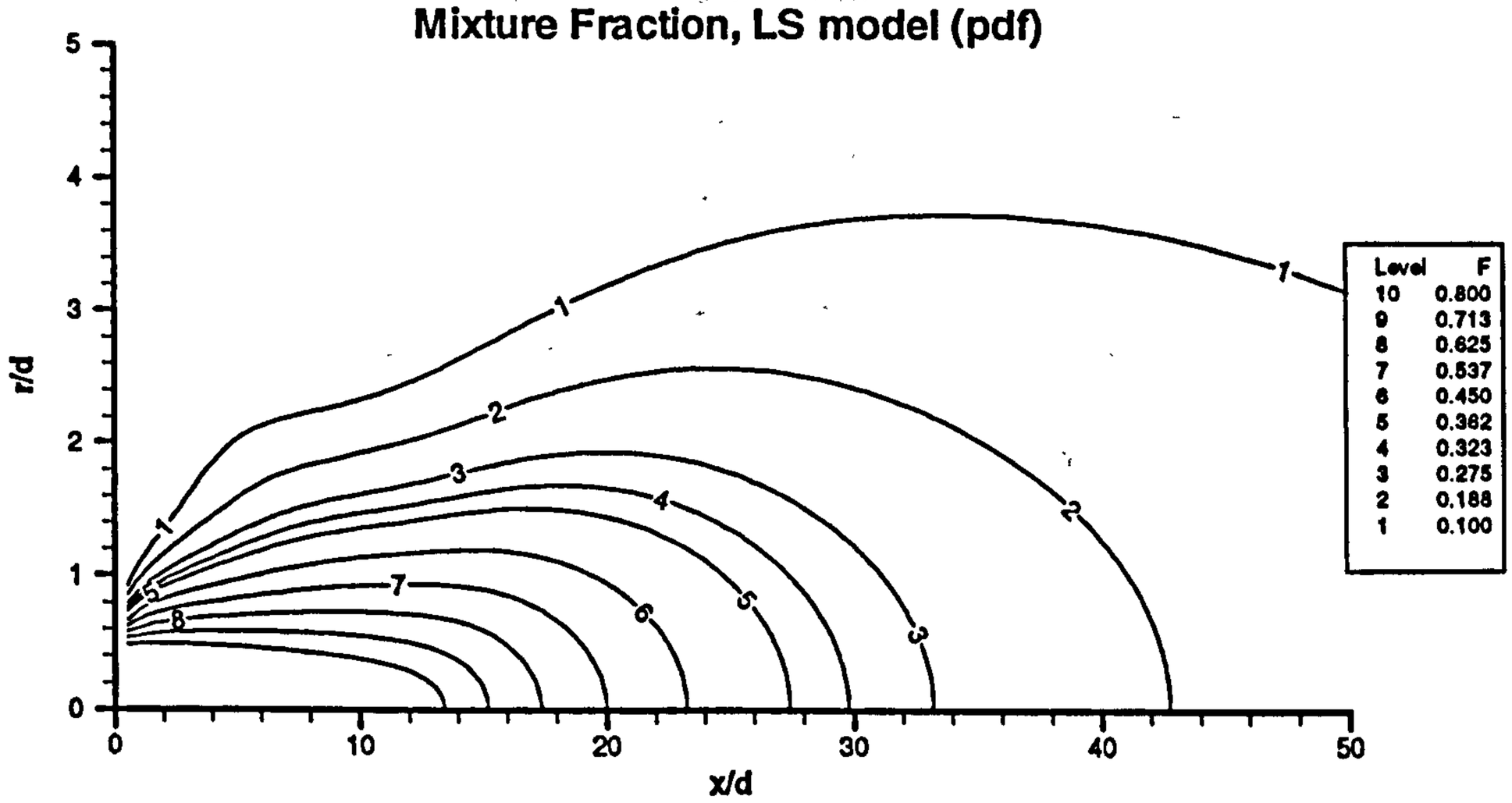

(d)

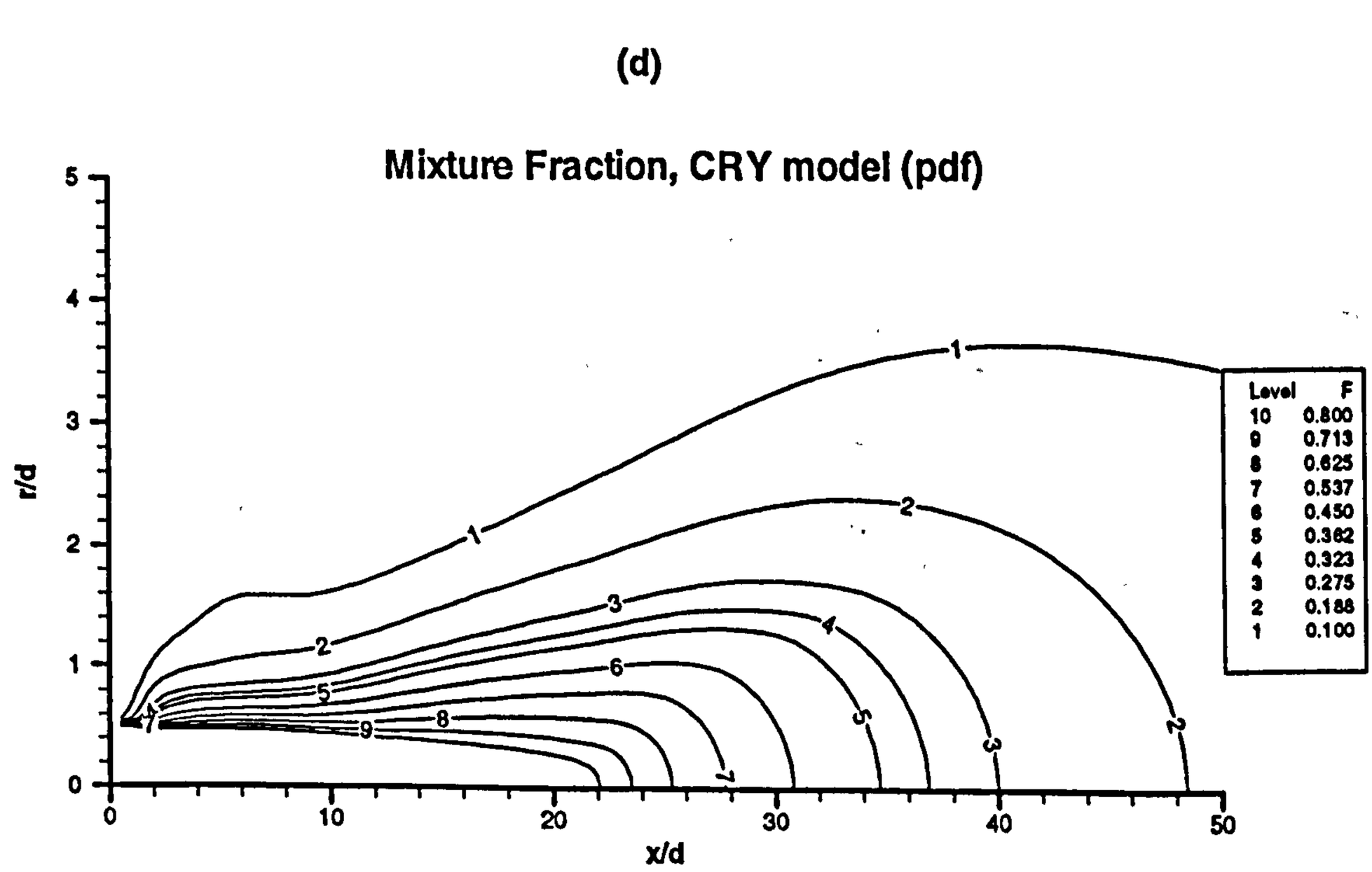

Figure 5.13 - continued.

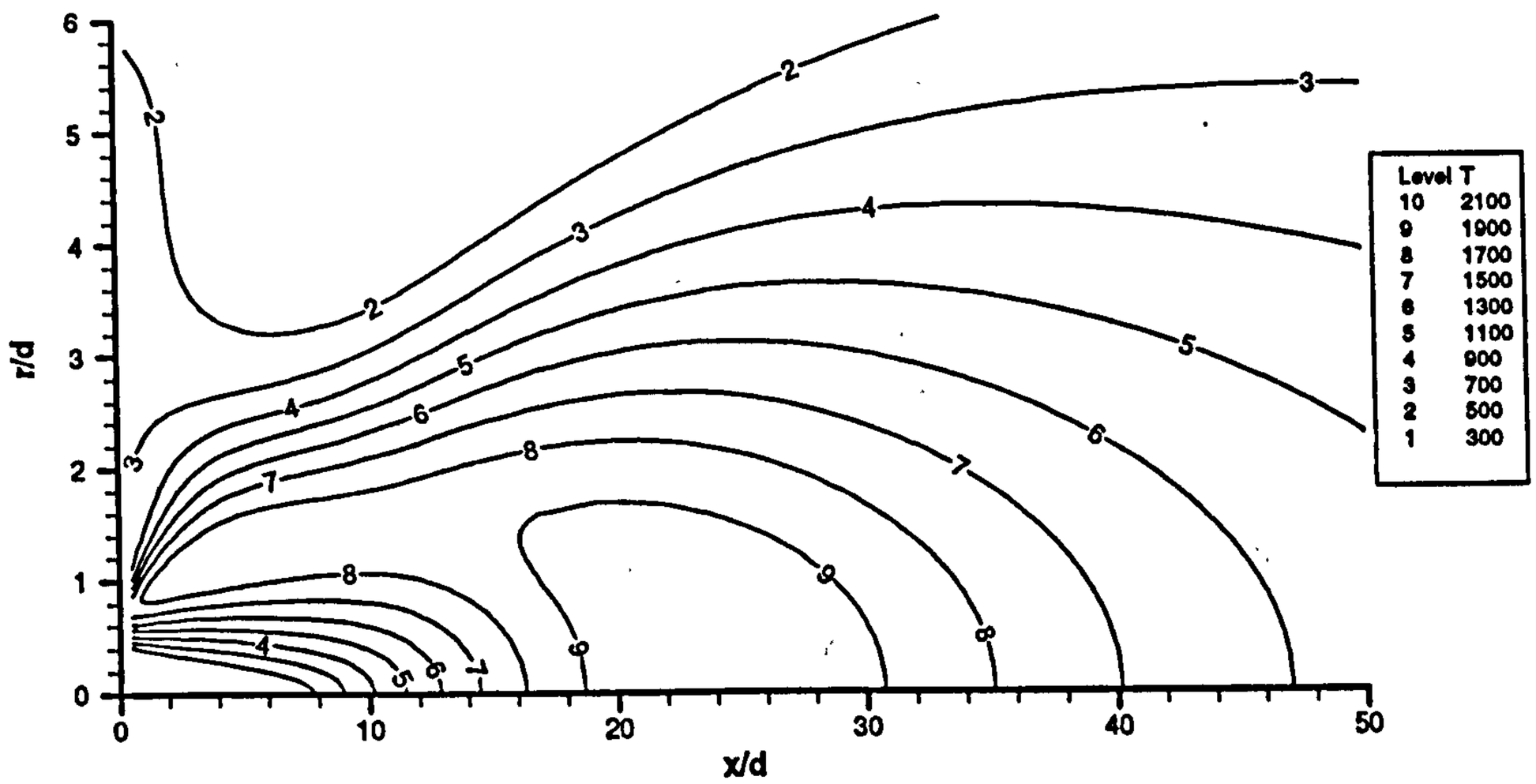

Figure 5.14: Temperature contour plots for the various turbulence models.

(c)

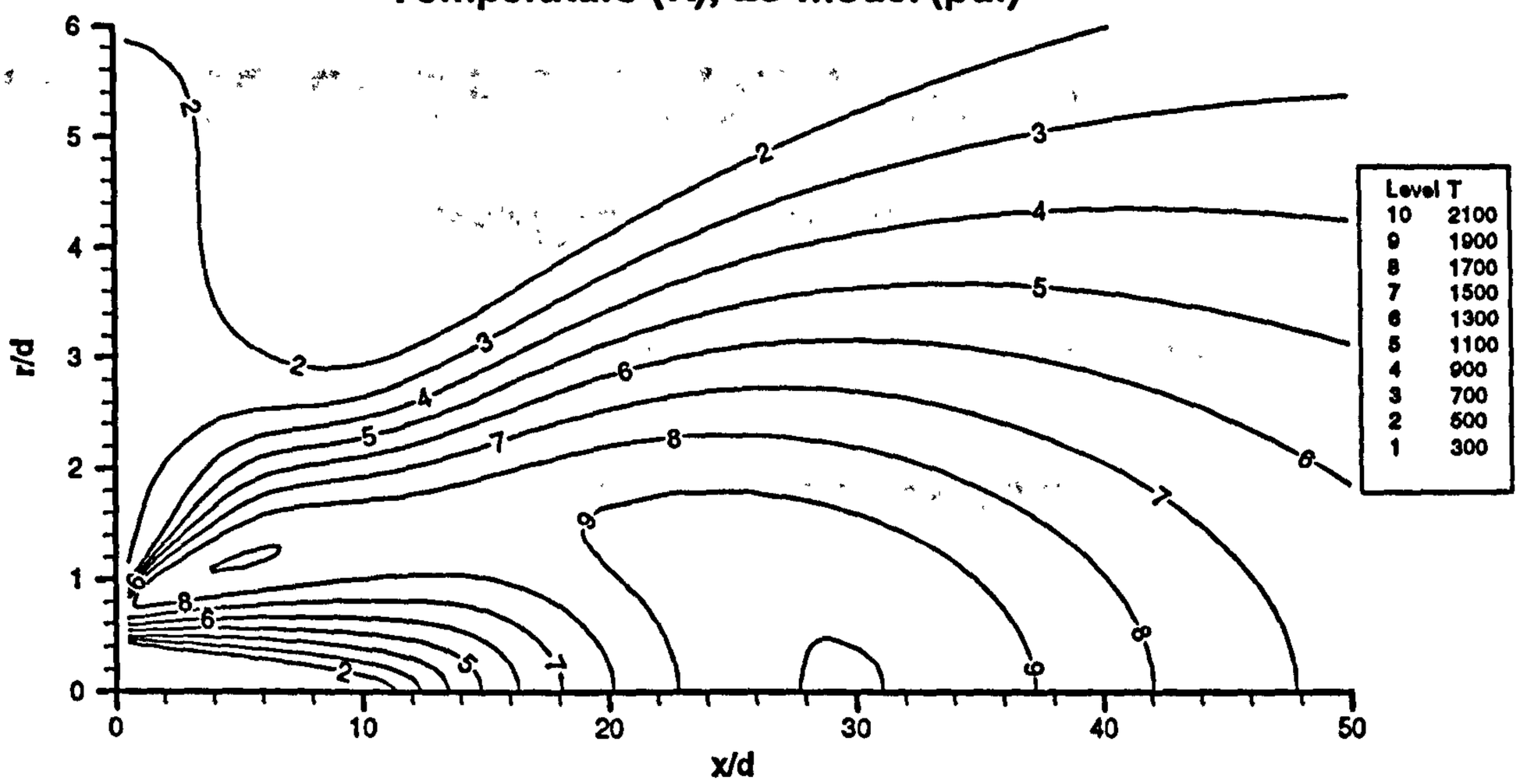

(d)

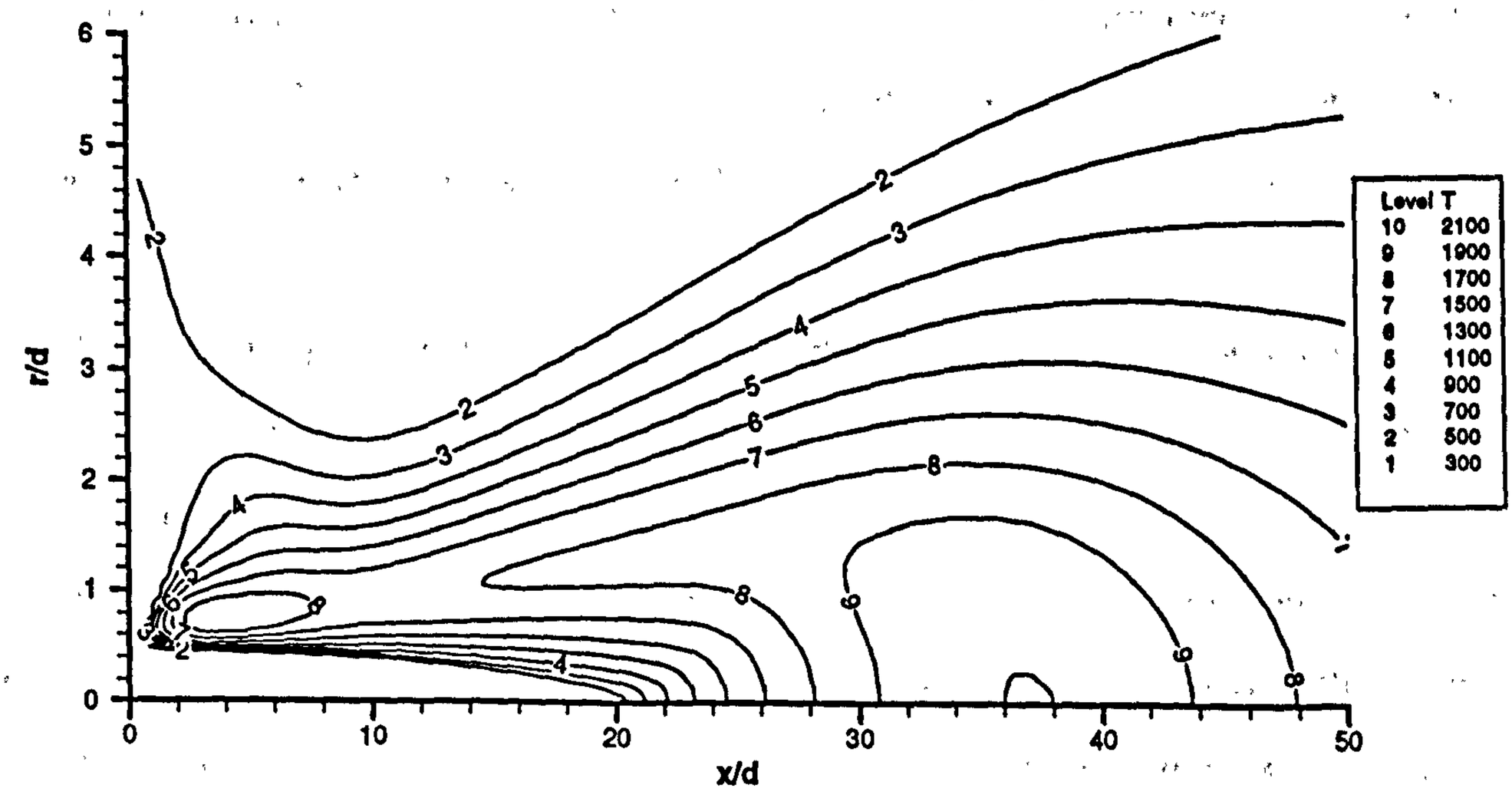

Figure 5.14 - continued.

CHAPTER 6: THE BLUFF-BODY COMBUSTOR: EXPERIMENTAL AND NUMERICAL WORK

The previous chapter confirmed that the flow within bluff-body combustors is indeed complex and revealed that the accuracy of combustion predictions is a strong function of the computed flow-field. The choice of turbulence model was seen to have a significant impact, and the nonlinear model resulted in improved predictions for mixture fraction and temperature. Thorough validation of the cubic turbulence model, however, requires comparison with detailed experimental velocity distributions.

Throughout all the simulations conducted so far, the cubic turbulence model has proven to be somewhat numerically unstable. Confinement of the flame is desirable for the simple reason that it permits wall boundary conditions to be applied rather than pressure boundary conditions, which were reported to lead to convergence difficulties (Jones, 1998, and Hossain, 1998). Modelling considerations aside, this type of configuration (as opposed to the unconfined variety) was reported as being a more realistic simulation of industrial combustors and is a future experimental objective of the TNF Workshops (1st TNF Workshop, 1996). Thus detailed, experimental flowfield data for a confined, bluff-body burner was sought for the purpose of validating the cubic turbulence model.

An extensive search of the public domain revealed an absence of the required experimental data. In light of this, a confined, bluff-body combustor was built for use with non-intrusive, optical measurement techniques. The aim of this chapter is to compare numerical and experimental results for this combustor.

The present chapter begins with a literature survey regarding available sets of experimental data for the geometry in question. Once the need for experimental flow-field data has been established, the major aspects of the design procedure are considered and the exact geometry is specified. The choice of measurement technique is then justified, after which the method of Particle Image Velocimetry is introduced. Subsequently, the experimental procedure is described, including the setup, the procedure and the results and errors. Finally, the CFD simulations are presented and the performance of the cubic turbulence model is compared against the experimental data and other turbulence models. The main findings of the chapter are then summarised.

6.1 SURVEY OF EXPERIMENTAL DATA

A review of the literature shows that the emphasis of most experimental work involving bluff-body burners, is placed on results for the validation of combustion models. For instance, Masri et al (1992, 1998) and various other groups pooling their results under the TNF Workshop scheme, report extensive distributions for temperature, mixture fraction and various species concentrations. Detailed optical measurements of velocity and turbulence fields have been reported by Schefer et al (1987, 1994) as well as by the research team at Sydney University; however, these are for unconfined flames only. A noteworthy conclusion of the 1998 TNF Workshop (Masri, 1998) was that more flowfield data was required for reacting and non-reacting, bluff-body stabilised flows. In their study of confinement effects on burners, Schefer et al (1996) noted that Elliman et al (1978) had obtained velocity measurements for a confined burner using pitot tubes; however, this intrusive method was believed to interfere significantly with the sensitive flow field. Roquemore et al (1980) utilised laser techniques to quantify the flow field, but the blockage ratio was so low (0.22) that confinement had very little effect. Schefer et al (1996) did investigate confined, bluff-body stabilised flames, but

no detailed velocity distributions were recorded (Schefer, 1997). An exhaustive search of the public domain, including contacting other key workers in this field (Barlow, 1997, Geiss, 1997, Masri, 1997, Meier, 1997), resulted in the finding that no experimental velocity measurements were available for confined, higher blockage-ratio, bluff-body combustors.

6.2 DESIGN OF THE EXPERIMENT

The present section highlights the main features of the design process. Since the main purpose of the experiment is to provide results with which predictions can be compared, the rig is designed with the following modelling requirements in mind.

6.2.1 Modelling Requirements

Design of any experiment should proceed in a manner which affords the most control over the experimental environment. In order for the combusting flow to be simulated with the TEACH code, the reacting flow must be steady and axisymmetric. The flow should be free of swirl (the current investigation is concerned with the bluff-body induced vortices), but simple modifications should allow for swirl generation in future studies. Since no radiation models are employed, the flow should also be as soot-free as possible. Promoting adiabatic conditions further simplifies the computational task because a separate transport equation for enthalpy need not be solved (see equation 2.63).

Correct boundary conditions are crucial to successful simulations, otherwise the results can be adversely affected. Ideally, velocity and turbulence energy measurements would be available at the inlet plane, which could then be employed as inlet conditions in the simulation. To this effect, the inlet plane should be optically accessible. Realistically speaking, however, it is often difficult to obtain accurate measurements at the boundaries of the flow-field. Furthermore, the fuel jet is not seeded (seeding is required for optical velocity-measurement techniques), meaning that no measurements can be made at the fuel inlet. The most feasible option is to ensure that the fuel and air

streams are fully-developed at the inlet. Reasonably accurate inlet profiles can then be obtained from simulations of developing pipe and annulus flow. As far as exit boundary conditions are concerned, the exhaust tube should be long enough such that the flow becomes redeveloped at the outlet, and to prevent external flows from affecting the test area.

6.2.2 Principal Design Considerations

The key feature of the rig is optical access to the recirculation region; thus the confining walls near the bluff body must be transparent. The following criteria were considered:

- Test section length: Schefer et al (1996) noted that the recirculating zone length was typically equal to the diameter of the bluff body, and that confinement could extend this to approximately three such diameters. Optical access was thus required for at least three bluff-body diameters downstream of the inlet, but measurements would be extrememly useful further away too, such that a significant portion of the flame can be investigated should it be of the fuel-dominant type (which extends much further downstream than an air-dominated flame).
- Confinement material: Due to the exothermic nature of the flow, perspex is obviously not a candidate for the enclosing structure. Fused silica is the only alternative; it is temperature resistant and its refractive index does not vary significantly with temperature. Strength is not an issue in the present case since combustion occurs at constant, ambient pressure. A 350mm long, drawn, quartz tube seemed to meet these requirements, but unfortunately the drawing process resulted in the formation of striations which cause undesired interference patterns upon illumination with coherent light. The only remaining option was a hand-polished, 'Suprasil' fused-silica cylinder made to order.
- Cylinder dimensions: The greatest available length of a 'Suprasil' cylinder was 150mm; the bore (84.45mm) and wall thickness (12.775mm) were selected so as to provide a degree of interchangeability (in the event of breakage) with a similar, shorter cylinder already in use in the lab. The rather thick wall raised concerns that any optical diagnostics measurements would be distorted as the wall is approached. However, Thompson et al (1984) reported that acceptable velocity results could be

obtained out to a normalised tube radius of r/R=0.83, provided a correction lens was adopted. Design of such a lens, though, was an additional, undesired complexity.

Once the dimensions of the confining cylinder had been selected, it was possible to proceed with a more precise specification of the bluff-body geometry and also with the determination of the overall main dimensions of the rig.

- Bluff body: The simplest method of creating the bluff-body geometry was by utilising pipes arranged in a concentric manner. The diameters of these tubes had to be such that the bluff-body radius was at least ten times that of the fuel pipe. Furthermore, a fairly narrow air jet was desired such that the blockage ratio is not too low (else confinement has little effect). Due to restrictions on commercially available pipe diameters, meeting these requirements led to the design incorporating a pipe expansion at the inlet plane.

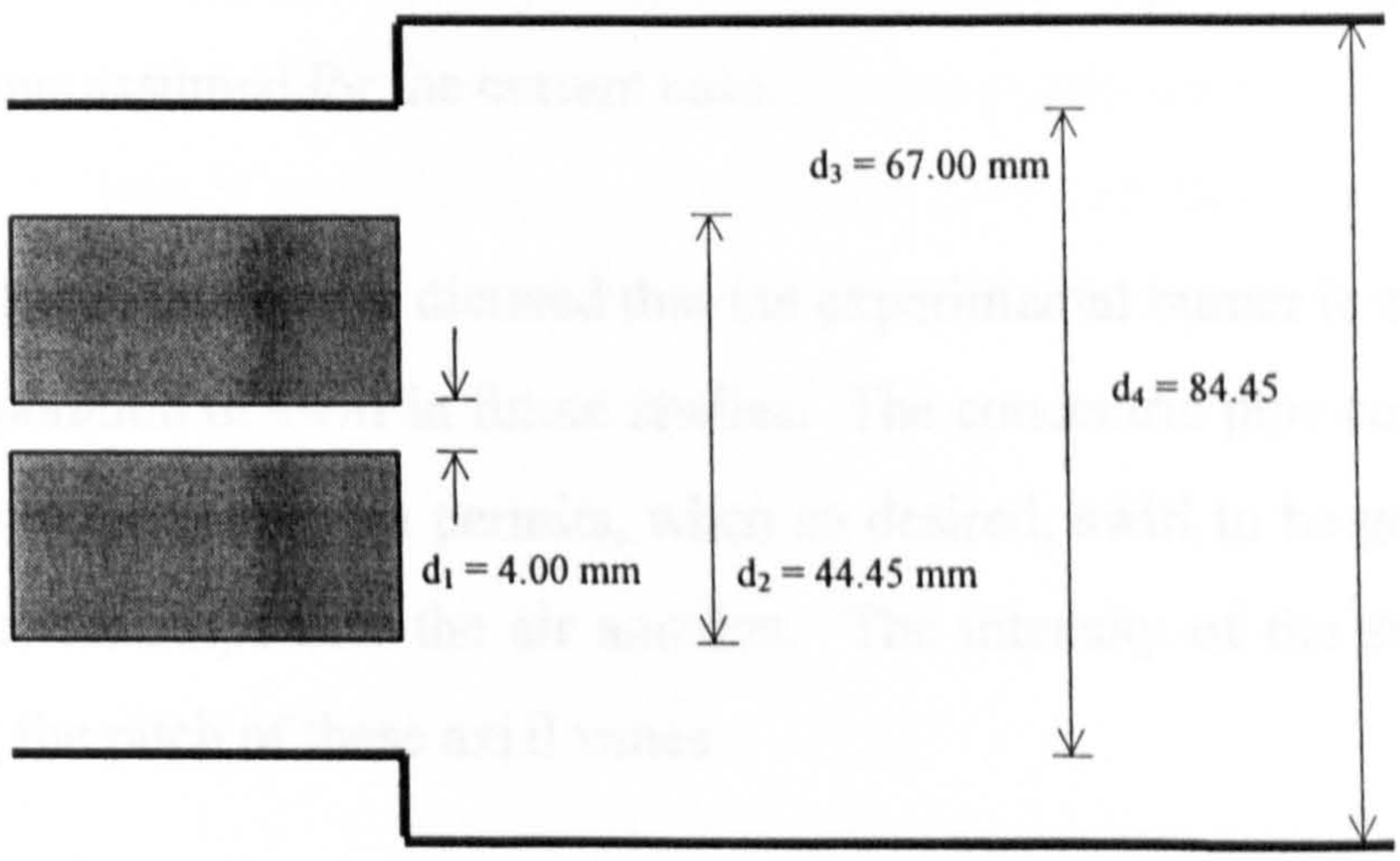

Figure 6.1: Main dimensions of the bluff-body combustor.

Schefer et al (1996) noted that this was not uncharacteristic of industrial burners. This design has a small advantage when optical diagnostic tools are utilised; since the cylinder distorts measurements near the walls, moving the walls further from the core flow will result in less potential distortion at the outer bluff-body diameter. The exact dimensions of the setup are shown in figure 6.1; the geometry is characterised by an intermediate blockage ratio BR=0.44.

- Inlet section: In order for the inlet fuel and air flows to approach the fully-developed state, the minimum development lengths needed to be found. For simple pipe flows,

this can safely be taken as 100 fuel pipe diameters (note that Durst et al, 1993, used only 40 diameters). No general rule of thumb was found concerning annulus development lengths. Therefore, other experimental burners were used as a guide. That investigated by Roquemore et al (1980) featured an inlet development length of 3.1 annulus outer diameters ($3.1d_3$ with reference to figure 6.1), whilst a burner investigated by Gaz de France (1992) employed 8 such diameters. Since neither flow was specifically quoted as being fully developed, the inlet length for the current combustor was selected as approximately $12d_3$, which ensures that both fuel and annulus-air flows approach the fully-developed state at the inlet.

- Exhaust: Even fewer guidelines existed for determining exit lengths. In the first instance, recovery lengths in pipe expansions were drawn upon. Approximately 50 step heights are required (see Chapter 3), corresponding to 440 mm. Sheen et al (1997) utilised 9.2 confining diameters ($9.2d_4$ with reference to figure 6.1) whilst the Gaz de France burner only featured an exhaust section $3d_4$ long. A length of $9.0d_4$ (700 mm) was thus assumed for the current case.

The modelling requirements dictated that the experimental burner is supposed to allow for the incorporation of swirl in future studies. The concentric pipe configuration within the inlet development region permits, when so desired, swirl to be generated by simply inserting helical strips into the air annulus. The intensity of the swirl can be varied by changing the pitch of these axial vanes.

An important aspect of the combustor is the cooling system, which is required for the following reasons.

- Cooling provides greater control over the experimental environment. Without any such provisions in place, the combustor would require long periods of time to achieve steady-state conditions with respect to its surroundings.
- Cooling prevents the burner from expanding; since the expansion coefficient of fused silica is much smaller than that of steel, lack of cooling could easily result in the quartz cylinder breaking.
- Cooling ensures that the bluff-body assembly does not heat up and maintains the inlet fuel and air temperatures at ambient levels (which is one of the simulation assumptions).

- Extraction facilities within the laboratory dictate that the exhaust gases be under 70°C before arriving at the fan.

It was initially thought that the cooling requirements would conflict with the adiabatic assumption for the burner. However, consideration of the system led to the following developments:

- A thin layer of ceramic paste (approximately 1mm thick) was applied to the face of the bluff-body, thereby minimising heat transfer to the base of the burner.
- The air flow rates through the annulus are generally high, which results in the heat of reaction being convected downstream rather than diffusing across to the confining walls. Furthermore, the high air mass flow rate, relative to that of the fuel, results in low bulk temperatures of the exhaust gases. Thus the exit cooling system is mainly a precautionary feature.

To avoid rapid corrosion, the bulk of the rig needed to be manufactured from either stainless steel or aluminium. Most of the burner components were made of stainless steel. Due to weight considerations (the rig was to be mounted on a traversing mechanism), though, aluminium was the material of choice for the exhaust pipe and the associated cooling jacket.

6.2.3 Further Design and Operational Aspects

Consideration of the features discussed in the previous section led to the combustor design illustrated in figure 6.2. The actual burner is shown in the photograph in figure 6.3, and the detailed design drawings are given in Appendix H.

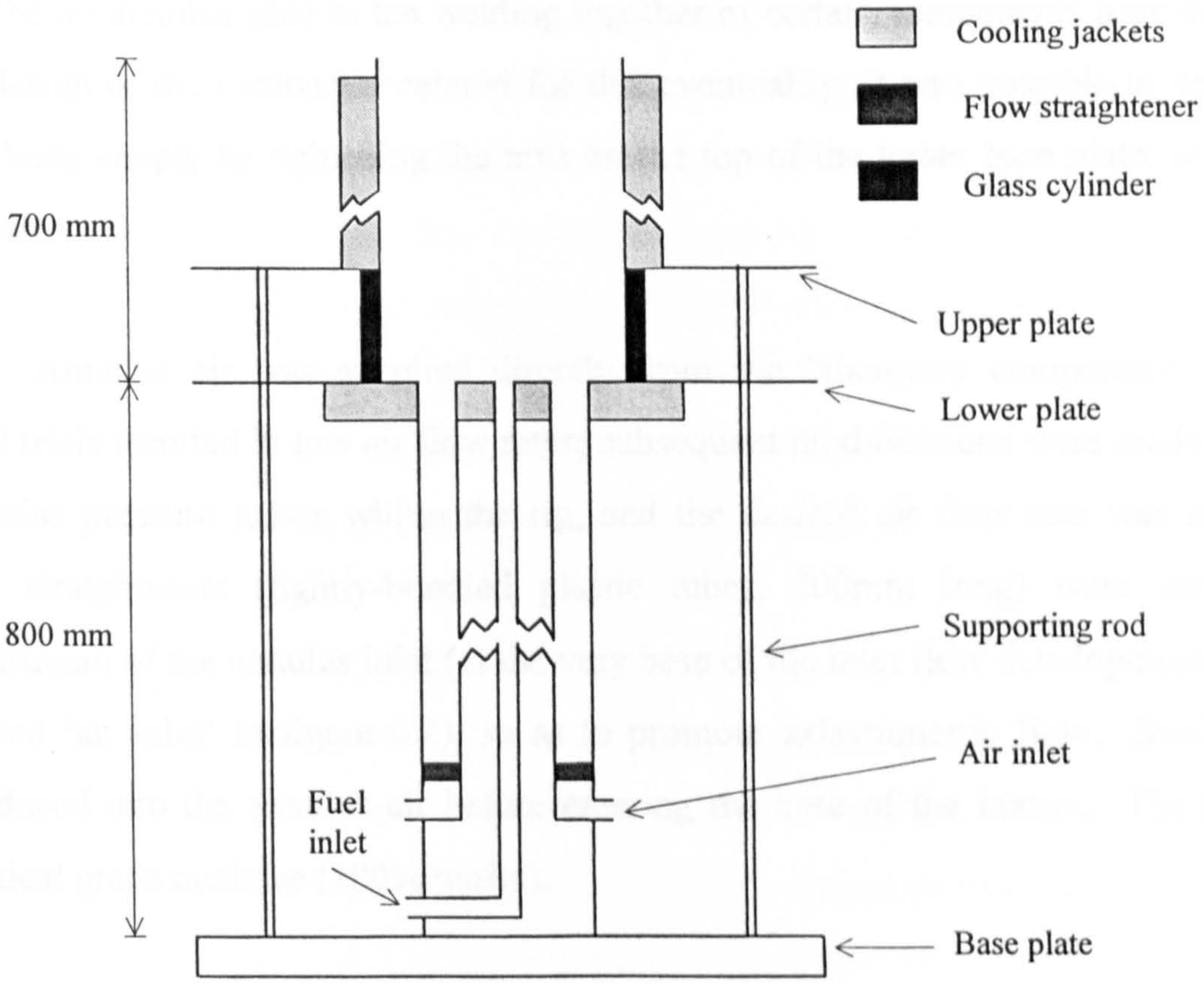

Figure 6.2: Schematic of complete burner.

Lateral supporting rods (threaded) were required such that the glass cylinder does not bear the weight of the exhaust pipe and the associated cooling jacket. The 'Suprasil' cylinder was located by means of shallow, annular grooves machined into both the lower and upper plates. Nuts either side of the plates ensured that a reasonably tight fit was obtained between the glass and the plates; gaskets were employed so as to form a seal and also to prevent direct contact between quartz and steel. An airtight fit was not necessary since the burner operated at atmospheric pressure.

Optical measurement techniques involving flow quantities require tracer particles. Since these particles tend to foul the glass cylinder, thereby impeding optical access, the burner was designed such that the 'Suprasil' cylinder could be easily

removed, cleaned and reinstalled (a procedure which took only ten minutes). For this reason, the upper plate and top water jacket were located and fastened only by the lateral supporting rods.

An initial concern was the effect of the bluff-body not being perfectly concentric with the air annulus (due to the welding together of certain components near the base). The design of the combustor catered for this eventuality; it was possible to centre the bluff body simply by tightening the nuts on the top of the lower base plate, to various degrees.

Annulus air was supplied directly from the laboratory compressed air line. Initial trials resulted in low air flow rates; subsequent modifications were made so as to minimise pressure losses within the rig, and the desired air flow rate was achieved. Flow straighteners (tightly-bundled plastic tubes, 200mm long) were added just downstream of the annulus inlet (at the very base of the inlet flow development section, labelled 'air inlet' in figure 6.2), so as to promote axisymmetric flow. Seeding was introduced into the annulus air before entering the base of the burner. The fuel was technical grade methane (100% purity).

During the initial phases of the design, an internal ignition system was desireable. However, it quickly became apparent that the only non-intrusive ignitor, i.e. one utilising a spark across the bluff-body face, would in fact not work due to the poor conductance of the quartz walls. As a result, the ignition consisted of filling the exhaust tube with a premixed mixture (using a very low air flow rate), igniting it at the exit, and reducing the air flow rate so as to draw the flame back to down to the bluff-body face.

6.3 OPTICAL TECHNIQUES

The relatively small dimensions of the bluff-body signified that any intrusive probes would distort the flow and strongly affect any experimental results. Optical techniques are ideal for this type flow since they do not disturb the highly-sensitive flow-field. The design of the burner permitted the application of numerous optical techniques (eg LDA, PIV, CARS, LIF) to investigate both the flow-field and scalars (i.e. temperatures, species concentrations) of the turbulent, non-premixed flame. Time constraints, however, made it clear that optical methods could only be used to obtain flowfield data. Particle image velocimetry (PIV) was the most suitable technique to image the flow field because:

- Information is provided on the whole field.
- Turbulence quantities can be obtained with suitable data processing.

Particle image velocimetry is a technique which makes use of the fact that if tracer particles are introduced in a flow and are illuminated in a stroboscopic manner, then, provided their respective positions are recorded and the time between light pulses is known, instantaneous velocities can be calculated. Although this principle is simple and certainly not new, PIV has the advantage that it can be applied to high-speed, turbulent flows. This versatility is entirely due to the fact that lasers are used to illuminate the tracking particles; higher light intensities signify that smaller particles can be used whilst still returning a decent signal. The tracer particles are small enough to follow the intricacies of the flow without affecting it. A good overview of this technique is given by Grant (1997). The subject is also treated thoroughly be Reeves (1995), who notes that the successful application of PIV to complex flows requires a judicious compromise between many different, often conflicting, experimental parameters. The purpose of the following section is to highlight the most important of these issues and to demonstrate that not all of them need to be specifically addressed if certain measures are taken.

The main components comprising a typical PIV system are shown in figure 6.4. Using suitable optics, laser light is formed into a sheet which illuminates a plane within the seeded flow. The recording medium, typically a photographic or a CCD (charge

coupled device) camera, is placed such that its optical axis is perpendicular to the light sheet; this ensures that the laser sheet and the focal plane of the camera lens are parallel. Failure to do so results in an image of varying sharpness which causes velocity measurement errors. Sharp images are obtained by ensuring that the illuminated particles are within the depth of field of the camera lens and are also coplanar. Although formulae can be used to calculate the required depth of field, Grant (1997) notes that the use of a thin sheet of light which coincides with the in-focus plane is sufficient to guarantee in-focus images.

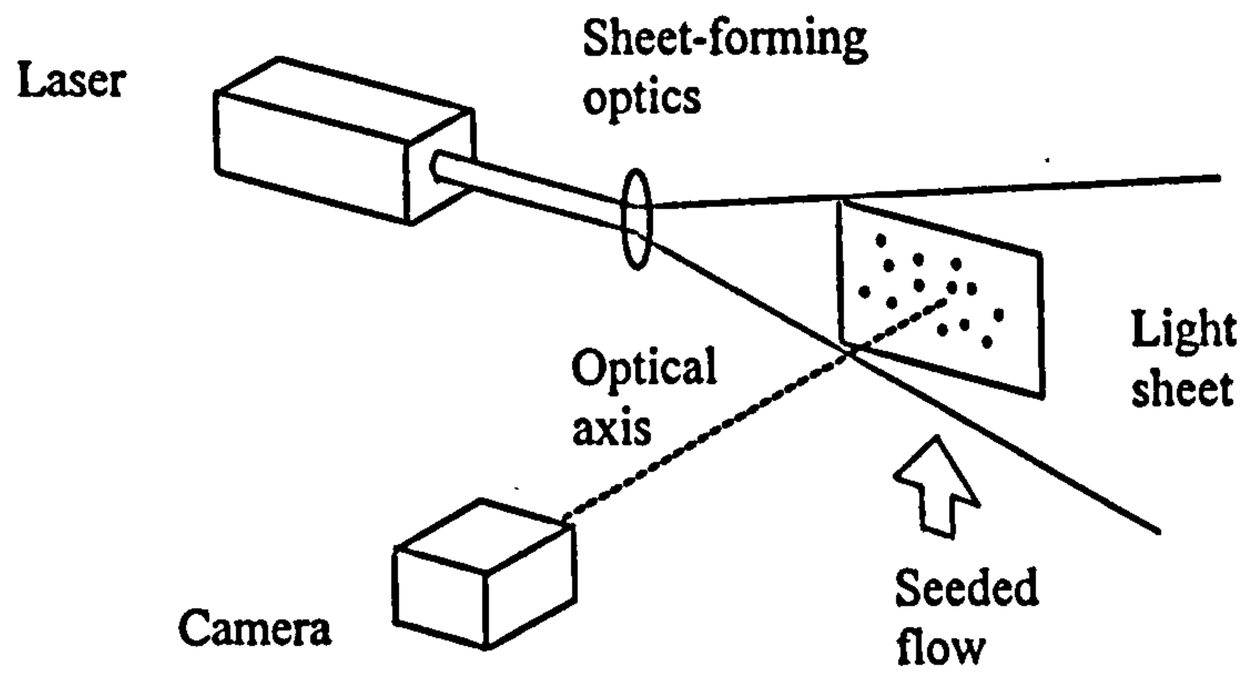

Figure 6.4: Principle of PIV.

Difficulties can arise when the seeded flow is enclosed by curved surfaces. Refractive effects (due to the incident light not being normal to the surface) can prevent the light sheet in the flow from being coplanar with the external sheet, thereby resulting in positioning errors. Fortunately, corrective optics are not required for 2-D, axisymmetric flows because only a single plane is of interest, namely that passing through the centreline. No optical aberration occurs because the light sheet is perpendicular to the quartz cylinder surrounding the flame.

Vertical light sheets passing through a cylinder result in stray illumination due to multiple reflections from the walls; the problem is exacerbated by thick confining walls. Flare, as it is known, introduces significant experimental errors (Reeves, 1997). This phenomenon is minimised in the current investigation by simply blackening

approximately one quarter of the internal quartz cylinder wall. The cylinder was then positioned such that the far side of the light sheet impinged upon the darkened surface.

A standard aspect of the PIV technique involves discretising the inspected flowfield into numerous cells, called interrogation volumes, for each of which a representative velocity is obtained. This is found by simply averaging the velocities calculated for all the particle image pairs within the interrogation volume. Since the range of velocities in each cell can be considerable, it is likely that the image pairs for higher velocities are incomplete due to the particles falling outside the illuminated zone during the second exposure. In other words, the largest velocities may not be represented and the average cell velocity can be biased towards lower values. Velocity bias, as this phenomenon is known, is a function of several criteria which are listed below. Grant (1997) quantifies these parameters whilst further guidelines and references are provided by Reeves (1995).

- A high image density (10-20 image pairs per interrogation cell) should be selected so as to optimise the signal/noise ratio. This is a direct function of seeding density.
- The time delay between successive light sheets should not be so large that non-pairing occurs as a result of the particle having moved outside the confines of the interrogation volume.
- Particle movement normal to the light sheet should be avoided since this also results in non-pairing. Reeves (1997) found that in predominantly 2-D flows, the errors associated with out-of-plane motion can be neglected.
- Velocity gradients imply velocity variations within an interrogation region. Smaller cells thus reduce the range of velocities.

Since the turbulent diffusion flame in the current investigation is axisymmetric and contains no swirl, the flow is essentially 2-D and thus out-of-plane motion is not expected to be of concern. Furthermore, Grant (1997) concluded that velocity bias is generally not a problem in high image density PIV since the ratio of unpaired images to paired images is small. Dense seeding can therefore be employed to minimise velocity bias.

6.4 EXPERIMENTAL WORK

This section reports on the experimental work carried out using the bluff-body combustor described previously in this chapter. It begins with a description of the experimental layout and then outlines the actual experimental procedure (including selection of air/fuel flow rates, PIV parameters and postprocessing). Errors and corrections are quoted, and finally the results are presented.

6.4.1 Setup

The experimental layout is depicted in figure 6.5. Digital flowmeters were used to measure the fuel and air flow rates (accuracy: ±0.4% and ±0.8%, respectively, of the reading). One of these controlled the air supply through the seeder (secondary air flow) which essentially consisted of a fluidised bed. The tracer particles were drawn into the primary air supply by virtue of its much higher flow rate (and hence lower static pressure). In order to ensure that a sufficient pressure difference existed between the seeder and the junction with the primary air flow, the pipework to and from the seeder (which was adapted from a previous experiment) had to be enlarged so as to minimise the pressure losses across the device. The seeding particles were Zirconium Oxide of a 1 micron nominal diameter, selected because of their availability and temperature resistance. Precise control of the seeding density was impossible given that the fluidisation process had to be aided by physically shaking the seeder, thereby ensuring adequate seeding levels.

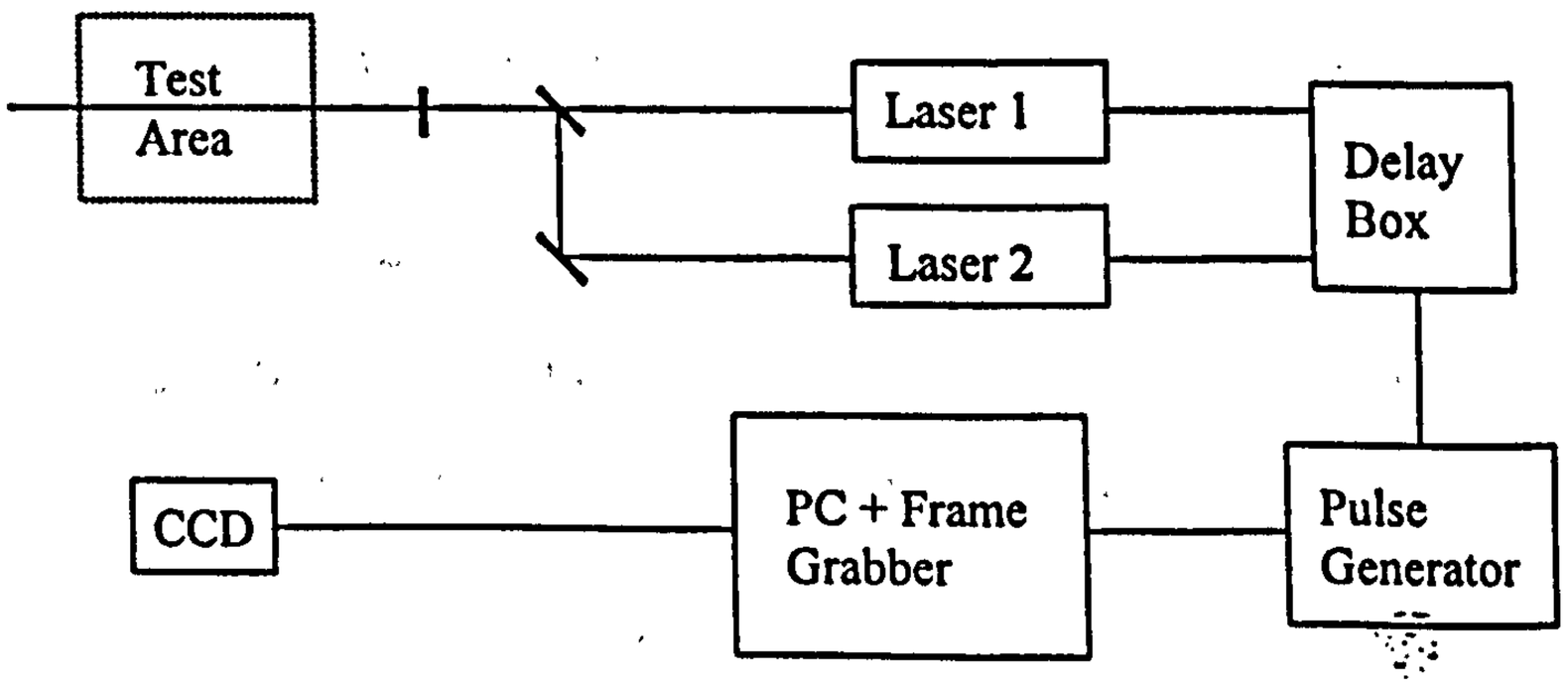

Figure 6.5: Experimental layout.

The burner was placed on a specially adapted traversing mechanism which permitted both horizontal (in the same plane as the laser light sheets) and vertical motion. The light sheets (approximately 100mm wide and less than 1mm thick) were directed through the centreline of the burner such that the first region to be investigated was the recirculation zone immediately behind the bluff-body face. Downstream areas could be subsequently examined by lowering the burner. Once initially aligned, the optical setup required no further adjustment since the burner itself was displaced as needed.

Two lasers (Continuum Surelite II, 532nm Nd:Yag, 200mJ) were utilised to illuminate the seeded flow. Although each laser could operate in a stroboscopic mode, greater control over the delay interval was afforded by using two light sources in conjunction with a delay mechanism. The two light sheets were aligned visually (a lengthy procedure due to the three-dimensional nature of the problem), and the delay between successive sheets was verified with a photodiode and an oscilloscope.

A CCD camera (Kodak Megaplus ES1.0, 1000×1000 pixels) was used to record the illuminated flow regions. Although its optical axis was not entirely perpendicular to the light sheets, all the image pairs remained in focus. The CCD was linked to a frame grabber; operation of the entire system was initiated by a pulse generator.

Since temperatures are also of interest, measurements were made by traversing a thermocouple (0.8mm diameter, K-type, Ni-Cr/Ni-Al, range: -200°C to 1250°C) through the test section. Although intrusive and disturbing the flow-field somewhat, this served to give an indication of the temperature field. The thermocouple was mounted on a rigid bar which passed through the exhaust tube and was connected to a small traversing mechanism (for horizontal movement along the radius of the burner) which in turn was attached to the extraction hood above the burner. Longitudinal positioning was afforded by moving the burner along its vertical axis.

6.4.2 Procedure

6.4.2.1 Selection of Flow Rates

Prior to any measurements being made, the exact air and fuel flow rates had to be determined. To this effect, a study was conducted which assessed the effects of various air and fuel flow rate combinations, on flame structure. Four types of flames were found:

1. Fuel-jet dominant (figure 6.6(a)): the annulus air has no effect, meaning there is no significant recirculation region (if any).
2. Fuel-jet dominant, weak recirculation (figure 6.6(b)): the weak recirculation zone (possibly created by the fuel jet rather than the annulus air) interacts with the fuel jet to produce a flame whose base is similar to the diameter of the bluff-body.
3. No clear dominance (figure 6.6(c)): neither the fuel jet nor annulus air dominate. Instead, there exists a central flame which is controlled by the fuel jet, but combustion also occurs in the large toroidal recirculation region, which extends downstream and envelopes the central fuel jet, created by the air annulus.
4. Air dominant (figure 6.6(d)): the central fuel jet is broken down sooner and the toroidal recirculation zone dominates.

A type-4 flame (which is far from blow-off) was selected for investigation because of the high turbulence levels and its complete domination by the large, toroidal recirculation region. Furthermore, the high air flow rate and the fact that the flame was lifted off the base of the burner, meant that the system approached the adiabatic state (one of the modelling requirements). The corresponding air and fuel flow rates are given in the table below. The Reynolds numbers for the inlet fuel and air are based on the pipe diameter and annulus width, respectively.

	Flow rate (lpm)	Density (kg/m^3)	Viscosity ($Pa \cdot s$)	Bulk velocity (m/s)	Reynolds number
Air	480	1.225	1.79×10^{-5}	4.053	3130
Fuel	4	0.67	1.09×10^{-5}	5.305	1300

Table 6.1: Air and fuel flow rates.

The Reynolds number of the fuel in the inlet pipe implies that the flow is laminar. However, the flow is so dominated by the annulus air jet that the flow regime of the fuel jet is of little consequence.

In order to assess the effects of combustion on the flow-field, isothermal flow through the bluff-body combustor was also investigated. In this instance the fuel flow rate was zero.

6.4.2.2 Data Acquisition

The CCD camera was positioned such that the field of view extended from the centreline of the burner to a point near the confining quartz wall, corresponding to a 40mm by 40mm area (thus the resolution was 40.8μm/pixel). Measurements right up to the wall were avoided because the bright reflections from seeding particles which had stuck to the fused-silica, interfered with the correct signals. A pulse separation of the light sheets of 100μs was selected. Since half the diameter of the combustor was captured in one image, horizontal traversing was not necessary. Thus only vertical traversing was required; measurements were also taken in the region $40<x<80$ and $80<x<120$ (where x is in millimetres). Approximately 180 image pairs were captured and recorded, over a continuous period, at each location. A greater quantity would have been desirable, but each image was approximately 1Mb large and memory limitations prevented a greater number of images from being taken.

Temperature measurements were subsequently made so as to obtain radial profiles (6 points along each radius, spaced at 5mm, starting at the bluff-body centreline) at the following axial locations: $x = 0.5R_b$, $1.5R_b$, $2.5R_b$, $3.5R_b$ and $4.5R_b$, where R_b is the radius of the bluff-body ($0.5\times d_2$ in figure 6.1). Ideally, measurements should have been taken at locations even further from the centreline, but time constraints dictated otherwise. In many areas of the flame, the flowfield was rather complex and locally-unsteady; due to the fairly fast response of the thermocouple, the indicated temperatures in certain locations tended to fluctuate significantly. Since no data-logging system was in place, an average temperature was estimated and the extents of the fluctuations about the mean were noted. Generally the temperature fluctuated by approximately ±15°C about the mean, although this could be more in regions where entrainment of annulus air was significant. The deviations were smaller near the base of the flame where the temperatures were lower (typically ±5°C).

6.4.2.3 Post-Processing

The 40mm by 40mm image area was divided into a matrix consisting of 60×60 interrogation zones, each being a square of 2.608mm (achieved by using 64×64 pixels per interrogation region, with a 50% overlap). A vector plot was computed for each image pair by using a cross-correlation algorithm in the flow visualisation software VISIFLOW. This calculated a representative velocity vector for each interrogation region. A filter was used to remove any vectors whose magnitude was greater than 7m/s. Each image pair gives rise to an instantaneous velocity field because the actual flow is turbulent. However, the TEACH code assumes steady flow. For this reason, 180 or so consecutive flowfields were averaged, thereby allowing the mean quantities U and V and the fluctuating components $\overline{u'^2}$, $\overline{v'^2}$ and $\overline{u'v'}$ to be computed. Rather than averaging the entire flowfield, this process was performed along selected traverses, resulting in radial profiles of the above quantities at the axial locations $x = 0.5R_b$ to $x = 5.0R_b$, in increments of $0.5R_b$. Although it was not possible to measure the tangential stresses, it was assumed that $\overline{w'^2} \approx \overline{v'^2}$ for the purpose of estimating the experimental turbulence energy (using equation 4.7). Whilst this is of course an approximation, it will be shown that the axial stresses are generally significantly larger than $\overline{v'^2}$, so the error in the above assumption is likely to be small.

In combusting environments, heat transfer occurs between the thermocouple and the reacting flowfield; this interaction modifies the thermocouple temperature reading. If instantaneous temperatures are required, then the thermal inertia of the thermocouple must also be accounted for. Vachon et al (1986) developed a correction method which takes into consideration all these issues. In the present case, however, we are only interested in mean temperatures; thus thermal inertia effects are neglected. Furthermore, conduction is assumed to be several orders of magnitude smaller than convective heat transfer. Thus a temperature correction can be calculated by assuming thermodynamic equilibrium between the thermocouple junction and the reacting gases, whereby heat gained by convection is promptly radiated to the gases. This loss by radiation is approximated by using a method similar to that of Bĕçker & Yamazaki (1978):

$$T = T_j + \frac{\varepsilon\sigma}{h}\left(T_j^4 - T_\infty^4\right) \qquad (6\text{-}1)$$

where T is the actual gas temperature (in Kelvin), T_j is the temperature (Kelvin) recorded by the thermocouple, T_∞ is the ambient temperature (293K in this case), ε is the emissivity of the probe, σ is the Stefan-Boltzman constant (5.67×10^{-8} W/m^2·K^4) and h is the heat transfer coefficient (a relationship between Nusselt number and Reynolds number is used for circular cylinders). Becker & Yamazaki (1978) utilised a silica-coated thermocouple (which minimises catalytic effects) with an emissivity $\varepsilon = 0.22$. Gengembre et al (1984), on the other hand, employed an emissivity of $\varepsilon = 0.9$ for soot-covered probes. In the present case, the thermocouple junction glowed bright red at the highest temperatures, indicating that the soot deposits were largely being eliminated by combustion. No emissivity data was found for K-type thermocouples, so the average of the emissivities for oxidised Chromega (Ni-Cr, $\varepsilon \approx 0.87$ for the temperature range 600°C to 1300°C) and Alomega (Ni-Al, $\varepsilon \approx 0.15$ for the temperature range 200°C to 800°C) was used. The resulting value was $\varepsilon = 0.5$. At the highest temperatures, the radiation correction was approximately 20% of T_j.

6.4.2.4 Initial Results

Prior to averaging out the vector fields as described in the previous section, several flow-field images were examined so as to determine the extent of axisymmetry. Inspection of the non-combusting flow (only annulus air was present) revealed that the isothermal flow field was strongly asymmetric. It was found that two fixed recirculation zones of unequal size existed, as shown in figure 6.7. Efforts were made to ensure that the asymmetry was not due to manufacturing problems, but after several adjustments the asymmetry persisted. The CFD work assumes the flow to be axisymmetric, but the above finding meant it was not possible to compare simulation predictions with the experimental data. For this very reason, the isothermal flow through the bluff-body combustor was not investigated any further.

A similar inspection was conducted for the reacting case. Although the flame was visibly unsteady, its overall shape did not change over time and remained confined

to a certain envelope. Statistical averaging of the vector plots either side of the longitudinal axis of the combustor revealed that the reacting flow was axisymmetric. Figure 6.8 clearly shows that the resulting radial profiles of U (at two different axial locations) are axisymmetric in a trend-wise sense, if not in absolute values.

6.4.3 Errors

Before the experimental results are presented, it is important that the sources of experimental error are highlighted and their effects assessed. Three main areas exist in which errors could occur.

1. Biasing: In areas of low seeding density, the velocities are biased toward smaller values (as explained in section 6.3.2). This is anticipated to cause problems near the centreline because the fuel jet is not seeded (time constraints meant that it was not possible to design and construct a seeding device for very low flow rates). Velocities in this region, particularly near the bluff-body face, are only computed by virtue of the tracer particles entrained into the fuel jet from the recirculation vortex. This implies that the experimental velocities along the centreline should be higher than those measured.
2. Post-Processing: (a) Correlating image pairs occasionally leads to some vectors which are clearly in error (either in magnitude or direction or both). Many of these so-called rogue vectors are removed by a filtering algorithm; for example, section 6.4.2.3 describes how an upper limit of 7m/s was applied. However, there still exists the opportunity for rogue vectors below the 7m/s threshold to be computed (see figure 6.9, for example), and these can particularly affect results where the surrounding velocities are much smaller. Mean velocities tend to be least compromised by this phenomenon, but quantities based on the deviation from the mean (i.e. the Reynolds stresses) can be significantly distorted. However, such misrepresentation is purely a local event; hence any discontinuities seen in the radial profiles of experimental results are likely to be due to rogue vectors. (b) Had the seeding intensity been any higher, there would have been a serious risk of flame quenching occurring, thereby altering the flow. For the given level of seeding, the optimum parameters were deemed to be those described in section 6.4.2.3. The only problem with the relatively large interrogation zone (2.608mm square, 64×64 pixels)

is that the velocity profiles tend to be smoothed out in areas of steep gradients. Normally, a 32×32 pixel (1.304mm square) interrogation region would more accurately resolve the issue of large gradients. However, in the present case, such processing parameters yield many rogue vectors which cause the statistically-averaged profiles to be inaccurate. This is clearly observed in the U profiles in figure 6.10, which compares the results for data which was processed using 64×64 and 32×32 pixel interrogation regions. The 32×32 pixel resolution results in a significantly lower peak velocity in the annulus area; this is entirely due to insufficient seeding densities. More accurate results could possibly have been obtained if the CCD had been focussed onto a smaller area of the flow, but this would have required more memory and thus fewer images could have been captured (resulting in a smaller sample from which to calculate the statistical means). It is evident that a compromise must be reached at some point; this is why the cross-correlation parameters employed in the experiment were those described in section 6.4.2.3.

3. Positioning: During the application of the PIV technique, only vertical traversing was necessary. This was achieved by raising or lowering the entire burner; the spatial accuracy was approximately ±0.5mm, which is small relative to the area captured by the CCD at any time. The same vertical accuracy applied to the thermocouple position. The horizontal placement of the thermocouple was only accurate to within ±1mm because the thermocouple actually vibrated laterally. However, the accuracy of the location of the thermocouple is not particularly relevant because (a) the flow-field was locally-unsteady at most locations, causing the temperature to fluctuate noticeably, and (b) the radiation correction procedure results in temperature alterations which are much larger than those due to positioning errors.

A worst-case estimate for the velocity error resulted in an error band of ±4%, based on U = 5m/s, 40.8μm per pixel, and assuming that the particle displacement is accurate to within ±0.5 pixel. Theoretically, this error increases at smaller velocities. In actual fact, though, the averaging of many velocity vectors within each interrogation region, in conjunction with the cross-correlation procedure utilised by VISIFLOW, reduces this error significantly, by up to as much as several orders of magnitude

(Hargrave, 1999). Thus the worst-case figure of ±4% is applied to the entire range of velocities. In any case, this error is expected to be small compared to those present in the CFD simulations.

6.4.4 Results

The flow within the bluff-body combustor, at the given fuel and air supply rates, is truly complex; this is clearly demonstrated by the results which are presented in the current section. The overall characteristics of the flow-field are reported, after which more detailed flow and temperature distributions are presented.

6.4.4.1 Overall Features

Although the main flow feature, the toroidal recirculation zone, exhibited lateral fluctuations, the visible flame envelope itself did not vary significantly in time; it was approximately 3.5 bluff-body diameters high and slightly wider than the bluff body. As seen in figure 6.6(d), the visible flame is lifted from the bluff-body face, which is covered by a black layer of soot. Other researchers (e.g. Masri et al, 1996) reported that their bluff-body flames caused an insulating ceramic tile at the base of the burner to glow red-hot, citing this as evidence of heat transfer to the base. In the present case, heat transfer to the bluff-body is negligible. Furthermore, the exhaust gas temperature was rather low (the outside temperature of the exhaust was found to be around 50°C to 60°C) and seemingly uniform; this confirms that most of the heat of reaction is indeed convected away from the flame by the annulus air.

Figure 6.9 is a vector plot of half the reacting flow field, extending from x = 0mm to x = 80mm, where the longitudinal axis and the bluff-body face occur at the right and bottom of the illustration, respectively. Although it only represents instantaneous velocities, it still captures the essence of the flow. The principal feature is clearly the large recirculation zone (marked 'A' in figure 6.9), approximately 2.8R_b long, which is driven by the air annulus (marked 'B') and breaks down the central fuel jet. Due to velocity bias problems, the readings along the centreline are somewhat suspect, however the data suggests that the central fuel jet persists further than x/R_b =

3.5. The presence of several eddy-like structures between the main recirculation zone and the centreline is observed. Another recirculation region occurs near the base of the burner, extending from $x/R_b = 0$ to roughly $x/R_b = 1$ (marked 'C'). The last clearly-defined recirculation area occurs behind the step towards the outer radius of the burner (marked 'D'). Figure 6.9 indicates the extent of this region to be approximately $1.3x/R_b$ (or 28.9mm). After completion of the experiment, it was observed that seeding had remained attached to the quartz cylinder along the range x = 25mm to 35mm, an indication of the extent of the fluctuations of the stagnation point.

6.4.4.2 Detailed Distributions

Radial profiles of experimental mean U, V, $\overline{u'v'}$, $\overline{u'^2}$, $\overline{v'^2}$ and T are plotted at the axial locations $x = 0.5R_b$, $1.5R_b$, $2.5R_b$, $3.5R_b$ and $4.5R_b$, in figures 6.11 to 6.16. Each graph is briefly examined and the observations are recorded below.

Figure 6.11 is in good agreement with the vector plot (figure 6.9) and shows the correct trends; the peak mean axial velocity in the annulus region is seen to expand outwards radially as the flow progresses downstream. The profile at $x = 4.5R_b$ suggests that the central fuel jet persists to approximately this location. However, the centreline values of U at $x = 0.5R_b$ and $x = 1.5R_b$ are likely to be too low as a result of the biasing due to insufficient seeding, particularly if one considers that the centreline inlet velocity was 7.2m/s. As x increases, more seeding is entrained into the central region and the centreline measurements of U are expected to become more accurate. Thus the indication that the central fuel jet is largely broken down by $x = 4.5R_b$ (where U at the centreline is zero) is entirely plausible.

Figure 6.14 reveals high peaks for $\overline{u'^2}$ at the centreline, for the axial locations $x = 0.5R_b$ to $x = 2.5R_b$. Clearly this is a consequence of the error in velocity measurement, described above. However, the radius of the fuel jet is only 2mm (0.0455R) and relatively high values of $\overline{u'^2}$ persist to r = 0.25R, far outside the region influenced by the poor seeding levels. This signifies that the instantaneous axial velocities u' can differ from the mean velocity U by large amounts (in the region

0.05<r/R<0.25), of the order of magnitude of U itself. These large fluctuations in instantaneous velocity in this particular region are in all likelihood due to the lateral oscillations of the flame. They could also be due to vertical motion of the large structures, but visual evidence does not corroborate this. In fact, as mentioned previously, observations of the flame revealed radial fluctuations of the toroidal vortices and an approximately constant flame height.

Since the mean radial velocities are significantly smaller than U, any fluctuation in u' is bound to cause a change in v' (by continuity) which is much larger relative to its mean than the variation in u' is compared to U. Thus the V profiles are much more sensitive to fluctuations in the flow-field. Nevertheless, figure 6.12 indcates that the trends are correct. The profiles of V in the lower region of the main recirculation zone are positive (in the direction away from the centreline) whilst those nearer the top are negative.

Figure 6.15 indicates that the radial stresses generally behave as do those in the axial direction, for similar reasons. The lateral fluctuations of the flame mean that v' varies with time at a point in space; this is supported by the high levels of $\overline{v'^2}$ which extend from near the centreline to r/R = 0.2. Again, only the values in close proximity to the centreline are suspect.

It is well known that in flows approximating free shear layers, the quantity $\overline{u'v'}$ is directly proportional to the predominant velocity gradient. However, the present flow has strong streamline curvature and involves significant radial velocities. Figure 6.13 reveals that there is no clear correlation between $\overline{u'v'}$ and the U profiles, except perhaps in the annulus region at $x = 1.5R_b$ (where the peaks in shear stress correspond to the steepest parts of the U curve).

The main feature in the temperature profiles (figure 6.16) is the fact that the peak temperatures occur rather far from the centreline. Masri et al (1996) noted that the low stoichiometric air/fuel ratio for methane causes the reaction zone to be moved away from the central jet, which is also observed in the present case. The location of the peak

temperature is seen to shift outwards radially from r/R = 0.37 to r/R = 0.47, remains at this location for the profiles x = 1.5R_b to 3.5R_b and then moves nearer to the centreline again (to r/R = 0.45) at x = 4.5R_b. Comparing this trend with figure 6.9 reveals that at x = 1.5R_b to x = 3.5R_b, the peak temperatures are located inside the main recirculation zone. The temperature drops rapidly as one moves further outwards, mainly because of the prevailing annular jet which is much cooler at its outer diameter. Another trend worth noting is that the centreline profiles become flatter in the streamwise direction. The shallow centreline temperature gradients are particularly evident at x = 4.5R_b which roughly coincides with the top of the principal recirculation region. The flatter centreline profiles are thus due to the convection of heat and reaction products from higher temperature areas towards the lower temperatures encountered at the centreline. A very interesting point to note is that the peak temperatures occur at the radial locations at which the axial velcocity is small. Furthermore, at these points the shear stress $\overline{u'v'}$ and normal stresses are also small. This indicates low levels of convection and relatively little diffusion at the points in question. In the current flame, this is as near to an adiabatic condition as possible. However, convection and diffusion, must still be of significance because they limit the peak temperatures to 1700K which is considerably lower than the stoichiometric adiabatic flame temperature of 2600K (Clarke, 1994).

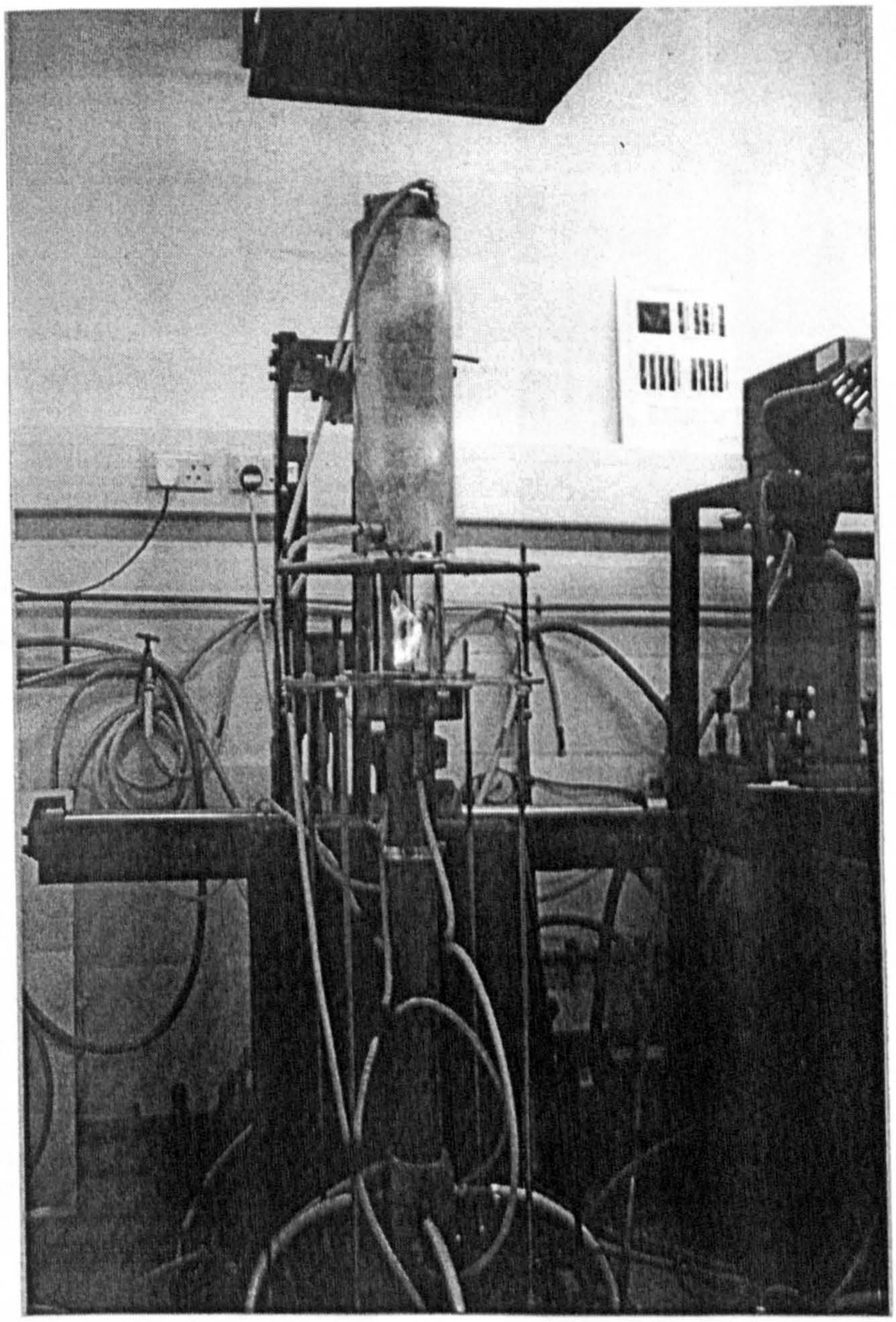

Figure 6.3: Photograph of the experimental rig.

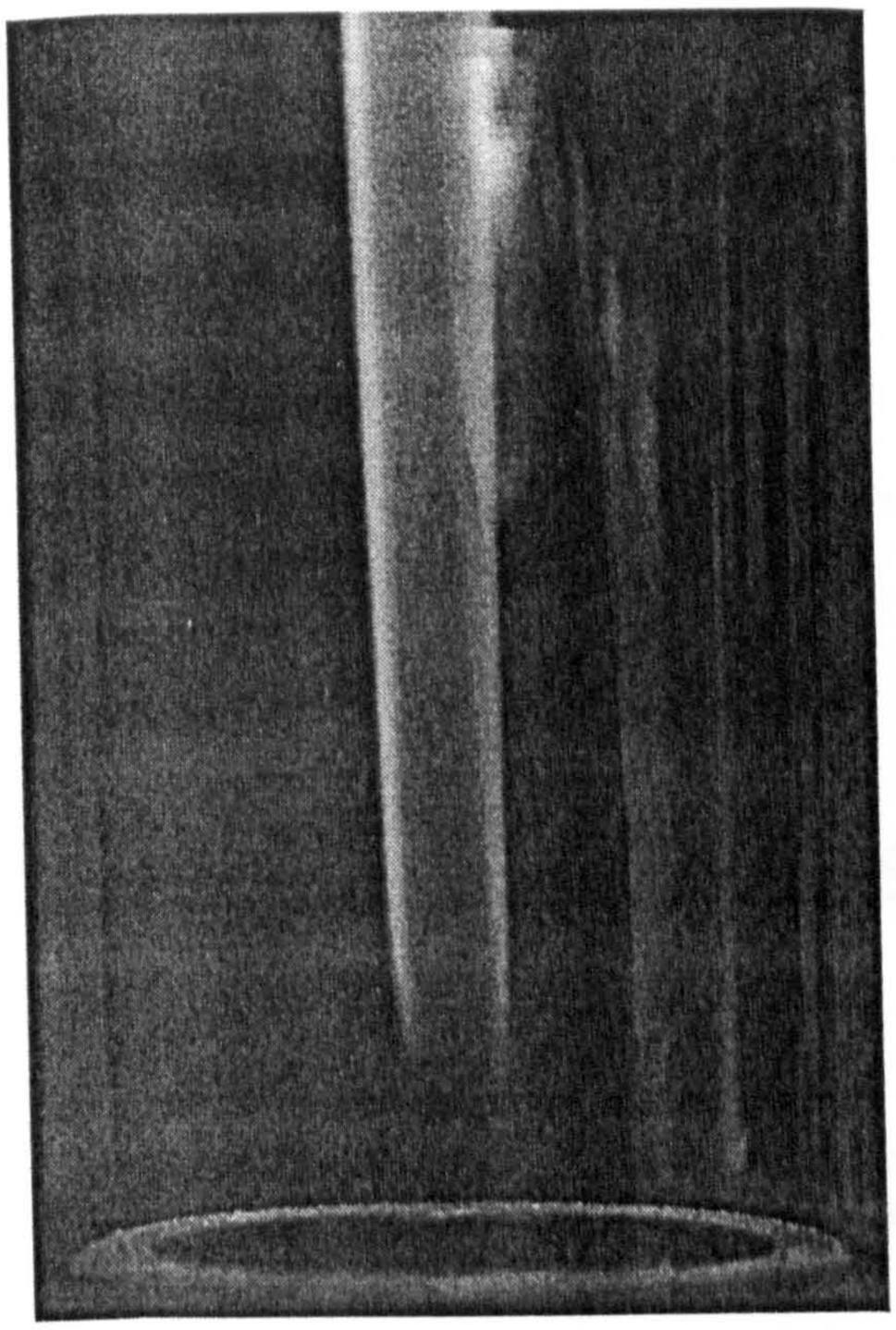

(a) Q_{air} = 63 lpm

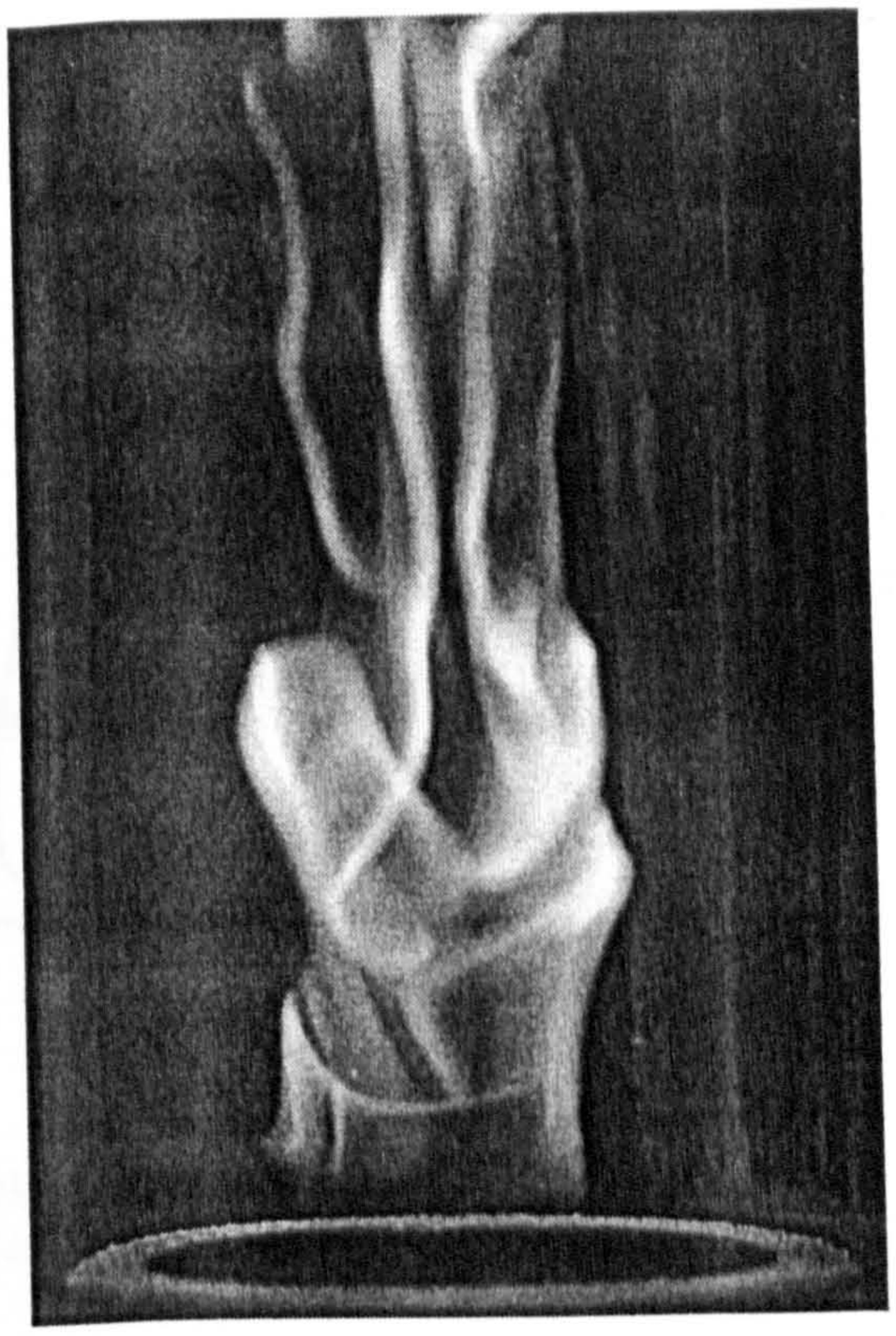

(c) Q_{air} = 282 lpm

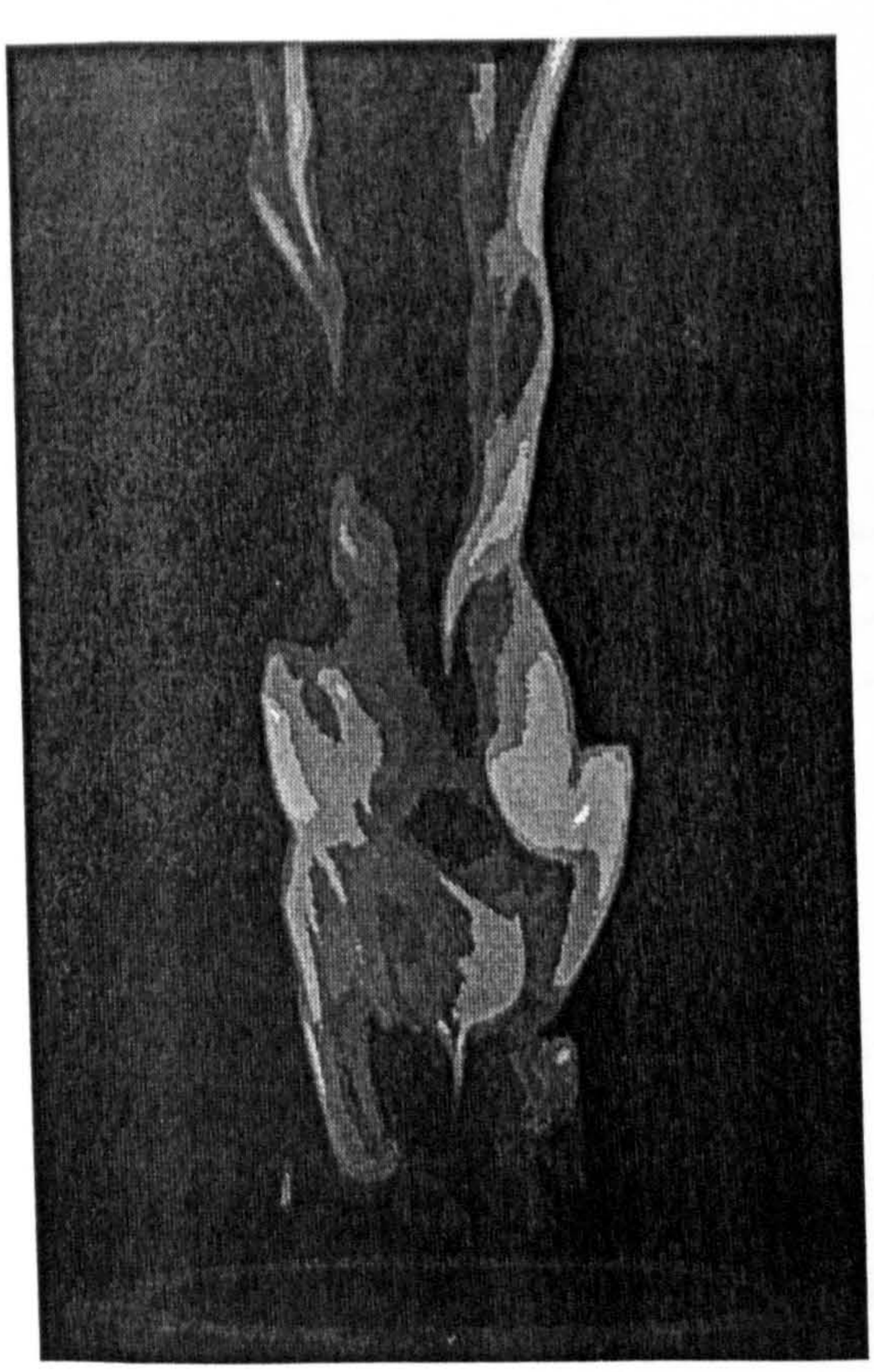

(b) Q_{air} = 220 lpm

(d) Q_{air} = 480 lpm

Figure 6.6: Flame structures at various air flow rates (all fuel flow rates are 4.0 litres per minute).

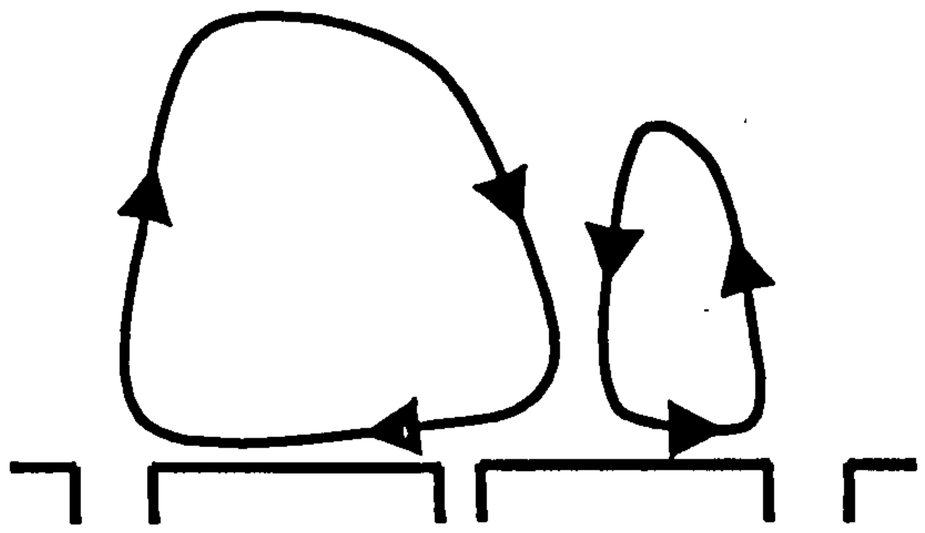

Figure 6.7: Illustration of the two recirculation zones of unequal size in the asymmetric, isothermal flow.

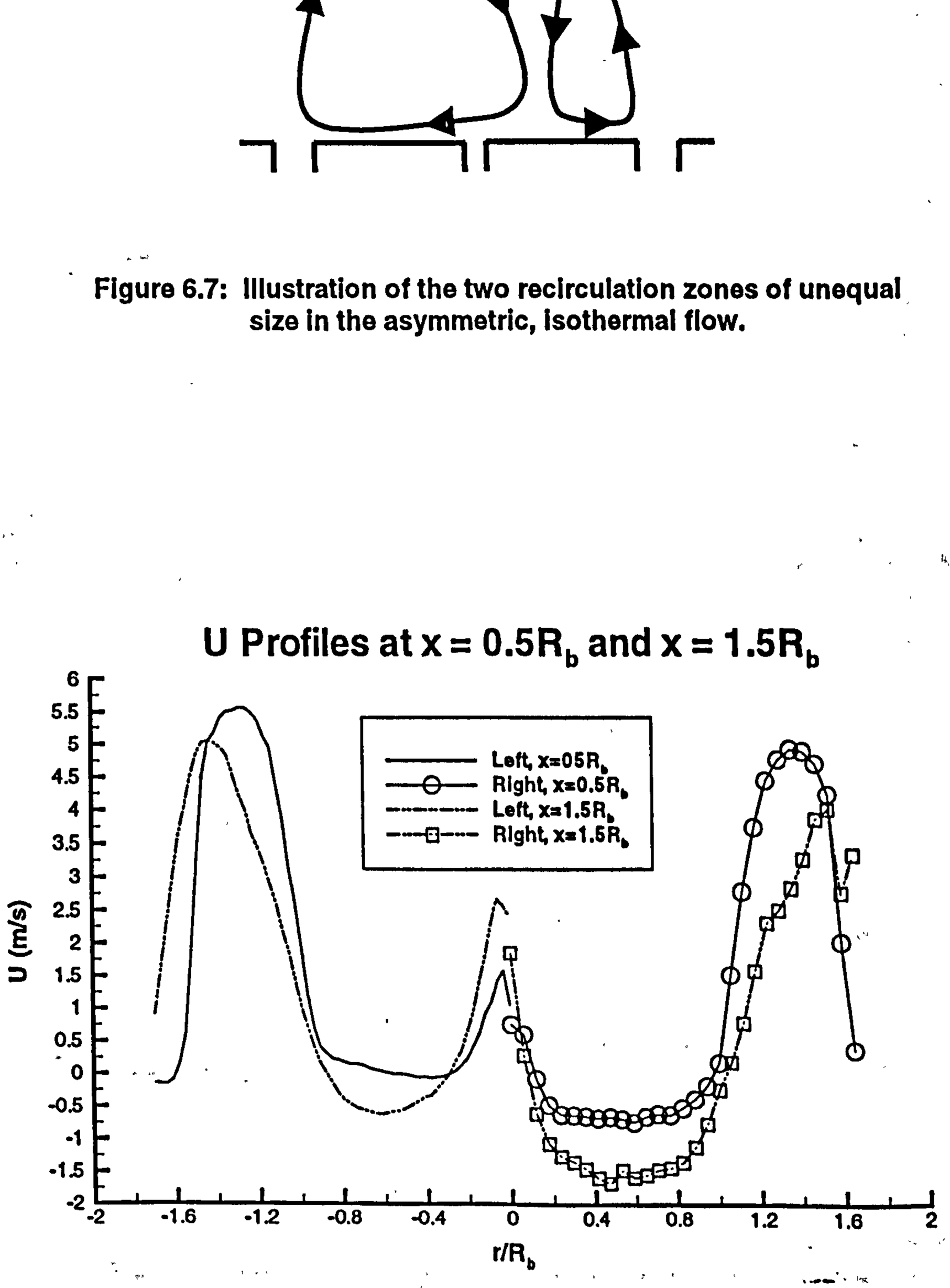

Figure 6.8: Radial profiles of axial velocity on both sides of the bluff-body longitudinal axis

Sample Instantaneous Velocity Field

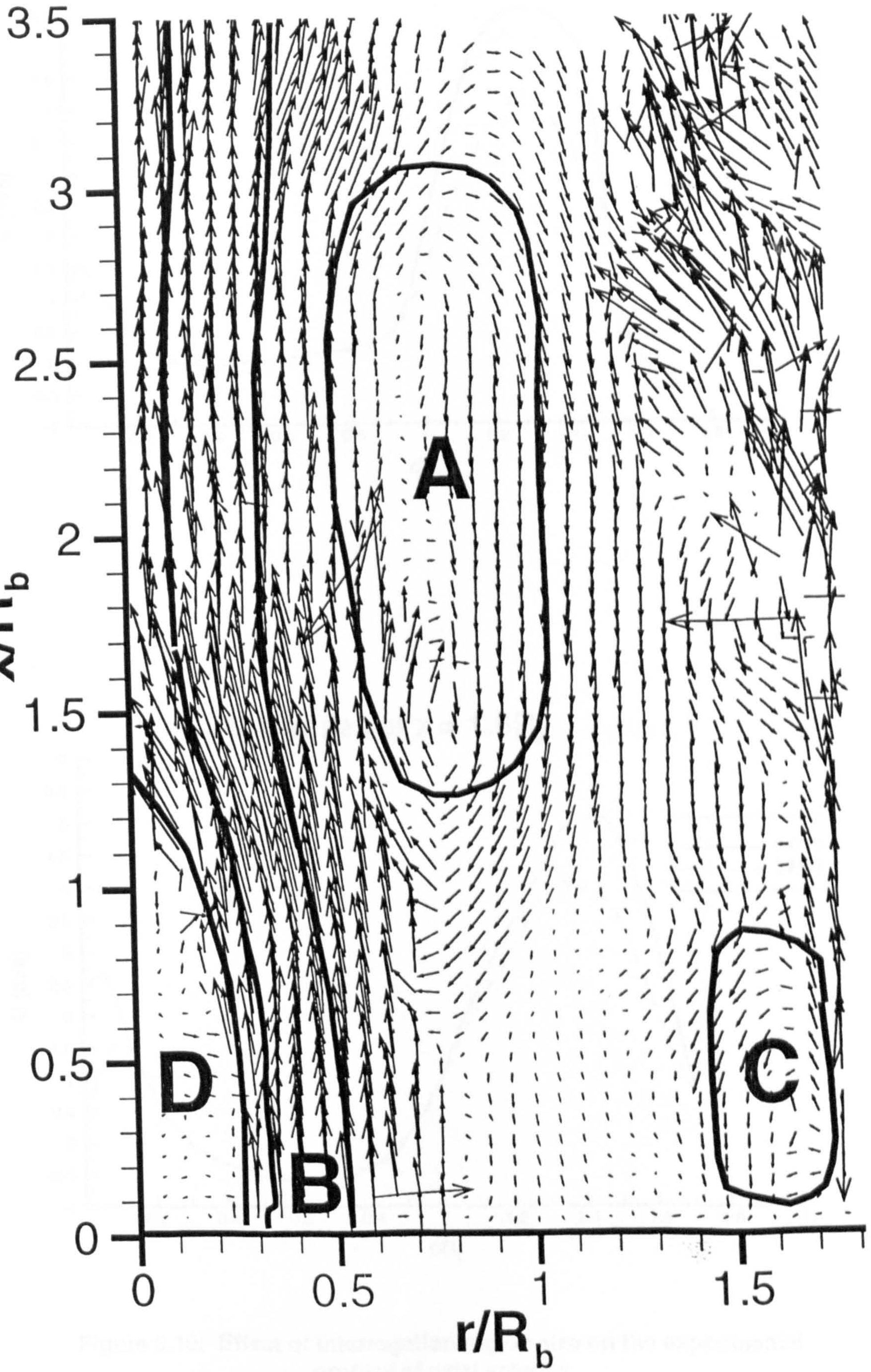

Figure 6.9: Instantaneous vector plot of the flow up to 1.75 bluff-body diameters downstream of the inlet. Note that the x-axis is labelled with respect to the wall (i.e. $r/R_b = 0$ and r/R_b correspond to, respectively, the wall and the centreline).

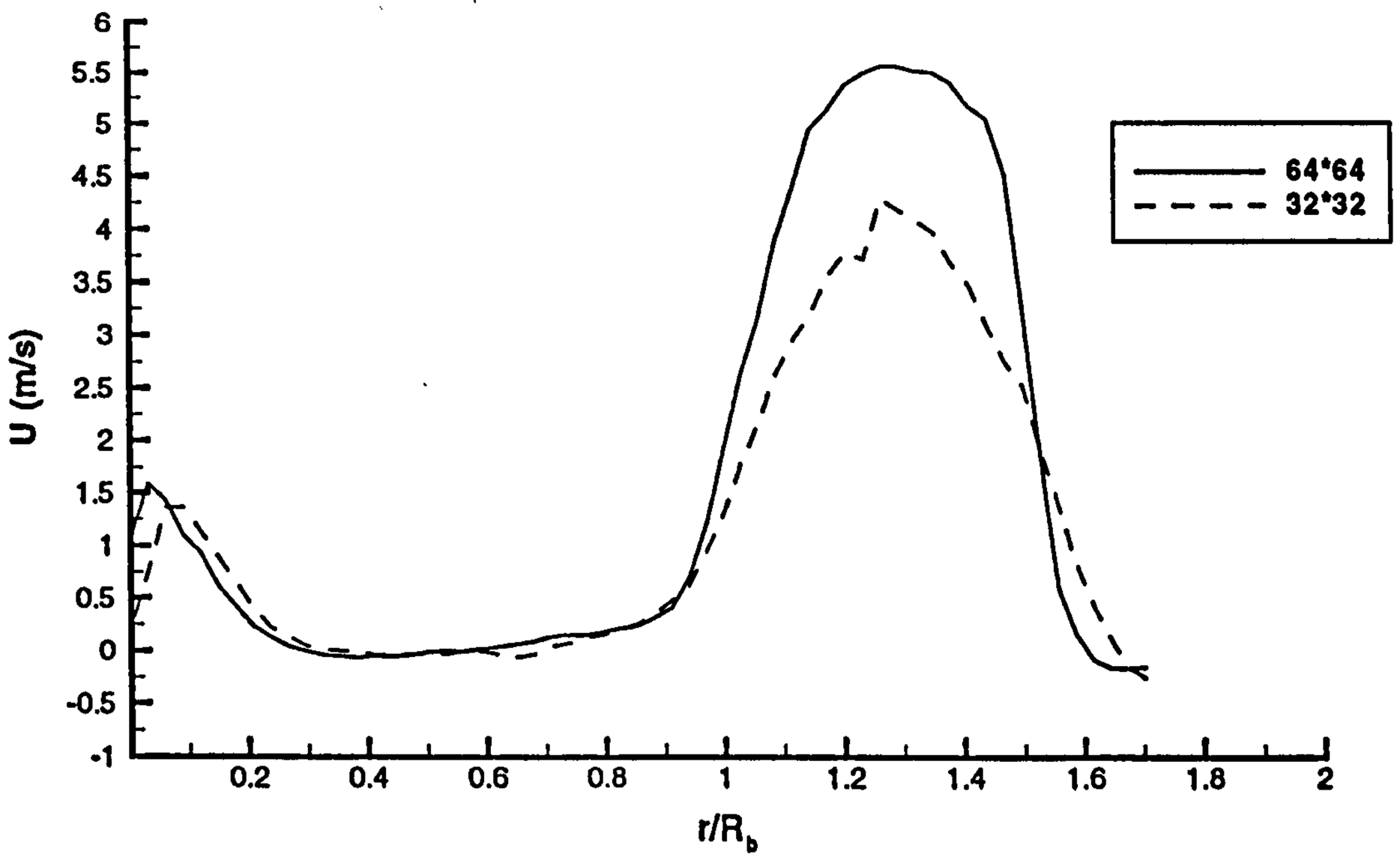

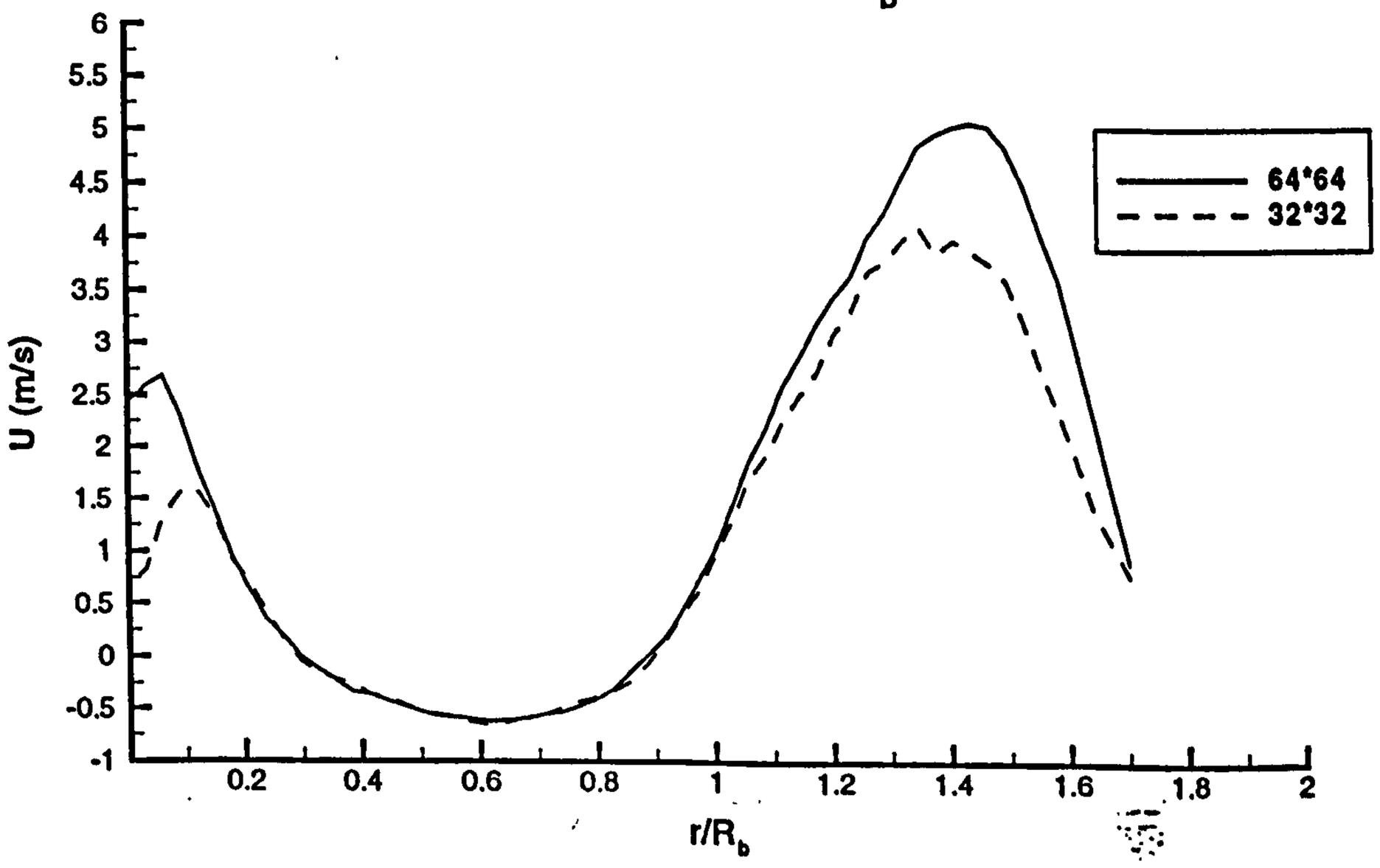

Figure 6.10: Effect of interrogation region size on the experimental profiles of axial velocity

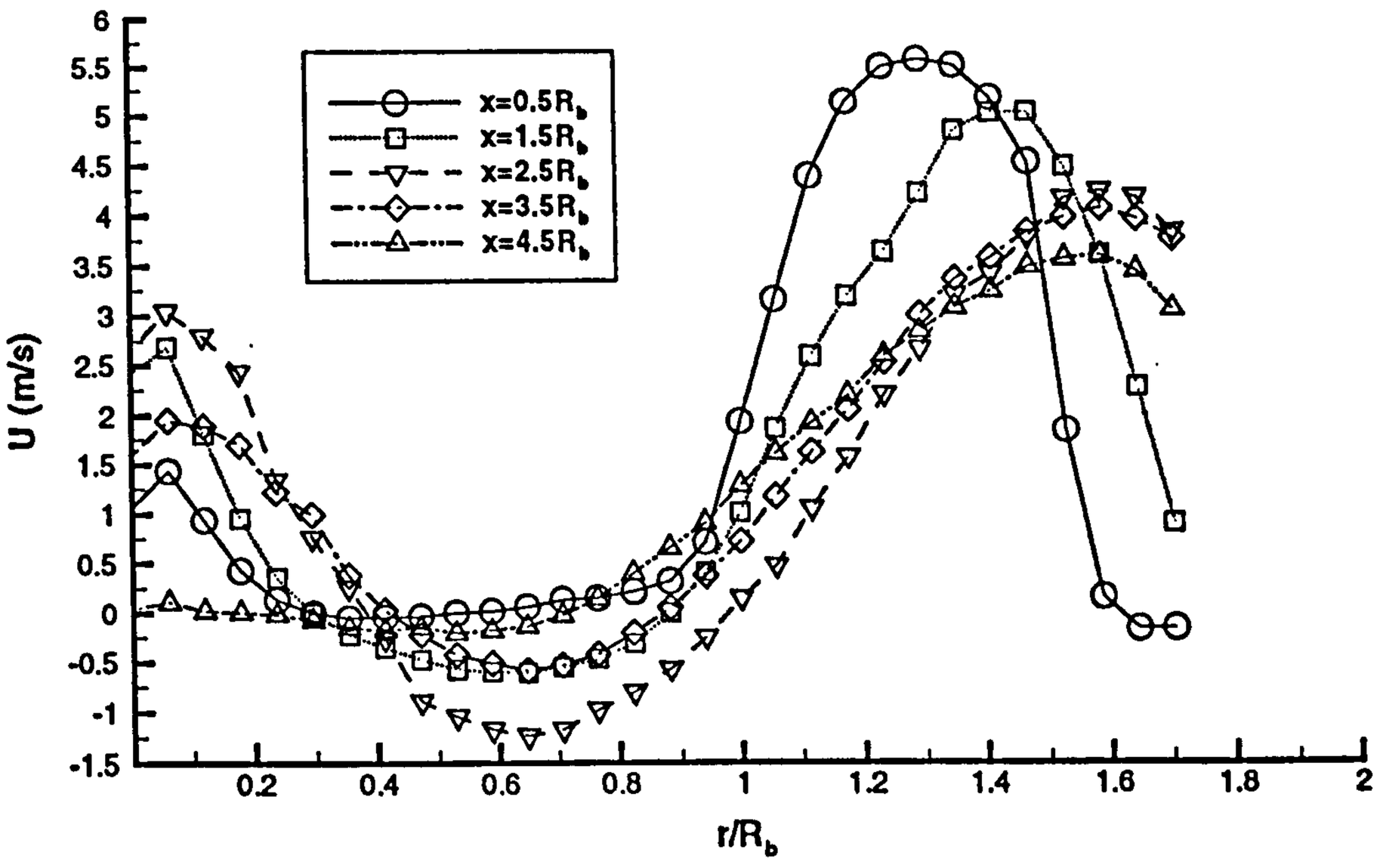

Figure 6.11: Experimental axial velocities.

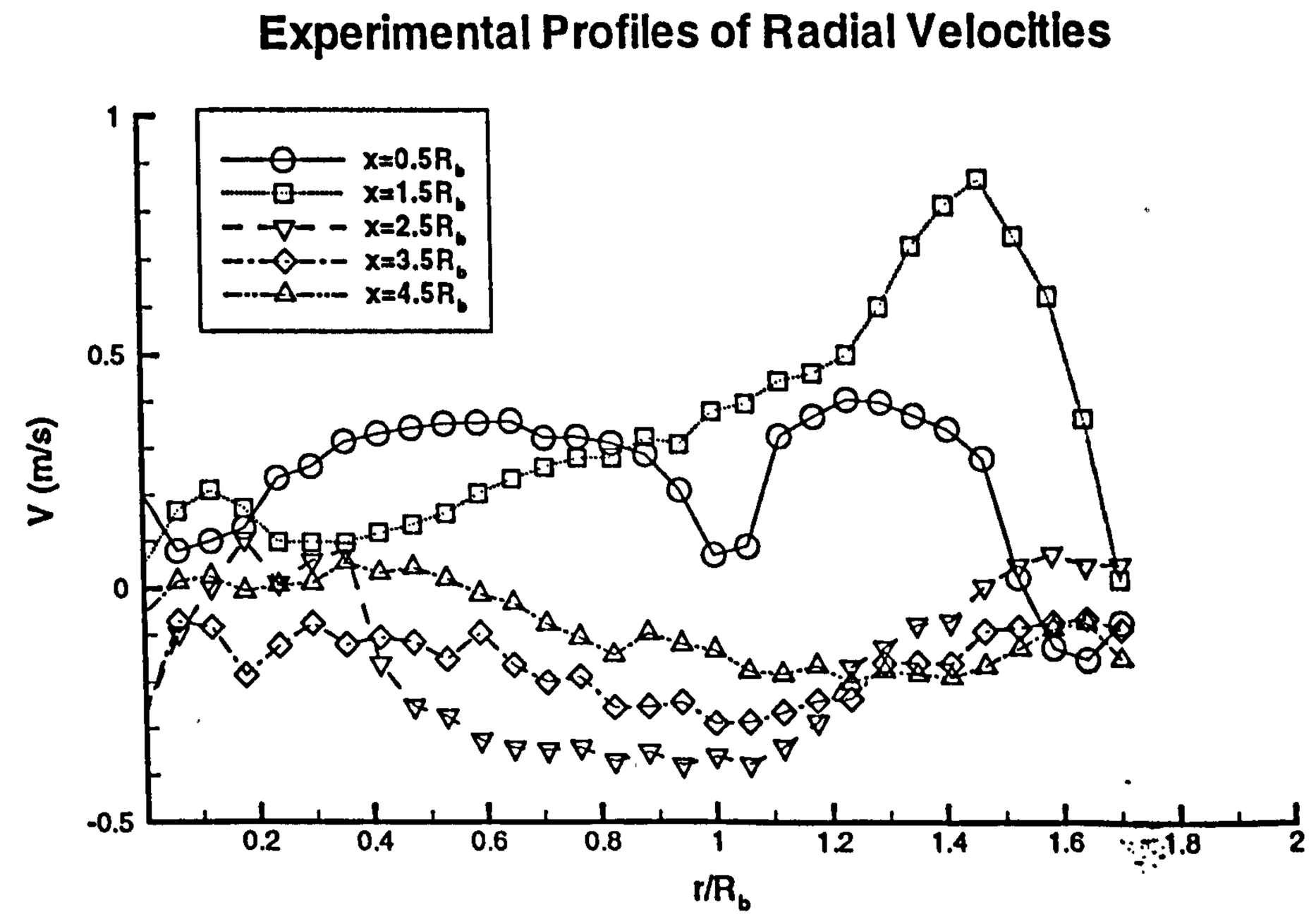

Figure 6.12: Experimental radial velocities.

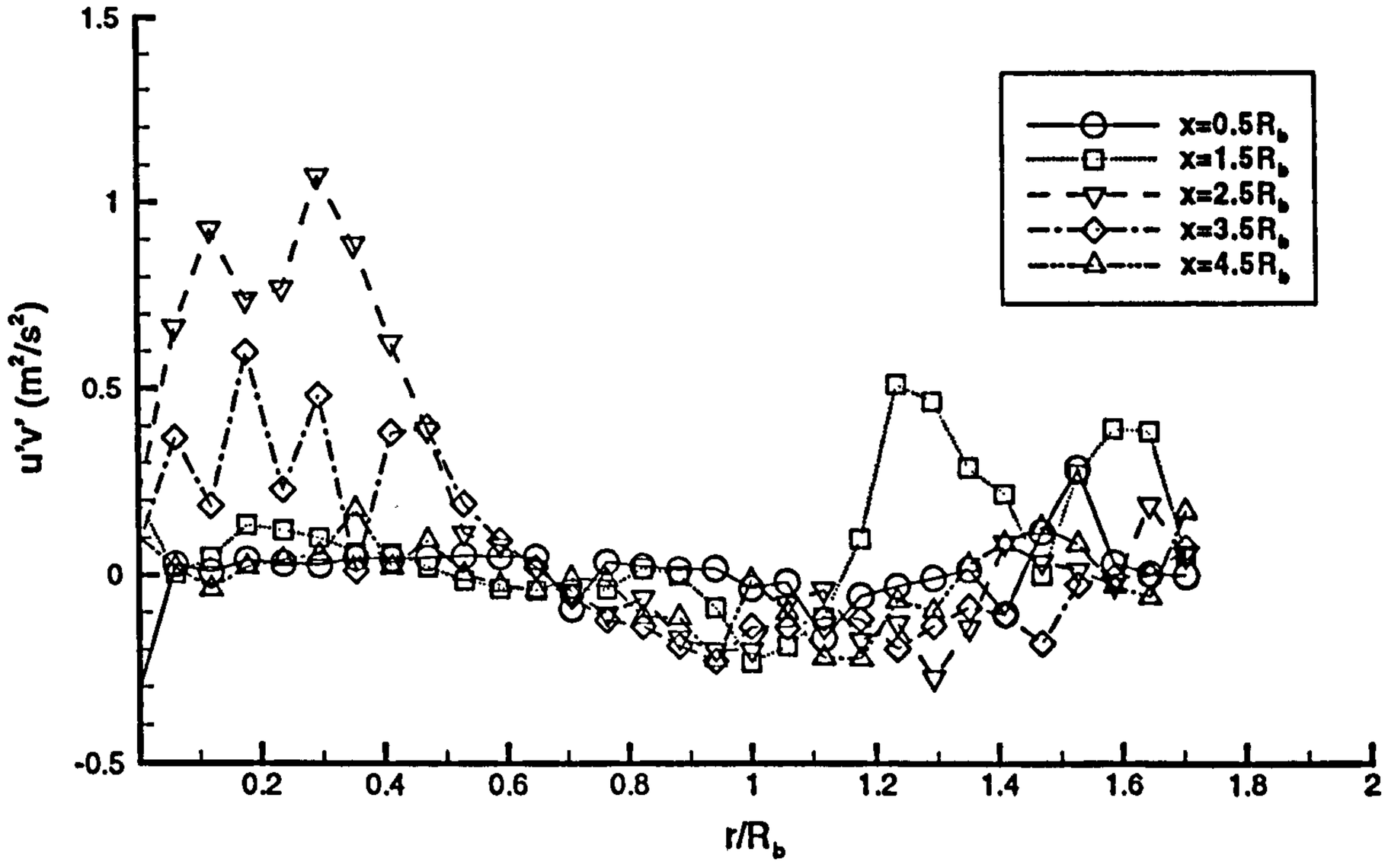

Figure 6.13: Experimental shear stresses (Reynolds).

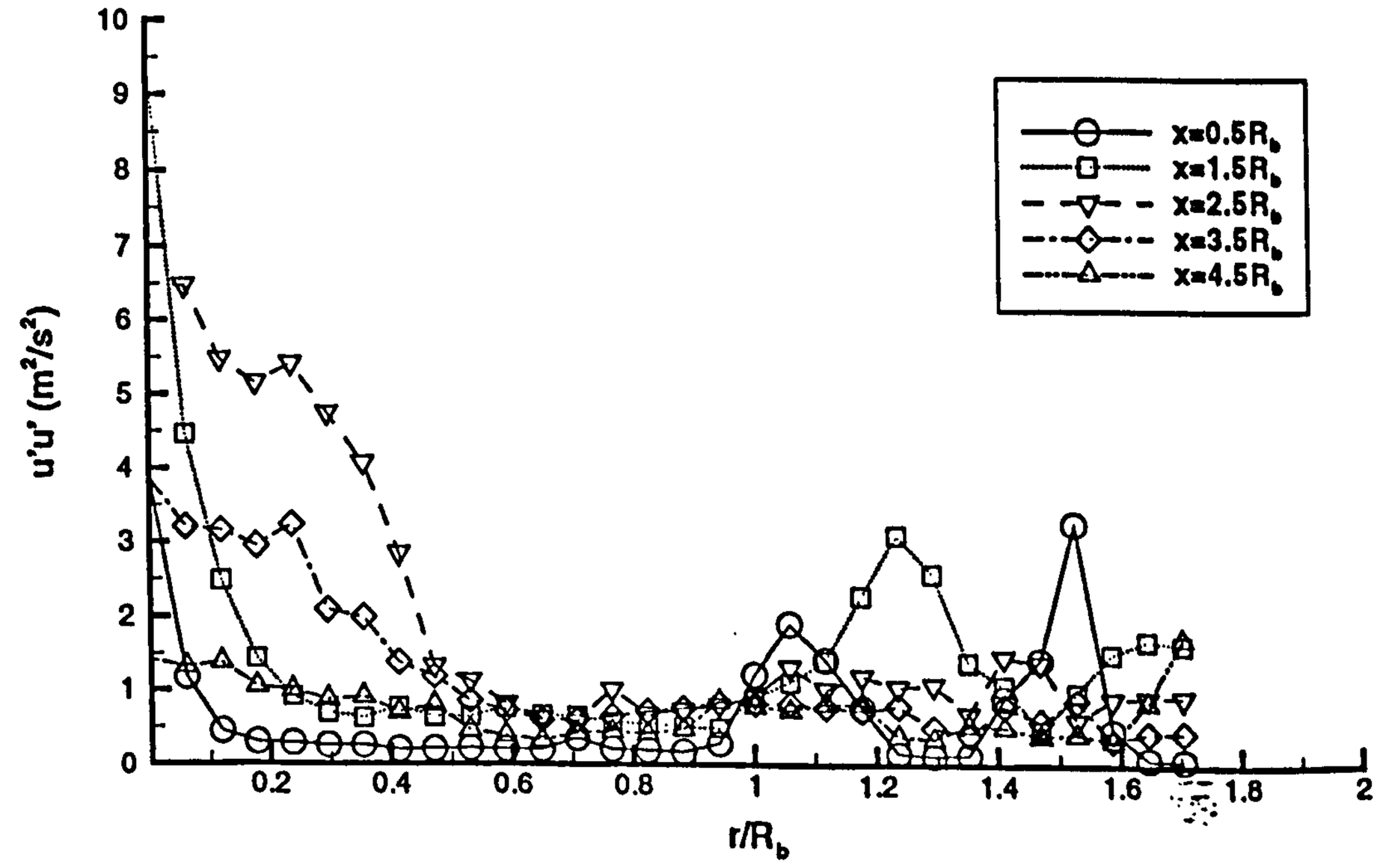

Figure 6.14: Experimental axial stresses (Reynolds).

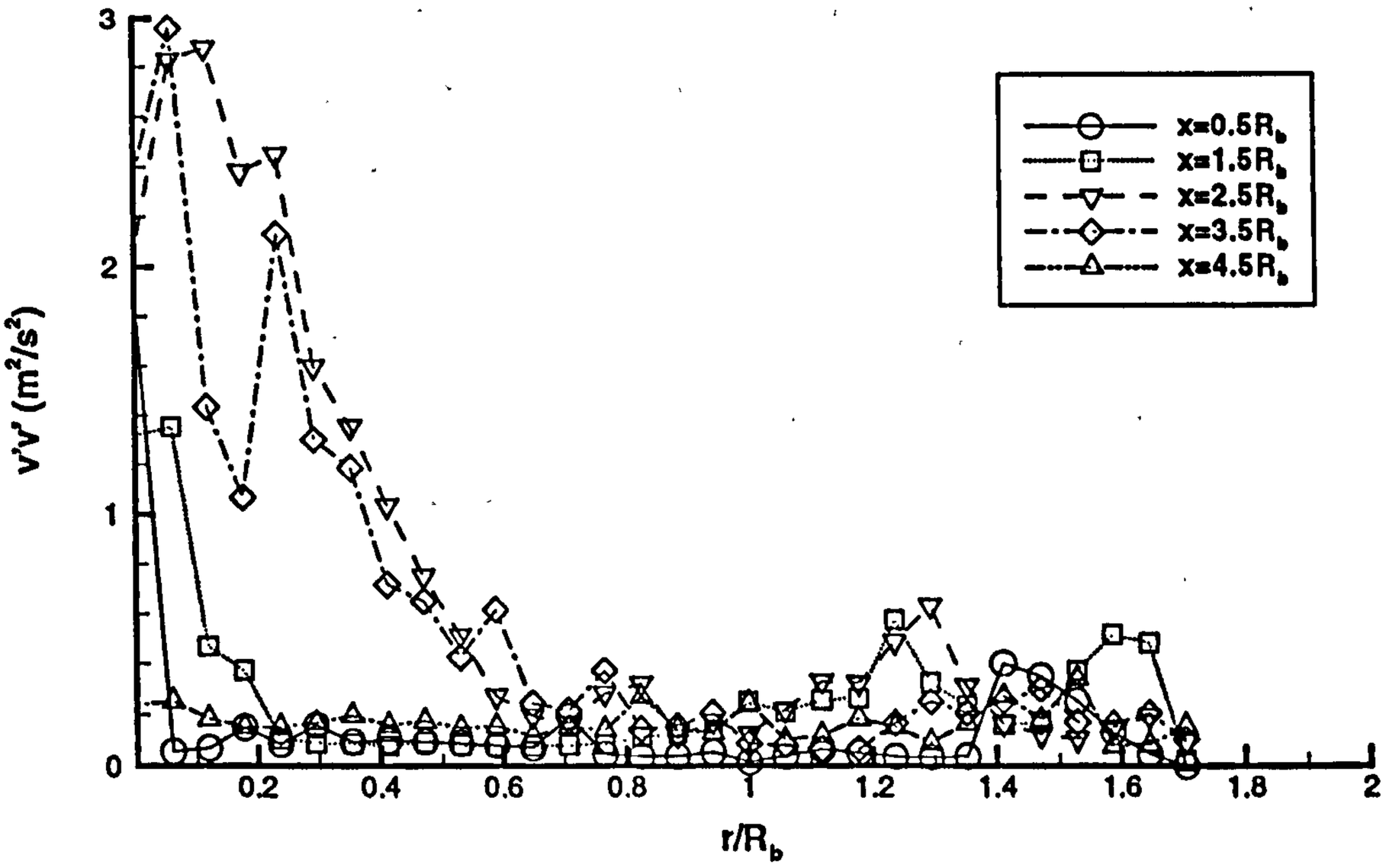

Figure 6.15: Experimental radial stresses (Reynolds).

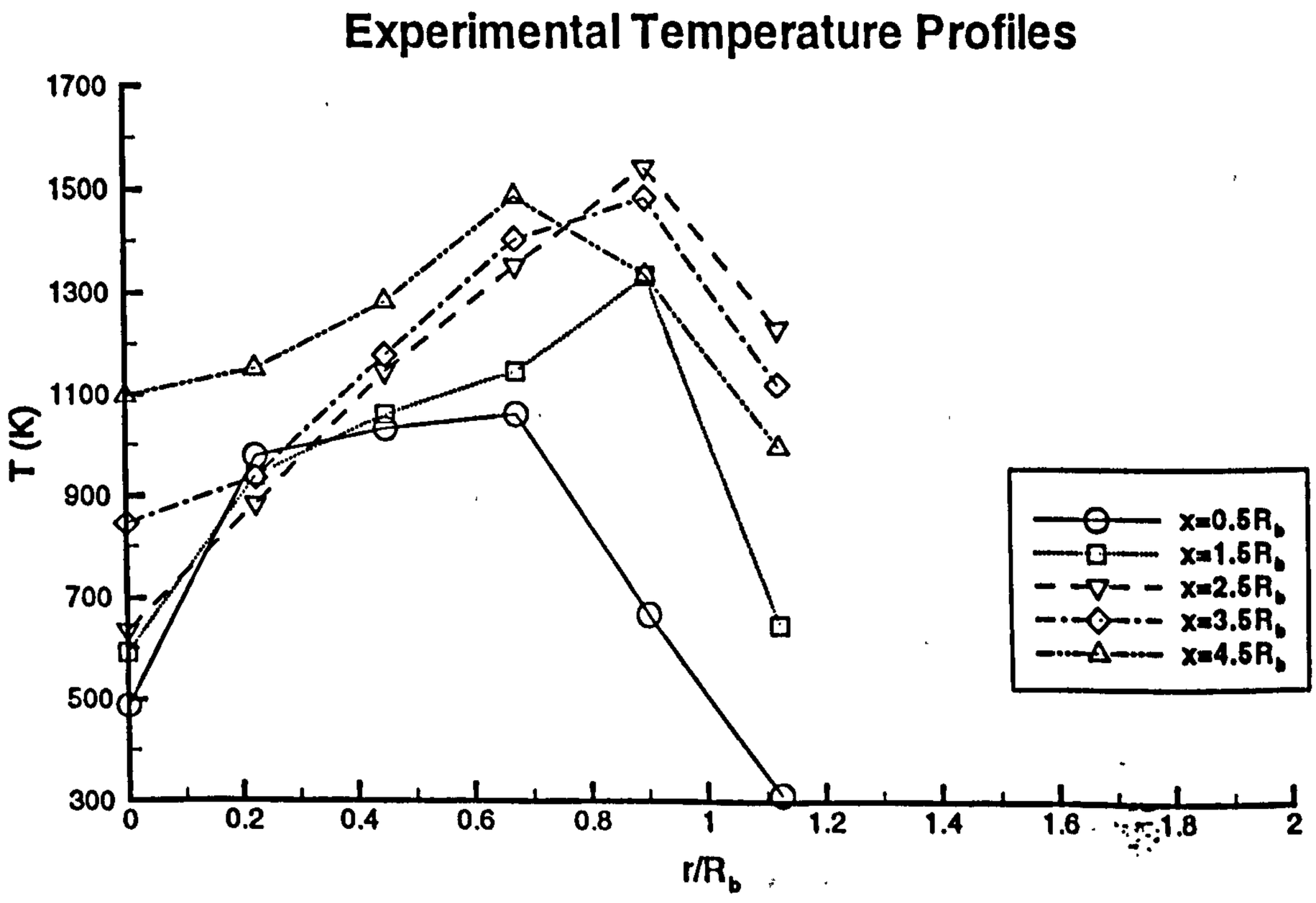

Figure 6.16: Experimental temperatures.

6.5 CFD SIMULATIONS

The previous section presented the experimental results which yielded a good representation of the flowfield and a rather more qualitative temperature field. In the present section, the CFD predictions are compared with the experimental results, and the performance of the cubic turbulence model is assessed relative to the other EVM's utilised in previous chapters.

The turbulence closures used are the standard k-ε, RNG, LS and CRY models and the flame-sheet combustion model was employed in conjunction with a β-pdf which is designed to account for interactions between turbulence and chemistry (these models are depicted in Chapter 2). The Reynolds Stress Model in Fluent is not used for comparative purposes because Dally et al (1995) reported that in isothermal bluff-body flows, it did not improve results relative to the standard k-ε model. The general CFD setup is described as follows:

- Inlet boundary conditions for U, k and ε were obtained from Fluent simulations of fully-developed pipe and annulus flows, using the standard k-ε model. It was assumed that $\tilde{\varepsilon} \approx \varepsilon$ at the inlet because the radial variation of $k^{1/2}$ was not excessive.
- The wall and exit boundary conditions are those described in Chapter 3.
- The domain length was taken as L = 0.3m, which is much further from the inlet than the visible flame height. The effect of using a longer domain, L = 0.45m, was explored; figures 6.17 to 6.22 revealed that this afforded no improvement.
- The densities and dynamic viscosities of air and methane are given in table 6.1. Despite the large temperature range encountered in the simulations, a constant laminar viscosity (taken at ambient conditions) was assumed throughout the flow field. This action is justified by the fact that the turbulent viscosity is much larger than its laminar counterpart, regardless of temperature.
- Grid independence was assessed using the k-ε and CRY models by (a) comparing radial profiles of U and k at the axial locations x = 0.05m and x = 0.15m (figures 6.17, 6.18, 6.20 and 6.21), and (b) examining plots of the normalised stream function to gauge whether the main flow features are dependent on the grid (figures

6.19 and 6.22). As a result, 60×90 and 60×85 meshes were employed for the CRY (and LS) and k-ε (and RNG) models, respectively.

6.5.1 Results

Examination of the computed stream functions (figure 6.23) is instructive because it highlights the differences between model predictions. All the linear EVM's (i.e. k-ε, RNG and LS models) predict main recirculation regions of very similar dimensions. This is also true for the small recirculating area immediately behind the bluff-body face (from $r/R_b = 0.1$ to $r/R_b = 0.5$) and for the separated flow behind the step (from $r/R_b = 1.5$ to the wall). The central fuel jet is seen to be broken down by the main recirculation region at x/R_b = 0.8, 1.0 and 1.3 for the k-ε, RNG and LS models, respectively. In contrast, the cubic turbulence model predicts much longer main and central recirculation zones, and the central fuel jet extends to x/R_b = 3.3. The comparison between experimental and computed values of mean U, V, k, $\overline{u'v'}$, $\overline{u'^2}$, $\overline{v'^2}$ and T is presented in the form of a series of radial profiles at the axial locations x = $0.5R_b$, $1.5R_b$, $2.5R_b$, $3.5R_b$ and $4.5R_b$ (figures 6.24 to 6.32).

Figure 6.24 reveals that all the turbulence models significantly overpredict the axial velocity in the annular air jet. As far as the main recirculation region is concerned, only the CRY model predicts the correct U profile at $x = 0.5R_b$; everywhere else, this area is not accurately computed by any model. Importantly, only the nonlinear model returns the correct centreline trends up to a point between $x = 2.5R_b$ and $x = 3.5R_b$, where the predicted fuel jet is completely eroded. The profiles at $x = 1.5R_b$ also indicate that the nonlinear model predicts a wall-stagnation point further downstream than the other models. Trendwise, the CRY model clearly returns the best results in the region $0.5R_b < x < 2.5R_b$. A glance at the mean radial velocities (figure 6.25) reveals no consistent trends. This is not surprising since V (which is an order of magnitude smaller than U) is heavily influenced by the U distributions which are seen to vary considerably. At $x = 3.5R_b$ and $x = 4.5R_b$, all the linear EVM's forecast very large negative velocities in the area corresponding to the main recirculation region. Interestingly, the RNG and LS models predict identical U profiles which differ noticeably from those computed

with the standard k-ε model. The same trend is observed in the V profiles, although differences between RNG and LS results do exist.

Definite trends are evident in the turbulence energy profiles (figure 6.26). At x = $0.5R_b$ and x = $1.5R_b$, all turbulence models predict a peak k either side of the annulus air jet where the gradient $\partial U/\partial r$ appears to be largest. Further downstream, the level of the outer peak drops significantly relative to that closer to the centreline. This is due to the annulus jet expanding outwards after x = $1.5R_b$ (this is particularly clear in figure 6.9) and the presence of smaller cross-stream U gradients for r/R > 0.8, which is in turn a result of the reattachment of the layer which separates from the wall at the inlet step. (see figure 6.24). Apart from the location x = $0.5R_b$, all turbulence models predict relatively flat profiles across the main recirculation region and centreline area. The k-ε model is seen to consistently return the highest levels of k; the RNG and LS profiles are very similar to each other (except at x = $0.5R_b$) and lower than the k-ε curves. The nonlinear model predicts the lowest levels of k and is generally in line with experimental values (which are obtained from the normal stresses using equation 4.7). The experimental turbulence energy at the centreline is inaccurate for the reasons stated in section 6.4.4.2

Figure 6.27 indicates that the computed shear stress profiles are strongly related to the turbulence energy distributions in the annulus region. Peaks of $\overline{u'v'}$ are seen to occur either side of the annulus jet for the linear EVM's, particularly at the first three axial locations. The radial location of the distinct inner peak, near r/R = 0.5, coincides with the point at which $\partial U/\partial r$ and k are highest for the k-ε, RNG and LS models. The k-ε model is seen to generally predict the largest magnitudes of $\overline{u'v'}$. In contrast, the CRY model predictions for $\overline{u'v'}$ are much lower and more faithful to the experimental values, compared to the linear EVM's.

All turbulence models generally underpredict $\overline{u'^2}$ in figure 6.28, although the CRY model does this less severely than the k-ε, RNG and LS models. This may be due to the unsteadiness of the actual flow field. The graphs also show that the nonlinear

model is the only one which does not predict negative axial stresses. Figure 6.29 shows the radial Reynolds stresses $\overline{v'^2}$; the performance of the nonlinear model is not much better than the linear EVM's.

Figure 6.30 displays a comparison of the experimental and computed temperature distributions. The profiles near the inlet ($x = 0.5R_b$) show minima at the centreline and at $r/R > 0.6$ since these are the locations where the cold reactants enter the combustor. Temperatures are elevated in the region $0.05 < r/R < 0.6$ due to combustion effects. All turbulence models generally resolve these trends, but to different degrees of accuracy. At $x = 0.5R_b$ at the centreline, the nonlinear model is seen to underpredict the experimental temperature by the largest amount. As one progresses downstream, the CRY model returns the slowest rate of increase of centreline temperature. Throughout the region behind the bluff body ($0.05 < r/R < 0.6$), all turbulence models are seen to either over- or underpredict the temperature significantly. The exact trend depends upon whether or not the centreal fuel jet is predicted to exist at that location. For example, the linear EVM's overpredict T at $x = 0.5R_b$ whilst the CRY model does so up to $x = 2.5R_b$. Once the main recirculation region extends to the centreline, all models underpredict the temperature. It is interesting to note that the CRY model predicts the maximum temperature at the radial point at which the mean axial velocity, turbulence energy and shear stress are all small. This is not evident in the case of the linear EVM's.

Although no experimental data was obtained for species concentrations, the computed mixture fraction contours reflect the diverse performance of the turbulence models. Figure 6.31 reveals that the mean mixture fraction distributions are rather similar for the three linear EVM's. The principal differences are the points at which the stoiciometric controur ($f = 0.05482$) intersects the horizontal axis; the k-ε, RNG and LS models compute this location as $x/R_b = 0.9$, 1.1 and 1.4, respectively. The cubic model calculates a rather different distribution, with the above point located at $x = 3.5R_b$. It is worth noting that the intersection of the stoichiometric contour with the centreline coincides with the location at which the central fuel jet is fully eroded, due to the low stoiciometric mixture fraction of methane.

6.5.2 Discussion

The focus of the ensuing discussion is accounting for the variations in performance of the turbulence models investigated. A second issue regards the very poor temperature predictions of all the turbulence models.

Prediction of the flowfield was seen to depend on the turbulence model employed. All EVM's returned similar trends whilst the cubic model yielded considerably different results. An examination of the computed Reynolds shear stresses (figures 6.32 and 6.33) provides a clue as to the origin of these differences. Figure 6.32 indicates that the maximum shear stresses are smaller for the RNG model than in the case of the k-ε model, thereby accounting for the divergence in radial U profiles (figure 6.24) The RNG and LS plots of $\overline{u'v'}$ are rather more similar, which explains why the U profiles for these two models are nearly identical in many cases. Figure 6.33 reveals that the CRY model, on the other hand, predicts much lower shear stresses in the bulk of the flow. This explains the elongated main recirculation region and longer central fuel jet. However, it is not initially clear which mechanism causes this significant moderation of $\overline{u'v'}$. In the case of the RNG model, the shear stresses are reduced (relative to the standard k-ε model) by the mechanism explained in Chapter 4 (section 4.2.3). The LS model seems to acheive similar results by using damping functions whose operation is clearly not confined to near-wall areas (see figure 6.34). In the case of the cubic model, several factors can give rise to the low stresses witnessed in figure 6.33.

The first of these mechanisms is the damping function f_μ (whose purpose is the same as that in the LS model). Figure 6.34 is a contour plot of f_μ for both the LS and CRY models; it reveals that the cubic model f_μ predictions deviate significantly from the turbulent Reynolds number limit of unity in areas far from the wall, particularly along the centreline. This behaviour was also observed in the unconfined burner simulations in Chapter 5, and can be explained by the presence of lower gas densities upon which the turbulent Reynolds number (Re_t) depends. Whilst the same effect is apparent in the LS model, the region of influence is considerably smaller, mainly because the reaction

zone was seen to broadly follow the contours of the dominant fuel jet. Since the low values of f_μ coincide with the elongated central fuel jet, it seems clear that this contributes to the reduced shear stresses in this region.

Figure 6.35 is a contour plot of the strain-dependent term C_μ which is constant (approximately 0.09) for the linear EVM's, but defined in equation 2.35 for the nonlinear model. Whilst the bulk of the principal recirculation zone is characterised by $C_\mu \approx 0.1$, it is interesting to note that the value of C_μ is much lower (≈ 0.03) along the inside of the annular jet. This has the effect of moderating the shear stresses in an area which should contain a significant shear layer, thereby allowing the central recirculation area to extend much further downstream. These findings also account for the abrupt change in U profile at $x = 0.5R_b$ to $x = 2.5R_b$ (figure 6.24) and the very low turbulence energy and shear stresses (figures 6.26 and 6.27).

The final factor which could influence the shear stresses in the CRY model is the contribution of the nonlinear terms in the cubic stress/strain relationship (equation 2.32). Figure 6.36 maps out these nonlinear terms; the nature of the plot suggests that they are strongly influenced by local events. Careful examination reveals that the predominant contours are numbers 7 to 9. Although the associated values are small, they are of the same order of magnitude as the total stresses in figure 6.33. Thus the nonlinear terms form a significant portion of the total shear stresses computed by the CRY model. Whilst it is not possible to separate the individual contributions of f_μ, C_μ and the higher-order terms, the above discussion regarding the cubic model has shown that all the factors mentioned participate in the modification of shear stress.

The previous section revealed that the temperature predictions tended to deviate significantly from experimental values. As seen below, this discrepancy is explained by the interactions between turbulence and chemistry, the latter being modelled such that it depends entirely on mixture fraction distributions. Masri (1996) noted that since methane has a low stoichiometric mixture fraction ($f_{st} = 0.05482$), the reaction zone of the resulting flame tends to lie outside the fuel jet. This agrees with the experimental observations of section 6.4. In fact, the present reaction zone is very broad because small, yet sufficient, quantities of methane are transported throughout the flow-field.

This spreading of the fuel is enhanced by the complex flow, as seen in figure 6.31, where the stoichiometric contour computed by each turbulence model actually bisects the predicted principal recirculating region. Clearly the mixture fraction contours depend entirely on the flow-field predictions, and hence on the turbulence models. Accurate mixture fraction predictions do not, however, guarantee correct temperature distributions. This is entirely due to the turbulence/chemistry interaction model, in this case the 'β' probability density function. Whilst this assumed distribution yielded adequate results for the simpler, fuel-jet dominated flame simulated in Chapter 5, in the present case it clearly cannot cope with the complex flow-field. The flame-sheet combustion model assumes that temperatures are purely a linear function of mixture fraction, whilst the β-pdf modfies this relationship somewhat to help resolve the effects of turbulence. The current flow is so turbulent and complex, however, that thermal transport attains a highly influential role, much more so than in the flame in Chapter 5. For example, the adiabatic flame temperature of methane is approximately 2600K whilst the peak experimental temperature is only 1500K. This is entirely due to the rapid removal of the heat of reaction. It is this additional complication which the β-pdf model fails to account for. Thus even if the turbulence models did yield the correct flow- and mixture-fraction fields, the simulated and experimental data suggests that the β-pdf approach would still not result in accurate temperature predictions.

6.6 SUMMARY

The purpose of this chapter was present the detailed experimental flow-field and temperature measurements and to compare them with the predictions of the various turbulence models, particularly the new cubic model. The main findings are as follows:

- A search of the public literature revealed no experimental velocity data for a confined, bluff-body combustor, thereby suggesting a need for such measurements.
- Such a combustor was designed for use with PIV, although optical techniques for the measurement of temperature and concentrations are also to be used in future work.
- An analysis of the experimental procedure revealed several sources of error which, given additional time and resources, could easily be eliminated. These rectification measures are recommended for further work in Chapter 7. Nevertheless, the current results are of sufficient quality and consistency for comparison with various turbulence model predictions, which is the aim of the investigation.
- The experimental results revealed a highly turbulent, complex flow-field, and the nonlinear turbulence model offered the closest agreement with the experimental data. The standard k-ε model was the most diffusive (highest levels of k and shear stress) whilst the RNG and LS models gave very similar results for all variables.
- The predicted temperature fields were completely dependent on mixture fraction distributions which were in turn a function of the turbulence closure. No turbulence model yielded reasonably accurate temperature predictions.
- An examination of the functions f_μ and C_μ and the nonlinear terms in the cubic stress/strain relationship, indicated that all these factors contributed to the improved results of the cubic turbulence model.
- A discussion regarding the temperature and mixture fraction distributions indicated that the β-pdf turbulence/chemistry interaction model is probably not adequate in complex flows such as the present one.

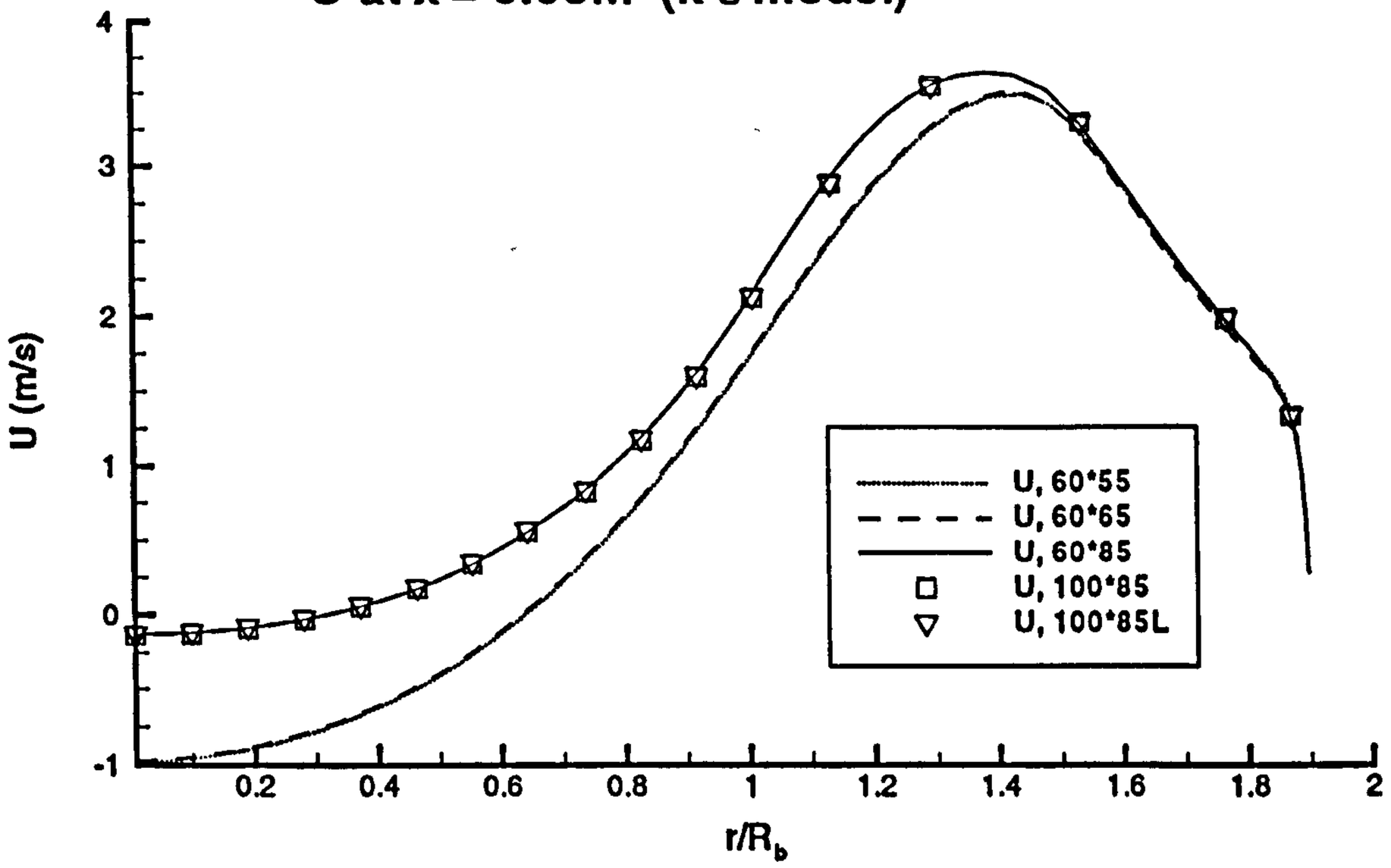

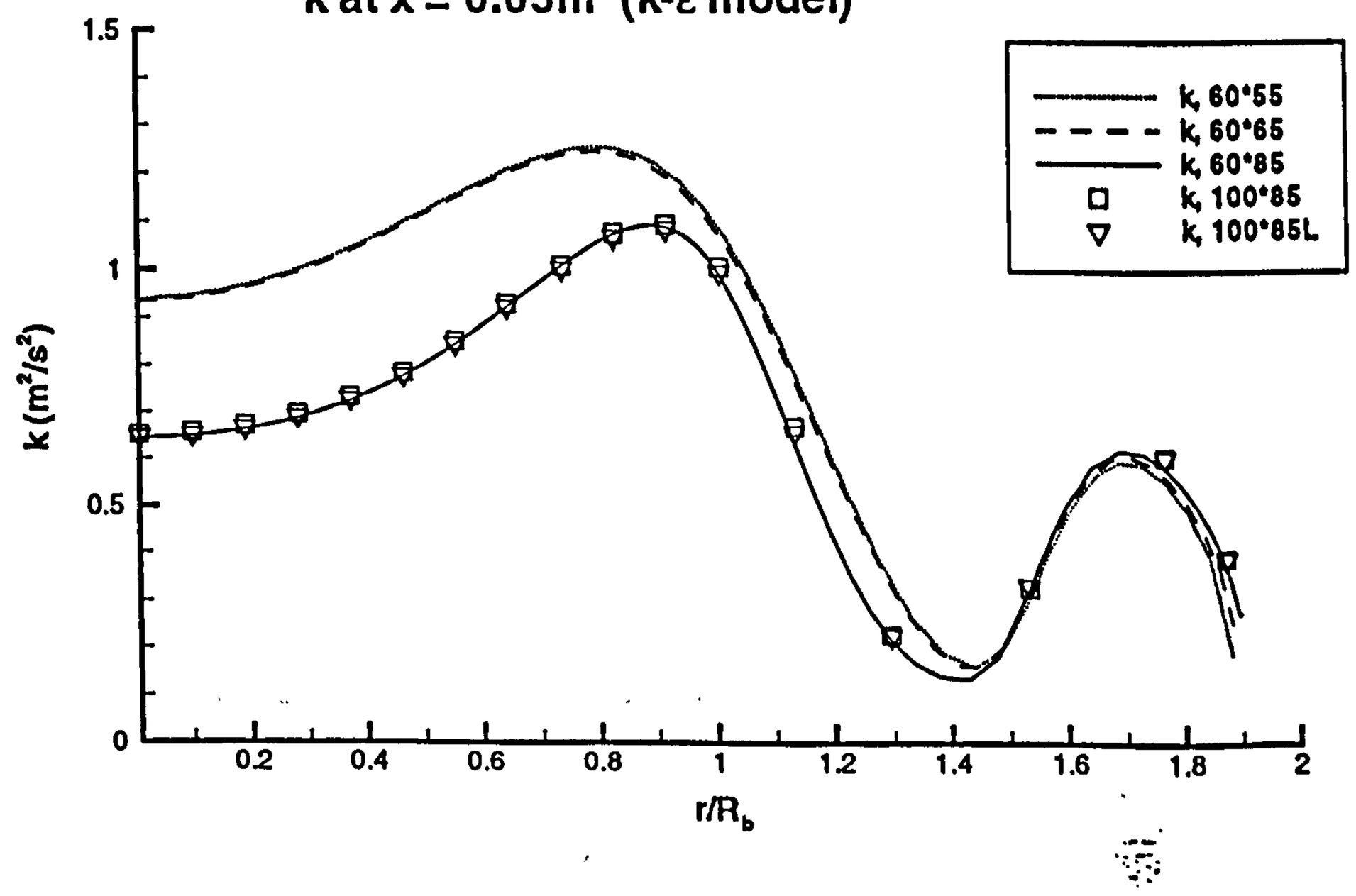

Figure 6.17: Profiles of *U* and *k* using the *k*-ε model. In the legend, L denotes a longer axial domain.

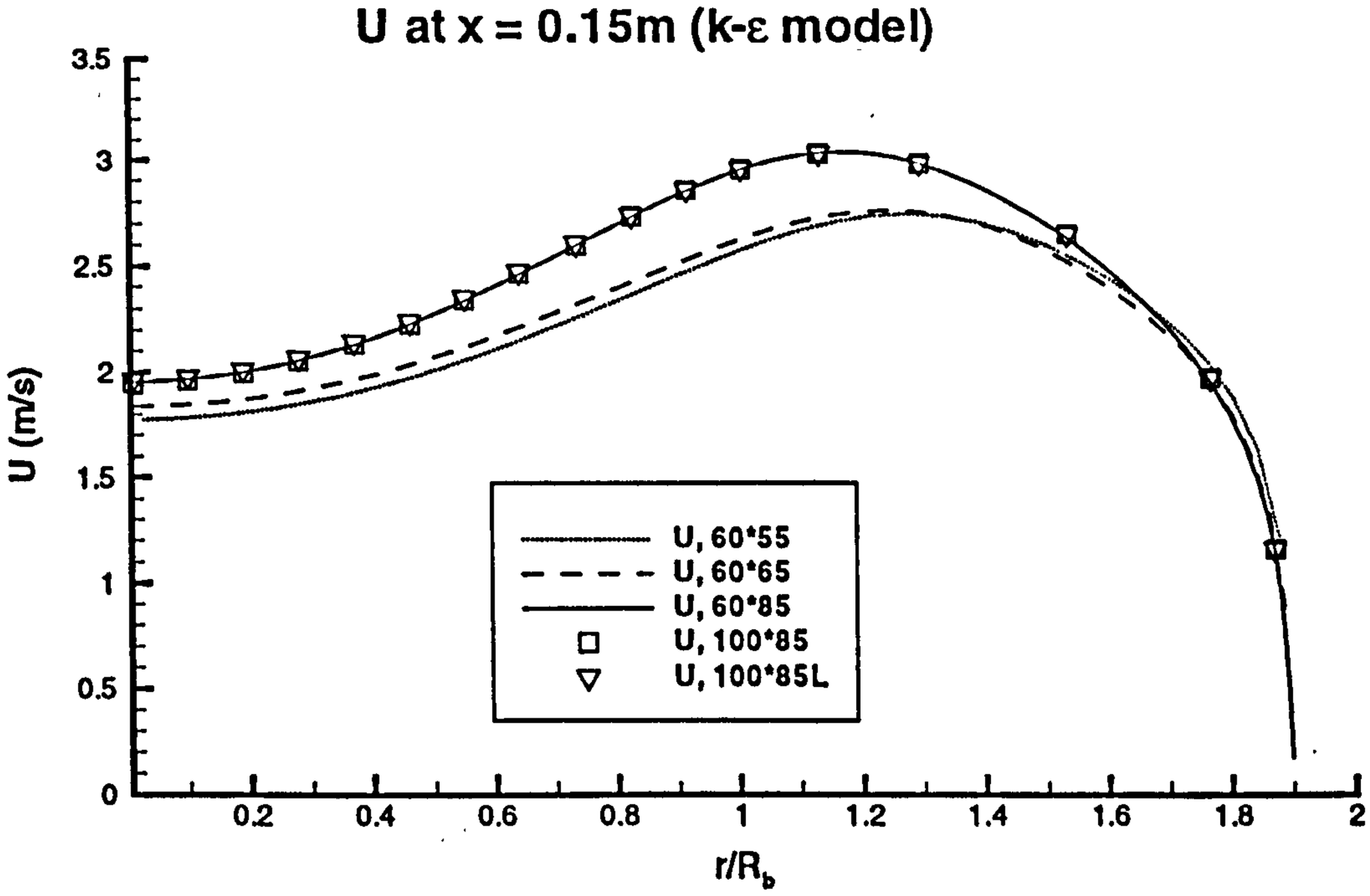

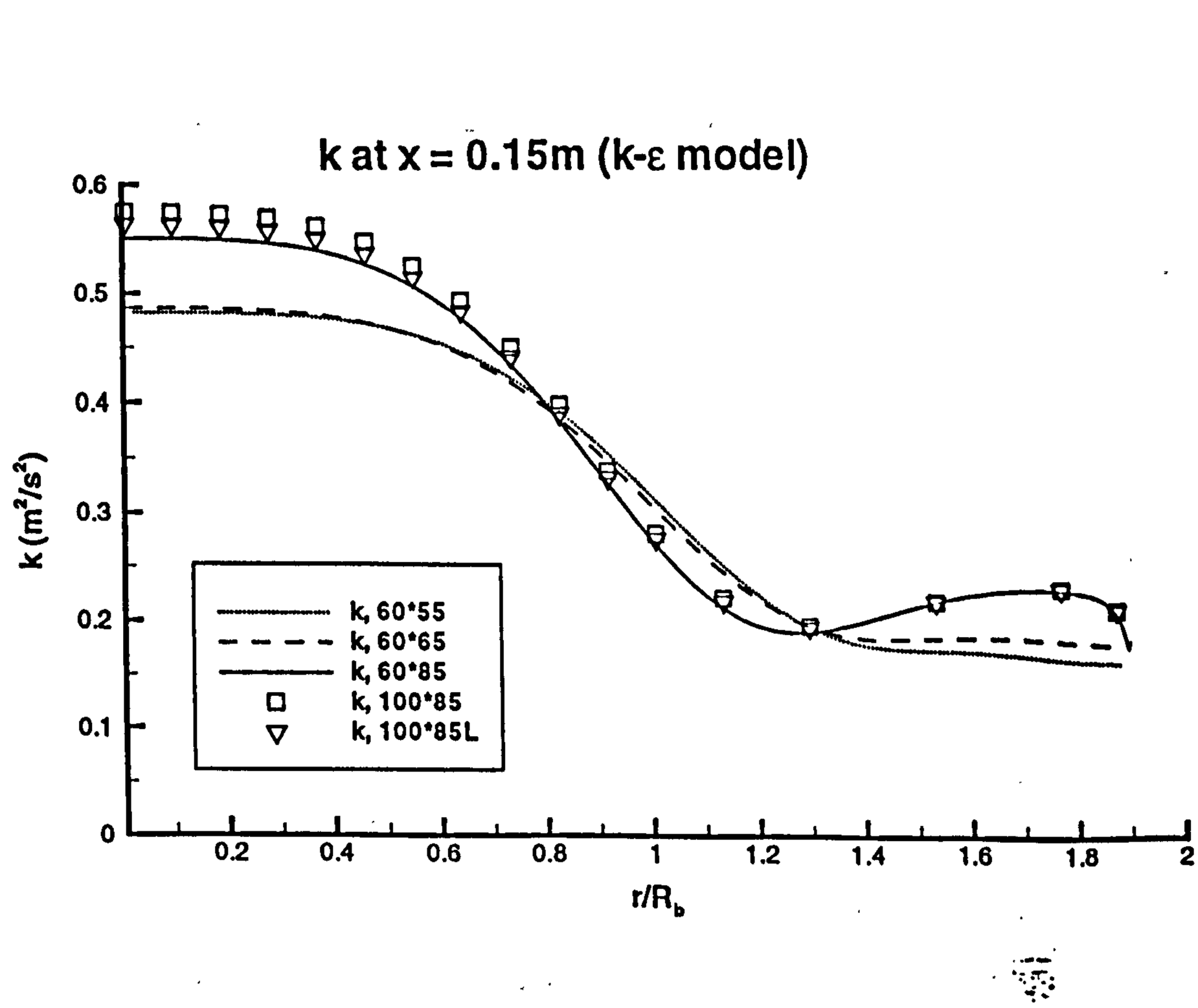

Figure 6.18: Profiles of *U* and *k* using the *k*-ε model. In the legend, L denotes a longer axial domain.

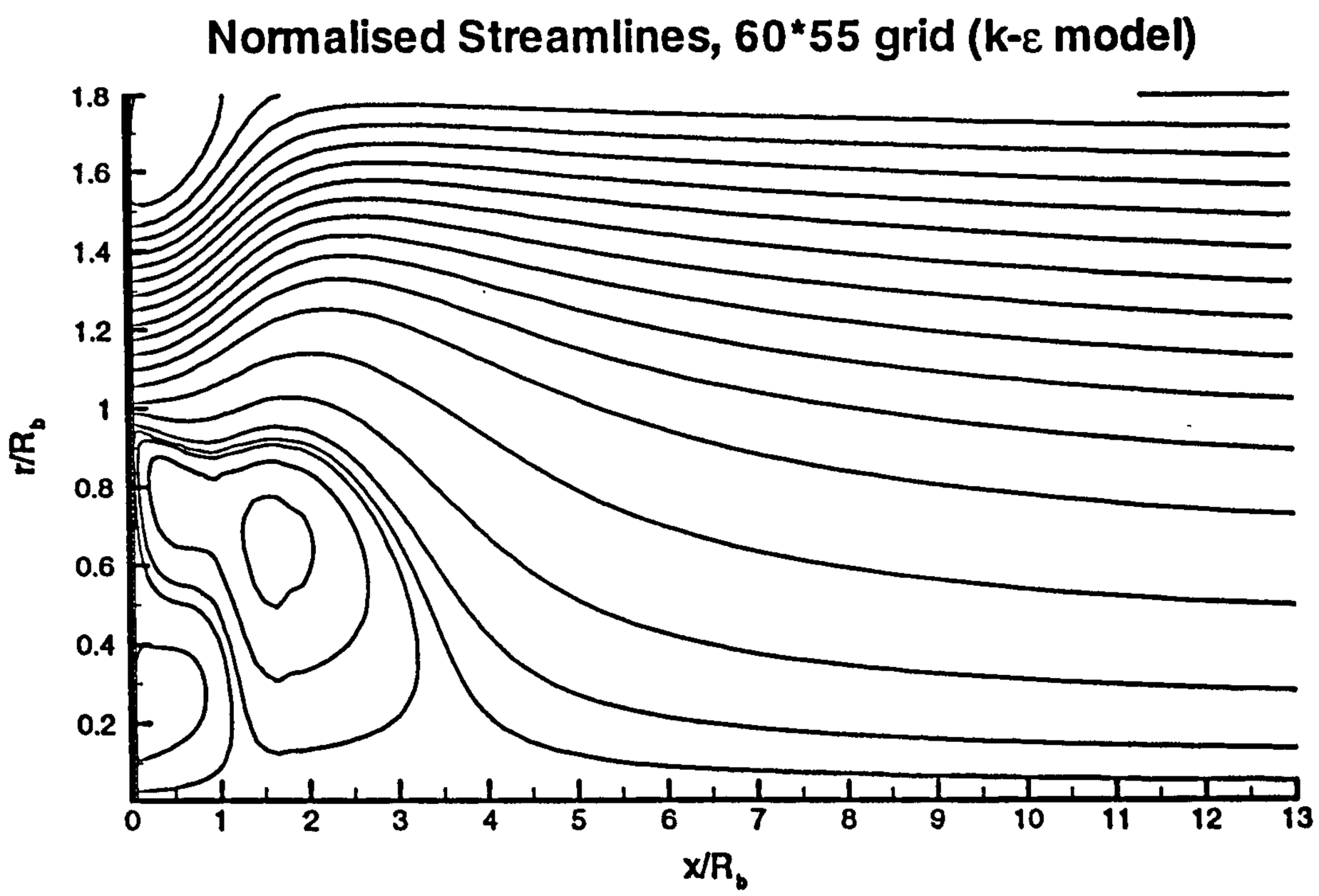

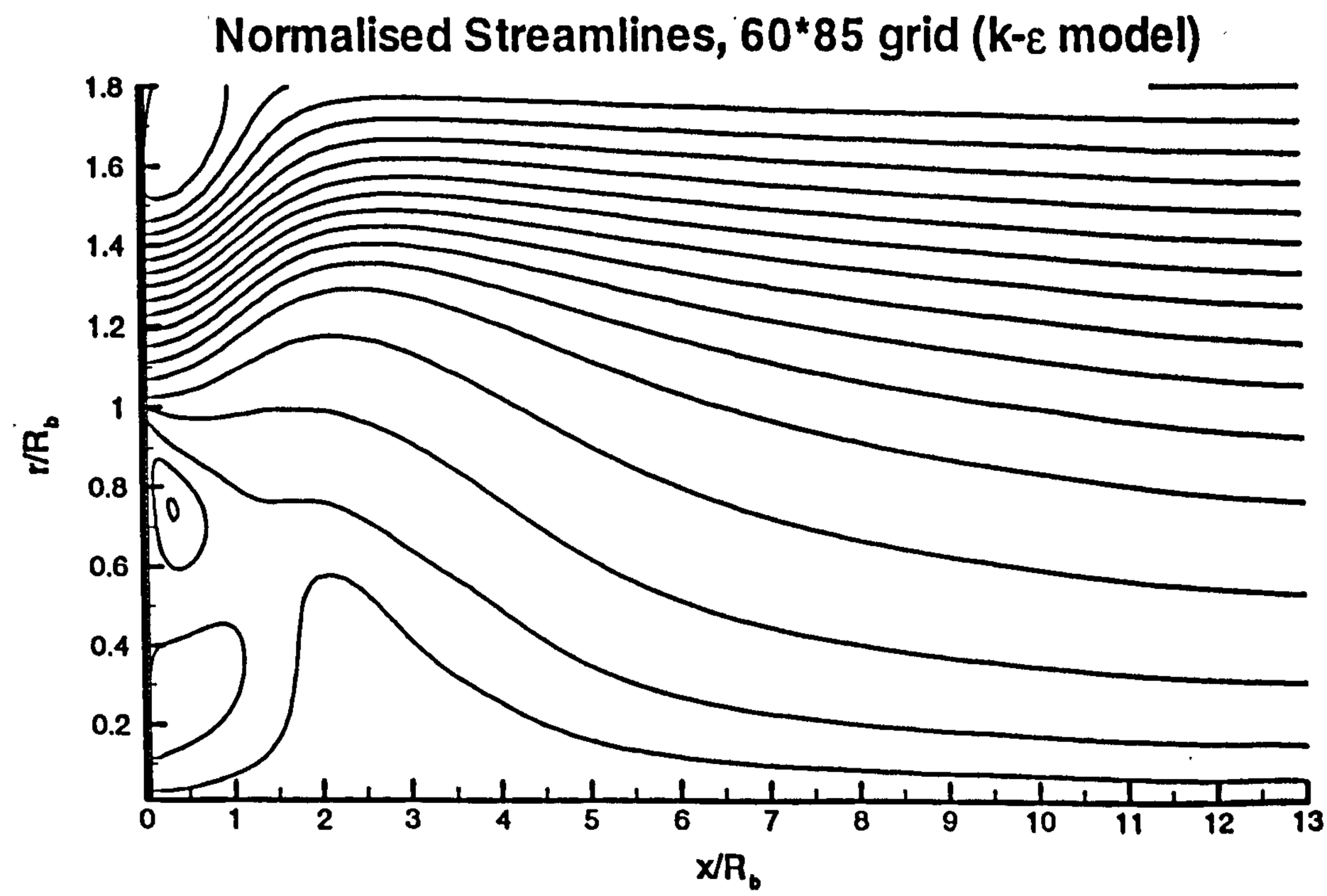

Figure 6.19: Normalised streamlines for various grid sizes.

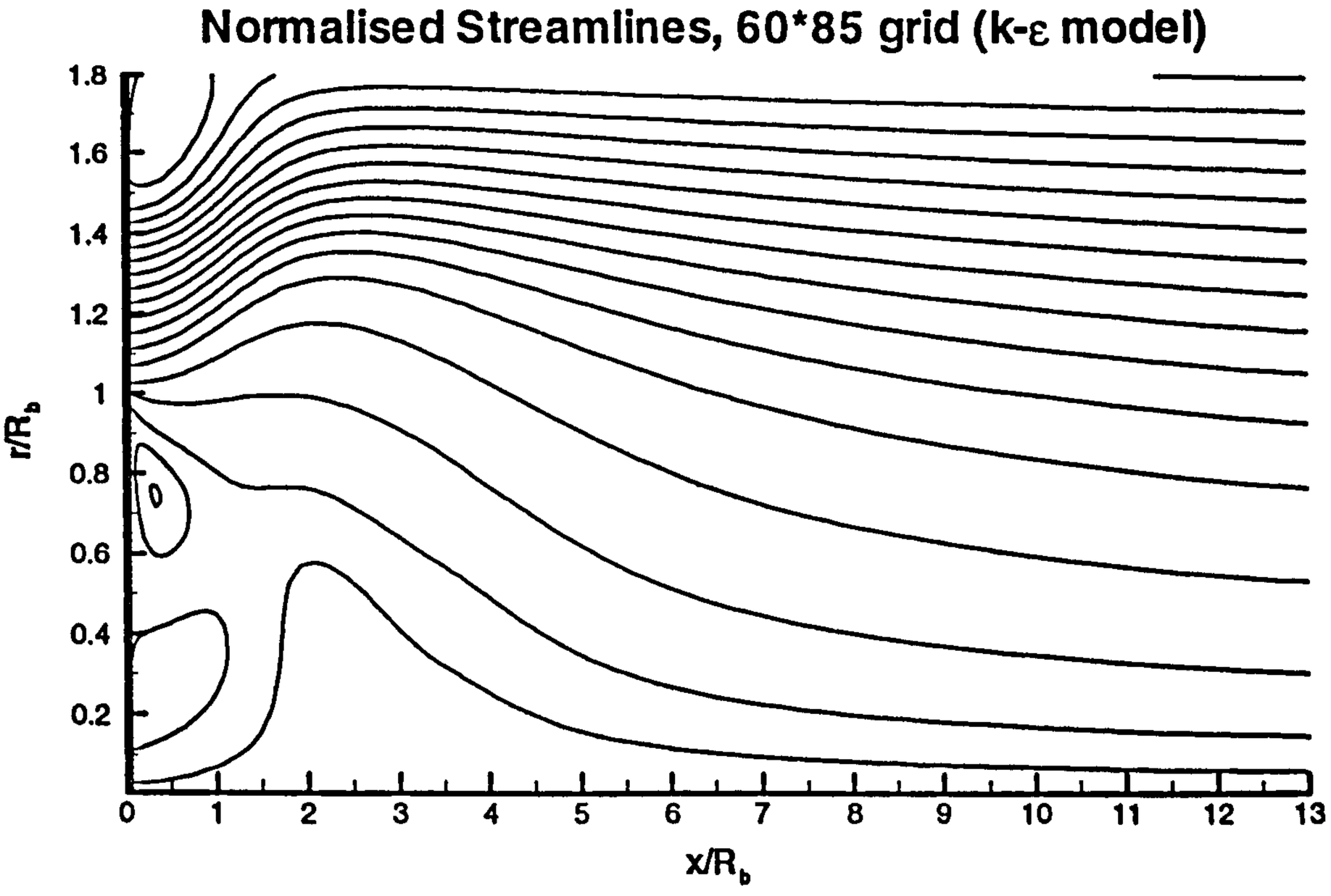

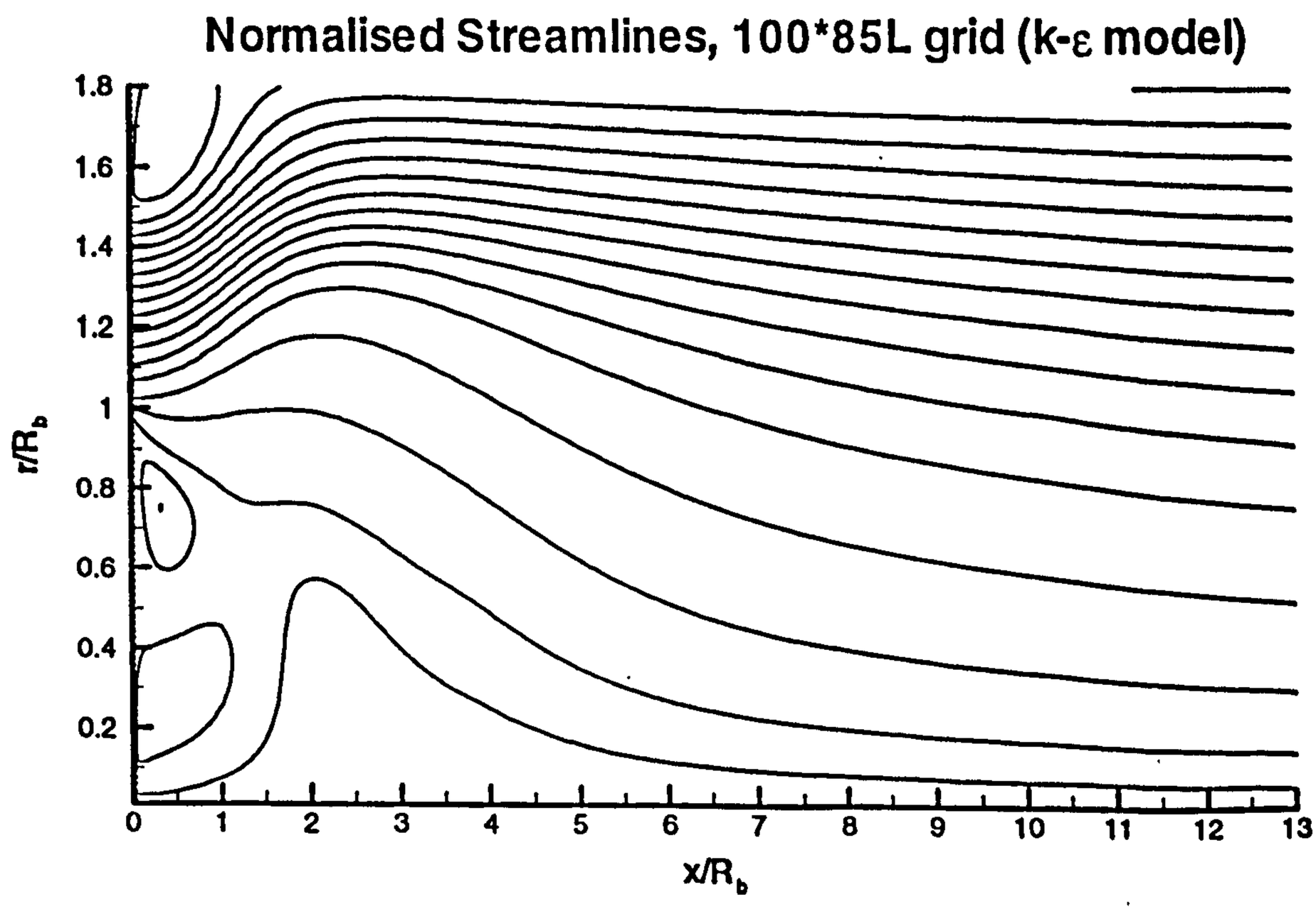

Figure 6.19 - continued.

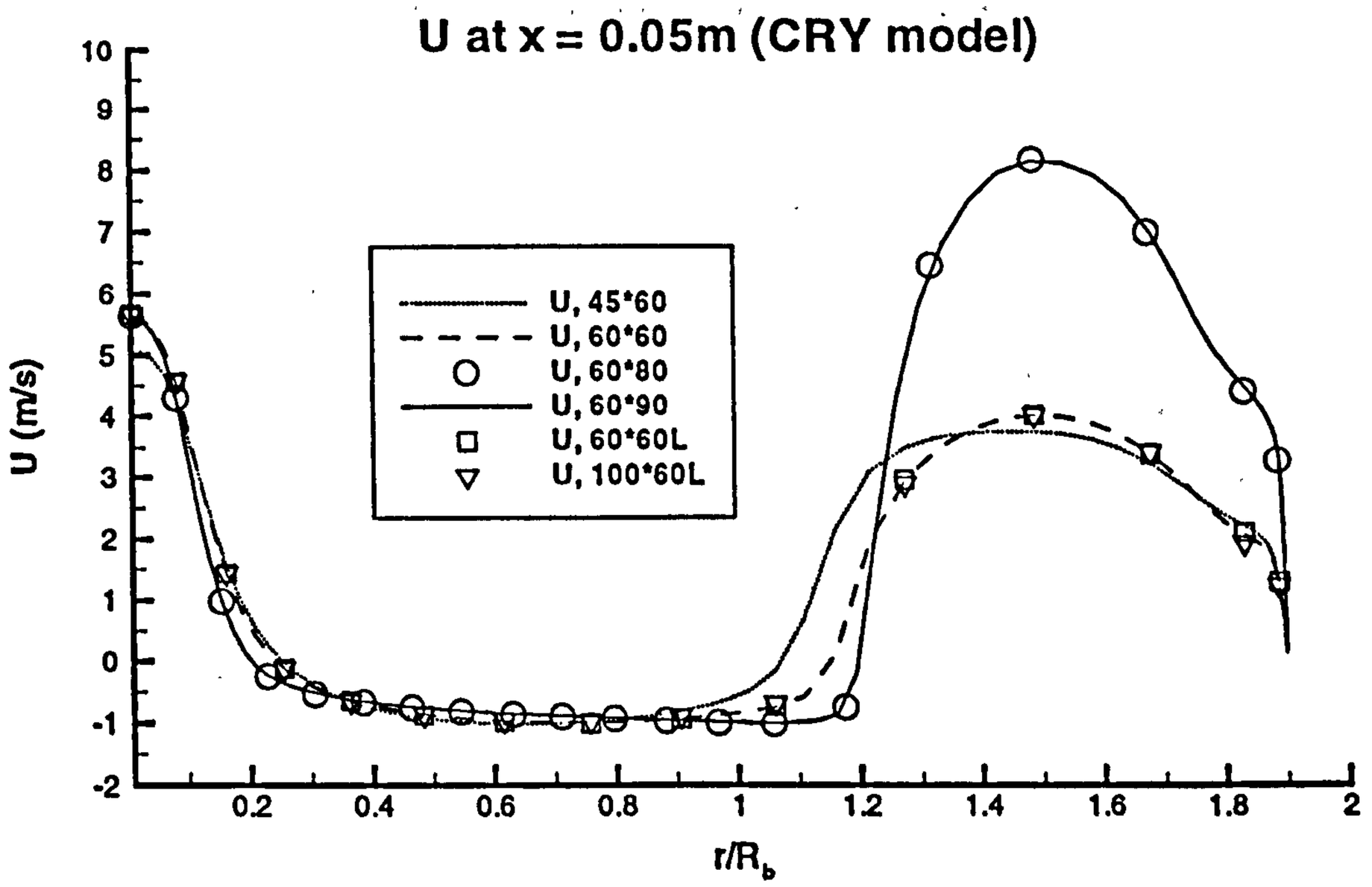

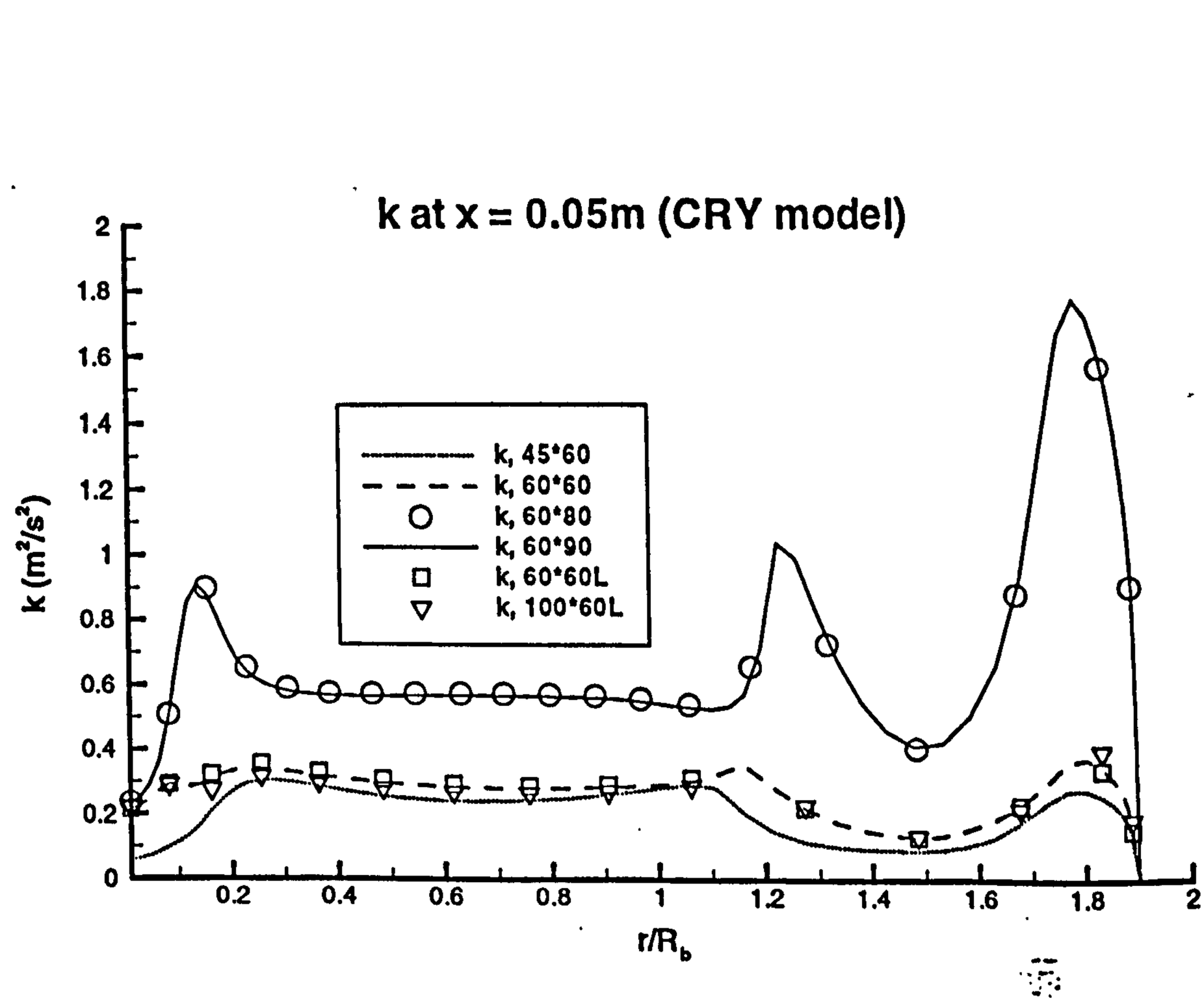

Figure 6.20: Profiles of *U* and *k* using the CRY model. In the legend, L denotes a longer axial domain.

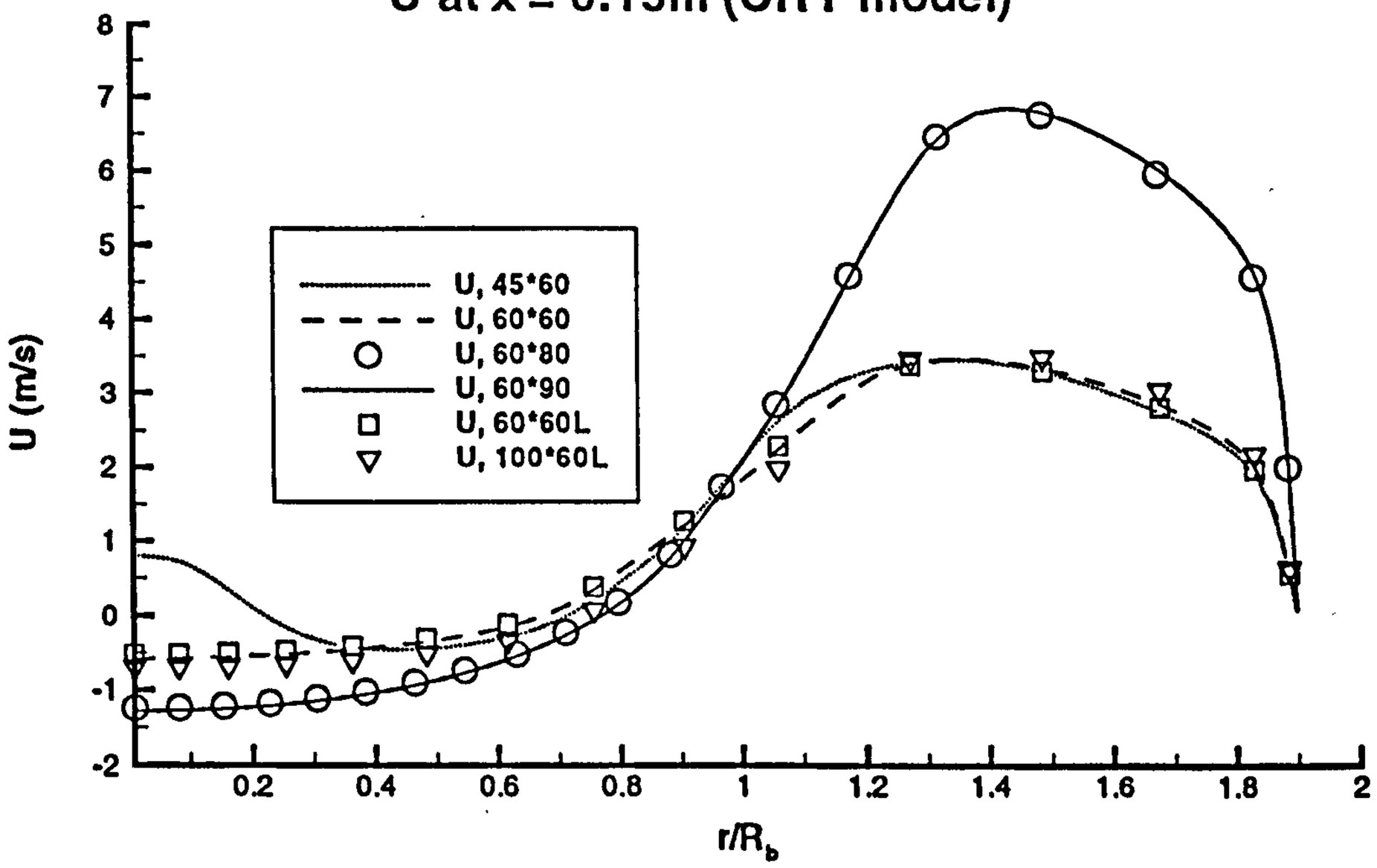

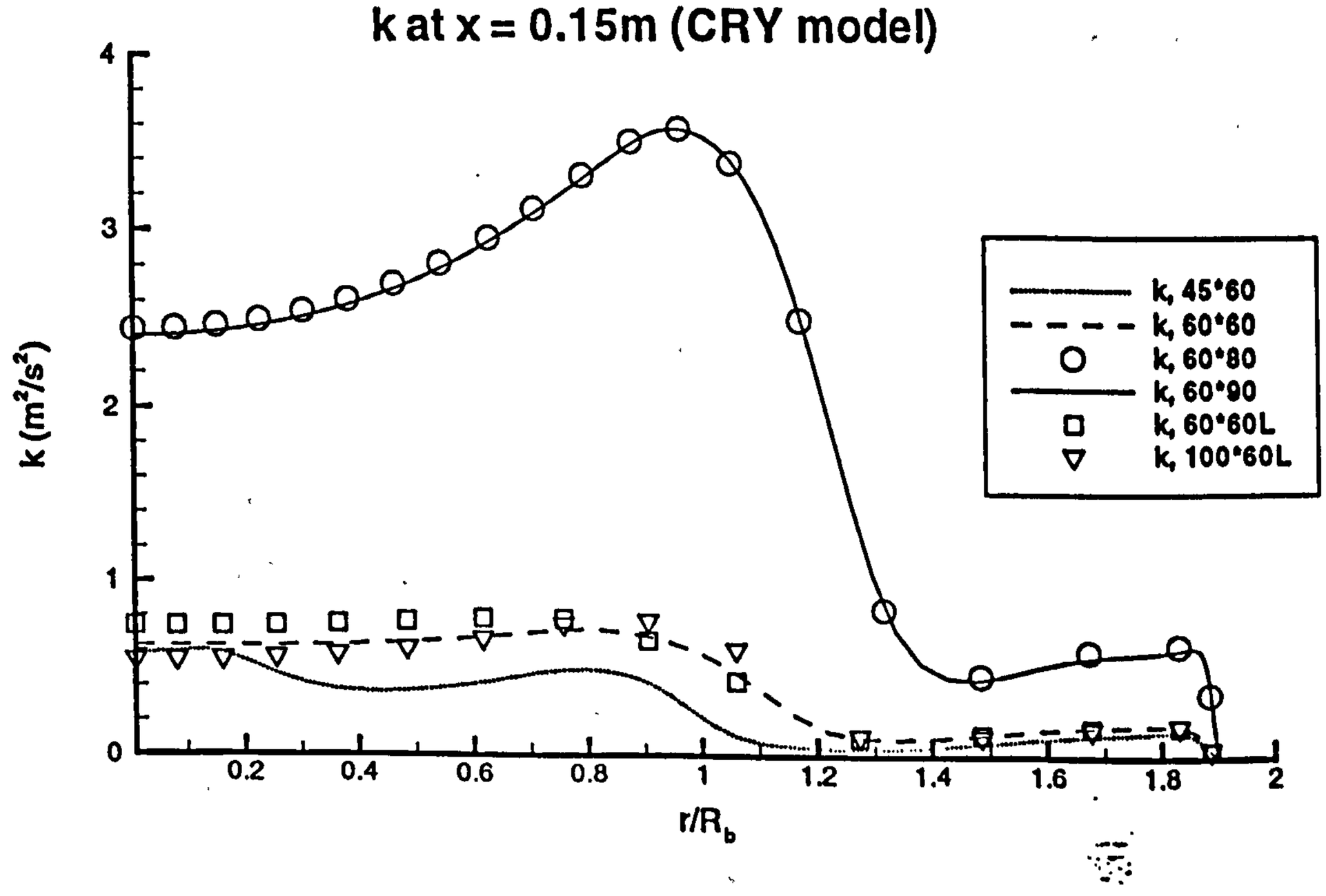

Figure 6.21: Profiles of *U* and *k* using the CRY model. In the legend, L denotes a longer axial domain.

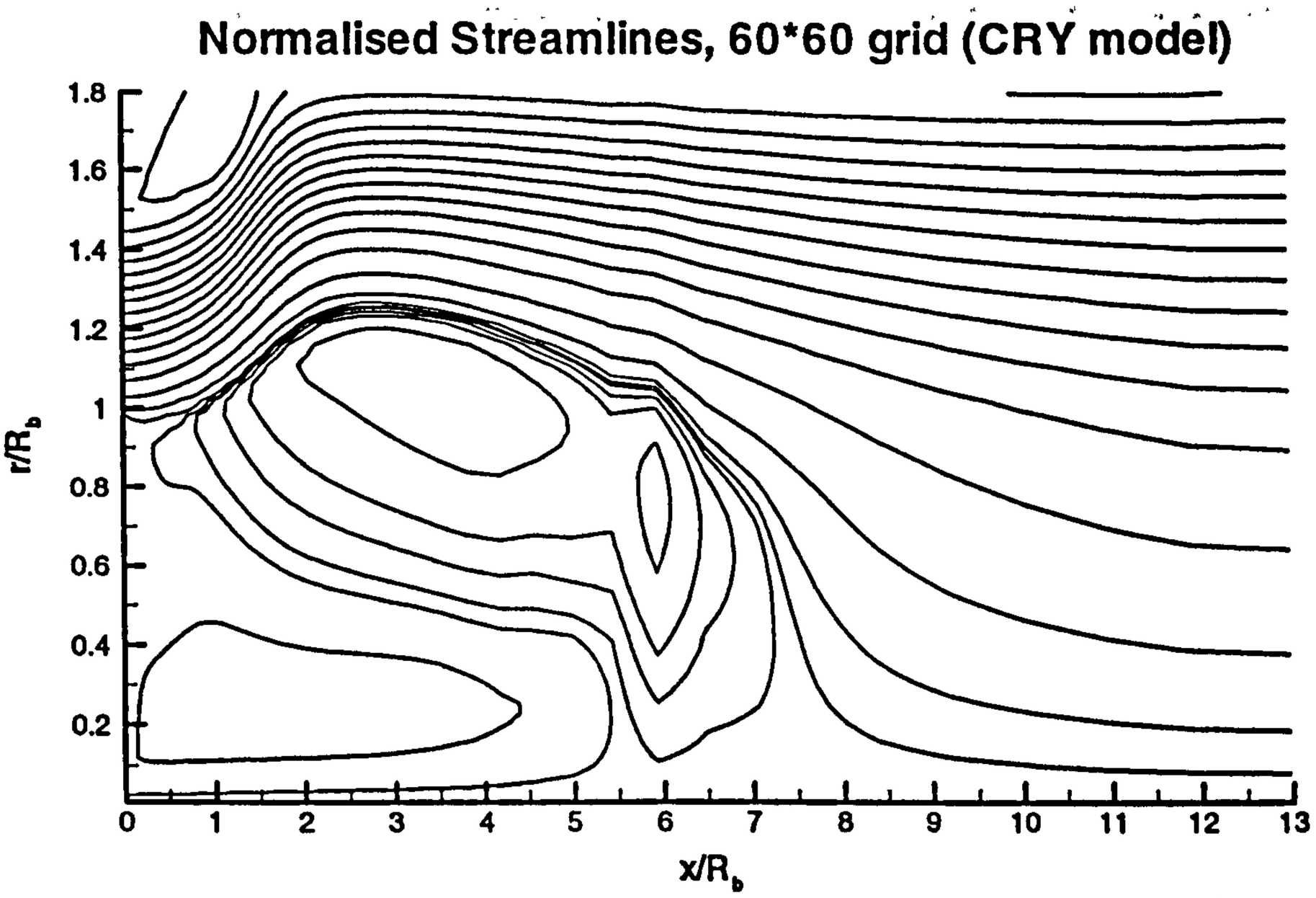

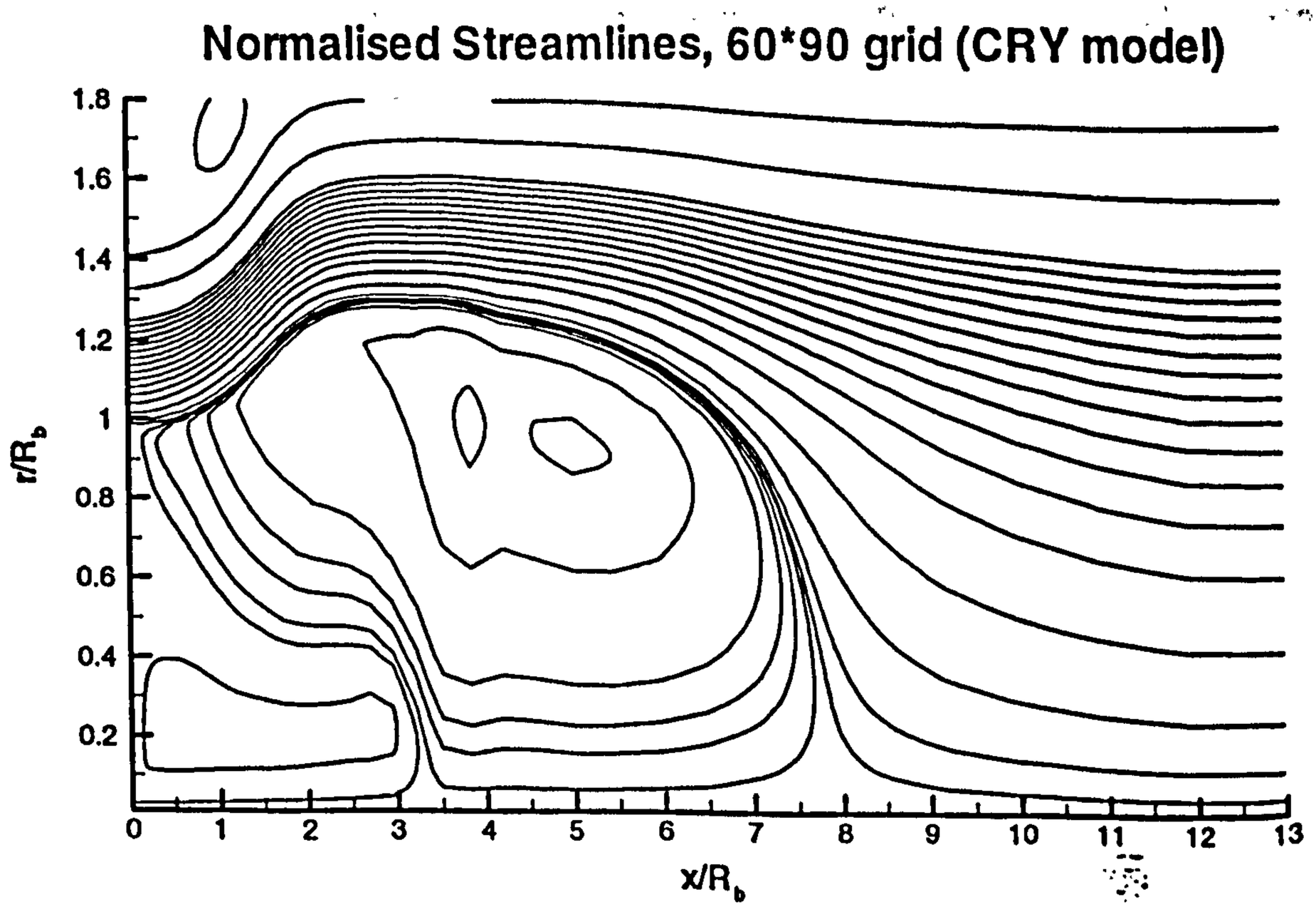

Figure 6.22: Normalised streamlines for various grid sizes.

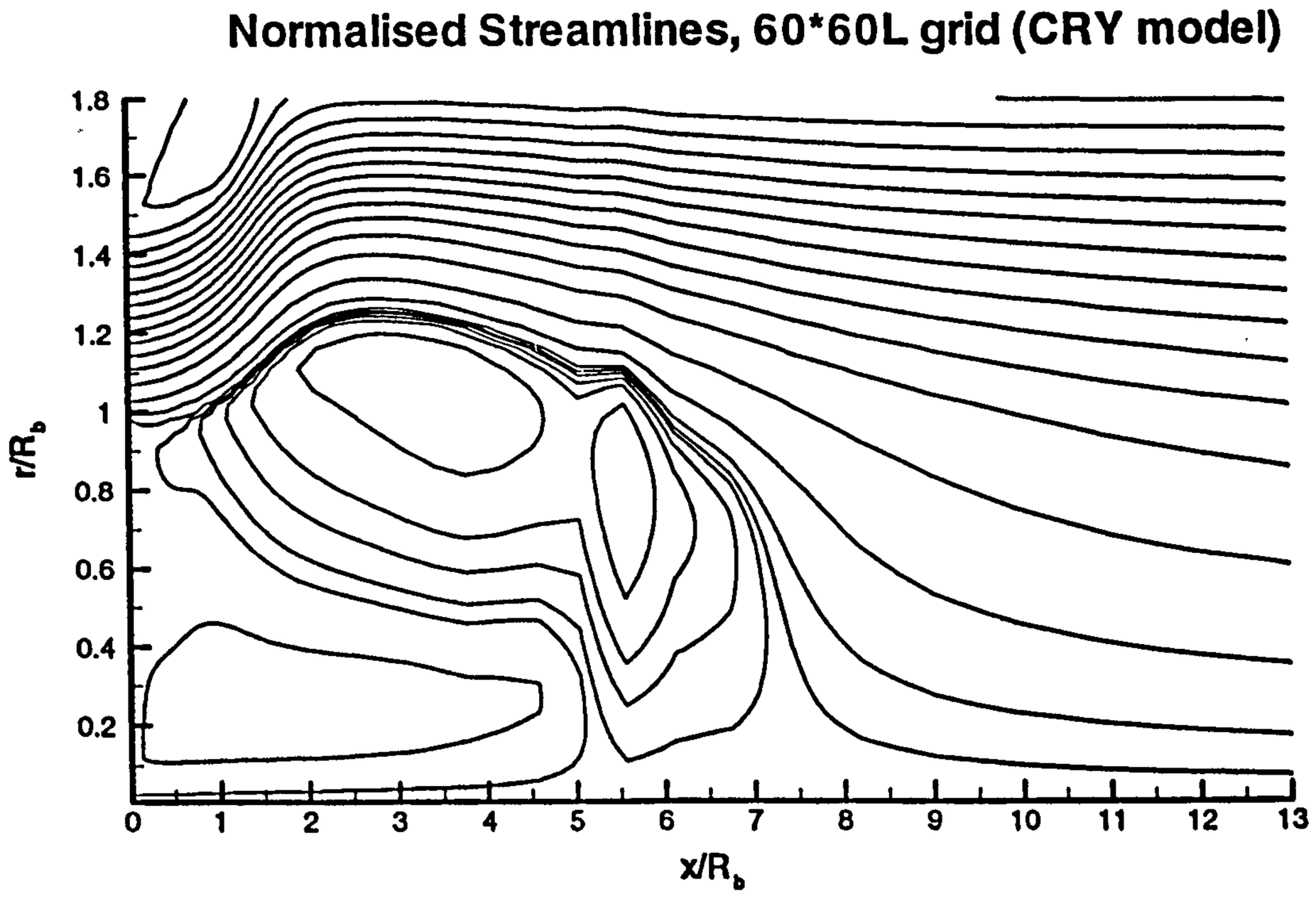

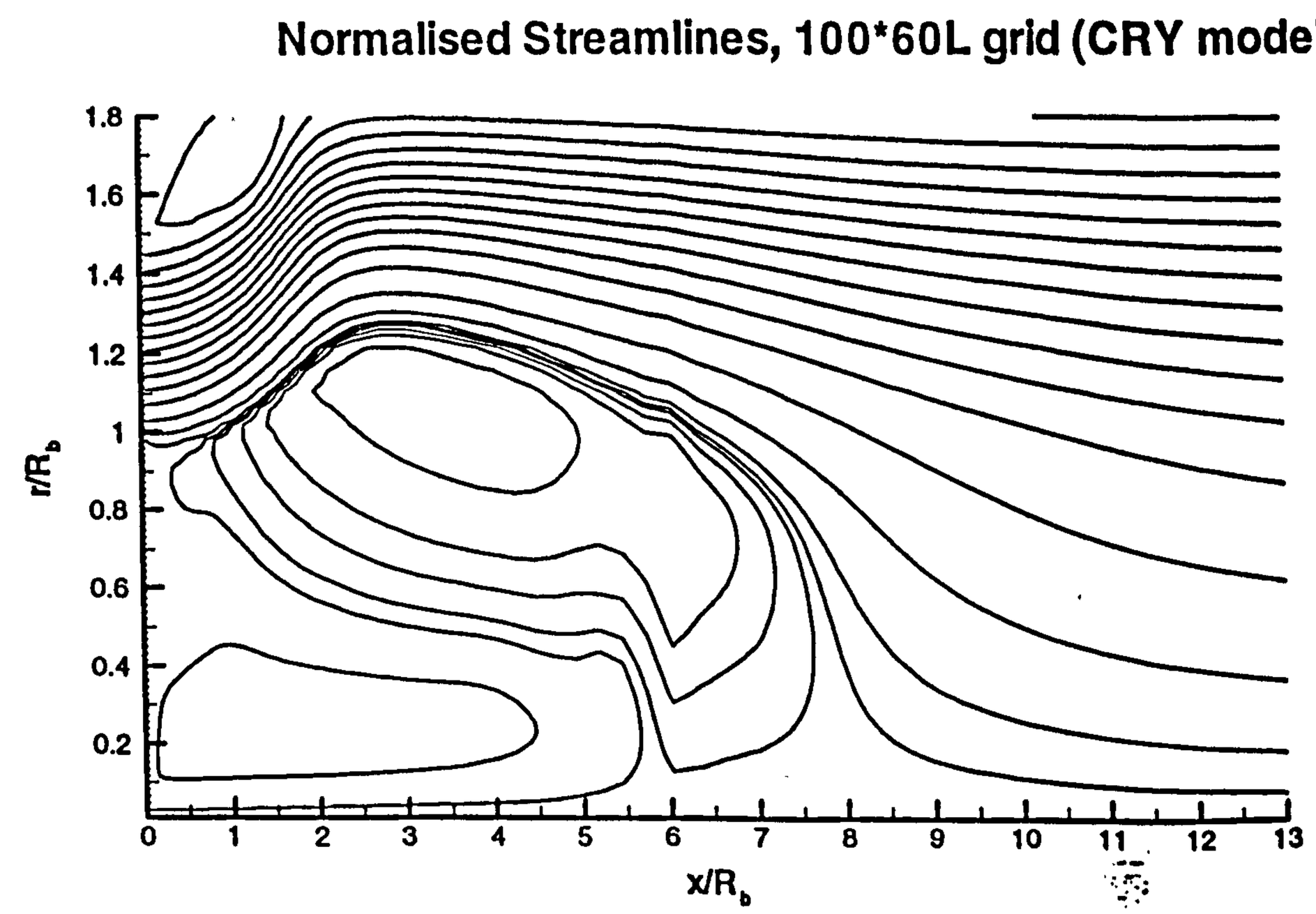

Figure 6.22 - continued.

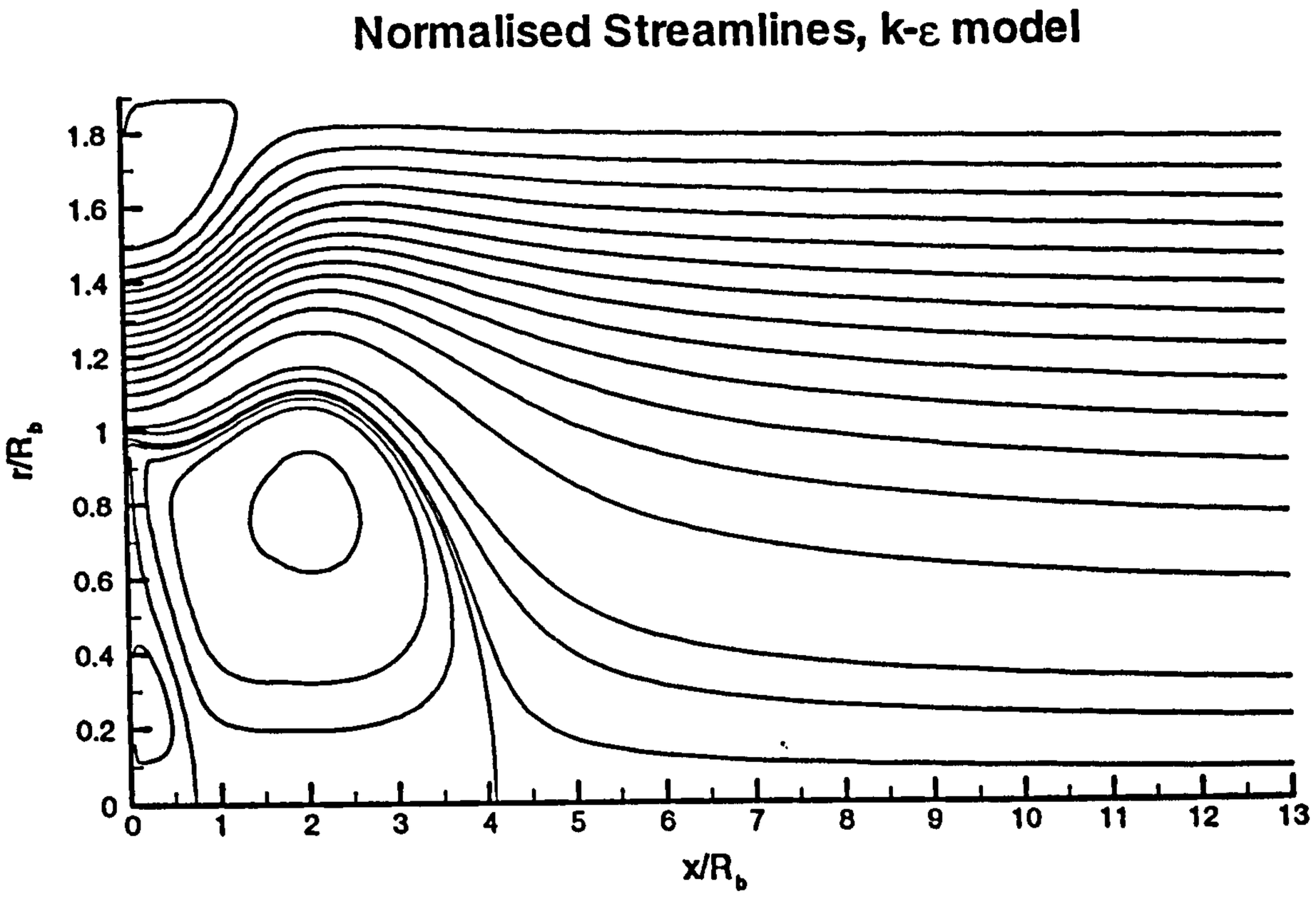

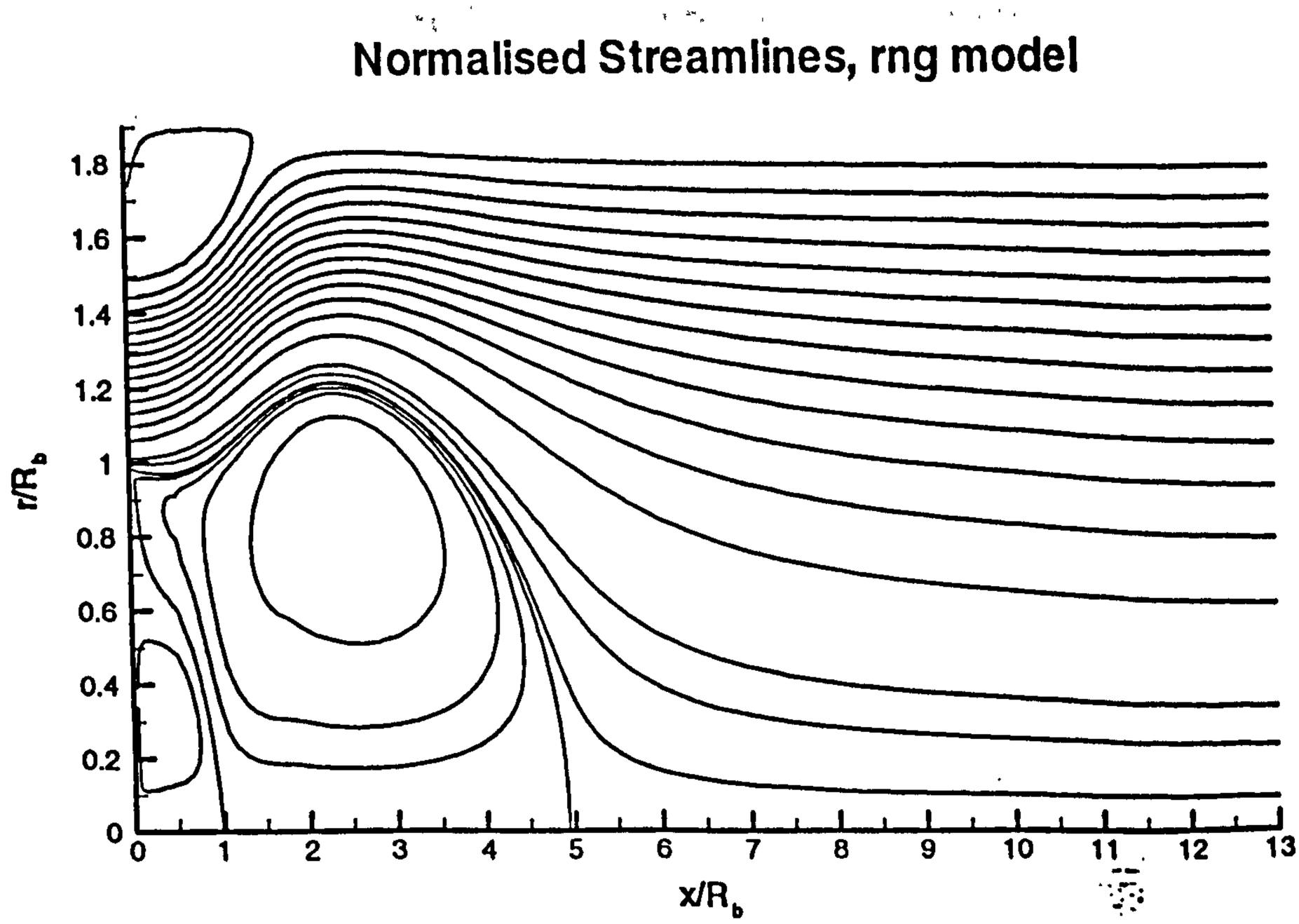

Figure 6.23: Normalised streamlines for the various turbulence models.

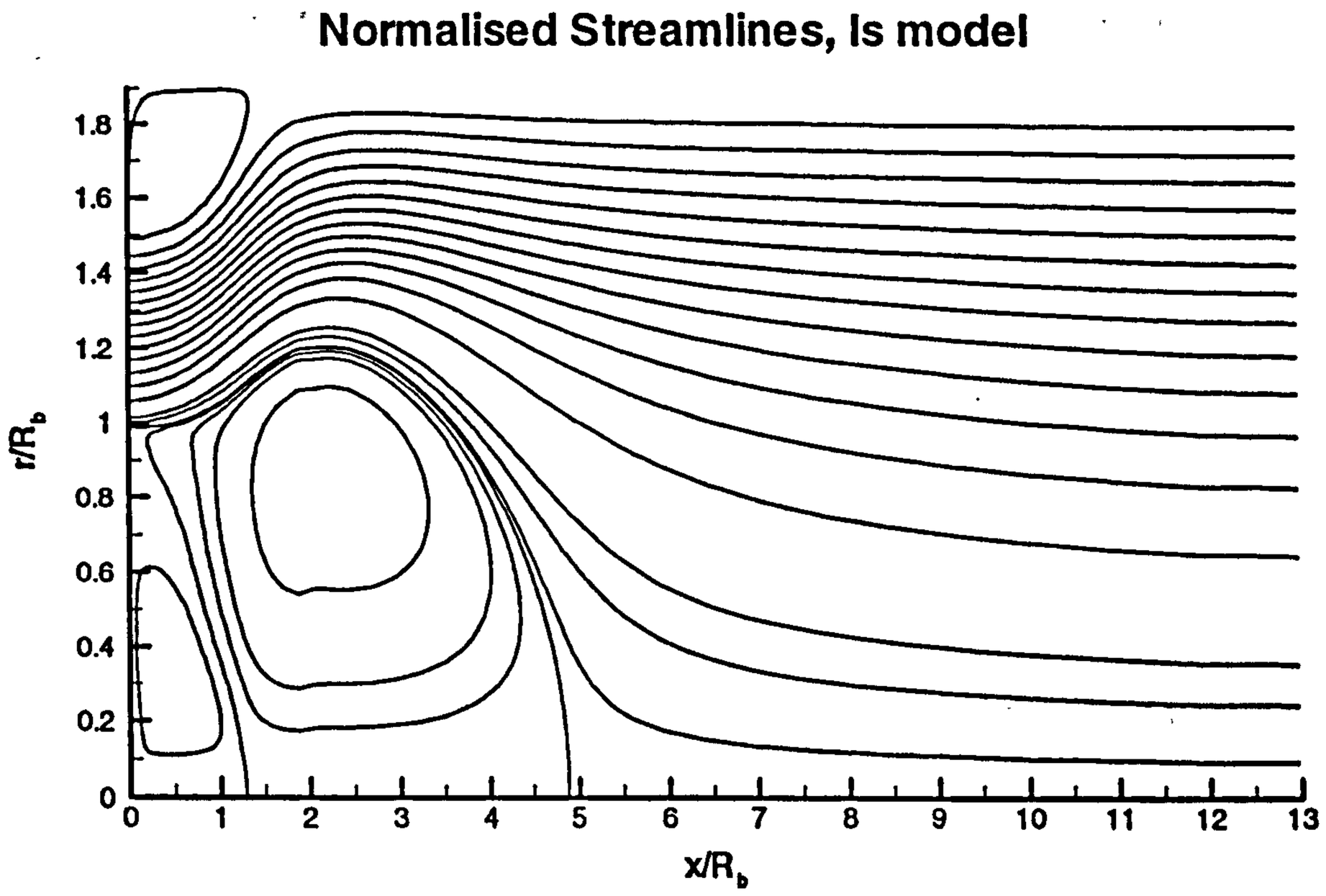

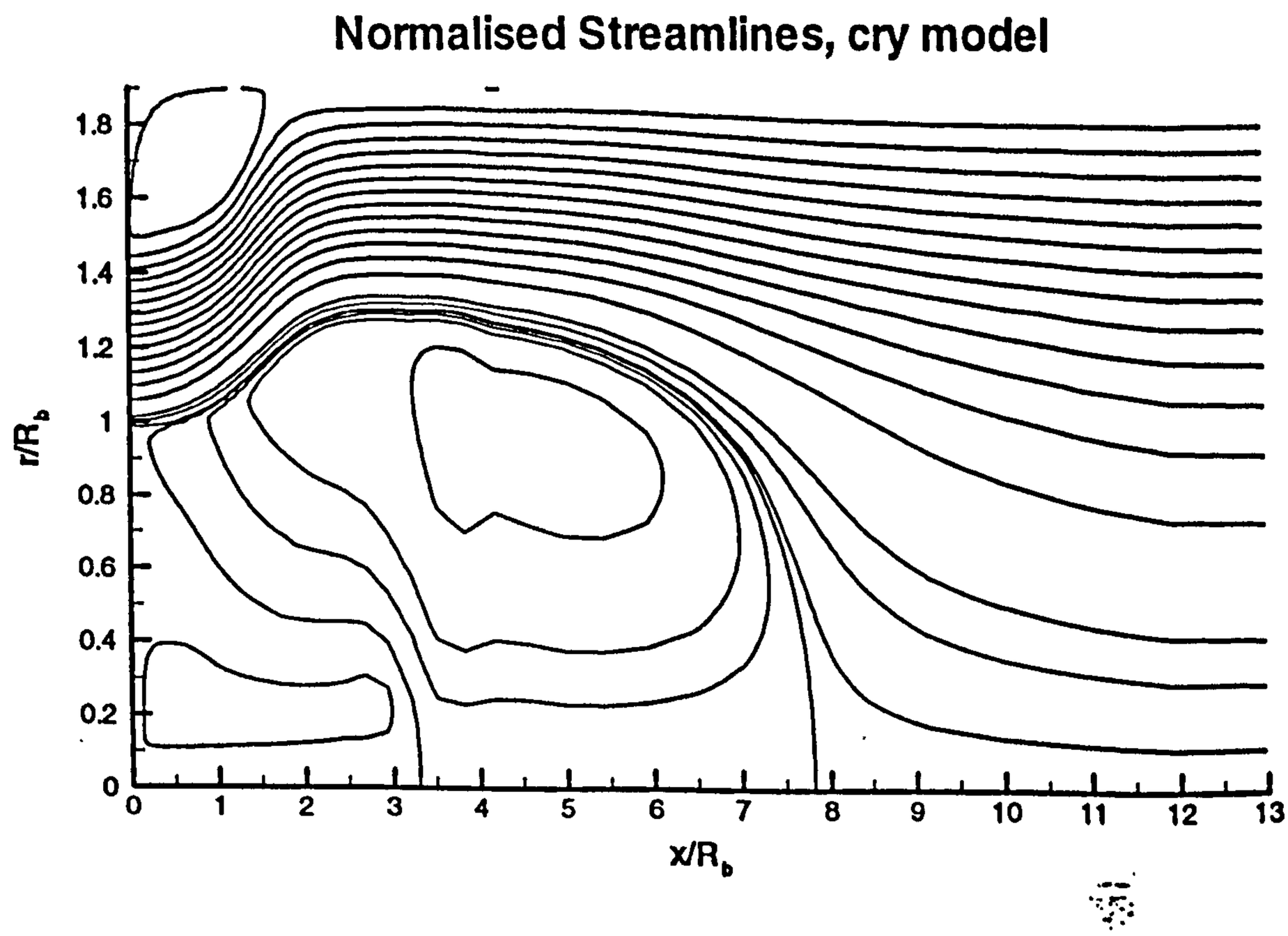

Figure 6.23 - continued.

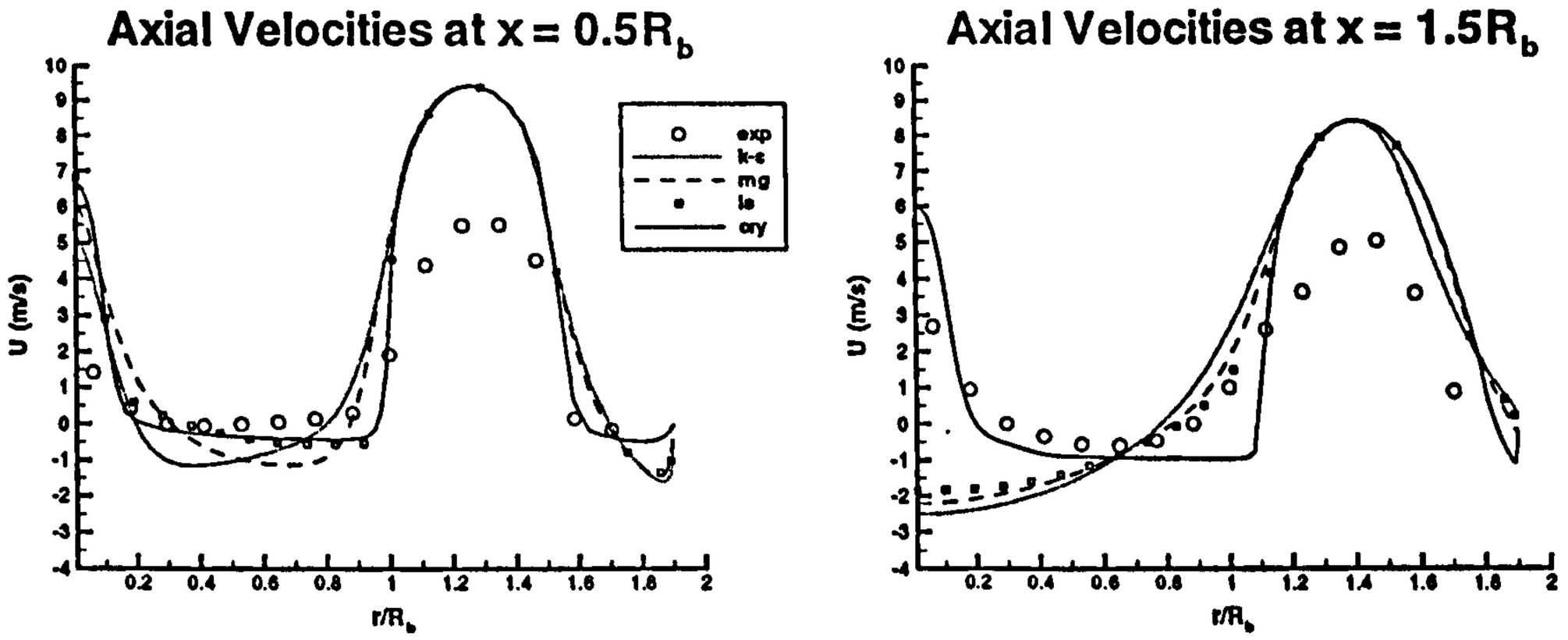

Figure 6.24: Experimental and predicted axial velocities.

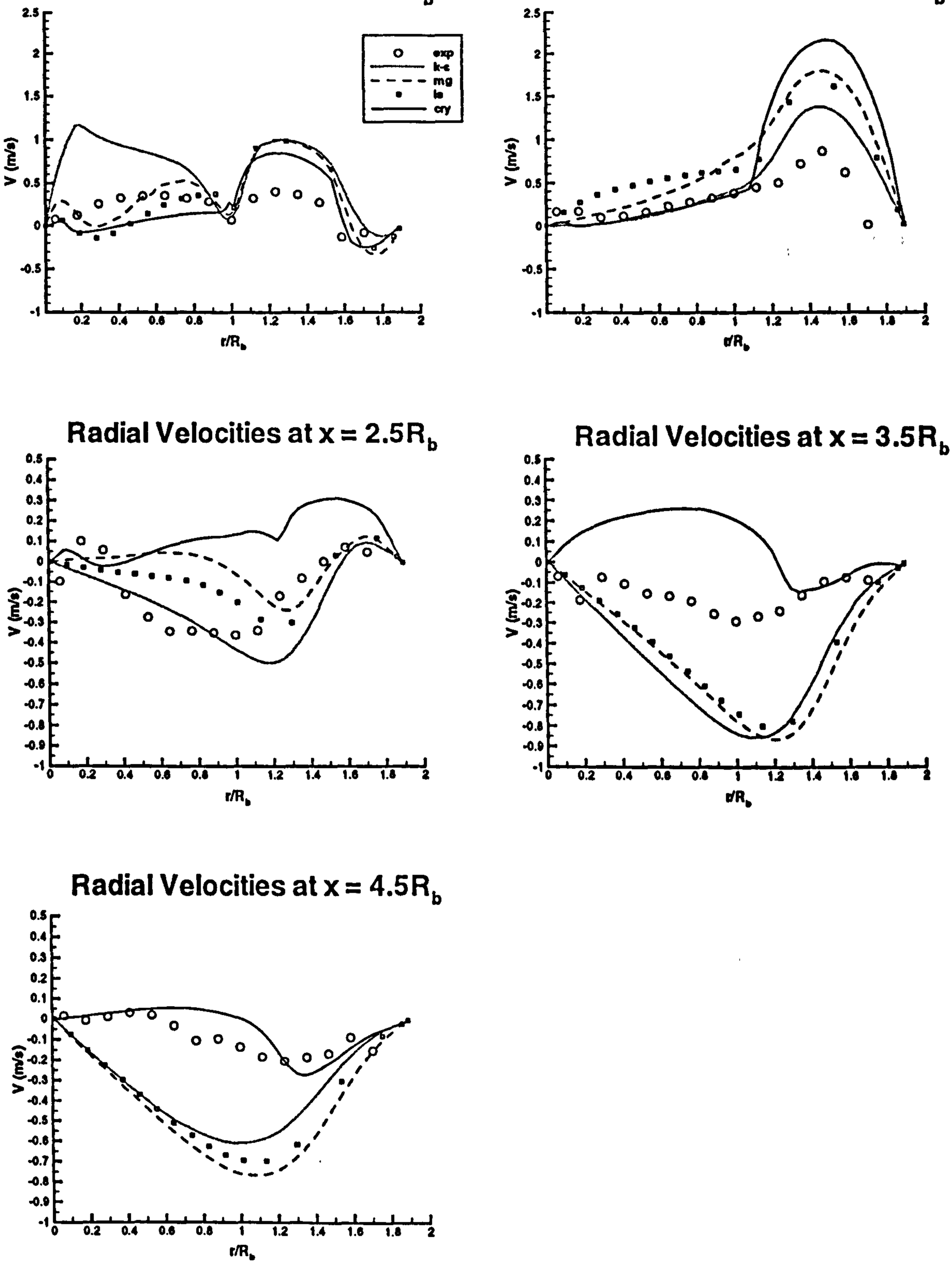

Figure 6.25: Experimental and predicted radial velocities.

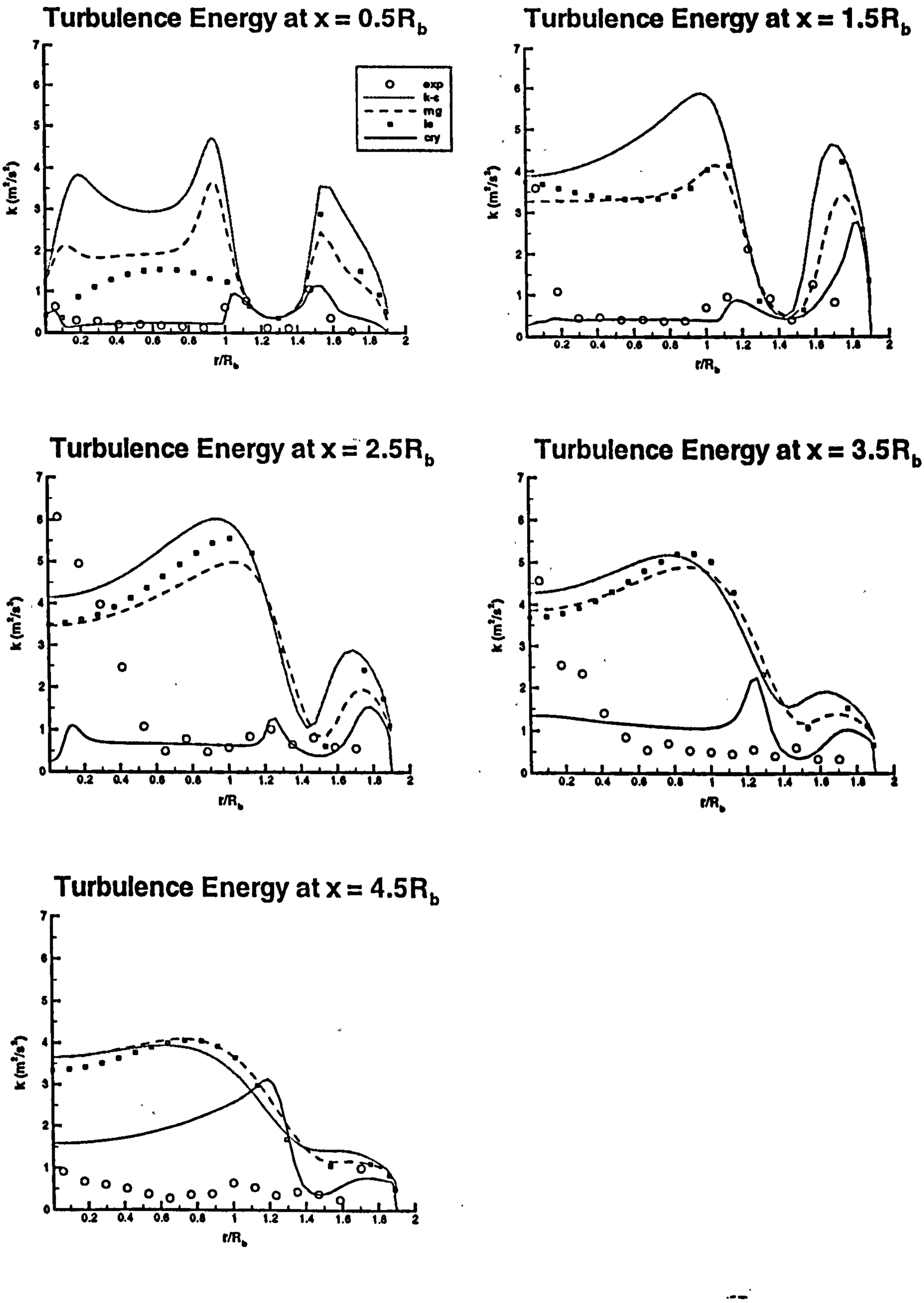

Figure 6.26: Experimental and predicted turbulence energy.

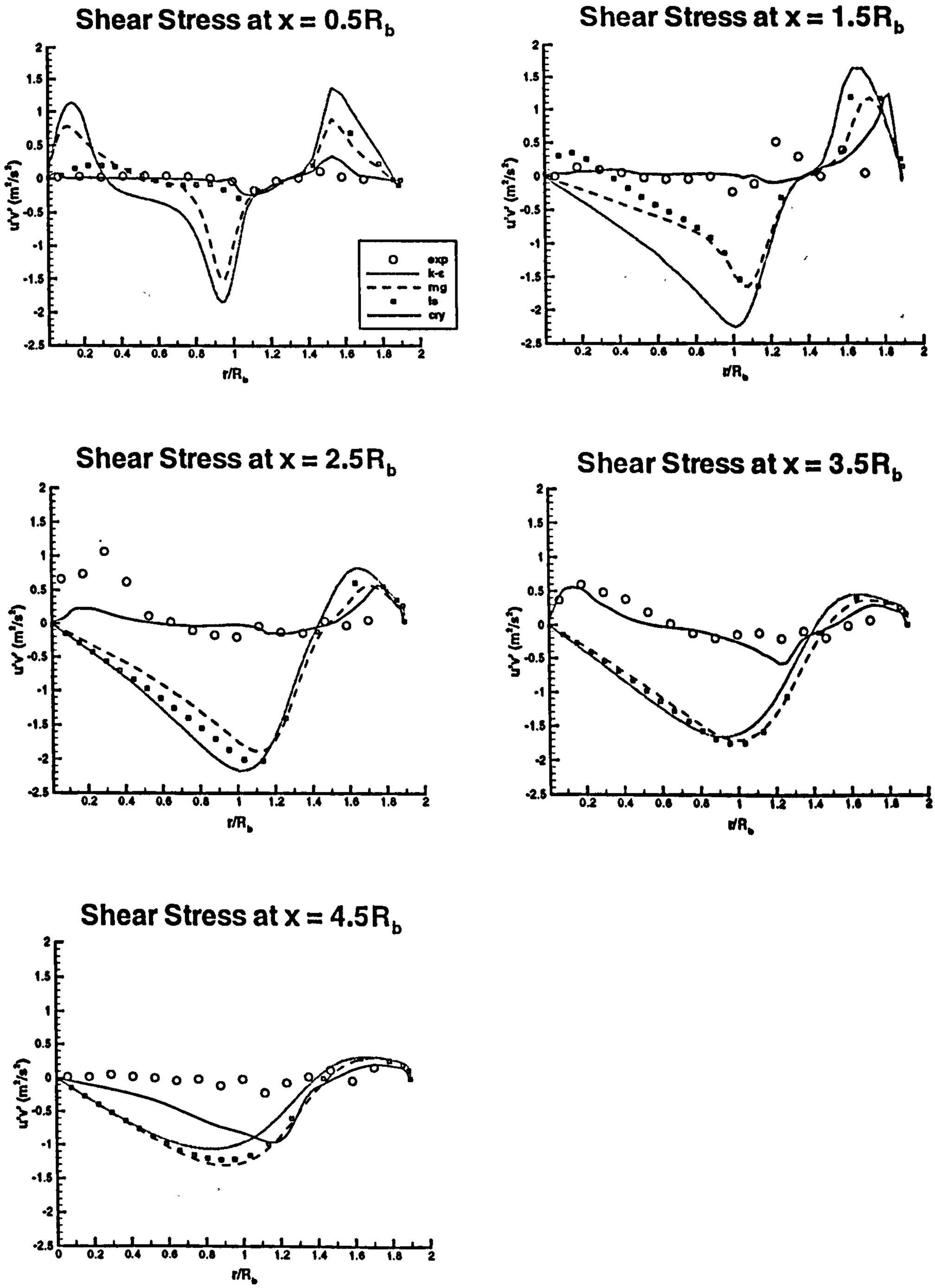

Figure 6.27: Experimental and predicted shear stresses.

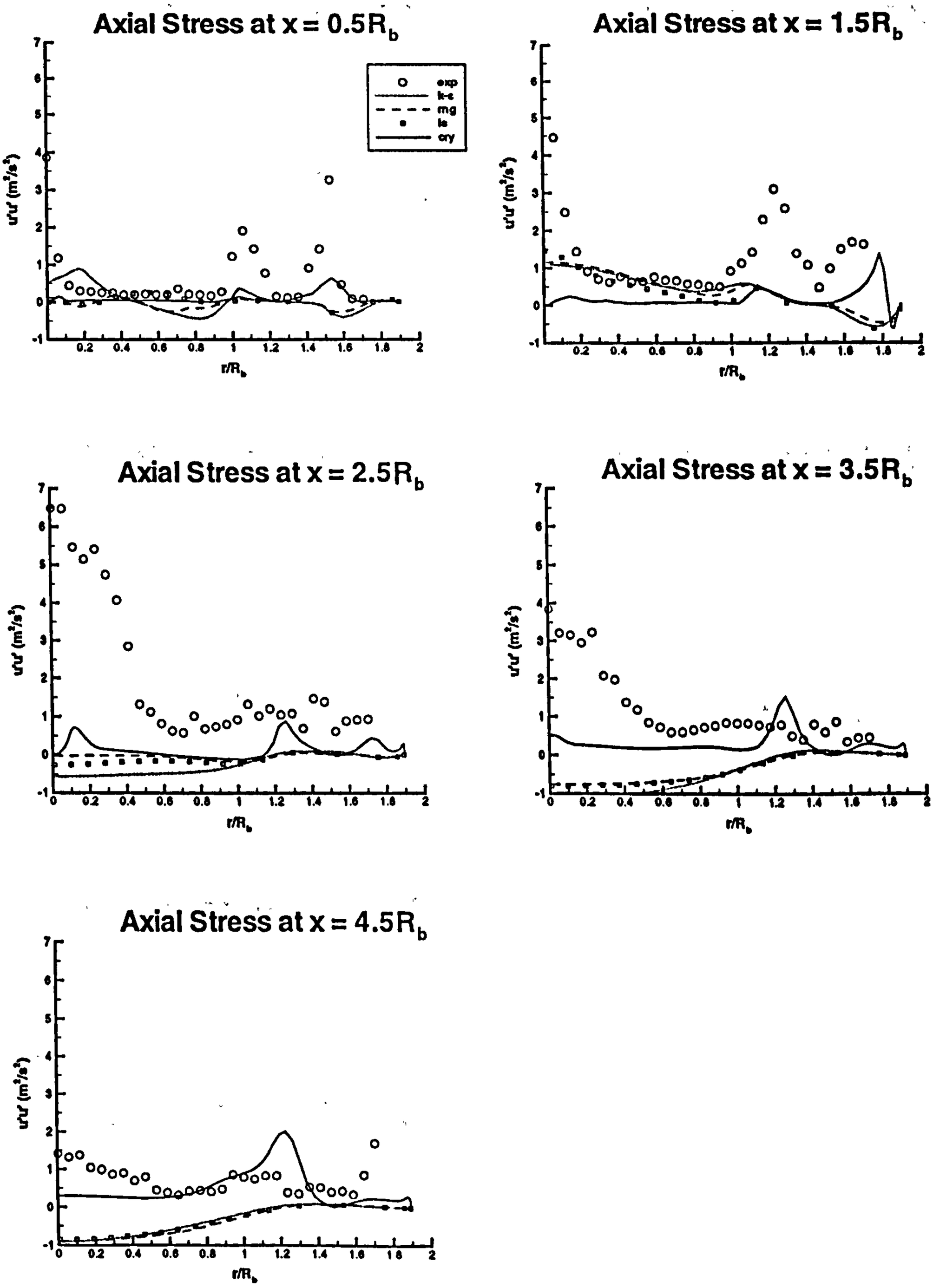

Figure 6.28: Experimental and predicted axial stresses.

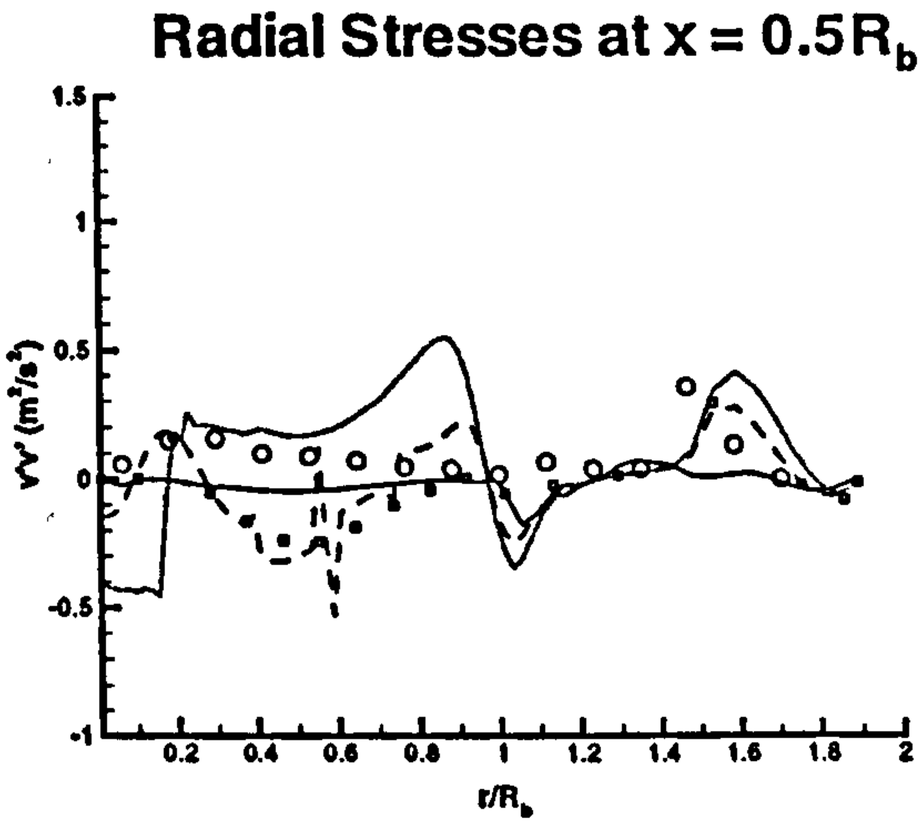

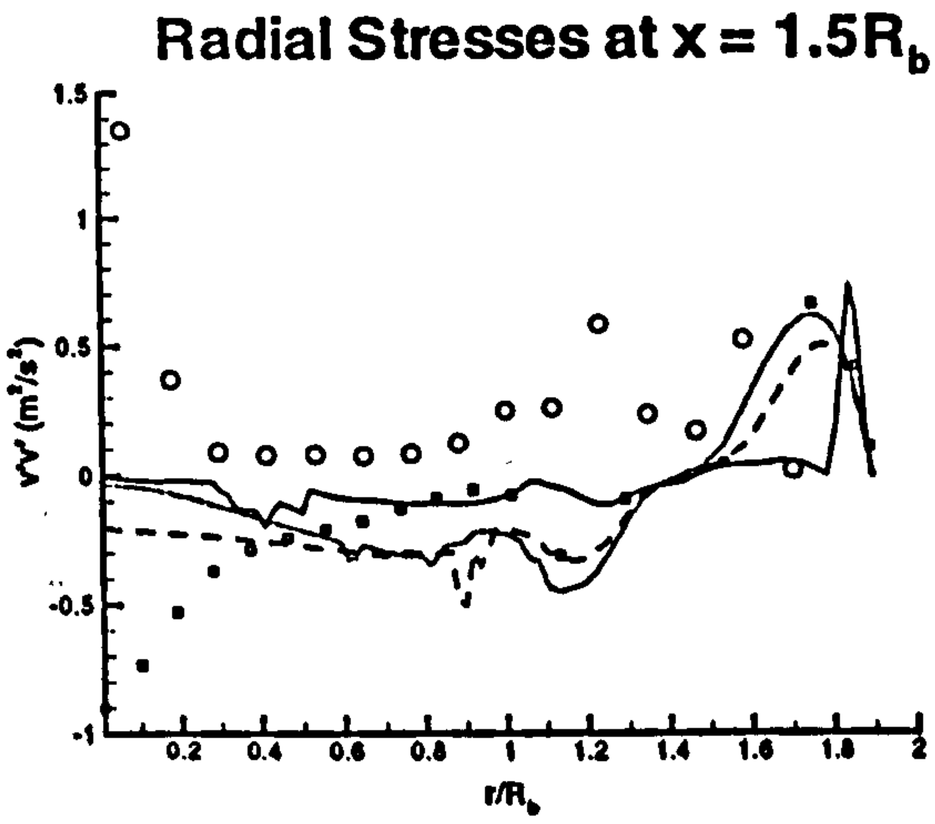

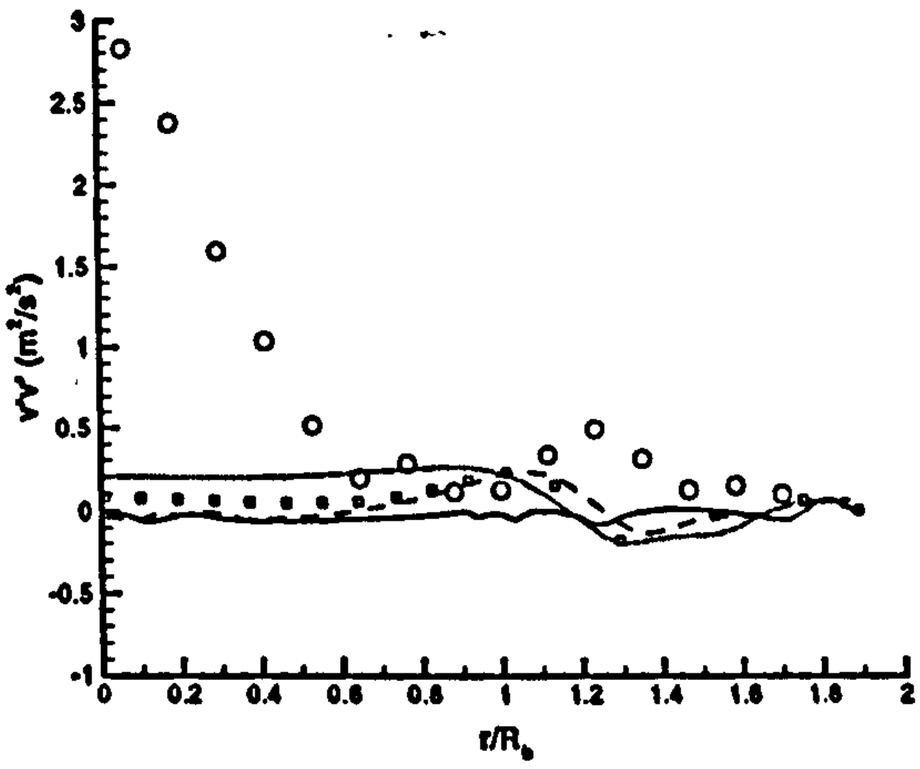

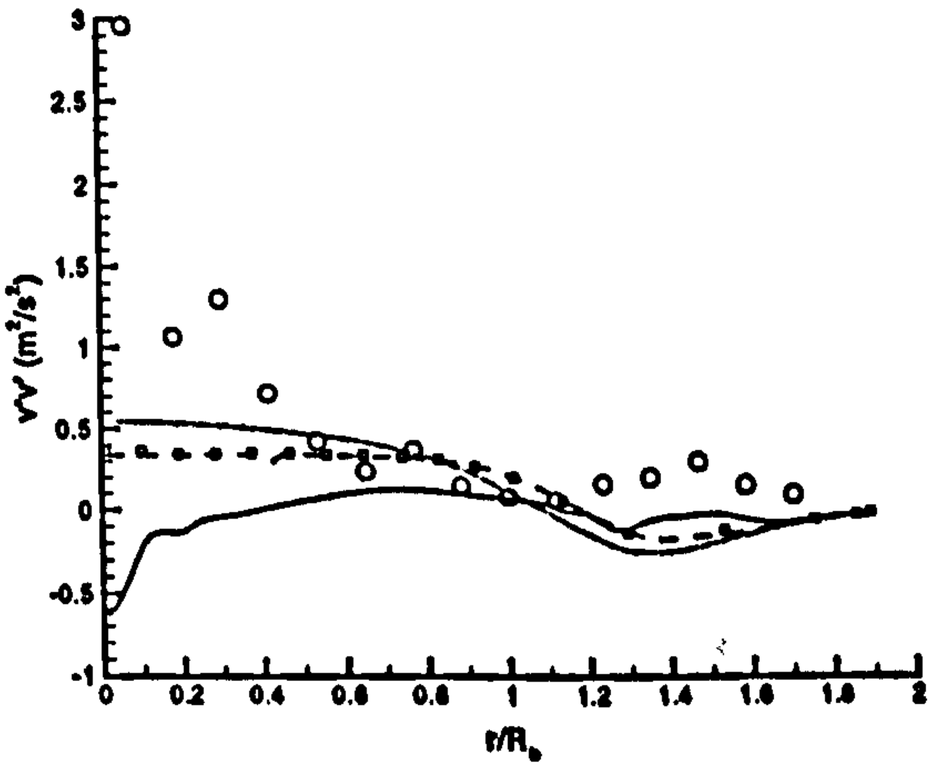

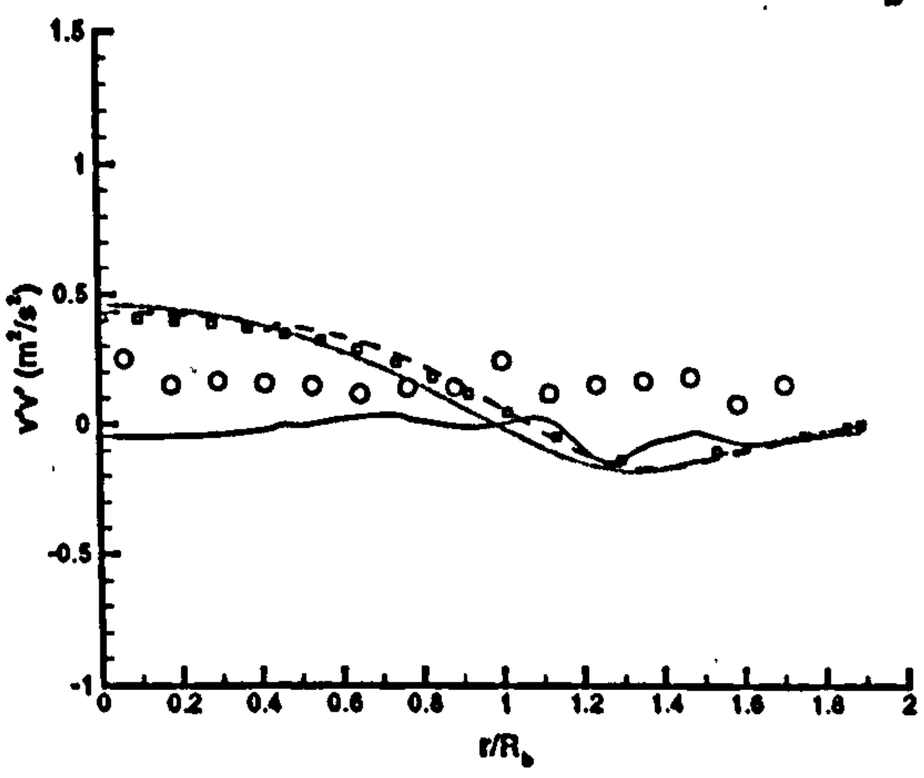

Figure 6.29: Experimental and predicted radial stresses.

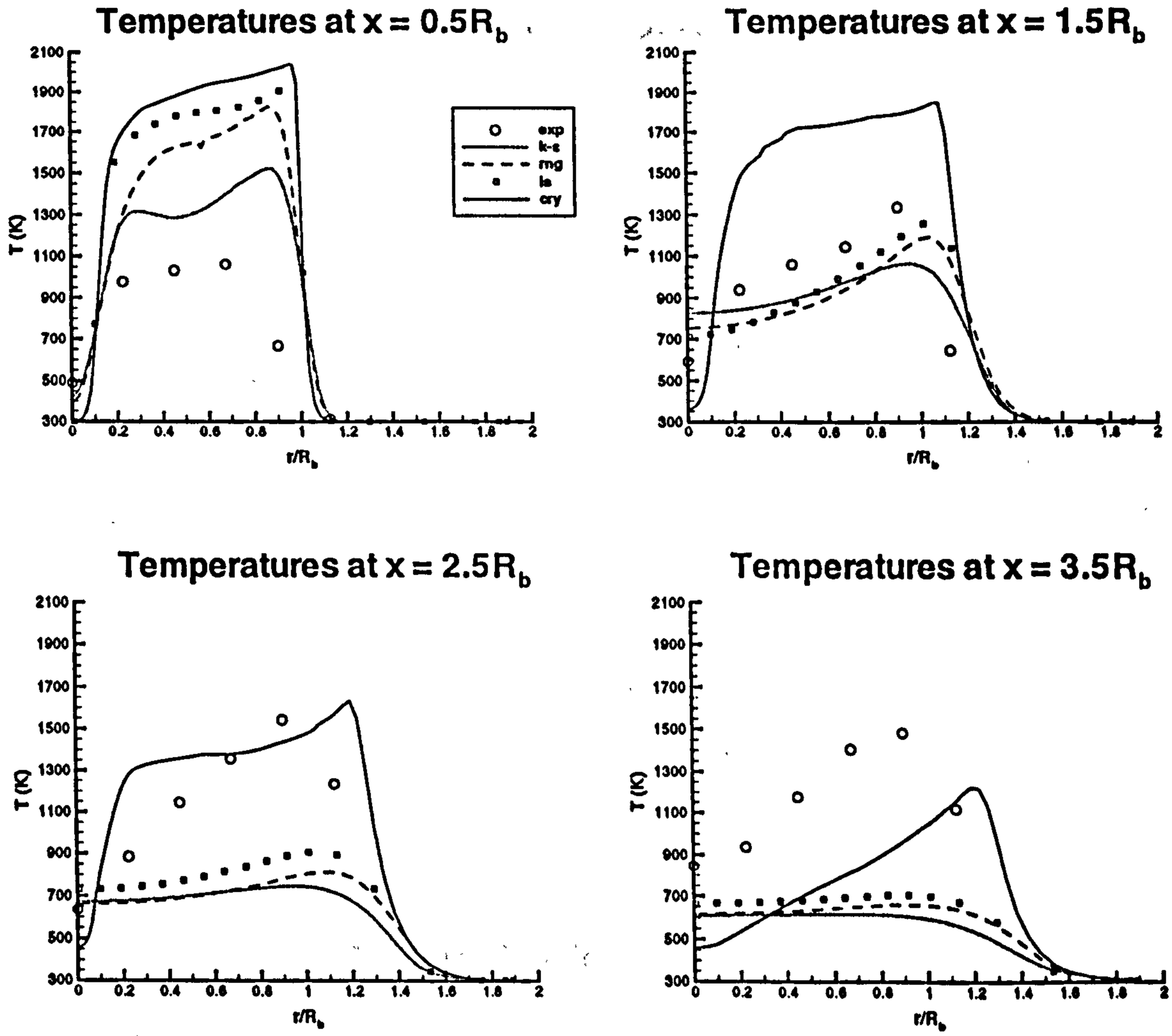

Figure 6.30: Experimental and predicted temperatures.

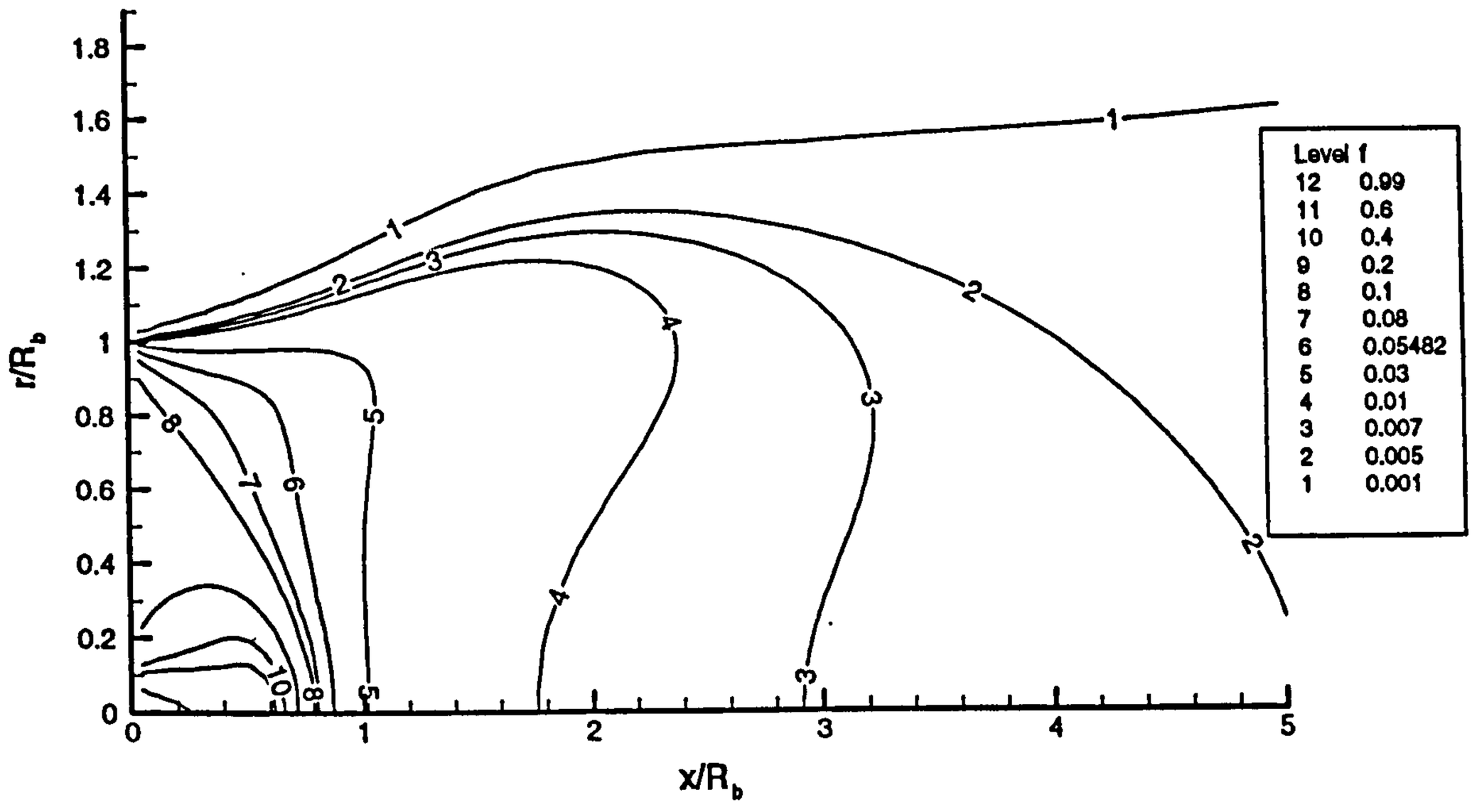

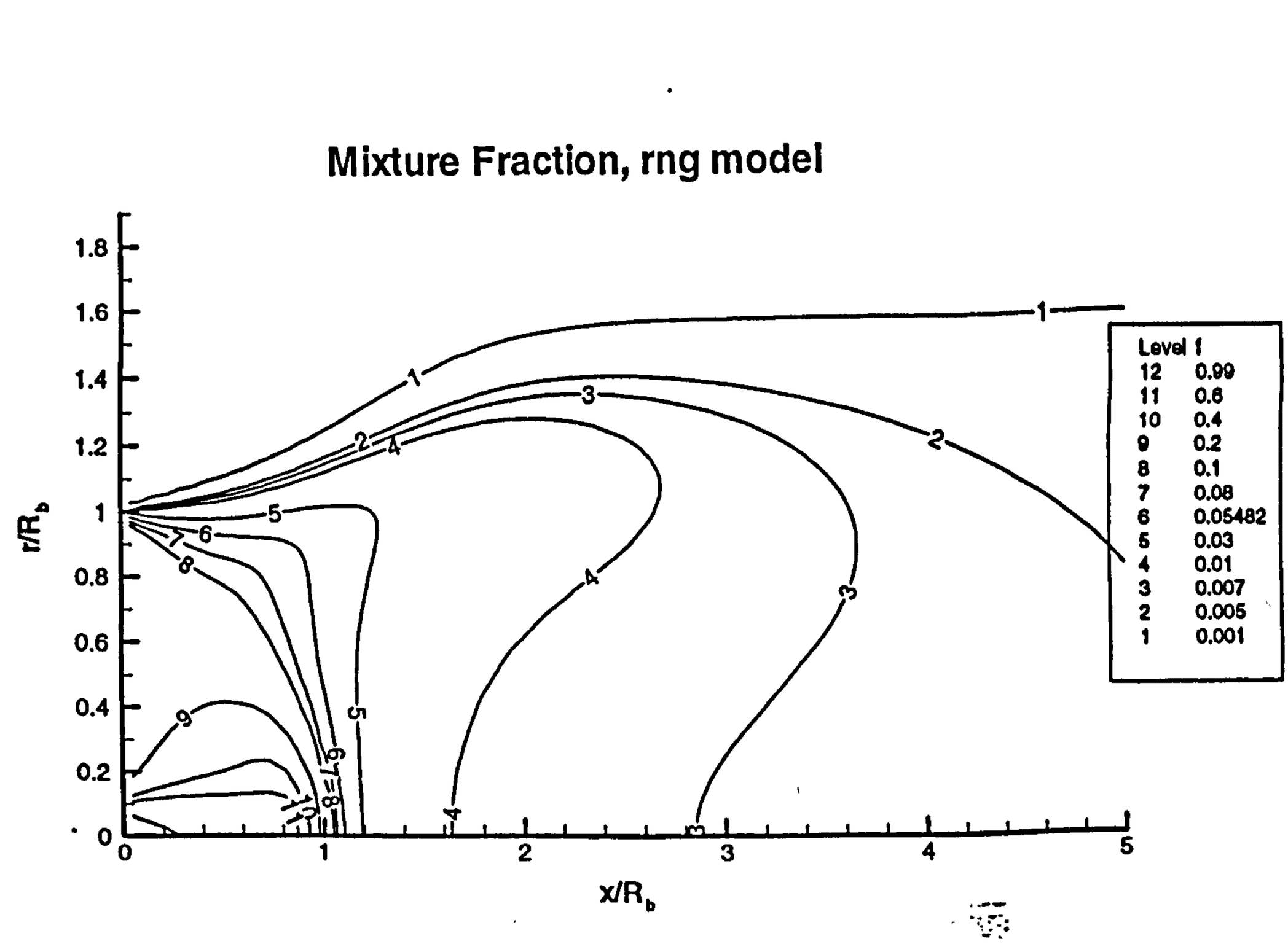

Figure 6.31: Mixture fraction contours for the various turbulence models.

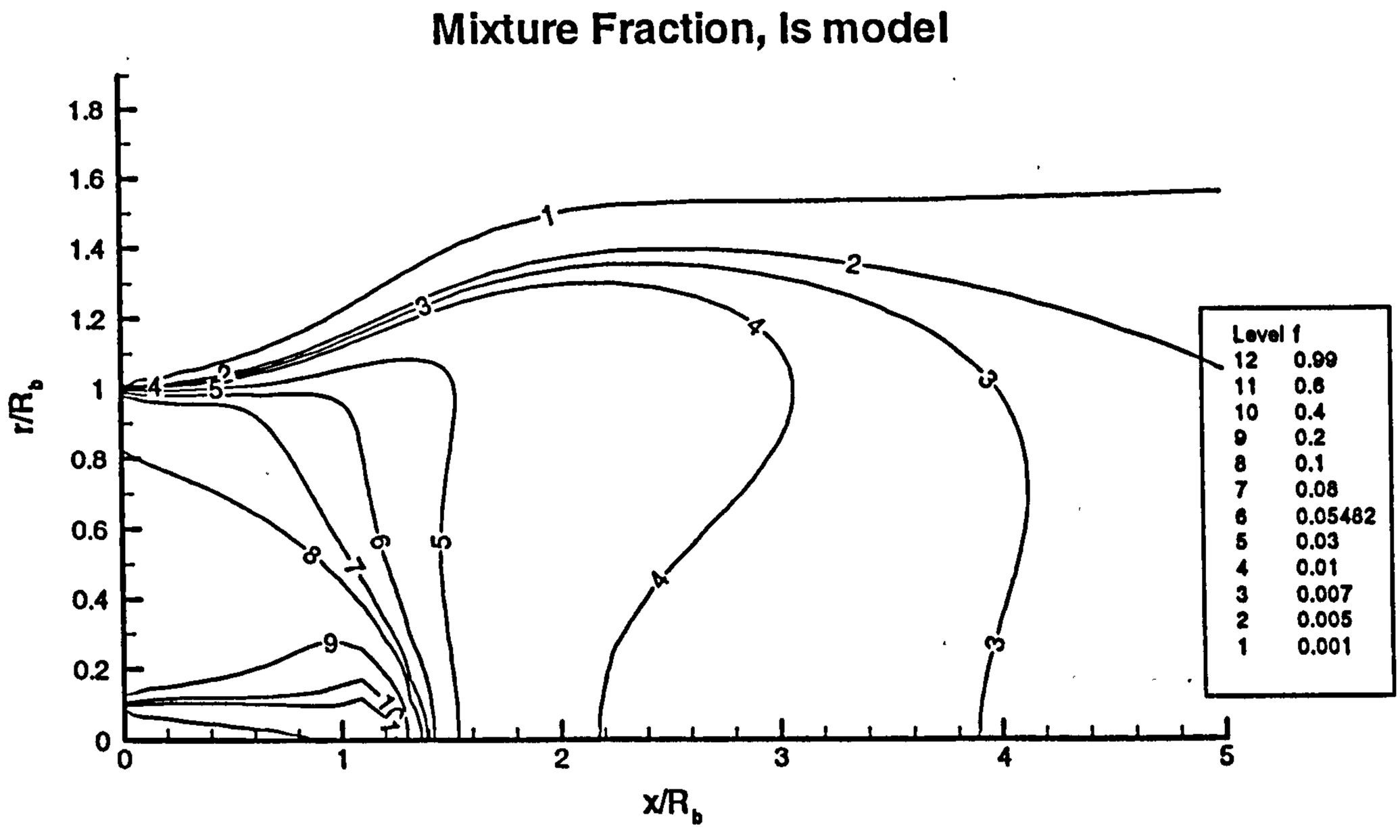

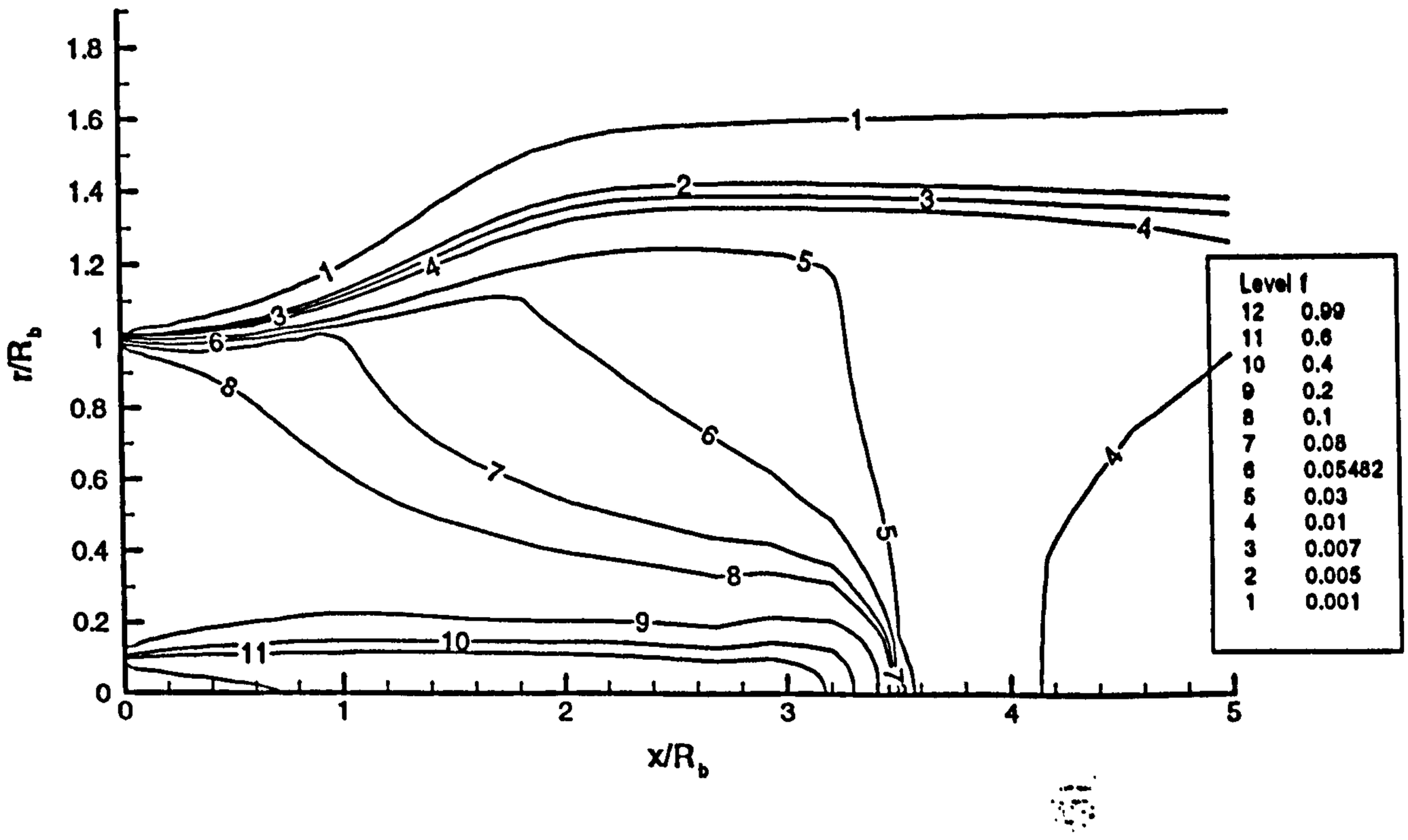

Figure 6.31 - continued.

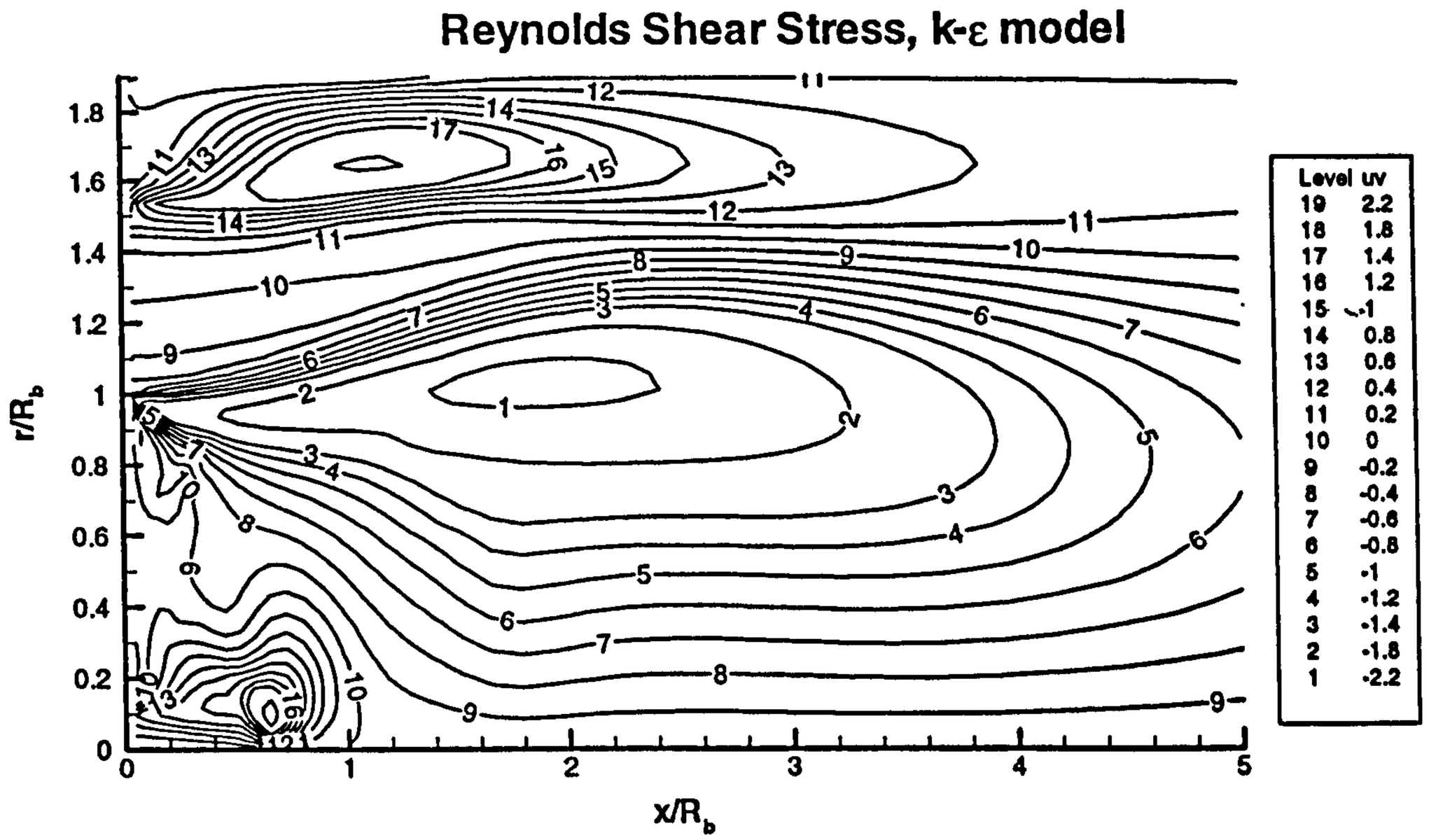

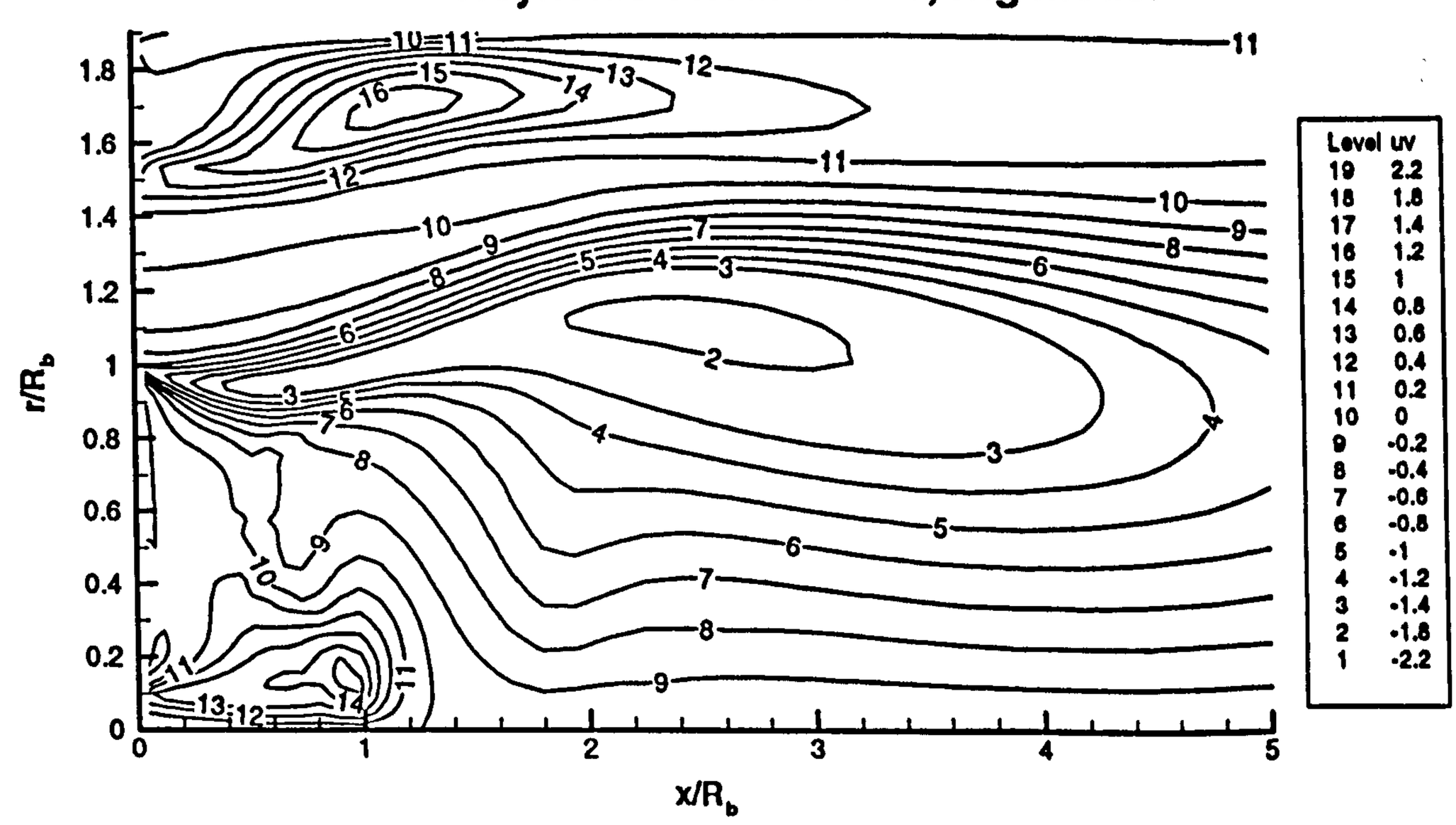

Figure 6.32: Reynolds shear stresses computed with the *k*-ε and RNG models.

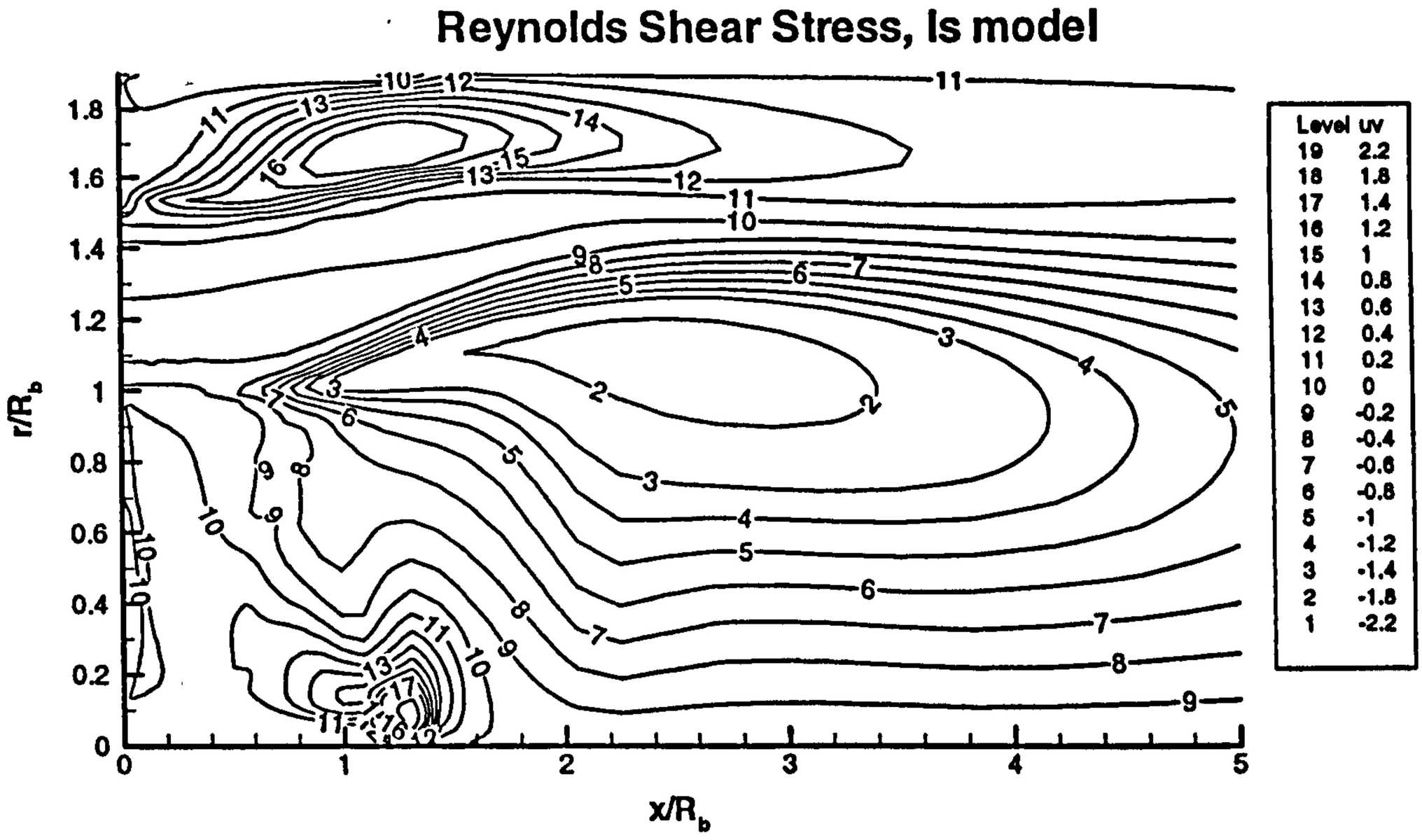

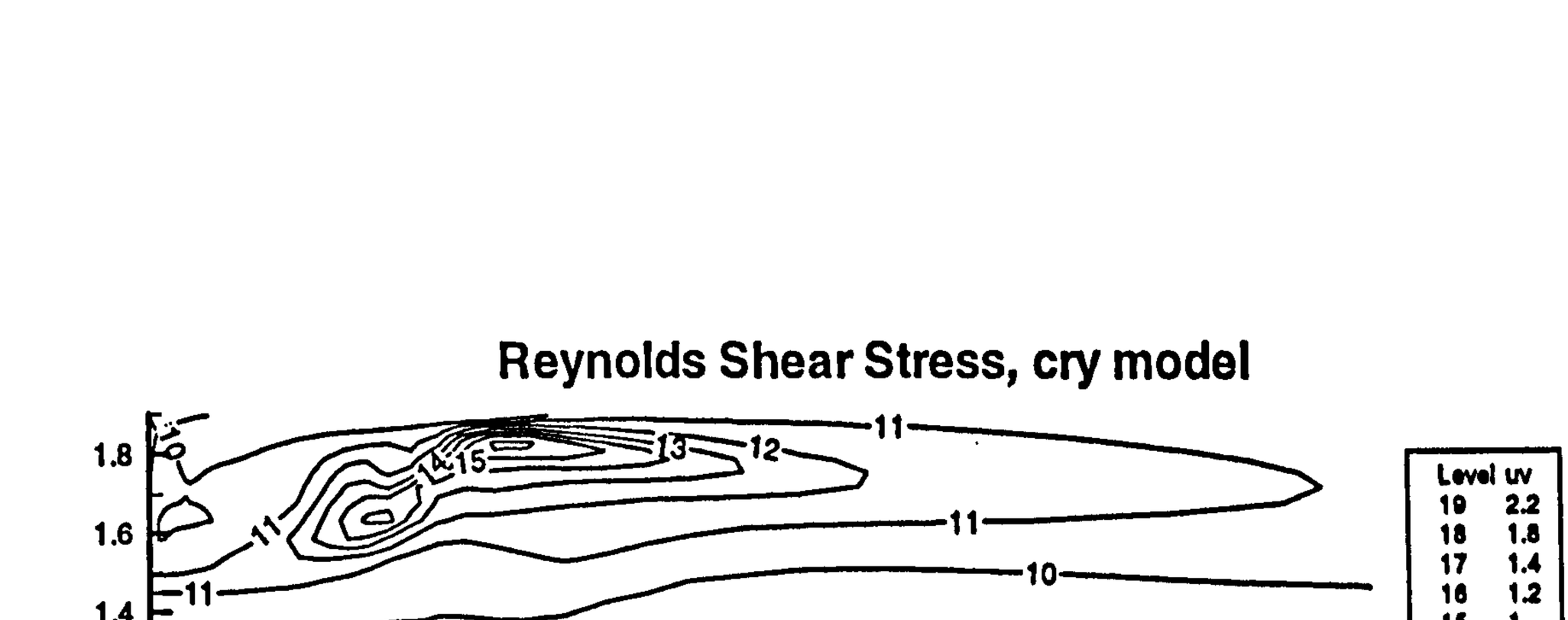

Figure 6.33: Reynolds shear stresses computed with the LS and CRY models.

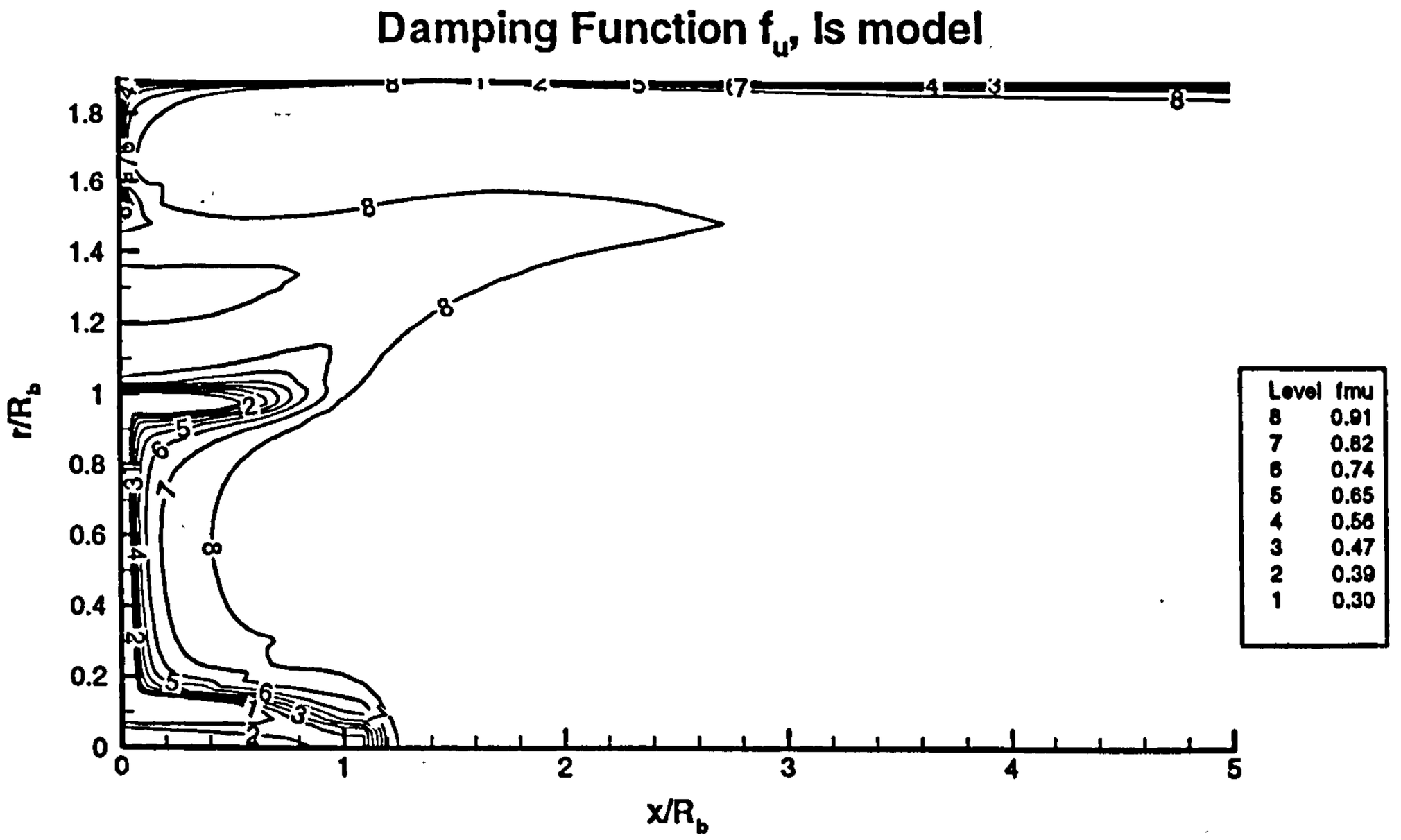

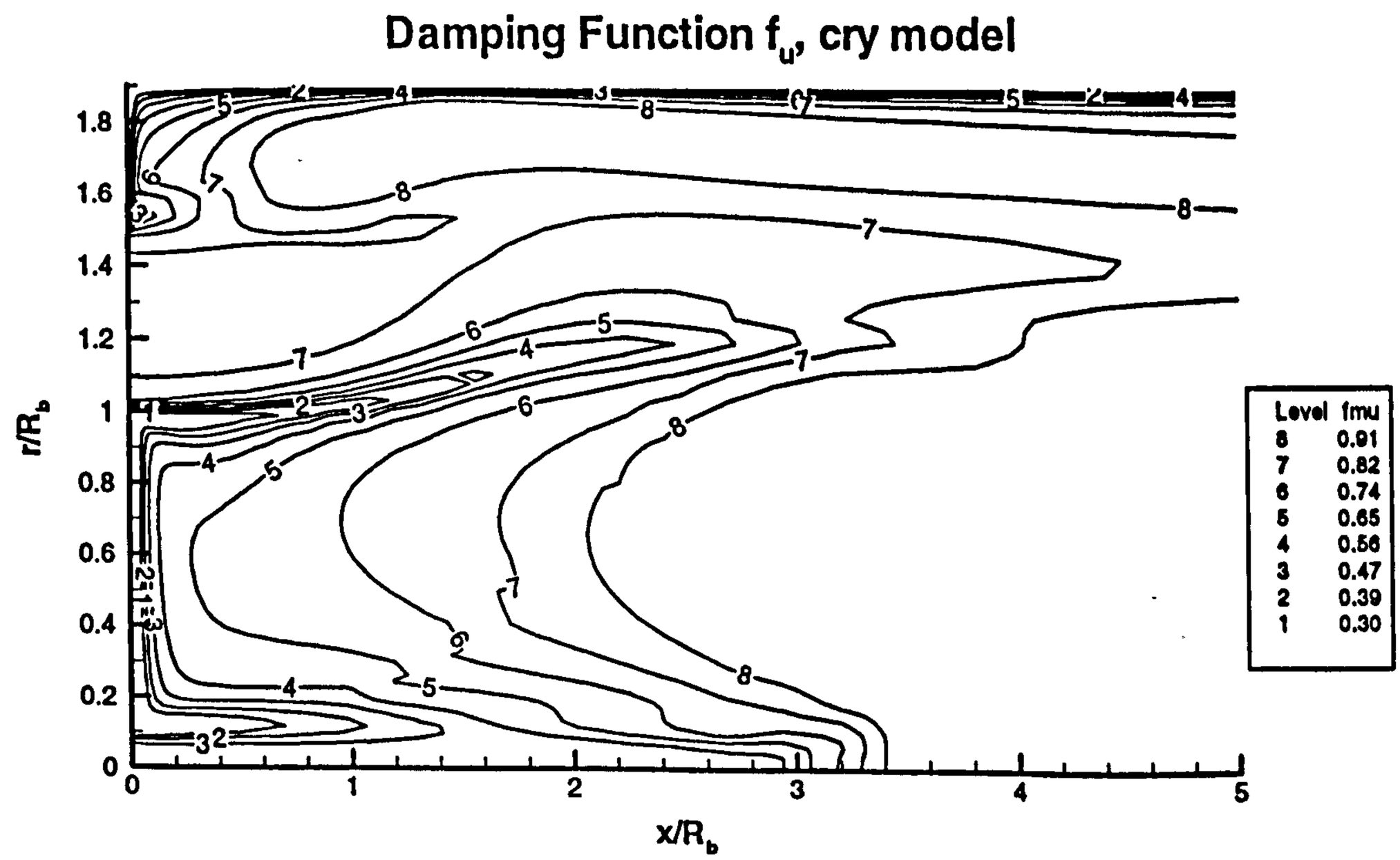

Figure 6.34: Comparison of the damping function f_μ used by the LS and CRY models.

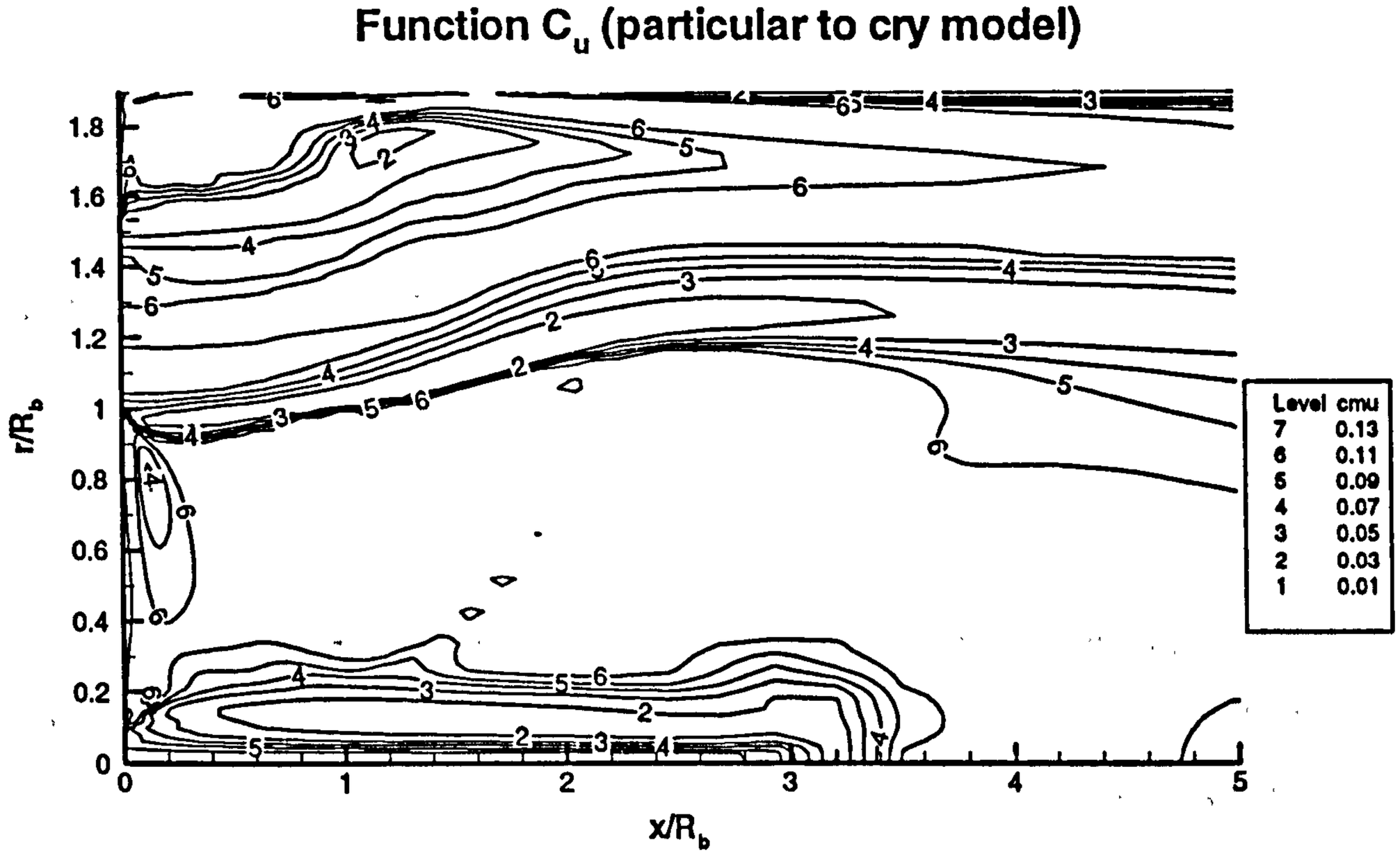

Figure 6.35: Contour plot of the function C_μ (which is only applicable to the CRY model).

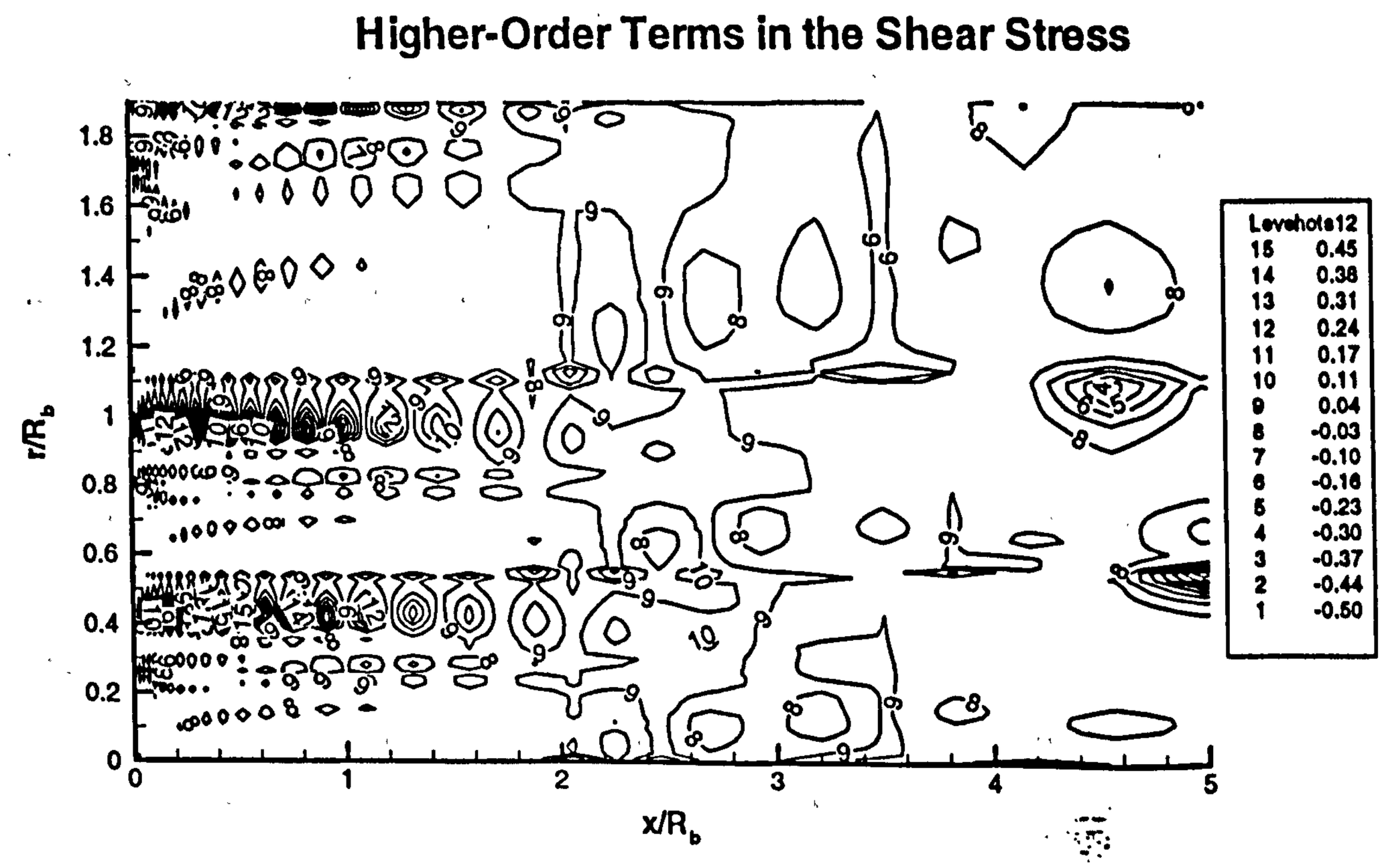

Figure 6.36: Contour plot of the higher-order terms in the nonlinear Reynolds shear stress formulation.

CHAPTER 7: CLOSURE

The purpose of this chapter is to draw together all the major findings of the previous chapters with regard to the turbulence models, and to present the overall conclusions. The contributions of the thesis are stated and finally areas of further work are recommended.

7.1 CLOSING DISCUSSION

Application of the turbulence models to the various flows described in Chapters 4, 5 and 6 has resulted in interesting findings for each separate case. In order to obtain an overall picture of the performance of the turbulence models and their application to a complex flow with combustion, particularly the cubic model, the following discussion draws together the key elements from all the individual investigations.

With the exception of fully-developed pipe flow, all the cases investigated have featured strong streamline curvature effects and recirculation regions which had important functions in the flows:

- Pipe expansions (Chapter 4): Separation of flow due to a sudden step resulted in a large recirculation zone bounded by a free shear layer and a wall.

- High swirl-intensity pipe flow (Chapter 4): Redistribution of pressure caused a large area of flow reversal to be formed along the longitudinal axis of the pipe. Streamlines are distorted due to the decay of tangential velocities.
- Unconfined bluff-body combustor (Chapter 5): A large recirculating structure was formed by the flow of an annular jet past a bluff-body. However, the strong, central fuel jet was not affected.
- Confined bluff-body combustor (Chapter 6): Annular air flowing past a bluff-body resulted in an elongated (due to confinement) recirculation area which in this case completely dominated the fuel jet.

Regardless of the cause of these recirculation zones, they are all areas of strong streamline curvature, which is a feature that eddy-viscosity models are generally not capable of dealing with. In all the flows investigated, the standard k-ε model was seen to be least able to resolve the recirculating structures, as demonstrated by its underpredictions of recirculation zone length. This is generally due to its excessively diffusive nature, which is supported by consistent overpredictions of turbulence energy and shear stress in key regions of the flows. The LS model generally followed similar trends. The RNG model was found to be less consistent; in the pipe expansion cases it accurately resolved the free shear layers but not the reattachment lengths, for various Reynolds numbers. In the swirling flow and bluff-body combustor cases, however, it offered little, if any, improvement over the k-ε and LS models. In contrast to the linear EVM's, the cubic turbulent model consistently returned the lowest shear stresses (apart from the swirling pipe case) and generally provided improved predictions.

Detailed investigation of the pipe expansion cases revealed the mechanisms by which the CRY and RNG models provided the most accurate predictions.

- The cubic model was strongly influenced by the nonlinear terms in the stress/strain relationship and also by the strain-dependent functional form of C_μ; in reacting flows, the damping function f_μ further contributed in a positive manner.
- The RNG model relied upon a strain-dependent modification of the production term in the dissipation-rate transport equation, as well as having a reduced value of the constant $C_{\varepsilon 2}$.

Interestingly, these devices did not aid the RNG model in the bluff-body burner simulations, whilst they clearly had a large, positive impact on the CRY predictions for the combustors. Although the nonlinear model did not match the experimental data everywhere in the combined combustor, it did yield significant improvements. The one case with which all EVM's struggled was the pipe flow with high-intensity swirling motion. The reason for this difficulty was presumed to be the inadequacy of the eddy-viscosity assumption for complex flows in which local velocity gradients did not seem to correlate with shear stresses. Although the nonlinear model did not accurately predict the swirling flow, it tended towards some of the correct trends, particularly for the axial velocities. Whilst incapable of resolving the central flow reversal, it did at least predict much lower axial velocities in the core region than the linear EVM's. This partial success was attributed to the presence of cubic terms.

The above discussion clearly demonstrates that the cubic turbulence model offers more potential than the linear EVM's, simply because it consistently returned the best results for a variety of taxing flows. The only other model which behaved in a consistent manner was the standard k-ε model, whose predictions were always the worst. However, this improvement was gained at a certain cost; the nonlinear model required integration to the walls (increasing the computational expense) and tended to be quite numerically unstable. Various practices had to be adopted in order to obtain meaningful solutions with any turbulence model; the standard issues of grid-independence and false diffusion are described in Chapter 3. All turbulence models were more sensitive to cell distributions in the reacting cases than in the isothermal cases. However, additional measures were required for the cubic model in order to avoid instability and obtain converged solutions:

- Relaxation factors were applied to the nonlinear terms; the values were several orders of magnitude smaller than those for the main flow variables, typically 0.05 or less.
- The cubic model required additional grid refinement in areas of steep gradients in the combusting flows, otherwise the simulations would diverge.
- In the initial stages of most simulations, the nonlinear model tended to predict negative values for turbulence energy, thereby causing divide-by-zero errors. This was avoided by adopting the k-production term defined for the LS model in the event that this quantity, as calculated for the cubic model, was negative.

- The CRY model places a constraint upon the gradient dissipation term such that its effect is confined to areas of low turbulent Reynolds number; however, this involves a discontinuity and promotes instability. Thus for all complex flows, this constraint had to be removed.

7.2 CONCLUSIONS

The conclusions regarding the CFD simulations and experimental work are summarised in the following three sections.

7.2.1 Turbulence Modelling

1. The cubic turbulence model was generally found to yield the most accurate results, compared to the linear EVM's, in the flows investigated.
   - The Reynolds Stress Model, however, proved superior in the highly-swirling pipe flow. In this case, the cubic model distinguished itself from the linear EVM's by tending towards the correct trends.
   - The RNG model only improved results for pipe expansion geometries.
   - The standard k-ε and LS models were found to be too dissipative in that they constantly overpredicted shear stresses and turbulence energy.
2. The CRY and RNG models were seen to contain devices which reduce shear stresses. These proved effective for nearly all the flows investigated with the CRY model, but in the case of the RNG model their tuning gave satisfactory performance only for the pipe expansion flows.
   - The cubic model was found to owe its success to a combination of:
     - Nonlinear terms in the stress-strain relationship.
     - Strain-dependent formulation for C_μ.
   - In the combusting cases, the nonlinear model was also aided by the damping function f_μ in regions far from the wall, simply because this function, which depends on the turbulent Reynolds number Re_t, was activated by the lower densities occurring at higher gas temperatures. The same is true of the LS model, although the improvement was much smaller.
   - The nonlinear model contained the Yap correction term which was seen to have no effect on the bulk of the flow in pipe expansion cases, but did affect results somewhat in the swirling pipe case. It was also found to cause a deterioration in fully-developed pipe flow simulations (CRY model).
3. All EVM turbulence models were found to occasionally predict negative normal stresses. In spite of this 'non-realisability,' the computations showed that the main

variables were not affected; it was demonstrated in several cases that all gradients involving the normal stresses are relatively small.

4. The nonlinear turbulence model was the least stable from a numerical point of view; it was seen to be more sensitive to the grid than any other model investigated, and the following measures were required in order for converged solutions to be obtained for the complex flows:
   - Applying under-relaxation factors to the nonlinear terms; very low values were necessary.
   - Preventing the attainment of negative turbulence energy.
   - Lifting of certain constraints placed upon the gradient production term.

7.2.2 Combustion Modelling

1. Predictions for scalar quantities in the reacting simulations were found to be highly sensitive to the turbulence model used.
   - Ad-hoc modification of the standard k-ε model (i.e. increasing the value of the constant $C_{\varepsilon 1}$ in the dissipation rate equation) dramatically improved results for the unconfined bluff-body combustor simulations.
   - Altering the value of the turbulent Prandtl number in the scalar transport equations (for mean mixture fraction and variance) had a much smaller impact.
   - The confined bluff-body combustor computations highlighted the dependence of scalar quantity predictions on flow fields.
2. The β-pdf turbulence/chemistry interaction model was found to be adequate in the unconfined bluff-body burner in which the reaction zone occurred along the central fuel jet. It had the desired effect of simulating heat removal and moderating the temperatures. However, in the case of the confined bluff-body combustor where the reaction zone was spread over the entire diameter of the bluff-body, the β-pdf model failed to account for the large effects of heat transfer, thereby resulting in incorrect temperature predictions.

7.2.3 Experimental Results

1. The flow fields obtained with PIV were used for comparison with the CFD simulations. The trends in the flow were clearly captured. The uncertainty regarding absolute values of velocities and turbulence data was estimated at 4%, a worst-case error based on pixel size only. Cross-correlation parameters are known to affect results, but it was not possible to quantify the extent of any such effects.
2. The temperature field was obtained using a thermocouple probe, but the results were only a qualitative representation of the thermal distributions because:
   - A data-logging facility was not available with which to compute the mean temperature in a statistical manner.
   - The correction for radiation losses from the thermocouple depends entirely on the emissivity, for which a value was not available.

7.3 CONTRIBUTION OF PRESENT WORK

The scope of the thesis is to apply the cubic NLEVM to a range of flows, including bluff-body combustors, to determine whether this model does indeed offer improvements over linear, two-equation models. The work carried out whilst achieving this objective consisted of the following:

- Modification of the well-known TEACH CFD code to include various well-documented turbulence models (k-ε, RNG and Launder & Sharma low Reynolds number model).
- Inclusion of a combustion model (flame sheet model with assumed 'β' probability density function).
- Testing the above turbulence models in the following isothermal cases:
  - Fully-developed, turbulent pipe flow.
  - Axisymmetric pipe expansions (three different Reynolds numbers).
  - High-intensity, swirling pipe flow.

- Implementation of the new cubic turbulence model, and its validation against the above benchmark cases and comparison of its performance with that of the previous models.
- Conducting initial simulations of non-premixed combusting flow in a bluff-body burner, using all the above turbulence and combustion models.
- Designing and constructing an experimental confined, bluff-body combustor for use with optical measurement techniques (e.g. LDV, PIV, CARS, LIF).
- Obtaining detailed measurements for velocities and turbulence quantities using Particle Image Velocimetry (PIV).
- Validating the cubic turbulence model for reacting flows in the confined combustor by comparing predicted results with the measured experimental data, and also with the predictions of the other turbulence models.

The concrete contribution of this thesis is an assessment of the cubic NLEVM's performance in several different isothermal and combusting flows, as compared with experimental data and predictions using 'industry-standard' turbulence models. A valuable feature of the thesis is a description of all the numerical problems encountered with the new turbulence model, and the appropriate remedies. Furthermore, an experimental bluff-body burner is made available for future studies concerning combusting flows.

7.4 FURTHER WORK

The present study has raised several issues which require further investigation. Some of these are:

1. Examining in detail several factors which affect the performance of the nonlinear turbulence model, including:
   - Investigating the effect of solving an additional transport equation for the anisotropic stress invariant A_2. This could potentially improve the predictions for highly-swirling flows.
   - Quantifying the effect of the Yap correction term in combusting flows.
   - Assessing the contribution of the damping functions by testing the cubic model in conjunction with high Reynolds number wall functions.
   - In future studies involving flows in which normal stresses are more important, the effect of calculating these in the manner described by equation 4.5 should be examined.
2. Validating the cubic model for a wider range of isothermal flows in order to further test its ability to correctly resolve the features of complex flows and physical processes:
   - Other swirling pipe flows (of various swirl intensities). A particularly good case would be a swirling annulus jet because experimental data for this flow can be obtained from the confined bluff-body combustor rig.
   - Impinging jets, in which normal stresses play a more dominant role.
   - Rotating flows.
   - Buoyant flows.
   - More complex geometries such as pipe contraction/expansion configurations and 90° or 180° bends.
3. Improving experimental results by taking the following measures:
   - Seeding the central fuel jet so as to obtain accurate measurements along the centreline.
   - Investigating the effects of higher seeding densities and various parameters used in the cross-correlations for computing vector fields from the PIV data.

- Utilising a greater number of vector plots for statistical analysis. Hargrave (1999) found that using 100-200 image pairs yielded the correct trends, and that 800-1000 pairs further refined the predictions.
- Sifting through all the vector plots and removing rogue vectors prior to the statistical analysis.
- Conducting a study to determine the dependence of emissivity of the thermocouple junction, on temperature and soot formation.

4. Extending the experimental and numerical study of the confined bluff-body combustor to include the following cases:
   - Reacting flow with a more dominant central fuel jet.
   - Combusting flow with swirling annulus air jet.
5. Obtaining measurements for species concentration and temperature within the confined bluff-body burner, using optical techniques.
6. Investigating the performance of other combustion models (including the Eddy Dissipation Concept) in the above reacting flows.

REFERENCES

CHAPTER 1

Abe, K., Kondoh, T., Nagano, Y., (1994), "A New Turbulence Model for Predicting Fluid Flow and Heat Transfer in Separating and Reattaching Flows - I. Flow Field Calculations," Int. Journal of Heat and Mass Transfer, Vol. 37, No. 1, pp. 139-151.

Apsley, D.D., Leschziner, M.A., (1998), "A New Low Reynolds Number Nonlinear Two-Equation Turbulence Model for Complex Flows," Int. Journal of Heat and Fluid Flow, Vol. 19, pp. 209-222.

Boussinesq, J., (1877), "Théorie de l'écoulement tourbillant," Mém. Présentés par divers Savants Acad. Sci. Inst. Fr., Vol. 23, pp. 46-50.

Chen, W.L., Leschziner, M.A., (1999a), "Turbulence Modelling of Rotor-Stator Interaction with Linear and Non-linear Eddy-viscosity Models," I.Mech.E. Conference.

Chen, W.L., Leschziner, M.A., (1999b), "Modelling Turbomachine Blade Flows with Non-linear Eddy-viscosity Models and Second-moment Closure," I.Mech.E. Conference.

Cho, H.H., Goldstein, R.J., (1994), "An Improved Low Reynolds-Number $k-\varepsilon$ Turbulence Model for Recirculating Flows," Int. J. Heat and Mass Transfer, Vol. 37, No. 10, pp. 1495-1508.

Cotton, M.A., Ismael, J.O., (1993), "Development of a Two-Equation Turbulence Model with Reference to a Strain Parameter," Proc. 5th Int. Symp. on Refined Flow Modelling and Turbulence Measurements, Paris.

Craft, T.J., Launder, B.E., Suga, K., (1993), "Extending the Applicability of Eddy Viscosity Models Through the Use of Deformation Invariants and Non-linear Elements," 5th Int. Symp. on Refined Flow Modelling and Turbulence Measurement, Paris.

Craft, T.J., Launder, B.E., Suga, K., (1996), "Development and Application of a Cubic Eddy-Viscosity Model of Turbulence," Int. Journal of Heat and Fluid Flow, Vol. 17, pp. 108-115.

Craft, T.J., Launder, B.E., Suga, K., (1997), "Prediction of Turbulent Transitional Phenomena with a Nonlinear Eddy-Viscosity Model," Int. Journal of Heat and Fluid Flow, Vol. 18, pp. 15-28.

Duncan, B.S., Liou, W.W., Shih, T.H., (1993), "A Multiple-Scale Turbulence Model for Incompressible Flow," NASA Technical Memo TM-106113.

Hanjalic, H., Launder, B.E., Schistel, R., (1979), "Multiple-Time-Scale Concepts in Turbulent Transport Modelling," Proc. Turbulent Shear Flows, Vol. 2, pp. 10.31-10.36.

Harlow, F.H., Nakayama, P.I., (1967), "Turbulent Transport Equations," Physics of Fluids, Vol. 10, p. 2323.

Jones, W.P., Launder, B.E., (1972), "The Prediction of Laminarisation with a Two-Equation Model of Turbulence," Int. J. Heat and Mass Transfer, Vol. 15, pp. 301-314.

Jones, W.P., Launder, B.E., (1973), "The Calculation of Low Reynolds-Number Phenomena with a Two-Equation Model of Turbulence," Int. J. Heat and Mass Transfer, Vol. 16, pp. 1119-1130.

Kobayashi, T., Togashi, S., (1996), "Comparison of Turbulence Models Applied to Backward-Facing Step Flow," JSME International Journal, Series B, Vol. 39, No. 3, pp. 453-460

Kolmogorov, A.N., (1942), "The Equations of Turbulent Motion in an Incompressible Fluid," Izv. Acad. Sci. USSR, Phys. 6, pp. 56-58.

Launder, B.E., (1981), "Turbulence Modelling in the Vicinity of a Wall," Stanford Conference on Complex Turbulent Flows, Volume 2, pp. 691-699.

Launder, B.E., (1989), "Second-moment Closure: Present .... and Future?" Int'l. Journal of Heat & Fluid Flow, Vol. 10, No. 4, pp. 282-300.

Launder, B.E., Sharma, B.I., (1974), "Application of the Energy-Dissipation Model of Turbulence to the Calculation of Flow Near a Spinning Disc," Letters in Heat and Mass Transfer, Vol. 1, pp. 131-137.

Launder, B.E., Spalding, D.B., (1972), Lectures in Mathematical Models of Turbulence, Academic Press, London.

Launder, B.E., Spalding, D.B., (1974), "The Numerical Computation of Turbulent Flows," Computer Methods in Applied Mechanics and Engineering, Vol. 3, pp. 269-289.

Lee, M.J., Kim, J., Moin, P., (1990), "Structure of Turbulence at High Shear Rate," Journal of Fluid Mechanics, Vol. 216, pp. 561-583.

Lien, F.S., Chen, W.L., Leschziner, M.A., (1996), "Low Reynolds-Number Eddy-Viscosity Modelling Based on Nonlinear Stress-Strain/Vorticity Relations," 3rd Symposium on Engineering Turbulence Modelling and Measurements, Crete.

Lien, F.S., Leschziner, M.A., (1994), "Assessment of Turbulence-Transport Models Including Nonlinear, RNG Eddy-Viscosity Formulation and Second-Moment Closure for Flow Over a Backward-Facing Step," Computers Fluids, Vol. 23, No. 8, pp. 983-1004.

Lumley, J.L., (1970), "Toward a Turbulent Constitutive Equation," Journal of Fluid Mechanics, Vol. 41, pp. 413-434.

Magagnato, F., (1999), "Unsteady Flow Past a Turbine Blade Using Non-linear Two-equation Turbulence Models," I.Mech.E. Conference.

Myong, H.K., Kasagi, N., (1990a), "A New Approach to Improved k-ε Turbulence Model for Wall-Bounded Shear Flows," JSME International Journal, Series II, Vol. 33, pp. 63-72.

Myong, H.K., Kasagi, N., (1990b), "Prediction of Anisotropy of the Near Wall Turbulence with an Anisotropic Low Reynolds-Number k-ε Turbulence Model," Journal of Fluids Engineering, Vol. 112, pp. 521-524.

Nagano, Y., Hishida, M., (1987), "Improved Form of the k-ε Model for Wall Turbulent Shear Flows," ASME Journal of Fluids Engineering, Vol. 109, pp. 156-160.

Nagano, Y., Kondoh, M., Tagawa, M., (1994), "Multiple-Scale Turbulence Model for Wall and Free Turbulent Flows," Transactions of the JSME: Part B, Vol. 60-572, pp. 1188-1195.

Nagano, Y., Shimada, M., (1995), "Computational Modeling and Simulation of Turbulent Flows," Computational Fluid Dynamics Review, Ed. Hafez, M. and Oshima, K., John Wiley & Sons.

Nagano, Y., Tagawa, M., (1990), "An Improved k-ε Model for Boundary Layer Flows," ASME Journal of Fluids Engineering, Vol. 112, pp. 33-39.

Nallasamy, M., (1987), "Turbulence Models and Their Applications to the Prediction of Internal Flows: A Review," Computers & Fluids, Vol. 15, No. 2, pp. 151-194.

Patel, V.C., Rodi, W., Scheuerer, G., (1985), "Turbulence Models for Near-Wall and Low Reynolds-Number Flows: A Review," AIAA Journal, Vol. 23, No. 9, pp. 1308-1319.

Rabbitt, M.J., (1997), "Some Validation of Standard, Modified and Nonlinear k-ε Turbulence Models," Int. Journal for Numerical Methods in Fluids," Vol. 24, pp. 965-986.

Rodi, W., (1972), The Prediction of Free Turbulent Boundary Layers by Use of a Two-Equation Model of Turbulence, Ph.D. Thesis, University of London.

Rodi, W., (1980), Turbulence Models and their Applications in Hydraulics, IAHR, Delft, Netherlands.

Rotta, J.C., (1968), "Statistische Theorie nichthomogener Turbulenz," Zeitschrift für Physik, Band 192, pp. 547-572 and Band 131, pp. 51-77 (1951). English Translation: Imperial College, Dept. Mech. Eng., Reports TWF/TN/38,39 (1968).

Rubinstein, R., Barton, J.M., (1990), "Non-linear Reynolds Stress Models and the Renormalisation Group," Physics of Fluids A, Vol. 2, No. 8, pp. 1472-1476.

Saffman, P.G., (1970), "A Model for Inhomogeneous Turbulent Flow," Proc. Royal Society, Series A, Vol. 317, p. 417.

Saffman, P.G., (1977), "Results of a Two-Equation Model for Turbulent Flows and Development of a Relaxation Stress Model for Application to Straining and Rotating Flows," Proc. Proj. SQUID Workshop on Turbulence in Internal Flows, ed. S. Murthy, pp. 191-231, Hemisphere, New York.

Sharif, M., Wong, Y., (1995), "Evaluation of the Performance of Three Turbulence Closure Models in the Prediction of Confined Swirling Flows," Computers & Fluids, Vol. 24, No. 1, pp. 81-100.

Shih, T.H., Lumley, J.L., (1993), "Kolmogorov Behaviour of Near-Wall Turbulence and its Application in Turbulence Modelling," International Journal of Computational Fluid Dynamics, Vol. 1, pp. 43-56.

Spalding, D.B., (1971), "The $k-\omega$ Model of Turbulence," Imperial College, Dept. Mech. Eng., Report (TM/TN/A/16).

Speziale, C.G., (1987), "On Nonlinear $k-l$ and $k-\varepsilon$ Models of Turbulence," Journal of Fluid Mechanics, Vol. 178, pp. 459-475.

Speziale, C.G., (1991), "Analytical Methods for the Development of Reynolds-Stress Closures in Turbulence," Ann. Rev. Fluid Mech., Vol. 23, pp. 107-15 7.

Speziale, C.G., Thangam, S., (1992), "Analysis of an RNG Based Turbulence Model for Separated Flows," Int. Journal of Engineering Science, Vol. 30, No. 10, pp. 1379-1388.

Suga, K., (1995), "Development and Application of a Non-linear Eddy-Viscosity Model Sensitised to Anisotropy," PhD Thesis, UMIST.

Thangam, S., Speziale, C.G., (1992), "Turbulent Flow Past a Backward-Facing Step: A Critical Evaluation of Two-Equation Models," AIAA Journal, Vol. 30, No. 5.

Yakhot, V., Orszag, S.A., (1986), "Renormalisation Group Analysis of Turbulence, Part 1: Basic Theory," J. Sci. Computing, Vol. 1, pp. 3-51.

Yakhot, V., Orszag, S.A., Thangam, S., Gatski, T.B., Speziale, C.G., (1992), "Development of Turbulence Models for Shear Flows by a Double Expansion Technique," Physics of Fluids A, Vol. 4, No. 7, pp. 1510-1520.

Yoshizawa, A., (1984), "Statistical Analysis of the Deviation of the Reynolds Stress from its Eddy Representation," JSME International Journal, Vol. 27, p. 1377.

CHAPTER 2

Borghi, R., (1988), "Turbulent Combustion Modelling," Prog. Energy Combustion Science, Vol. 14, pp. 245-292.

Boussinesq, J., (1877), "Théorie de l'écoulement tourbillant," Mém. Présentés par divers Savants Acad. Sci. Inst. Fr., Vol. 23, pp. 46-50.

Brizuela, E.A., (1995), "Brief Communication: Errors Due to Correlations in Evaluating Mean Density from Favre-Averaged Enthalpy and Composition in Turbulent Reactive Flow," Combustion & Flame, Vol. 103, pp. 343-347.

Chang, K.C., Hsieh, W.D., Chen, C.S., (1995), "A Modified Low Reynolds Number Turbulence Model Applicable to Recirculating Flow in Pipe Expansion," Journal of Fluids Engineering, Vol. 117, pp. 417-423.

Chomiak, J., Nisbet, J.R., (1995), "Modeling Variable Density Effects in Turbulent Flames -- Some Basic Considerations," Combustion & Flame, Vol. 102, pp. 371-386.

Chung, T.J., (1993), "Finite Element Methods in Turbulent Combustion," Numerical Modeling in Combustion, T.J. Chung (ed.), Taylor & Francis, Washington D.C.

Craft, T.J., Launder, B.E., Suga, K., (1996), "Development and Application of a Cubic Eddy-Viscosity Model of Turbulence," Int. Journal of Heat and Fluid Flow, Vol. 17, pp. 108-115.

Craft, T.J., Launder, B.E., Suga, K., (1997), "Prediction of Turbulent Transitional Phenomena with a Nonlinear Eddy-Viscosity Model," Int. Journal of Heat and Fluid Flow, Vol. 18, pp. 15-28.

Daly, B.J., Harlow, F.H., (1970), "Transport Equations in Turbulence," Physics of Fluids, Vol. 13, pp. 2634-2649.

Fluent 4.3 Manual, 1995.

Gran, I.R., Magnussen, B.F., (1996), "A Numerical Study of a Bluff-Body Stabilised Diffusion Flame, Parts 1 & 2," Combustion Science & Technology, Vol. 119, pp. 171-217, 1996.

Hanjalic, K., Launder, B., (1972), "A Reynolds Stress Model of Turbulence and its Applications to Thin Shear Flows," Journal of Fluid Mechanics, Vol. 52, pp. 609-638.

Jones, W.P., Kakhi, M., (1996), "Mathematical Modelling of Turbulent Flames," Unsteady Combustion, F. Culick et al (eds.), pp. 411-491, Kluwer Academic Publishers, Netherlands.

Jones, W.P., Launder, B.E., (1972), "The Prediction of Laminarisation with a Two-Equation Model of Turbulence," Int. J. Heat and Mass Transfer, Vol. 15, pp. 301-314.

Jones, W.P., Whitelaw, J.H., (1982), "Calculation Methods for Reacting Turbulent Flows: A Review," Combustion & Flame, Vol. 48, pp. 1-26.

Kuo, K., (1986), Principles of Combustion. John Wiley & Sons, New York.

Lau, J.H.W., (1995), "Brief Communication: Comparison of Pdf and Eddy-Dissipation Combustion Models Applied to a Propane Jet Flame," Combustion & Flame, Vol. 102, pp. 209-215.

Launder, B.E., (1981), "Turbulence Modelling in the Vicinity of a Wall," Stanford Conference on Complex Turbulent Flows, Vol. 2: Taxonomies, Reporters' Summaries, Evaluation, and Conclusions, pp. 691-699.

Launder, B.E., Sharma, B.I., (1974), "Application of the Energy-Dissipation Model of Turbulence to the Calculation of Flow Near a Spinning Disc," Letters in Heat and Mass Transfer, Vol. 1, pp. 131-137.

Launder, B.E., Spalding, D.B., (1974), "The Numerical Computation of Turbulent Flows," Computer Methods in Applied Mechanics and Engineering, Vol. 3, pp. 269-289.

Libby, P.A., Williams, F.A., (1994), Turbulent Reacting Flows, Academic Press, Oxford.

Lien, F.S., Leschziner, M.A., (1994), "Assessment of Turbulence-Transport Models Including Nonlinear, RNG Eddy-Viscosity Formulation and Second-Moment Closure for Flow Over a Backward-Facing Step," Computers Fluids, Vol. 23, No. 8, pp. 983-1004.

Lumley, J.L., (1978), "Computational Modelling of Turbulent Flows," Adv. Appl. Mech., Vol. 18, pp. 123-176.

Magnussen, B.F., Hjertager, B.H., (1976), "On Mathematical Modelling of Turbulent Combustion with Special Emphasis on Soot Formation and Combustion," 16th Symposium (International) on Combustion / The Combustion Institute, pp.719-729.

Nallasamy, M., (1987), "Turbulence Models and Their Applications to the Prediction of Internal Flows: A Review," Computers and Fluids, Vol. 3, pp. 151-194.

Patel, V.C., Rodi, W., Scheuerer, G., (1985), "Turbulence Models for Near-Wall and Low Reynolds-Number Flows: A Review," AIAA Journal, Vol. 23, No. 9, pp. 1308-1319.

Pun, W.M., Spalding, D.B., (1967), "A Procedure for Predicting the Velocity and Temperature Distributions in Confined, Steady, Turbulent, Gaseous Diffusion Flames," Proc. Int. Astronautical Federation Meeting, Belgrade.

Rodi, W., (1980), Turbulence Models and their Applications in Hydraulics, IAHR, Delft, Netherlands.

Rubinstein, R., Barton, J.M., (1990), "Non-linear Reynolds Stress Models and the Renormalisation Group," Physics of Fluids A, Vol. 2, No. 8, pp. 1472-1476.

Savill, A.M., (1993), "Some Recent Progress in the Turbulence Modelling of By-Pass Transition," Near-Wall Turbulent Flows, R.M.C. So, C.G. Speziale, B.E. Launder (eds.), Elsevier Science, New York, pp. 829-848.

Spalding, D.B., (1976), "Development of the Eddy-Break-Up Model of Turbulent Combustion," 16th Symposium (International) on Combustion/The Combustion Institute, pp. 1657-1663.

Speziale, C.G., (1991), "Analytical Methods for the Development of Reynolds-Stress Closures in Turbulence," Ann. Rev. Fluid Mech., Vol. 23, pp. 107-15 7.

Speziale, C.G., Thangam, S., (1992), "Analysis of an RNG Based Turbulence Model for Separated Flows," Int. Journal of Engineering Science, Vol. 30, No. 10, pp. 1379-1388.

Starner, S.H., Bilger, R.W., (1980), Eighteenth Symposoium (International) on Combustion, The Combustion Institute, Pittsburgh, pp. 912-930.

Suga, K., (1995), "Development and Application of a Non-linear Eddy-Viscosity Model Sensitised to Anisotropy," PhD Thesis, UMIST.

Tennekes, H., Lumley, J.L., (1972), A First Course in Turbulence, Cambridge, Mass., MIT Press.

Warnatz, J., Maas, U., Dibble, R.W., (1996), Combustion, Springer Verlag, Heidelberg.

Yakhot, V., Orszag, S.A., (1986), "Renormalisation Group Analysis of Turbulence, Part 1: Basic Theory," J. Sci. Computing, Vol. 1, pp. 3-51.

Yakhot, V., Orszag, S.A., Thangam, S., Gatski, T.B., Speziale, C.G., (1992), "Development of Turbulence Models for Shear Flows by a Double Expansion Technique," Physics of Fluids A, Vol. 4, No. 7, pp. 1510-1520.

Yakhot, V., Smith, L.M., (1992), "The Renormalisation Group, the ε-expansion and Derivation of Turbulence Models," Journal of Scientific Computing, Vol. 7, p. 35.

Yap, C.R., (1987), "Turbulent Heat and Momentum Transfer in Recirculating and Impinging Flows," PhD Thesis, University of Manchester.

CHAPTER 3

Apsley, D.D., Leschziner, M.A., (1998), "A New Low Reynolds Number Nonlinear Two-Equation Turbulence Model for Complex Flows," Int. Journal of Heat and Fluid Flow, Vol. 19, pp. 209-222.

Back, L.H., Roschke, E.J., (1972), "Shear-layer Flow Regimes and Wave Instabilities and Reattachment Lengths Downstream of an Abrupt Circular Channel Expansion," Journal of Applied Mechanics (Transactions of the ASME), pp. 677-681.

Craft, T.J., Launder, B.E., Suga, K., (1997), "Prediction of Turbulent Transitional Phenomena with a Nonlinear Eddy-Viscosity Model," Int. Journal of Heat and Fluid Flow, Vol. 18, pp. 15-28.

Eaton, J., Johnston, J., (1980), "Turbulent Flow Reattachment: An Experimental Study of the Flow and Structure Behind a Backward-Facing Step," Stanford University Report TR MD-39, Stanford, CA.

Gosman, A.D., Pun, W.M., (1974), Calculation of Recirculating Flows. Lecture Notes, Rep. No. HTS/74/2, Dept. Mechanical Engineering, Imperial College, London.

Gran, I.R., Ertesvag, I.S., Magnussen, B.F., (1997), "Influence of Turbulence Modelling on Predictions of Turbulent Combustion," AIAA Journal, Vol. 35, No. 1, pp. 106-110.

Jones, W.P., (1994), "Turbulence Modelling and Numerical Solution Methods for Variable Density and Combusting Flows," Turbulent Reacting Flows, P.A. Libby and F.A. Williams (eds.), Academic Press, Oxford, pp. 309-374

Launder, B.E., (1981), "Influence of Numerics and Computor Variance in the Computation of Complex Turbulent Flows," Stanford Conference on Complex Turbulent Flows, Vol. 2: Taxonomies, Reporters' Summaries, Evaluation and Conclusions, pp. 691-699.

Launder, B.E., Sharma, B.I., (1974), "Application of the Energy-Dissipation Model of Turbulence to the Calculation of Flow Near a Spinning Disc," Letters in Heat and Mass Transfer, Vol. 1, pp. 131-137.

Leschziner, M.A., (1980), "Practical Evaluation of Three Finite Difference Schemes for the Computation of Steady-State Recirculating Flows," Computer Methods in Applied Mechanics and Engineering, Vol. 23, pp. 293-312.

McGuirk, J., (1996), Private communication, Loughborough University.

McGuirk, J., (1998), Private communication, Loughborough University.

Nallasamy, M., (1987), "Turbulence Models and Their Applications to the Prediction of Internal Flows: A Review," Computers and Fluids, Vol. 3, pp. 151-194.

Patankar, S.V., Spalding, D.B., (1972), "A Calculation Procedure for Heat, Mass and Momentum Transfer in Three-Dimensional Flows," Int. Journal of Heat and Mass Transfer, Vol. 15, p. 1787.

Rabbitt, M.J., (1997), "Some Validation of Standard, Modified and Non-Linear $k-\varepsilon$ Turbulence Models," Int. Journal for Numerical Methods in Fluids, Vol. 24, pp. 965-986.

Ramos, J.I., (1993), "Finite-Difference Methods in Turbulent Combustion," Numerical Modeling in Combustion, T.J. Chung (ed.), Taylor and Francis, Washington D.C., pp. 281-373.

Spalding, D.B., (1972), "A Novel Finite Difference Formulation for Differential Expressions Involving Both First and Second Derivatives," Int. Journal for Numerical Methods in Engineering, Vol. 4, pp. 551-559.

Thangam, S., Speziale, C.G., (1992), "Turbulent Flow Past a Backward-Facing Step: A Critical Evaluation of Two-Equation Models," AIAA Journal, Vol. 30, No. 5.

Tropea, C., Stieglmeier, M., Weiser, N., Nitsche, N., (1989), "Experimental Investigation of the Flow Through Axisymmetric Expansions," ASME Journal of Fluids Engineering, Vol. 111, pp. 464-471.

Vahl Davis, G., Mallinson, G.D., (1976), "An Evaluation of Upwind and Central Difference Approximations By a Study of Recirculating Flow," Computers & Fluids, Vol. 4, pp. 29-43.

CHAPTER 4

Apsley, D.D., Leschziner, M.A., (1998), "A New Low Reynolds Number Nonlinear Two-Equation Turbulence Model for Complex Flows," Int. Journal of Heat and Fluid Flow, Vol. 19, pp. 209-222.

Back, L.H., Roschke, E.J., (1972), "Shear-layer Flow Regimes and Wave Instabilities and Reattachment Lengths Downstream of an Abrupt Circular Channel Expansion," Journal of Applied Mechanics (Transactions of the ASME), pp. 677-681.

Bish, E.S., (1998), "An Evaluation of Practical Numerical Approaches for Modelling the Near-Field Dynamics in a Step Swirl Combustor," Abstract, Proceedings of the

Third International Workshop on Measurements and Computation of Turbulent Nonpremixed Flames, 30 July - 1 Aug, Boulder, CO

Chang, K.C., Hsieh, W.D., Chen, C.S., (1995), "A Modified Low-Reynolds-Number Turbulence Model Applicable to Recirculating Flow in Pipe Expansion," ASME Journal of Fluids Engineering, Vol. 117, pp. 417-423.

Chen, Q., Nieuwstadt, F., (1993), "Numerical Prediction of Turbulent Swirling Flow in a Straight Pipe," Refined Flow Modelling and Turbulence Measurement, Proceedings of the 5th Int. Symposium, Sept. 7 – 10th, Paris.

Chieng, C., Launder, B., (1980), "On the Calculation of Turbulent Transport Downstream from an Abrupt Pipe Expansion," Numerical Heat Transfer, Vol. 3, pp. 189-207.

Craft, T.J., Launder, B.E., Suga, K., (1996), "Development and Application of a Cubic Eddy-Viscosity Model of Turbulence," Int. Journal of Heat and Fluid Flow, Vol. 17, pp. 108-115.

Craft, T.J., Launder, B.E., Suga, K., (1997), "Prediction of Turbulent Transitional Phenomena with a Nonlinear Eddy-Viscosity Model," Int. Journal of Heat and Fluid Flow, Vol. 18, pp. 15-28.

Driver, D., Seegmiller, H., (1985), "Features of a Reattaching Turbulent Shear Layer in Divergent Channel Flow," AIAA Journal, Vol. 23, pp. 163-171.

Durrett, R., Stevenson, W., Thompson, H., (1988), "Radial and Axial Turbulent Flow Measurements with an LDV in an Axisymmetric Sudden Expansion Air Flow," ASME Journal of Fluids Engineering, Vol. 110, pp. 367-372.

Durst, F., Jovanovic, J., Sender, J., (1993), "Detailed Measurements of the Near-Wall Region of Turbulent Pipe Flow," ASME FED Vol. 146, Data for Validation of CFD Codes.

Durst, F., Jovanovic, J., Sender, J., (1995), "LDA Measurements in the Near-Wall Region of Turbulent Pipe Flow," Journal of Fluid Mechanics, Vol. 295, pp. 305-335.

Eaton, J., Johnston, J., (1980), "Turbulent Flow Reattachment: An Experimental Study of the Flow and Structure Behind a Backward-Facing Step," Stanford University Report TR MD-39, Stanford, CA.

Hinze, J., (1975), Turbulence: An Introduction to its Mechanism and Theory. 2nd edition, McGraw-Hill, New York.

Hogg, S., Leschziner, M., (1989), "Computation of Highly Swirling Confined Flow with a Reynods Stress Turbulence Model," AIAA Journal, Vol. 27, No. 1, pp. 57-63.

Kim, J., Kline, S., Johnston, J., (1980), "Investigation of a Reattaching Turbulent Shear Layer: Flow Over a Backward-Facing Step," ASME Journal of Fluids Engineering, Vol. 102, pp. 302-308.

Kitoh, O., (1991), "Experimental Study of Turbulent Swirling Flow in a Straight Pipe," Journal of Fluid Mechanics, Vol. 225, pp., 445-479.

Kobayashi, T., Yoda, M., (1987), "Modified k-ε Model for Turbulent Swirling Flow in a Straight Pipe," JSME International Journal, Vol. 30, p. 66.

Laufer, J., (1954), "The Structure of Turbulence in a Fully-developed Pipe Flow," NACA Technical Report 1174.

Launder, B., (1989), "Second-Moment Closures: Present ... and Future?", Int. J. Heat and Fluid Flow, Vol. 10, No. 4, pp. 282-300.

Lien, F.S., Leschziner, M.A., (1994), "Assessment of Turbulence-Transport Models Including Nonlinear, RNG Eddy-Viscosity Formulation and Second-Moment Closure for Flow Over a Backward-Facing Step," Computers Fluids, Vol. 23, No. 8, pp. 983-1004.

Lilley, D., Chigier, N., (1971), "Nonisotropic Turbulent Stress Distribution in Swirling Flows from Mean Value Distributions," Int. Journal of Heat and Mass Transfer, Vol. 14, pp. 573-585.

Masri, A., (1998), "Computation of Bluff-Body Stabilised Jets and Flames," Proceedings of the Third International Workshop on Measurements and Computation of Turbulent Nonpremixed Flames, 30 July - 1 Aug, Boulder, CO.

Moon, L., Rudinger, G., (1977), "Velocity Distribution in an Abruptly Expanding Circular Duct," ASME Journal of Fluids Engineering, pp. 226-230.

Myong, H.K., Kasagi, N., (1990), "A New Approach to Improved $k-\varepsilon$ Turbulence Model for Wall-Bounded Shear Flows," JSME International Journal, Series II, Vol. 33, pp. 63-72.

Nallasamy, M., (1987), "Turbulence Models and Their Applications to the Prediction of Internal Flows: A Review," Computers & Fluids, Vol. 15, No. 2, pp. 151-194.

Patel, V.C., Rodi, W., Scheuerer, G., (1985), "Turbulence Models for Near-Wall and Low Reynolds-Number Flows: A Review," AIAA Journal, Vol. 23, No. 9, pp. 1308-1319.

Pope, S., (1975), Journal of Fluid Mechanics, Vol. 72, Part 2, p. 331.

Qin, H., (1984), "The Flow Characteristic of a Sudden Axisymmetric Expansion," PDR/CPDU IC/4, Imperial College, London.

Sampers, W., Lamers, A., von Steenhoven, A., (1993), "Analysis of Experimental and Numerical Results of a Turbulent Swirling Flow in a Tube," Chem. Eng. Comm., Vol. 125, pp. 187-196.

Sharif, M., Wong, Y., (1995), "Evaluation of the Performance of Three Turbulence Closure Models in the Prediction of Confined Swirling Flows," Computers & Fluids, Vol. 24, No. 1, pp. 81-100.

Sindir, M., (1982), "Numerical Study of Separating and Reattaching Flows in a Backward-Facing Step Geometry," Doctoral Thesis, University of California, Davis, CA.

Speziale, C.G., Thangam, S., (1992), "Analysis of an RNG Based Turbulence Model for Separated Flows," Int. Journal of Engineering Science, Vol. 30, No. 10, pp. 1379-1388.

Suga, K., (1995), "Development and Application of a Non-linear Eddy-Viscosity Model Sensitised to Anisotropy," PhD Thesis, UMIST.

Tennekes, H., Lumley, J.L., (1972), A First Course in Turbulence, Cambridge, Mass., MIT Press.

Thangam, S., Speziale, C.G., (1992), "Turbulent Flow Past a Backward-Facing Step: A Critical Evaluation of Two-Equation Models," AIAA Journal, Vol. 30, No. 5.

Thompson, H., Stevenson, W., Durrett, R., (1984), Laser Velocimeter Measurements and Analysis in Turbulent Flows With Combustion - Part III: A Correction Lens for Laser Dopple Measurements in a Cylindrical Tube, AFWAL - TR - 82 - 2076.

Tropea, C., Stieglmeier, M., Weiser, N., Nitsche, W., (1989), "Experimental Investigation of Flow Through Axisymmetric Expansions," ASME Journal of Fluids Engineering, Vol. 111, pp. 464-471.

Yakhot, V., Orszag, S.A., Thangam, S., Gatski, T.B., Speziale, C.G., (1992), "Development of Turbulence Models for Shear Flows by a Double Expansion Technique," Physics of Fluids A, Vol. 4, No. 7, pp. 1510-1520.

CHAPTER 5

Correa, S.M., Gulati, A., (1992), "Measurements and Modelling of a Bluff Body Stabilised Flame," Combustion & Flame, Vol. 89, pp. 195-213.

Correa, S.M., Pope, S.B., (1992), "Comparison of a Monte Carlo PDF / Finite-Volume Mean Flow Model with Bluff-Body Raman Data," 24th Symposium (International) on Combustion/The Combustion Institute, pp. 279-285.

Dally, B.B., Fletcher, D.F., Masri, A.R., (1995), "Computations of a Non-Reacting Bluff Body Jet Flow," First Asian CFD Conference Proceedings, Hong Kong, Volume 1, pp. 177-182.

Elghobashi, S.E., (1977), "Studies in the Prediction of Turbulent Diffusion Flames," Studies in Convection - Vol. 2 (Ed. Launder, B.E.), Academic Press, London.

Elghobashi, S.E., Pun, W.M., (1974), "A Theoretical and Experimental Study of Turbulent Diffusion Flames in Cylindrical Furnaces," 15th Int. Symposium on Combustion, pp. 1353-1365.

Gran, I.R., Magnussen, B.F., (1996), "A Numerical Study of a Bluff-Body Stabilised Diffusion Flame, Parts 1 & 2," Combustion Science & Technology, Vol. 119, pp. 171-217.

Gran, I.R., Ertesvag, I.S., Magnussen, B.F., (1997), "Influence of Turbulence Modelling on Predictions of Turbulent Combustion," AIAA Journal, Vol. 35, No. 1, pp. 106-110.

Jones, W.P., Kakhi, M., (1996), "Mathematical Modelling of Turbulent Flames," Unsteady Combustion, F. Culick et al (eds.), pp. 411-491, Kluwer Academic Publishers, Netherlands.

Kim, Y.M., Chung, T.J., (1989), "Finite-Element Analysis of Turbulent Diffusion Flames," AIAA Journal, Vol. 27, pp. 330-339.

Lockwood, F.C., El-Mahallawy, F.M., Spalding, D.B., (1974), "An Experimental and Theoretical Investigation of Turbulent Mixing in a Cylindrical Furnace," The Combustion Institute, pp. 283-293.

Masri, A.R., (1998), "Computation of Bluff-Body Stabilised Jets and Flames," Proceedings of the Third International Workshop on Measurements and Computation of Turbulent Nonpremixed Flames, 30 July - 1 Aug, Boulder, CO.

Masri, A.R., Dibble, R.W., Barlow, R.S., (1992), "Raman-Rayleigh Measurements in Bluff-Body Stabilised Flames of Hydrocarbon Fuels," 24th Symposium (International) on Combustion/The Combustion Institute, pp. 317-324.

Roquemore, W.M., Britton, R.L., Sandhu, S.S., (1983), "Dynamic Behaviour of a Bluff-Body Diffusion Flame," AIAA Journal, Vol. 21, No. 10, pp. 1410-1417.

Schefer, R.W., Namazian, M., Kelly, J., Perrin, M., (1996), "Effect of Confinement on Bluff-Body Burner Recirculation Zone Characteristics and Flame Stability," Combustion Science & Technology, Vol. 120, pp. 185-211.

Weinberg, F.J., (1986), "Introduction," Advanced Combustion Methods, editor F.J. Weinberg, Academic Press.

CHAPTERS 6 AND 7

Barlow, R.S., (1997), Private communication, Sandia National Laboratories.

Becker, H.A., Yamazaki, S., (1978), "Entraiment, Momentum Flux and Temperature in Vertical Free Turbulent Diffusion Flames," Combustion & Flame, Vol. 33, pp. 123-149.

Clarke, A., (1994), D. Phil: Thesis, Oxford University.

Elliman, D.G., Fussey, D.E., Hay, N., (1978), "Predictions and Measurements of a Turbulent, Axisymmetric Ducted Diffusion Flame," International Journal of Heat Transfer, Vol. 21, pp. 1393-1402.

Gaz de France, (1992), GDF Report 92102-3-A.

Geiss, S. (1997), Private communication, TH Darmstadt.

Gengembre, E., Cambray, P., Karmed, D., Bellet, J., (1984), "Turbulent Diffusion Flames with Large Buoyancy Effects," Combustion Science & Technology, Vol. 41, pp. 55-67.

Grant, I., (1997), "Particle Image Velocimetry: A Review," Proc. Inst. Mech. Engrs, Vol. 211, Part C, pp. 55-76.

Hargrave, G.K., (1999), Private communication, Loughborough University

Hossain, M., (1998), Private communication, Loughborough University.

Jones, J.C., (1998), Private communication, Loughborough University.

Masri, A.R., (1997), Private communication, University of Sydney.

Masri, A.R., (1998), "Computation of Bluff-Body Stabilised Jets and Flames," Proceedings of the Third International Workshop on Measurements and Computation of Turbulent Nonpremixed Flames, 30 July - 1 Aug, Boulder, CO.

Masri, A.R., Dibble, R.W., Barlow, R.S., (1992), "Raman-Rayleigh Measurements in Bluff-Body Stabilised Flames of Hydrocarbon Fuels," 24th Symposium (International) on Combustion/The Combustion Institute, pp. 317-324.

Masri, A.R., Dibble, R.W., Barlow, R.S., (1996), "The Structure of Turbulent Nonpremixed Flames Revealed by Raman-Rayleigh-LIF Measurements," Prog. Energy Combustion Science, Vol. 22, pp. 307-362.

Masri, A.R., Kelman, J.B., Dally, B.B., (1998), "The Instantaneous Spatial Structure of the Recirculation Zone in Bluff-Body Stabilised Flames," 27th Symposium (International) on Combustion/The Combustion Institute, pp. 1031-1038.

Meier, W., (1997), Private communication, DLR (Deutsche Forschungsanstalt für Luft- und Raumfahrt).

Reeves, M., (1995), "Particle Image Velocimetry Applied to Internal Combustion Engine In-Cylinder Flows," PhD Thesis, Loughborough University.

Roquemore, W.M., Bradley, R.P., Stutrud, J.S., Reeves, C.M., Krishnamurthy, L., (1980), "Preliminary Evaluation of a Combustor for Use in Modelling and Diagnostics Development," ASME Gas Turbine Conference and Products Show, New Orleans, LA.

Sheen, H., Chen, W., Jeng, S., (1996), "Recirculation Zones of Unconfined and Confined Annular Swirling Jets," AIAA Journal, Vol. 34, No. 3, pp. 572-579.

Schefer, R.W., (1997), Private communication, Sandia National Laboratories.

Schefer, R.W., Namazian, M., Kelly, J., (1987), "Velocity Measurements in a Turbulent Nonpremixed Bluff-Body Stabilised Flame," Combustion Science & Technology, 1987, Vol. 56, pp. 101-138.

Schefer, R.W., Namazian, M., Kelly, J., (1994), "Velocity Measurements in Turbulent Bluff-Body Stabilised Flows," AIAA Journal, Vol. 32, No. 9, pp. 1844-1851.

Schefer, R.W., Namazian, M., Kelly, J., Perrin, M., (1996), "Effect of Confinement on Bluff-Body Recirculation Zone Characteristics and Flame Stability," Combustion Science & Technology, Vol. 120, pp. 185-211.

Sydney University Group, http://www.me.su.oz.au/research/energy/energy.html

Thompson, H., Stevenson, W., Durrett, R., (1984), Laser Velocimeter Measurements and Analysis in Turbulent Flows With Combustion - Part III: A Correction Lens for Laser Doppler Measurements in a Cylindrical Tube, AFWAL - TR - 82 - 2076.

TNF (Turbulent Nonpremixed Flames) Group, http://www.ca.sandia.gov/ - tdf/Workshop.html

Vachon, M., Cambray, P., Maciaszek, T., Bellet, J., (1986), "Temperature and Velocity Fluctuation Measurements in a Diffusion Flame with Large Buoyancy Effects," Combustion Science & Technology, Vol. 48, pp. 223-240.

PUBLICATIONS

Carroni, R., Versteeg, H.K., "Investigation of a Third-Order, Nonlinear, Eddy-Viscosity Turbulence Model Applied to a Pipe Expansion Flow," Proceedings of the 3rd ASME/JSME Joint Fluids Engineering Conference, July 18-23, 1999, San Francisco, California.

APPENDIX A: Mean Strain- and Vorticity Rates, and Momentum Transport Equations.

Note that the subscripts 1,2,3 refer to the axial (x), radial (r) and tangential (θ) directions, respectively. In axisymmetric, swirling flows, all gradients in θ are zero.

Mean-strain rates:

$$S_{11} = \left[2\frac{\partial U}{\partial x} - \frac{2}{3}\left(\nabla \cdot \vec{U}\right) \right]$$

$$S_{12} = S_{21} = \left[\frac{\partial U}{\partial r} + \frac{\partial V}{\partial x} \right]$$

$$S_{13} = S_{31} = \left[\frac{\partial W}{\partial x} + \frac{1}{r}\frac{\partial U}{\partial \theta} \right]$$

$$S_{22} = \left[2\frac{\partial V}{\partial r} - \frac{2}{3}\left(\nabla \cdot \vec{U}\right) \right]$$

$$S_{23} = S_{32} = \left[r\frac{\partial}{\partial r}\left(\frac{W}{r}\right) + \frac{1}{r}\frac{\partial V}{\partial \theta} \right]$$

$$S_{33} = \left[2\left(\frac{1}{r}\frac{\partial W}{\partial \theta} + \frac{V}{r}\right) - \frac{2}{3}\left(\nabla \cdot \vec{U}\right) \right]$$

where $\nabla \cdot \vec{U} = \frac{1}{r}\frac{\partial}{\partial r}(rV) + \frac{1}{r}\frac{\partial W}{\partial \theta} + \frac{\partial U}{\partial x}$

Mean-vorticity rates:

$$\Omega_{11} = \Omega_{22} = \Omega_{33} = 0$$

$$\Omega_{12} = \left[\frac{\partial U}{\partial r} - \frac{\partial V}{\partial x}\right]$$

$$\Omega_{21} = -\Omega_{12}$$

$$\Omega_{13} = \left[\frac{1}{r}\frac{\partial U}{\partial \theta} - \frac{\partial W}{\partial x}\right]$$

$$\Omega_{31} = -\Omega_{13}$$

$$\Omega_{23} = \left[\frac{1}{r}\frac{\partial V}{\partial \theta} - \frac{1}{r}\frac{\partial}{\partial r}(rW)\right]$$

$$\Omega_{32} = -\Omega_{23}$$

Momentum transport equations for swirling flows (using cylindrical coordinates):

Axial momentum:

$$\rho\left[\frac{\partial U}{\partial t} + V\frac{\partial U}{\partial r} + \frac{W}{r}\frac{\partial U}{\partial \theta} + U\frac{\partial U}{\partial x}\right] = -\frac{\partial p}{\partial x} - \left[\frac{1}{r}\frac{\partial}{\partial r}(r\tau_{12}) + \frac{1}{r}\frac{\partial \tau_{13}}{\partial \theta} + \frac{\partial \tau_{11}}{\partial x}\right]$$

Radial momentum:

$$\rho\left[\frac{\partial V}{\partial t} + V\frac{\partial V}{\partial r} + \frac{W}{r}\frac{\partial V}{\partial \theta} - \frac{W^2}{r} + U\frac{\partial V}{\partial x}\right] = -\frac{\partial p}{\partial r} - \left[\frac{1}{r}\frac{\partial}{\partial r}(r\tau_{22}) + \frac{1}{r}\frac{\partial \tau_{23}}{\partial \theta} - \frac{\tau_{33}}{r} + \frac{\partial \tau_{12}}{\partial x}\right]$$

Tangential momentum:

$$\rho\left[\frac{\partial W}{\partial t} + V\frac{\partial W}{\partial r} + \frac{W}{r}\frac{\partial W}{\partial \theta} + \frac{VW}{r} + U\frac{\partial W}{\partial x}\right] = -\frac{1}{r}\frac{\partial p}{\partial \theta} - \left[\frac{1}{r^2}\frac{\partial}{\partial r}(r^2\tau_{23}) + \frac{1}{r}\frac{\partial \tau_{33}}{\partial \theta} + \frac{\partial \tau_{13}}{\partial x}\right]$$

APPENDIX B: COMPARISON OF β-PDF AND EDC METHODS

Gran & Magnussen (1996) reported that the inclusion of detailed chemistry in the eddy dissipation concept (EDC) yielded good agreement with experimental results, particularly in conjunction with the Reynolds stress turbulence closure. However, it was also observed that the choice of turbulence model had a greater effect than varying the combustion models, particularly when the fast-chemistry assumption is valid. In order to test the predictive and computational merits and drawbacks of both assumed-pdf and EDC, simulations of the Correa & Gulati (1992) burner (described in Chapter 5) were run with the Fluent code, using k-ε, RNG and RSM turbulence models (a fully-developed pipe flow inlet profile was utilised for the fuel jet). The domain dimensions and boundary conditions are the same as those for the TEACH code simulations described in Chapter 5.

Grid independence was demonstrated by comparing radial profiles at x/d = 10 and x/d = 20, which were computed on highly non-uniform 180×77 and 230×100 meshes. Gran & Magnussen (1996) had utilised a 75×75 grid which was reportedly nearly of sufficient density. Execution of the simulations confirmed the fact that the EDC required far greater CPU times than the β-pdf model.

The computed results are compared with the limited experimental data provided by Correa & Gulati (1992) and Correa & Pope (1992). Figures B.1 to B.3 demonstrate that the results with the β-pdf and EDC models are similar, and that the difference between the RNG and RSM models is small. The standard k-ε model seems to be less affected by choice of combustion model than the RNG and RSM models; this is particularly evident in figure B.3. The radial temperature profiles (figures B.4 and B.5) reveal similar trends.

In the light of the available comparisons between experimental and simulated data, the EDC does not apparently return vastly improved results relative to the β-pdf

combustion model, particularly when one takes into account the additional computational resources required for the solution of transport equations of all the major species. Gran & Magnussen (1996) concluded that the choice of turbulence model has the greatest impact on the predictions. More importantly, when fast-chemistry is assumed, the effects of EDC and β-pdf combustion models are overshadowed by the influence of the turbulence model. These findings lend support to the use of the β-pdf combustion model in bluff-body, reacting flows.

Conclusions:

- EDC requires much larger CPU times than β-pdf.
- Judging from the comparisons with the available experimental data, the EDC has no significant advantage over the β-pdf in bluff-body burners.
- Turbulence models have a larger impact than the choice of combustion model.

(a)

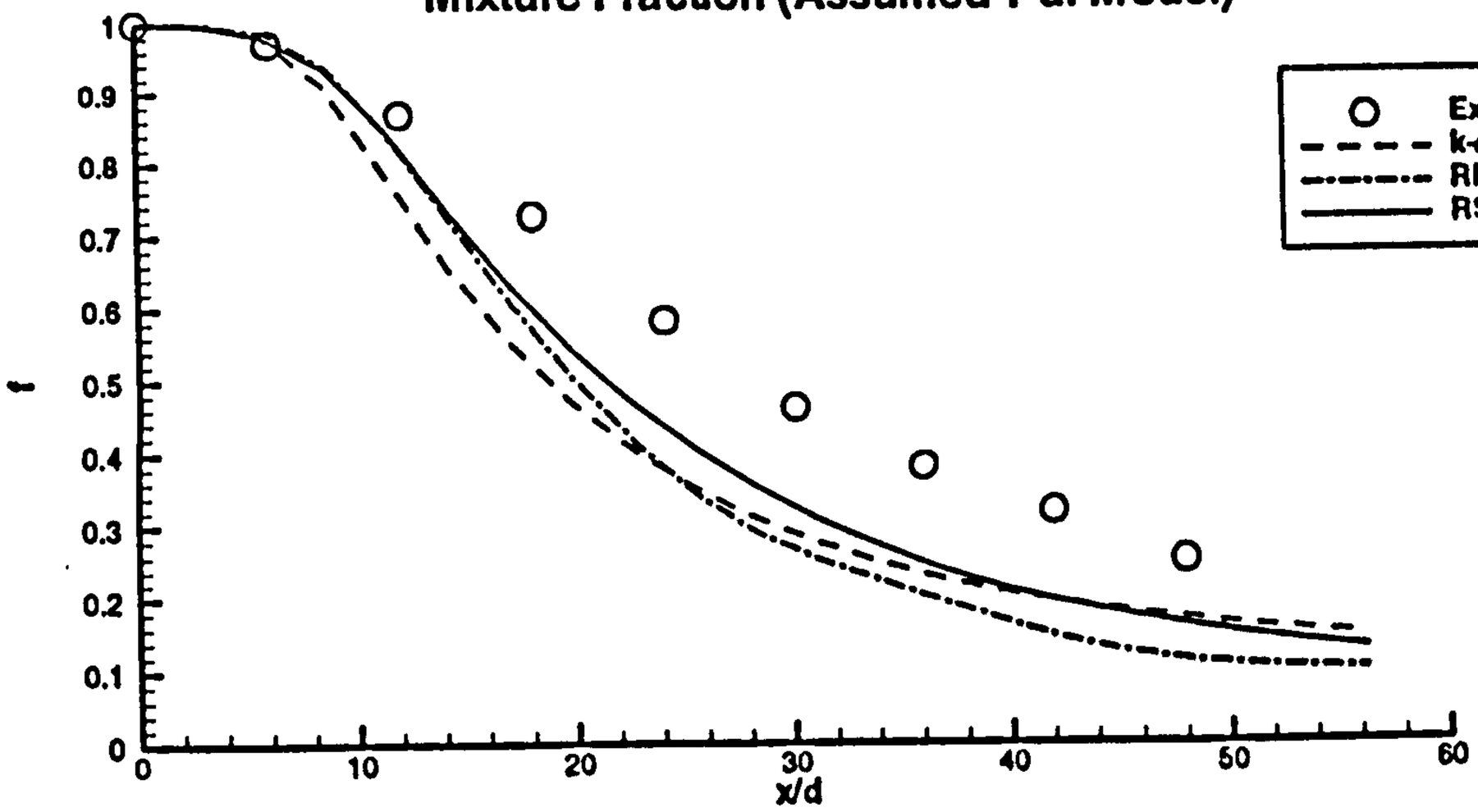

(b)

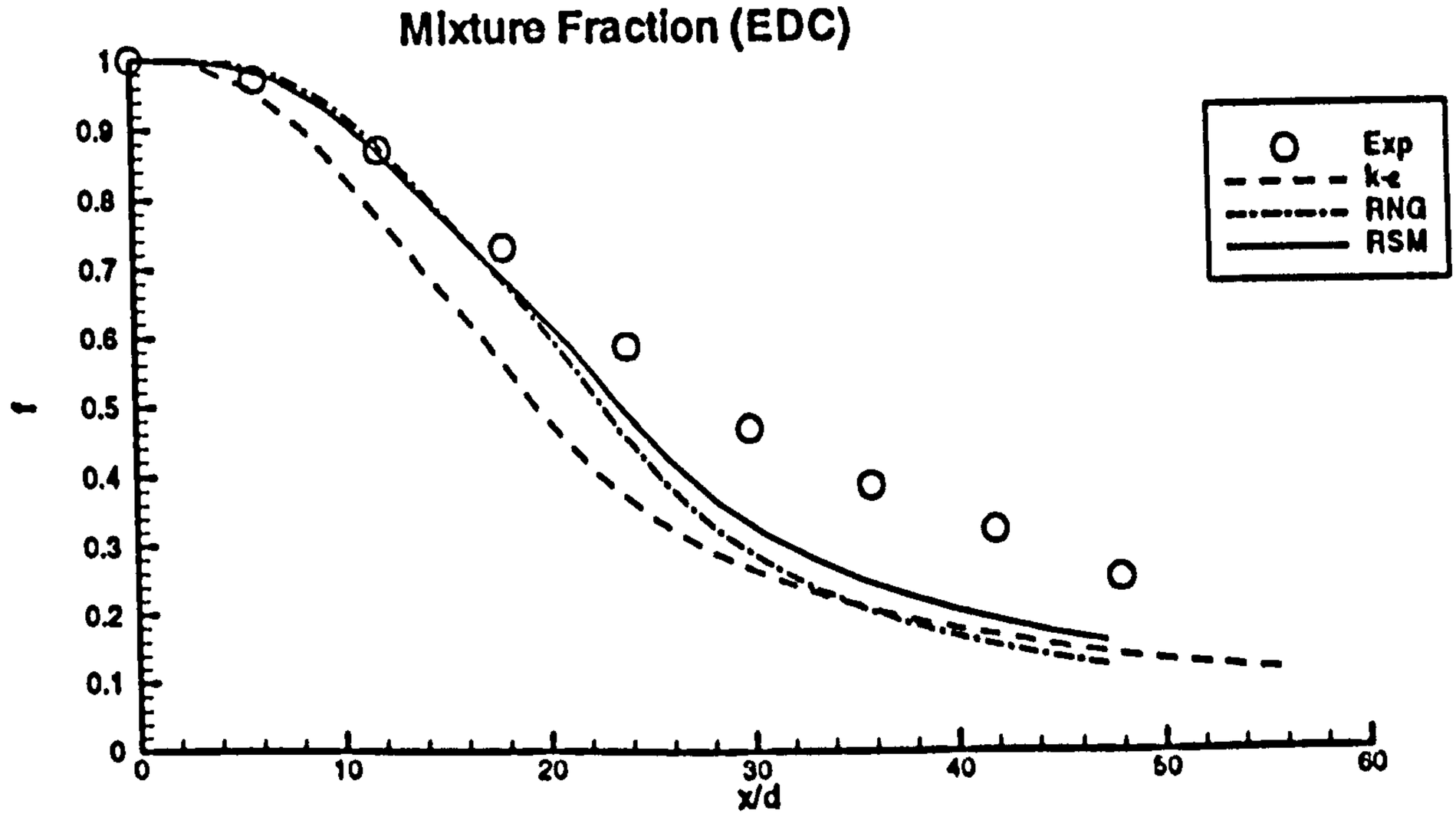

Figure B.1: Axial distribution of the mixture fraction along the centreline, using (a) assumed-pdf and (b) EDC combustion models.

(a)

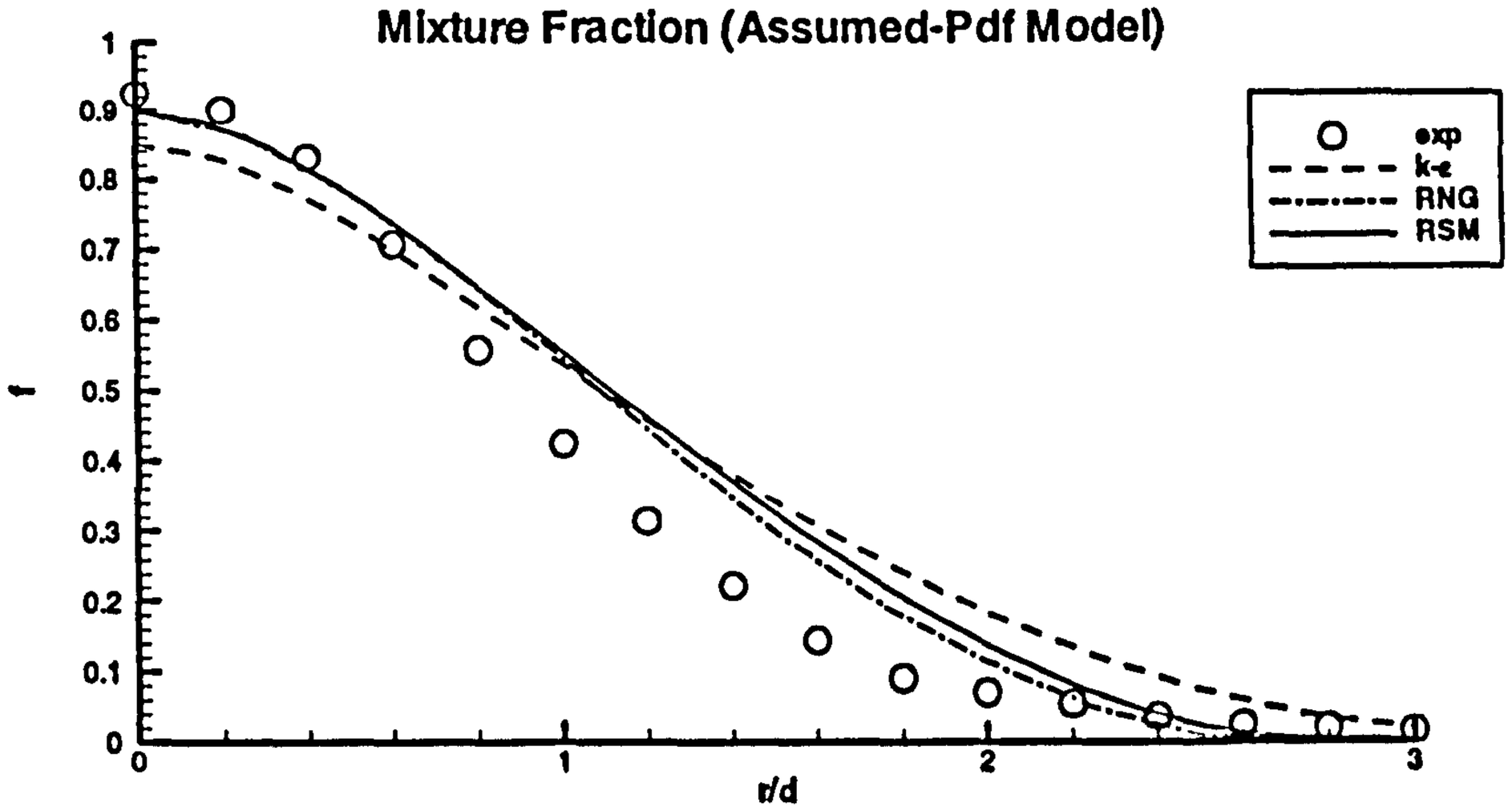

(b)

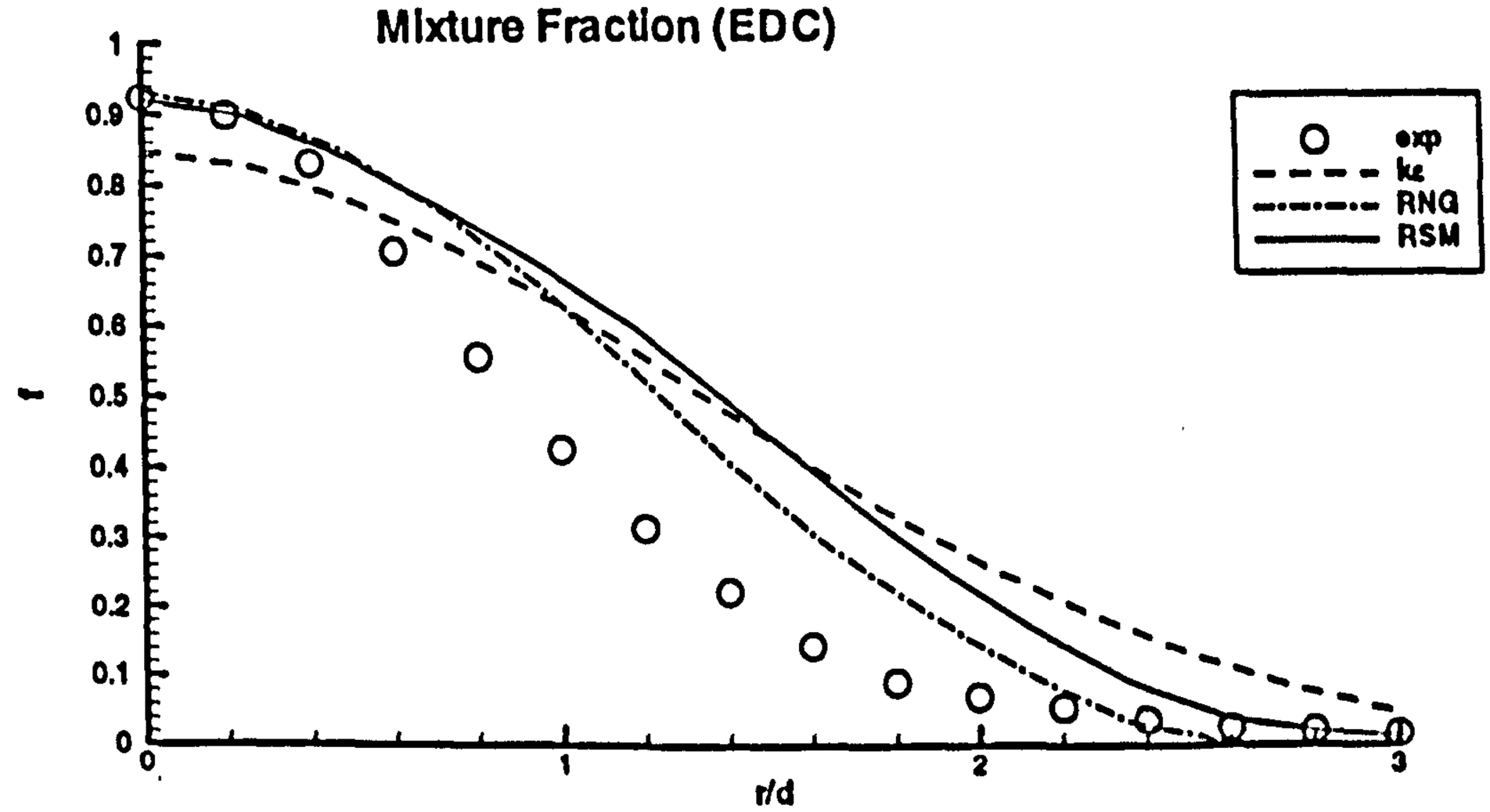

Figure B.2: Radial distribution of the mixture fraction at x/d = 10, using (a) assumed-pdf and (b) EDC combustion models.

(a)

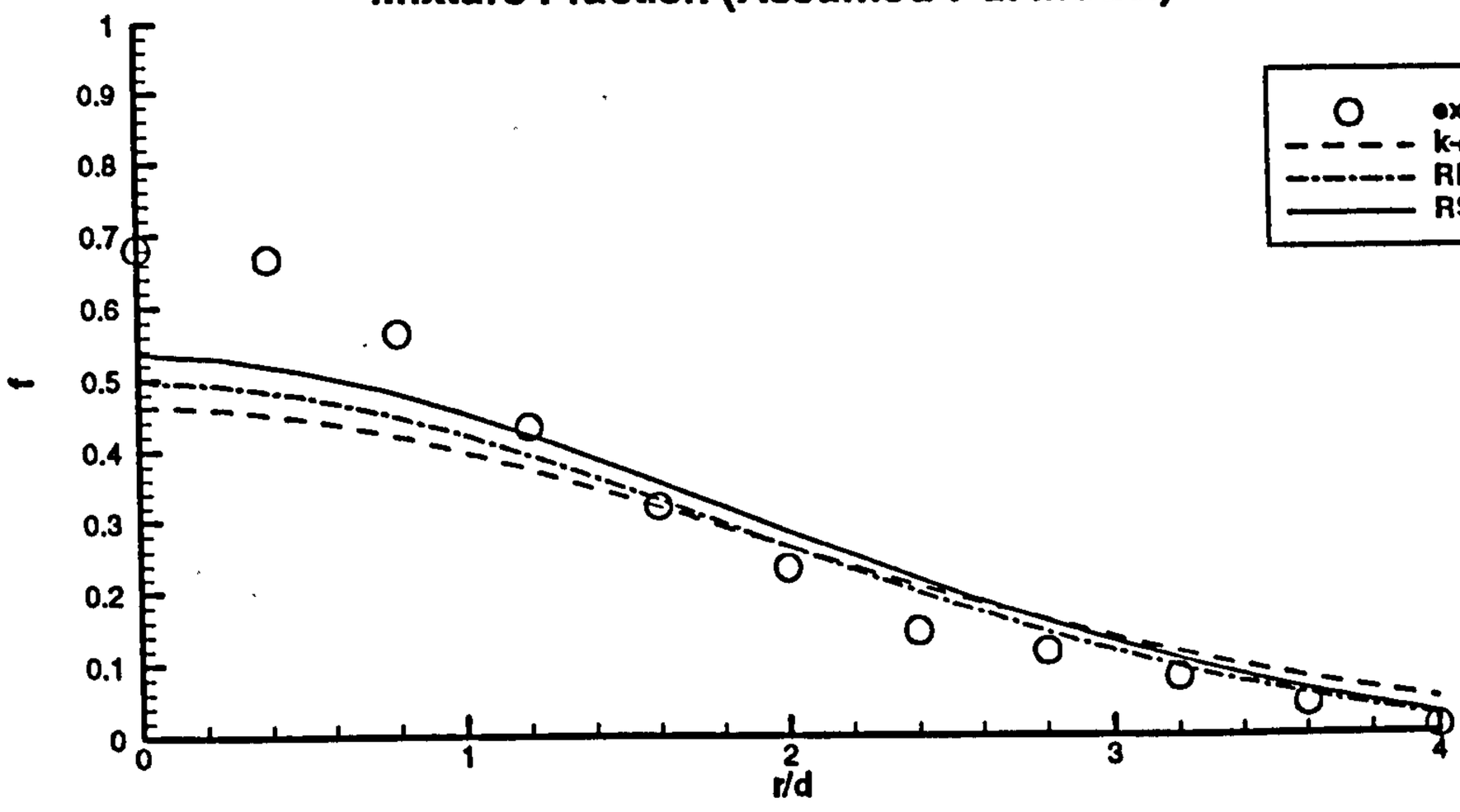

(b)

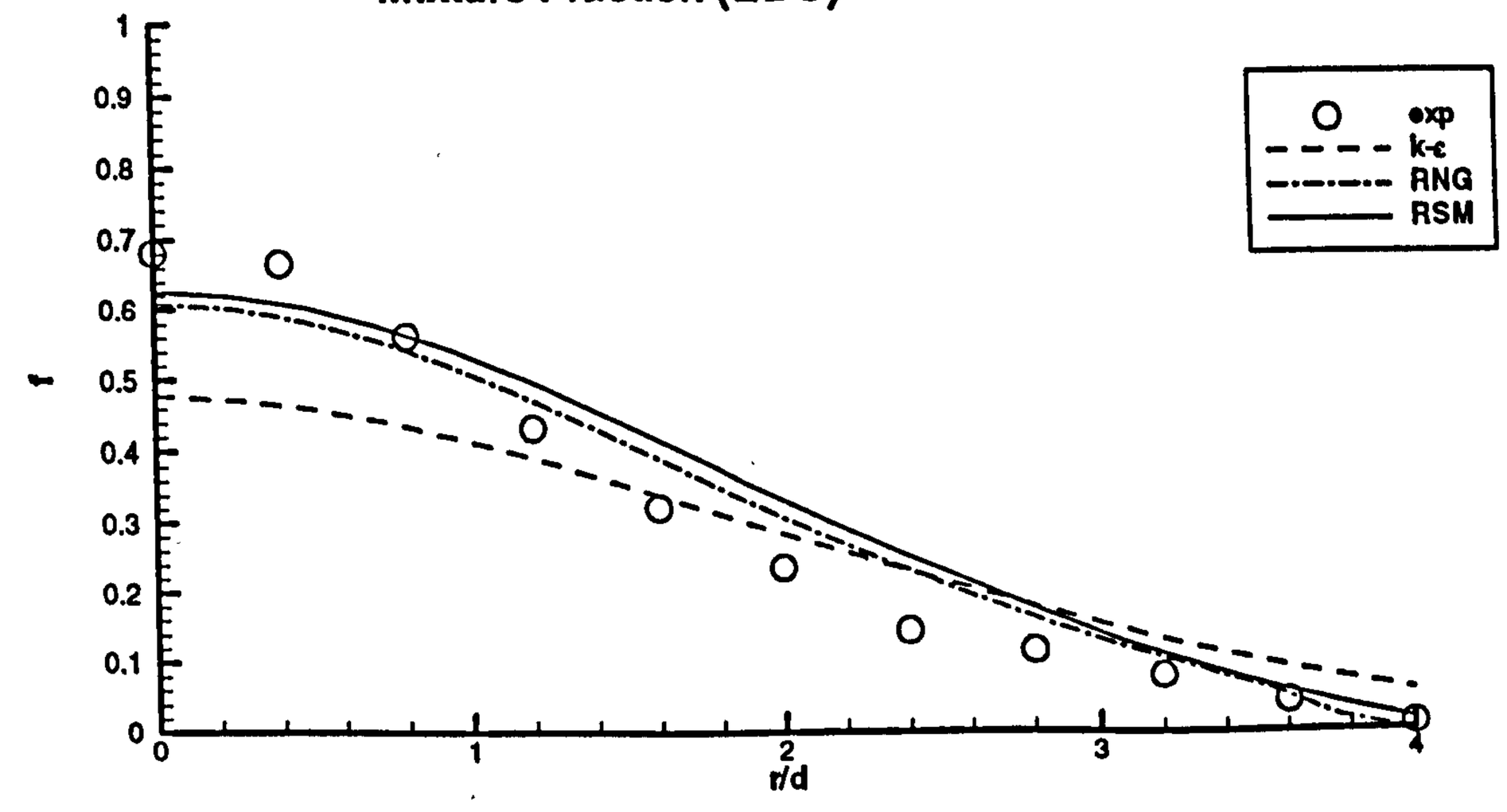

Figure B.3: Radial distribution of the mixture fraction at x/d = 20, using (a) assumed-pdf and (b) EDC combustion models.

(a)

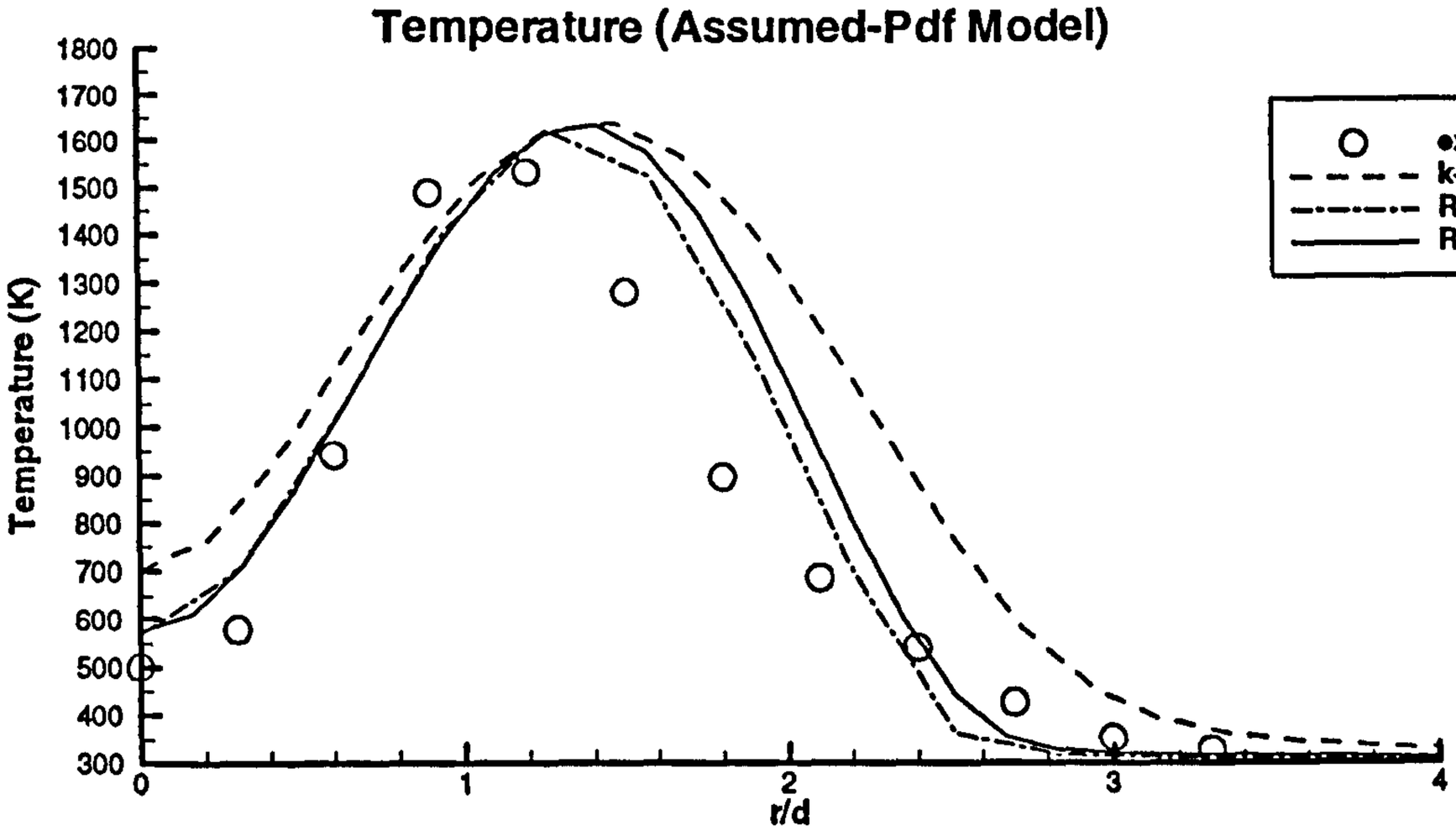

(b)

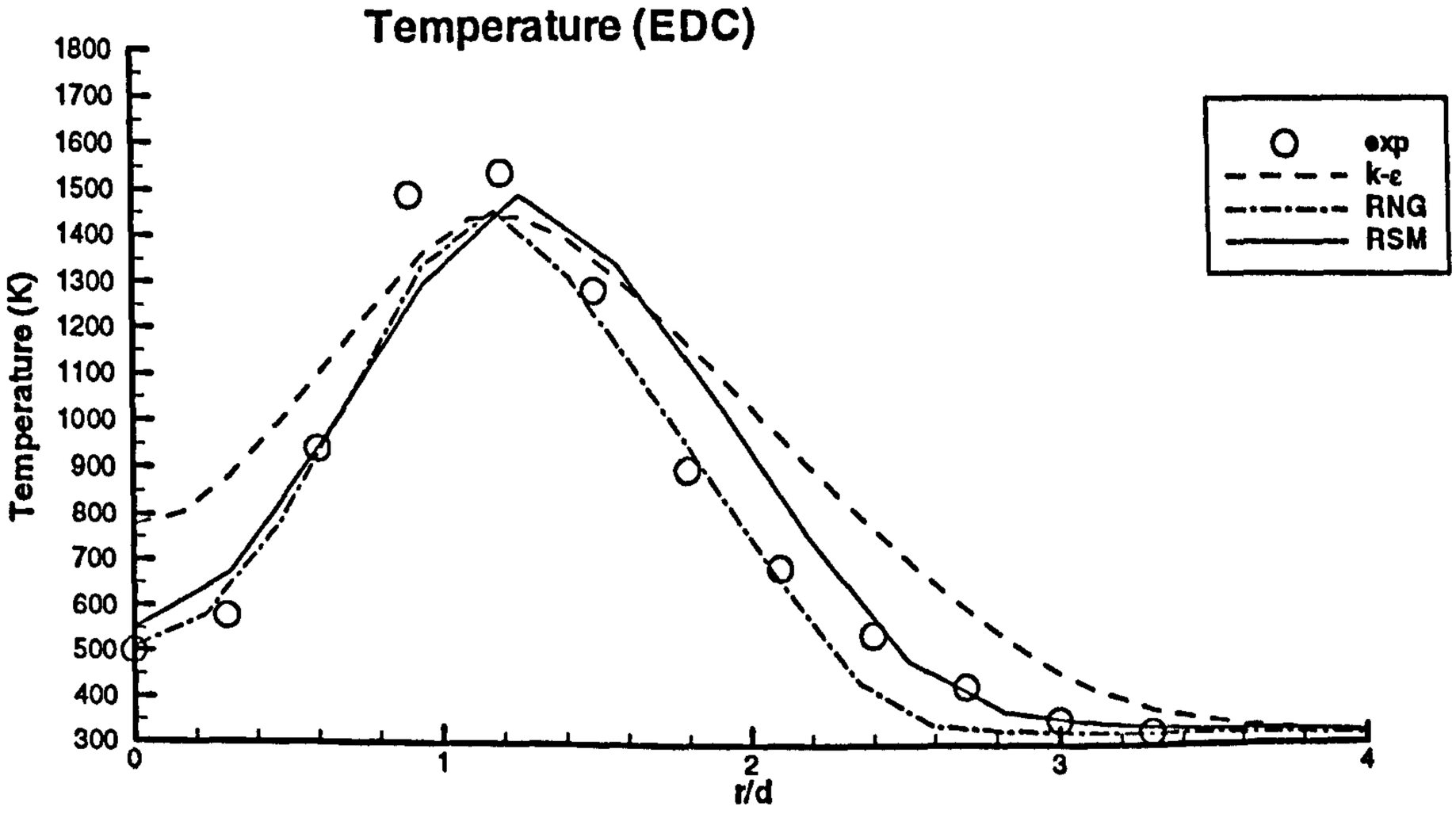

Figure B.4: Radial distribution of temperature at x/d = 10, using (a) assumed-pdf and (b) EDC combustion models.

(a)

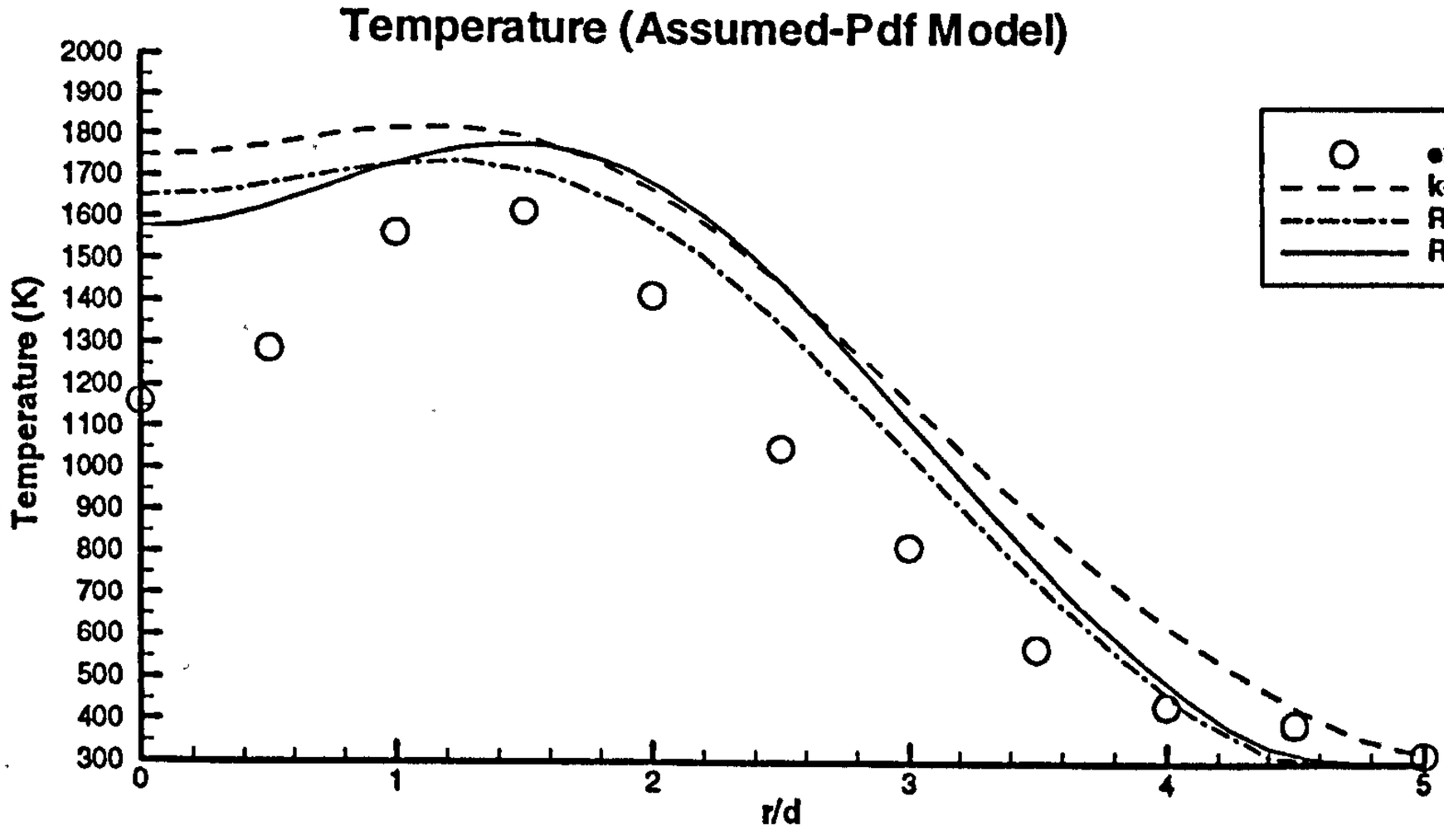

(b)

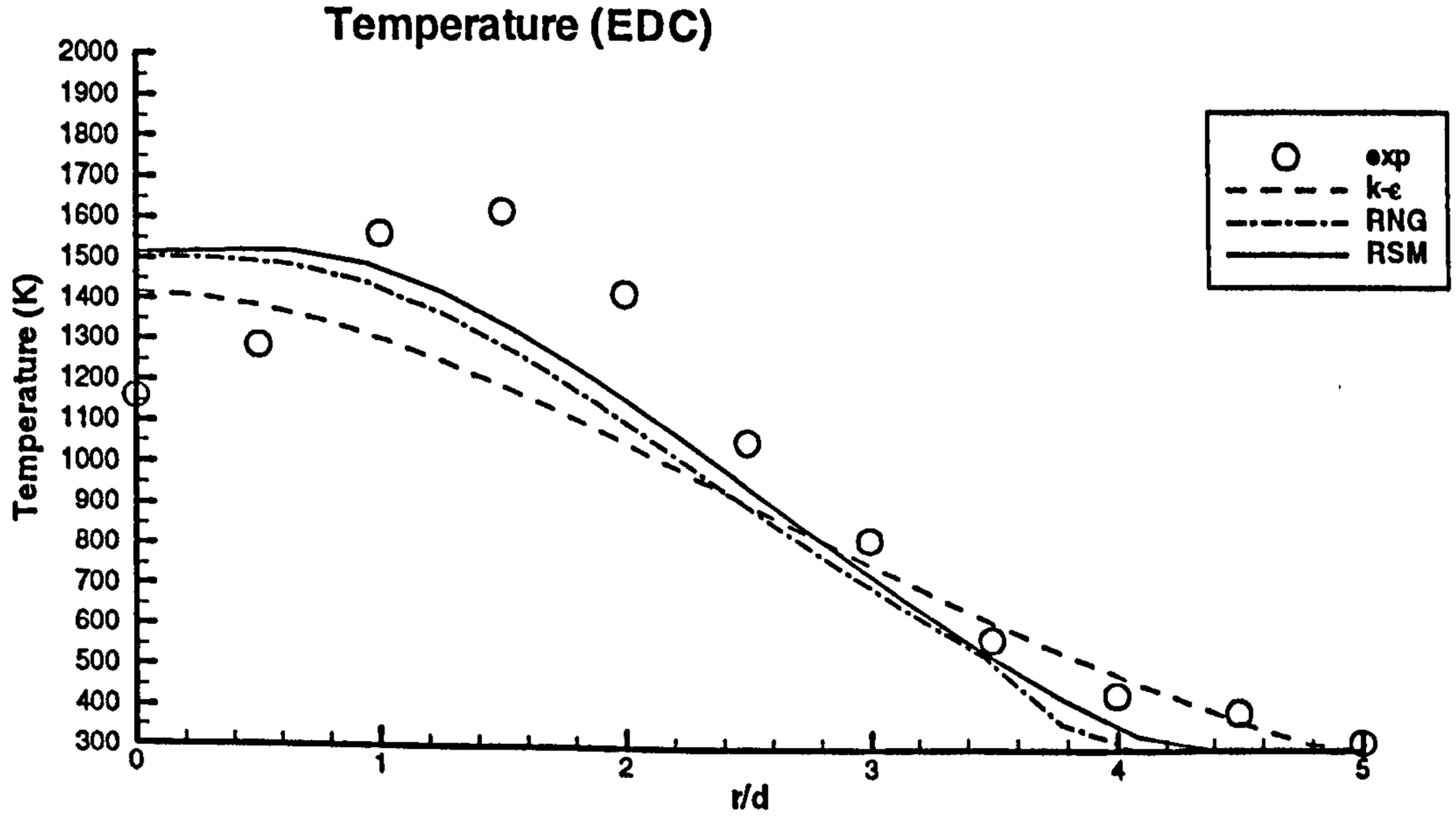

Figure B.5: Radial distribution of temperature at x/d = 20, using (a) assumed-pdf and (b) EDC combustion models.

APPENDIX C: TESTING OF SWIRL-RELATED MODIFICATIONS

In order to verify that the tangential momentum equation and associated wall boundary conditions had been correctly implemented in the TEACH code, a highly-swirling pipe flow (described in detail in Chapter 4) was simulated using the TEACH and Fluent codes. The computational meshes were identical and the standard k-ε turbulence model was used in both cases. The only known difference between the codes is that Fluent utilises a second-order accurate upwinding within the hybrid scheme, whilst TEACH employs first-order accurate upwinding. Plots of velocities and turbulence energy (figures C.1 to C.4) reveal that the two sets of predictions are in close agreement. This demonstrates that:

- The swirl-related modifications in TEACH have been correctly implemented.
- The effect of using second-order upwinding is much smaller than the errors introduced by the turbulence model, as witnessed by the difference between computed and experimental results.

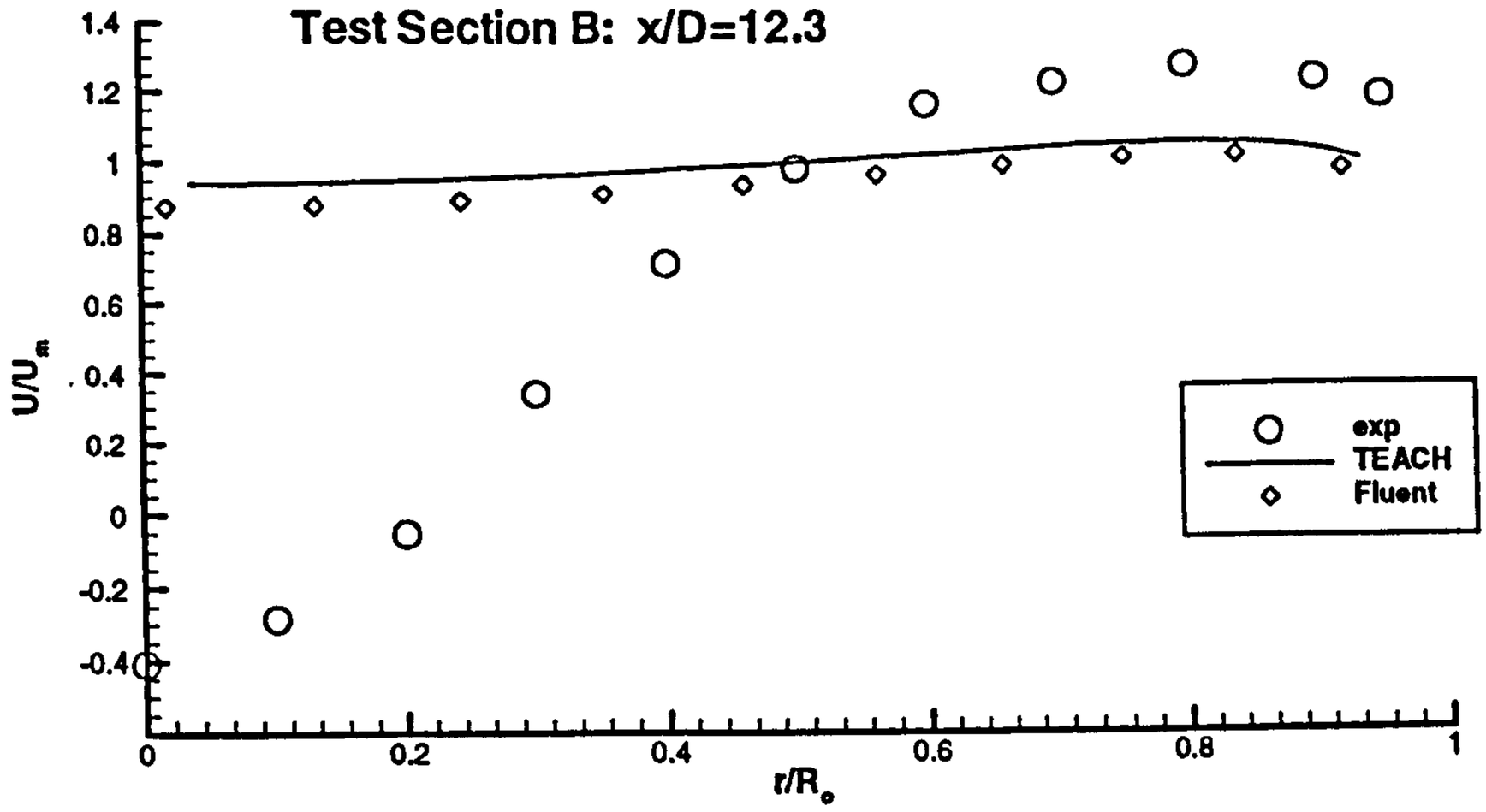

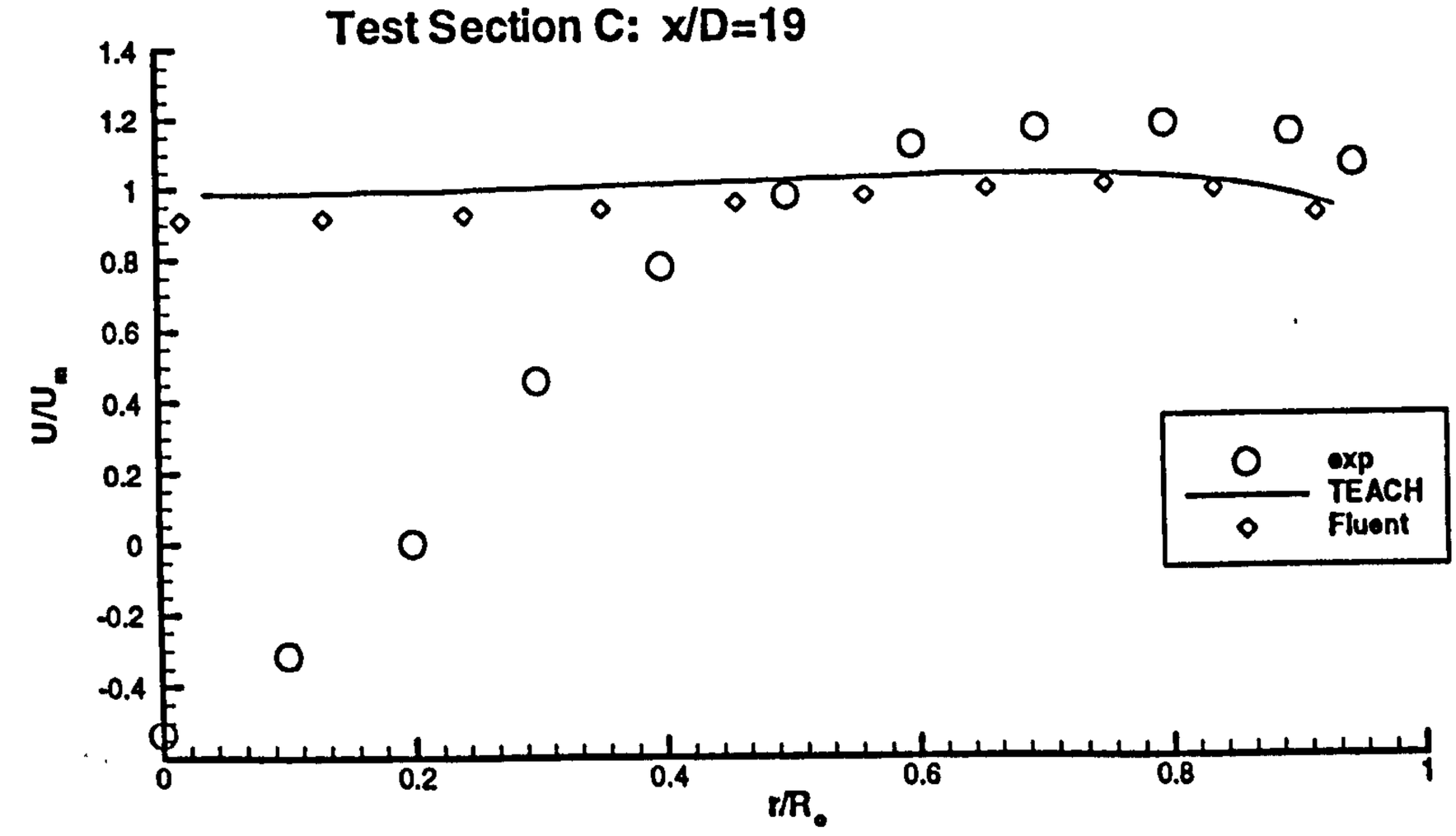

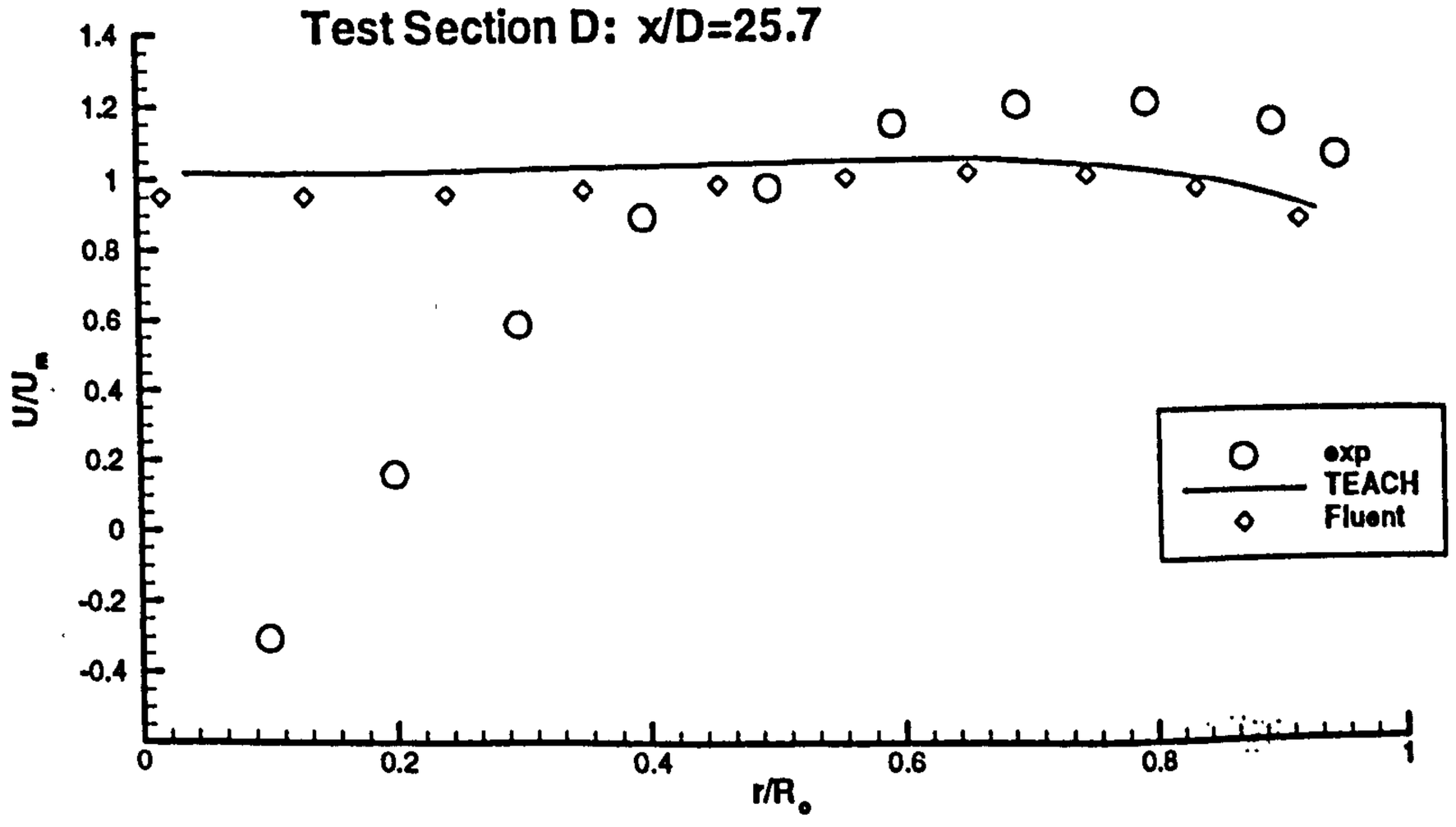

Figure C.1: Comparison of TEACH and Fluent axial velocities for the swirling pipe flow of Kitoh (1991).

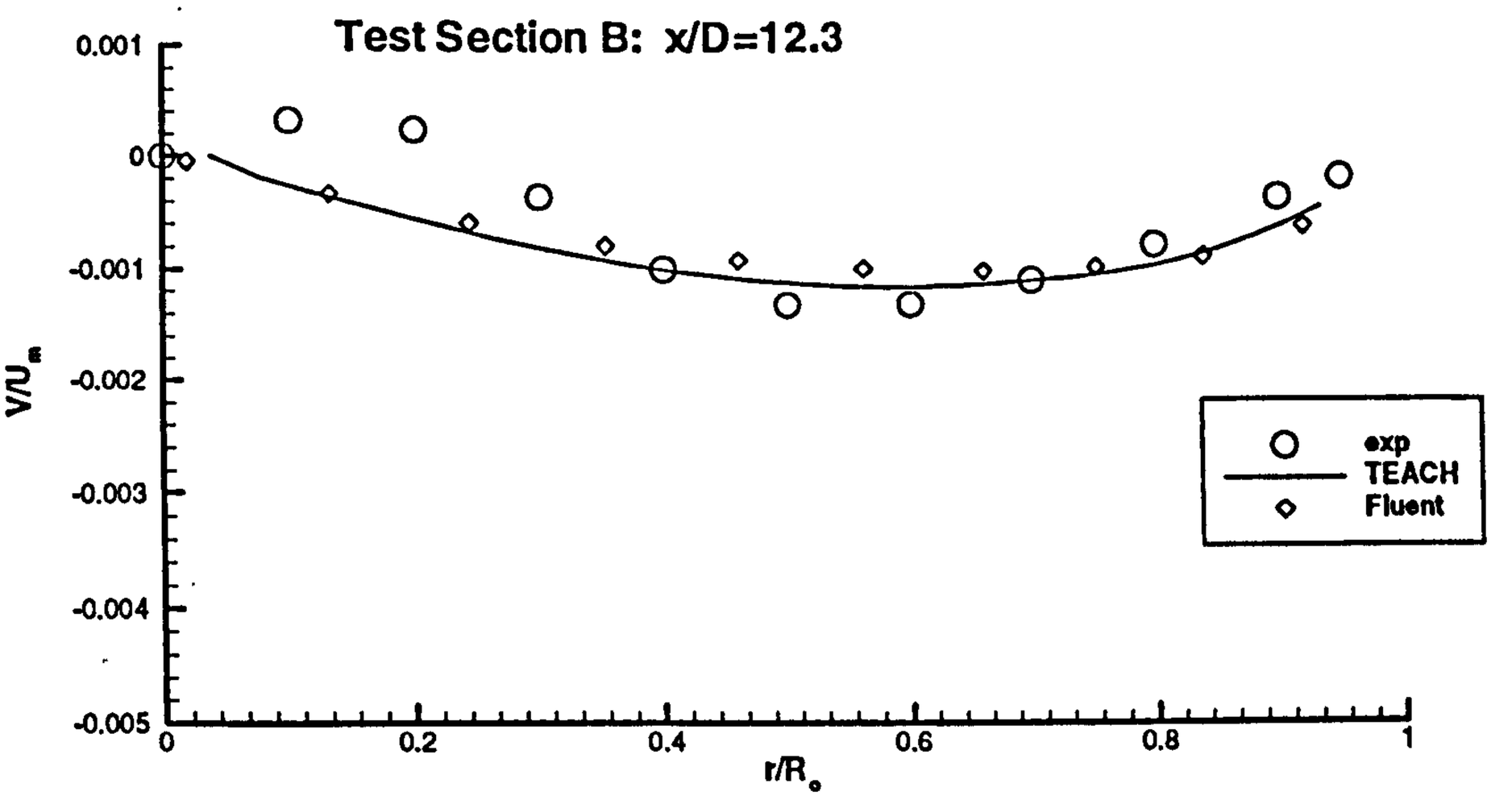

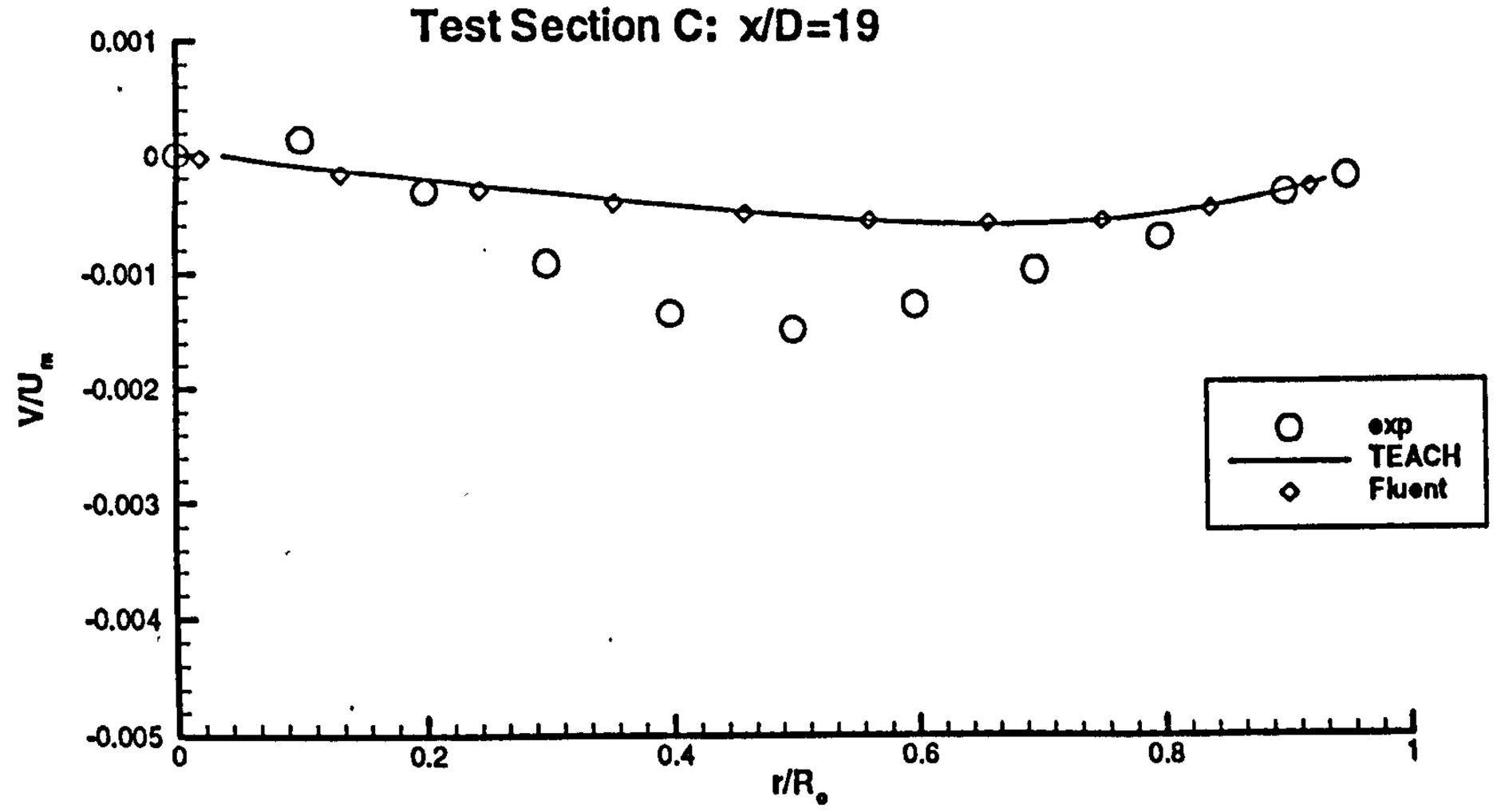

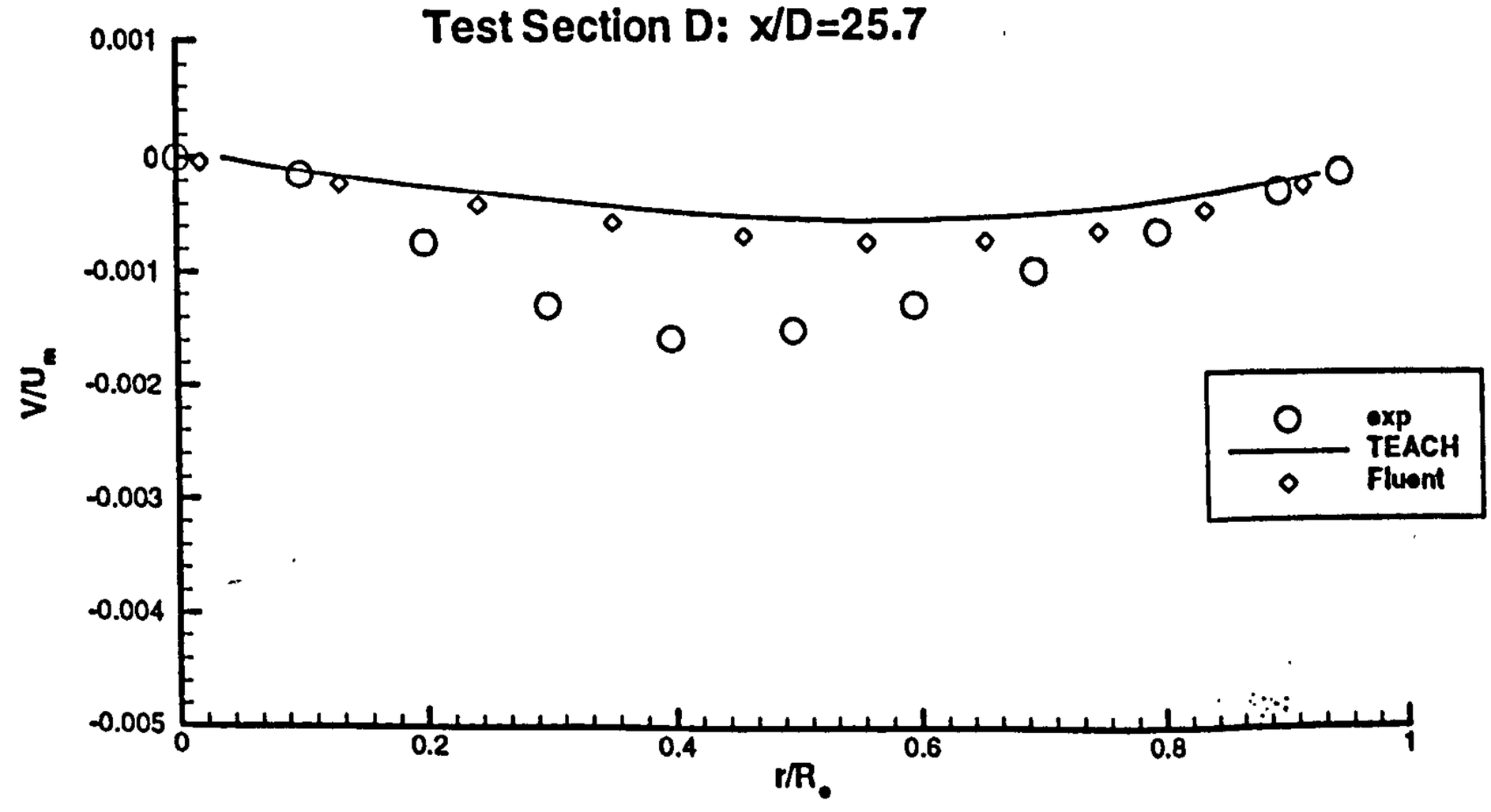

Figure C.2: Comparison of TEACH and Fluent radial velocities for the swirling pipe flow of Kitoh (1991).

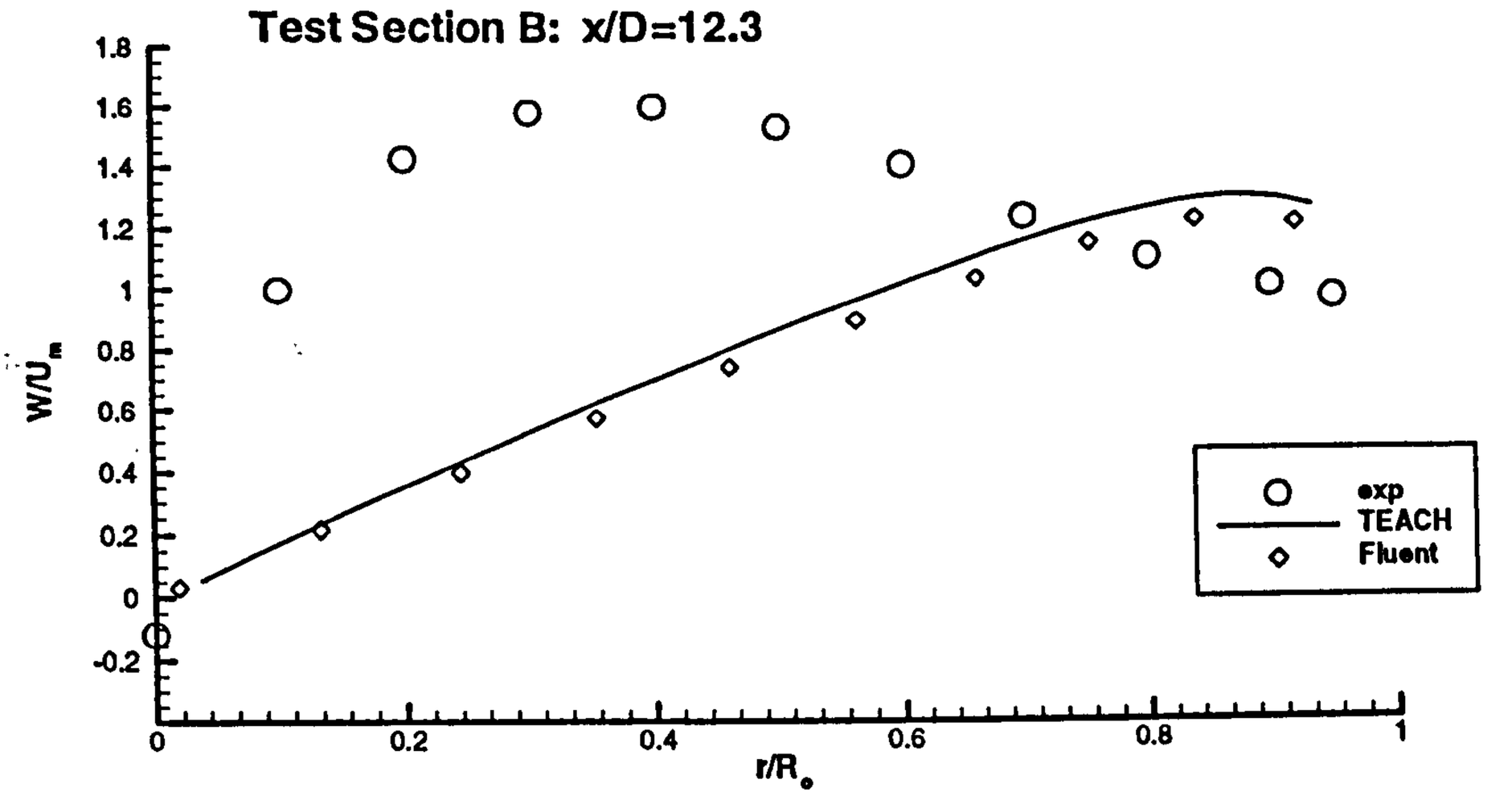

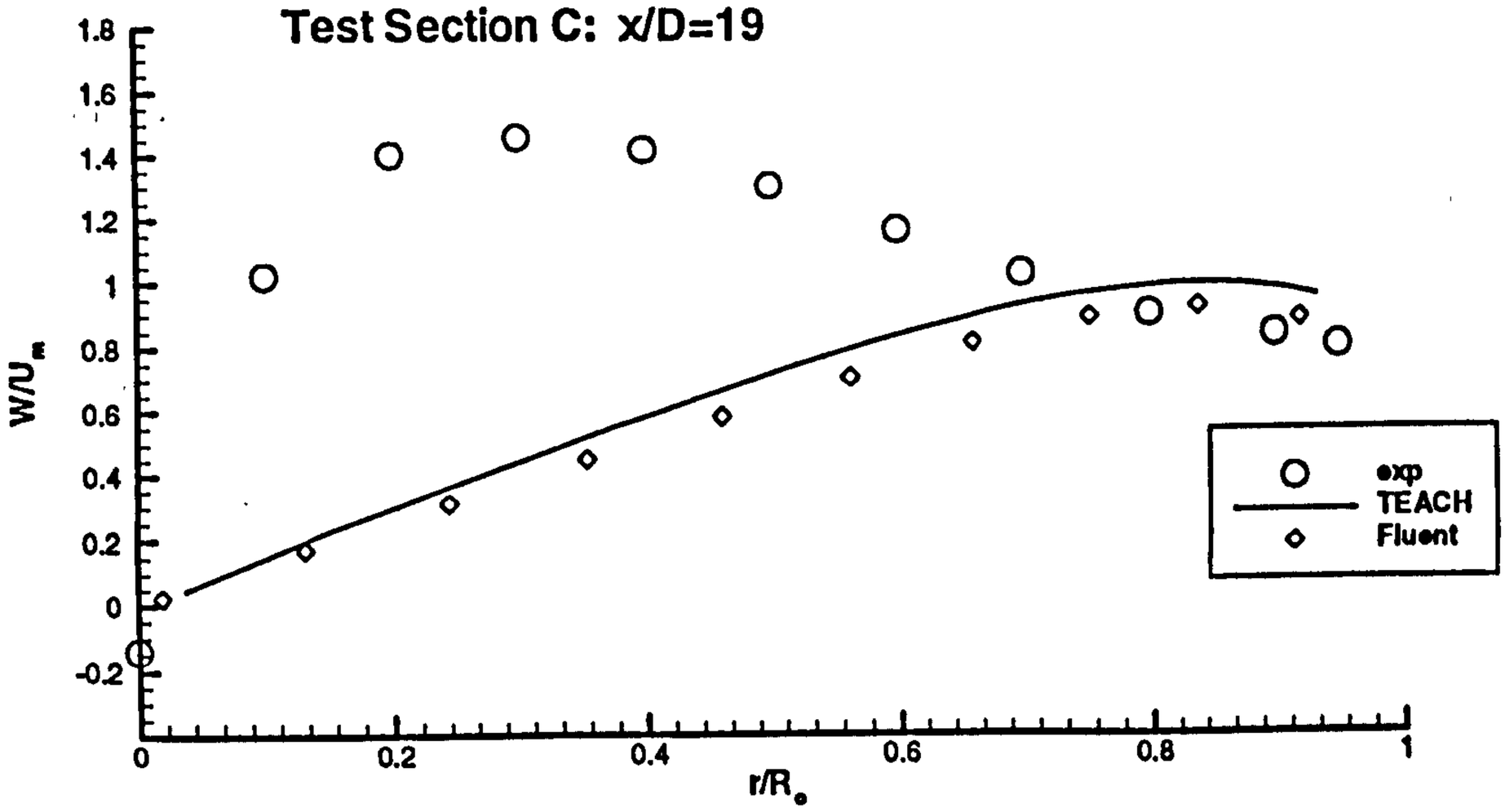

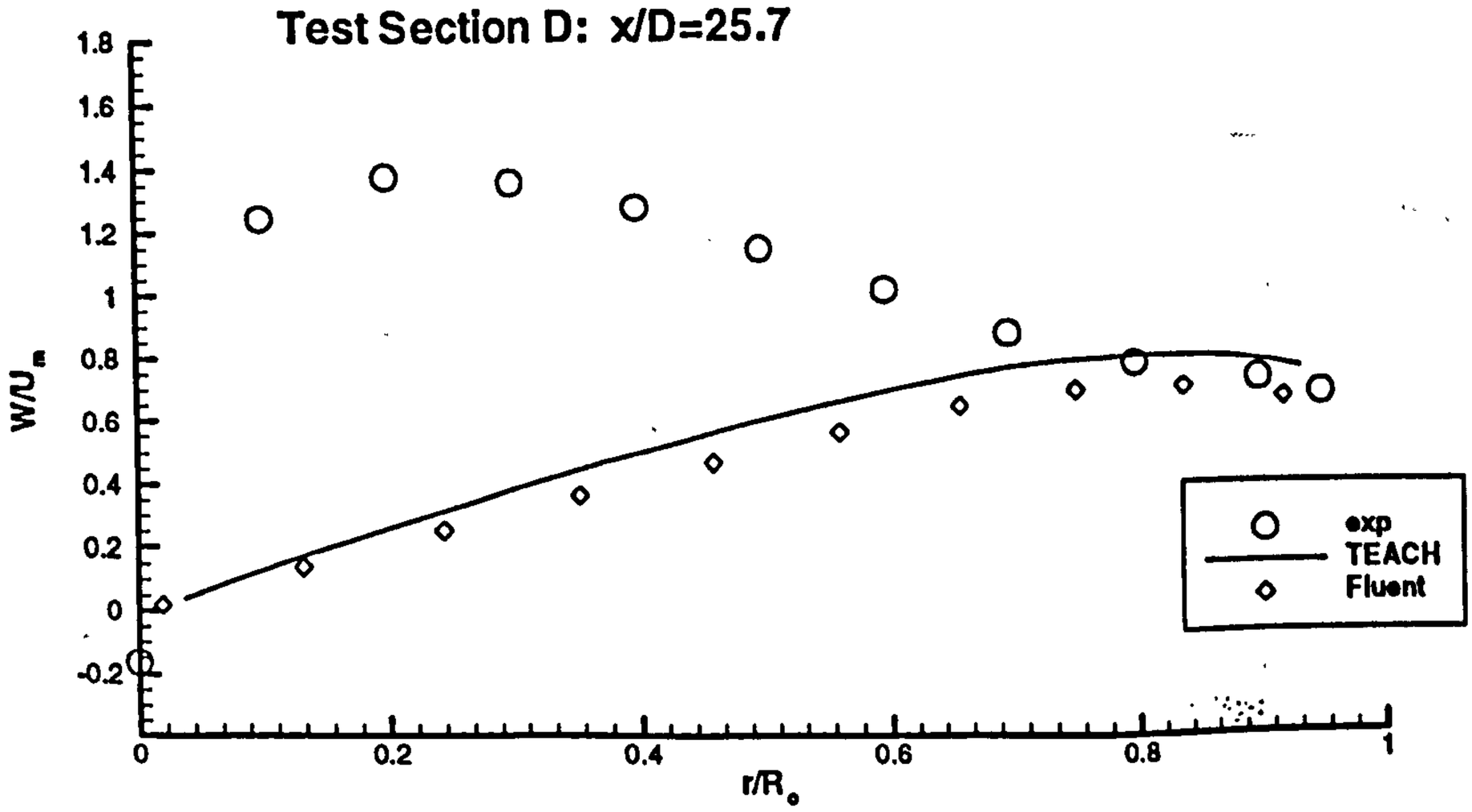

Figure C.3: Comparison of TEACH and Fluent tangential velocities for the swirling pipe flow of Kitoh (1991).

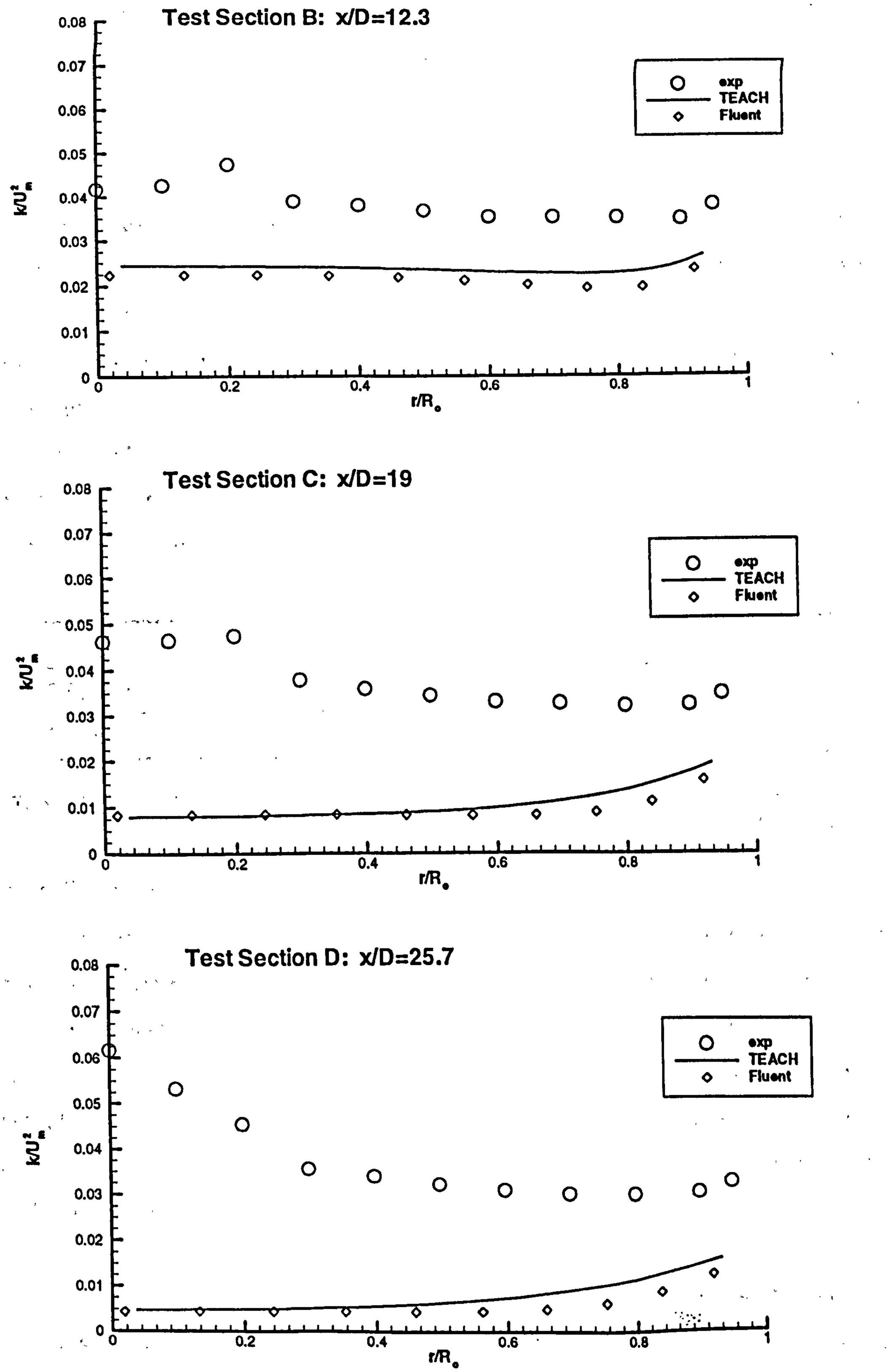

Figure C.4: Comparison of TEACH and Fluent turbulence energy for the swirling pipe flow of Kitoh (1991).

APPENDIX D: EFFECT OF DISCRETISATION SCHEME

The advantage of employing a second-order accurate upwind scheme in the context of the hybrid scheme, relative to a first-order approach, was ascertained during simulations of the Tropea et al (1989) pipe expansion (studied in detail in Chapter 4) using the k-ε model in the TEACH and Fluent codes. The computational grids were very similar, but slight differences existed near the wall (these were found after the study had been conducted). Radial profiles of normalised axial velocity and turbulence energy at two axial locations, one upstream and the other downstream of the reattachment point, are depicted in figures D.1 to D.4.

	X_r / D_2
TEACH	1.19
Fluent	1.21

Table D.1: Predicted reattachment lengths.

	X_r / D_2
Power law	1.23
QUICK	1.21

Table D.2: Effect of discretisation scheme on reattachment length.

The predicted reattachment lengths (normalised with the exit diameter D_2) are seen from table D.1 to be nearly identical. This demonstrates that using second-order upwinding in the hybrid scheme does not significantly change the reattachment lengths compared to first-order upwinding, provided the grid is sufficiently dense. The power-law and QUICK discretisation schemes (details available in the Fluent manual) were also employed in Fluent; their forecast values of X_r / D_2, shown in table D.2, also reveal that, in this case, the choice of discretisation scheme does not have a significant influence on reattachment length predictions.

The relatively small discrepancies in tables D.1 and D.2 and in figures D.1 and D.2 indicate that, provided adequate grid resolution is ensured, the effects of false diffusion can be assumed as being negligible. The good match between the TEACH and Fluent simulations in Appendix C concur with this finding.

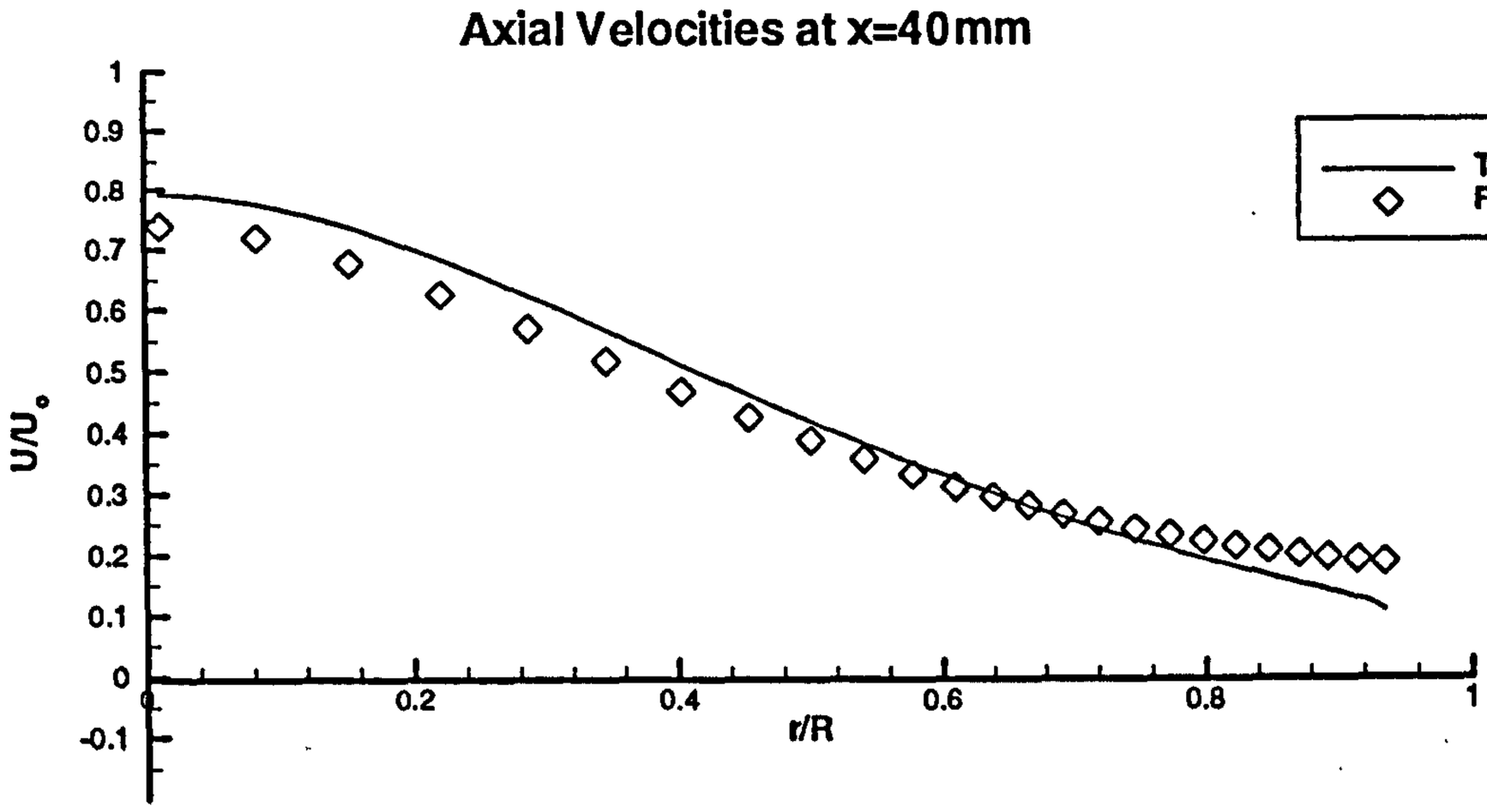

Figure D.1: Comparison of TEACH and Fluent for the pipe expansion of Tropea et al (1989).

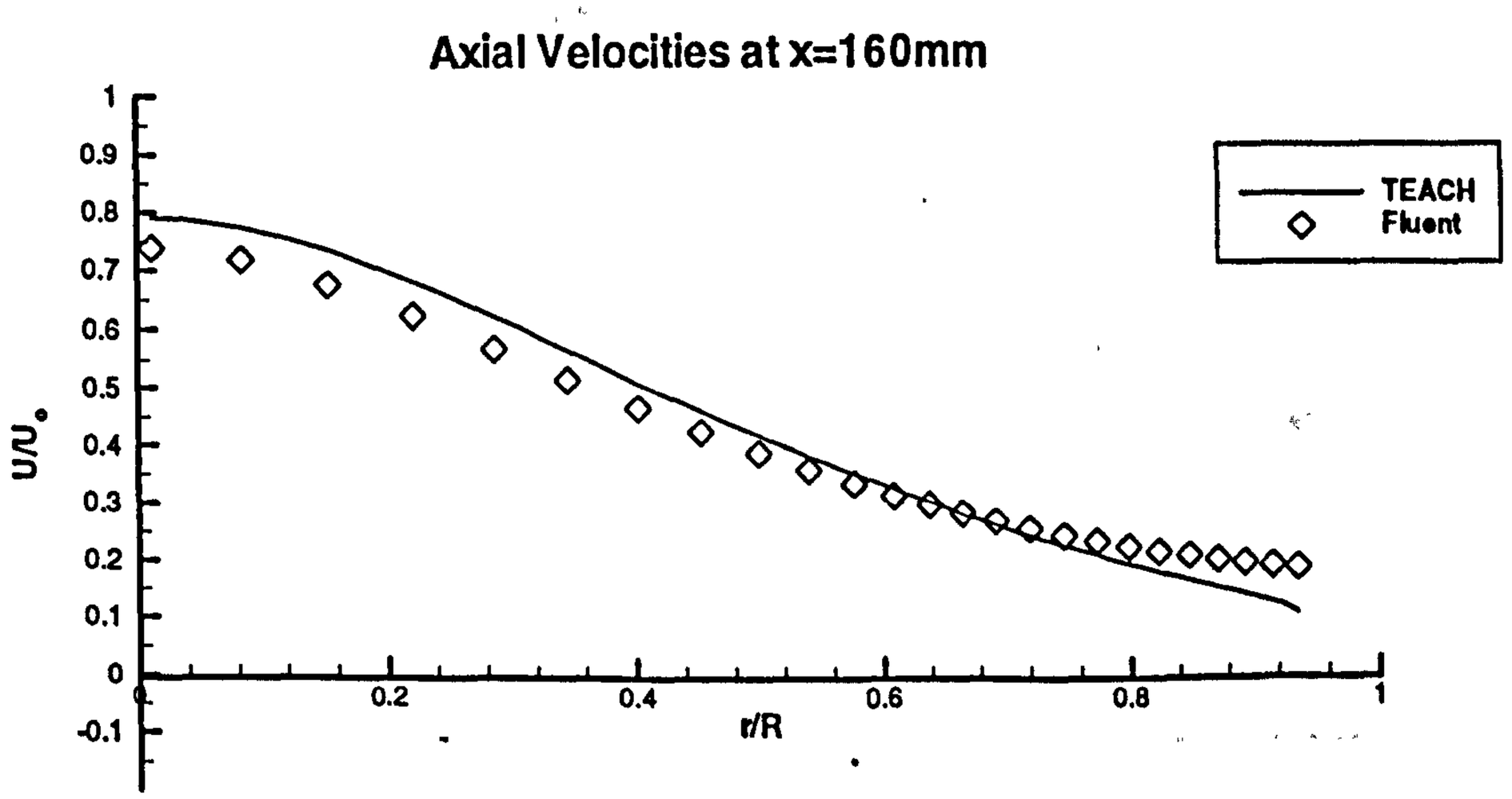

Figure D.2: Comparison of TEACH and Fluent for the pipe expansion of Tropea et al (1989).

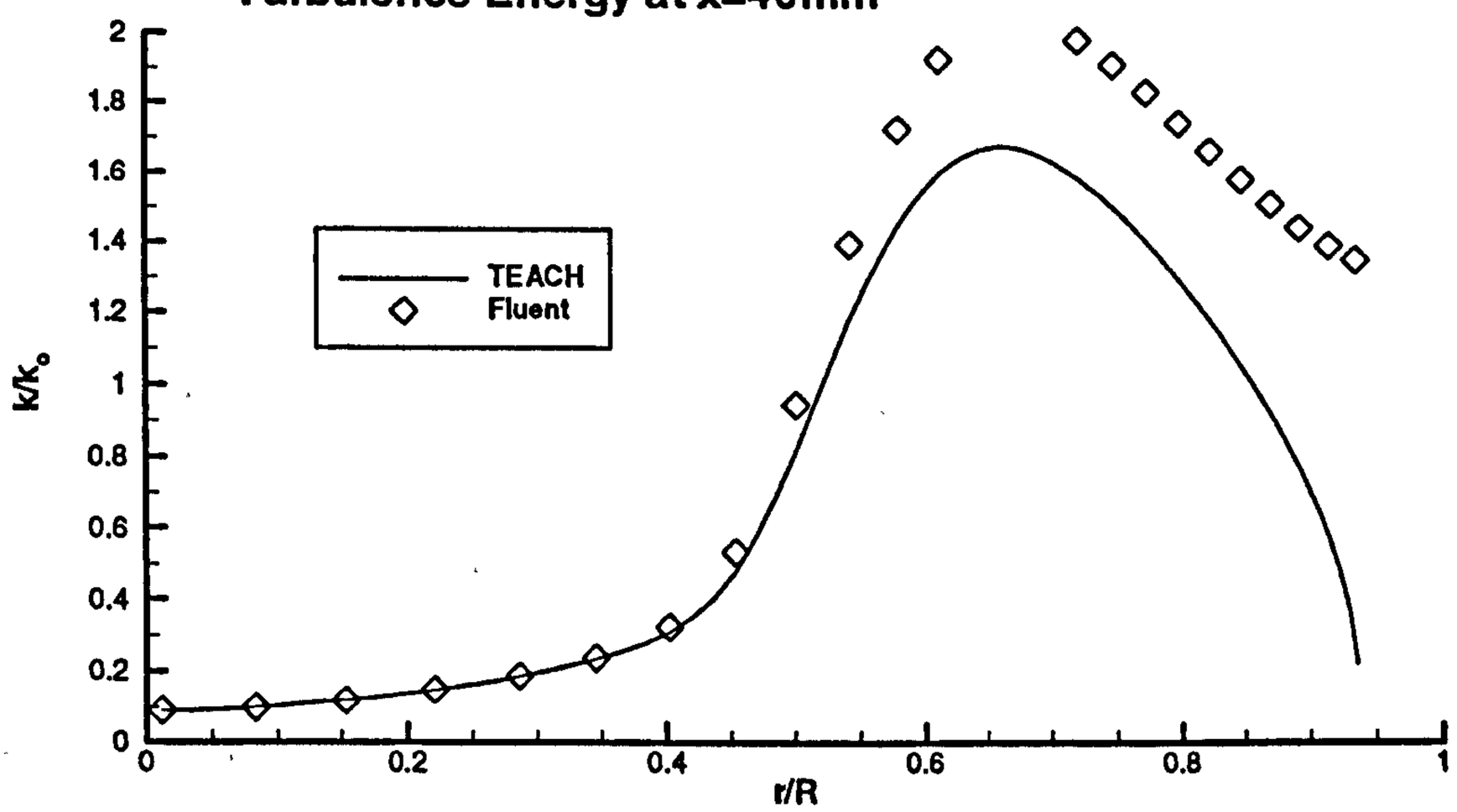

Figure D.3: Comparison of TEACH and Fluent for the pipe expansion of Tropea et al (1989).

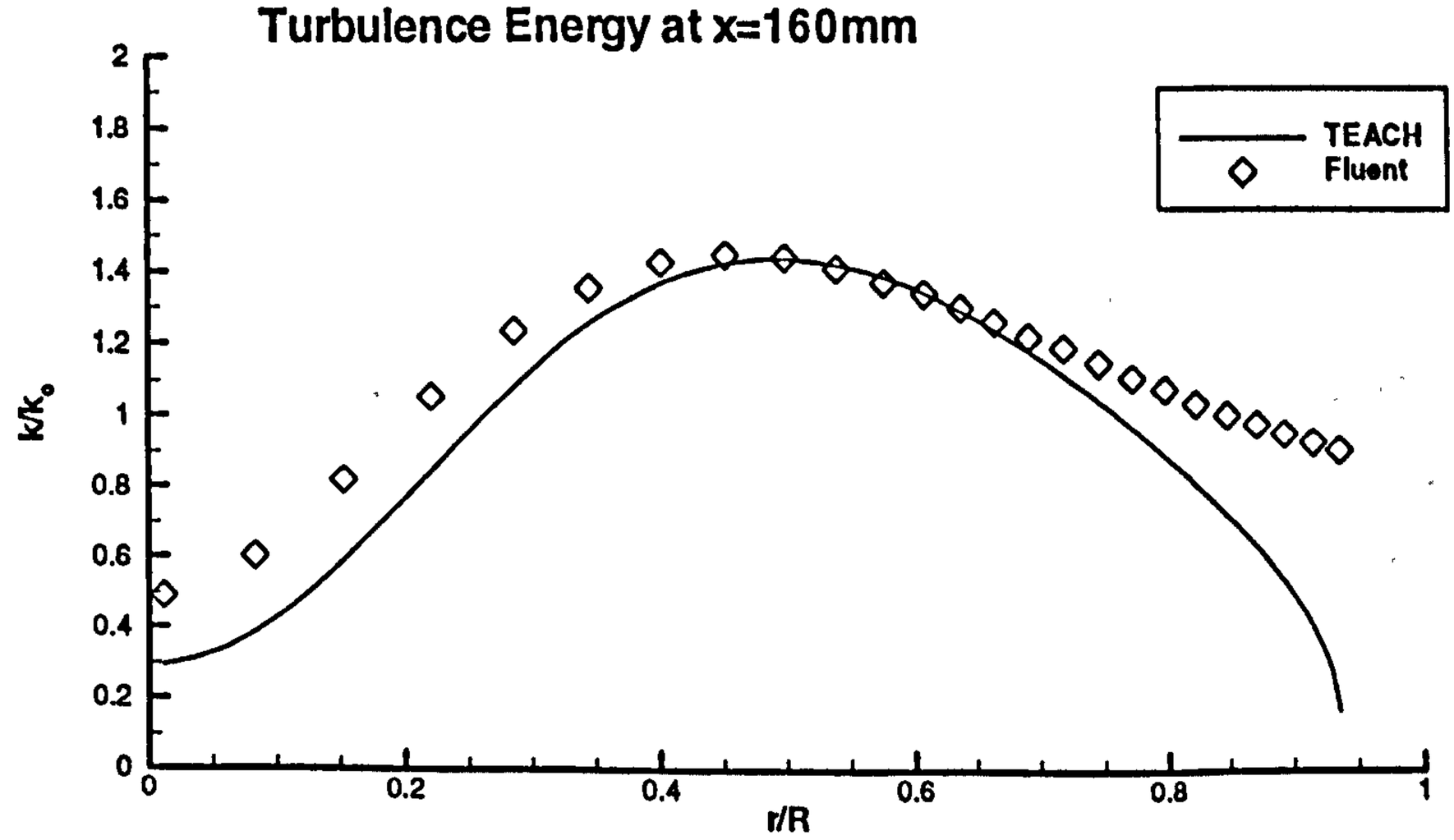

Figure D.4: Comparison of TEACH and Fluent for the pipe expansion of Tropea et al (1989).

APPENDIX E: EFFECTS OF INLET PROFILES

In the pipe expansion case of Tropea et al (1989), detailed inlet profiles of U and k are given; however, a value for ε is also required. Since no information is presented concerning the latter, it is standard practice to apply a relation of the form of equation 3.5 to obtain an average value for ε (i.e. flat profile), using an average k. Alternatively, one could calculate a curved profile by feeding the experimental distribution of k into relations 3.5. It is important to examine the sensitivity of the predicted results obtained using various combinations of curved and flat inlet profiles for the three inlet parameters U, k and ε. The four cases explored are outlined in table E.1. Average inlet values for velocity and turbulence energy are $U_{avg} = 1.966$ m/s and $k_{avg} = 0.03U_{avg}^2$ (based on a turbulence intensity of 3%).

	U	k	ε
Case 0	exp. curve	exp. curve	eqtn (3.6) using exp. k
Case 1	exp. curve	exp. curve	eqtn (3.6) using k_{avg}
Case 2	exp. curve	k_{avg}	eqtn (3.6) using k_{avg}
Case 3	U_{avg}	k_{avg}	eqtn (3.6) using k_{avg}

Table E.1: Various combinations of inlet boundary conditions.

The effects of the various cases on reattachment length (X_r/D_2 where D_2 is the exit diameter), using three different turbulence models, are displayed in table E.2. The experimental value for X_r/D_2 is 1.87. The discrepancy between the largest and smallest reattachment lengths is 17%, 36% and 44% for the CRY, k-ε and RNG models, respectively. It is interesting to note that the nonlinear model is least affected by varying the nature of the inlet profiles.

	CRY	k-ε	RNG
Case 0	1.87	1.11	1.62
Case 1	1.99	1.24	1.69
Case 2	1.70	0.94	1.30
Case 3	1.81	0.91	1.17

Table E.2: Reattachment lengths (X_r/D_2).

Inspection of detailed distributions of U, k and $\overline{u'v'}$ (figures E.1 to E.6), however, emphasises the differences brought about by using the various inlet profiles. Radial plots are shown at two representative axial locations; the first (X=40mm) lies within the recirculation zone whilst the second (X=160mm) is downstream of the reattachment point. Figures E.1 and E.2 suggest that it is important to specify the velocity distributions correctly. Utlising a flat inlet profile for ε only (Case 1) does not significantly alter the predicted distributions of U, k and $\overline{u'v'}$. However, doing so for k (Case 2) has a decidedly negative impact on the results. Finally, the assumption of a plug flow at the inlet (Case 3) causes a large deterioration in predicted results, particularly at locations not far from the step (as shown at x = 40mm).

This study has shown that the nature of the U profile at the inlet is the most influential regarding the computed results, whilst the ε profile has the least impact. Whilst this may seem obvious, it emphasises the need for quantities such as dissipation rate, for which no direct experimental data is available, to be properly represented. The conclusion to be drawn is that the inlet conditions must be as similar as possible to the actual inlet flow.

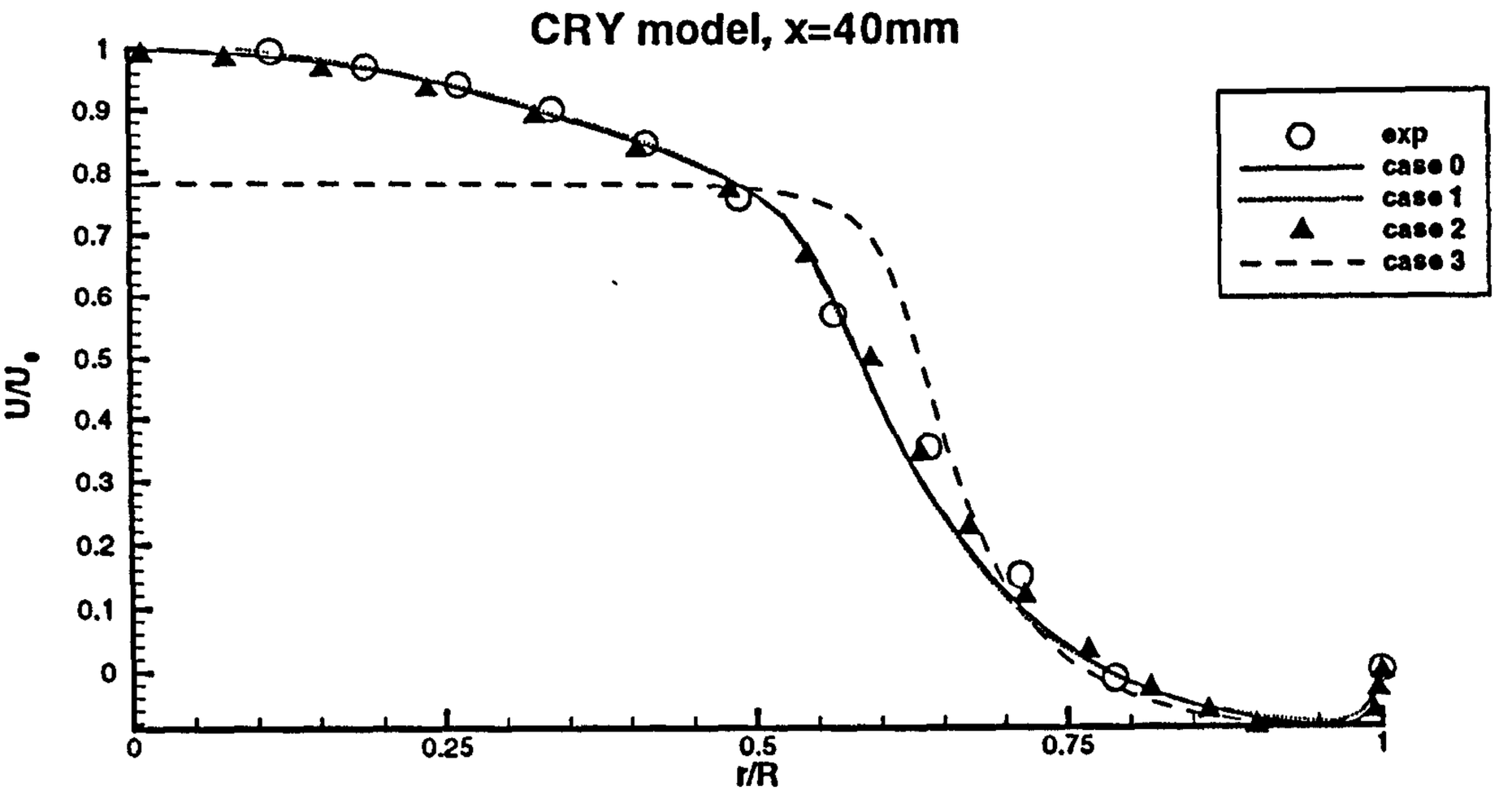

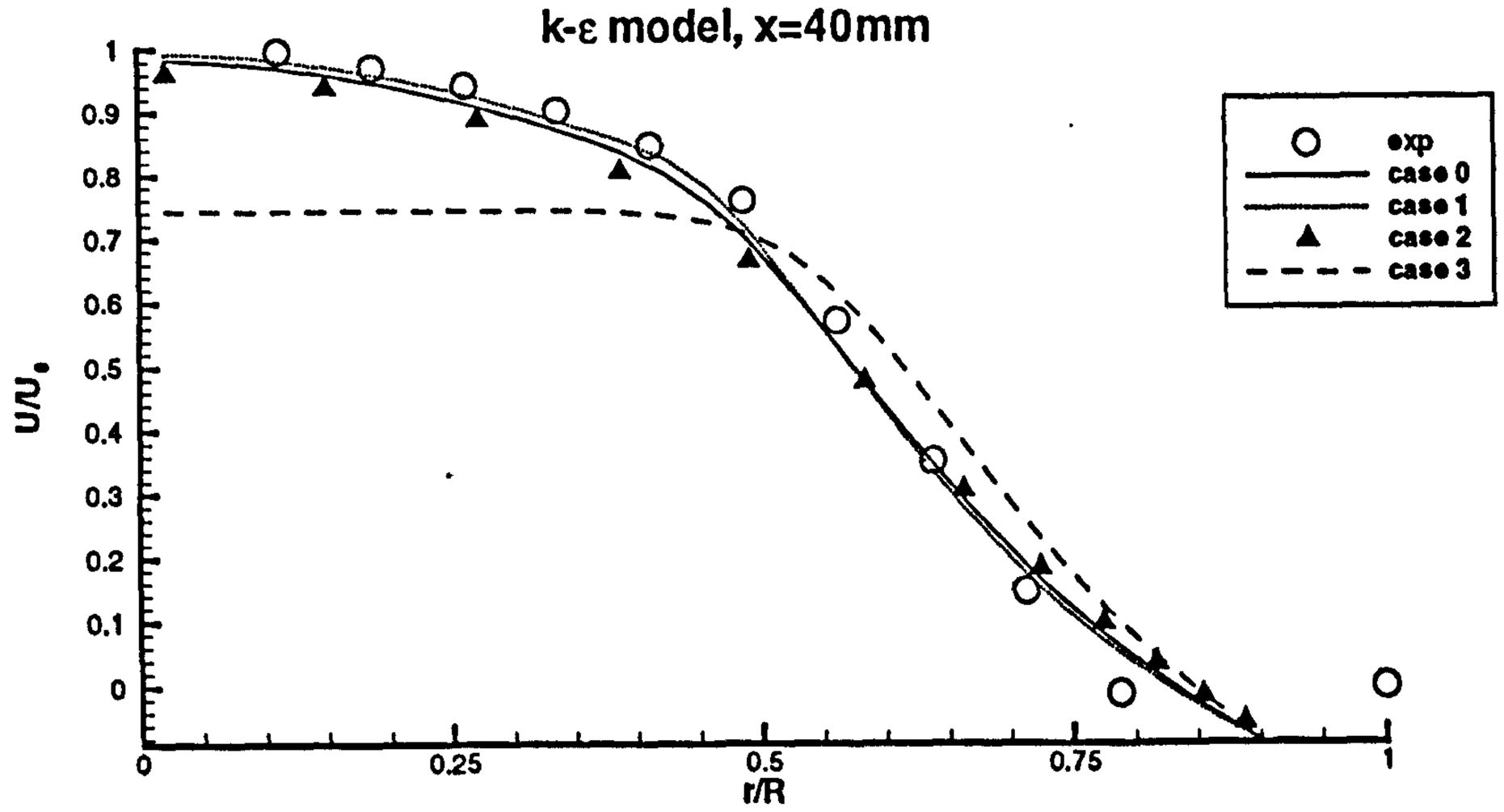

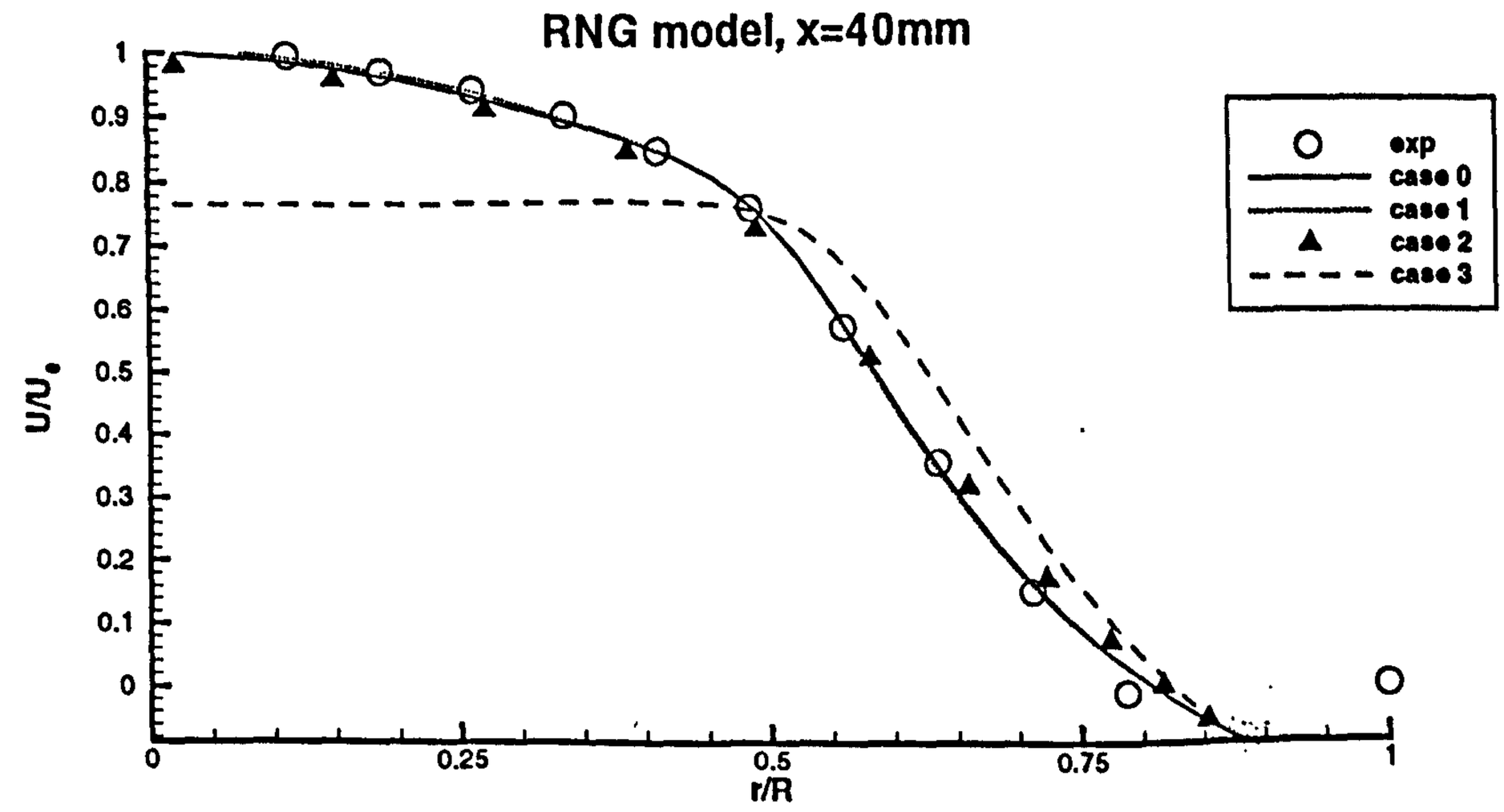

Figure E.1: Effect of inlet condition on axial velocity, for the pipe expansion of Tropea et al (1989).

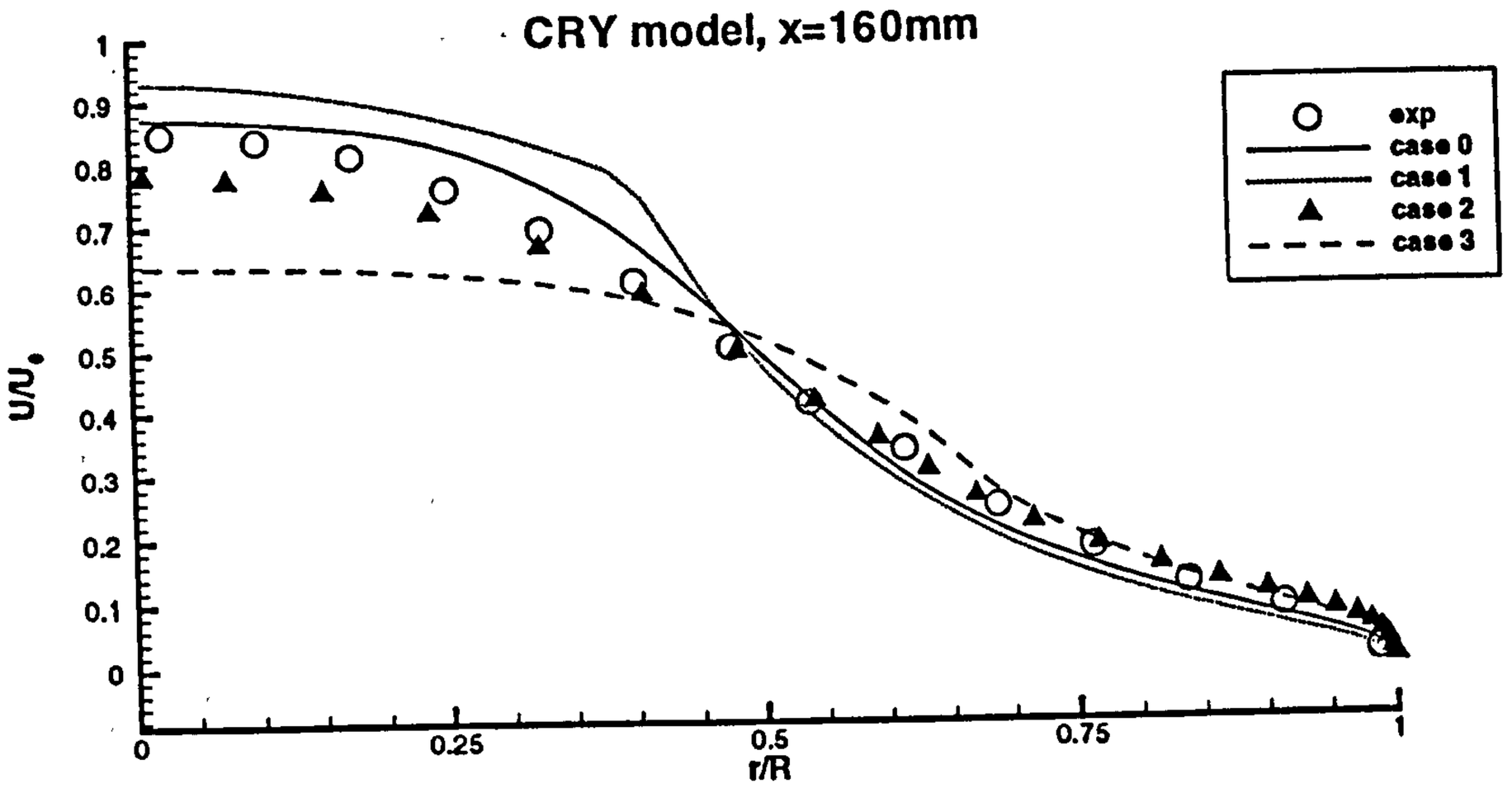

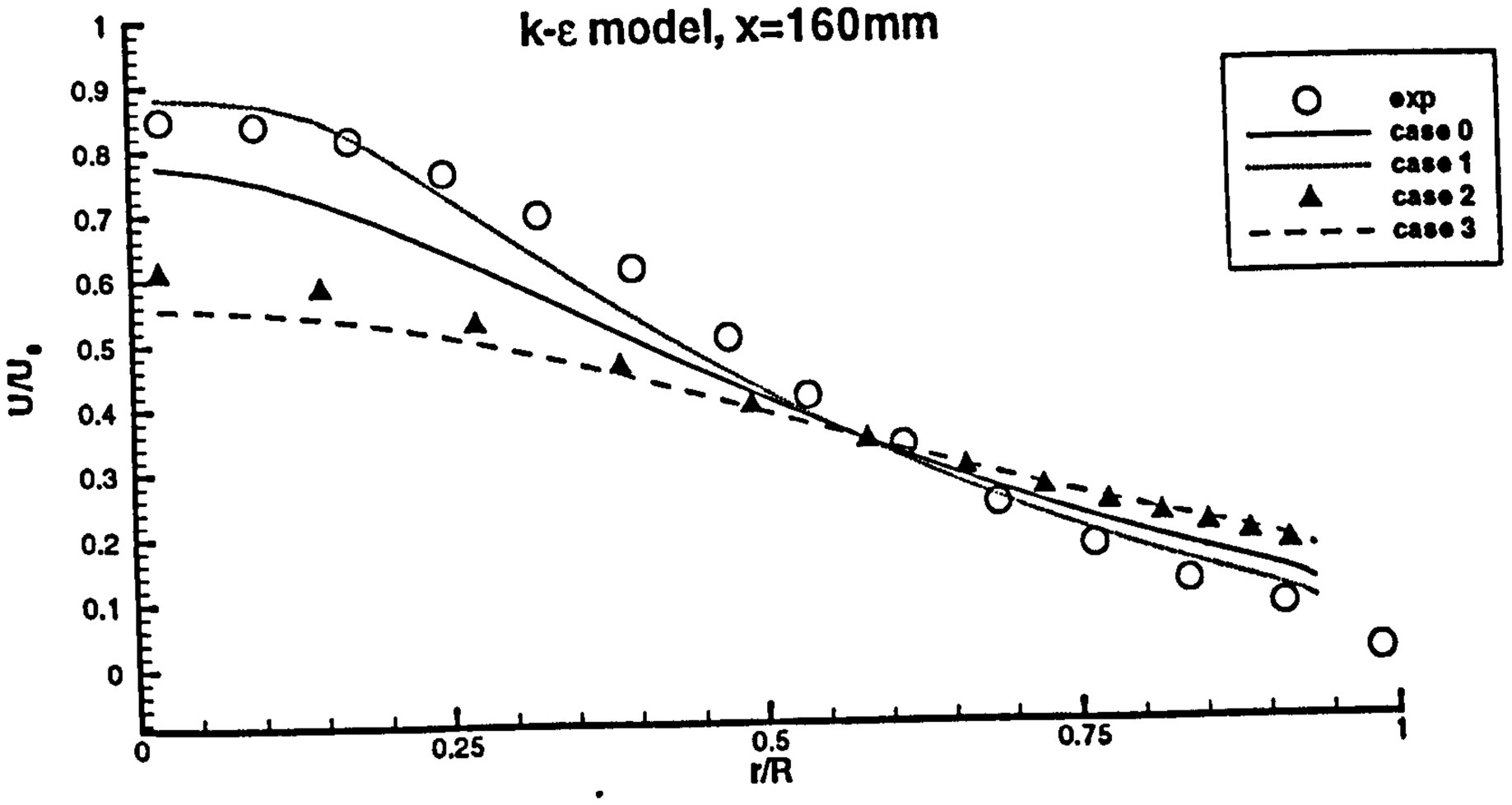

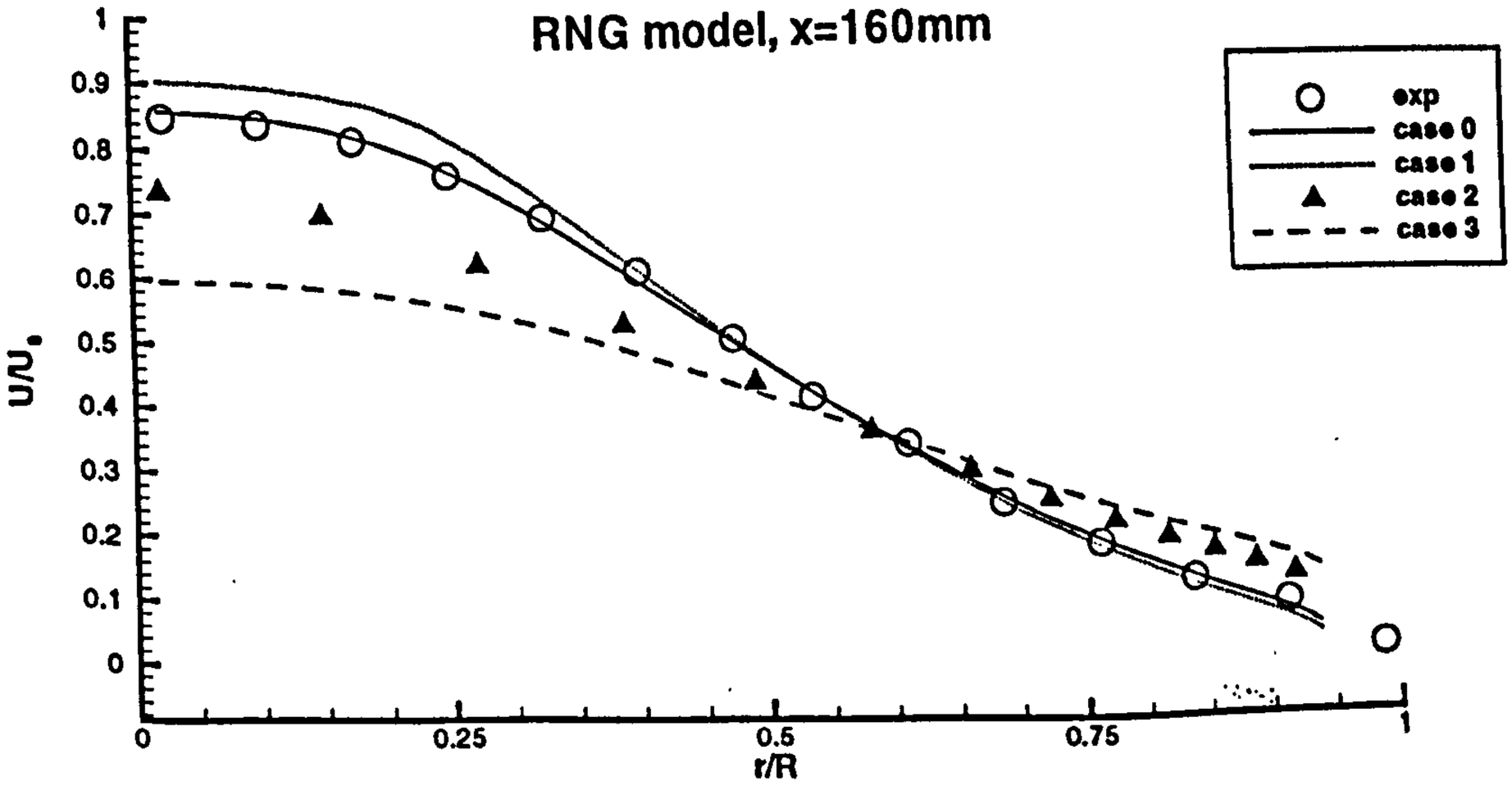

Figure E.2: Effect of inlet condition on axial velocity, for the pipe expansion of Tropea et al (1989).

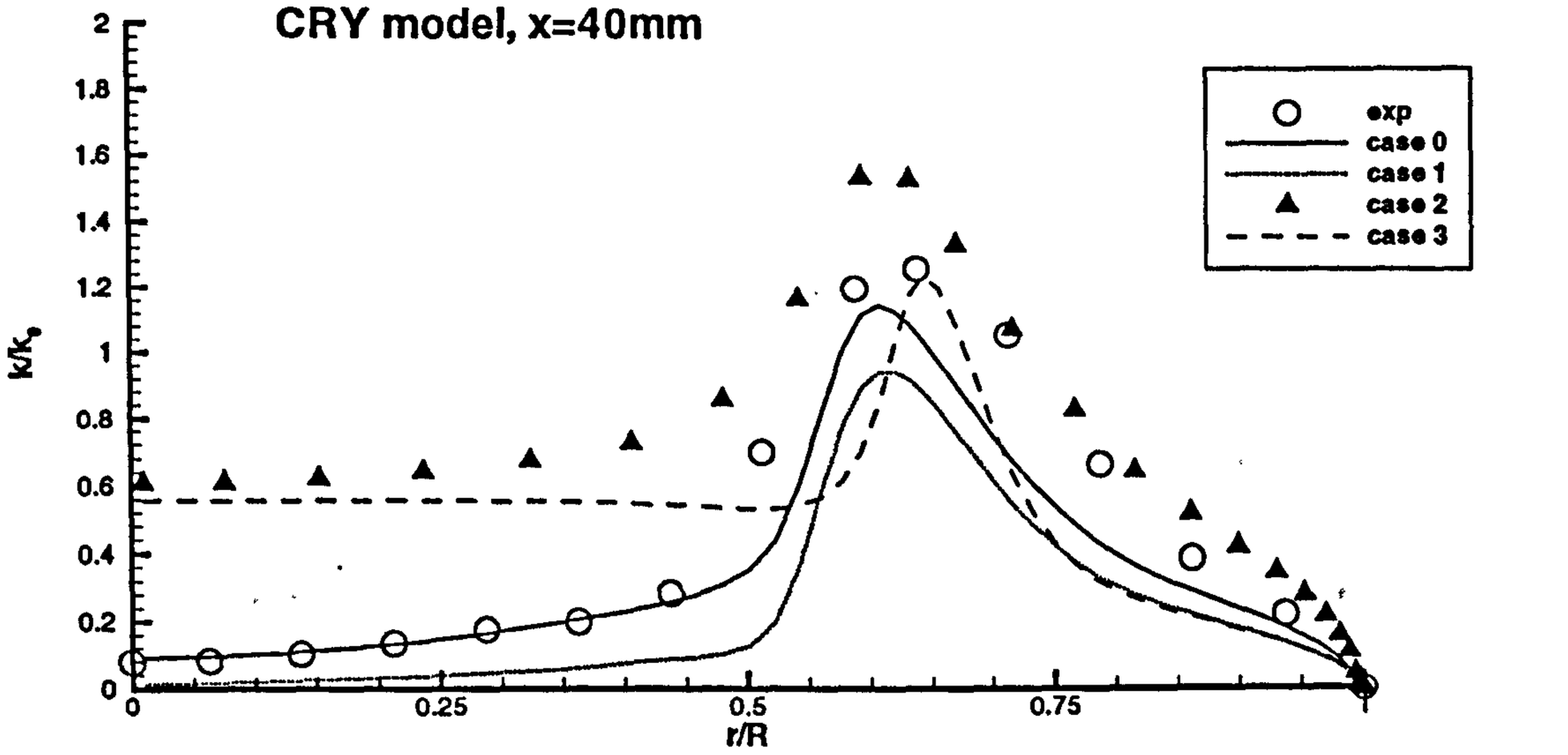

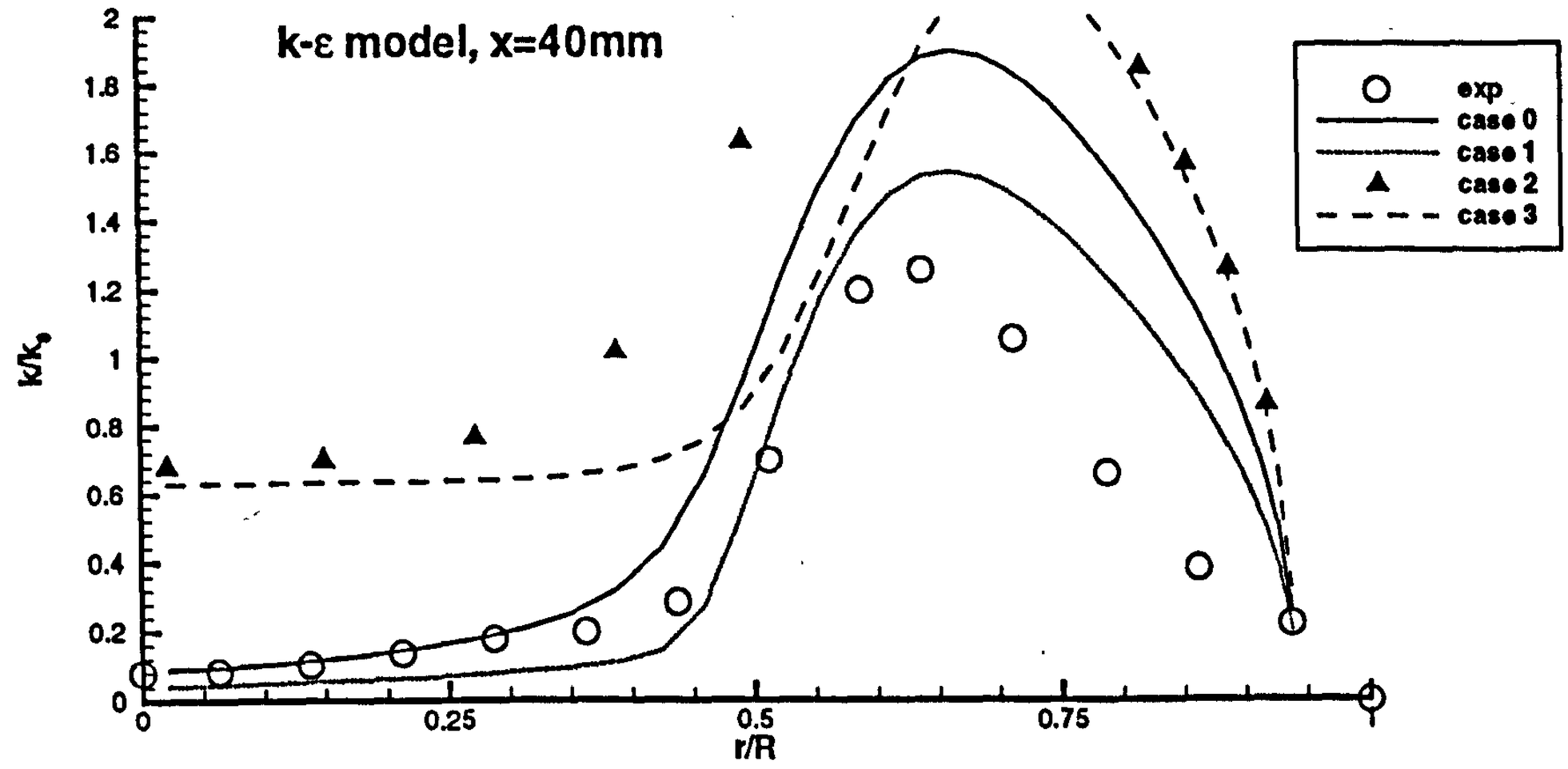

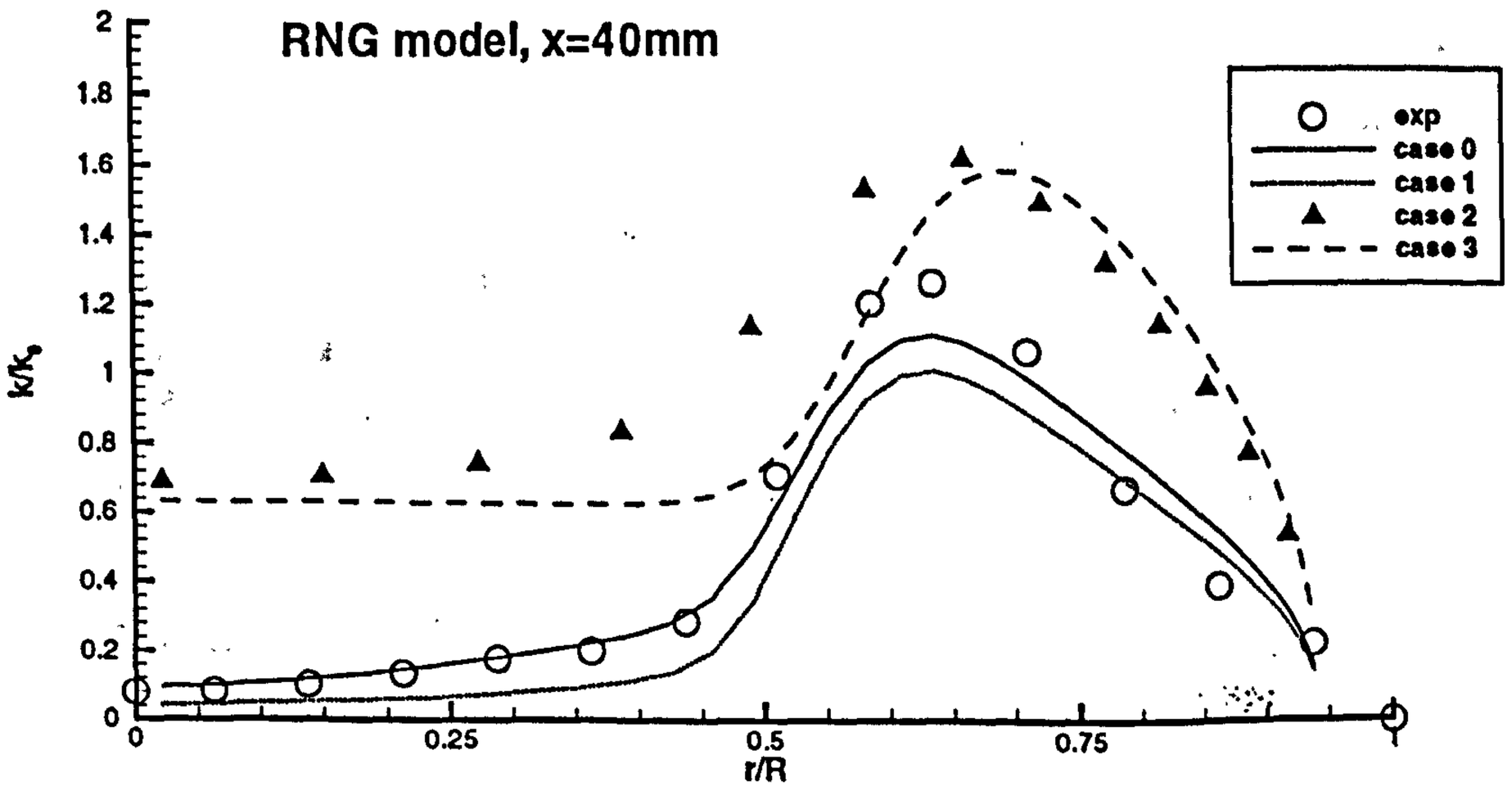

Figure E.3: Effect of inlet condition on turbulence energy, for the pipe expansion of Tropea et al (1989).

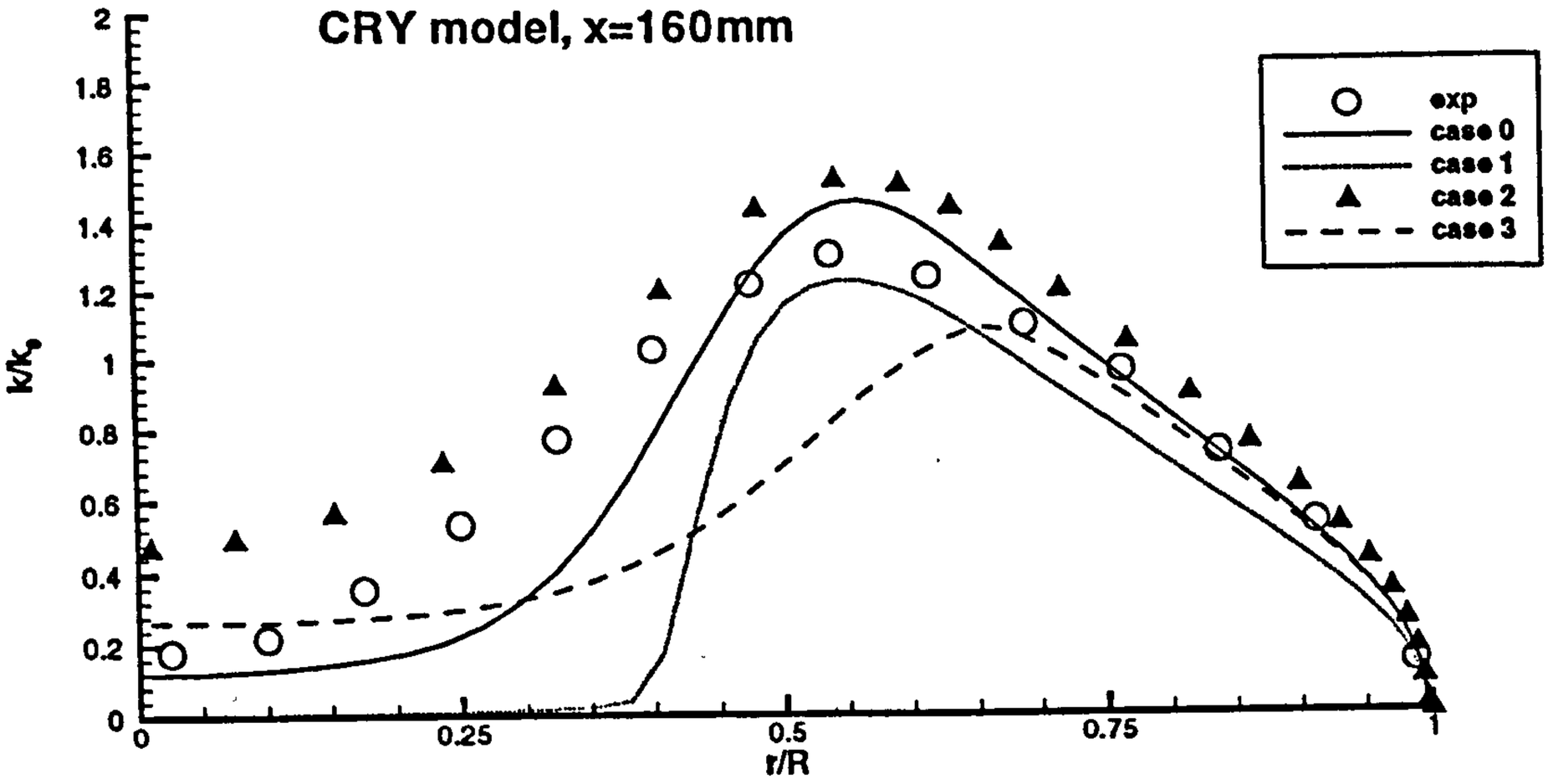

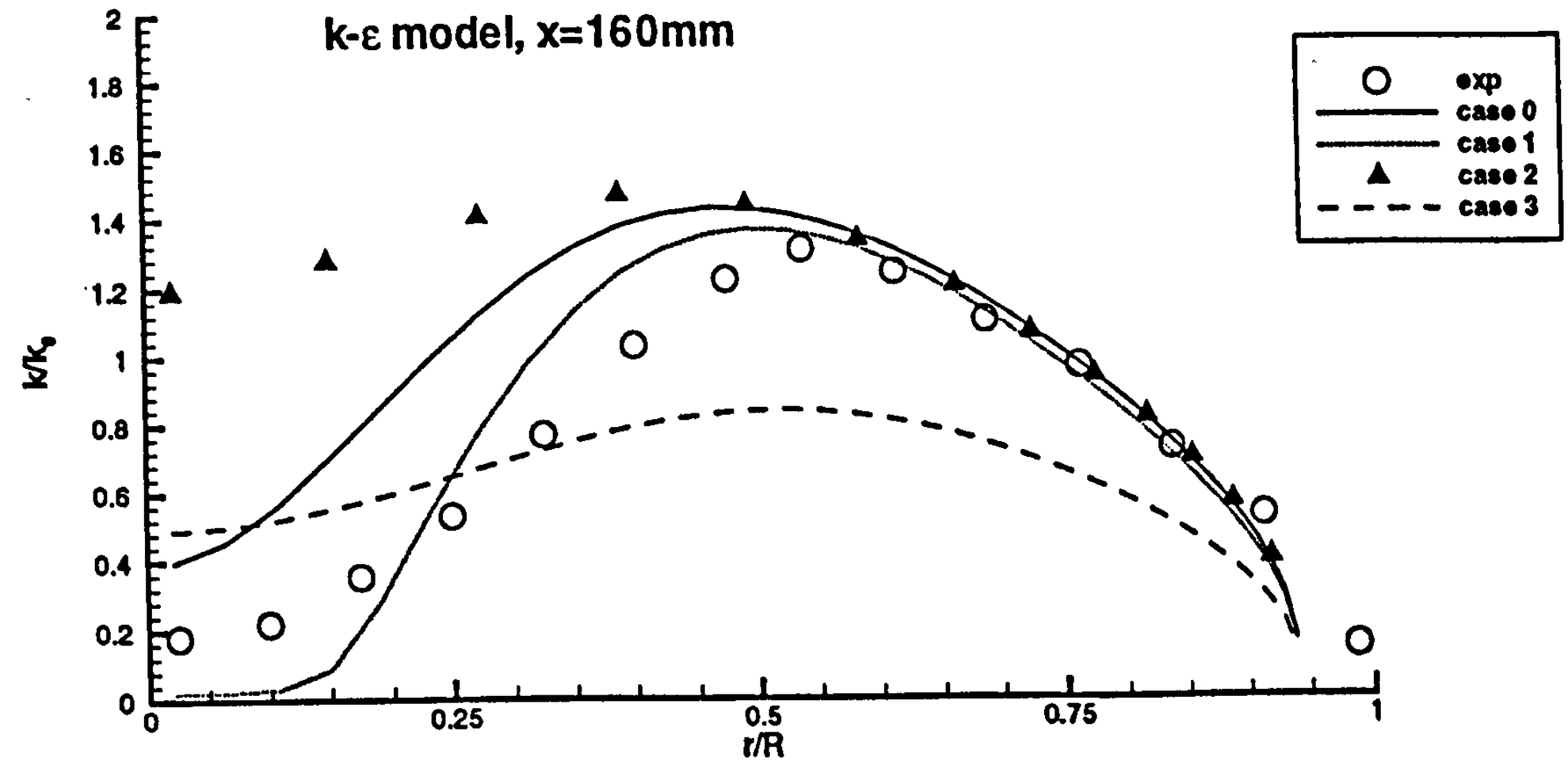

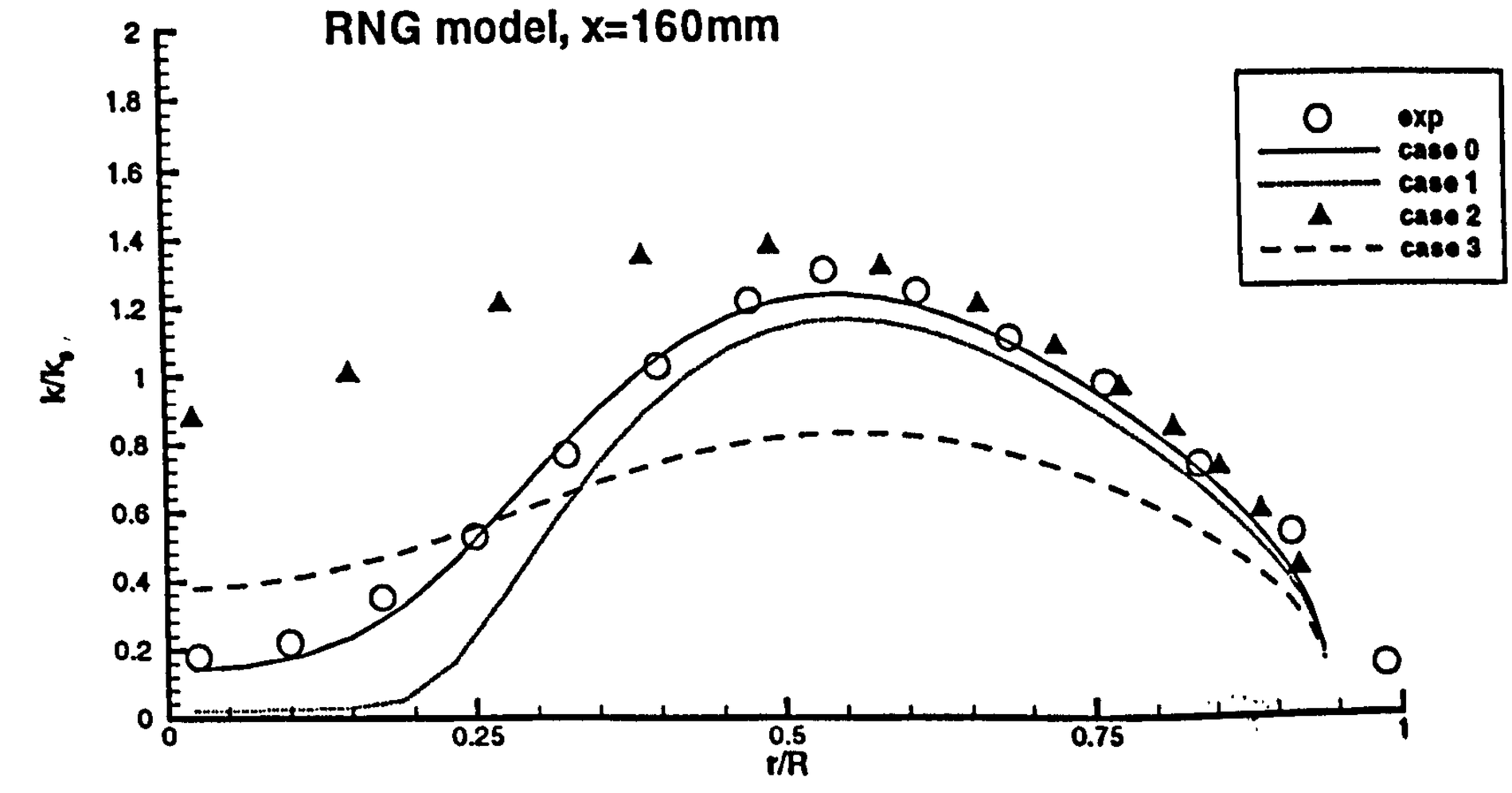

Figure E.4: Effect of inlet condition on turbulence energy, for the pipe expansion of Tropea et al (1989).

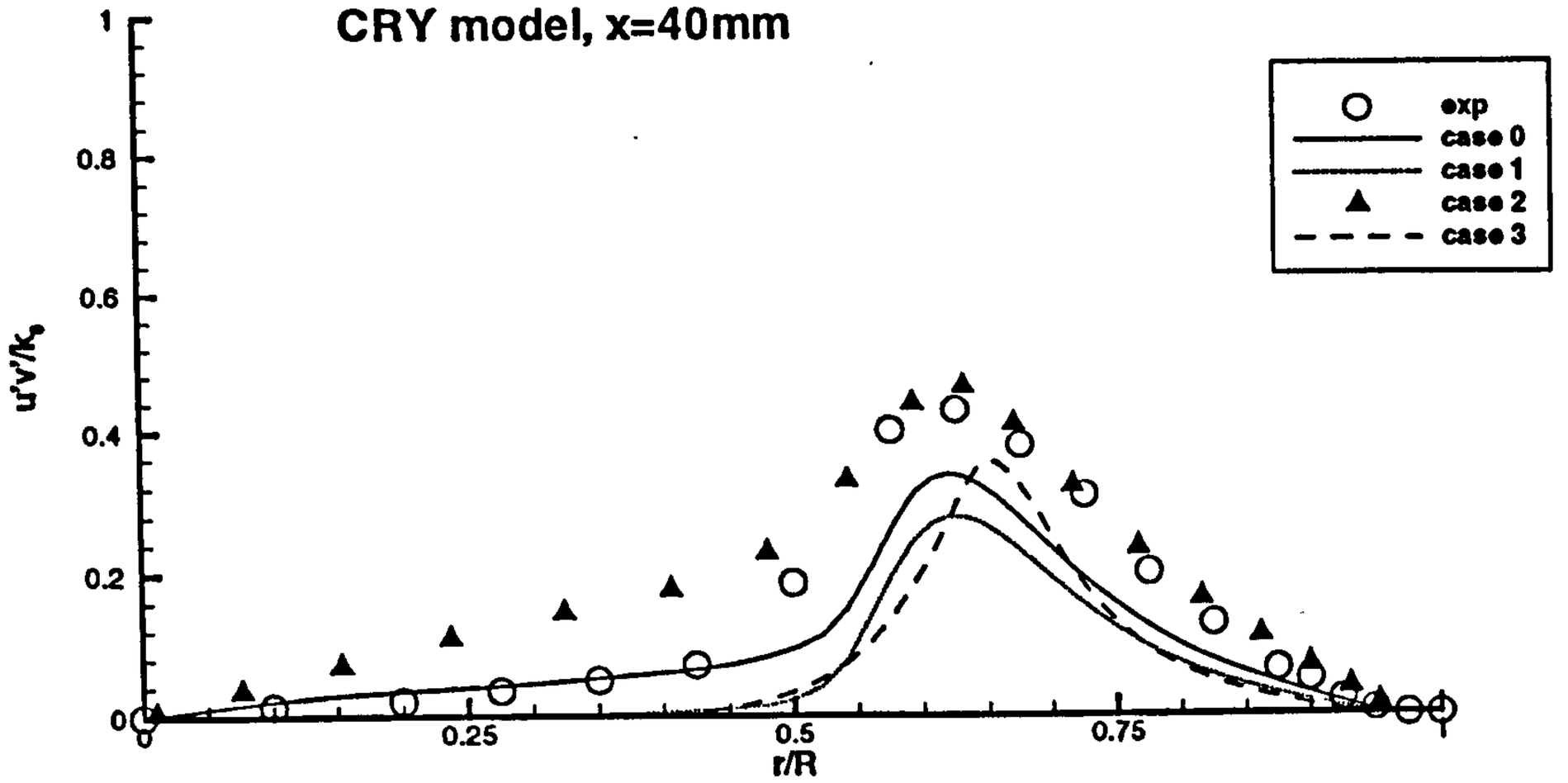

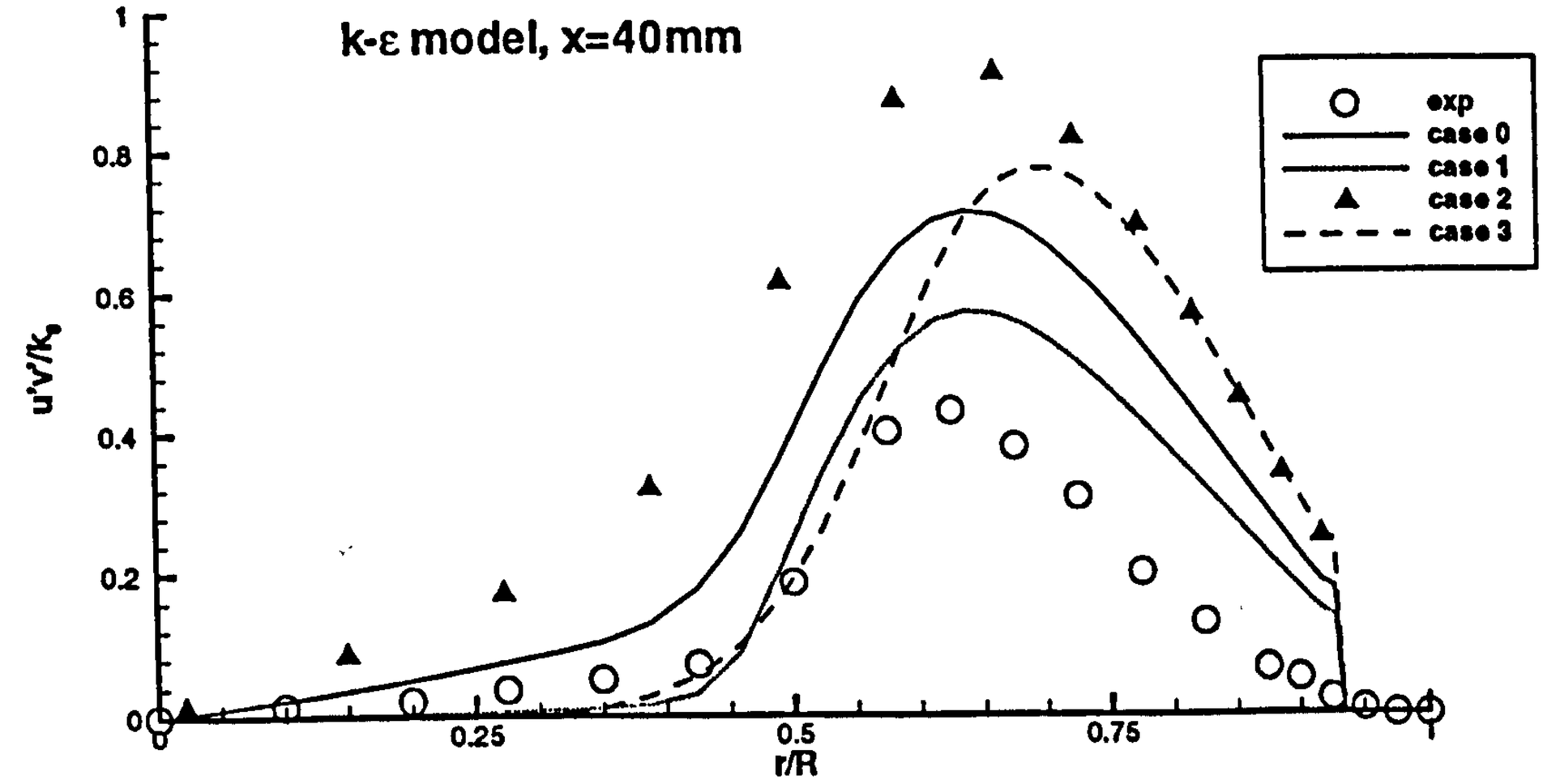

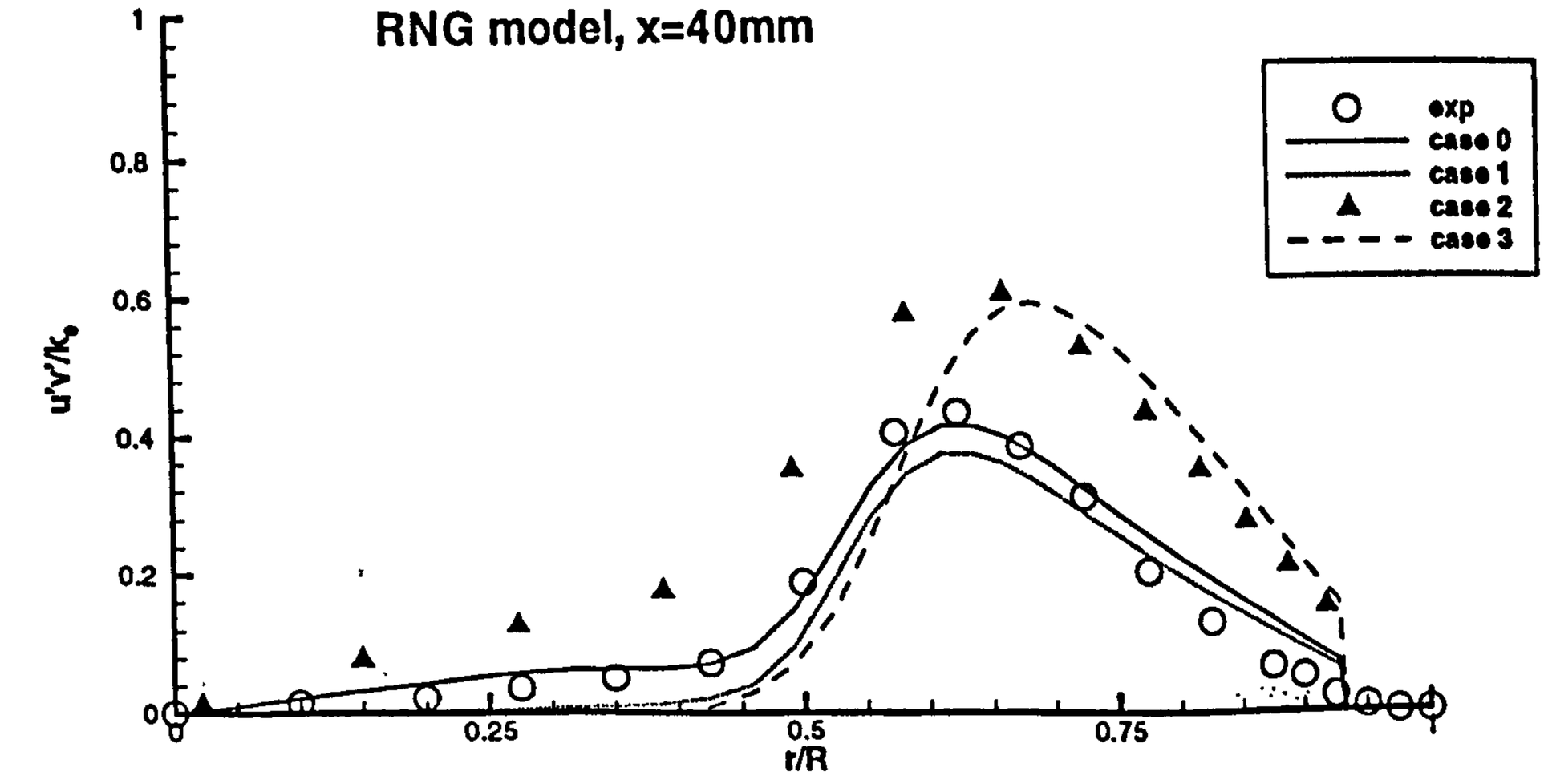

Figure E.5: Effect of inlet condition on Reynolds stress, for the pipe expansion of Tropea et al (1989).

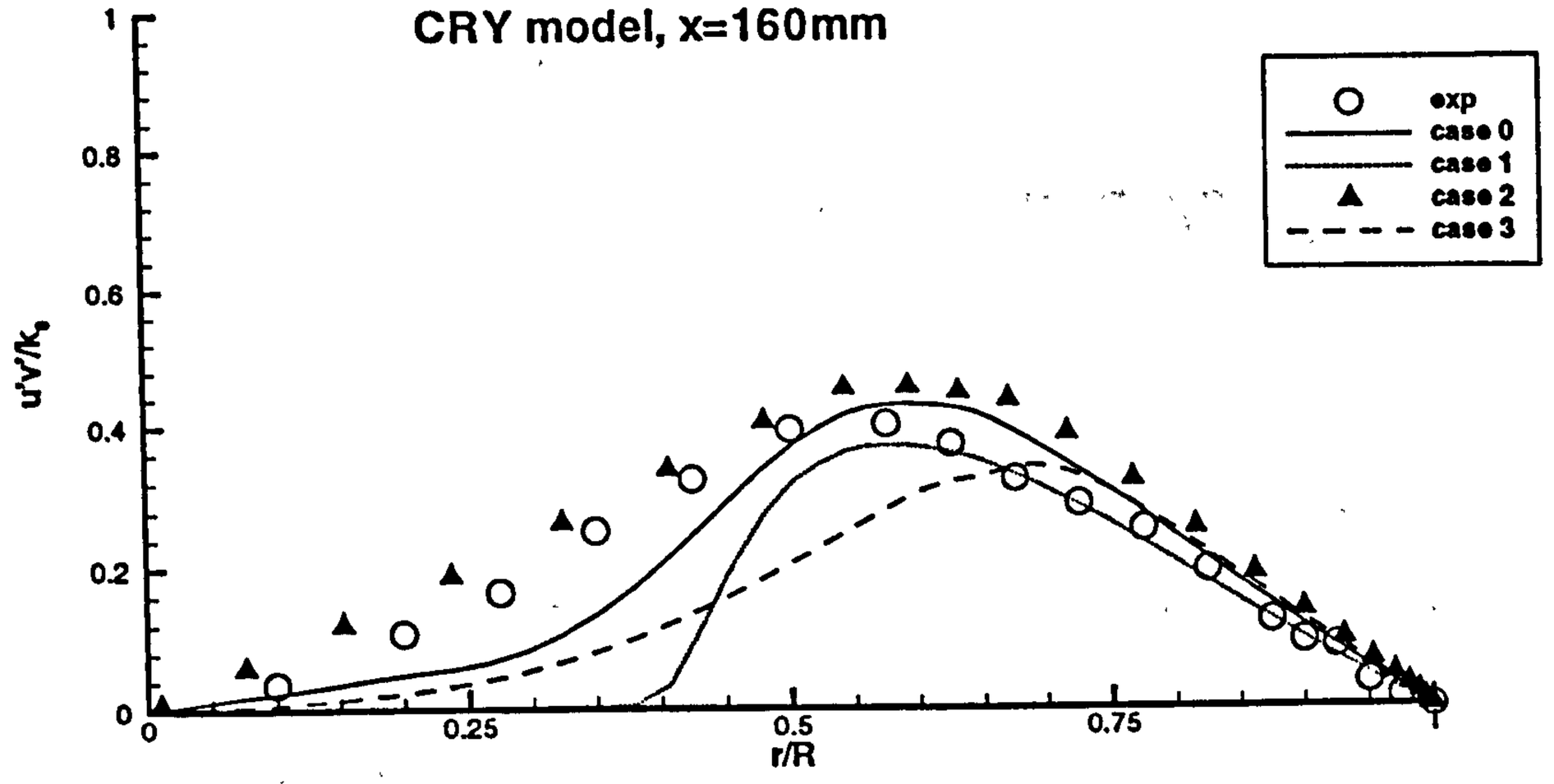

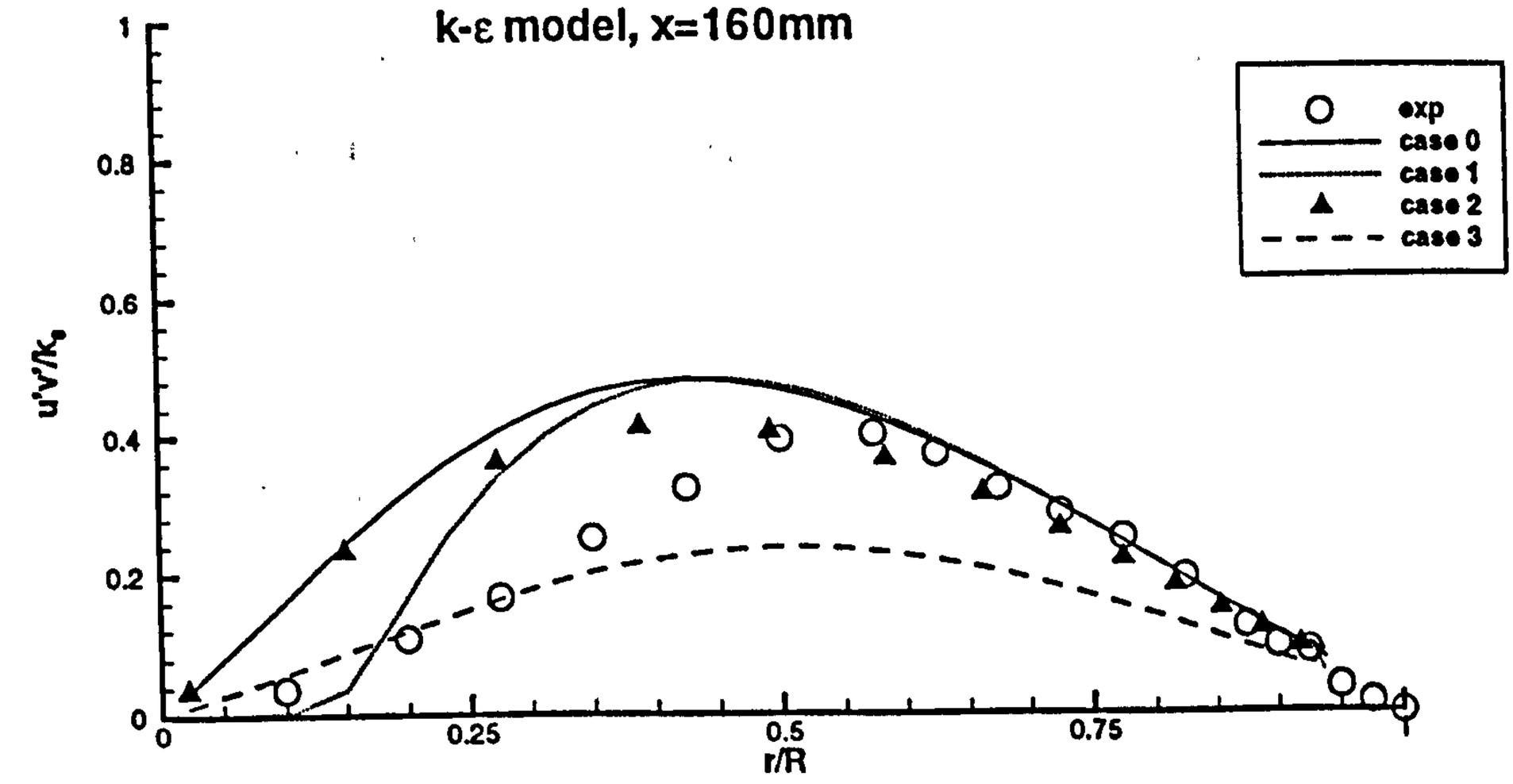

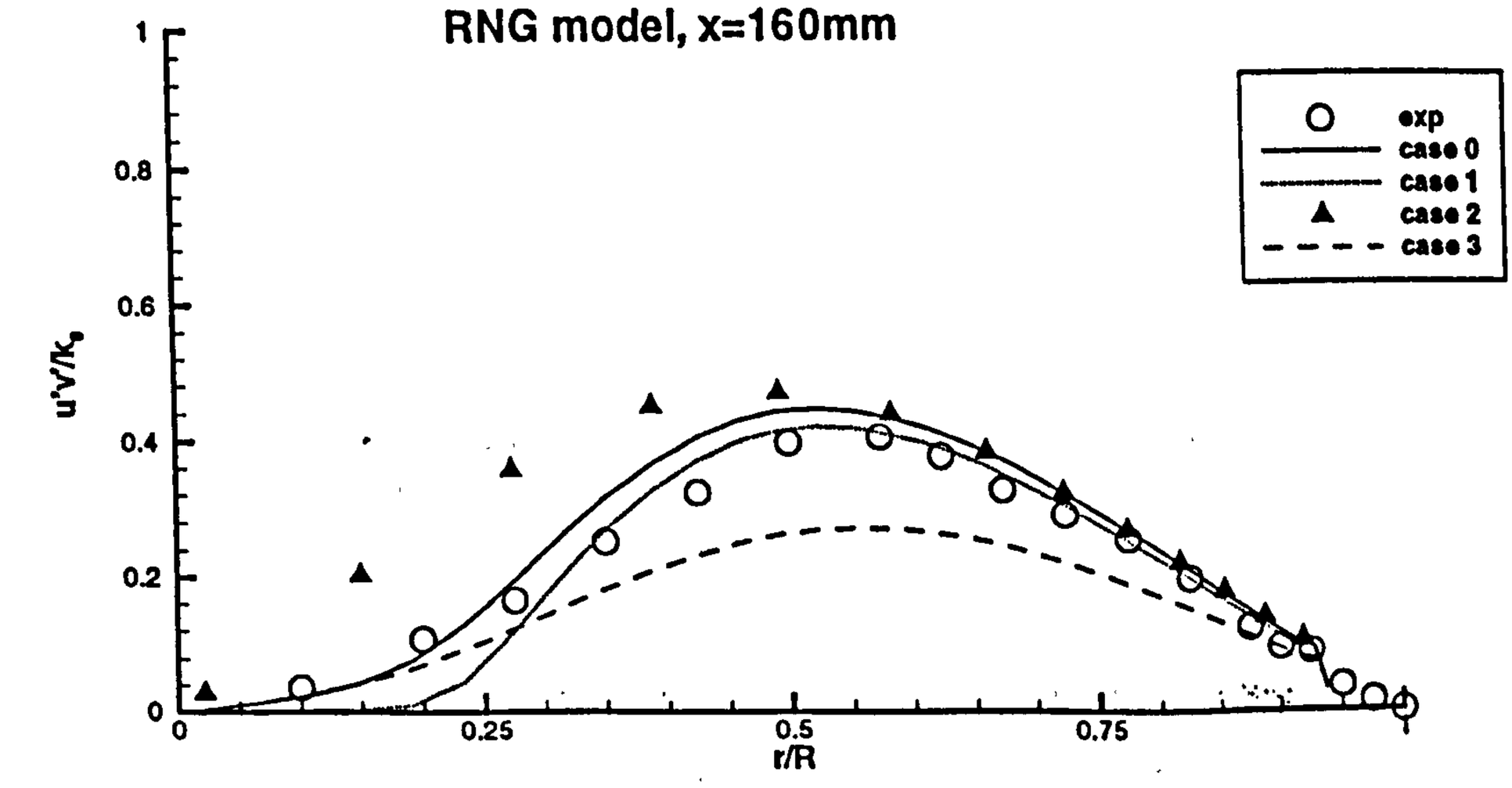

Figure E.6: Effect of inlet condition on Reynolds stress, for the pipe expansion of Tropea et al (1989).

APPENDIX F: SENSITIVITY OF COMPUTATIONS TO LEVELS OF INLET DISSIPATION RATE

Equations 3.6 and 3.7 are two examples of inlet specifications for dissipation rate, in the context of pipe expansions. It is useful to gauge the sensitivity of pipe expansion predictions to these inlet parameters. Nallasamy (1987) provided a graph which quantifies the dependence of the reattachment length (X_r) on inlet levels of turbulence energy k and dissipation rate ε, using the standard k-ε turbulence model. Figure F.1 clearly indicates that X_r does not vary over a wide range of l/H, which is the ratio of the length scale ($l = k^{3/2}/\varepsilon$) to the step height (H). The reattachment length is more dependent on the inlet turbulence energy.

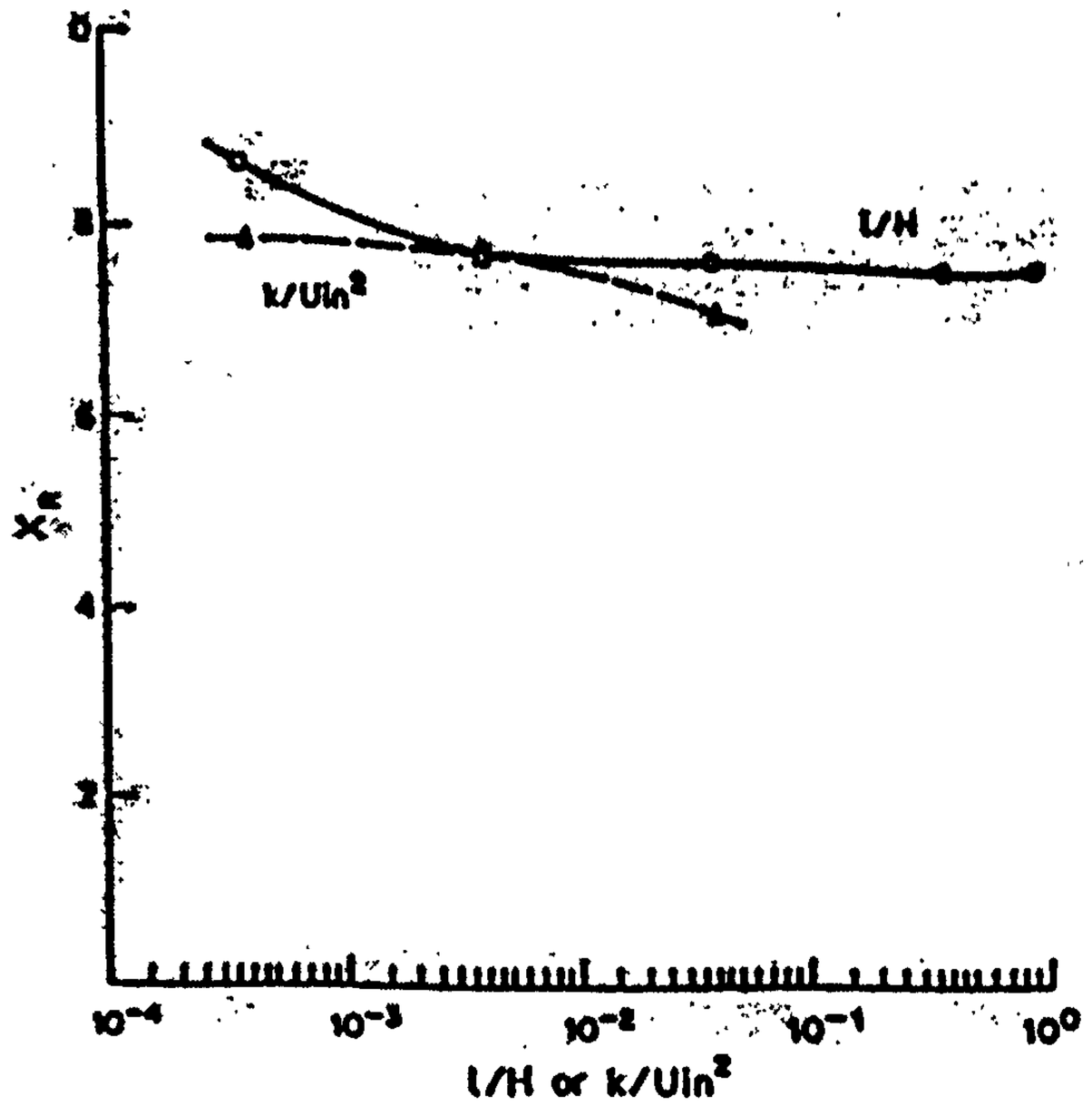

Figure F.1: Variation of reattachment length X_r with inlet k and ε levels (Nallasamy, 1987).

It is possible to check whether equations 3.6 and 3.7 have any bearing on the predicted reattachment length by calculating the ratio *l/H* for each formula, as indicated in table F.1. The dimensions are those of the Tropea et al (1989) pipe expansion which is thoroughly investigated in Chapter 4.

ε (using equation 3.6)	ε (using equation 3.7)
$\varepsilon = C_\mu^{3/4} k^{3/2} / (0.07 \times 0.05) = 46.95 k^{3/2}$	$\varepsilon = C_\mu k^{3/2} / (0.03 \times 0.025) = 120 k^{3/2}$
$l = k^{3/2} / 46.95 k^{3/2} = 2.13 \times 10^{-2}$	$l = k^{3/2} / 120 k^{3/2} = 8.33 \times 10^{-3}$
$l/H = 2.13 \times 10^{-2} / 0.015 = 1.42$	$l/H = 8.33 \times 10^{-3} / 0.015 = 0.555$

Table F.1: Calculation of dimensionless inlet parameter *l/H*.

The resulting values of *l/H* are 1.42 and 0.555, respectively, for formulations 3.6 and 3.7. The *l/H* curve in figure F.1 demonstrates that these two inlet prescriptions have little effect on computations. Simulations of the Tropea et al (1989) pipe expansion with the TEACH code, using the two different inlet conditions for ε, confirmed that use of relations 3.6 and 3.7 yields identical reattachment lengths (X_r/D_2 = 1.1), as predicted in figure F.1.

The main purpose of this exercise was to demonstrate that simulation results are relatively insensitive to the inlet prescriptions for dissipation rate. Similar conclusions were also drawn for pipe expansion simulations by Chang et al (1995). This finding is useful because it implies that when isotropic dissipation rates are employed, they can be simply approximated as $\tilde{\varepsilon}_{in} \approx \varepsilon_{in}$ rather than being derived from equation 2.23.

APPENDIX G: PIPE EXPANSION - BACK & ROSCHKE (1972)

The original flow studied with the aid of the TEACH code was the pipe expansion for which Back & Roschke (1972) provided experimental evidence of the variation of reattachment length with Reynolds number. The case was thus further investigated using the RNG, LS and CRY models. Inlet and exit diameters are $D_1=9.525\times10^{-3}$ m and $D_2=2.4765\times10^{-2}$ m, respectively, whilst the length of the test section (and of the computational domain) was 31.5H (0.235 m). The fluid medium was water, having density 1000 kg/m^3 viscosity 8.0×10^{-4} Pa·s. A plug profile (i.e. flat U, k and ε) was prescribed at the inlet because Back & Roschke (1972) reported the inlet flow as being nearly uniform. Back & Roschke concluded that the reattachment length remained constant beyond Re = 5000; since this is a low value as far as turbulence models are concerned, it was decided to simulate the case for Re = 20000 instead. The bulk inlet velocity was 1.68m/s. A turbulence intensity of 3% was assumed, whilst equation 3.4 was used to specify the inlet dissipation rate. Again, the assumption $\tilde{\varepsilon}_{in} \approx \varepsilon_{in}$ is justified by the flat inlet profiles.

Grid independence studies showed that a 200×50 mesh was sufficient for the CRY and LS models. Radial cells were removed from this grid to create a 200×35 mesh for the k-ε and RNG models, ensuring that the near wall node was mostly in the inertial sublayer. A 200×54 grid for the high Reynolds number models (which was also constructed such that $y_p^+>30$) yielded the same reattachment length. The maximum cell Reynolds number in the axial direction was 18.5 (calculated at the inlet, near the centreline), whilst the peak radial Peclet number for the CRY model was 1.11. The corresponding values were 3.43 and 1.69 for the k-ε model, using the 200×35 and 200×54 grids, respectively. Figures G.1 and G.2 present the distributions of numerical diffusion as a percentage of local eddy viscosities, using he method described in Chapter 3. Again, one sees that false diffusion is generally a small fraction of the local eddy viscosity (except in the region directly behind the step where the percentage is larger

because μ_t is much smaller than elsewhere in the flow) and hence contributes very little to the overall results. The 200×35 and 200×54 grids used for the high Reynolds number models resulted in reattachment lengths of $X_r/H = 6.79$ and $X_r/H = 6.82$, respectively, despite the presence, in the former case, of several cells in which radial Peclet numbers were larger than 2. This confirms that the computational grids are not subject to excessive errors.

The only experimental data provided by Back & Roschke (1972) are reattachment lengths; table G.1 summarizes the predictions of the various turbulence models. It should be emphasised that the experimental result is at Re = 5000 whilst the computations were carried out at Re = 20000; this is justified because

- Above a certain Reynolds number, the reattachment length remains constant for a given geometry.
- The turbulence models do not perform well at low bulk Reynolds number flows.

	Experimental	k-ε	RNG	LS	LSY	CR	CRY
X_r/H	9.5	6.79	8.20	6.90	8.07	8.63	10.26
Error	-	-28.5%	-13.7%	-27.4%	-15.1%	-9.2%	+8.0%

Table G.1: Experimental and computed reattachment lengths.

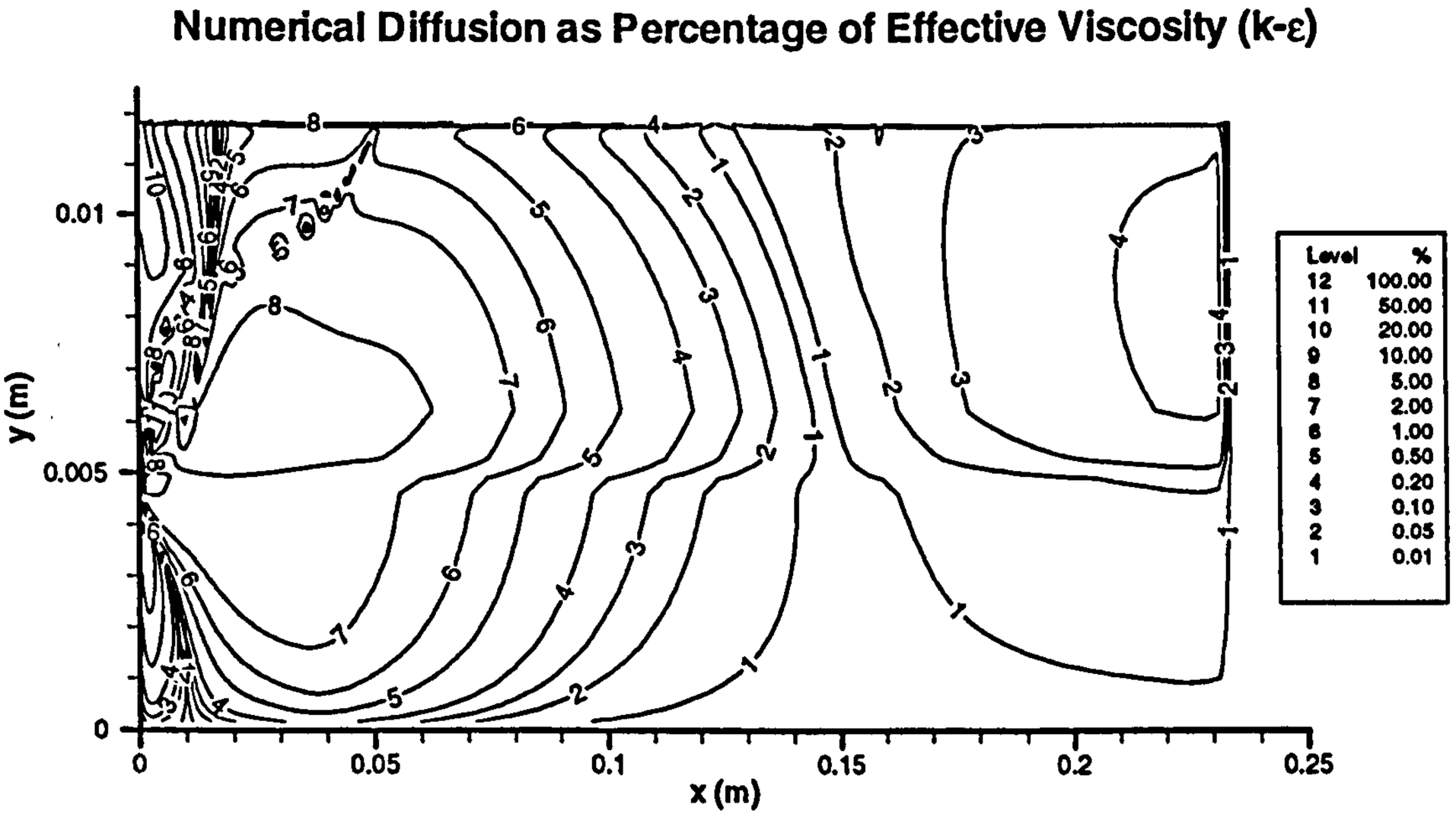

Figure G.1: Contour plot of artifical diffusion (*k*-ε model), Back & Roschke (1972) pipe expansion case.

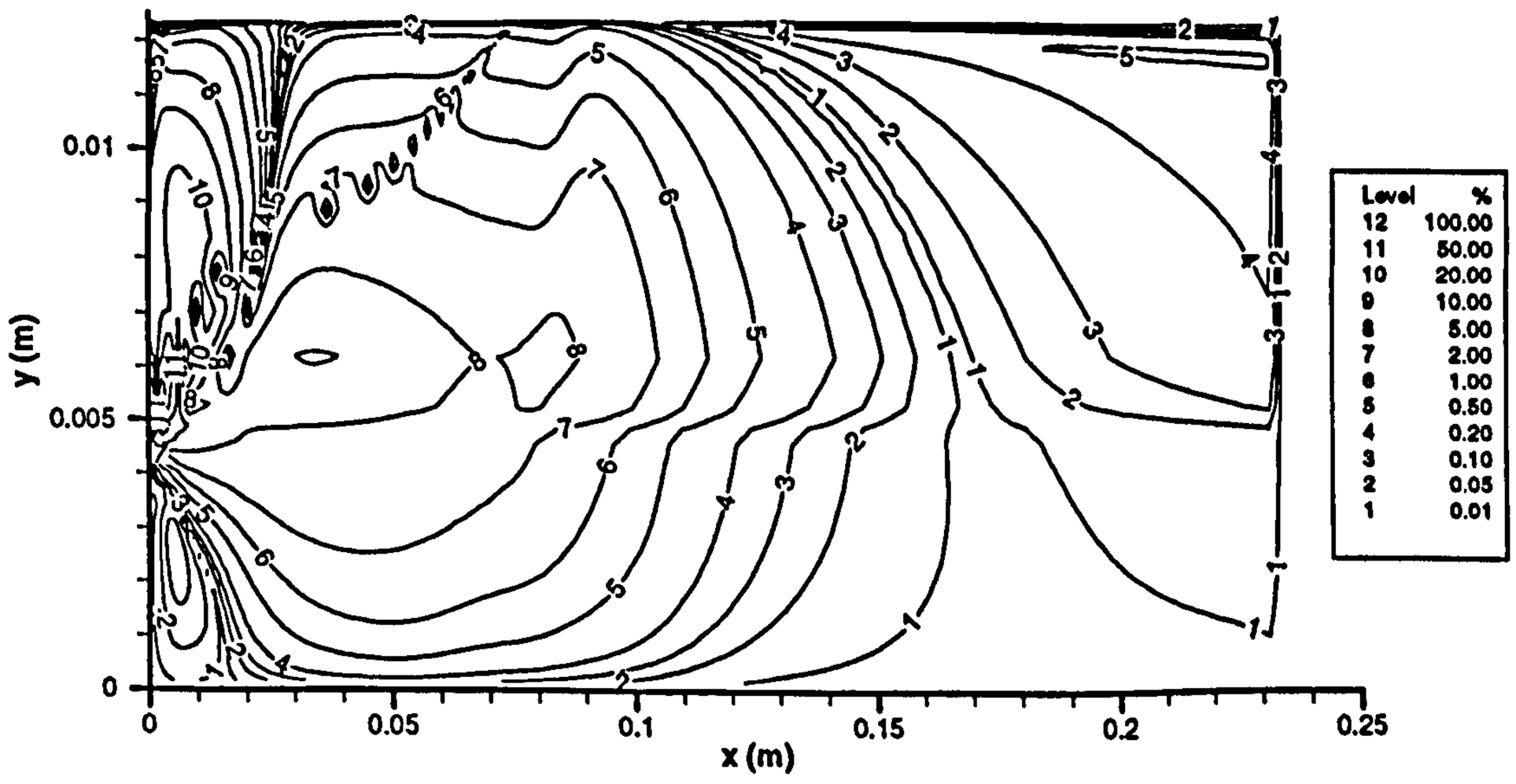

Figure G.2: Contour plot of artifical diffusion (CRY model), Back & Roschke (1972) pipe expansion case.

APPENDIX H: DETAILED DRAWINGS

Detailed drawings of individual components and the entire bluff-body burner assembly are shown in the following pages. Due to a change in circumstances, various components of the experimental combustor eventually had to be welded together. This necessitated several internal design changes; however, these drawings were not updated accordingly.

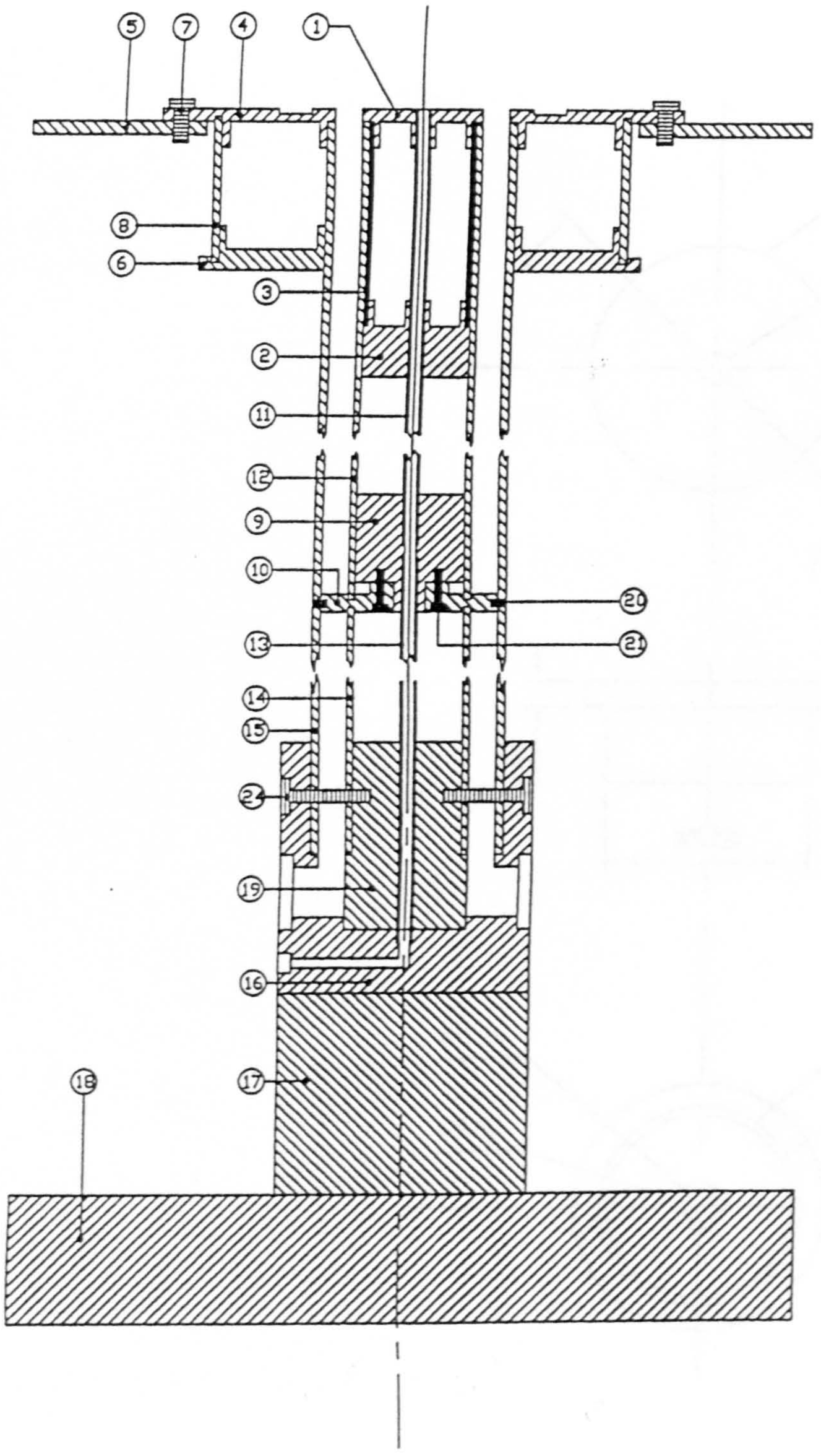

Units: millimetres

All components are made of stainless steel (304) except parts 5 and 18 (to be made of non-stainless material).

PART	DESCRIPTION	QTY.	SUPPLIER	RAW MATERIAL
1	See detailed drawing	1	Workshop	Round bar, ø50
2	See detailed drawing	1	Workshop	Round bar, ø50
3	See detailed drawing	1	Workshop	Pipe: I.D.=37 O.D.=50
4	See detailed drawing	1	Workshop	To be found
5	See detailed drawing	1	Workshop	To be found
6	See detailed drawing	1	Workshop	To be found
7	Bolt	4		
8	Pipe: L=60.00 I.D.=154.00 O.D.=168.00	1	EMA	
9	See detailed drawing	1	Workshop	Round bar, ø50
10	See detailed drawing	1	Workshop	Plate, approx. 9.5 thick
11	Pipe: L=240.00 I.D.=4.00 O.D.=6.00	1	AALCO	
12	Pipe: L=257.00 I.D.=41.20 O.D.=44.45	1	EMA	
13	Pipe: L=555.00 I.D.=4.00 O.D.=6.00	1	AALCO	
14	Pipe: L=502.00 I.D.=41.20 O.D.=44.45	1	EMA	
15	Pipe: L=760.00 I.D.=67.00 O.D.=73.00	1	EMA	
16	See detailed drawing	1	EMA	Square block, 95X95X100
17	See detailed drawing	1	EMA	Square block, 95X95X80
18	See detailed drawing	1	Workshop	To be found
19	See detailed drawing	1	Workshop	Round bar, ø50
20	grub screw	4		
21	bolt	4		
22	Pipe: L=145.00 I.D.=8.00 O.D.=10.00	4	AALCO	
23	Pipe: L=630.00 I.D.=8.00 O.D.=10.00	4	AALCO	
24	bolt	4		

Component 8 requires turning down from O.D.=168.00 to O.D.=160.00

We also require 4 bolts (approx. 240mm long) to fasten parts 16, 17 and 18 together.

PART 1

Not necessarily drawn to scale

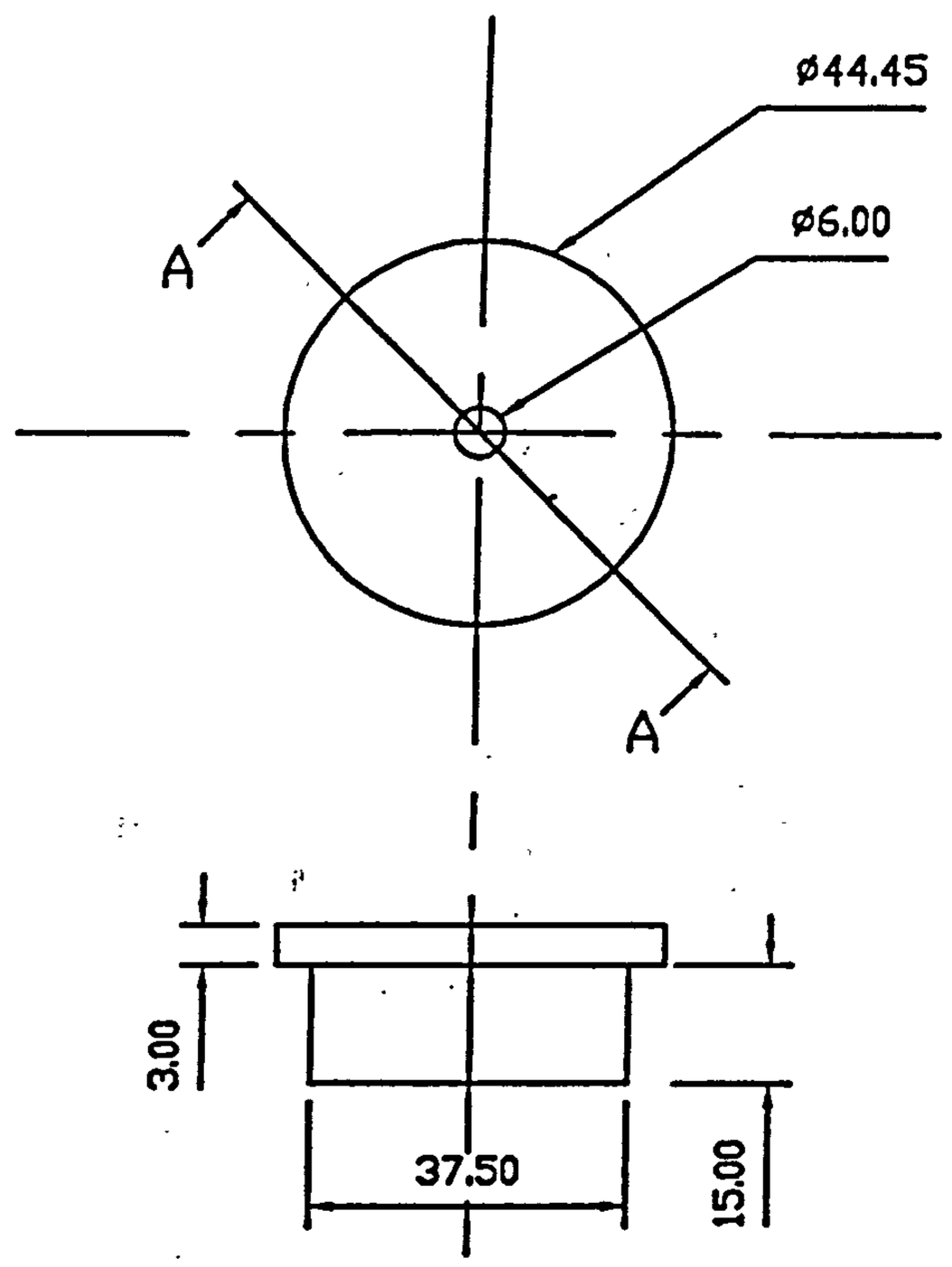

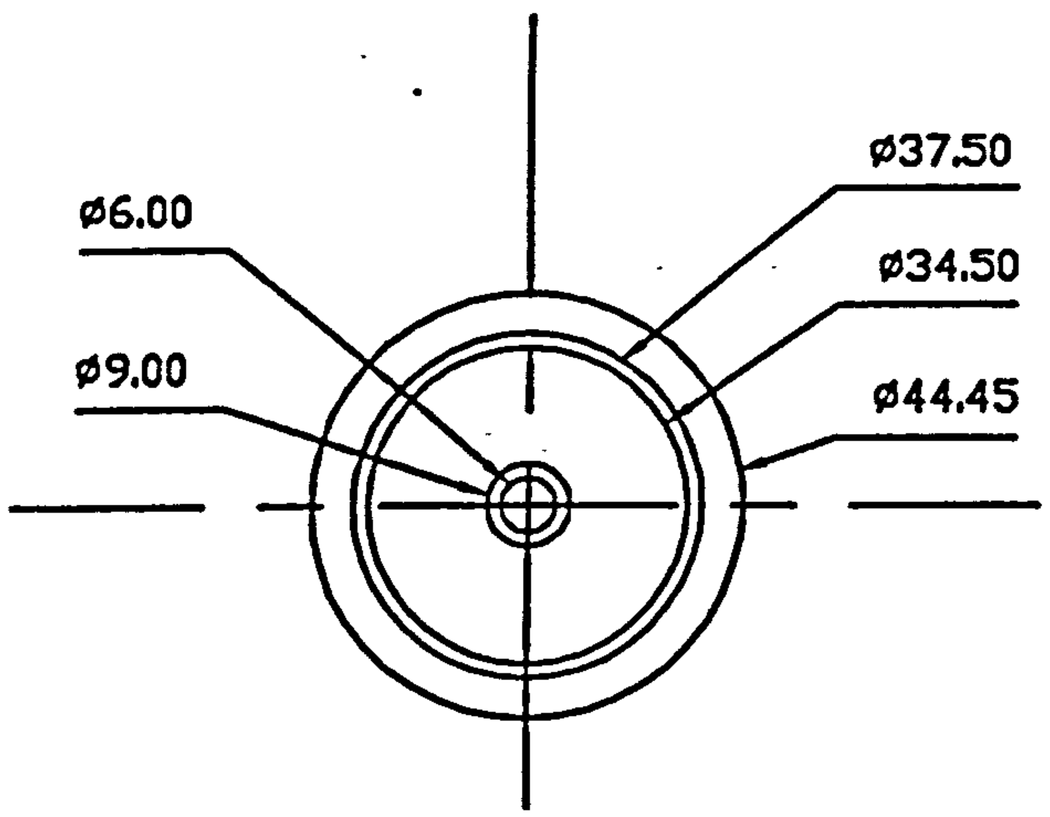

Section A-A

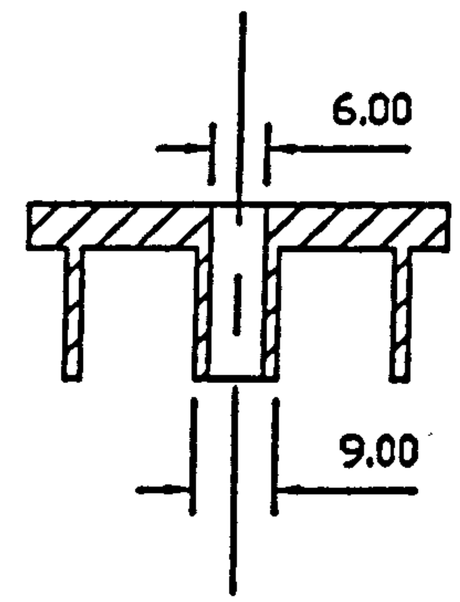

PART 2

Not drawn to scale

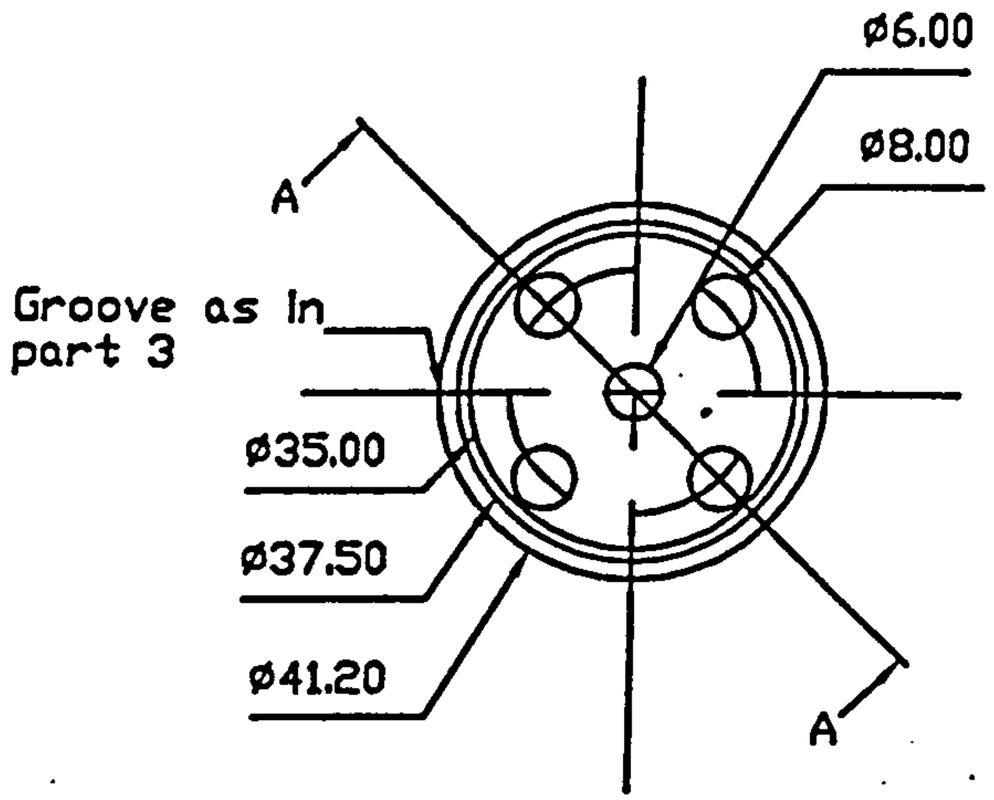

Section A-A

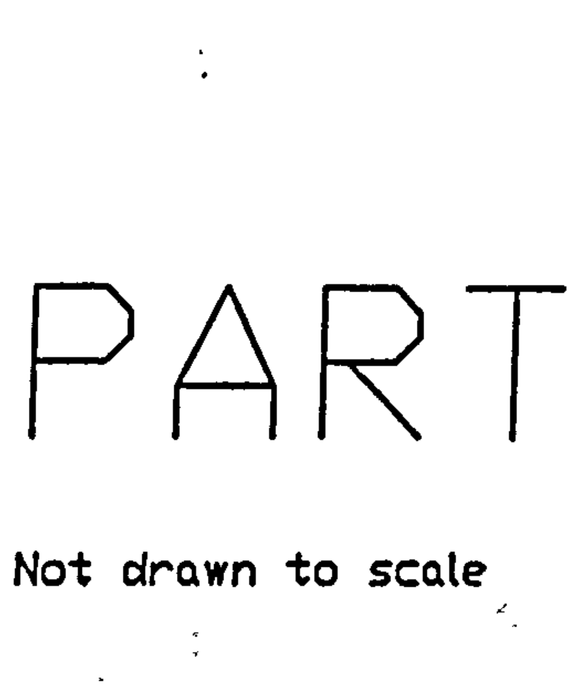

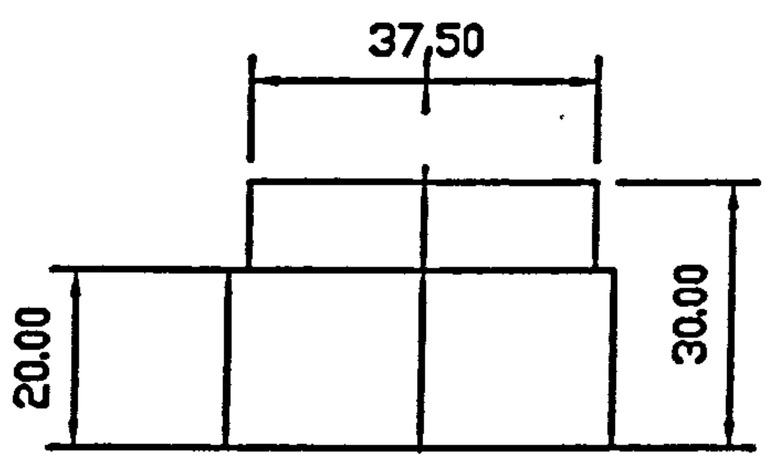

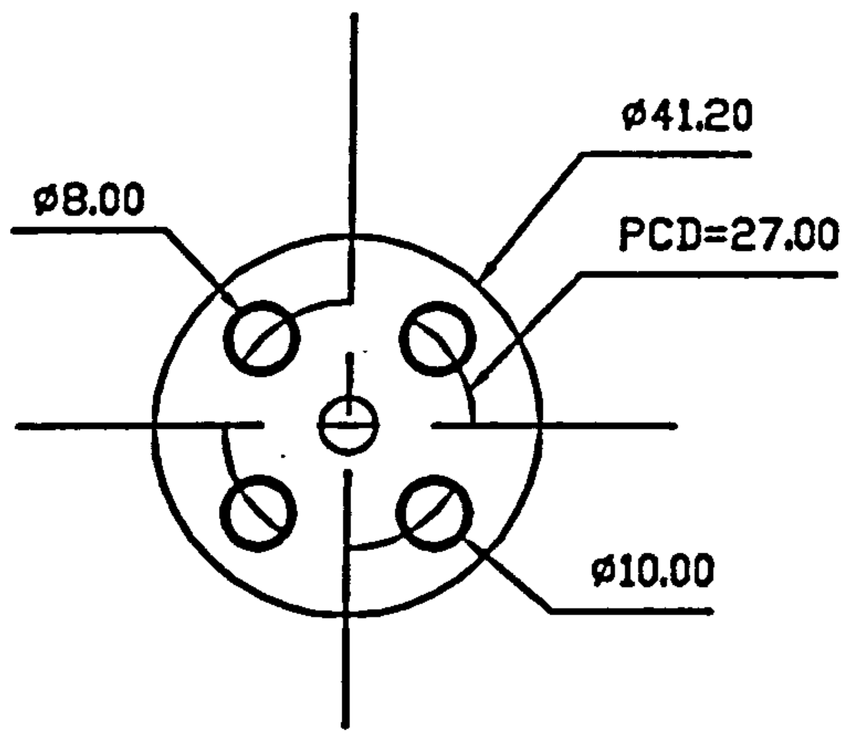

PART 3

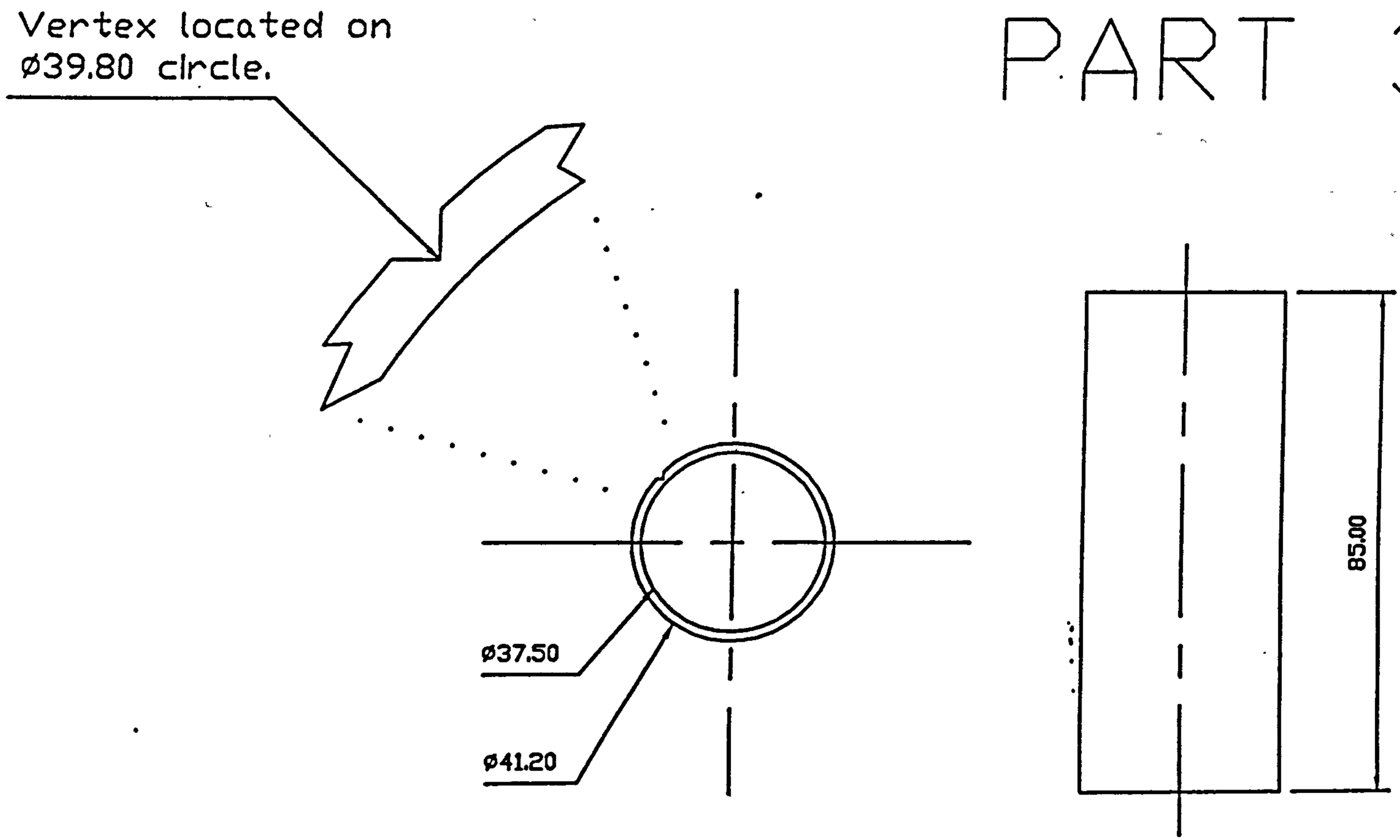

BOTTOM VIEW

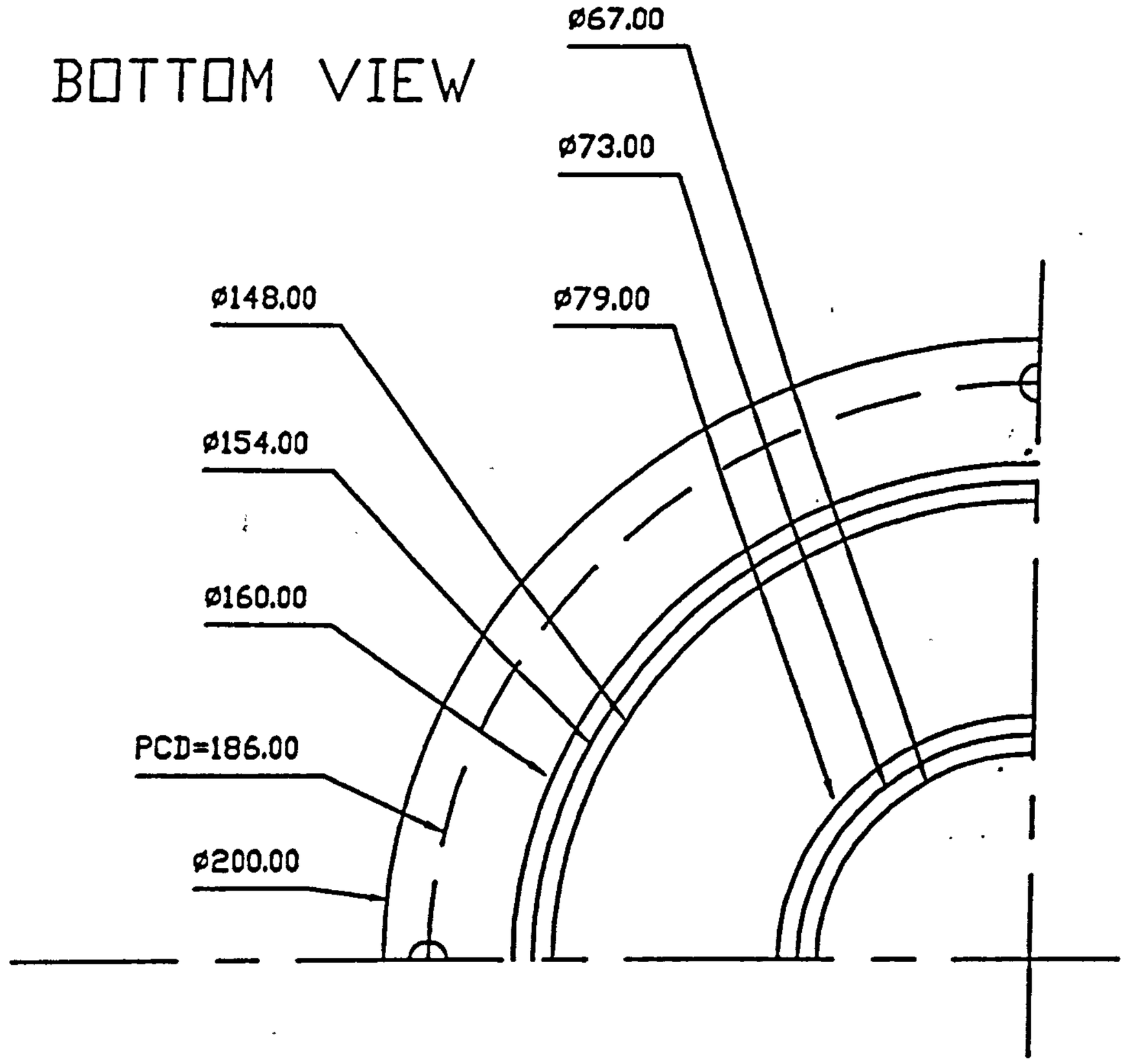

TOP VIEW

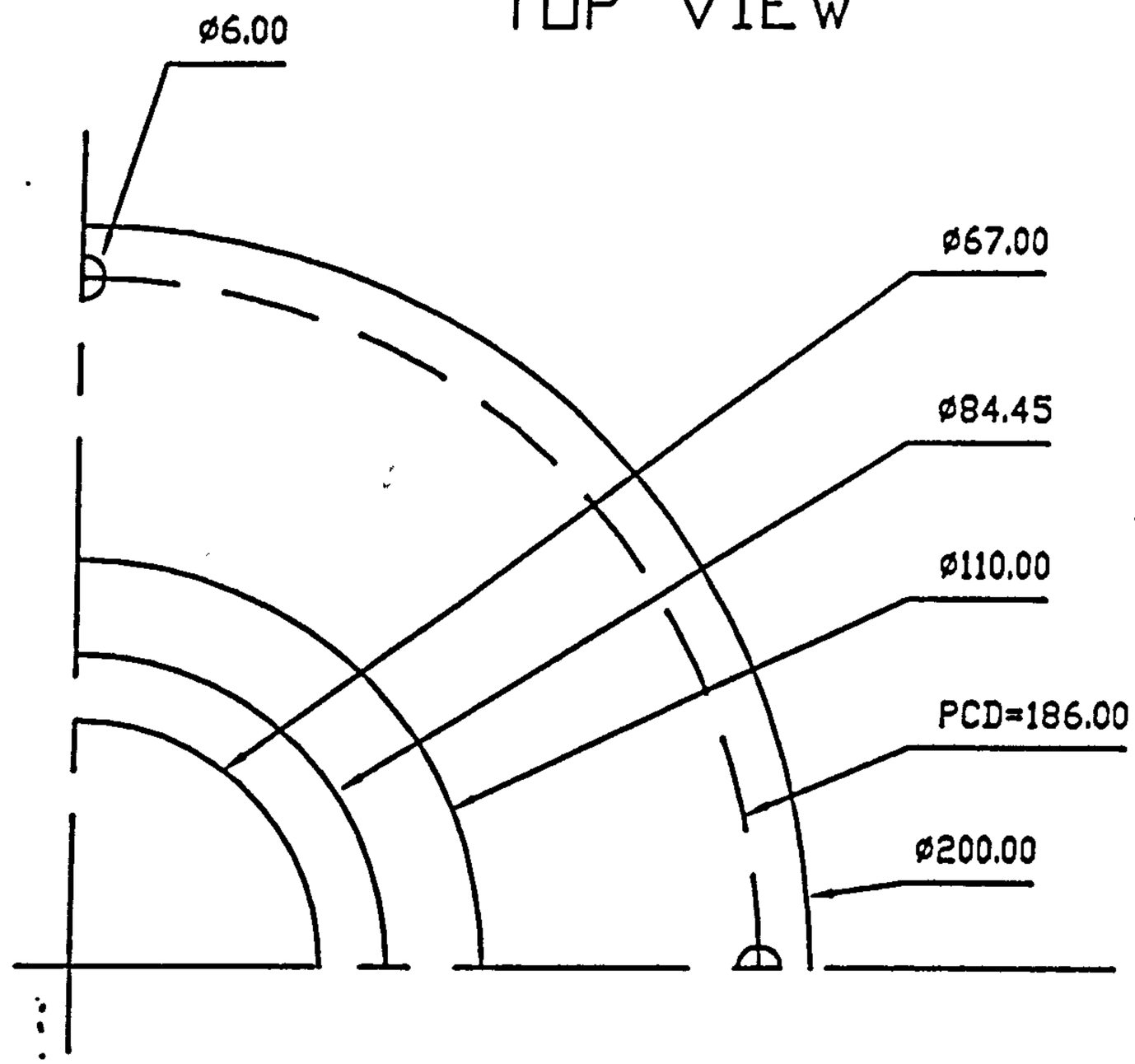

PART 4

Not drawn to scale

Section of component

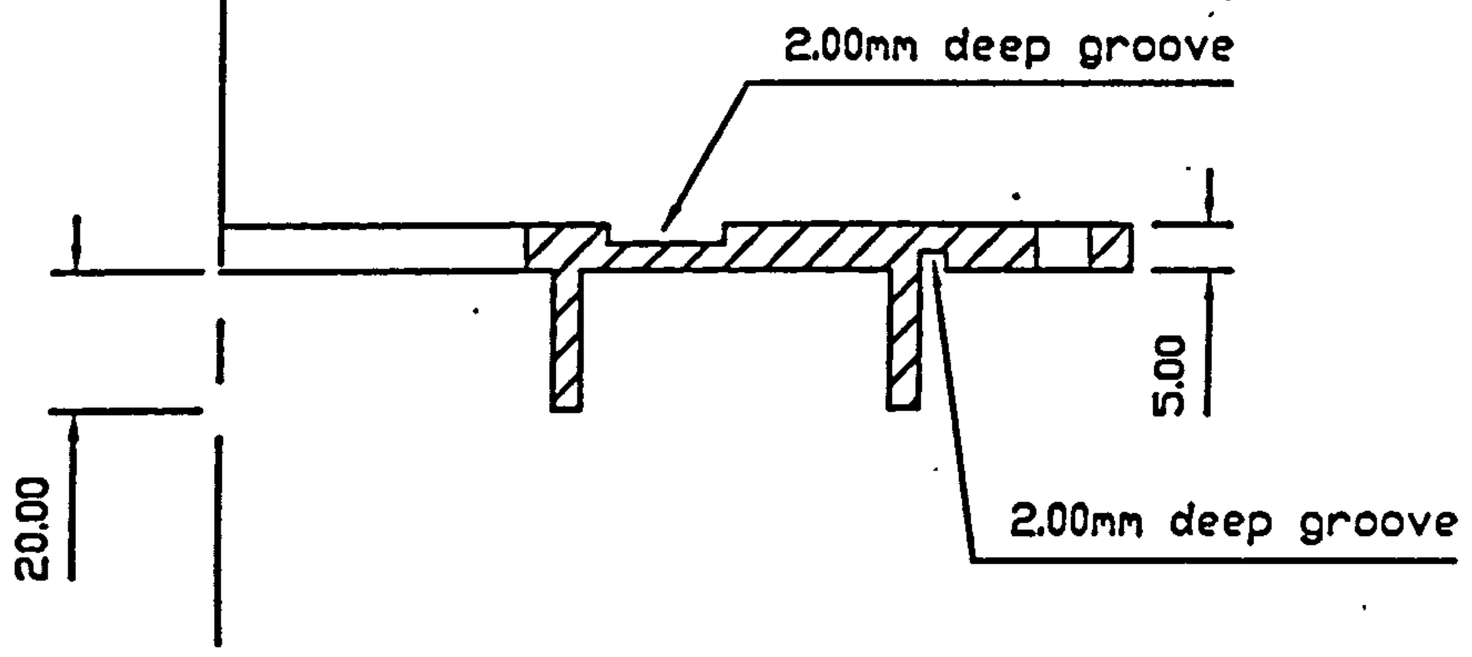

PART 5

Not drawn to scale

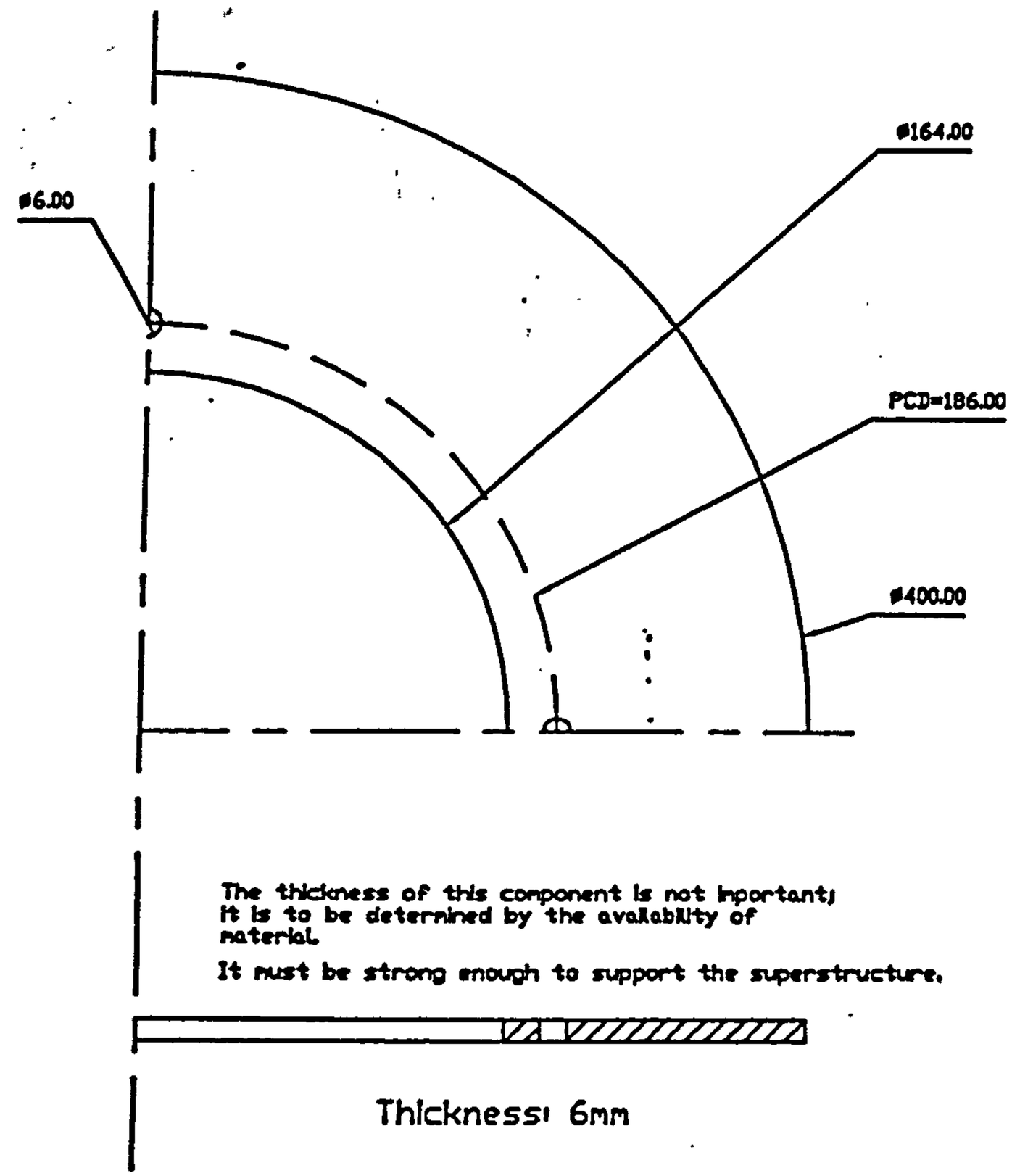

The thickness of this component is not important; it is to be determined by the availability of material.

It must be strong enough to support the superstructure.

Thickness: 6mm

PART 6

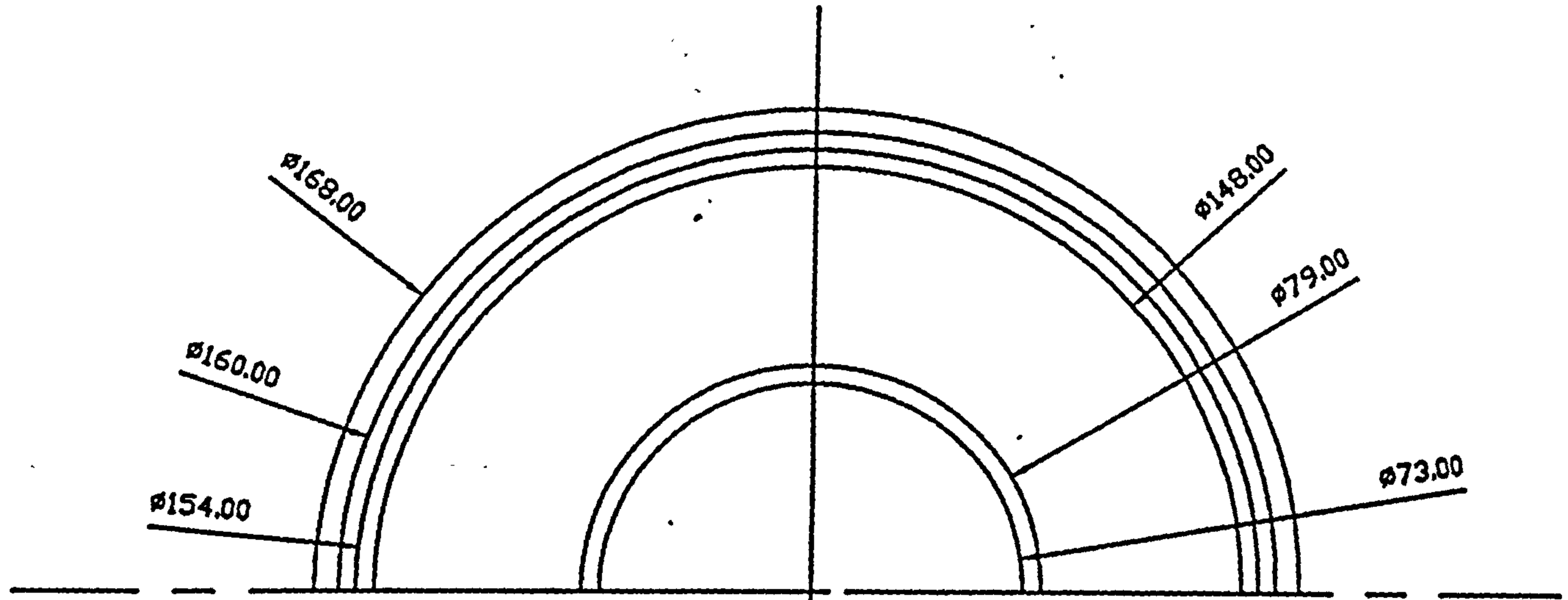

Not drawn to scale

Sectional View

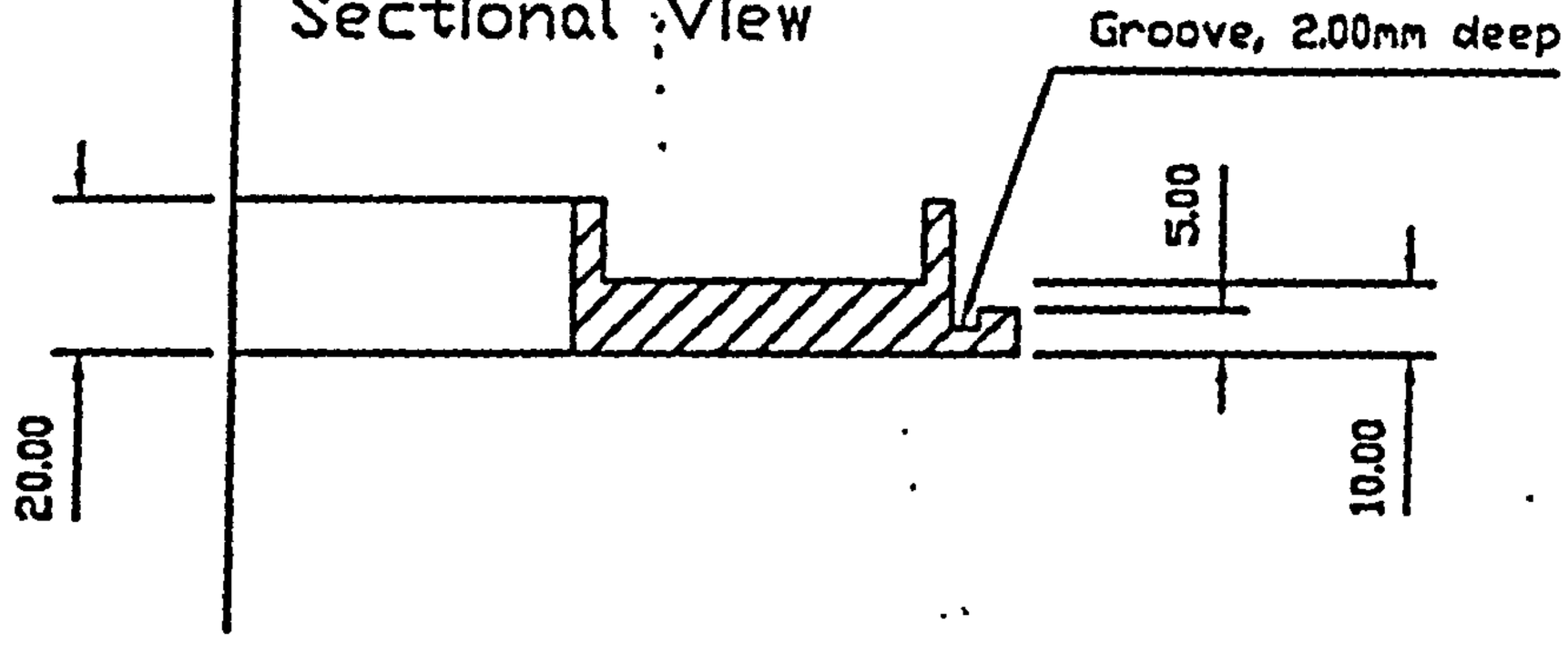

PART 9

Not drawn to scale

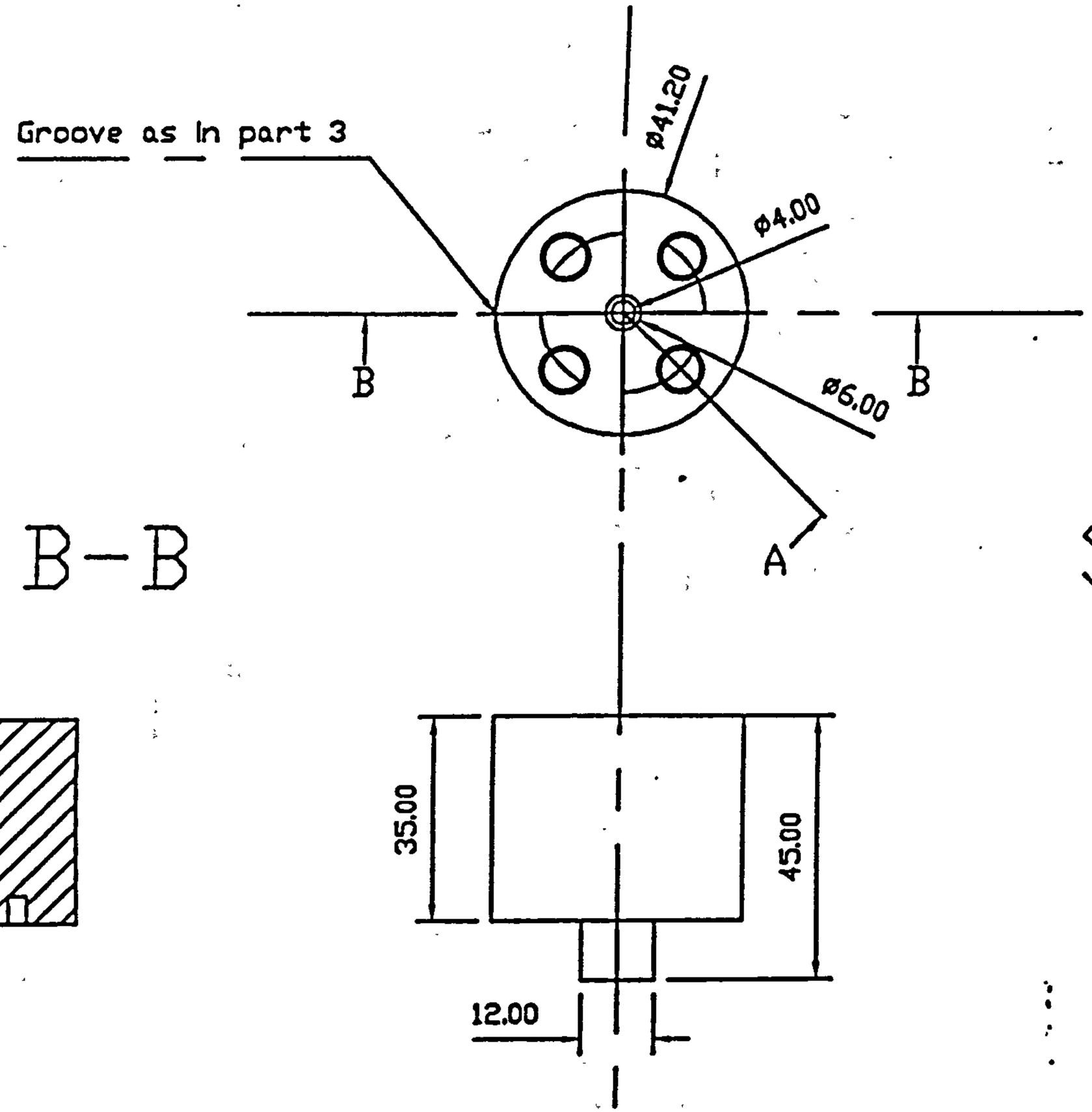

Section B-B

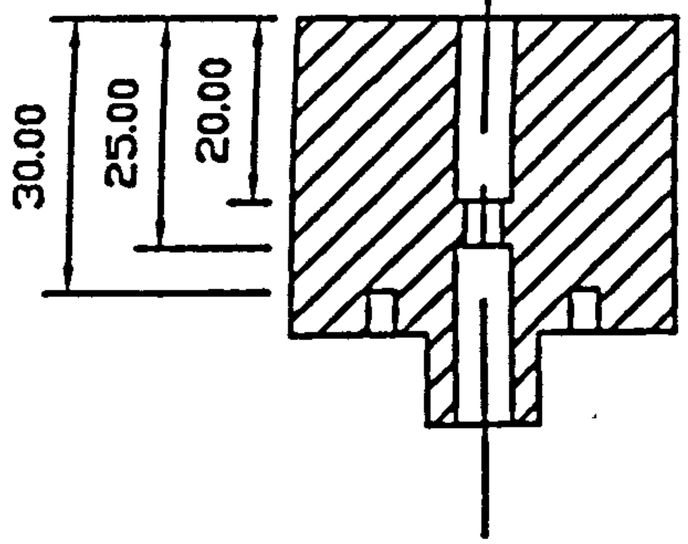

Section A

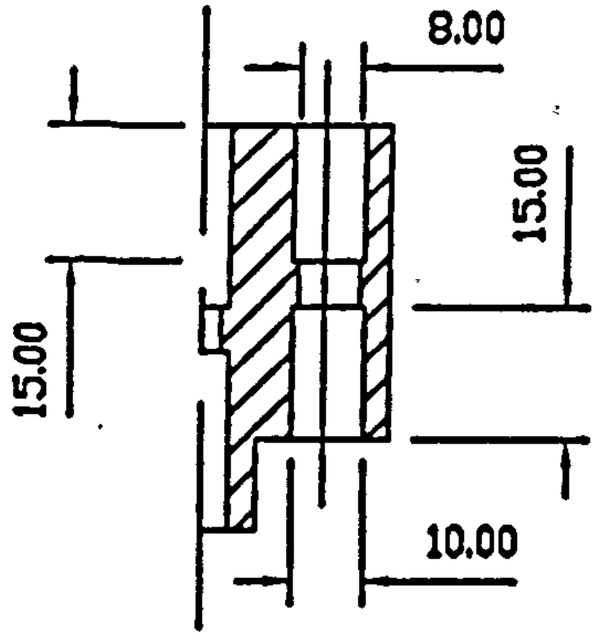

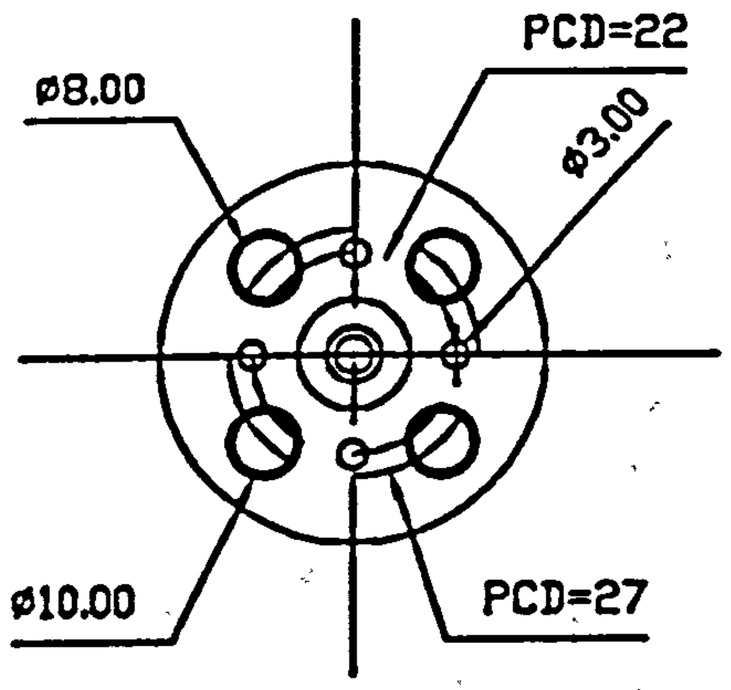

PART 10

Not drawn to scale

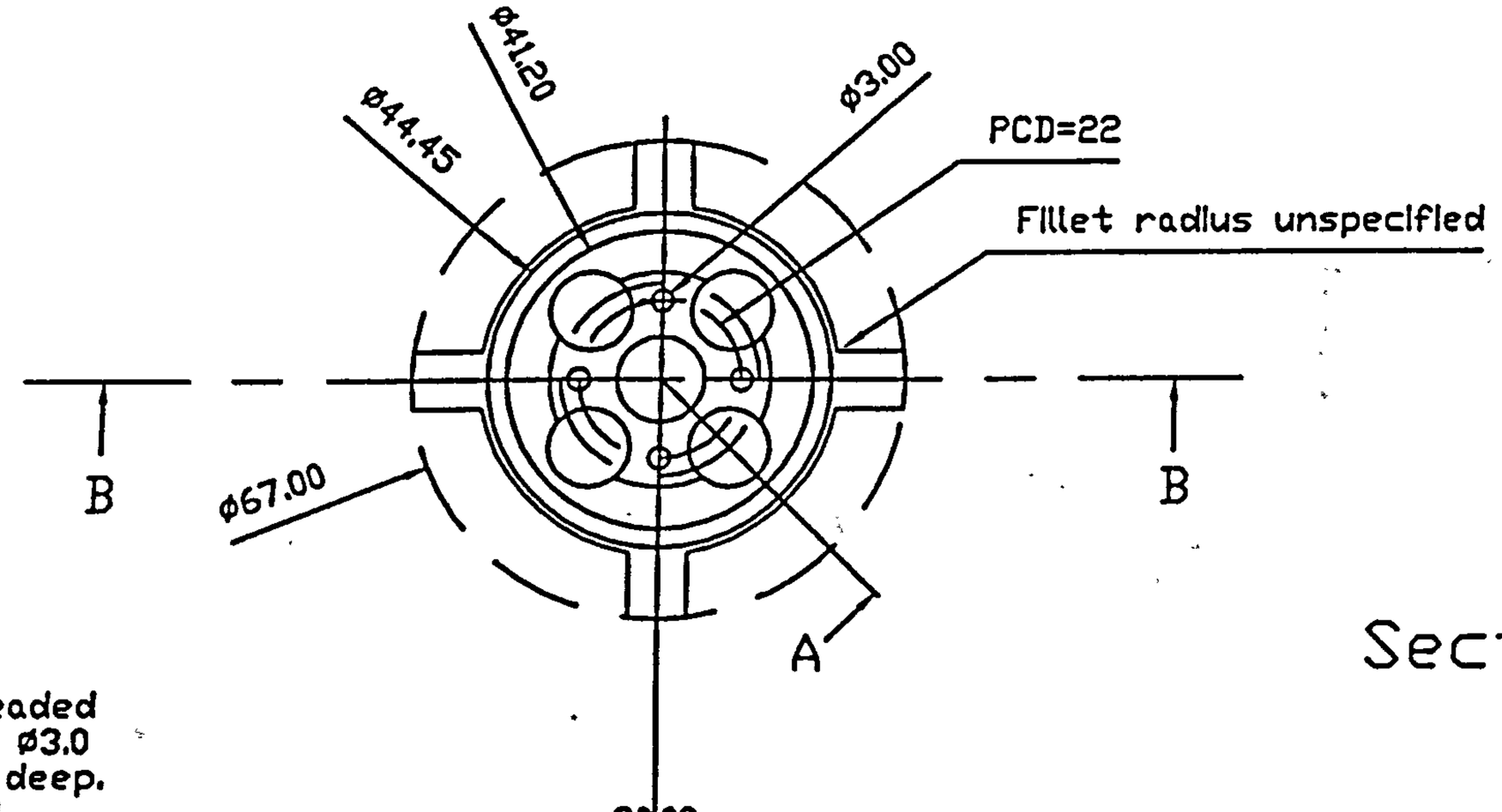

Section B-B

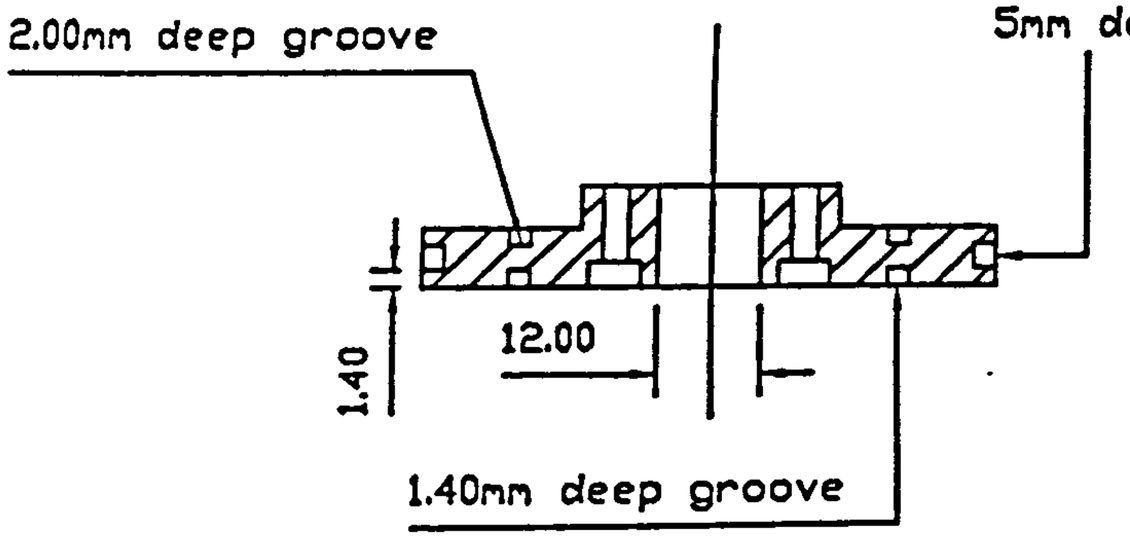

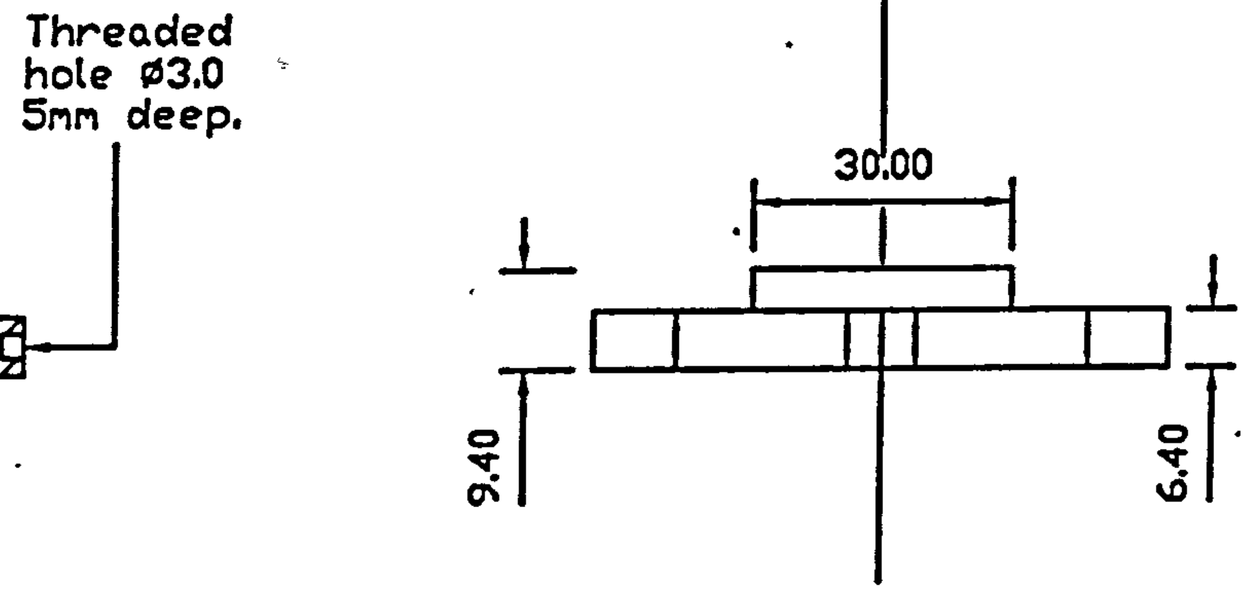

Section A

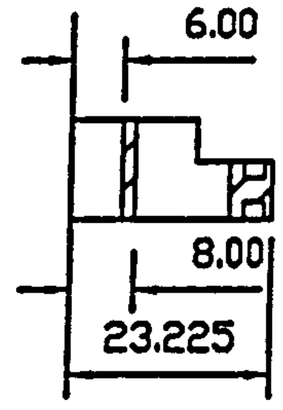

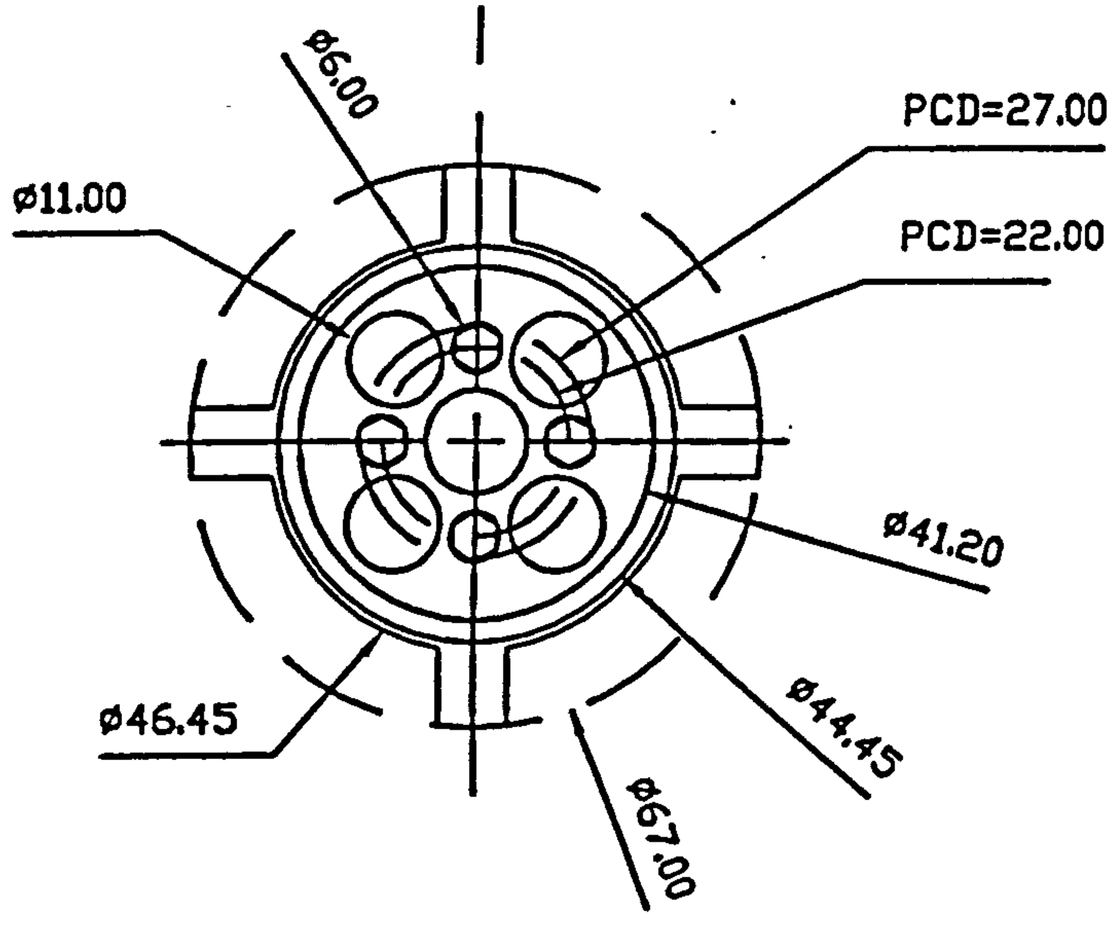

PART 16

Not drawn to scale

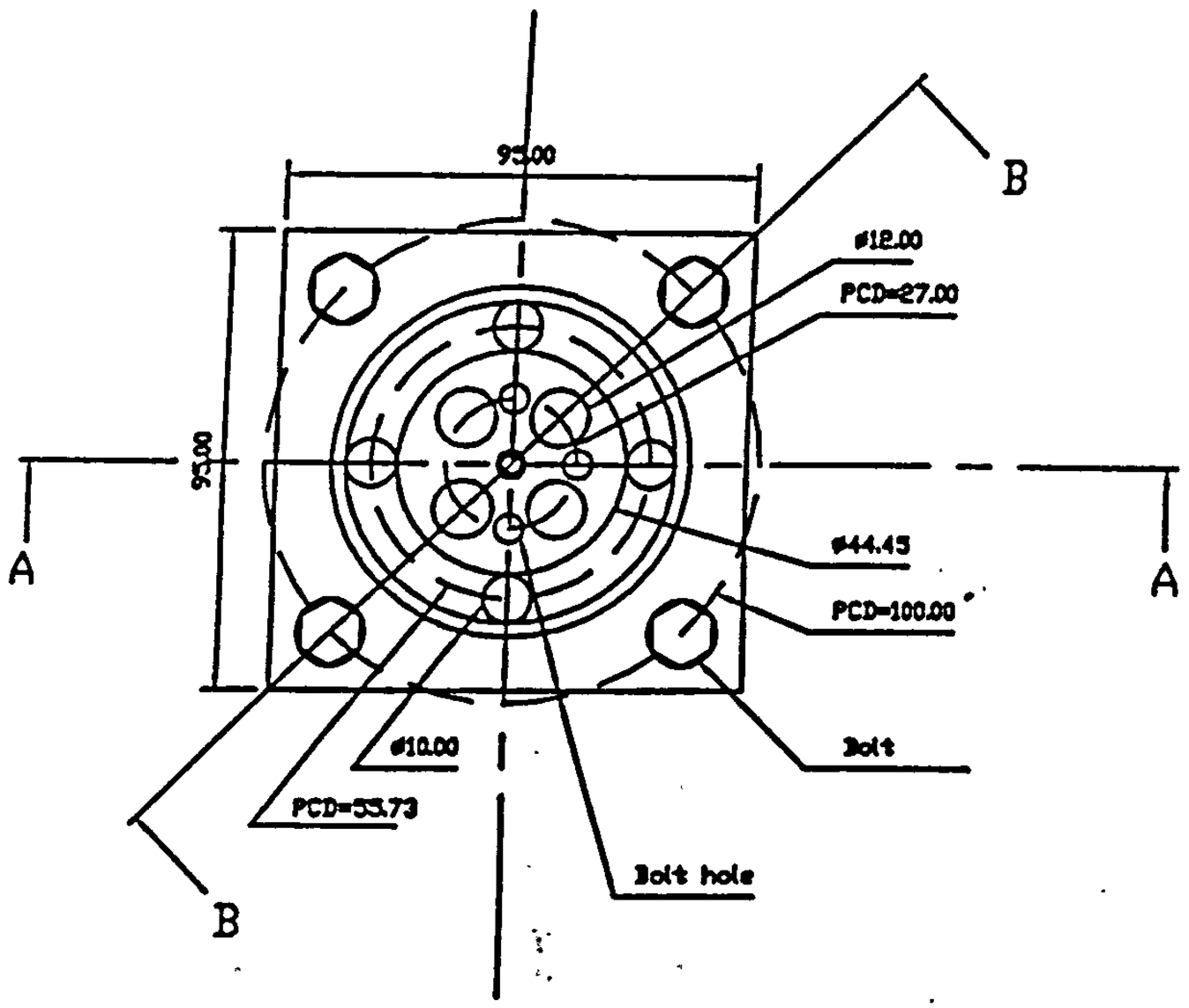

Section A-A

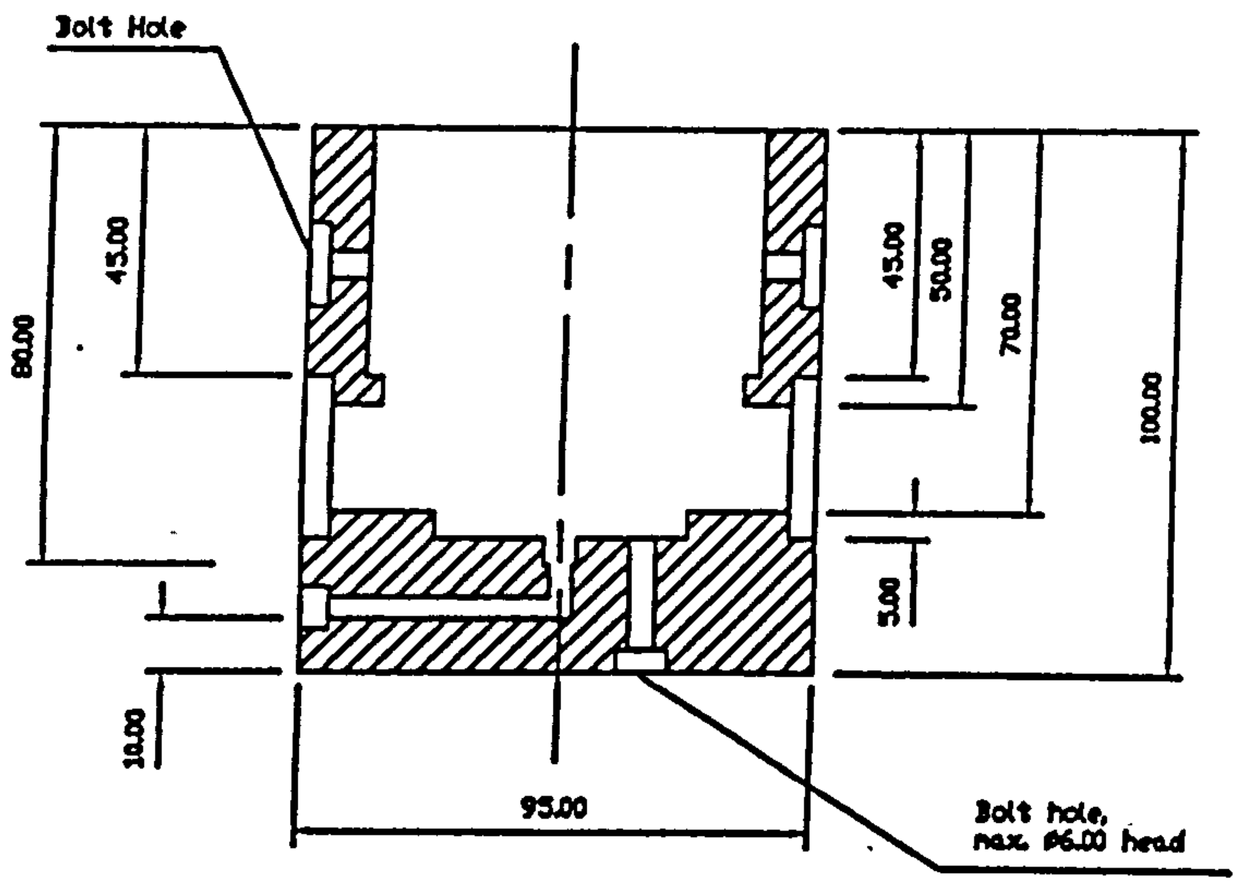

Section B-B

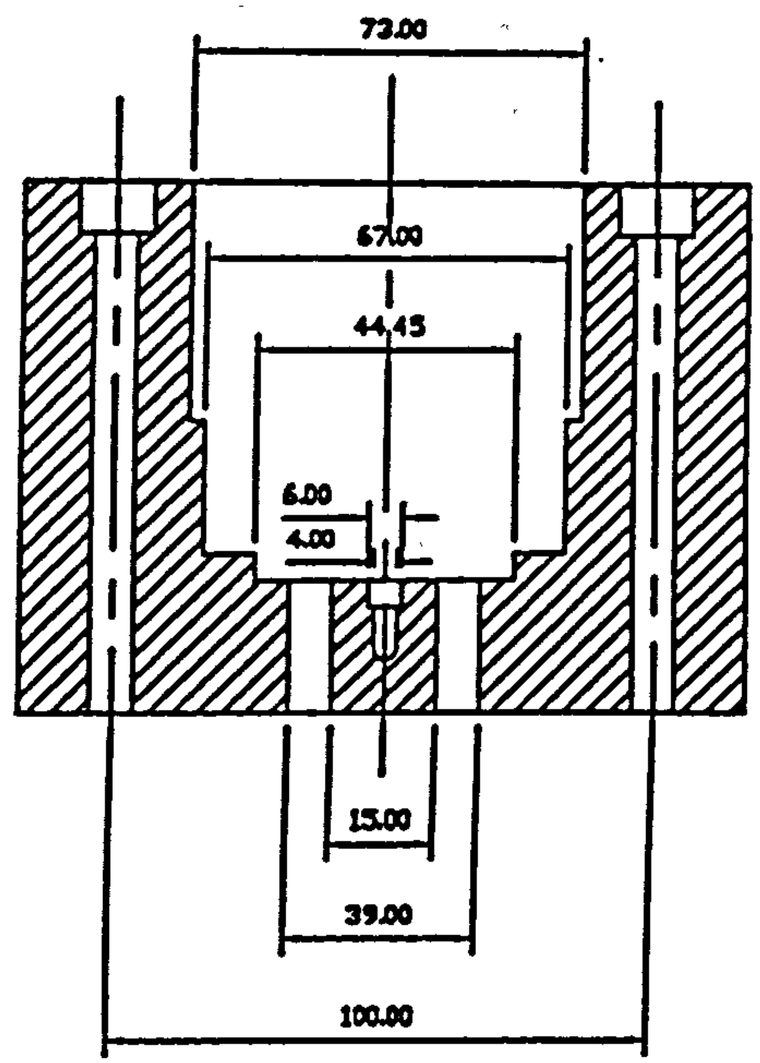

PART 17

Not drawn to scale

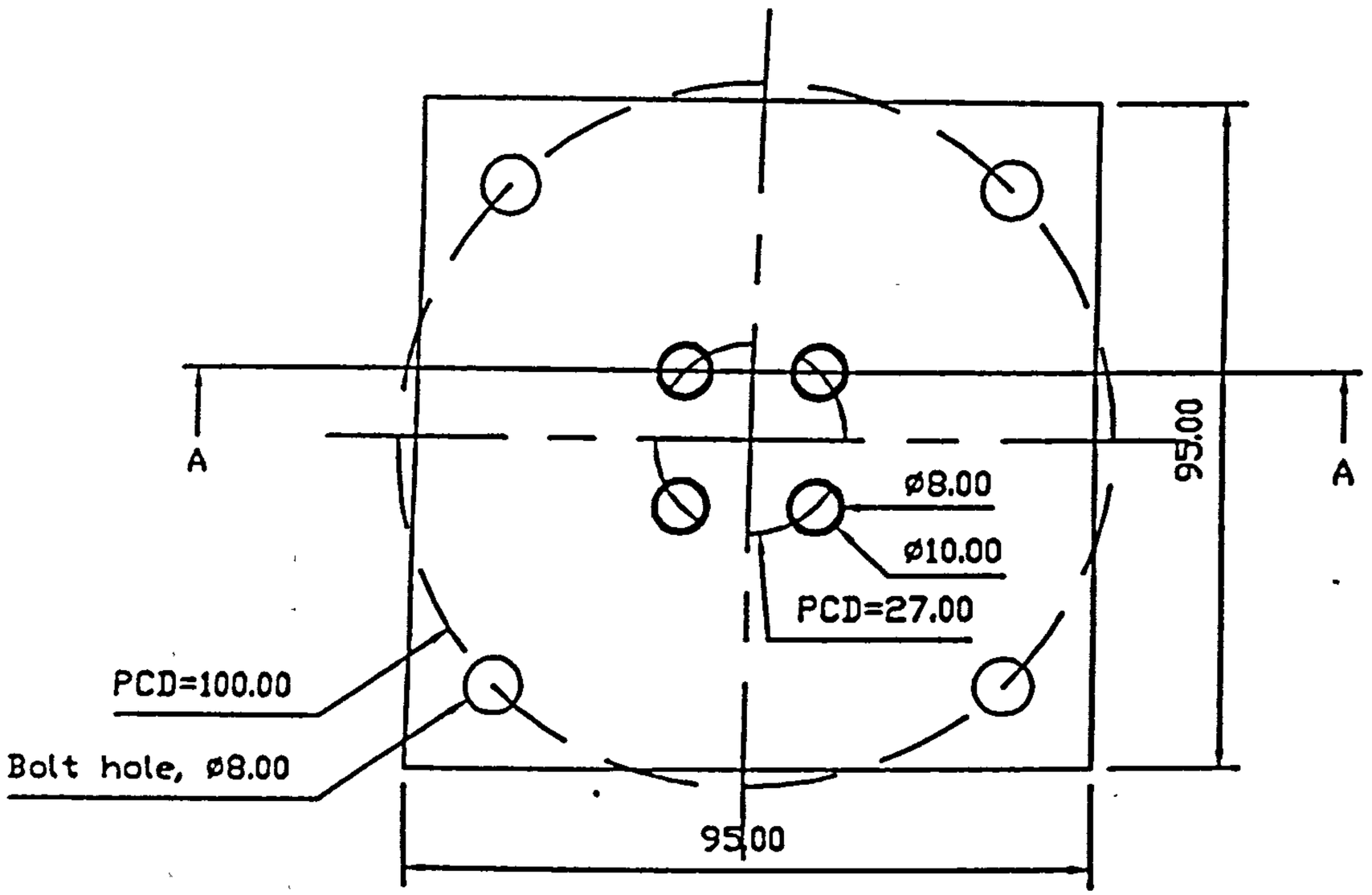

Section A-A

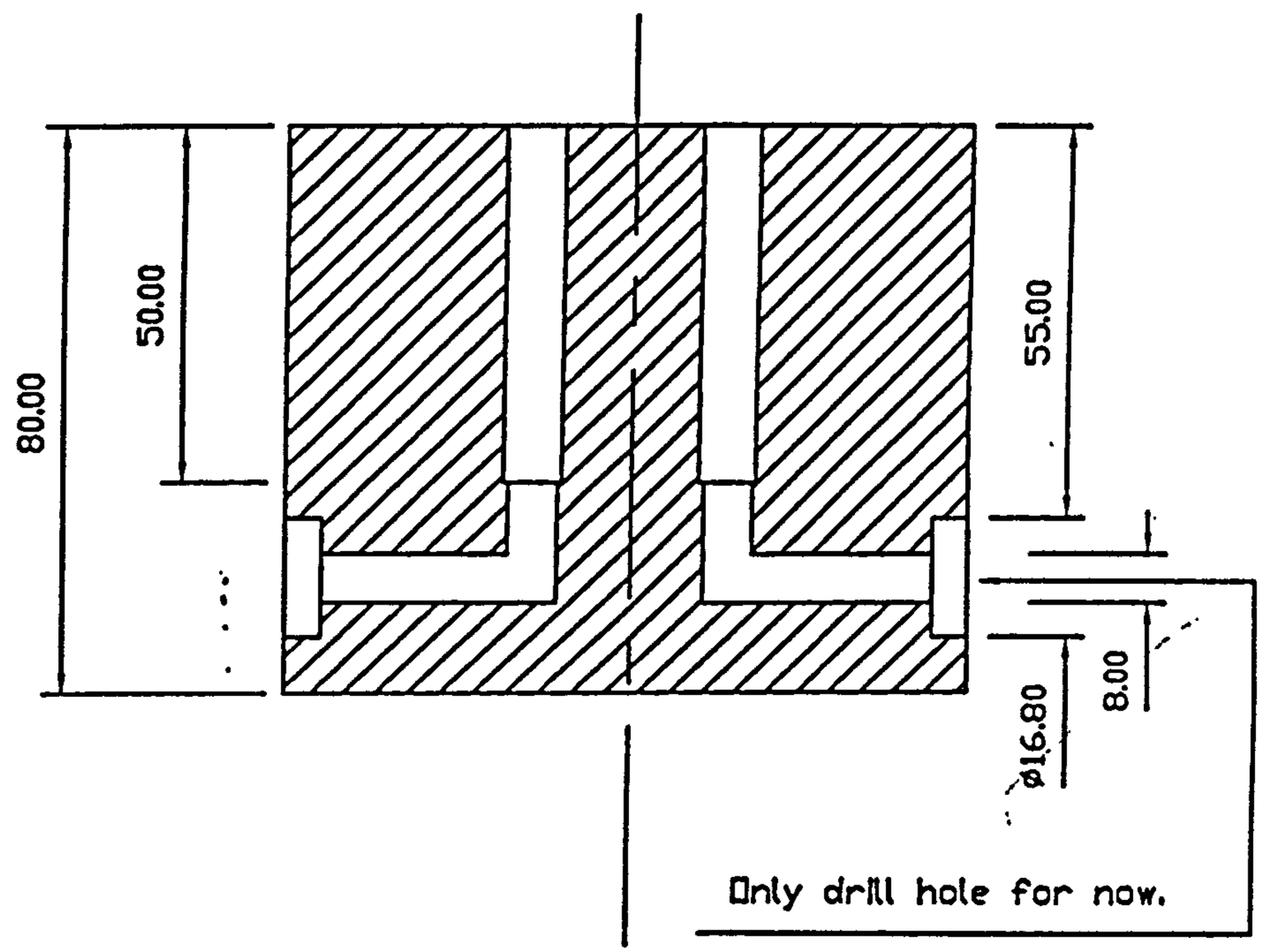

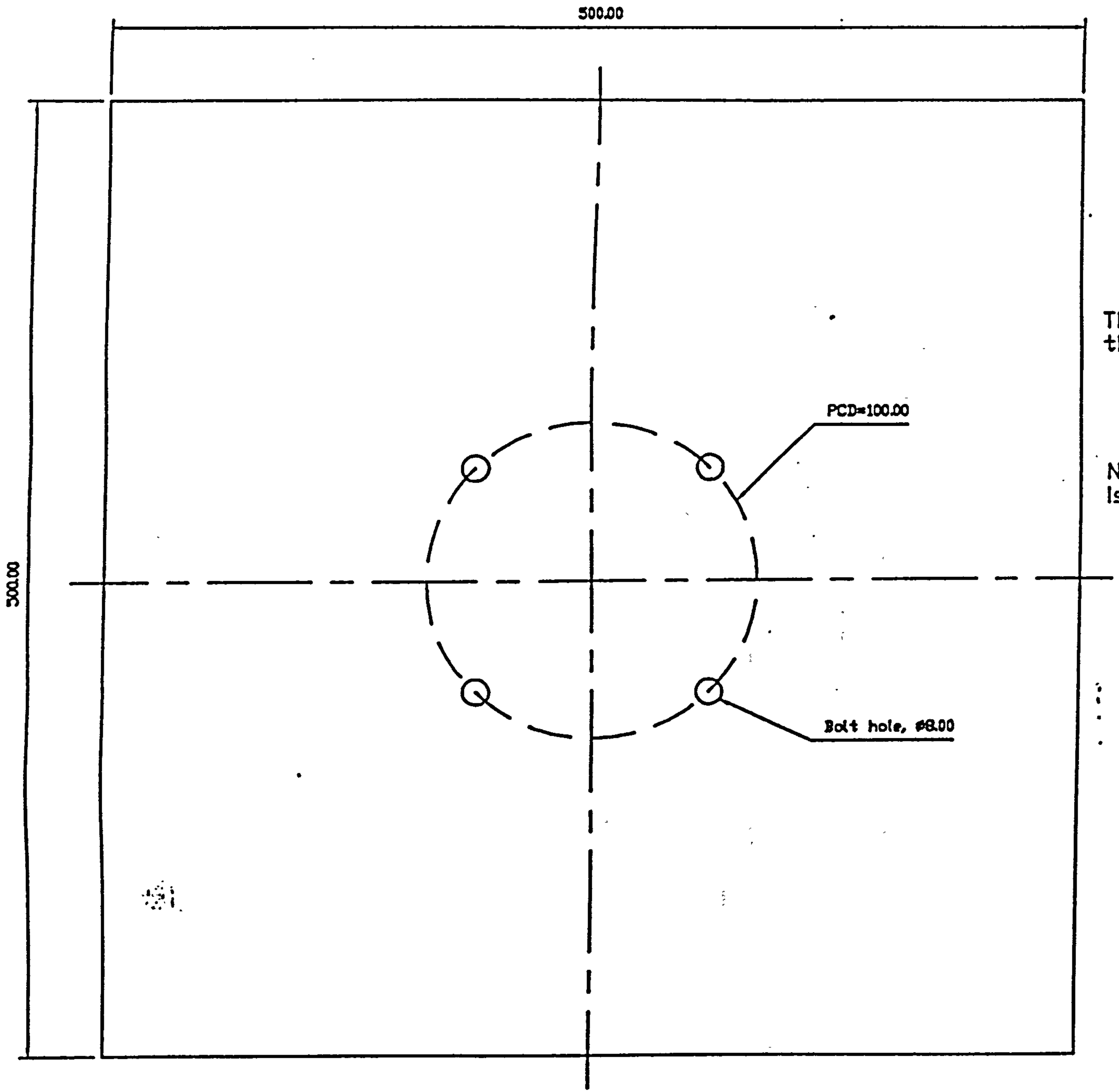

PART 18

This component is the base; it is 80.00mm high and the bolt holes are 60.00mm deep.

Note that a cheap grade of steel (or cast iron) is used for this base.

PART 19

Top View

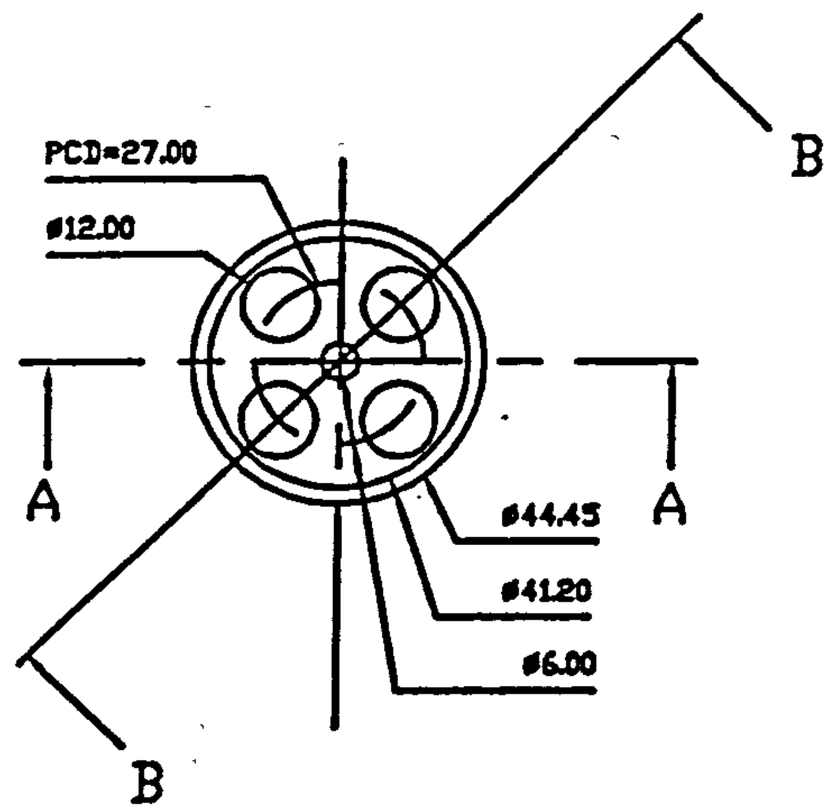

Section A-A

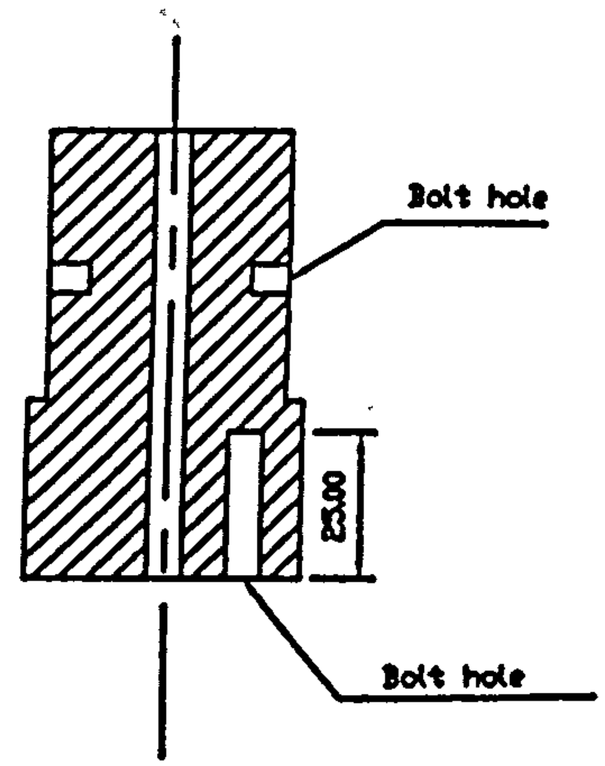

Bottom View

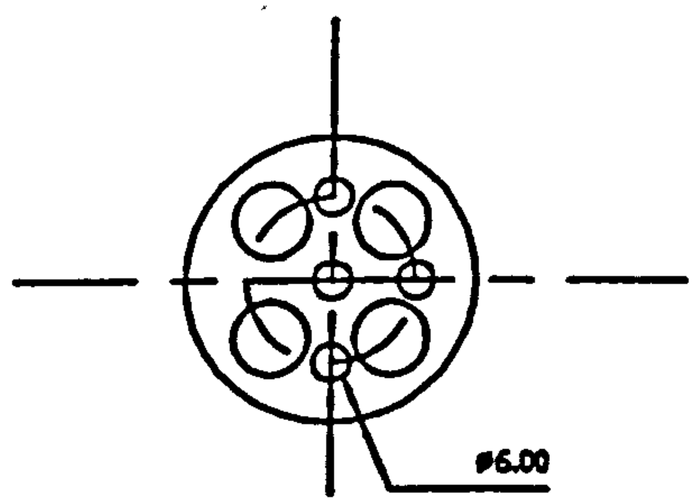

Section B-B

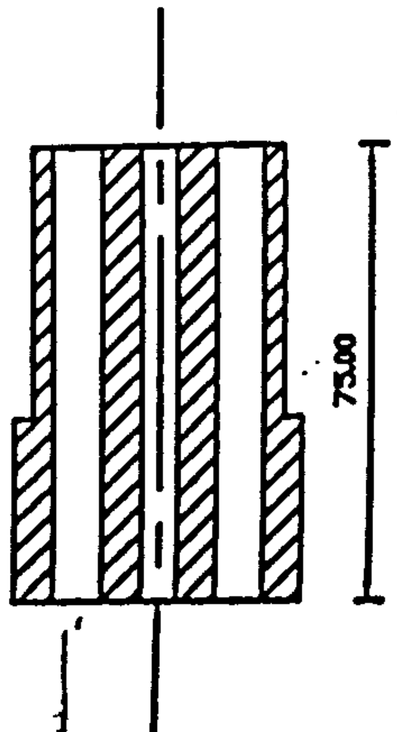

ASSEMBLY OF SUPERSTRUCTURE

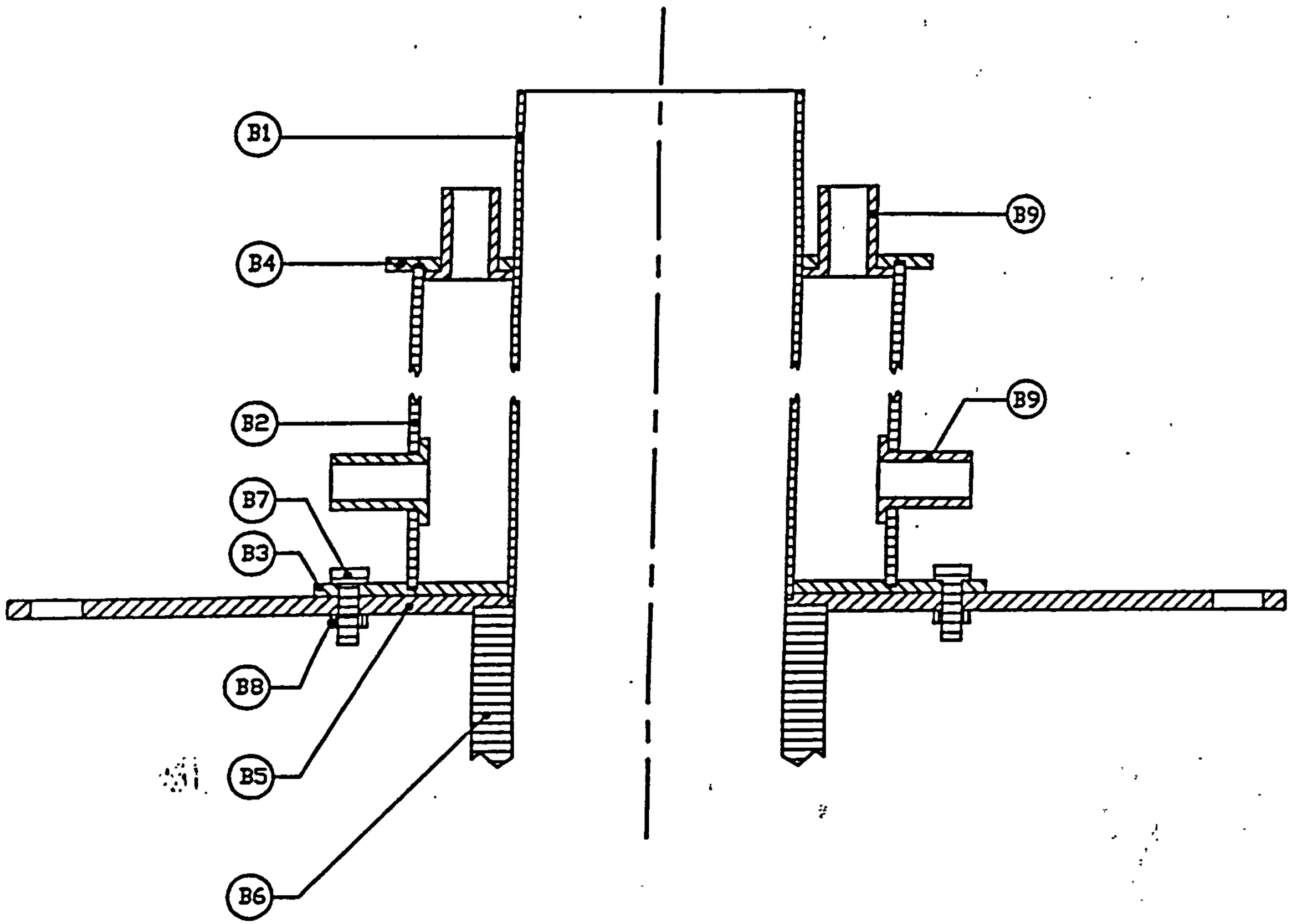

Units: millimetres

Components B1,B2,B3,B4 and B9 are made of aluminium.
Component B5 is made of stainless steel.

PART	DESCRIPTION	QTY.
B1	Pipe: L=550.00 I.D.=84.45, O.D.=88.90	1
B2	Pipe: L=500.00 I.D.=146.05, O.D.=152.40	1
B3	See detailed drawing	1
B4	See detailed drawing	1
B5	See detailed drawing	1
B6	Optical cylinder (I.D.=84.45, O.D.=110.00)	1
B7	M6*20 hex. bolt (steel)	4
B8	M6 hex. nut (steel)	4
B9	See detailed drawing	4

NOTE THAT COMPONENT B9 IS NOT REALLY IN THIS PLANE; IT IS ACTUALLY IN THE PLANE ROTATED 45° ABOUT THE LONGITUDINAL AXIS.

FURTHERMORE, COMPENENT B9 IS WRONGLY MOUNTED IN THIS DRAWING.

PARTB3

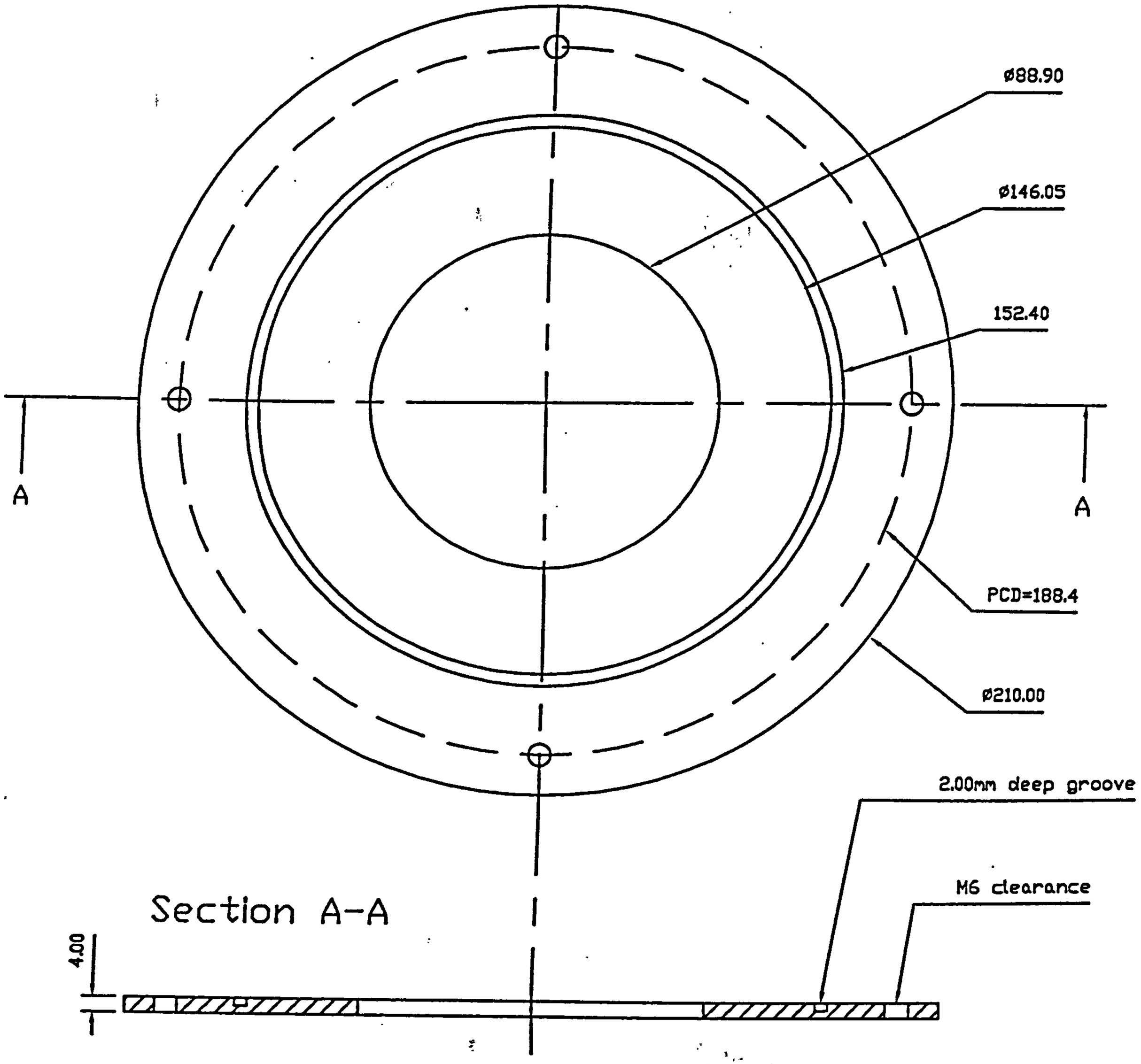
ø88.90
ø146.05
152.40
A
A
PCD=188.4
ø210.00
2.00mm deep groove
M6 clearance
Section A-A
4.00

PARTB4

Section A-A

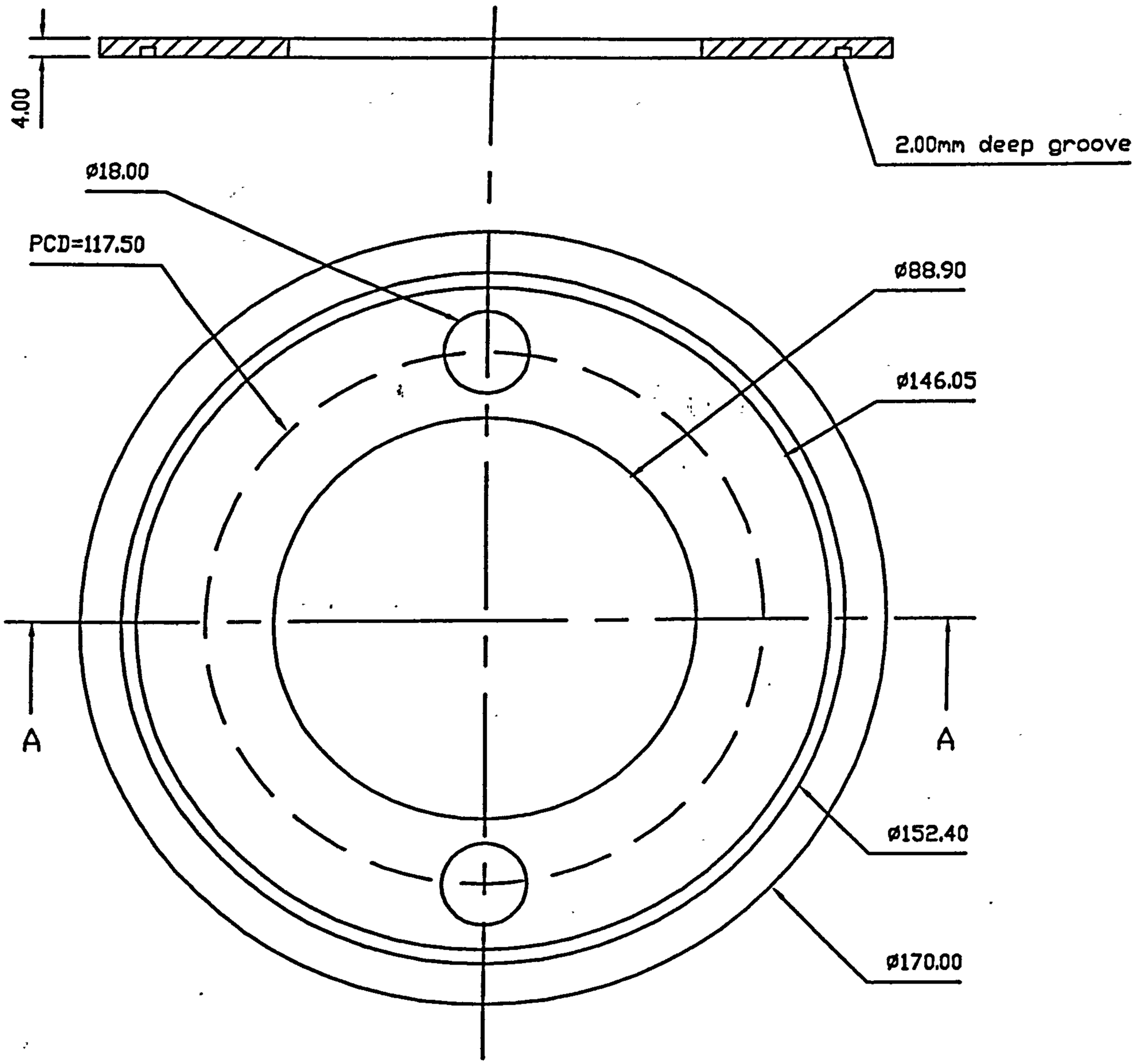

PARTB5

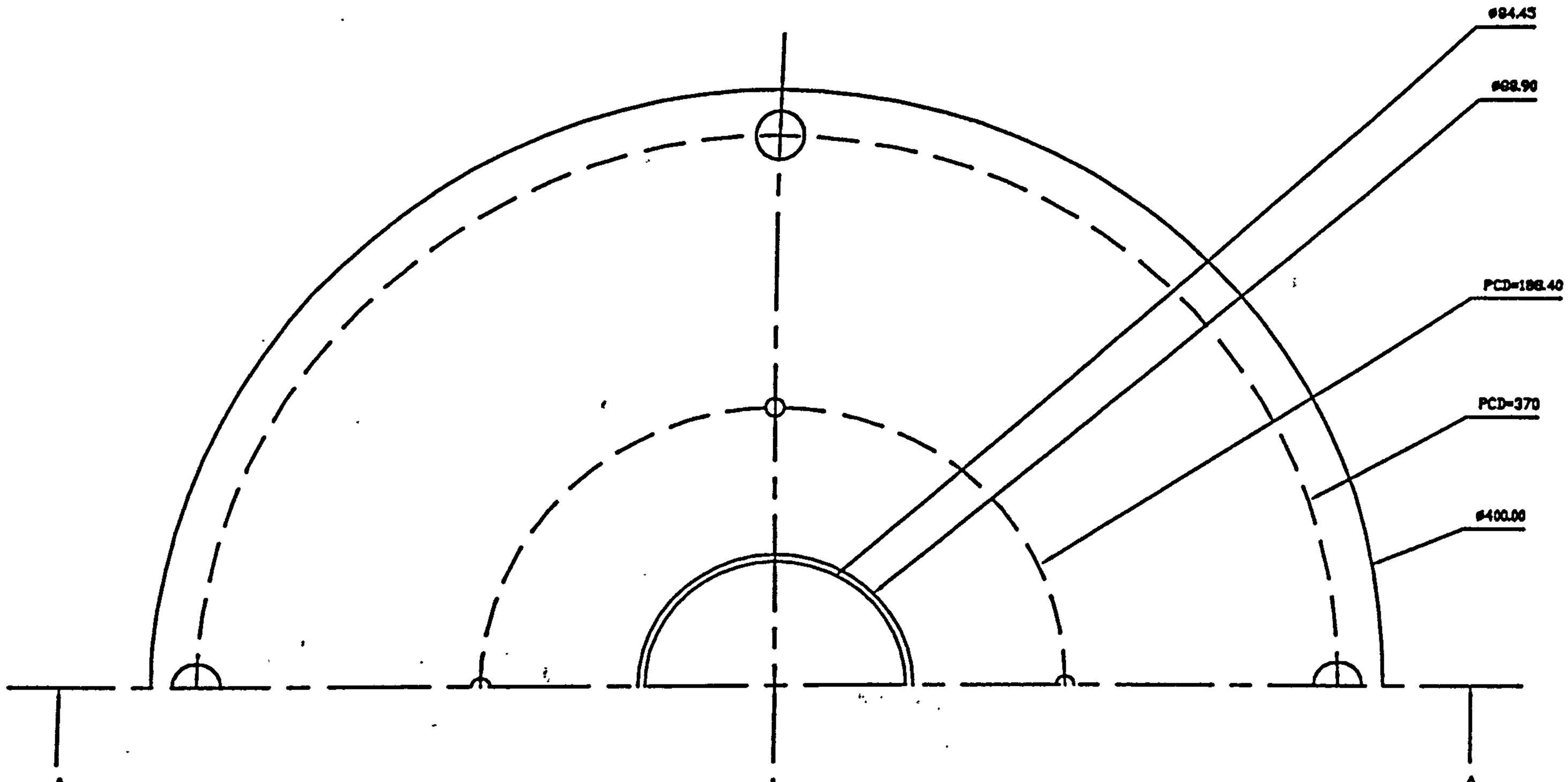

Section A-A

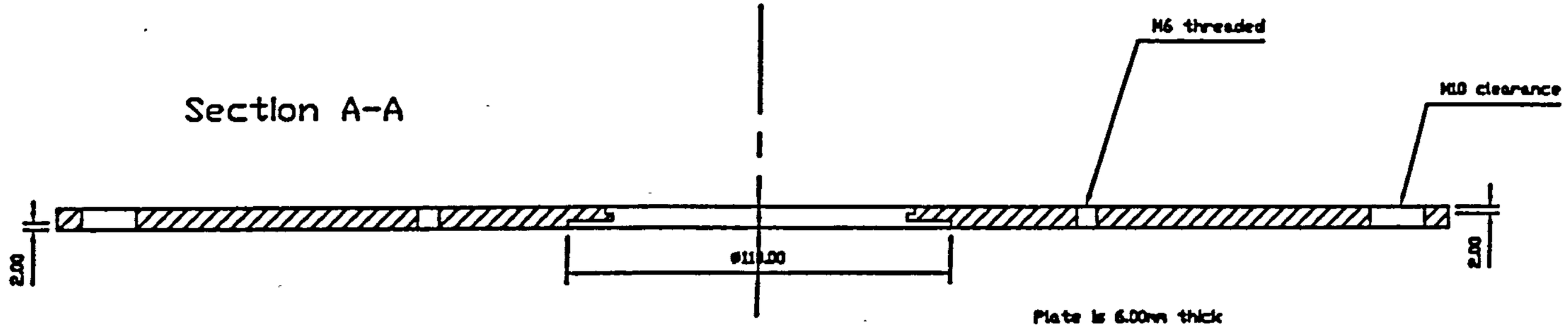

Plate is 6.00mm thick

PART B9

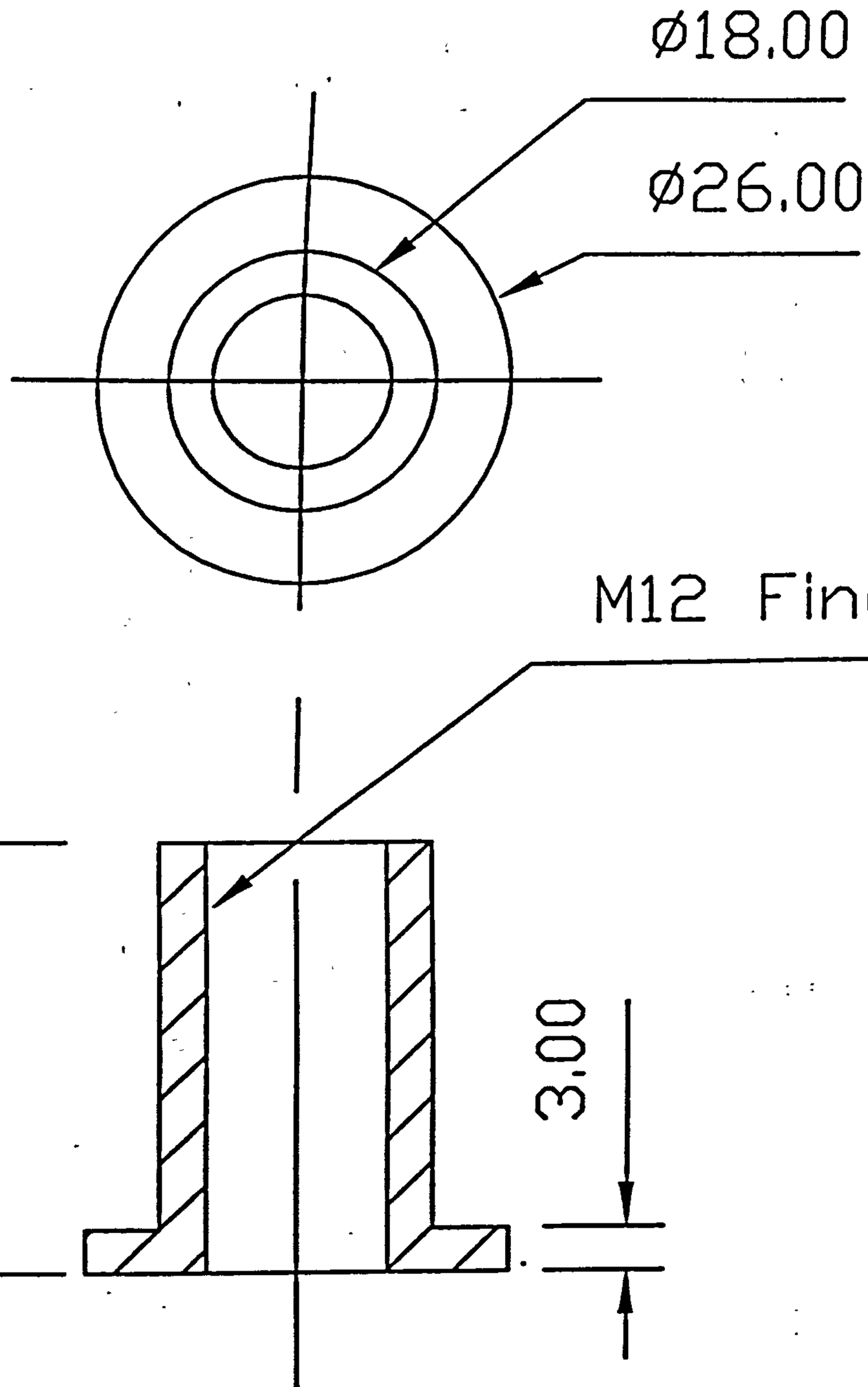

SUPPORTING RODS

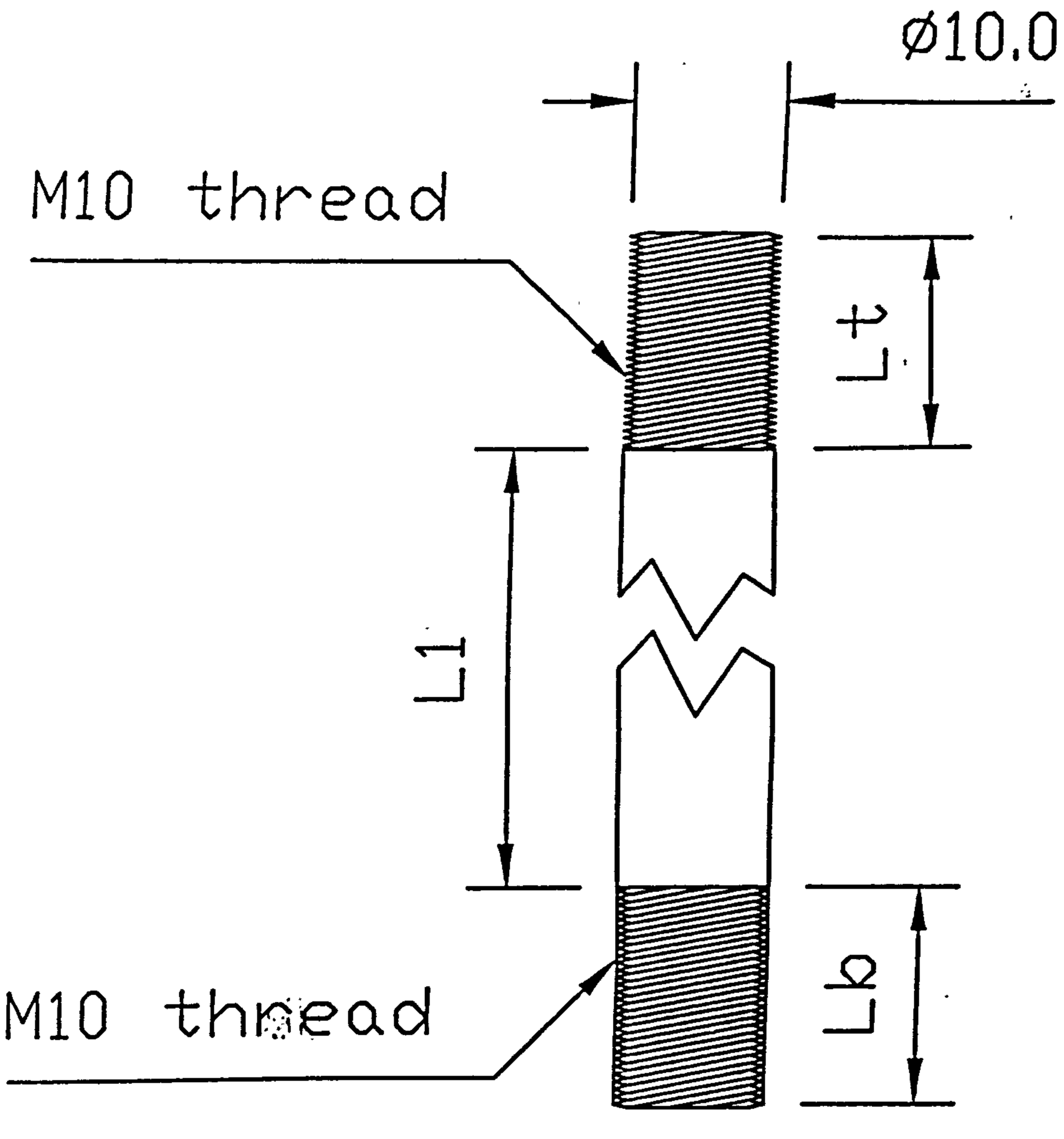

Units: millimetres

	L1	Lt	Lb
Bar 1	151	40	40
Bar 2	889	40	71

Material: Mild steel

Quantity: 4 of each bar.

Additional components:

40 off M10 nut (thick, hex.)